Tensile-Loaded Suction Bucket Foundations for Offshore Structures in Sand

Von der Fakultät für Bauingenieurwesen und Geodäsie

der Gottfried Wilhelm Leibniz Universität Hannover

zur Erlangung des Grades

Doktor-Ingenieur

Dr.-Ing.

genehmigte Dissertation von

Dipl.-Ing. Patrick Sven Gütz

geboren am 29. März 1988

in Berlin

2020

Die vorliegende Arbeit wurde als Dissertation im Rahmen des Promotionsverfahrens an der Fakultät für Bauingenieurwesen und Geodäsie der Leibniz Universität Hannover eingereicht und angenommen.

Referent:	Prof. Dr.-Ing. Martin Achmus
Korreferent:	Prof. Lars Bo Ibsen, PhD (Aalborg University, Denmark)
Kommissionsmitglied:	Prof. Dr.-Ing. Peter Schaumann
Vorsitz:	Prof. Dr.-Ing. Arndt Hildebrandt

Tag der Promotion: 22.09.2020

To my beloved wife for her endless support,
and to my newborn son who has motivated me unknowingly.

Vorwort des Herausgebers

Die Offshore-Windenergie ist für den Ausbau der Erneuerbaren Energien von großer Wichtigkeit. In den letzten Jahren sind große Anstrengungen unternommen worden, um die Konstruktion und auch die Bemessung der Tragstrukturen zu optimieren und gleichzeitig an die immer größer werdenden Dimensionen anzupassen. Eine zumindest für Offshore-Windenergieanlagen relativ neue Gründungslösung besteht darin, Jacketstrukturen statt auf Pfählen auf „Suction Buckets" zu gründen. Dies ist eine potentiell wirtschaftliche Gründungsform, die auch insofern umweltfreundlich ist, als die Installation durch Unterdruck erfolgt und deshalb kein Rammschall auftritt.

Problematisch ist, dass im Betrieb das Auftreten von Zuglasten meist nicht vollständig vermeidbar ist, wenn man die Abstände der einzelnen Buckets nicht sehr groß und das Jacket damit sehr teuer macht. Unter transienter Zugbelastung treten günstige, weil den Widerstand des Buckets erhöhende Porenwasserunterdrücke im Boden auf. Deren Größe ist von der Belastungsgeschwindigkeit abhängig. Wie sich die Porenwasserunterdrücke bei wiederholter (zyklischer) Zuglast entwickeln und welche bleibenden Hebungen im Zuge der zyklischen Belastung entstehen, ist bislang noch nicht vollständig geklärt. Deshalb müssen Jacket-gründungen mit Buckets bislang so bemessen werden, dass zumindest im Normalbetrieb nur sehr geringe zyklische Zuglasten auftreten, die unterhalb der dränierten Tragfähigkeit bleiben.

Herr Gütz hat sich der Aufgabe angenommen, das Tragverhalten von Suction Buckets unter zyklischer Zuglast zu untersuchen. Dafür hat er aufwendige Modellversuche durchgeführt und ausgewertet, mit deren Hilfe er ein numerisches Simulationsmodell validiert und dann für die Prognose des Tragverhaltens von Suction Buckets im Originalmaßstab eingesetzt hat. Schließlich hat er noch eine analytische, auf einem komplexen Feder-Dämpfer-Modell basierende Methode zur Prognose des Verschiebungsverhaltens weiterentwickelt.

Aus den Modellversuchen ergaben sich höchst interessante Ergebnisse. Herr Gütz konnte bestätigen, dass zyklische Belastungen mit der Maximallast unterhalb der dränierten Tragfähigkeit zu nur marginalen bleibenden Hebungen eines Buckets führen. Er konnte darüber hinaus zeigen, dass sich eine Hebungsakkumulation ergibt, wenn die Maximallast größer ist als die dränierte Tragfähigkeit, wobei die Akkumulationsrate nicht nur von der Maximallast, sondern auch von der zyklischen Lastamplitude und der Belastungsfrequenz abhängt.

Im hydraulisch-mechanisch gekoppelten numerischen Simulationsmodell wurde bewusst – u. a. auch um numerische Probleme zu umschiffen – ein relativ einfaches elastoplastisches Stoffgesetz verwendet. Dennoch gelingt die Nachrechnung der experimentellen Versuche recht gut, was ein Hinweis darauf ist, dass das Verformungsverhalten bei der zyklischen

Zugbelastung mit nicht zu großen Lasten durch den hydraulischen Prozess dominiert wird. Die Berechnungen des Tragverhaltens von Buckets im Originalmaßstab zeigen auf, dass zyklische Zuglasten oberhalb der dränierten Tragfähigkeit zulässig sein könnten, wenn sie nicht zu groß sind bzw. ihre Anzahl begrenzt bleibt.

Natürlich bleiben noch viele weitere Fragen zu klären, bevor ein auch in der Praxis anwendbares Berechnungsmodell zur Prognose akkumulierter Hebungen vorliegt. Die Arbeit von Herrn Gütz liefert aber wertvolle grundlegende Erkenntnisse und stellt damit einen wichtigen Schritt auf dem Weg zu einem solchen Berechnungsmodell dar.

M.Achmus

Author's preface

Offshore structures generating renewable energy are required to assure the future's energy supply. These structures necessitate reliable and efficient foundations and multipod substructures with suction buckets are a promising alternative to commonly used piles. The economical advantages of suction buckets are currently limited due to a lack of knowledge in terms of their tensile bearing behaviour. The most essential uncertainties are related to the drainage condition and the cyclic response. While the first aspect refers to a substantially larger resistance if the consideration of partially drained conditions is applicable, the latter concerns the potentially accumulating displacement or differential pressure. These circumstances require a conservative design of the foundation by either limiting tensile loads to the drained resistance or to totally omit those.

The potential for an optimised design motivated the research on which this thesis is based on. Therefore, the present uncertainties were systematically evaluated by multiple methods and the attained results illustrate the significant capabilities of the suction bucket's tensile bearing behaviour. Consequently, the present design recommendations might be too cautious and the conceivable consideration of tensile loads within the scope of design would facilitate the suction bucket's economical competitiveness.

I acknowledge Prof. Dr.-Ing. Martin Achmus for the opportunity of conducting this research and for always supporting me with his deep expertise and clear focus. Additionally, I convey my thanks to Prof. Lars Bo Ibsen as co-examiner for the comprehensive and critical assessment. Another thanks goes to Prof. Dr.-Ing. Peter Schaumann as member of the committee and Prof. Dr.-Ing. Arndt Hildebrandt acting as head of the committee.

Thanks to my colleagues with whom I spent a convenient time and who have contributed to this thesis. In particular, I thank Bernd Howind with his technical competence as well as Dennis Frick and Christian Schröder for their collaboration regarding the physical model tests and for spreading good mood. Jann-Eike Saathoff helped me with our discussions of numerical issues and shared some special 'Aloha'-experiences with me. Furthermore, I got assistance from the students Laurenz Borm, Bjarne Halbfas and Jannik Meyer.

Last but not least, I appreciate my family's great encouragement, of which I can be sure of at any time. Most essentially, I emphasize my wife's support and understanding during this exceptional and sometimes turbulent time in which our wonderful son was born. Lisa, these few words cannot describe how grateful I am how we managed all that.

P. Gütz

Abstract

Currently, a great demand for renewable energy exists and offshore wind turbines (OWTs) supply a relevant share, which is expected to further increase in the future. The foundations for these structures must fulfill strict requirements to ensure a safe and reliable operation of the OWTs while minimising the costs. Suction buckets for multipod foundations are considered as a promising alternative and demonstrated their applicability in commercial projects. The multipod substructure transfers the horizontal loads acting on the OWT to axial loads on the opposing foundations. Owing to the self weight of the OWT, the suction bucket's mean load is generally compressive and superimposed by a variation of the axial load. Except for wide spacing of the foundations or large self weight of the OWT, tensile loads arise. Due to incomplete knowledge regarding the suction bucket's tensile bearing behaviour, the particular economic and ecological advantages are still limited.

Although numerous studies investigated the suction bucket's response to axial loads, the tensile bearing behaviour was not yet elucidated holistically. If the suction bucket is subjected to very low tensile load rates and the soil's hydraulic conductivity is sufficiently high, the tensile resistance constitutes from the drained skin friction inside and outside the suction bucket's skirt. Major uncertainties exist in terms of the response to cyclic loads and the assessment of loading under constrained drainage, where the presence of negative differential pressure beneath the suction bucket's lid contributes to the tensile resistance. It is neither possible to quantify the magnitude of the invoked suction force nor is there any reliable method to predict the required displacement to generate this resistance. Moreover, the displacement accumulation induced by recurring tensile loads cannot be determined with confidence. As a consequence, a conservative design of OWTs by means of prohibiting the occurrence of tensile loads is often recommended.

This thesis presents results of comprehensive analyses with specific focus on gaining knowledge concerning the suction bucket's tensile bearing behaviour under partial drainage and assessing the applicability of tensile loads. Based on a holistic literature review, the response to a wide range of load types was examined by physical model tests and numerical simulations. Finally, these observations were used to improve an existing analytical model.

The physical model tests revealed a significant increase of the tensile resistance with decreasing drainage, but its mobilisation required a larger displacement. Force-controlled tests enabled the determination of the displacement accumulation. Depending on the load magnitude, a significant number of cyclic loads were withstood until relevant displacement took place. Cyclic loads substantially exceeding the drained resistance caused severe

displacements after few cycles, but the occurrence of only a limited number of cycles might be acceptable if certain displacement would be tolerable. The results of the physical model tests provided an essential database for the development and validation of a finite element (FE) model. In general, the numerical simulations agreed with the observations of the model tests and extended the range of investigated specifications within the scope of a broad parametric study at prototype scale. The stiffness as well as the interaction of the resistances were evaluated depending on the drainage condition and the size of the suction bucket. Moreover, the induced displacement rates due to monotonic and cyclic loading were examined for various load configurations and suction bucket geometries. Finally, a concept for defining a cyclic equivalent load was proposed and demonstrated successfully. The conclusions from the physical model tests and numerical simulations were utilised for developing and calibrating an existing analytical model. Although the analytical model exhibited certain limitations, the attained results were reasonable.

The findings of this thesis indicate that the occurrence of few tensile load cycles might be acceptable depending on their magnitudes and provided that these loads do not recur in short-term to allow for dissipation. A practical approach to estimate the cyclic displacement accumulation by a simplified load was proposed. Additionally, the applicability of an analytical model was demonstrated. It is remarked that the investigated loads were only tensile, although there is usually an interaction with compressive loads of different magnitudes, which would induce certain downward displacement and a variation of stiffnesses.

Key words: *suction bucket, tensile loading, sand, partially drained conditions, physical model tests, finite element analyses, analytical model, offshore*

Kurzfassung

Der aktuell große Bedarf an regenerativen Energien wird sich in Zukunft erwartungsgemäß weiter steigern. Offshore Windenergieanlagen (OWEAs) produzieren bereits jetzt einen großen Anteil der benötigten regenerativen Energie und es wird von einem fortschreitenden Ausbau ausgegangen. An die Gründungen von OWEAs werden hohe Anforderungen gestellt, um einen sicheren und zuverlässigen Betrieb bei gleichzeitig geringen Kosten gewährleisten zu können. Die Gründung einer OWEA auf mehrere Suction Buckets stellt hierbei ein vielversprechendes Konzept dar, dessen Umsetzbarkeit bereits in Form von Prototypen in mehreren kommerziellen Windparks nachgewiesen wurde. Die OWEA erfährt hauptsächlich horizontale Belastungen, welche durch die Unterstruktur in axiale Belastungen auf die gegenüberliegenden Gründungen übertragen werden. Das Eigengewicht einer OWEA bedingt eine mittlere Drucklast, sodass diese zusätzlichen Belastungen eine Variation der axialen Last hervorrufen. Sofern die Gründungen nicht besonders weit voneinander entfernt angeordnet sind oder die OWEA ein übermäßiges Eigengewicht aufweist, werden zeitweilig Zugkräfte auf die Gründungen einwirken. Das Tragverhalten von Suction Buckets unter Zugbelastung ist bislang nicht vollständig bekannt, weshalb die ökonomischen und ökologischen Vorteile dieser Gründung eingeschränkt sind.

In der Vergangenheit befassten sich unterschiedliche Studien mit dem axialen Tragverhalten von Suction Buckets, jedoch konnte das Verhalten unter Zugbelastung bislang nicht ganzheitlich bewertet werden. Unter sehr langsamen Belastungsraten und in durchlässigem Boden verhält sich das Suction Bucket dräniert, sodass dessen Widerstand aus der Mantelreibung resultiert. Hingegen bestehen Unsicherheiten hinsichtlich des Verhaltens unter zyklischer Belastung und höheren Belastungsraten, bei denen die Entwicklung eines Unterdrucks hinzukommt, der als zusätzlicher Widerstand unter dem Deckel des Suction Buckets der einwirkenden Kraft entgegenwirkt. Weder die Größe der daraus resultierenden Unterdruckkraft noch die Verschiebung des Suction Buckets zur Mobilisierung des Unterdrucks können bislang zuverlässig bestimmt werden. Darüber hinaus können zyklisch wiederkehrende Zugkräfte zu einer Akkumulation der Verschiebungen führen, welche ebenfalls noch nicht prognostiziert werden können. Aus diesen Gründen wird das Auftreten von Zugkräften im Rahmen einer konservativen Bemessung von OWEAs konstruktiv verhindert.

In dieser Dissertation werden die Ergebnisse von umfassenden Untersuchungen vorgestellt, welche auf die Ermittlung des Zugtragverhaltens im partiell drainierten Zustand und die Bewertung der Anwendbarkeit zum Auftreten von Zuglasten ausgerichtet waren. Hierzu wurde der aktuelle Stand der Wissenschaft ausführlich dargestellt und daraus die

zielgerichtete Analyse mit Hilfe von physikalischen Modellversuchen und numerischen Simulationen abgeleitet und durchgeführt. Schließlich wurden die gewonnenen Erkenntnisse in die Verbesserung eines bestehenden analytischen Modells übertragen.

Die physikalischen Modellversuche ergaben höhere Zugwiderstände bei geringerer Drainage, jedoch erforderte deren Mobilisierung größere Verschiebungen. Kraftgesteuerte Versuche ermöglichten die Ermittlung der Verschiebungsakkumulation. In Abhängigkeit der hierbei aufgebrachten Belastungen widerstand das Suction Bucket einer gewissen Anzahl von Zyklen bis schließlich größere Verschiebungen hervorgerufen wurden. Bei Belastungen, die die dränierte Tragfähigkeit um ein Vielfaches überschritten, trat dies bereits nach wenigen Zyklen auf, jedoch wäre das Eintreten einzelner Lastereignisse unter Berücksichtigung tolerierbarer Verschiebungen zulässig. Aus den Beobachtungen der Modellversuche wurden die essentiellen Merkmale abgeleitet, welche in dem numerischen Modell implementiert wurden. Außerdem lieferten die gemessenen Ergebnisse die Basis für die Validierung des numerischen Modells, dessen Ergebnisse mit denen der Modellversuche grundlegend übereinstimmten. Eine weitreichende Parameterstudie wurde mit Hilfe von numerischen Simulationen im Prototypmaßstab durchgeführt, um die Bandbreite der in den Modellversuchen untersuchten Randbedingungen zu erweitern. Hierin wurden die Einflüsse der Drainagebedingung und der Abmessung des Suction Buckets auf dessen Steifigkeit und Zugwiderstand ausgewertet. Darüber hinaus wurden die Verschiebungen und Verschiebungsraten in Folge unterschiedlicher statischer und zyklischer Belastungen in Abhängigkeit der Größe des Suction Buckets untersucht. Abschließend wurde ein Ansatz formuliert und erfolgreich demonstriert, der die Abschätzung der zyklischen Verschiebungsakkumulation durch eine äquivalente Last approximiert. Die gewonnenen Erkenntnisse aus den Modellversuchen und Simulationen wurden in der Weiterentwicklung und Kalibrierung eines analytischen Modells berücksichtigt, welches trotz gewisser Einschränkungen adäquate Abschätzungen liefert.

Die Ergebnisse dieser Dissertation zeigen auf, dass die Einwirkung einiger Zuglasten zulässig sein könnte, sofern gewährleistet ist, dass die Belastung gewisse Größen nicht überschreitet und solche Lasten nicht wiederholt in zu kurzem Abstand auftreten, um eine zwischenzeitliche Dissipation des Porendrucks zu ermöglichen. Ein anwendungsorientierter Ansatz wurde vorgeschlagen, der die zyklische Verschiebungsakkumulation durch eine vereinfachte Belastung abschätzt. Außerdem wurde die Anwendbarkeit eines analytischen Modells aufgezeigt. Es sei darauf hingewiesen, dass diese Untersuchungen ausschließlich Zugkräfte berücksichtigten, diese jedoch üblicherweise mit Drucklasten interagieren, welche abwärtsgerichtete Verschiebungen und unterschiedliche Steifigkeiten hervorrufen.

Schlagworte: *Suction Bucket, Zugbelastung, Sand, teilweise dränierte Bedingungen, physikalische Modellversuche, Finite Elemente Simulationen, analytisches Modell, Offshore*

Contents

List of Figures

List of Tables

List of Symbols

Latin letters

A	Area of the suction bucket's lid	L^2
a	Differential pressure ratio	1
b	Empirical correction parameter of the analytical model	1
c'	Cohesion	$\mathrm{F/L}^2$
$C_{0\ldots2}$	Coefficients for CPT correlation	1
C_5	Damper coefficient of the analytical model	$\mathrm{F/(L/T)}^\xi$
C_C	Coefficient of curvature	1
C_U	Uniformity coefficient	1
c_v	Consolidation coeffcient	L^2/T
D	Diameter of the suction bucket	L
d	Thickness of the suction bucket's skirt	L
E	Young's modulus	$\mathrm{F/L}^2$
e	Void ratio	1
E_s	Oedometric stiffness of the soil	$\mathrm{F/L}^2$
$\bar{F}$	Force divided by drained resistance	1
$\hat{F}_\mathrm{suc}$	Moving mean of suction force	F
F	Vertical load	F
f	Load frequency	1/T
$F_{1\ldots5}$	Elements' forces of the analytical model	F

F_ampl	Load amplitude	F
F_dr	Drained resistance	F
F_eq	Equivalent load	F
F_fric	Frictional resistance	F
F_mean	Mean load	F
F_suc	Suction Force	F
g	Gravitational acceleration	L/T^2
h_w	Water depth	L
i	Hydraulic gradient	1
i_cr	Critical hydraulic gradient	1
I_D	Relative density	1
K	Stiffness	F/L
k	Earth pressure coefficient	1
k_0	Earth pressure coefficient at rest	1
$K_{1\ldots4}$	Elements' stiffnesses of the analytical model	F/L
$K^*_{1\ldots4}$	Elements' initial stiffnesses of the analytical model	F/L
k_f	Hydraulic conductivity of the soil	L/T
k_int	Integral hydraulic conductivity	L/T
k_i	Inner hydraulic conductivity	L/T
k_i/k_o	Permeability ratio	1
K_w	Bulk modulus of the pore fluid	F/L^2
L	Length of the suction bucket	L
l_dr	Length of the drainage path	L
m	Buoyant mass of the suction bucket	M
N	Cycles	1

n	Stress relief constant	1
p_0	Hydrostatic pressure	$\mathrm{F/L}^2$
p_{atm}	Atmospheric pressure	$\mathrm{F/L}^2$
p_{cav}	Cavitation pressure	$\mathrm{F/L}^2$
$\tilde{q}_{\mathrm{soil}}$	Normalised water volume rate	$(\mathrm{L}^3/\mathrm{T})/(\mathrm{F/L}^2)$
q_{c}	Cone resistance	$\mathrm{F/L}^2$
q_{soil}	Water volume rate	L^3/T
R	Coefficient of determination	1
r	Radial coordinate	L
s	Spacing of the foundations	L
T	Period	T
t	Time	T
t_{acc}	Preloading (or acceleration) duration	T
t_{hold}	Holding duration	T
T_{k}	Dimensionless drainage parameter	1
t_{unload}	Unloading duration	T
T_{v}	Dimensionless time	1
T_{w}	Temperature of the pore fluid	°C
u	Pore pressure	$\mathrm{F/L}^2$
v	Displacement rate	L/T
z	Vertical coordinate	L
$z_{1\dots2}$	Displacements of the analytical model	L
z_{gap}	Gap height	L
z_{plug}	Plug heave	L

Greek letters

α, β	Regressed coefficients for displacement accumulation	
Δu	Differential pressure	F/L^2
Δu_{cr}	Critical negative differential pressure	F/L^2
Δz_{gap}	Gap expansion	L
Δ	Change of particular value	
δ	Interface friction angle	°
$\Delta \hat{u}$	Moving mean of differential pressure	F/L^2
$\Delta \hat{z}$	Moving mean of displacement	L
η	Arbitrary function or parameter	
γ'	Effective unit weight of the soil	F/L^3
γ_{w}	Weight of the pore fluid	F/L^3
$\tilde{\gamma}$	Effective unit weight of the soil influenced by hydraulic gradient	F/L^3
κ	Stiffness factor	1
λ	Stiffness exponent	1
ν	Poisson's ratio	1
ψ	Dilation angle	°
φ'	Internal friciton angle	°
ρ	Correlation coefficient	1
σ'	Effective stresses	F/L^2
τ	Skin friction	F/L^2
ξ	Damper exponent of the analytical model	1

Subscripts

$_{an}$	Analytical model
$_{cyc}$	Cyclic
$_{eq}$	Equivalent
$_{ext}$	Outside the suction bucket in the soil
$_{FE}$	Finite element model
$_{i}$	Inside of the suction bucket's skirt
$_{j}$	Arbitrary index
$_{lid}$	Beneath suction bucket's lid
$_{max}$	Maximum value
$_{min}$	Minimum value
$_{m}$	Model scale
$_{o}$	Outside of the suction bucket's skirt
$_{p}$	Prototype scale
$_{r}$	Radial direction
$_{ref}$	Reference case
$_{tip}$	At the skirt's tip
$_{z}$	Vertical direction

Legend

Length	L
Mass	M
Time	T
Force	$F=ML/T^2$

Abbreviations

ALS   accidental limit state

CPT   cone penetration testing

DPS   differential pressure sensor

DT   displacement transducer

EU   European Union

FE   finite element

FLS   fatigue limit state

GS   gap sensor

OWT offshore wind turbine

REB   reverse end bearing

SLS   serviceability limit state

ULS   ultimate limit state

VS   volume sensor

1 Introduction

1.1 Offshore renewable energy

1.1.1 Demand

At the present time, there are several aspects driving the development of renewable energy resources. Fossil fuels on earth are limited and their usage expedites the global climate change so that alternative sources of energy are sought. The German government decided to shut down all nuclear power plants until 2022 and the last coal-fired power plant in 2038, which will cause a gap of energy supply and makes the situation even more critical. This goes along with the political and societal demand for sustainable development based on renewable energy resources. As part of the Europe 2020 strategy, the European Commission defined the target of achieving a share of 20% of renewable energy in gross final energy consumption in the European Union (EU) until 2020 (Eurostat, 2019). Although the capacity of renewable energy was steadily increased in the recent years, the imposed goal for the year 2020 is likely to be missed. Nevertheless, the EU enacted a recast renewable energy directive in 2018, which introduces the new binding target of at least 32% renewable energy in the gross final energy consumption of the EU until 2030 (The European Parliament and the Council, 2018).

Various potential renewable energy resources exist, but their regional potential depends on site-specific characteristics, such as the availability of biomass, the topography for hydro-power plants, the steadiness and intensity of sunshine or wind for photovoltaic systems or wind turbines respectively. The development of energy production in the EU is shown in Figure 1.1. Obviously, the capacity of fossil energy sources decreased (mainly coal and oil, while gas is on a stable level) and the amount of renewable energy increased significantly (solar, wind and biomass). As it is evident from the evolution of the hydro-power shown in Figure 1.1, the capacity of some renewable energy resources are constrained due to previously mentioned criteria. Similarly, there are limitations of the available spaces for solar and wind farms (especially onshore), due to societal disapproval or competing land usage. Although these limits are not yet reached, as it can be seen in the steadily enlarging cumulative capacity, it might become a relevant issue in the near future.

The exploitation of offshore renewable energies is seen as a promising prospect. The societal acceptance is generally higher than onshore and the resources to be used have a great potential in terms of their energy capacity. Until now, the focus is on offshore wind energy, but other concepts such as wave converters or turbines driven by tidal currents are possible as well. Wind Europe (2019b) forecasts that the EU requires 230 GW to
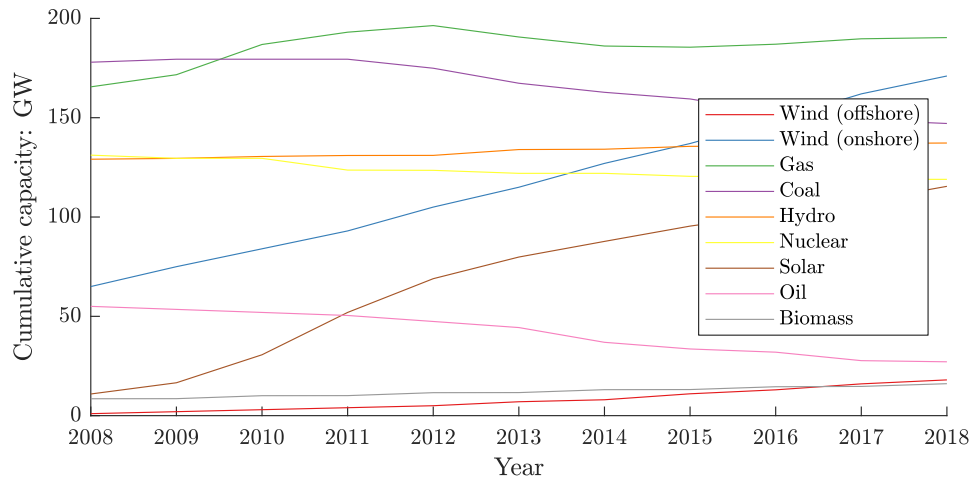
Figure 1.1: Total power energy capacity in the EU (Wind Europe, 2019c).

450 GW offshore wind capacity by 2050, where the higher capacity would cover 30% of the predicted electricity demand. At the end of 2019, there was a total offshore wind capacity of 22 GW with an increase of 3.6 GW within the last year (Wind Europe, 2020). Although the annually installed capacity grew steadily so far, the formulated target is still ambitious. According to Wind Europe (2019b), the annual installation rate has to rise up to more than 20 GW per year to achieve this target. In recent years, the growing experience and technological advance enhanced the capacity of offshore wind turbines (OWTs) and enabled more effective constructions so that the capital expenditure per capacity reduced drastically. The cost reduction due to this development interacts with increasing costs for offshore wind farms in deeper water further away from shore. Nevertheless, offshore wind exhibits a decline of the levelised cost of energy by about 50% from 2012 to 2017 (UN Environment's Economy Division et al., 2018; Wind Europe, 2019a) and tends to become economically competitive to other energy sources, which intensifies further development.

In comparison to onshore wind, the offshore wind provides higher and more continuous energy production due to generally steadier wind with less turbulences and higher average speeds. Larger turbine sizes (concerning capacity and geometric dimension) can be deployed with appropriate vessels and rigs to transport the large components to location and assemble the OWTs, while the onshore turbine size is limited due to constraints in terms of transportation. The currently largest capacity per OWT in commercial operation is 9.5 MW (Skopljak, 2020), but new nacelles and rotors are under development having more than 10 MW capacity (Durakovic, 2019a,b). Although there are many advantages regarding offshore wind, the erection, maintenance and decommission of OWTs is challenging in the harsh offshore environment, which implies technical, logistical and economical drawbacks. Thus, periods with good weather conditions have to be used in most efficient manner by steadily optimising construction processes to gain the highest economical output.

The design of an OWT must consider substantial exposures, such as corrosion of the structure, cyclic environmental loads (aero- and hydrodynamic loads resulting from wind

as well as waves and currents), but also operational and accidental loads. These loads affect the entire structure and have to be safely transferred to the subsoil. Due to the increasing size of the turbines and greater water depths, the environmental loads become larger leading to higher requirements on both the structure and the foundation.

1.1.2 Marine foundations

The Renewables Advisory Board (2010) published an analysis of the costs related to the planning, commissioning and operation of OWTs. The capital expenditure attributed to the foundation is 16% of the lifetime costs from which the highest share of 9.3% is associated with costs for materials. The installation and commissioning of the foundation constitute further 7% of the total capital expenditure, of which a significant proportion is related to the operation of construction vessels. These figures highlight that foundation costs have a relevant contribution to the overall costs of an OWT. The ongoing research on foundations for OWTs attest the great potential for innovation and optimisation. Within the context of larger turbine sizes and deeper waters, the development of foundations for OWTs aspires reduced material costs and effective installation methods allowing for shorter operational times of the vessels and less expansive equipment.

Currently, foundations of OWTs are either gravity bases, piles or suction buckets. Monopiles are the most frequently used foundations with a share of 81% in Europe (Wind Europe, 2020). Figure 1.2 depicts a range of possible combinations of foundation types adopted for a substructure consisting of either single foundation or multiple foundations per OWT. The selection of the suitable foundation and substructure mainly depends on the water depth and the concomitant environmental loads, but also on economical aspects. While gravity base and monopod structures are applicable in shallow water depth, monopile foundations are erected in water depths up to 40 m. As the water depth increases, the resulting loads (especially the overturning moment due to wind and wave loading) become too large to be resisted by the soil's bedding resistance around a large-diameter monopile. As an alternative, substructures with multiple foundations, such as centric or eccentric tripod or jackets, are more effective with less use of material. If the water depth exceeds roughly 60 m, fixed structures become unprofitable and floating structures are favoured.

Houlsby et al. (2005a) stated that the design of the foundation is driven by the stiffness and the behaviour under fatigue loads rather than by the ultimate capacity. Therefore, the foundation must ensure serviceability as well as integrity for the entire lifetime and respect certain eigenfrequency of the OWT outside the range of potential excitation frequencies, i.e. frequencies of rotor, blade passing, wind and wave, to avoid dynamic amplification. Monopile foundations are commonly designed to have the eigenfrequency between the frequencies of the rotor and the blade passing (soft-stiff), which is a narrow bandwidth, especially since both frequencies are expected to be not constant, but change over the lifetime of an OWT (Bhattacharya et al., 2013; Houlsby et al., 2005a). To ensure the serviceability, the tilt must be inside a strict criterion of generally 0.5° (DNVGL-ST-0126). The installation of the foundation, substructure and tower has a total tolerance

3
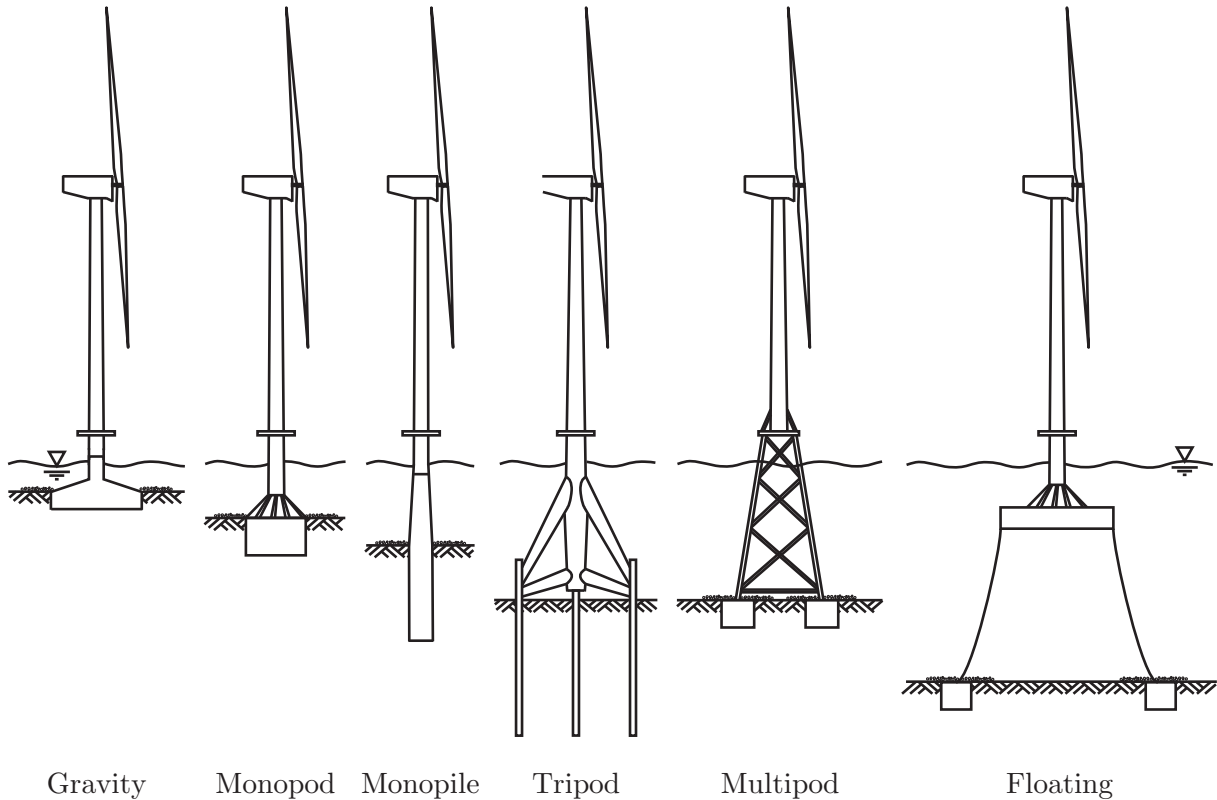
Figure 1.2: Substructures and foundations for OWTs.

of 0.25° so that the additional permanent tilt is restricted to 0.25°. Consequently, the displacement or rotation of the foundation must be limited, which is a difficult task due to the large number of cyclic loads under changing directions.

Most OWTs are built on piles, which are driven into the soil. Beside the technical aspect, the already installed offshore wind farms revealed two main reasons dominating the research on alternatives to pile foundations, namely ecological impact and economic efficiency. The driving process leads to high noise emissions causing harm to animals in the surrounding area. Cost-intensive noise mitigation systems were developed to reduce the noise to an acceptable level. Furthermore, the installation process requires a large amount of energy and heavy equipment (specialised vessels and pile hammers) to drive the piles into the soil. The steadily increasing size of the piles in diameter and length complicates the installation in regard of higher penetration resistance of the soil, which is faced by larger pile hammers. Hence, the financial costs are high due to the large amount of steel and expensive equipment needed for the long duration required for installation. Making the process even more complex, the installation can only be conducted during good weather periods, which are rare, and bad weather conditions cause cost-intensive downtimes. Finally, it has to be marked that pile foundations are difficult to extract from the soil once the OWT shall be decommissioned after reaching its lifetime.

Recently, suction bucket foundations were applied for OWTs as an alternative that is expected to offer cost savings and ecological advantages. A suction bucket is usually

made of steel and has a cylindrical shape (skirt) with a plate closing its top (lid) and an open bottom. It has at least one opening on the lid, which is open during the initial installation phase, where the suction bucket penetrates the soil by its own weight. The self weight installation stagnates at certain depth, once the penetration resistance of the soil is equal to the own weight of the suction bucket. Then, the installation process is continued by connecting a pump to the opening, which extracts water from the inside and creates a negative differential pressure (suction). This induces a seepage flow, which reduces the penetration resistance, and an additional force on the lid. After complete installation, the pump is disconnected, the potential gap between the lid and the soil surface is grouted and the opening is sealed.

Houlsby (2016) stated that the costs for a suction bucket are similar to those of a pile with equivalent capacity, but the installation does neither require expensive equipment nor noise mitigation systems. Further benefits, which are likely to reduce the costs indeed, are that suction buckets can be pre-assembled with the substructure (jacket or transition piece) and installed within a single operation. This reduces the number of actions to deploy an OWT and therefore the required time for installation. Moreover, decommissioning is easily achievable by inverting the installation process (applying a positive differential pressure by pumping water into the suction bucket).

The usage of the suction piles for mooring began in the 1970s and evolved in the subsequent decade to the first offshore platforms founded on large piles that adopted negative differential pressure to achieve the final penetration depths (Tjelta, 2015). In the 1990s, the suction foundations gained prominence and it was the novel foundation concept for the Draupner E riser platform giving the name bucket foundations (Tjelta, 1994). The installation of the Draupner E and Sleipner T platforms in the North Sea were the first application of suction buckets made of steel that rely on the tensile resistance of the foundation in non-cohesive soils (Bye et al., 1995; Randolph and Gourvenec, 2011). Since then, numerous offshore platforms for the oil and gas industry were erected on suction bucket foundations.

Byrne (2000) considered suction bucket foundations for OWTs and conducted physical model tests to investigate the bearing behaviour. In contrast to heavy offshore platforms, OWTs are more lightweight so that the portion of the cyclic horizontal and moment loads is much more pronounced in comparison to the own weight of the structure (Randolph and Gourvenec, 2011). In case of multipod foundations with three or four individual foundations, the horizontal and moment loads due to wind and wave are mainly transferred to the subsoil by vertical loads on the opposing foundations (cf. Figure 1.3). As a result of the relatively low weight of the OWT, the occurrence of tensile loads at the windward foundation is likely (except it is prevented by large spacing or increased weight of the OWT, which might considerably increase the costs (Achmus and Schröder, 2014)). Universal Foundation (2014) conducted a field test-campaign, wherein the installation of suction buckets was investigated with two different structures having diameters of 8 m and 4 m with identical skirt lengths of 6 m. These structures were successfully installed 29 times in partly challenging soil conditions representing a variety of potential locations for OWTs. In 2014, the first prototype of a suction bucket jacket for an OWT was erected in
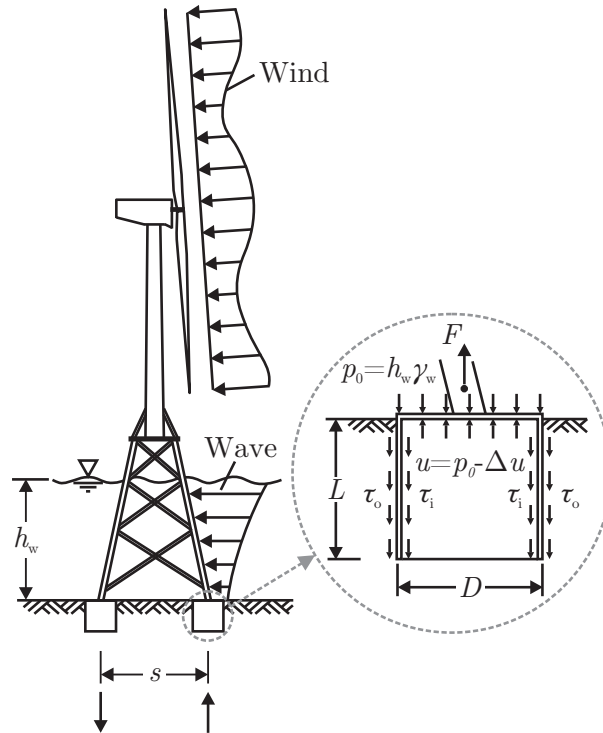
Figure 1.3: OWT on multipod suction bucket foundation.

the offshore wind farm Borkum Riffgrund 1 located in the German North Sea (Shonberg et al., 2017). Moreover, suction bucket jackets were deployed in two commercial wind farms in 2018 (Borkum Riffgrund 2 and European Offshore Wind Deployment Centre) proving their economical applicability and demonstrating their advantages such as fast installation with low noise emission. According to BVG associates and InnoEnergy (2017), an increasing number of offshore wind farms will adopt suction bucket foundations and relevant cost savings are anticipated.

Taking the previous aspects into account, the renewable energy supply of the future has to regard the technical, ecological and economical aspects related to the foundations for OWTs. Further research provides valuable insights, novel structures and optimised design recommendations that can considerably reduce the costs for the foundations and make OWTs more competitive and interesting for investors. Beside OWTs, other offshore energy constructions, such as wave or current converters, might also profit from the current research on suction bucket foundations.

1.1.3 Loading condition

According to DNVGL-ST-0126, four distinct limit states must be met in order to ensure the fulfilment of design criteria, i.e. ultimate limit state (ULS), serviceability limit state (SLS), fatigue limit state (FLS) and accidental limit state (ALS). These limit states define distinct failure mechanisms, which relate to certain geotechnical problems. Table 1.1

Table 1.1: Limit states with examples according to DNVGL-ST-0126.

State	Load	Geotechnical issue
ULS	50-year design storm	Bearing capacity
SLS	Loads during operation	Differential settlement inducing tilt
FLS	Repeated or cyclic loading	Foundation stiffness affecting the eigenfrequency
ALS	Accidental vessel impact	Bearing capacity

provides examples for the particular limit states. To establish a certain level of safety, load and resistance factors are applied to the characteristic values (partial factor method). The relevant design load cases to be analysed are defined in DNVGL-ST-0437, where the installation, operation and decommissioning are of particular interest.

OWTs are exposed to environmental, operational and accidental loads acting mainly horizontally and induce an overturning moment. Besides the horizontal loads, a vertical compressive force resulting from the self weight of the entire structure acts on the foundations. These loads can be classified as either quasi-static (e.g. current, mean wind or self weight), cyclic (e.g. regular waves or tower-shadow of the blades), stochastic (e.g. irregular sea states or turbulence) or transient (e.g. breaking waves, gusts or turbine shutdown). The foundation must ensure the secure transfer of the loads to the subsoil. The loads are categorised in wind, wave, current, ice, seismic as well as accidental collision. Subsequently, an overview is given to identify relevant loads as defined in DIN 18088-1:2019-01 for multipod suction bucket foundations.

The wind provides the kinetic energy to be converted by the OWT to electrical energy. Therefore, the wind velocity reduces when passing the rotor. This implies the generation of a force in the direction of the wind. Current turbines are able to vary the pitch of the blades to optimise the energy output at variable mean wind velocities, but also to rotate the turbine or the blades out of the wind during storm events. Beside the wind driving the turbine, it also acts on the entire structure and invokes additional loading. Andersen and Løvseth (2006) found out in an offshore measurement campaign that relevant high spectral densities have frequencies lower than 0.01 Hz, which is significantly lower than onshore (Andersen and Løvseth, 2006). However, gusts may have frequencies between 0.07 Hz and 0.1 Hz (Senders, 2009). Thus, wind loads can be treated as quasi-static, but gusts are rather transient.

Waves are induced by wind acting on the sea surface and transferring energy via friction and pressure differences. As a consequence, the water surface becomes rougher and more energy is fetched by the sea. The mobilisable wave height and velocity depend on the wind speed, wind duration and fetch length, i.e. the distance where the wind acts on the sea. If the fetch length is sufficiently long and the wind acts continuously over a long duration, the wave velocity reaches the same speed as the wind at the water surface and no further energy is absorbed from the sea, i.e. a fully developed sea state is reached. The characteristics of waves were analysed and described by Pierson and Moskowitz (1964). Based on this, the work of Hasselmann et al. (1973) accounted for the limited fetch length

in the German North Sea and its impact on the sea state. The evaluation of the model proposed by Pierson and Moskowitz (1964) with a peak frequency of 0.1 Hz provides a wave spectrum with energy rich frequencies between 0.05 Hz and 0.2 Hz (Bhattacharya et al., 2013). Lower frequencies correlate with greater wave heights, which is in accordance with typical wave characteristics summarised in Lesny (2008) and DNVGL-ST-0437. Based on the determined wave spectra, the wave loads due to drag and inertia forces can be quantified. The occurrence of many waves over the lifetime of an OWT implies that waves are responsible for high cyclic loads in both number and magnitude. The worst combination of wind and wave arises when the wind speed is moderate with the turbine in operation causing high wind loads, but the sea is at a rather extreme state with additional significant wave loads (Byrne and Houlsby, 2003).

Among others, changes of the water elevation due to the tide induce currents in the sea. The velocity of the water flow and the associated frequency of currents are low. Consequently, the load magnitude on offshore structures is very small in the North Sea and Baltic Sea. The impact on OWTs is anticipated to be of minor importance and the load characteristic is expected to be quasi-static.

Ice loads may be relevant in the Baltic Sea, but to a much lower extent in North Sea, where the occurrence of ice is unlikely (Lesny, 2008). Different types of ice loads on OWTs are possible, e.g. ice on the structure and blades (inducing additional harmonic excitation), cyclic ice breaking due to continuous ice flow or quasi-static ice pressure on the substructure. The first two aspects are issues related with the eigenfrequency of the structure and require detailed investigations, especially since the cyclic frequency of ice breaking is potentially in the range of the eigenfrequency of the OWTs.

Seismic loads are not likely to occur in the North Sea or Baltic Sea. If there is certain potential for earthquakes at other offshore locations, the probability for liquefaction of the soil has to be assessed, which is a relevant problem for loose to medium dense sands. Cyclic shearing of the soil induces volumetric strain with a reduction of the void ratio and an increase of the pore pressure, which reduces the effective stresses. This goes along with a loss of the soil's stiffness and strength.

The accidental collision of large maintenance vessel or the planned boat impact of a crew transfer vessel has to be simulated numerically. Usually, the probability of the collision is determined and assessed whether such a detailed analysis is required (BSH No. 7005). It has to be noted that the resulting load on the offshore wind turbine is highly affected by the type of the substructure and the size of the vessel (Lesny, 2008).

The previously described loads vary in terms of their magnitude, frequency of occurrence, probability and load rate (defined by load frequency or duration). The dominantly horizontal loads invoke an overturning moment, which is counteracted by the vertical resistance of the foundations of a multipod suction bucket (see Figure 1.3). In course of this, tensile loads, which are critical for this type of foundation due to considerably lower stiffness and resistance, may arise. Especially the load rate has an essential impact on the tensile bearing behaviour of a multipod suction bucket foundation, since it affects the drainage condition.

In case of very slow load application, the behaviour is drained and solely the outer and inner skin friction (τ_o and τ_i) resist the upward loading. As the load rate increases, a negative differential pressure Δu is mobilised, which acts on the bottom of the lid and contributes to the tensile resistance. Moreover, the pore pressure field in proximity to the suction bucket exhibits a certain differential pressure, which induces a seepage flow in the soil, but also affects the soil's stress state and skin friction. The behaviour is then partially drained or even undrained.

Cyclic tensile loads may cause a displacement accumulation over the lifetime of an OWT, which has to be limited within the serviceability criteria. It is still an open question, to which extent this accumulation occurs for certain loads, soil permeability as well as stiffness. Offshore Wind Accelerator (2019) remarked that tensile loads may be considered in the design, but relevant displacement may take place as tensile loads exceed the drained resistance. However, no guidance is provided how to determine the permanent displacement.

Despite multipod suction bucket foundations are sensitive to tensile loads, their general bearing behaviour combines two beneficial aspects (Byrne, 2000; Tjelta, 2015). Firstly, the quasi-static long term loads are sustained by the drained resistance, since temporarily arising differential pressures can dissipate. Therefore, degradation of the soil strength resulting from accumulation of positive differential pressure does not take place. It has to be noted that these loads might be for instance environmental loads that must not induce tensile forces on the foundation. Secondly, the exceptionally high magnitude cyclic or transient loading over a short period of time is resisted by the partially drained to undrained response of the foundation. Thus, additional capacities can be considered for singular loads in the ULS or ALS. Nevertheless, these loads may imply significant permanent displacements (Houlsby, 2016).

1.2 Outline of the thesis

1.2.1 Motivation

The need for a renewable energy supply is evident and the offshore wind is expected to contribute a significant share. To date, ongoing development leads to increasing capacity of OWTs while reducing the levelised cost of energy, which strengthens the competitiveness of offshore wind against other energy sources. However, the capital expenditure is still on a high level and the costs attributed for the foundation constitute a significant portion. Forthcoming offshore wind farms will be deployed further away from shore in deeper water, where substantially higher environmental loads are present. These aspects highlight the need for a cost-effective and reliable foundation for the numerous offshore structures to be built.

To face the described demands, the multipod suction bucket foundation is a promising concept, which is worth of intensive investigations. At the present stage, however, many

uncertainties exist and conservative assumptions are adopted. Hence, the economic benefits are diminished or even vanished. In that context, the response to tensile loads is crucial. So far, it cannot be relied on the partially drained tensile resistance as it is not yet completely understood. Especially the development of the differential pressure cannot be predicted with certainty, although it is known to highly contribute to the partially drained to undrained bearing behaviour. Assuming that tensile resistances higher than the drained one are accounted for, their mobilisation necessitates larger vertical displacements. Since the required displacement cannot be determined so far, it is not possible to assess whether it is tolerable in regard of the SLS. The offshore loading regime is cyclic, which extends the complexity even more by a potential accumulation of pore pressure or displacement over the operational time. Obviously, this accumulation must be limited or avoided to ensure integrity and serviceability of the OWT.

Ongoing research on suction buckets expands the knowledge in terms of the previous aspects. Once the bearing behaviour of this innovative foundation is understood, the design can be optimised and a highly efficient foundation concept becomes available. Subsequently, common design recommendations and standards, such as DNVGL-ST-0126 or DIN 18088-4:2019-01, may include a comprehensive design concept in future revisions. The explicit definition of verified design guidelines is expected to enhance the applicability and a gain of prominence. In order to achieve this, fundamental research is required.

1.2.2 Objective and concept

The main target of the research presented in this thesis is to enhance the applicability of suction bucket foundation as an efficient concept for OWTs. To achieve this purpose, the design of the suction buckets has to optimally utilise the capacities of that foundation. This optimisation is restricted so far due to incomplete understanding of the tensile bearing behaviour. This is where the present thesis focuses on by investigating the response of suction buckets to tensile loads via diverse approaches.

The structure of this thesis follows the methodology of the conducted research on which it is based on. Hence, the individual aspects, i.e. physical model tests, numerical simulations and analytical calculation methods, are addressed separately. Each chapter is introduced by basic considerations on the particular approach. Thereafter, the tensile bearing behaviour is analysed with regard of the different loading conditions. Eventually, every chapter is finalised with a conclusion.

This thesis initially provides a state of the art of suction bucket foundations with emphasis to the bearing behaviour under tensile loads in sand. The present knowledge was fundamentally gained by physical modelling supplemented with numerical simulations. The findings and methodologies of previous studies are analysed and summarised. The current design practice and available methods to analytically determine the tensile bearing behaviour are presented.

Despite the conduction of many physical model tests in the past, the results suffer from certain insufficiencies, e.g. small scale, inappropriate boundary conditions or deficient

documentation. For a comprehensive analysis of the tensile response, new physical model tests were performed in an exclusively erected testing facility. The results of the medium-scaled model tests improved the understanding of the tensile bearing behaviour of suction buckets. Furthermore, a large database of high-sophisticated results was built up.

A finite element (FE) model was developed, which incorporates essential aspects in terms of the tensile bearing behaviour of suction buckets. The formerly mentioned database of model tests was used for verification and validation of the FE model. As the FE model was proven to give accurate results for different model scales, an extrapolation of the geometric dimensions was established. By doing so, the response of suction buckets at prototype scale was investigated in a parametric study. In addition to the parametric study, specific focus was on the investigations of load types that either represent probable loads on OWT or simplify the complex cyclic displacement accumulation by an equivalent load.

The findings of the model tests and FE analyses were adopted to formulate a new calibration and implementation of an existing analytical calculation method. The input parameters were derived from regression of the results of FE simulations in conjunction with basic theoretical considerations so that the determination of the input parameters is consistent and straightforward. Additionally, the analytical mode was verified for various load conditions including cyclic equivalent load and testified its applicability.

The thesis closes with a synopsis of the outlined scope in which the main findings are aggregated and rated. An outlook is given, where the potential for future applications of suction bucket foundations is evaluated and the relevance for proceeding research is marked. Finally, a brief summary of the new results is provided.

1.2.3 Scope

The scope of this thesis is on multipod suction bucket foundations for OWTs, with the particular focus on tensile loading in sand. For a holistic evaluation of the suction bucket's response, various monotonic and cyclic loading conditions were investigated. Although a wide range of cyclic load configurations was considered, the applied loads are exclusively tensile (swell loads). The investigated drainage condition is the partially drained to undrained state, albeit the drained resistance is utilised for reasons of comparability. The conducted research considers dense to very dense sand since it is a predominant soil condition in the German North Sea.

In case that anything else but the previously described scope is considered, it is clearly marked as such. For instance, when analysing the state of the art, certain publications are relevant for specific aspects, but consider different boundary conditions, such as the loading condition. Nevertheless, the results of these studies may reveal significant information on e.g. installation effects.

2 Suction bucket foundations

2.1 Definitions

In order to facilitate analysis and interpretation of the results presented in this thesis, general definitions are introduced. The results of previous studies were edited to ensure conformity or if not possible, it is marked and explained appropriately. The following sign conventions apply:

- Depth below soil surface z is negative

- Upward displacement Δz is positive

- Upward movement of the soil plug Δz_{plug} is positive

- Gap expansion Δz_{gap} is positive

- Upward loads F acting on the suction bucket are positive

- Negative differential pressure (suction) Δu is positive

- Suction force F_{suc} is positive

- Downward frictional resistances $F_{\mathrm{fric}} = F_{\mathrm{i}} + F_{\mathrm{o}}$ are positive

Figure 2.1 illustrates the sign conventions and provides specifications on geometric dimensions, load and resistances. An axisymmetric coordinate system, which is justified by the axisymmetric geometry of the suction bucket and the axially applied load, is introduced by vertical z and radial r directions. While the absolute magnitude of certain quantity is for instance depth z or gap height z_{gap} the change of the particular value is specified by the vertical displacement of the suction bucket Δz or the gap expansion Δz_{gap} respectively. Derivatives, such as the displacement rate, are defined as $v_z = \mathrm{d}z/\mathrm{d}t$. If it is not explicitly specified, Δu refers to the negative differential pressure beneath the suction bucket's lid.

The allowable permanent load-induced tilt of an offshore wind turbine (OWT) during lifetime may be $0.25°$ (see subsection 1.1.2). The spacing s of the foundations is commonly $2D$ to $3D$ with $2D$ being more critical with regard to acceptable displacement (see Figure 1.3). Thus, the allowable displacement can be determined by trigonometry to $\Delta z/D = 2 \tan 0.25° = 0.009$ for $s = 2D$ and $\Delta z/D = 3 \tan 0.25° = 0.013$ for $s = 3D$. These dimensionless quantities are valid under the consideration of the introduced relations and only if foundations located on one side of the jacket displace while the opposing ones remain at their origin. In that regard, the introduced displacements are referred
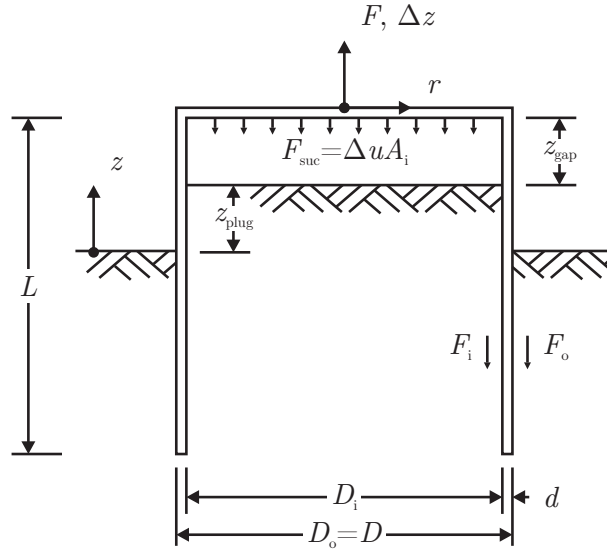
Figure 2.1: Definition of geometric quantities.

to in order to give an indication where serviceability limits might be reached. It should be noted that these values are assumed only for that purpose and do not have a general validity for the serviceability limit state (SLS).

Three load types are distinguished according to Figure 2.2, namely constant displacement rate, constant force and cyclic force. While the first two load types aim at investigating the monotonic bearing behaviour, either displacement-controlled or force-controlled, the last one idealises the irregular cyclic loading condition on OWTs.

The analysis of the response of a suction bucket subjected to a constant displacement rate v_z is a severe simplification of the actual offshore loading condition, but allows for the controlled investigation of different drainage conditions. Furthermore, it provides fundamental insights into the mobilisation of the individual resistances that depend on both displacement and displacement rate. Therefore, the initial stiffness and the development of the negative differential pressure can be quantified. Since the displacement rate mainly affects the drainage, the plug heave corresponds to the displacement rate and can be assessed as well.

Loading with constant force F induces time-dependent displacement, which is an essential benchmark for the evaluation of the much more complex cyclic bearing behaviour. Moreover, the allocation of the load to the individual resistances (frictional resistances and suction force) is possible. The loading condition is characterised by three parameters, i.e. preloading duration t_{acc}, holding duration t_{hold} and load magnitude, and allows for the analysis of drainage condition, displacement accumulation and permanent displacement after unloading.

Cyclic loading is the most realistic load type, despite the idealisation of the irregular offshore load characteristics to a regular load sequence. The load is defined by mean load F_{mean}, load amplitude F_{ampl} and load frequency f or period T respectively. The analysis
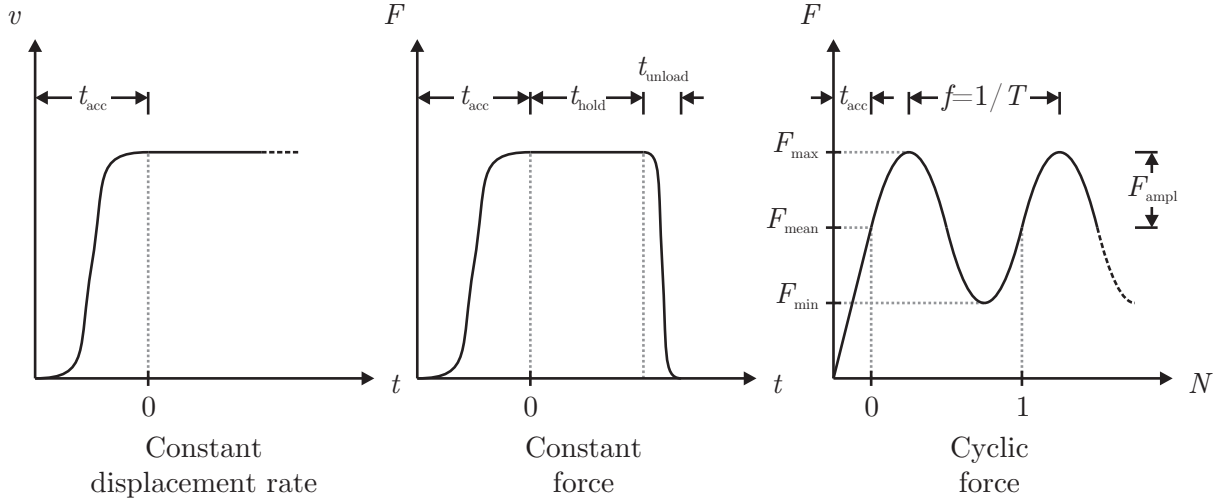
Figure 2.2: Definition of load characteristics.

of cyclic loads enables the assessment of potential accumulation of differential pressure and displacement, which is essential for the evaluation of serviceability.

In case of force-controlled loading and to enhance comparability, the applied loads are generally divided by the drained resistance (see Equation 2.1). Furthermore, the frictional resistance, which is affected by the drainage condition, is divided by the drained resistance as well to qualitatively assess the hydraulic effects on the frictional resistance.

$$\bar{F} = \frac{F}{F_{\mathrm{dr}}} \tag{2.1}$$

2.2 Tensile bearing behaviour

The tensile bearing behaviour of a suction bucket depends on the actual failure mechanism, which is dictated by the drainage condition, i.e. the drained, partially drained or undrained response (see Figure 2.3). The drainage condition itself is governed by the hydraulic conductivity of the soil, geometric dimensions of the suction bucket, but also the load rate. While the soil's permeability relates to its void ratio and the connectedness of the voids, the hydraulic conductivity k_{f} further accounts for the pore fluid's viscosity and density (assuming fully saturated conditions).

On the one hand, very slow load rates invoke the drained response with negligible change of the pore pressure in the soil. The effective stresses σ' are not affected by the pore water seepage flow, which slowly, but continuously fills the gap between the soil surface and the suction bucket's lid. The soil next to the skirt exhibits minor upward displacement as a matter of shearing at the interface along the skirt, but beside that there is no plug heave.
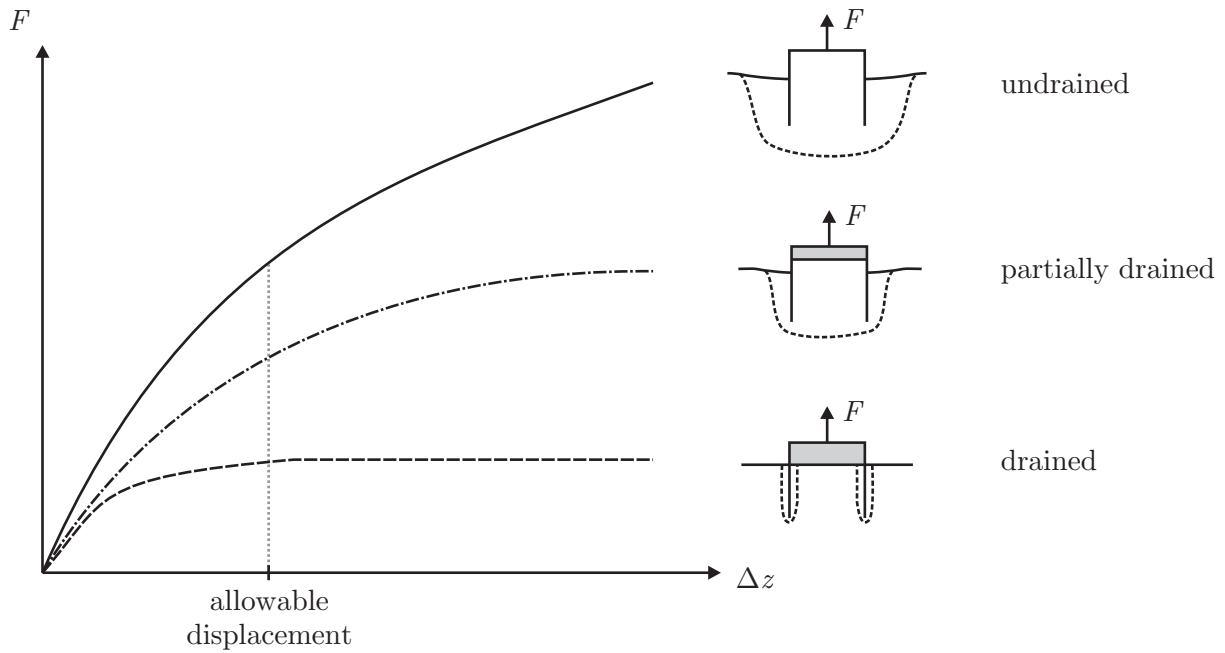
Figure 2.3: Drainage dependent failure mechanisms and qualitative resistances (following Senders, 2009).

Thus, the height of the gap between the suction bucket's lid and the soil surface is almost equal to the displacement of the suction bucket.

On the other hand, the undrained condition takes place if the load rate is very fast prohibiting dissipation of differential pressure. Consequently, the pore water seepage flow inside the suction bucket and thus the formation of the water filled gap is prevented. As a result, the shear resistance of the soil outside the suction bucket is mobilised. The significant stress changes of the pore pressure induce an equivalent shift of the effective stresses in the soil according to the principle of effective stresses (Terzaghi and Jelinek, 1954). Consequently, not only the tensile resistance is magnified by the suction force but also the frictional resistance is affected. The plug heave and the displacement of the suction bucket are essentially of the same value.

The drained and undrained condition are both rather unlikely to take place in sand. The load rates are generally too high and invoke at least certain differential pressure so that it cannot be treated as drained. Contrary, the considerably high hydraulic conductivity prohibits the occurrence of the undrained condition for realistic load rates as described in subsection 1.1.3. The actual drainage condition is expected to be partially drained along with the intermediate failure mechanism as depicted in Figure 2.3. Despite this, the drained and undrained condition represent the lower and upper bound of the tensile resistance of a suction bucket and are thus essential for the appropriate evaluation of the partially drained bearing behaviour.

As it is evident from Figure 2.3, the drainage condition does not solely affect the resistance, but also the displacement to mobilise the particular resistance. This implies two major aspects. Firstly, the initial stiffness $K = \mathrm{d}F/\mathrm{d}z$ increases the more the response

tends to be undrained. Secondly, assuming certain allowable displacement, the resistance is significantly higher for rather undrained conditions. Or vice versa, a distinct load magnitude will require less displacement if the suction bucket behaves more undrained.

In the following, the individual components forming the monotonic tensile resistance of a suction bucket are individually described. The qualitative discussion addresses especially the effect of different drainage conditions on the particular resistance. Four distinct components are regarded, namely the outer friction, inner friction, differential pressure beneath the suction bucket's lid and self weight. The effect of the differential pressure at the tip of the suction bucket's skirt is neglected since the circular ring area on which it acts is very small and hence no relevant resistance can be generated.

Theoretically, the drained resistances of the outer and inner friction can be estimated by the integration of the skin friction along the skirt (see Equation 2.2 and Equation 2.3). If it is assumed that $\tau = \gamma' k \tan \delta$, this formulation neglects the effect of the upward shear stresses at the soil-structure interface on the surrounding soil. Consequently, the actual tensile resistance is less than the theoretically calculated resistance because of stress relief in the soil.

$$F_\mathrm{o} = \pi D_\mathrm{o} \int_0^L \tau_\mathrm{o} \, \mathrm{d}z = \pi D_\mathrm{o} \int_0^L \gamma' z k \tan \delta \, \mathrm{d}z \tag{2.2}$$

$$F_\mathrm{i} = \pi D_\mathrm{i} \int_0^L \tau_\mathrm{i} \, \mathrm{d}z = \pi D_\mathrm{i} \int_0^L \gamma' z k \tan \delta \, \mathrm{d}z \tag{2.3}$$

In regard to the partially drained to undrained condition, the outer friction is increased by the negative differential pressure outside the skirt and the induced downward pore water seepage flow. Although it strongly simplifies the complex interaction, this effect can be described by the hydraulic gradient i_o, which is adopted to enhance the effective unit weight of the soil by $\tilde{\gamma}_\mathrm{o} = \gamma' + i_\mathrm{o} \gamma_\mathrm{w}$ to be considered in Equation 2.2 instead of γ'. The mobilisation of the frictional resistance requires certain relative displacement in the interface between the suction bucket and the soil, but this will differ from that under drained condition since the soil itself displaces considerably (see Figure 2.3).

While the pore water seepage flow is downward on the outside of the suction bucket, the flow is upward inside the suction bucket. The effective unit weight of the soil is reduced by the upward hydraulic gradient i_i resulting in $\tilde{\gamma}_\mathrm{i} = \gamma' - i_\mathrm{i} \gamma_\mathrm{w}$. As a consequence, the inner friction is diminished. The upper limit of the previously described effect is reached when the effective unit weight of the soil becomes zero and liquefaction theoretically takes place. Additionally, the more undrained the suction bucket behaves, the more plug heave occurs impeding relative displacement at the interface on the inside of the skirt and thus adversely affect the mobilisation of the inner friction (see Figure 2.3).

Even under drained condition, certain negative differential pressure arises, which evokes pore water seepage flow to fill the gap beneath the suction bucket's lid. However, the magnitude of the differential pressure is negligible and does not provide relevant tensile

resistance. The partially drained and undrained loading of a suction bucket develops significantly higher negative differential pressures. While the partially drained response still requires considerable displacement, the undrained bearing behaviour does not need substantial displacement to mobilise negative differential pressure. In general, the generated negative differential pressure induces pore water seepage flow since the pore pressure field differs from hydrostatic state. The seepage flow fills voids, whose localisation depends on the failure mechanism depicted in Figure 2.3, e.g. beneath the suction bucket's bottom in undrained or beneath its lid in drained condition. It is to be noted that the resulting pore pressure field is even more complex due to dilation and contraction of the soil that locally affects the differential pressure along with the seepage flow.

The negative differential pressure is limited by cavitation. The sum of the hydrostatic $p_0 = h_{\mathrm{w}}\gamma_{\mathrm{w}}$ and atmospheric p_{atm} pressure defines the cavitation limit $p_{\mathrm{cav}} = p_0 + p_{\mathrm{atm}}$ (see Figure 1.3). As a consequence, the water depth dominates the pressure at which cavitation occurs and hence it is a relevant issue in shallow water. Beside the limitation of the maximum negative differential pressure beneath the suction bucket's lid, the local occurrence of cavitation due to dilation of the soil has to be considered as well. Although the dilation-induced reduction of pore pressure increases the strength of dense sand, its behaviour changes abruptly from undrained to drained if cavitation takes place (McManus and Davis, 1997). This will affect the global response of the suction bucket likewise.

Finally, a distinct share of the self weight of the OWT contributes to the tensile resistance of each particular foundation of a multipod substructure. It is straightforward to determine the appropriate compressive mean load on each suction bucket. Contrary to the previously described components forming the tensile resistance, the self weight does not require any displacement for mobilisation. Additionally, dynamic loads with high acceleration would generate extra inertial forces, but such high load rates are not likely to occur at prototype scale except for excitation from earthquakes.

Although the knowledge on the monotonic bearing behaviour is essential, the suction bucket foundation of an OWT is predominantly exposed to cyclic loads. Frequent loading and unloading with various magnitudes and load directions (compressive and tensile) are expected to occur. This may potentially lead to incomplete dissipation of differential pressure during subsequent cycles, which in turn has an impact on the frictional resistances such as strength or stiffness degradation.

The previous description adopted the terms 'drained', 'partially drained' and 'undrained' to qualitatively introduce the tensile bearing behaviour. However, these terms oversimplify this much more complex issue. It is not possible to exactly predict the drainage condition and there are no strict distinctions of the failure mechanism, but rather a transition from one state to the next. Even though a qualitative determination is potentially feasible, it is hardly possible to reliably and accurately ascertain the response of a suction bucket subjected to arbitrary tensile loading.

In the past, physical model tests at different scales and numerical investigations were employed to analyse the bearing behaviour of suction buckets. Based on these findings

and additional theoretical considerations, analytical methods and scale analyses were proposed, which aim at describing the bearing behaviour or evaluate scale effects respectively. An overview on the current state is provided in section 2.3.

2.3 Literature review

2.3.1 Physical model tests

According to DIN EN ISO 19901-4:2017-01 it is recommended to conduct model tests if 'a high degree of uncertainty exists as to how the structure or its foundation will behave', which applies for the tensile bearing behaviour of suction buckets in sand. Physical model tests can be either at prototype, field, laboratory or centrifuge scale. All physical testing methods have assets and drawbacks. Thus, the choice of the appropriate method requires intensive considerations of the individual demands and constraints to attain the objective pursued.

While prototype and field testing are expected to provide the most realistic results, these test methods are expensive and the number of executable tests is generally limited. Consequently, the bandwidth of investigated parameters is constrained. Although the boundary conditions, e.g. soil profile and properties, can be examined, they can hardly be changed to the desired characteristics.

Laboratory testing at $1g$ suffers from the low stress state in the soil. Bolton (1986) stated that soil's internal friction angle φ' and dilation angle ψ decrease slightly with soil's effective stress and increase rapidly with relative density thus implying high dilation in dense sand at low stress. This has a major effect on stress changes in shear bands as it was analysed by Hettler (1982, 2010), who identified increasing normalised tensile resistances of piles with decreasing diameters at laboratory scale. To reduce dilation, it is possible to conduct model tests at laboratory scale with reduced relative density (Byrne, 2014). Furthermore, scaling of the obtained results is a crucial but highly discussed aspect since there is no unique and generally accepted procedure. For instance, the soil's stiffness non-linearly depends on the actual stress and strain so that linear scaling of displacements is not applicable. Laboratory testing is advantageous because of the relatively large scale, which allows for the high quality measurement of many quantities in numerous tests. Additional features such as a pressure chamber or enhanced effective stress allow for the simulation of higher water depth (higher ambient pressure) or increased embedment depth (higher effective stresses in the soil) respectively.

Physical modelling in a geotechnical centrifuge linearly scales the geometric dimensions with the level of acceleration and generates soil's stresses appropriate to scaled conditions. A major disadvantage for testing of suction buckets in sand is the accelerated rate of consolidation, which is dealt with by more viscous pore fluids, whereby not only the bulk moduli differ from the one of water but also the different pore fluid potentially affects the soil's strength and stiffness. Depending on the size of the centrifuge and the model,

Table 2.1: Overview of preceding physical model tests on vertically (partly tensile) loaded suction buckets in sand.

Reference	Type [*]	Length L: mm	Diameter D: mm	Thickness d: mm	Loading [†]
Iskander et al. (1993, 2002)	L	194	110	5	Mon, Cyc
Tjelta and Haaland (1993)	F	1700	1500	12	Mon, Cyc
Jones et al. (1994)	L		127	16	Mon, Cyc
Bye et al. (1995)	L	210	550		Mon, Cyc
Byrne (2000)	L	50	150	0.45	Mon, Cyc
Feld (2001)	L	100	200		Mon, Cyc
Kelly et al. (2004, 2006b)	L (PC)	180	280	3.125	Mon, Cyc
Houlsby et al. (2006)	F	1000	1500		Mon, Cyc
Senders (2009)	C ($100g$)	60	60	0.3	Mon, Cyc
Kakasoltani et al. (2011)	L	80–320	80	2.5	Mon
Vaitkunaite et al. (2014)	L (OP)	500, 1000	1000	3	Mon
Vaitkunaite et al. (2016)	L (PC)	250	500	2	Mon
Hung et al. (2017)	L	75, 150	150	1	Mon, Cyc
Vaitkune et al. (2017)	L	500	1000	3	Mon, Cyc
Zhang et al. (2017)	L	120, 240	120	2	Mon
Bienen et al. (2018a,b)	C ($100g$)	40	80	0.5	Mon, Cyc
Wang et al. (2019)	C ($30g$)	9–70	70	0.49	Mon
Jeong et al. (2020)	C ($50g$)	200	143	1.5	Mon, Cyc

[*] L: laboratory; F: field; C: centrifuge; PC: pressure chamber; OP: overburden pressure.

[†] Mon: monotonic; Cyc: cyclic.

the variation of acceleration with distance to the axis of rotation is a relevant issue. Moreover, the operation of a centrifuge is complex and expensive so that the number of tests is limited. In terms of geometric dimensions, the size of the model is generally small in comparison to the size of the measurement devices and soil's grain size (Byrne, 2014). As a consequence, the number and locations of measured quantities are restricted, but also the relation of grain size to the size of the structure is not appropriately scaleable.

Table 2.1 provides a chronological overview of preceding physical model tests being relevant for the vertical bearing behaviour of suction buckets in sand. This compilation is a selection of physical model tests where at least some tests of any particular study deal with the tensile response of a suction bucket. The main findings of these studies are summarised afterwards. Controversial results as well as limitations of the test environment or conclusions are highlighted.

Iskander et al. (1993) conducted physical model tests at laboratory scale to systematically investigate the effect of the installation method and different conditions during tensile loading. The suction bucket was installed either by jacking, or hydraulic installation by applying different magnitudes of negative differential pressure. Subsequently, the suction bucket was loaded by a constant displacement rate of 7.6 mm/s with a valve at the suction
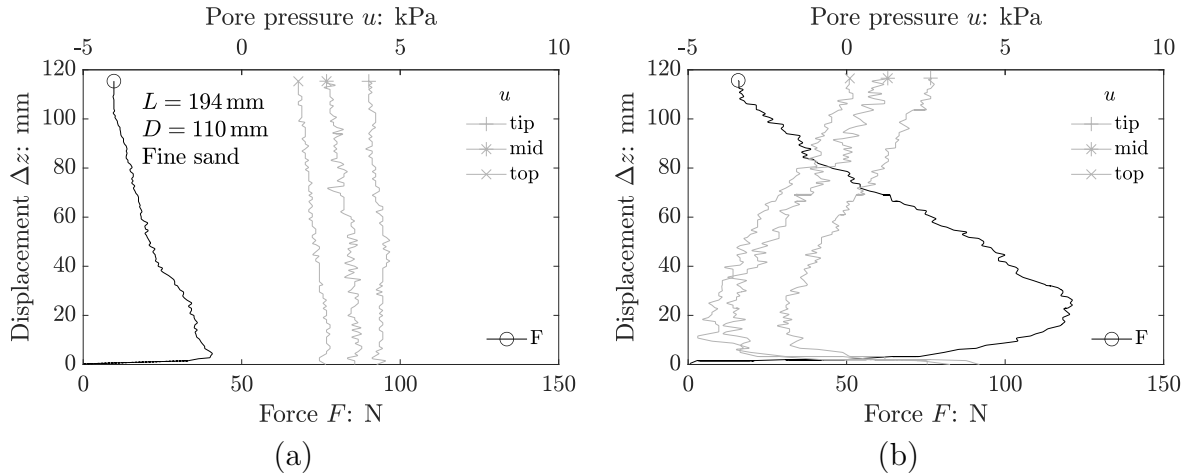
Figure 2.4: Drained (a) and undrained (b) response (following Iskander et al., 2002).

bucket's lid being either open (drained condition) or closed (undrained condition) (see Figure 2.4). The pore pressure was measured beneath the suction bucket's lid and at two positions inside the suction bucket's skirt. As expected, no negative differential pressure occurred under drained condition and the soil plug inside the suction bucket remained at its origin. Under undrained condition, the negative differential pressure was found to substantially increase the tensile resistance, but also to affect the outer frictional resistance due to higher effective stresses in the soil. The highest negative differential pressure during installation implied the lowest frictional resistance under tensile loading. This indicates that the soil was loosened during installation, which is confirmed by the highest plug heave measured after installation. Since the soil plug remained inside the suction bucket under undrained condition, the authors concluded that the soil's weight contributes to the tensile resistance, but prevents the mobilisation of inner friction. In terms of the displacement required to achieve the maximum resistance, it was found that the drained resistance is reached quickly, but higher displacement is needed to reach the undrained resistance (see Figure 2.4). Despite the methodical analysis of crucial aspects, this study is not comprehensive and the investigated aspect ratio is greater than it would be applicable for OWTs. The readings of the differential pressure sensors (DPSs) exhibit certain offsets and their relation to a distinct origin is not provided. The interpretation of these measurements can therefore only be qualitative.

Based on Iskander et al. (1993), Jones et al. (1994) conducted tests with a suction bucket having a double-walled acrylic skirt to provide space for strain measurements and DPSs to monitor the differential pressure at the inside and outside of the skirt at different depths. The length of the model is not provided, but the embedment depths are given between 100 mm and 125 mm. The drained and partially drained response were evaluated and the results are consistent with those of Iskander et al. (1993). Moreover, the readings of the additional DPSs point out the existence of negative differential pressure outside the suction bucket. Additionally, findings from cyclic tests with load frequencies between 4 Hz and 15 Hz are discussed. A cyclic test, where the minimum and maximum load were $\bar{F}_{\min} = 0.47$ and $\bar{F}_{\max} = 0.88$ respectively, is presented in detail. The cyclic load-

ing invoked little negative differential pressure, but caused continuous displacement with decreasing increments per cycle. It has to be noted that the use of acryl for the suction bucket's skirt is expected to affect the frictional resistance (especially its roughness during repeated cyclic loading) and the skirt thickness is too large in comparison to prototype scale. Furthermore, the high load frequencies may invoke inertial forces if the resulting displacements are sufficiently large.

The publication of Iskander et al. (2002) refers back to the results of Iskander et al. (1993) and Jones et al. (1994), but provides a more detailed theoretical analysis and comments on cyclic tests. It is stated that the suction bucket was extracted from the soil within 5 s if $\bar{F}_{max} > 1.25$, but extraction took several hours if $1.0 > \bar{F}_{max} > 1.1$ and no displacement was observed for $\bar{F}_{max} = 0.9$. Therefore, the analysis of the cyclic response is contradictory to the results discussed in Jones et al. (1994).

In advance of the construction of the Draupner E and Sleipner T platforms, a laboratory and field testing campaign was executed (Tjelta and Haaland, 1993; Bye et al., 1995). Although the results of the tests are mainly confidential for commercial reasons, crucial findings were qualitatively documented. Dilation of the soil was identified to be a dominant factor affecting the tensile resistance, but also the drainage and duration of the load were found to be relevant. Dilation and insufficient pore water seepage flow generate significant negative differential pressure and hence increase the effective stress. As a result, the soil's strength and therefore the tensile resistance of the suction bucket are magnified. Opposed to this effect, tensile loads may also decrease the effective stress due to upward shear stresses that reduce the soil's strength. As a consequence, only very low frictional resistance remains after dissipation of negative differential pressure. However, for short load duration, substantial tensile forces may be applicable. During cyclic loading, contraction of the soil takes place. Distinct zones of sustainable cyclic amplitudes were identified, but their breach evoked rapid degradation. The monotonic resistance was observed to not decrease after cyclic loading (Bye et al., 1995), but certain results indicate even higher resistances and stiffnesses after cyclic loading (Tjelta and Haaland, 1993). For scaled model tests, the issues of low stress level and adequate drainage condition were identified, which compete with the desire of using the actual in-situ soil type. While the first issue was encountered by large scale field test, the latter was dealt with by more viscous pore fluid and less permeable soil to attain reduced hydraulic conductivity. Tjelta (2015) re-published results of Bye et al. (1995), where the quantitative values were initially not provided (see Figure 2.5). Obviously, higher displacement rates significantly enlarge the tensile resistances and lead to higher initial stiffnesses. However, the stated displacement rates are partly inconsistent with those of the original publication (Bye et al., 1995).

Byrne (2000) and Byrne and Houlsby (2002) pointed out uncertainty in terms of the tensile response. While the drained resistance is low, the resistance is significantly higher if dilation and typical load rates such as those induced by waves are considered. To incorporate appropriate drainage characteristics for in-situ condition, silicon oil was used as pore fluid. The suction bucket model was installed by jacking. A stiff symmetric response under low compressive load magnitudes was observed, but gradual transition to an asymmetric response with substantial displacement took place when tensile loads
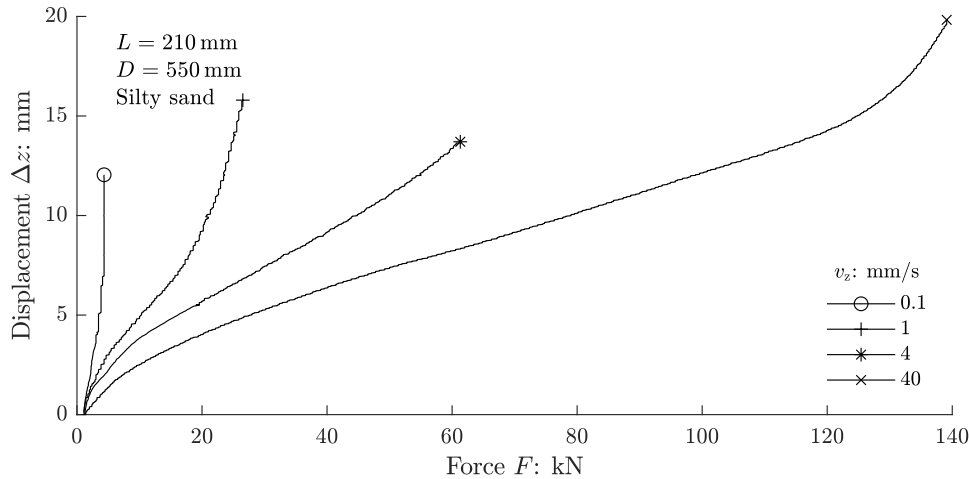
Figure 2.5: Tensile resistance affected by displacement rate (following Bye et al., 1995; Tjelta, 2015).

arose. As long as the displacements were relatively small, little degradation, affecting the tensile resistance and stiffness, appeared. Nevertheless, the resistance continuously degraded to the drained resistance for large displacements. Opposed to that, Byrne and Houlsby (2002) stated that the degradation approached to a resistance consisting of the weight of the soil plug and a certain share of outer friction. Redensification of the soil by vertical compression load as well as horizontal and moment cycling caused regain and even improvement of the tensile response in comparison to initial tensile loading. In terms of the load rate (i.e. period), no significant change of the response was observed. Monotonic tests with constant displacement rates revealed little effect of the displacement rate on the initial stiffness, but it was noticed to affect the tensile resistance at large displacements (limited by cavitation). The load sharing of the suction force to the total force was found to be hardly affected by the displacement rate. The authors identified a correlation between the monotonic and cyclic response suggesting that the cyclic bearing behaviour can be possibly derived from monotonic tests. The asymmetric response when transitioning from compressive to tensile loads and the large displacement necessary to mobilise the tensile resistance led to the conclusion that serviceability requirements will govern the design. Drained triaxial tests on samples saturated with silicon oil in comparison to water saturated samples revealed that the soil's internal friction angle (by approximately 3°) and the dilation angle were reduced.

The physical model tests of Feld (2001) dealt with the effect of preceding cyclic loading and the displacement rate on the tensile response. While the tensile resistance increased with displacement rate, the initial stiffness did not seem to be affected (see Figure 2.6). The gain of the post-cyclic tensile resistance is apparent from the tests at $v_z = 2\,\mathrm{mm/s}$ depicted in Figure 2.6, where the values in parentheses represent the number of antecedent cyclic load sequences. If only one cyclic load sequence instead of two sequences was applied, the stiffness and maximum resistance were substantially lower. According to Feld (2001), this effect related to the densification during cyclic loading. Although the negative differential pressure was monitored, their readings were doubted by the author (Feld, 2001).
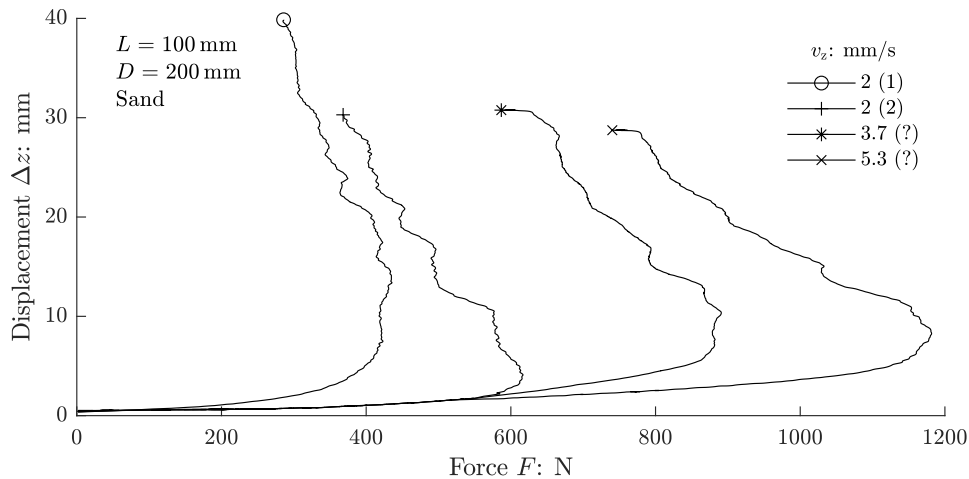
Figure 2.6: Tensile resistance affected by displacement rate and cyclic preloading (following Feld, 2001).

Kelly et al. (2003) conducted tests in a pressure chamber. The soil was saturated with de-aired water and cyclic loads with constant compressive mean load but increasing load amplitudes in packages were applied on a mechanically installed suction bucket model. The load amplitude in the last sequence exceeded the mean load so that it comprised tensile loads. A sudden reduction of the stiffness was observed as tensile loads were present (see Figure 2.7 (a)). However, the net displacement remained downward. Subsequently, the suction bucket model was extracted from the soil by applying a constant displacement rate of 5 mm/s. Contrary to Byrne (2000), cavitation was not observed. Kelly et al. (2003) attributed this finding to the significantly lower hydraulic conductivity due to the more viscous pore fluid used by Byrne (2000), which evoked more undrained response of the suction bucket. The authors concluded that tensile loads shall be kept within the sum of the self weight of the suction bucket, the weight of soil plug and the outer friction to prevent crucial upward displacement (Kelly et al., 2003).

Further test series were presented in Kelly et al. (2004) and Kelly et al. (2006b). Among other tests, the same load configuration as previously described was applied on a suction bucket installed in a different sand being thousand times less permeable than the one used in Kelly et al. (2003). Despite the ten times lower load frequency, the loading invoked higher changes in differential pressure indicating more undrained behaviour (see Figure 2.7 (b)). Moreover, higher tensile loads were applicable, but these were accompanied by larger displacements. Although a slight increase of stiffness due to cyclic loading in compression was observed, the application of cyclic loads was found to degrade the tensile response when extracting the suction bucket by a constant displacement rate. The drainage characteristics of the different cyclic tests (load frequency and soil type) were compared by one-dimensional consolidation analysis with the aim of identifying the most realistic test in terms of prototype dimensions and load rate (see subsection 2.3.4). Interestingly, the authors identified different test configurations to be most relevant in representing the prototype behaviour, when assuming either a constant consolidation coefficient c_v (Kelly et al., 2004) or accounting for the non-linear dependency of the soil's stiffness on
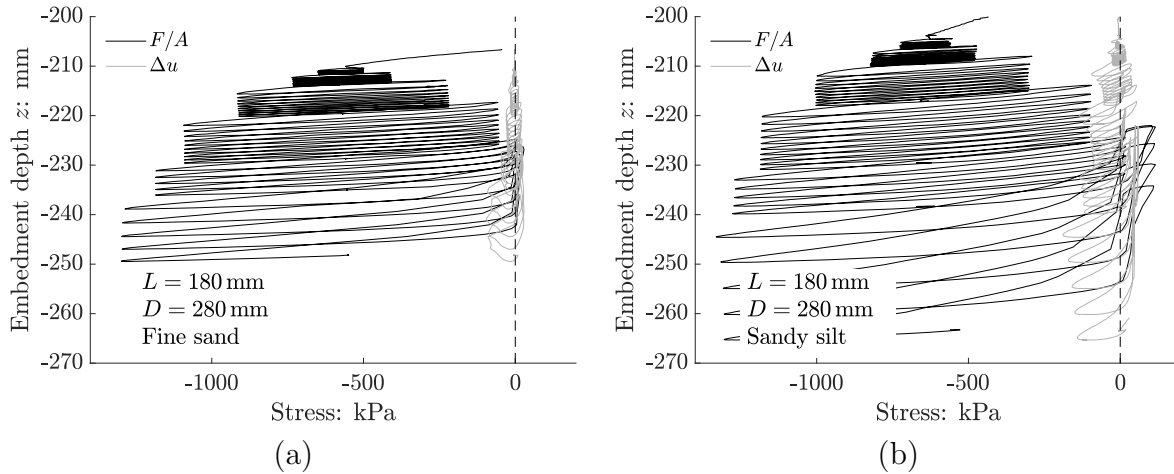
Figure 2.7: Cyclic test results in high permeable (a) and low permeable (b) sand (following Kelly et al., 2006b).

effective stresses (Kelly et al., 2006b). In addition, Kelly et al. (2006b) performed a phase analysis to assess the drainage conditions of particular cyclic tests. Therefore, the authors assumed that under drained condition, the phase angle of the differential pressure relates to the displacement rate, but under undrained condition it is expected to be in phase with the displacement. These hypotheses were successfully proven and individual tests were characterised to approach either drained or undrained behaviour. Furthermore, it was found that the more undrained the response is, the higher is the share of differential pressure on the total resistance. While Kelly et al. (2004) recommended limiting tensile loads to the drained frictional resistance at the skirts, Kelly et al. (2006b) were more stringent and suggested to totally avoid the occurrence of tensile forces.

Following the cyclic loading, the suction bucket model was extracted by applying different constant displacement rates at atmospheric or elevated ambient pressure (Kelly et al., 2006b). The test results pointed out a crucial increase of tensile resistance due to a higher displacement rate (see Figure 2.8). However, substantially more displacement was required, which might imply issues regarding the SLS. As reported by Kelly et al. (2004), no cavitation occurred under a displacement rate of 5 mm/s, but evidently at $v_z = 100$ mm/s since the negative differential pressure could not exceed the value of 100 kPa. When raising the ambient pressure by 200 kPa, the negative differential pressure was enabled to be significantly higher, which confirmed that cavitation took place in the previously described test. During initial displacement, the negative differential pressures exceeded the applied stresses, which is physically questionable. Beside this aspect, the high displacement rate may also invoke dynamic effects. The results of one test presented in Kelly et al. (2006b) revealed that the majority of the tensile resistance was generated within less than 0.1 s. Assuming a constant acceleration up to the displacement rate of 100 mm/s leads to $\mathrm{d}v/\mathrm{d}t_{\mathrm{acc}} = 100\,\mathrm{mm/s}/0.1\,\mathrm{s} = 1\,\mathrm{m/s}^2 \approx 0.1g$ and thus dynamic effects may be relevant as a result of the considerable acceleration.

Referring to the investigations of Kelly et al. (2003), Kelly et al. (2004) and Kelly et al. (2006b), the embedment depths evidently exceed the length of the suction bucket as a
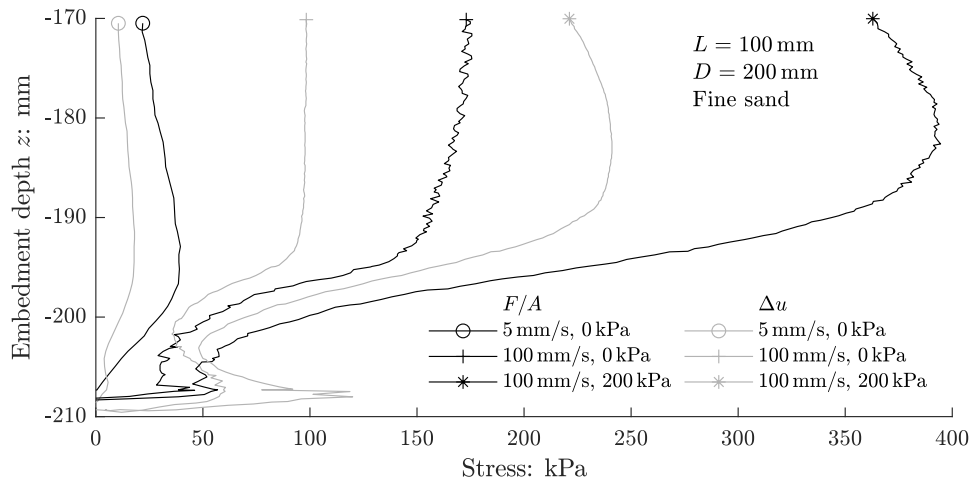
Figure 2.8: Tensile resistance affected by displacement rate and ambient pressure (following Kelly et al., 2006b).

result of the application of serious load magnitudes ($L = 180\,\mathrm{mm}$ in comparison with Figure 2.7 and Figure 2.8). As a consequence of the immense load amplitudes, very high vertical displacements per cycle were observed. Potentially, the investigated load magnitudes exceed the relevant loading for this particular model size, which can be partly verified by the estimation of the bearing capacity for an embedded footing. Unfortunately, the authors do not explain, how the load magnitudes were defined.

Houlsby et al. (2006) presented and analysed results of field tests on hydraulically installed suction buckets. The suction buckets were subjected to cyclic load sequences analogous to Kelly et al. (2006b) (constant compressive mean load and increasing load amplitudes). As the geometric dimension was larger, the applied load magnitudes were greater as well. The observed load-displacement response is qualitatively similar to the ones of Kelly et al. (2006b), but it is remarkable that the absolute vertical displacement is less than in the small-scale model tests despite a comparable number of load cycles. This indicates that the load magnitude of the field tests is likely to be relatively lower than the one of the laboratory tests regarding the different geometric scales. The drainage condition of the cyclic test cannot be assessed since neither the soil's permeability, nor the load frequency or differential pressure readings are provided. After cyclic loading, a monotonic test with a constant displacement rate was performed. The evaluation of the monotonic test suffers from uncertainty regarding the displacement rate (personal communication with B. W. Byrne described in Thieken et al., 2014) as well as the unknown soil's permeability and the premature cessation as the capacity of the load cell was reached.

Senders (2009) conducted numerous model tests in a geotechnical centrifuge. The pore fluid used in most of the tests was silicon oil and the models were installed either by jacking or hydraulically by extracting the pore fluid from inside the suction bucket. After installation, the global hydraulic conductivity was determined by generating distinct constant water volume rate and measuring the invoked negative differential pressure. The testing programme consisted of monotonic and cyclic loading. The cyclic loads were ap-

plied until tensile failure occurred and if it was not reached for certain load configuration, the load parameters were adjusted to provoke failure. The monotonic tests accounted for extraction of the suction bucket by various constant displacement rates with either open or closed vent at the suction bucket's lid to achieve different drainage conditions. The test results revealed higher tensile resistances for increasing displacement rates, which was found to be mainly due to higher negative differential pressures. However, the generation of the negative differential pressure appeared to not depend on the displacement rate. The frictional resistance was observed to be reduced from drained to partially drained condition, but its mobilisation did not seem to be affected by the displacement rate. Cavitation was noticed for high displacement rates, but it took place prior to the expected value consistently in several tests. The cyclic tests pointed out minor negative differential pressure for low load frequencies and in contrast to Byrne (2000), increasing load frequencies led to higher negative differential pressures. The evaluation of the results was focused on the development of an analytical calculation method, which is introduced in subsection 2.3.3.

Kakasoltani et al. (2011) and Zeinoddini et al. (2016) provided results of model tests on upright and conical suction buckets. After their mechanical installation, the suction buckets were extracted by applying a constant displacement rate. The conically shaped models provided higher tensile resistances. However, in comparison to the upright models, the mobilisation of the resistance required more displacement and the initial stiffness was found to be lower as well. A higher displacement rate was observed to evoke higher tensile resistance, which is more pronounced for upright suction buckets. An increase of the soil's relative density enhanced the tensile resistance especially for conical models. Although the bearing behaviour of conical suction buckets may have certain advantages, the authors neither explained how the installation of these foundations may be achieved at prototype scale nor provided a discussion on the effect of mechanical installation of these conical suction buckets on the soil. In Zeinoddini et al. (2016), the load-displacement curves for installation are given and reveal that significantly higher loads are needed to achieve the full penetration of the conical model, especially for higher relative density. Furthermore, the aspect ratio is relatively high and probably not suitable for OWTs.

Vaitkunaite et al. (2014) introduced a new testing facility to investigate the axial bearing behaviour of mechanically installed suction bucket foundations at relatively large scale. A particular feature is the possibility for applying overburden pressure on the soil surface to increase the effective stresses in the soil, which was realised by evacuating air from a membrane that was placed on top of the soil. The enhanced effective stresses in the soil were scaled to a higher equivalent embedment depth. However, the results were inconsistent and the method of scaling required revision (Vaitkunaite et al., 2014). In Vaitkunaite (2016), leakage of the system was given as possible reason for diverging results since the extraction of the pore fluid invoked partial saturation of the soil instead of full saturation as it was supposed. This affects the weight of the soil and therefore the effective stresses. As a consequence, the results may be misinterpreted. Further constraints are that tests can solely be conducted under drained condition and the dimensions of the suction bucket are relatively large in comparison to the size of the sand container so that its boundaries may affect the suction bucket's bearing behaviour.

Based on the testing facility described in Vaitkunaite et al. (2014), Vaitkune et al. (2017) investigated the drained cyclic and (post-cyclic) monotonic response without the previously described overburden pressure. The cyclic loads were defined in relation to the drained tensile resistance. During cyclic loading, the suction bucket either remained at initial position or displaced upwards, which agrees with the stiff elastic response of the suction bucket when subjected to small load magnitudes as observed by Byrne (2000), but is contradictory to observations of other studies, where the load magnitudes were significantly higher (Kelly et al., 2003, 2004, 2006b; Houlsby et al., 2006). Vaitkune et al. (2017) identified distinct ranges of mean loads and load amplitudes, where the displacement of the suction bucket is characterised as either stable, slightly upward or substantially upward. It was found that mean tensile loads implied constant incremental upward displacement during cyclic loading. Certain cyclic tests developed an accumulation of negative differential pressure, which disagrees with the definition of drained condition. The negative differential pressure was found to correlate with the displacement of the suction bucket. After cyclic loading, the monotonic stiffness was significantly higher than the original stiffness and the skin friction was analysed to be similar or slightly lower. The cyclic unloading stiffness was even higher than the monotonic one. If significant tensile loads were present, the cyclic stiffness was substantially lower and only then serious degradation was observed. These findings point out that a relevant number of cycles can be withstood even if tensile loads were implied, but certain displacement would be provoked.

Vaitkunaite et al. (2016) investigated the drainage condition from partially drained to undrained within the scope of monotonic physical model tests in a pressure chamber. In accordance with previous studies (Iskander et al., 1993; Bye et al., 1995; Byrne, 2000; Feld, 2001; Kelly et al., 2006a; Senders, 2009; Kakasoltani et al., 2011), higher displacement rates led to larger tensile resistance, which required more displacement to be mobilised (i.e. the secant stiffness from origin to maximum resistance is greatest for lowest displacement rate). Nevertheless, assuming a specified displacement (less than the required one to actuate the maximum resistance), the resistances were greater for higher displacement rates, which indicate relevant capacities exceeding the drained resistance. The readings of the DPSs at the skirt gave insight into the degree of drainage for different displacement rates (see Figure 2.9). The negative differential pressure is almost constant for the highest displacement rate so that no pore water seepage flow takes place and undrained conditions are prevalent. However, Vaitkunaite et al. (2016) stated that cavitation occurred in this test, although the theoretical cavitation limit was not reached (in agreement with Senders, 2009). Moreover, it is questionable, whether dynamic effects due to high acceleration can be neglected (see discussion of Kelly et al., 2006b) and if the highest displacement rate effectively represents a realistic loading condition. After the entire extraction of the suction bucket during the test, the soil surface was inspected. While under low displacement rates a slight mark of the skirt became visible, higher displacement rates invoked significant disturbance of the soil volume and formed a considerable hill as a result of plug heave. Finally, based on the findings of the model tests, the authors recommended to include partial drainage in ultimate limit state (ULS) design.

The study of Hung et al. (2017) was focused on the analysis of the cyclic displacement accumulation and development of unloading stiffness in dry and saturated sand consid-
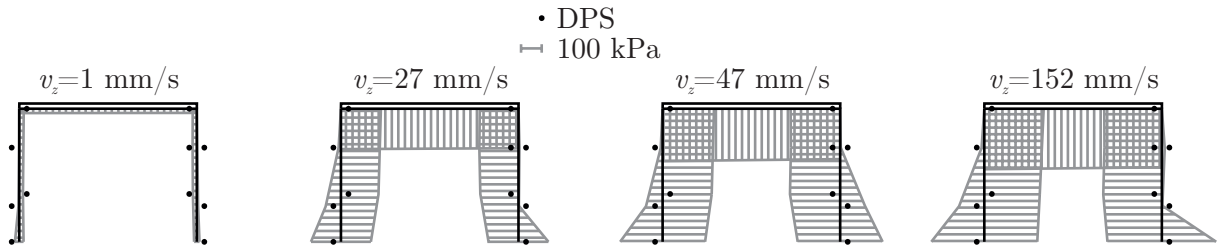
Figure 2.9: Distribution of maximum negative differential pressure (following Vaitkunaite et al., 2016).

ering two aspect ratios. Initially, the tensile resistances of both models in either dry or saturated sand were determined. The respective resistances are hardly comparable due to different relative densities of the sand, the greater effective stresses in dry sand as a consequence of the higher weight of the soil and partial drainage implying relevant negative differential pressure in saturated sand. The magnitude of the cyclic swell load is divided by the previously determined tensile resistance to enable comparability, but since these normalised loads were not constant for multiple tests and the boundary conditions of the monotonic tests differ crucially, the assessment of the results is inconclusive. Nevertheless, the authors infer that the cyclic stiffness decreases with load magnitude and number of cycles, while the cyclic displacement increases correspondingly (Hung et al., 2017).

Zhang et al. (2017) conducted tests aiming at the installation, monotonic response and extraction of suction bucket models. Hydraulic installation was demonstrated to be successful by reaching embedment depth of $|z/L| \geq 0.9$ for aspect ratios $L/D \in [1, 2]$. A cone shaped subsidence around the skirt was formed during installation and the installation ended with a sudden loss of negative differential pressure, which potentially refers to the occurrence of hydraulic failure. The previously described behaviour under constant displacement rate in drained and partially drained condition was confirmed. The measured tensile resistances were lower for hydraulically installed models in comparison to mechanically installed ones. The authors related this aspect to the higher embedment depth achieved by mechanical installation, but did not consider the possibility of fabric changes of the soil due to different installation methods. In a suction bucket model made of perspex, the plug heave during hydraulic installation and under monotonic partially drained loading was visualised. The models were successfully extracted by pumping water into the suction bucket, but hydraulic failure occurred outside the skirt when the model was almost entirely extracted as a consequence of the high hydraulic gradient when the length of drainage path became too short.

Bienen et al. (2018b) investigated the hydraulic installation and monotonic bearing behaviour in a geotechnical centrifuge. Two different pore fluids, i.e. silicone oil and water with cellulose ether, were utilised in order to increase the viscosity. During installation, a minimum flow rate was identified to reach the pursued embedment depth. Slight plug heave but negligible loosening of the soil inside the suction bucket was observed. Both aspects were deduced from the achieved mean embedment depth of $|z/L| = 0.9$ with some tests reaching $|z/L| \approx 1$ and the application of calculation methods, where the best agreement was found when neglecting higher permeability inside the suction bucket as

a result of the loosening of the soil. The monotonic tests were conducted by applying a constant displacement rate. The drained response was found to be affected by the previous cyclic loading, where high compressive loads caused downward movement along with densification of the soil (in accordance with Kelly et al., 2006b), which led to higher drained resistance. The undrained tests were limited by cavitation, whereby tests under partially drained conditions reached only slightly lower tensile resistances. Unfortunately, readings of the negative differential pressure are not provided.

The study of Bienen et al. (2018a) on the cyclic bearing behaviour by centrifuge testing accompanies the one of Bienen et al. (2018b). A strong interrelation between mean load, load amplitude and drainage was determined. But also the load history was found to affect the cyclic response. No displacement occurred as long as the tensile loads did not exceed the drained resistance and still negligible displacement appeared if the loads doubled the drained resistance (while mean load is compressive). Low mean loads, which were slightly compressive or tensile, in conjunction with a cyclic amplitude reaching the drained tensile resistance at the most invoked inevitably upward displacement. For high magnitude cyclic loading, the direction of displacement varied as a matter of drainage. By way of explanation, more drainage required further displacement to generate negative differential pressure to withstand the tensile load and thus displaced upwards, but if drainage was constrained, the displacement might be even downward. Although an undrained behaviour was identified by analysing the load sharing between the suction bucket's skirt and lid, none or negligible accumulation of negative differential pressure was measured. Stiffer response was observed for higher compressive mean loads and more undrained conditions. To ensure an appropriate context of the cyclic tests, the cyclic load sequence used in Kelly et al. (2006b) was adopted and a successful comparison of the results is provided. It is evident that these tests were only considered for comparison, since all other tests exhibit much lower load magnitudes. Finally, Bienen et al. (2018a) concluded that cyclic tensile loads must be avoided as long as the complex interaction is not fully understood.

Wang et al. (2019) presented results of centrifuge tests, which were focused on the drained compressive and tensile resistance for four different aspect ratios. The tensile resistance was found to substantially increase with the aspect ratio. Beside the higher stresses in deeper embedment depth and larger skirt area, the soil inside the suction bucket is more constrained in slender models and the effective stresses are magnified due to the mechanical installation. The back-analysis pointed out that the tensile friction was lower than the compressive one. Since the model did not have drainage openings on the lid and no measurement of the negative differential pressure is provided, it is difficult to assess whether unhindered drainage was present.

Jeong et al. (2020) investigated the drained response to cyclic loading at low magnitude in a geotechnical centrifuge. The maximum loads were defined to be $\bar{F}_{max} = 0.3$ and $\bar{F}_{max} = 0.5$ to represent fatigue limit state (FLS) and SLS respectively. Upward displacement was measured for swell loads and alternating SLS-loads accompanied by major reduction of the stiffness within the first ten cycles, whereby the loss of stiffness was more pronounced for alternating loads. Despite drainage holes on the lid and the objective of drained condition,

Jeong et al. (2020) often considered the occurrence or accumulation of differential pressure as a possible reason for the observed behaviour. Firstly, it is questionable whether entire drainage will take place under prototype condition and secondly, the potentially existing, but not measured differential pressure constricts the usability of the results.

Numerous physical model tests on suction bucket foundations were conducted in the past. There is general agreement in the following aspects. The monotonic tensile resistance depends on the drainage condition and the dilation of the soil, which are affected by the displacement rate and the effective stresses in the soil respectively. Substantial tensile resistance can be generated in partially drained to undrained condition, but the displacement to mobilise the particular resistance is up to $0.1D$ and therefore breach the SLS. The potential for cavitation is discussed controversially and is a relevant issue in model tests. However, it is not expected to be critical in-situ, where the water depth exceeds 35 m, permeable soils are present and realistic load rates apply so that partial drainage takes place. Moreover, the tensile stiffness is lower than the compressive one for both monotonic and cyclic loading and depends on the load magnitude, load rate as well as number of cycles (and consequently changes over the lifetime of an OWT). In terms of cyclic loading, the suction bucket displaces continuously downwards even if parts of the cyclic load are tensile, provided that the counteracting compressive loads are large (although the practical relevance of the high magnitude of the compressive loads is not verified). The reduction of the compressive mean load, in particular zero or tensile mean loads, invokes continuous upward displacement causing inevitable extraction of the suction bucket if the cyclic load is maintained. However, it has to be noted that the displacement rates are very low for specific load magnitudes. It can be concluded that the SLS is critical for axially loaded suction bucket foundations and tensile loading dictates the design.

Despite the relevancy of physical model tests, it is essential to verify these measurements with observations from prototypes. Shonberg et al. (2017) presented selected findings from the monitoring of a prototype at Borkum Riffgrund 1 over a period of seventeen months. In this time, none of the suction buckets experienced tensile loading, but still relevant insights were pointed out. The stiffness depended non-linearly on the wind direction, but also on the load magnitude, with decreased stiffness for substantially low loads. An accurate analysis of the vertical response requires the consideration of an appropriate stiffness of the suction bucket's lid and skirt (Shonberg et al., 2017). During storm, neither the vertical stiffness was observed to degrade nor did the differential pressure accumulate. The magnitude of the vertical cyclic load was dominated by wave loads. The differential pressure sustained a significant share of the vertical load with only little phase shift, which indicates almost undrained response. The drainage was exemplarily analysed within the frequency domain to identify the transition from drained to undrained behaviour. A transfer function was visualised that highlights the fluent shift of drainage and enables qualitative classification. The results demonstrate undrained behaviour for rather low load frequencies, which is unexpected in the mainly non-cohesive soil, but can be potentially explained by a less permeable layer in the site specific soil strata.

The analysis of the published results of physical model tests revealed partly questionable testing conditions as well as uncertain or insufficient documentation. As a consequence,

the usability of previous model tests is limited. So far, there is no holistic evaluation of the tensile resistance at a wide range of drainage conditions and different model dimension. As a result of both, the present knowledge does neither allow for the utilisation of the partially drained resistance with confidence, nor is it possible to adequately scale the findings of the model tests. Furthermore, there is a lack of comprehensive understanding of the cyclic tensile response, especially in terms of the identification of permissible load magnitudes for distinct number of cycles, whereby even the consideration of a single load cycle, e.g. to be accounted for in ULS, would be an advancement from the current state.

As a conclusion from the literature review concerning physical model tests, the hydraulic installation is essential in order to approximate prototype condition since it affects the soil fabric, especially in small to medium-scale tests. Cyclic preloading at low magnitude may be applied to simulate calm weather situations, where the soil and soil-structure interaction gain strength and stiffness, though it is conservative and thus acceptable to neglect this preloading. The cyclic load parameters shall be defined appropriately to prototype loads, but consider the reduced scale of the model test, since otherwise the measured response does not relate to the actual behaviour. However, precise scaling of the results of physical model tests remains uncertain and it is probably reasonable to establish a method, which is validated for different model scales and adopted to extrapolate the geometric dimensions.

2.3.2 Numerical simulations

Numerical studies on the tensile bearing behaviour of suction buckets by means of finite element (FE) analyses are scarce, but the issue to be analysed can be associated to some extent with investigations of the (cyclic) response of other foundations for OWT. For instance, monopiles or gravity bases were analysed recently and essential features for reliable simulations were pointed out (Grabe et al., 2004; Taşan et al., 2010; Safinus et al., 2011; Cuéllar et al., 2012, 2014). Most importantly, the FE model has to incorporate the multiphase properties of the soil material, whereby it is appropriate to neglect the gas-phase for fully-saturated offshore condition. Therefore, a proper coupling between the effective stresses in the soil and the pore pressure is necessary to regard for changes of soil's stress and stiffness as a result of transient variation of differential pressure due to loading or dissipation (Grabe et al., 2004). The coupling of these two fields necessitates the definition of shape functions with a higher order in displacement field than in pore pressure field to prevent numerical problems, such as volumetric locking, spurious oscillations of pore pressure or even unphysical failure mechanisms (Taşan et al., 2010; Cuéllar et al., 2014). A main objective of the initially mentioned studies is on the investigation of differential pressure accumulation due to cyclic loading with regard to fundamental parameters (i.e. loading frequency, soil's permeability and size of the structure) as well as its effect on the soil's response (i.e. loss of strength and stiffness due to diminishing effective stresses until liquefaction sets on ultimately). The loading of monopiles or gravity bases generates differential pressure mainly due to volumetric strains in the soil as a result of its dilation or contraction. Consequently, sophisticated soil models are required, which are capable of

considering these aspects. In this case, rather simple soil models, e.g. elastic-ideal plastic stress-strain behaviour, invoke elastic changes of the differential pressure and are thus not able to adequately represent the actual soil response.

Early back-analysis of physical model tests on the tensile bearing behaviour of suction buckets by FE simulations were qualitatively adequate, but discrepancies were prevalent (Bye et al., 1995; El-Gharbawy and Olson, 2000). Moreover, the descriptions of the adopted model configurations were insufficient and the modelling techniques were not advanced. For instance, the contact behaviour of the soil-structure interaction at the skirt was neglected by bonding the nodes of the soil elements on the suction bucket's skirt. Furthermore, the interface between the soil surface and the suction bucket's lid was oversimplified by either treating it to be bonded or unbonded without considering continuity of the pore fluid (Deng and Carter, 2002).

The model deployed by Cao et al. (2002) was the first one, which properly took the hydraulic interaction at the suction bucket's lid into account. Two-phase elements with linear elastic properties were introduced, which simulate the water filled gap. To avoid the transfer of effective stresses, but enable unconstrained pore water seepage flow, the stiffness of these elements was set to a very low value and the hydraulic conductivity was chosen to be sufficiently high. The concept of the so called 'water elements' was adopted in subsequent studies (Achmus and Thieken, 2014; Thieken et al., 2014; Mana et al., 2014; Shen et al., 2017; Sørensen et al., 2017). Mana et al. (2014) investigated the effect of the properties of the water elements on the global suction bucket's response. Negligible influence was identified when varying the following properties of the water elements: void ratio, hydraulic conductivity, Poisson's ratio and mesh density. Exclusively the stiffness of the water elements essentially affects the results and consequently has to be sufficiently small to eliminate potential effect on the local and global response. Alternatively, interface elements can be defined, which are able to transfer the pore pressure between the interacting surfaces and allow for separation of the contact pair while maintaining continuity of the pore fluid to imitate the water filled gap (Cerfontaine et al., 2015b,c). The definition of the general soil-structure interaction itself is challenging as well. The modelling of concave and convex corners of the interacting surfaces leads to over-constrained nodes in the FE mesh and may cause numerical instabilities.

The loading of the suction bucket induces volumetric strains in the soil along with changes of the void ratio e. Since the permeability of the soil depends on its void ratio, the bearing behaviour of the suction bucket is potentially affected by changes of the permeability. Carrier (2003) discussed the approach of Kozeny and Carman, which provides an equation $k = \eta(e)$ that was adopted in several studies (Achmus and Thieken, 2014; Thieken et al., 2014; Shen et al., 2017; Taşan and Yilmaz, 2019). Beside the hydraulic conductivity, the compressibility is an essential property of the pore fluid. Although it is adequate for many geotechnical problems to consider water as incompressible, it has to be kept in mind that this simplification implies an immediate presence of the flow field rather than its continuous development over a distinct period of time. Except for the studies of Sørensen et al. (2017) and Taşan and Yilmaz (2019), the compressibility of the pore fluid was either neglected or not explicitly stated in the publications.

The mechanical properties of the suction bucket are of subordinate importance supposing that the focus is on the investigation of the geotechnical response. Thus, it is acceptable to assume the suction bucket as rigid body or at least assign a relatively high elastic modulus. Nevertheless, the suction bucket's skirt is thin in comparison to its diameter (typically in the range of $d/D \approx 0.003$), which leads to issues in terms of discretisation and distortion of the FE mesh. To overcome these difficulties, Shen et al. (2017) and Cerfontaine et al. (2014) adopted larger thicknesses of $d/D = 0.0125$ and $d/D = 0.0375$ respectively. Based on the model of Cerfontaine et al. (2014), Cerfontaine et al. (2015a) reduced the skirt thickness to $d/D = 0.0125$ and introduced a so called 'elastic toe', i.e. the soil is defined to behave linear elastic in the vicinity of the skirt's tip, to compensate for the overestimated skirt thickness (also adopted by Shen et al., 2017). However, none of the studies provided evidence that the 'elastic toe' does not affect the tensile bearing behaviour. Furthermore, the thin skirt is exposed to considerable longitudinal strains, which lead to less relative displacement in the soil-structure interface. This is particularly evident in greater embedment depth and affects the mobilisation of frictional resistances. Consequently, the overestimation of the skirt's thickness causes less strains and thus facilitate frictional resistance.

Simulations of suction buckets subjected to monotonic tensile loads were published in Thieken et al. (2014). The FE model was validated with the test results of Iskander et al. (1993) and Houlsby et al. (2006), but major uncertainties were identified regarding the latter so that it was categorised to be unsuitable for this purpose. A sophisticated constitutive law (hypoplasticity) and geometric non-linearity, which is relevant for the large displacements of up to $\Delta z/D = 0.02$, were adopted. Numerous simulations with different displacement rates revealed significantly larger tensile resistances for higher displacement rates. Further, the soil's permeability and the geometry of the suction bucket were identified to mainly affect the tensile response. The authors developed interaction diagrams, where the resistance including the load sharing can be evaluated based on the displacement rate and displacement (see Figure 2.10). It is evident that higher displacement rates invoke larger resistances, which mainly result from the increasing suction force. Moreover, the complex interaction of the frictional resistances is revealed, where the outer friction tends to increase under partial drainage, but decreases under undrained condition (while the inner friction behaves vice versa). Additionally, the responses to constant tensile forces were investigated. A load less than the drained resistance invoked an initial displacement along with negative differential pressure as a result of the relatively high load rate. The displacement did not progress further and the differential pressure dissipated quickly as soon as the constant load was reached. For loads exceeding the drained resistance it was found that the larger the applied load is, the higher is the resulting displacement rate and the more negative differential pressure is generated. Although the investigations of Thieken et al. (2014) are comprehensive, the FE model has some deficits. For instance, the shape functions of the elements have the same order and the Poisson's ratio of the 'water elements' is close to 0.5, which usually requires the use of an appropriate hybrid element-formulation. Both aspects may induce numerical problems and can lead to inaccurate results. Furthermore, the soil-structure interaction implies a considerable elastic slip, which provides numerical stability, but is not physically reasonable.
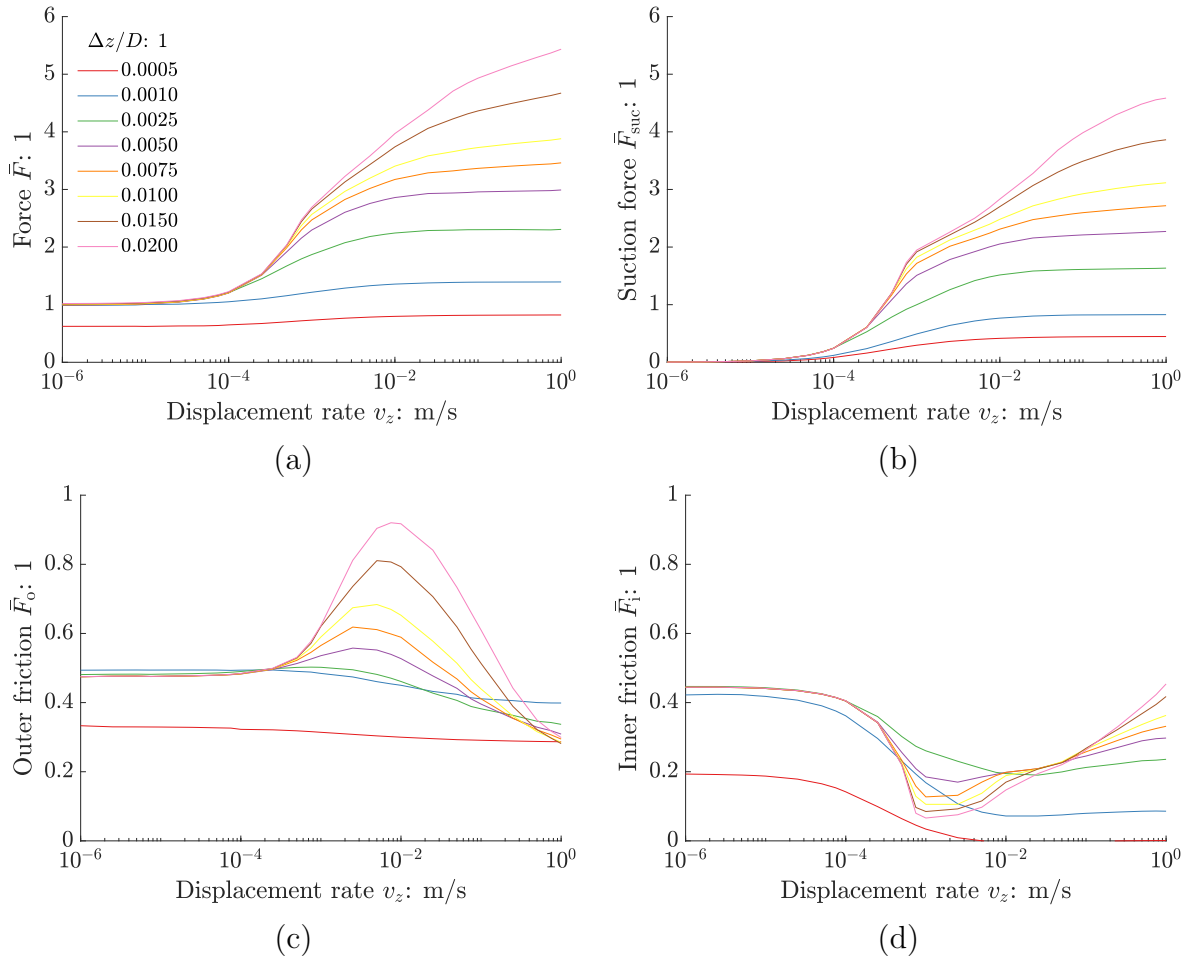
Figure 2.10: Interaction diagram with total resistance (a), suction force (b), outer friction (c) and inner friction (d) (following Thieken et al., 2014).

The study of Achmus and Thieken (2014) is based on the one of Thieken et al. (2014), but puts emphasis on the soil's liquefaction if the upward hydraulic gradient inside the suction bucket i_i exceeds the critical gradient $i_{cr} = \gamma'/\gamma_w$. Therefore, the authors defined an upper bound solution, where gradients $i > i_{cr}$ are possible and a lower bound solution, where the hydraulic gradient is limited to $i \leq i_{cr}$ by artificially increasing the soil's hydraulic conductivity. Marginal difference was found between both cases except for very high displacement rates and large displacements, where the substantial increase in permeability in the lower bound solution enables more dissipation inside the suction bucket so that the global response is more drained than in the upper bound solution. As a consequence, the inner friction is significantly reduced due to the lower effective stresses. Achmus and Thieken (2014) explained that this simplified approach does not take the stress state of the soil into account. The presence of effective stresses would prevent the soil from liquefying and thus the permeability from increasing. As a consequence, it was concluded that the upper bound solution is more accurate. Additionally, the authors stated that the applicable displacement of the suction bucket is limited by distortions of the finite element mesh.

Sørensen et al. (2017) investigated the monotonic tensile response by comparing three different FE formulations, from which two are dynamic formulations regarding for inertial forces on the pore fluid. In general, this study confirmed the findings of Thieken et al. (2014). The authors assessed the dynamic formulations to be of minor relevance for most of the considered displacement rates, except for highest ones, where inertia slightly influences the negative differential pressure beneath the suction bucket's lid. The results in terms of the resistances obtained by the dynamic simulations exhibit major oscillations. Thus, stability of these simulations may be a relevant concern.

Shen et al. (2017) presented results of a study on the monotonic tensile response, which is similar to Thieken et al. (2014) but utilised a bounding surface model based on critical state soil mechanics (SANISAND) and adopted questionable features from Cerfontaine et al. (2014, 2015a, 2016) (such as oversized skirt thickness and elastic toe). Although the results of Shen et al. (2017) generally confirmed the findings of Thieken et al. (2014), the undiscussed presence of negative inner friction under undrained condition and the discontinuous development of the frictional resistances at partially drained conditions are critical. The latter may be an example of instabilities resulting from the choice of an inappropriate element type with equal orders of the shape functions. Nevertheless, the analysis of the radial stress state under drained condition and comparison with an analytical approach (see Houlsby et al., 2005b, explained in subsection 2.3.3) give valuable insights into the stress relief.

While it is not straightforward to model the monotonic response of suction buckets, the simulation of the cyclic bearing behaviour is even more complex. The load characteristics (i.e. direction, magnitude, swell or alternating) and drainage are the main parameters defining the demands on the FE model. For instance, to simulate compressive loads, where permanent contact between the suction bucket's lid and the soil can be assumed, there is no need for 'water elements' or coupled interface formulations. The differential pressure results from soil's contraction, but also from rapid loading in comparison to soil's low permeability implying constrained dissipation. For suction buckets subjected to tensile loads, an adequate simulation of the water filled gap is necessary, but after load reversal in case of alternating loads, the minor stiffness of the 'water elements' is likely to produce numerical instabilities so that advanced interfaces are preferred. The implementation of highly sophisticated mechanical material models are more relevant to replicate the drained cyclic response of the soil. But as the drainage is constrained by the soil's permeability, the cyclic response of the suction bucket is likely to be dictated by the hydraulic response. Since the cyclic modelling is an intricate field, Offshore Wind Accelerator (2019) recommends validating numerical methods for cyclic loading against small-scale and field test results. So far, numerical studies on the cyclic bearing behaviour are limited to compressive loading or the occurrence of single tensile load cycles within a cyclic load sequence consisting various amplitudes.

Taşan (2015) investigated the cyclic response of a suction bucket subjected to compressive loading. The soil was modelled as a hypoplastic material with the extension for intergranular strains developed for the evaluation of the soil's response on cyclic excitation. Neither differential pressure accumulation nor progressive displacement was observed in a chosen

reference system. The increase of the load frequency invoked higher differential pressures, but less displacement of the suction bucket. The author concluded that lower frequencies enable dissipation that leads to higher effective stresses in the soil, which finally invoke larger strains.

The study of Taşan and Yilmaz (2019) aimed at the evaluation of installation effects on the cyclic compressive bearing behaviour. Therefore, different lower relative densities, which affect the mechanical and hydraulic properties of the soil, were attributed to the soil inside the suction bucket. Due to the lack of appropriate model tests under axial loading, the verification relied on the retrospective simulation of a cyclic horizontally loaded suction bucket. The authors found that the load sharing varies and higher accumulation of positive differential develops as a consequence of the looser soil inside the suction bucket, but also due to insufficient dissipation between two consecutive load cycles. The initially higher void ratio facilitates more contraction, which enlarges positive differential pressures and induces higher displacements. Furthermore, an interaction between the suction bucket's aspect ratio and the applied load magnitude on the load sharing was identified. Under the highest load magnitude investigated in this study, negative as well as positive differential pressure occurred. Moreover, negative skin friction was observed as the soil's strength inside the suction bucket is reduced due to positive differential pressure so that it displaces more than the suction bucket does.

Cerfontaine et al. (2014) analysed the cyclic response of an axially loaded suction bucket, whereby the compressive mean load was constant and the load amplitude varied so that slight tensile loads were implied in the load sequence. The load signal comprised of packages with different magnitudes and the effect of their arrangement was investigated. The soil was modelled as non-linear plastic material with a non-associated flow rule (Prevost model). The FE model had major simplifications, such as elastic soil behaviour near the surface outside the suction bucket, a load on the soil surface outside the suction bucket to artificially counteract the low stresses in the soil, isotropic initial stress state and a relatively high cohesion in the non-cohesive soil. Moreover, the skirt thickness is massive and the formation of a water filled gap beneath the suction bucket's lid is not considered. Two contact definitions at the inner skirt were analysed, namely without and with the capability of relative displacement. Except for low amplitude loading, where the contact is sticking anyway, the bonded contact definition was found to be not adequate. Despite the strong simplifications, the results are reasonably predicting the displacement and differential pressure development. The displacement was found to be hardly affected by the arrangement of the load packages. In contrast, the differential pressure development revealed different characteristics depending on the incidence of high amplitude loads (invoke differential pressure) and low amplitude sequences (enable dissipation).

The FE model utilised in Cerfontaine et al. (2014) was further developed in Cerfontaine et al. (2015a) and Cerfontaine et al. (2016) by implementing a coupled interface, reducing the skirt thickness and introducing an elastic soil behaviour at the skirt' tip to compensate the still overestimated skirt thickness. The 'elastic toe' was verified for compressive loading, but its necessity and functionality for tensile loading was not explained. For monotonic loading, the effect of different permeabilities and the adopted soil model were

evaluated. In case of tensile loading, it was found that a higher permeability allows for more drainage along with lower resistances and degrading stiffness. Regarding the soil model, the constitutive law is less decisive for tensile loads than for compressive loads, which is probably due to the frictional interaction at the skirt dominating the bearing behaviour. The analysed cyclic loading sequences were identical to Cerfontaine et al. (2014). Less displacement takes place when the applied load is partially drained rather than drained, which is due to differential pressure that bears certain share of the load. After load removal, the differential pressure dissipates and thus less changes in effective stresses are present. The authors distinguished between two consolidation processes, namely the short-term and long-term. While the short-term takes place within the scale of a load cycle and implies large variation of differential pressure, the long-term describes the dissipation of (accumulated) differential pressure that causes displacement due to volumetric strains in the soil.

The results of the previously described numerical simulations generally agree with the observations from physical model tests. Moreover, the analysis of the tensile response of suction buckets by means of FE simulations allows for detailed insights into the complex interaction of soil mechanics and hydraulics as well as the evaluation of the mobilisation of resistances or accumulation trends. These findings are essential to develop design recommendations or analytical calculation approaches. It can be concluded that numerical simulations are a powerful utility for gaining knowledge about the tensile bearing behaviour of suction bucket foundations. So far, there are few numerical studies on the axial bearing behaviour of suction buckets and even less are focused on the tensile response. Thus, the tensile bearing behaviour under various loading conditions was not yet comprehensively investigated by numerical simulations.

It was pointed out that the verification and validation of the FE models require sophisticated physical model tests, but their availability is scarce (Thieken et al., 2014; Taşan and Yilmaz, 2019). Moreover, the relevance to adequately consider certain aspects is evident. While some studies oversimplify the complex and interacting processes or neglect essentials of correctly modelling coupled problems, others clearly identified aspects that can be idealised without major loss of accuracy. The crucial issues to achieve accurate results are the hydraulic-mechanical coupling, appropriate modelling of the soil's hydraulic properties, a mechanical model that regards the fundamental behaviour of the soil and sophisticated modelling of the soil-structure interaction especially regarding the formation of a gap beneath the suction bucket's lid.

2.3.3 Analytical methods

Since model tests and numerical simulations are expensive and require large efforts, the research on suction bucket foundations also aims at deriving simplified analytical methods, which reliably predict the bearing behaviour. The number of studies focused on this aspect is limited until now. Thus, the introduced methods are not yet extensively developed.

Deng and Carter (2002) proposed a simple approach to calculate the tensile resistance of a suction bucket for either undrained, partially drained or drained condition. Since the first two conditions require the undrained shear strength of the soil as an input parameter, solely the drained condition is applicable for non-cohesive soils. The drained tensile resistance is the sum of the inner and outer friction, which is defined in Equation 2.4 assuming that inner and outer diameters are equal. A drained uplift factor was empirically determined by analysing FE simulations. Its purpose is the consideration of the ratio of interface friction angle and the soil's internal friction angle as well as the relation between horizontal and vertical effective stresses in the soil. The integration of Equation 2.4 and insertion of the uplift factor η leads to Equation 2.5. It is remarkable that the drained uplift factor depends on the aspect ratio and Equation 2.5 still implies an earth pressure coefficient ($k_0 = 1 - \sin \varphi'$ according to Jaky, 1948). Deng and Carter (2002) did not provide a physical explanation for the correlation of drained resistance and aspect ratio as it is defined by the drained uplift factor.

$$F = 2\pi D \int_0^L \sigma_r' z \tan \delta \, \mathrm{d}z = 2\pi D \int_0^L \eta k_0 \sigma_z' z \tan \varphi' \, \mathrm{d}z \tag{2.4}$$

$$F = 2.28\pi D^2 \left(\frac{L}{D}\right)^{0.54} (1 - \sin \varphi') \tan \varphi' \sigma_{z,z=-L}' \tag{2.5}$$

Moreover, Deng and Carter (2002) derived a dimensionless drainage parameter to assess the degree of drainage (see Equation 2.6). This parameter accounts for the displacement rate, suction bucket's diameter and the consolidation coefficient c_v, which accounts for soil's consolidation characteristics (see Equation 2.7 with hydraulic conductivity k_f and oedometric stiffness E_s). The analysis of FE simulations led to the definition of distinct boundaries with $T_k < 0.002$ and $T_k > 0.6$ for undrained and drained behaviour respectively (Deng and Carter, 2002). The introduction of a simple procedure to roughly evaluate the drainage condition of a suction bucket is essential. However, the general validity is limited and the approach is applicable only for distinct displacement rates.

$$T_k = \frac{c_v}{v_z D} \tag{2.6}$$

$$c_v = \frac{k_f E_s}{\gamma_w} \tag{2.7}$$

Iskander et al. (2002) distinguished between drained and undrained response of the suction bucket. Under drained condition, the tensile resistance results from friction along the suction bucket's skirt that can be calculated by Equation 2.2 and Equation 2.3. The authors suggested adopting reduced values for the earth pressure coefficient k and effective unit weight of the soil γ' to consider perturbation of the soil, but do not quantify the reduction. For back-analysis of physical model tests, a value of $k = 0.8$ was adopted which is considerably high and does not indicate reduction. If the behaviour is undrained, the soil plug inside the suction bucket is assumed to displace entirely upwards along with the suction bucket. Thus, no inner friction takes place, but the weight of the soil plug

contributes to the tensile resistance. Moreover, the negative differential pressure beneath the suction bucket's lid and outer friction give additional tensile resistance. The outer friction is enhanced by the effect of the downward hydraulic gradient on the weight of the soil $\tilde{\gamma}_o = \gamma' + i_o \gamma_w$. By back-analysis of a model test aiming at verification of the proposed calculation approach, the hydraulic gradient was determined to be $i_o = 2.1$, which is a rather high value.

The analysis of Iskander et al. (2002) was based on two types of model tests. While the drained condition is achieved by an open valve on the suction bucket's lid, it is not proven that totally no drainage occurred in the undrained test, where the valve was closed. Iskander et al. (2002) stated that the displacement rate affects the degree of drainage, but the study investigated solely a single displacement rate for undrained condition. Consequently, the proposed method cannot include the effect of distinct displacement rates. For prototype scale, partial drainage implying relevant plug heave along with certain gap expansion beneath the suction bucket's lid is more likely to take place rather than unmitigated plug heave. In addition, the calculation method for undrained condition neglects that the failure mechanism may transfer to a wider region outside the suction bucket (see Figure 2.3).

Houlsby et al. (2005b) provided methodologies to determine the tensile resistance for drained and partially drained conditions, but excluded the undrained resistance since cavitation in dilative sands is expected to always occur prior to the undrained failure. The calculation of the frictional resistance includes the stress relief due to upward shear stresses at the suction bucket's skirt as depicted in Figure 2.11. The proposed approach faces the previously described overestimation of the frictional resistance in Equation 2.2 and Equation 2.3. Therefore, the equilibriums of vertical stresses inside and outside the suction bucket were analysed separately assuming that the vertical stresses in the soil do not vary in radial direction and there are no shear stresses in the vertical plane at nD_o. This leads to Equation 2.8 for inside and Equation 2.9 for outside the suction bucket. The sum of the integrated Equation 2.8 and Equation 2.9 results in the drained resistance as given by Equation 2.10 (for constant n and with $\eta(x) = \exp(-x) - 1 + x$), whereby following substitutions apply: $Z_i = D_i/(4(k\tan\delta)_i)$ and $Z_o = D_o(n^2 - 1)/(4(k\tan\delta)_o)$.

$$\frac{\mathrm{d}\sigma_z'}{\mathrm{d}z} = \gamma' - \frac{4\sigma_z'(k\tan\delta)_i}{D_i} \tag{2.8}$$

$$\frac{\mathrm{d}\sigma_z'}{\mathrm{d}z} = \gamma' - \frac{4\sigma_z'(k\tan\delta)_o}{D_o(n^2-1)} \tag{2.9}$$

$$F_{\mathrm{dr}} = \gamma' Z_o^2 \eta\left(\frac{L}{Z_o}\right)(k\tan\delta)_o \pi D_o + \gamma' Z_i^2 \eta\left(\frac{L}{Z_i}\right)(k\tan\delta)_i \pi D_i \tag{2.10}$$

Partial drainage invokes negative differential pressure that firstly generates resistances beneath the suction bucket's lid and at the skirt's tip and secondly affects the frictional resistance by changes of the soil's weight. Houlsby et al. (2005b) considered these aspects in Equation 2.11. Empirical relations to calculate the negative differential pressures
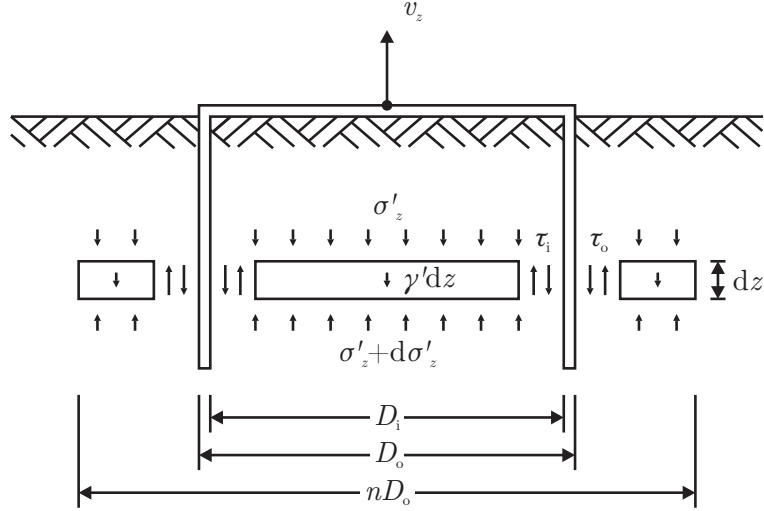
Figure 2.11: Vertical equilibrium in the soil along with skin friction at the suction bucket's skirt (following Houlsby et al., 2005b).

were derived from numerical simulations for different boundary conditions. These simulations assumed that the gap expansion is identical to the displacement of the suction bucket, which is unlikely under partially drained conditions (see Figure 2.3). The hydraulic gradients were supposed to be constants (i.e. linear distribution of differential pressure along the skirt's inside and outside) and were defined by $i_o = \Delta u_{tip}/(\gamma_w L)$ and $i_i = (\Delta u - \Delta u_{tip})/(\gamma_w L)$. Furthermore, the authors stated that it is appropriate to neglect the additional resistance due to negative differential pressure at the skirt's tip since the thickness and thus the area is small.

$$
\begin{aligned}
F = & \Delta u \frac{\pi D_i^2}{4} \\
& + \Delta u_{tip} \frac{\pi \left(D_o^2 - D_i^2\right)}{4} \\
& + \left(\gamma' + i_o \gamma_w\right) Z_o^2 \eta \left(\frac{L}{Z_o}\right) (k \tan \delta)_o \, \pi D_o \\
& + \left(\gamma' - i_i \gamma_w\right) Z_i^2 \eta \left(\frac{L}{Z_i}\right) (k \tan \delta)_i \, \pi D_i
\end{aligned}
\tag{2.11}
$$

Houlsby et al. (2005b) distinguished four cases in partially drained conditions, which can be treated as specifically simplified cases of Equation 2.11. The corresponding failure mechanisms are: small displacement rate (a), liquefaction without cavitation (b), cavitation without liquefaction (c) and cavitation with liquefaction (d). These cases can only occur in the following orders: (a)-(b)-(d) or (a)-(c). Although cavitation limits the negative differential pressure in model tests, its occurrence in deeper waters is rather unlikely. Since the proposed approach is not limited by an undrained failure, solely the onset of liquefaction constrains the tensile resistance. However, the occurrence of liquefaction of
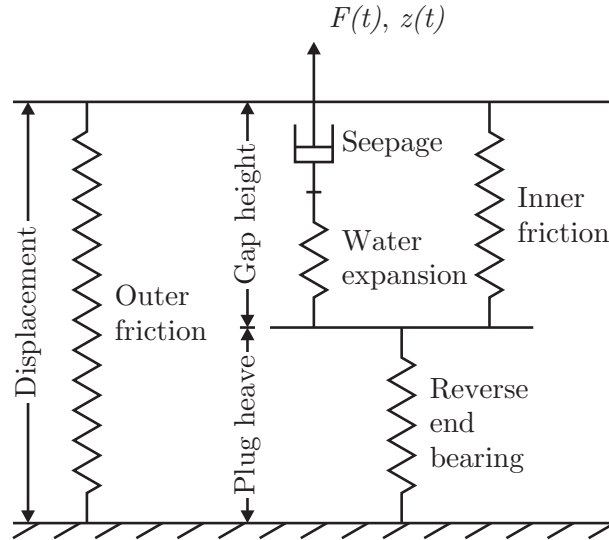
Figure 2.12: Arrangement of springs and damper in analytical model (following Senders, 2009).

the enclosed soil inside the suction bucket is questionable, since the suction bucket restricts the required volumetric expansion of the soil. Moreover, the neglect of plug heave for calculating the negative differential pressure causes overestimation. This effect magnifies the less drainage takes place. According to Houlsby et al. (2005b), the term $k \tan \delta$ is always considered jointly, despite both quantities are independent variables. Although the method enables the determination of the tensile resistance for particular displacement rates and failure mechanisms, it is not possible to assess the suction bucket's response to distinct tensile forces and the load-displacement response remains unknown.

Senders (2009) analysed the tensile bearing behaviour of suction bucket foundations under various drainage conditions as described in section 2.2 and derived an analytical model, which replicates the observed response (see Figure 2.12). The model consists of four springs and one damper. The individual elements of the model are passive or active depending on the drainage condition as summarised in Table 2.2. While the forces in the linear springs (outer and inner friction as well as water expansion) are limited by sliders (not depicted in Figure 2.12), the force of the spring that represents the reverse end bearing (REB) is constrained by its non-linear definition. The maximum frictional resistances are related to the integrated cone resistance profiles measured in cone penetration testings (CPTs). Furthermore, the maximum inner friction is linearly reduced by the ratio of negative differential pressure to the critical negative differential pressure that would invoke hydraulic failure (under quasi-static condition). The negative differential pressure itself is limited by cavitation.

The vertical stiffnesses of the inner and outer friction as well as REB are adopted from Doherty and Deeks (2003) and Doherty et al. (2005), who analysed the stiffness of rigid and flexible embedded foundations in elastic soil by means of numerical simulations. The allocation of these stiffnesses seems inaccurate since an overestimation of the differential pressure development was observed except for the undrained case. The water expansion depends essentially on the bulk modulus of water. However, Senders (2009) justified a

Table 2.2: Response of analytical model to different drainage conditions (following Senders, 2009).

Resistance	Drainage condition		
	drained	partially drained	undrained
Outer friction	active	active	active
Reverse end bearing	$\Delta z_{\mathrm{plug}} \approx 0$	active	$\Delta z_{\mathrm{plug}} \approx \Delta z$
Inner friction	active	active	$F_{\mathrm{in}} \approx 0$
Water expansion	$\Delta u \approx 0$	active	active
Seepage	$\Delta z_{\mathrm{gap}} \approx \Delta z$	active	$\Delta z_{\mathrm{gap}} \approx 0$

reduced stiffness of this element by potentially enclosed air beneath the suction bucket's lid, but also to provide stabilisation of the model. The damper coefficient is defined as a function of the soil's hydraulic conductivity and the length of drainage path.

Although the basic idea of the model proposed by Senders (2009) is sophisticated, severe deficits exist concerning its realisation. The model requires numerous parameters, but gives no strict specification on how to determine those. This aspect is evident from the back-analyses of physical model tests at different scales, where adjustments of the input parameters led to sophisticated results (Senders, 2009). These arbitrary alterations diminish the reliability of the model. In terms of the formulation, the description is insufficient to allow for straightforward implementation. Senders (2009) discussed multiple approaches defining the individual elements so that it is uncertain which equations are to be used. Furthermore, it was not stated whether specific parameters have to be calculated for each increment or only at the initial state. Moreover, the basic formulation of the model solely determines the response of the suction bucket subjected to certain displacement and the application of distinct time-dependent force is not included. With regard to the soil-structure interaction, only the maximum inner friction, but not the elastic response of the spring, is reduced by the occurrence of negative differential pressure (Senders, 2009). The assumed critical negative differential pressure is probably not appropriate for transient tensile loading, where the pore fluid flow is not constant. Moreover, the plug heave depends directly on the negative differential pressure, which may decrease as the suction bucket displaces upwards. Consequently, the plug heave would reduce as well, which is not reasonable since the soil plug will not lower once it has displaced.

Vaitkunaite et al. (2015) reviewed the calculation methods for determining the drained tensile resistance of suction buckets, whereas the methods of Senders (2009), Houlsby et al. (2005b), DNV No. 30.4 (β-approach) and ANSI/API RP 2GEO (four CPT-approaches) were regarded. The last two methods were originally established for piles and thus are not explicitly valid for suction buckets. It was found that the calculated tensile resistances differ significantly from one method to the others and that the results are also oversensitive on the aspect ratio. The method of Senders (2009) predicts the lowest tensile resistance in comparison to the other methods but provide good estimations of medium-scale model tests. Nevertheless, it has to be noted that the back-analyses of the model tests with the methods of Houlsby et al. (2005b) and DNV No. 30.4 led to substantially higher earth

pressure coefficients than the commonly adopted equation $k_0 = 1 - \sin\varphi'$ according to Jaky (1948). Especially the methods according to ANSI/API RP 2GEO are not capable to reliably estimate the drained tensile resistance and thus were declared inapplicable.

As it is described in subsection 2.3.1 and subsection 2.3.2, the mobilisation of the maximum tensile resistance needs certain displacement. Therefore, the required displacement might exceed the tolerable level in terms of the SLS. Thus, it is essential to predict the initial stiffness of the foundation or at least the necessary displacement to mobilise particular resistance. Furthermore, the mobilisations of skin friction and differential pressure are not identical and should be considered individually. As a consequence of these aspects, the methods of Deng and Carter (2002), Iskander et al. (2002) and Houlsby et al. (2005b) provide partly reasonable estimations of the tensile resistance, but are unsuitable for the detailed design of suction bucket foundations. Senders (2009) developed a promising approach, though the model exhibits deficiencies and suffers from inaccuracies. However, an efficient and consistent formulation as well as implementation of the model, but also an appropriate calibration of the parameters would significantly improve the model of Senders (2009). Further enhancements would be the ability for simulating both displacement-controlled and force-controlled loading, which could be even transient in further developments of the model. The explicit formulation and effective application would be great benefits of such an advanced analytical method for estimating the tensile bearing behaviour. This has to be seen within the context of high efforts to conduct physical model tests or FE simulations.

2.3.4 Scale analyses

Buckingham (1914) introduced a theorem for dimensional analysis of physical similarities, which was described and adapted for geotechnical application by Butterfield (1999). The dimensional analysis of a particular problem provides dimensionless groups of independent physical variables that govern the response of the underlying system. The dimensionless groups are frequently adopted for the design of scaled physical model tests or the evaluation of results from those as it was applied by Kelly et al. (2006a) for suction buckets. In terms of the axial resistance, the bearing capacity in non-cohesive soils scales by $\gamma'(0.5D)^3$ for densities that relate to similar bearing capacity factors at different scales (Kelly et al., 2006a). Similarity of bearing capacity factors can be obtained by lower densities at smaller scales taking the non-linear soil's internal friction angle into account. Kelly et al. (2006a) remarks that this aspect is less relevant as long as the applied loads are significantly lower than the maximum resistance.

The consideration of the stiffness leads to a dimensionless relation for vertical loading (see Equation 2.12 according to Kelly et al., 2006a). The stiffness exponent λ describes the non-linearity of the soil's stiffness, which is defined by Equation 2.13 as a function of the vertical effective stress σ'_z (Ohde, 1939). According to Equation 2.12, the response of a suction bucket shall be akin at different scales for similar normalised mean loads F_{mean}, aspect ratios L/D and soil's stiffness parameters κ and λ. The first two parameters are implied in the dimensionless function η. The derivation of this scaling approach is straightforward

and relatively simple. Although Kelly et al. (2006a) proved the comparability of tests at different scales, the application of this method did not provide perfect agreement. This imperfectness probably relates to different soil conditions and testing procedures (such as installation methods and load rates affecting drainage). For instance, it was found that the installation method substantially affects the bearing behaviour and that mechanical installation is detrimental specifically at small scale (Kelly et al., 2006a). Beside the high degree of simplification, the lack of regarding the actual drainage condition makes this method probably unsuitable for design purposes.

$$\frac{F}{\gamma' D^3} = \frac{\Delta z}{D} \left(\frac{p_{\mathrm{atm}}}{\gamma' D} \right)^{1-\lambda} \eta \left(\frac{F_{\mathrm{mean}}}{\gamma' D^3}, \frac{L}{D} \right) \tag{2.12}$$

$$E_{\mathrm{s}} = \kappa \sigma_{\mathrm{atm}} \left(\frac{\sigma_z'}{\sigma_{\mathrm{atm}}} \right)^{\lambda} \tag{2.13}$$

Kelly et al. (2006b) proposed an approach, which is based on the one-dimensional consolidation theory, to assess the drainage of model tests with regard to prototype condition (see Equation 2.14). The dimensionless time T_{v} incorporates the consolidation coefficient c_{v} as defined in Equation 2.7, the length of the drainage path l_{dr} and the time t required for a particular dissipation of differential pressure. Kelly et al. (2006b) concluded that if the dimensionless times at different scales are alike, similar drainage characteristics exist.

$$T_{\mathrm{v}} = \frac{c_{\mathrm{v}} t}{l_{\mathrm{dr}}^2} \tag{2.14}$$

To evaluate Equation 2.14, the following assumptions according to Kelly et al. (2006b) apply: the oedometric stiffness exhibits proportionality for $E_{\mathrm{s}} \propto (\sigma_z')^{\lambda}$, the length of the drainage path and the vertical stress are both proportional to the suction bucket's diameter, i.e. $l_{\mathrm{dr}} \propto D$ and $\sigma_z' \propto D$. Taking these relations into account and inserting Equation 2.7 in Equation 2.14, Equation 2.15 is obtained. Thus, the quantities of hydraulic conductivity, geometric dimension and time become comparable for different scales (with subscripts m and p representing model and prototype scale respectively). This also makes it possible to assess the validity of chosen boundary conditions in model tests. As evident from Equation 2.15, higher load rates or lower hydraulic conductivity at smaller scale are necessary to obtain similar drainage condition.

$$\frac{k_{\mathrm{f,m}}}{k_{\mathrm{f,p}}} = \frac{t_{\mathrm{p}}}{t_{\mathrm{m}}} \left(\frac{D_{\mathrm{m}}}{D_{\mathrm{p}}} \right)^{2-\lambda} \tag{2.15}$$

The shortcomings of the approach of Kelly et al. (2006b) are that it neglects the multidirectional seepage flow and assumes the length of drainage path to be proportional to the diameter of the suction bucket. However, it is more likely that under cyclic loading the

pore water seepage flow is not fully developed per cycle and frequently changes direction implying a much shorter length of drainage path. Nevertheless, for monotonic loading the proposed approach is probably more suitable since the seepage flow can be entirely mobilised. Moreover, the soil's stiffness is supposed to increase identically with effective stress for both scales, which is unlikely especially for different soils, soil's densities and stress states.

The presented methods for scaling of physical model tests reveal that it is difficult or even not possible to derive an appropriate scaling approach, which accounts for multiple essential aspects. Although the applicability was proven for particular examples and qualitatively sophisticated results were achieved with these methods, they still imply significant simplifications. Consequently, their general validity is constrained. It is questionable whether the complex tensile response of a suction bucket can be idealised by simple analytical equations. The results obtained from centrifuge testing overcome some major problems related to scaling, but other issues restraining the transferability and applicability were pointed out. Another alternative are numerical simulations with FE models at prototype scale, but these require highly sophisticated measurements for verification and validation. Observations at prototypes in field provide the most valuable results, but these data are scarce and mostly confidential. Finally, a great need is evident for an appropriate methodology that takes scaling issues into account.

2.4 Current design recommendations

The design of suction bucket foundations has to be consistent with relevant international (DIN EN ISO 19901-4:2017-01), European (DIN EN 1997-1:2014-03) and national (DIN 1054:2010-12; DIN 18088-4:2019-01) standards. Except for DIN 18088-4:2019-01, these standards do not refer specifically to suction bucket foundations. However, DIN 18088-4:2019-01 provides no particular guidance on the design and testifies the lack of generally accepted design methods. Consequently, the observation method according to DIN EN 1997-1:2014-03 for SLS and ULS is recommended alternatively (DIN 18088-4:2019-01).

The observation method stipulates the prediction of the expected foundation response, specification of distinct limits, which are monitored by a measuring system, along with associated mitigation measures. Therefore, it is suggested to utilise an appropriate numerical model to predict the bearing behaviour of the suction bucket (DIN 18088-4:2019-01). Especially the cyclic degradation in terms of differential pressure accumulation, displacement accumulation or loss of resistance are to be considered in the adopted method. The application of the observation method is in line with BSH No. 7005 and the utilisation of FE simulations is permissible according to DIN 1054:2010-12. However, it is remarked that complex processes can be modelled qualitatively, but quantitative replication is not necessarily reliable and that FE models imply relevant uncertainties and simplifications (BSH No. 7005). Thus, validation of the adopted models is essential, but as measured data from prototype is rare, comparisons with analytical methods along with sensitivity studies are recommended.

DNV-OS-J101 and DNVGL-ST-0126 refer to suction bucket foundations for multipod OWTs and suggest designing the foundation as gravity bases after completed installation. The description of suction buckets in DNVGL-ST-0126 is rather general and no particular procedures for the design are provided. It is classified that suction bucket foundations are not covered by available standards and individual evaluation is required. Essential aspects for the design are: the identification of drainage condition with reasonable confidence or conservative assumption instead, consideration of cyclic strength degradation for different load magnitudes (FLS potentially invoke strength increase, but ULS probably decrease strength), simultaneous regard of differential pressure accumulation and dissipation (both affect tensile resistance). These aspects are recommended to be assessed by means of FE simulations or model tests.

Most currently and specifically dedicated for suction bucket foundations for OWTs are the design guidelines of Offshore Wind Accelerator (2019), which summarise recommendations in terms of design principles, geotechnical investigations, loads, installation, operation and decommission. Regarding the tensile bearing behaviour, Offshore Wind Accelerator (2019) discusses drainage conditions, resistances, cyclic loads and load magnitudes, which are summarised in the following. The degree of drainage is determined by comparing a characteristic drainage period (similar to Equation 2.14) with the load period for distinct load cases. Although this procedure enables simple qualitative evaluation of drainage, the detriments discussed in subsection 2.3.4 apply. The drained tensile resistance is calculated by $F_{\mathrm{dr}} = F_{\mathrm{o}} + F_{\mathrm{i}}$ as defined in Equation 2.2 and Equation 2.3 optionally along with stress relief as proposed by Houlsby et al. (2005b) (see subsection 2.3.3). The undrained condition assumes cavitation to take place either beneath the lid or at the skirt's tip. As described in subsection 2.3.3, both approaches oversimplify the actual response. The effects of cyclic loading are commonly regarded by factors reducing strength, but more sophisticated approaches such as FE analyses are applicable to investigate cyclic accumulation of displacement or differential pressure. However, these FE models require validation and benchmarks by physical modelling.

In terms of the consideration of tensile loads, Offshore Wind Accelerator (2019) proposes multiple positions. Tensile forces exceeding the drained resistance may be considered within design, but care has to be taken for substantial displacement. However, no recommendations are provided on how to determine the displacement accumulation or the appropriate tensile resistance under partial drainage. It is qualitatively stated that for quantifying the tensile resistance, the following aspects must be considered: mean load, maximum load, number and duration of tensile cycles and drainage condition. Contrarily, it is also recommended omitting tensile loads or limit their magnitude to the drained resistance in order to keep displacements low. More specifically, it is suggested to consider tensile loads to nothing else than ULS due to the fatal failure mechanism in tensile cyclic loading. This statement is in line with DIN 18088-4:2019-01, where tensile resistances exceeding the drained resistance may be considered in the ULS-design. In particular, an increase of the suction bucket's resistance resulting from negative differential pressure can be considered up to $0.75p_{\mathrm{cav}}$, but the actual water depth, drainage condition and effects on subsoil as well as soil-structure interaction have to be regarded (DIN 18088-4:2019-01).

It is evident that the applicability of suction bucket foundations for OWTs is not only limited by lack of holistic knowledge on its response to tensile loads, but also by insufficient regulation within the scope of dedicated standards. The second aspect is a consequence of the first. No generally accepted design procedure was developed so far partly as a result of incomplete understanding of the complex tensile bearing behaviour. The consideration of the suction bucket's tensile resistance within the design is essential since otherwise the large spacing would make the application of multipod suction bucket foundations uneconomical (Achmus and Schröder, 2014). These aspects highlight the need for detailed investigations of this issue and the elaboration of an appropriate design method to be considered in common standards and guidelines.

3 Physical modelling

3.1 Model set-up

3.1.1 Scaling considerations

Physical model tests have to be designed appropriately to fulfil a given purpose. For instance, the following aspects have to be accounted for: functionality of all features and repeatability of the results must be ensured, the testing campaign has to be planned carefully to investigate the most relevant aspects, and the measurements must provide precise as well as evaluable data. Moreover, considerations in terms of scaling are of significant importance. It is usually not possible to adequately scale every physical dimension, but the most essential ones have to be regarded. In case of model tests on tensile-loaded suction buckets, beside the geometric dimensions, the hydraulic properties and stress state of the soil are relevant aspects to be considered. However, subsection 2.3.1 and subsection 2.3.4 highlighted that there is no generally accepted procedure to correctly scale the complex bearing behaviour of suction buckets subjected to tensile loads.

The physical model tests presented in here pursue an alternative approach. It was chosen not to aim at transferring the results via scaling laws to potential responses of a suction bucket under equivalent loading at prototype dimensions, but to adopt the measurements and findings of the model tests to develop and validate a sophisticated finite element (FE) model. Therefore, different model dimensions were tested and back-analysed by means of numerical simulations, which verified the scaleability of the FE model. Furthermore, the different model dimensions were subjected to similar loading conditions to directly compare the results and to qualitatively evaluate the effect of the scale, but not to derive a particular scaling law.

The dimensions of the different models are summarised in Table 3.1 with the names of the models representing their lengths L and diameters D both in mm. The model with the largest dimensions was expected to provide the most reliable results and was thus used for most of the tests. It has to be remarked that the suction bucket models had some geometric imperfections, which were most evident at the largest model (i.e. the model is not perfectly circular in plan view at tip level and thus, the skirt is not absolutely vertical in part). Although the potential impact on the observed tensile bearing behaviour cannot be determined, a locally larger subsidence of the soil in proximity to the imperfection was noticed after every installation.

Table 3.1: Dimensions and weights of the models.

Name	Length L: mm	Diameter D: mm	Skirt thickness d: mm	Buoyant mass m: kg
L500D510	500	510	5	85
L250D510	250	510	5	65
L250D260	250	260	5	27
L125D135	125	135	5	14

The low stresses in dense granular soil imply significant potential for dilation and highly affect shear strength as well as stiffness of the soil (see subsection 2.3.1). As a consequence, the results cannot be extrapolated directly, but still may be used for fundamental research aiming at the identification and quantification of basic relations as well as to provide data for validating FE models. The evaluation of the test results has to take into account the appropriate mechanical behaviour of the soil. Thus, it was crucial to determine the soil properties in laboratory tests under representative conditions for the environment of the testing facility. Moreover, it was essential that these relations were accurately implemented in an FE model, which is introduced in section 4.1.

The drainage condition at model scale has to be similar to prototype scale. Since the reduced scale implies shorter length of the drainage path, more drainage would take place at equal load rate in identical soil. Consequently, the soil's hydraulic conductivity may be decreased or the load rate may be increased to obtain less drainage. Finer soils can be used to reduce the permeability, but invoke deviating mechanical properties of the soil and additional issues regarding the preparation of the soil. Alternatively, more viscous pore fluids in comparison to water decrease the hydraulic conductivity as well, but also affect the soil's strength and are hardly applicable for the chosen size of the testing facility. Based on these considerations, sand with particle sizes as fine as possible along with higher load rates were chosen to achieve appropriate drainage conditions. Further, the chosen approach implied limitation to reasonable load rates in order to omit inertial forces at very high load rates. Beside this aspect, it has to be remarked that neither the displacement rate v_z nor the load frequency f are precisely scaleable from model scale to prototype scale (see subsection 2.3.4). Thus, the testing programme considered various displacement rates and two load frequencies that were approximately 6 or 12 times higher than the expected frequency of offshore wave loading (about 0.08 Hz). The practical relevance of the load rates were verified by retrospective FE simulations (see subsection 4.2.6).

3.1.2 Testing facility

Beside a cylindrical sand container, the testing facility comprised an actuator mounted on a loading frame. A personal computer controlled the load application and recorded the measurements of the sensors. A hydraulic system, which was used along with a vibrator to prepare the soil, was connected to the sand container. The soil's relative density was
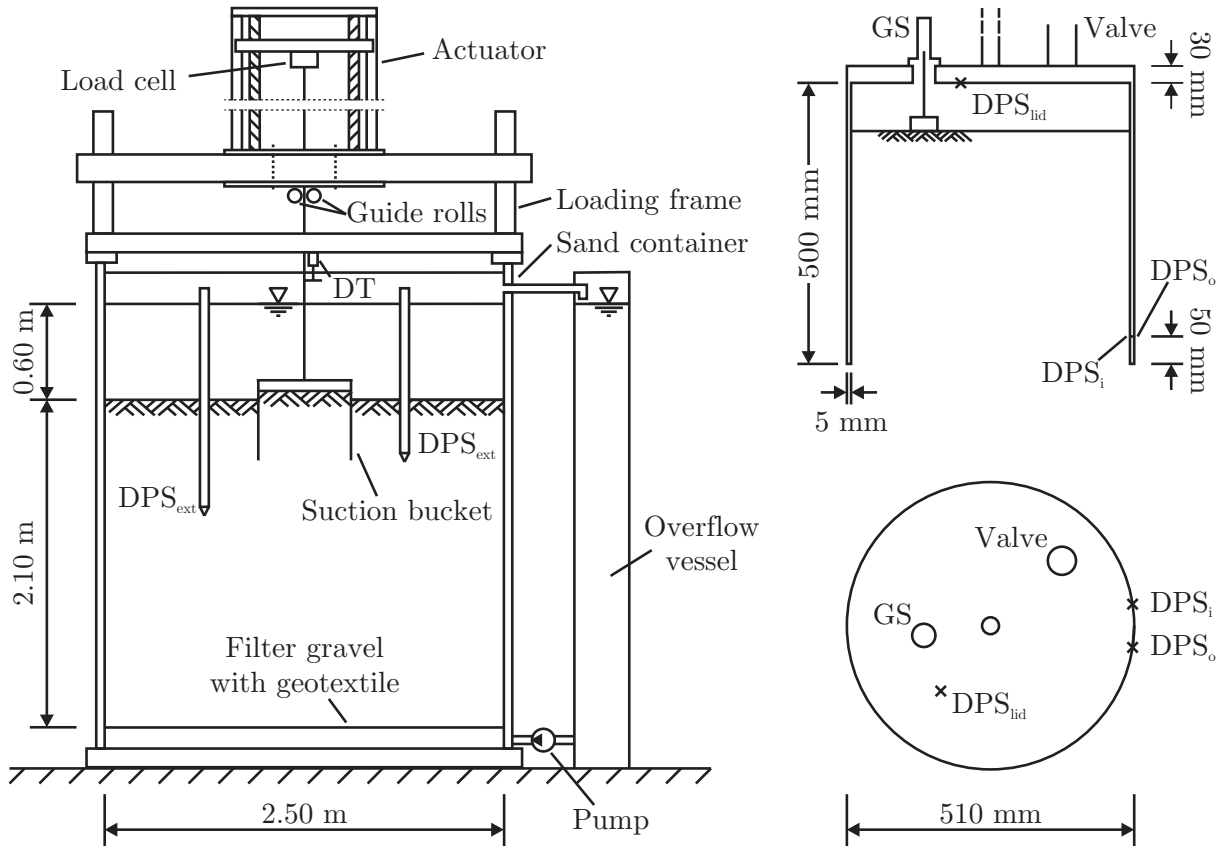
Figure 3.1: Sketch of testing facility and suction bucket model with sensors.

evaluated before each test by cone penetration testing (CPT). The suction bucket was generally installed by means of negative differential pressure, which was applied by a hydraulic system that utilised the principle of gravity flow. However, jacked installations were possible as well by using the actuator.

Figure 3.1 depicts the testing facility along with the suction bucket model L500D510. The other models were identical except for their dimensions (length L and diameter D, see Table 3.1) and did not have differential pressure sensors (DPSs) at the skirt. Further abbreviations of sensors depicted in Figure 3.1 are: displacement transducer (DT) and gap sensor (GS). The dimension of the testing facility, especially with regard to the sizes of the sand container and suction bucket models, was designed within preceding FE simulations aiming at minimising potential boundary effects. Spatial restrictions and the significant rise of effort for conducting model tests with increasing dimension of the facility were accounted for as well.

The diameter of the sand container was 2.50 m and the height of the soil was 2.10 m, which were sufficient to avoid effects from the boundary of the sand container on the suction bucket's response. Underneath the sand, a 0.40 m thick drainage layer was installed that consisted of filter gravel and a drainage pipe. The pipe was installed diagonally in the sand container and was connected to the hydraulic system for soil preparation. A geotextile was used to prevent erosion between the gravel and the sand. The water level exceeded
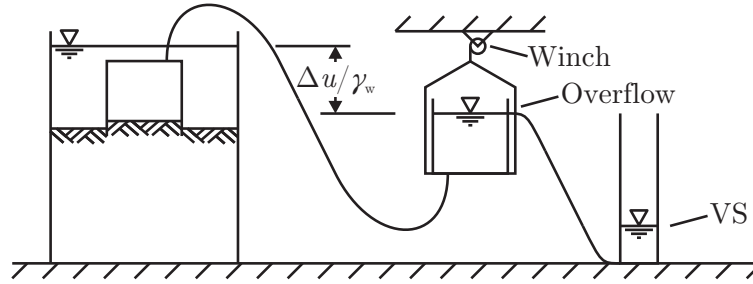
Figure 3.2: Sketch of hydraulic system for installation.

the soil surface by at least $0.60\,\mathrm{m}$ to provide sufficient water depth so that the largest suction bucket model was entirely submerged before the skirt's tip touched the sand. De-aired water was used in the testing facility. The actuator was moveable on the loading frame over the entire diameter of the sand container. The stroke of the actuator was $2\,\mathrm{m}$ and the maximum displacement rate and force were $v_{\mathrm{z}} = 100\,\mathrm{mm/s}$ and $F = 50\,\mathrm{kN}$ respectively. The load frequency for sinusoidal cyclic loads could be specified within the range of $0.1\,\mathrm{Hz} < f < 1.0\,\mathrm{Hz}$.

The sand container was connected to a hydraulic circular system, which pumped water through the soil from the bottom to the top (see Figure 3.1). The drainage layer provided uniform distribution of water pressure at the bottom of the sand container. The outflow at the top of the sand container gathered the surplus water, which ran in an overflow vessel providing the reservoir for the variable speed pump. This system was utilised for preparing the soil at specific relative density under reproducible conditions prior to each test.

The hydraulic installation of the suction bucket was achieved by the controlled application of negative differential pressure. A hydraulic system was erected to generate gravity flow (see Figure 3.2). A tube connected the valve on the suction bucket's lid with an overflow vessel, whose elevation could be modified by a manually driven winch. Depending on the difference between the two water levels inside the sand container and the overflow vessel, distinct differential pressures could be generated. The water flew out of the overflow vessel into another tank, where the current water level was measured by a volume sensor (VS). The VS facilitated the determination of the soil's (global) hydraulic conductivity.

3.1.3 Soil properties

The container of the testing facility was filled with 17 tons of silica sand with subangular shape of the particles (see Figure 3.3). The particle size distribution was analysed according to DIN EN ISO 17892-4:2017-04 with supplemental sieves for increasing the accuracy (see Figure 3.4). The uniformity coefficient and coefficient of curvature were determined to $C_{\mathrm{U}} = 1.36$ and $C_{\mathrm{C}} = 0.96$ respectively, so that the sand was categorised to be medium grained, poorly graded according to DIN EN ISO 14688-2:2018-05. The low uniformity coefficient minimised the potential for segregation of particle fractions that could result from repetitive soil preparation. Moreover, the relatively small particle size implied low

(a)   (b)
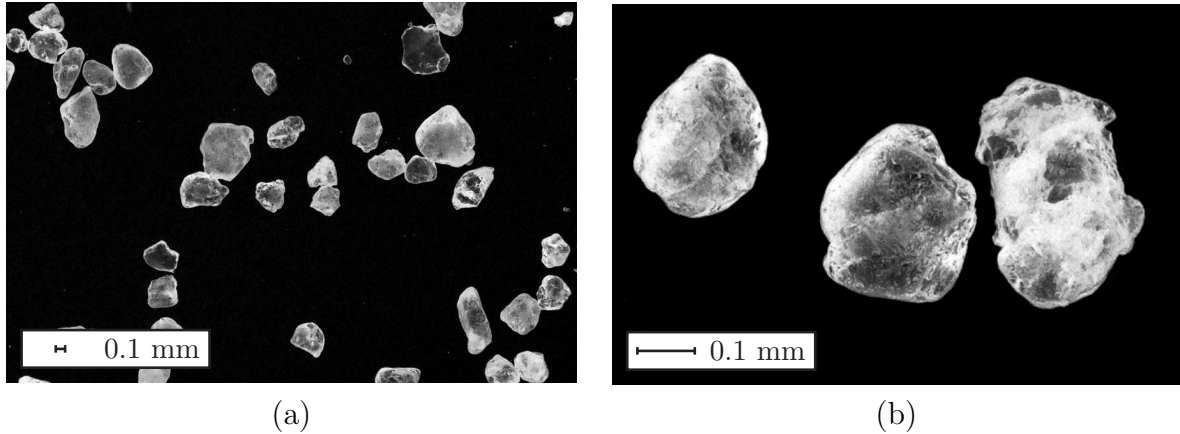
Figure 3.3: Microscopic images of the sand used in the testing facility with normal (a) and enhanced (b) visual enlargement.
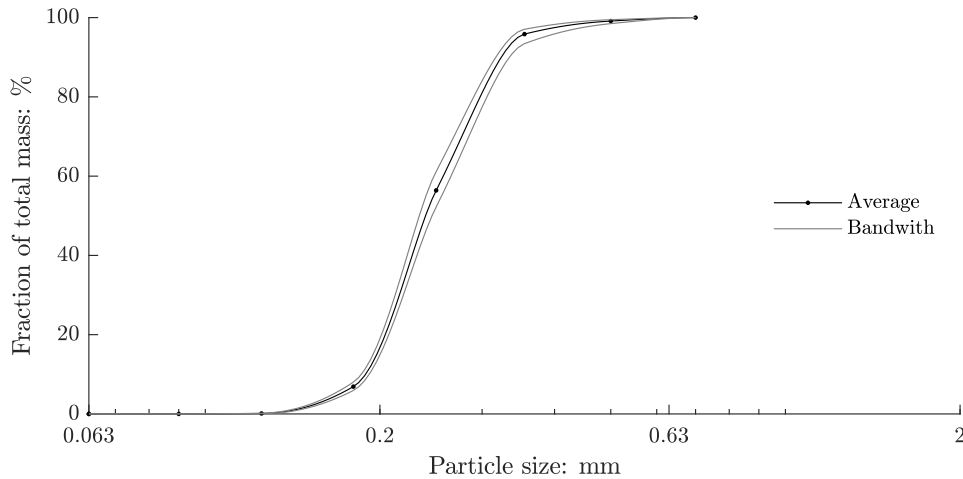
Figure 3.4: Particle size distribution.

permeability, which was necessary to reduce drainage for testing suction buckets under tensile loading. The minimum and maximum void ratio were analysed according to DIN 18126:1996-11 and led to $e_{\min} = 0.553$ and $e_{\max} = 0.873$ respectively.

The soil's hydraulic conductivity was investigated according to DIN EN ISO 17892-11:2019-05 with the particular aim of analysing the effect of the void ratio on the hydraulic conductivity (see Figure 3.5). There is an obvious tendency of increasing hydraulic conductivity with void ratio. Equation 3.1 was obtained by regression of the test results. As it is evident from Figure 3.5, the evaluation of Equation 3.1 within the range of the soil's minimum and maximum void ratio implies extrapolation along with potential inaccuracy for high void ratios. However, the scope was on high relative densities, whose hydraulic conductivities were well described by Equation 3.1 within the range of the experimental results. The hydraulic conductivity depends on the pore fluid's viscosity, which is affected by the temperature of the pore fluid T_{w}. Thus, an additional function $\eta(T_{\mathrm{w}})$ according to DIN EN ISO 17892-11:2019-05 was regarded in Equation 3.1.
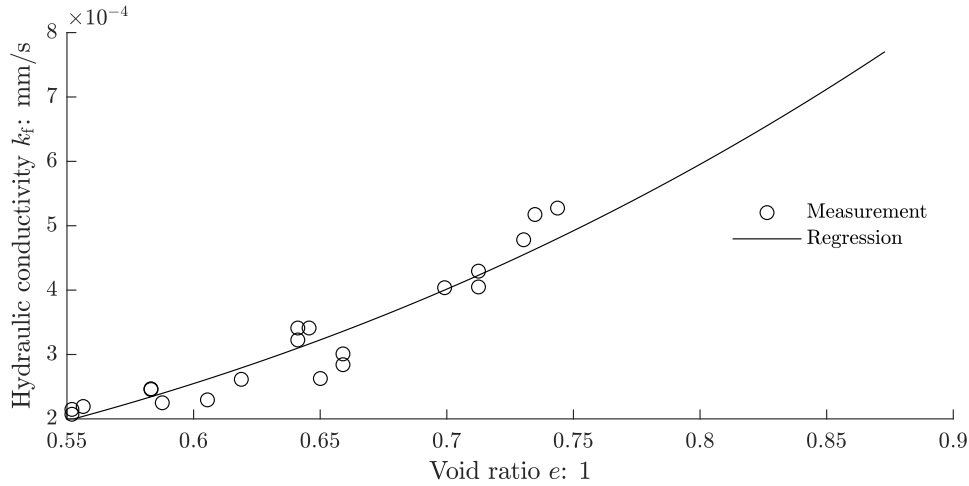
Figure 3.5: Hydraulic conductivity depending on void ratio at $T_\text{w} = 10°\text{C}$.

$$k_\text{f}(e, T_\text{w}) = 1.15 \times 10^{-3} \, \frac{\text{m}}{\text{s}} e^{2.95} \eta(T_\text{w}) \tag{3.1}$$

The oedometric stiffness of the soil depends on its void ratio and stress state. Numerous laboratory tests according to DIN EN ISO 17892-5:2017-08 were conducted to analyse this relation. Equation 2.13 was adopted to describe the stress dependency. The coefficients $\kappa = 350$ and $\lambda = 0.4$ provided the best approximation of the soil's measured stress-strain response regarding both the soil's relative density and estimated stress state in the testing facility.

A total number of 30 triaxial tests was executed in accordance with DIN EN ISO 17892-9:2018-07 for investigating the soil's monotonic shear strength regarding relative densities within the range of $0.5 \leq I_\text{D} \leq 0.9$ and effective radial stresses from $10\,\text{kPa}$ to $240\,\text{kPa}$. The determined maximum internal friction angles φ' and corresponding dilation angles ψ are presented in Figure 3.6. The results are in agreement with Bolton (1986) in terms of the increase of friction angle and a dilation angle with decreasing effective stress and void ratio. An internal friction angle of $\varphi' = 45°$ and dilation angle of $\psi = 20°$ were adopted in here as being representative for the soil's effective stress and void ratio in the testing facility.

Shear box tests either with sand-sand or sand-steel interface were conducted to determine the interface friction angle δ. A stainless steel plate with a comparable roughness to the suction bucket's skirt was utilised for these tests. It was found that the relation $\delta = 2/3\varphi'$ well approximates the test results.

It is crucial to evaluate the soil condition in the testing facility prior to each model test to facilitate an accurate interpretation of the measurements. Therefore, the soil was investigated by means of CPT. Foglia and Ibsen (2014) proved that CPT is capable of reliably assessing the relative density of sands in laboratory scale. Although there are published correlations for evaluating the soil's relative density based on CPTs, these
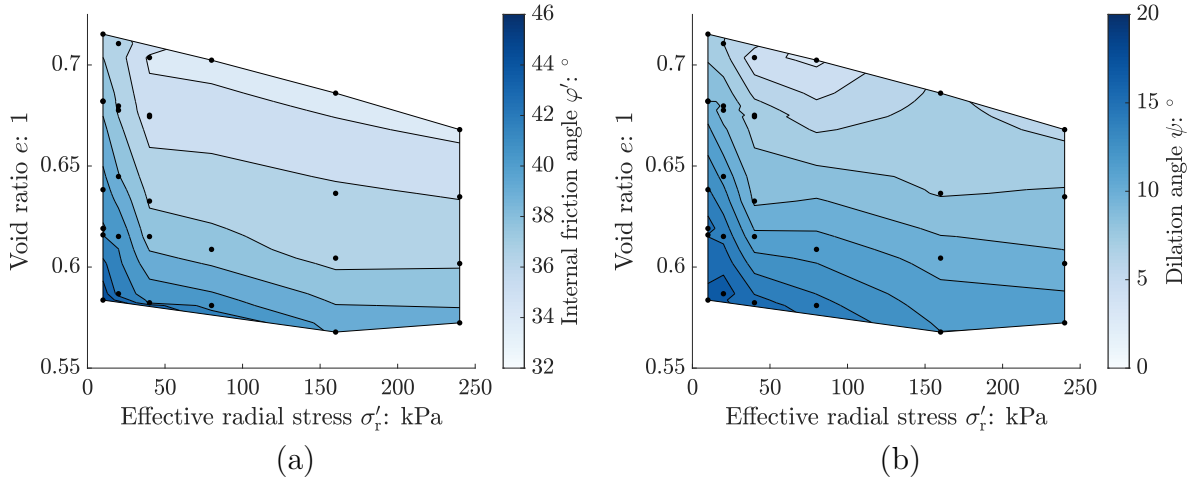
Figure 3.6: Effect of void ratio and effective stress on internal friction angle (a) and dilation angle (b).

relationships were established and calibrated for in-situ conditions and are not necessarily valid for the application in a testing facility. Thus, the utilised CPT device required an individual correlation for the particular conditions of this testing facility. Initially, the actual soil's relative densities were analysed by 80 soil samples using sampling tubes (in accordance with DIN 18125-2:2011-03), whereby eight distinct depths were examined. The obtained results enabled the investigation of both the homogeneity at each depth and distribution over depth. Then, these results were correlated with the cone resistance q_c measured in preceding CPTs with a cone diameter of 30 mm. Figure 3.7 presents a schematic top view of the sand container and specifies the locations of the ten samples taken at each depth as well as the locations of the CPTs.

Jamiolkowski et al. (2003) proposed Equation 3.2 to determine the relative density as a function of the effective stress and cone resistance. The empirically calibrated coefficients comprised in Equation 3.2 were modified in here. Figure 3.8 depicts the measured cone resistance profiles as well as the relative densities evaluated by means of the sample tubes. The coefficients $C_{0...2}$ were iteratively adjusted until good accordance between the predicted and measured relative densities was attained. The vertical effective stress in Equation 3.2 was continuously updated by considering the estimated effective unit weight of the soil, which was determined with regard to the minimum and maximum void ratio. Initially, the coefficients were calibrated individually for each CPT by exclusively taking into account the samples in direct proximity. Finally, a unique set of coefficients was defined that provided the best global accordance (see Table 3.2). The obtained approximations of the relative densities by CPT evaluation agreed well with the mean relative densities of the samples and were also within the bandwidth of the lowest and highest relative densities (see Figure 3.8 (b)). Obviously, the correlation exhibited minor accuracy for shallow depths up to approximately 200 mm, which was probably due to low vertical effective stresses. However, the accuracy of the estimated relative density improved for greater depths.
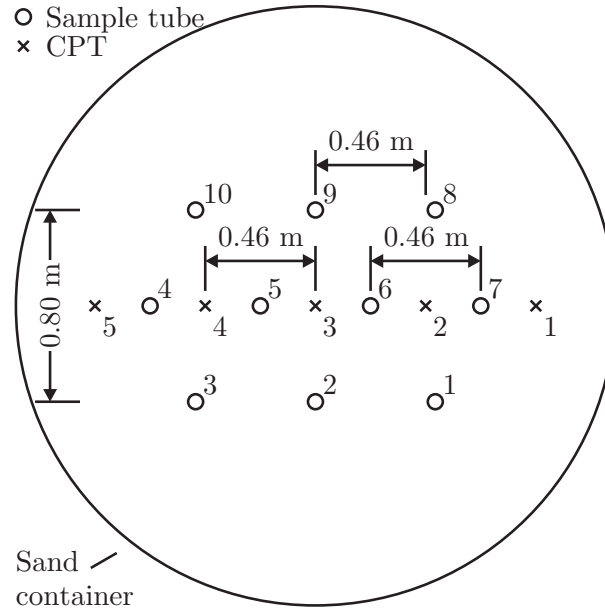
Figure 3.7: Locations of the CPTs and probes.

Table 3.2: Coefficients for CPT correlation.

Cone diameter	Coefficients		
	C_0: 1	C_1: 1	C_2: 1
30 mm	0.043	0.93	9.75
25 mm	0.043	1.1026	11.1824

$$I_\mathrm{D} = \frac{1}{C_2} \ln \left(\frac{\frac{q_\mathrm{c}}{p_\mathrm{atm}}}{C_0 \left(\frac{\sigma'_z}{p_\mathrm{atm}} \right)^{C_1}} \right) \tag{3.2}$$

Due to technical defect of the CPT device, an entirely new CPT system was established. Since the novel cone diameter was 25 mm and the technical properties differed substantially, a new calibration was required. Instead of taking another 80 soil samples, it was chosen to calibrate the coefficients by regressing the cone resistance profiles of four test series with a total number of 16 CPTs against the relative densities of the previously taken samples. The frequent soil preparations and investigations by CPT led to similar results until then, so that repeatable conditions were verified, which validates this procedure.

The regression process adopted the mean relative densities of the samples per depth as target values to be approximated by Equation 3.2 along with the mean cone resistance-profile of the 16 CPTs. The coefficient C_0 was kept constant, but C_1 and C_2 were varied to find the most accurate estimation (see Figure 3.9 (b)). The obtained coefficients are summarised in Table 3.2. Moreover, the sensitivity of the new coefficients was analysed by statistically evaluating the mean, minimum and maximum as well as standard deviation
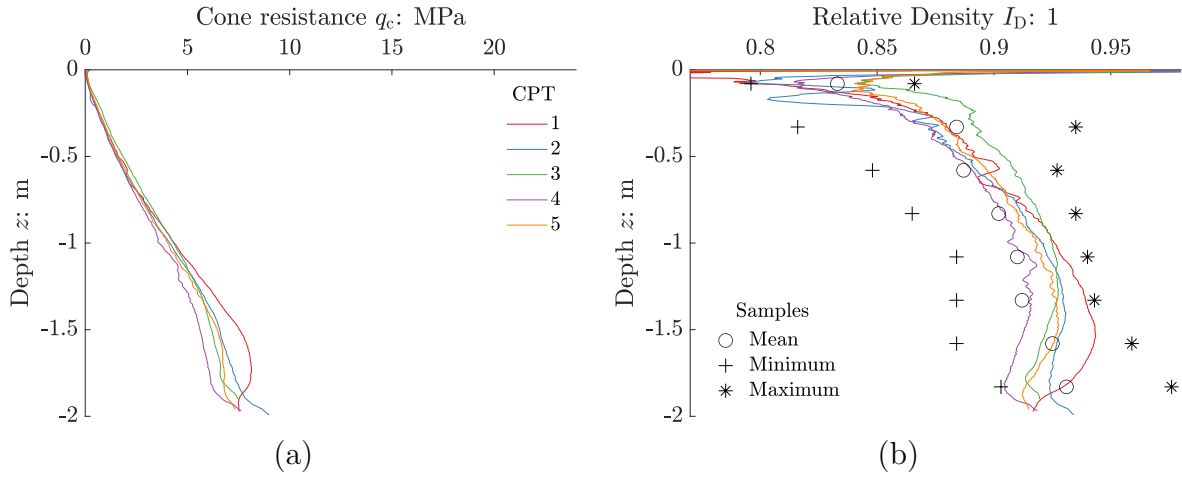
Figure 3.8: Measured cone resistances (a) and correlated relative densities along with samples (b) for 30 mm cone diameter.
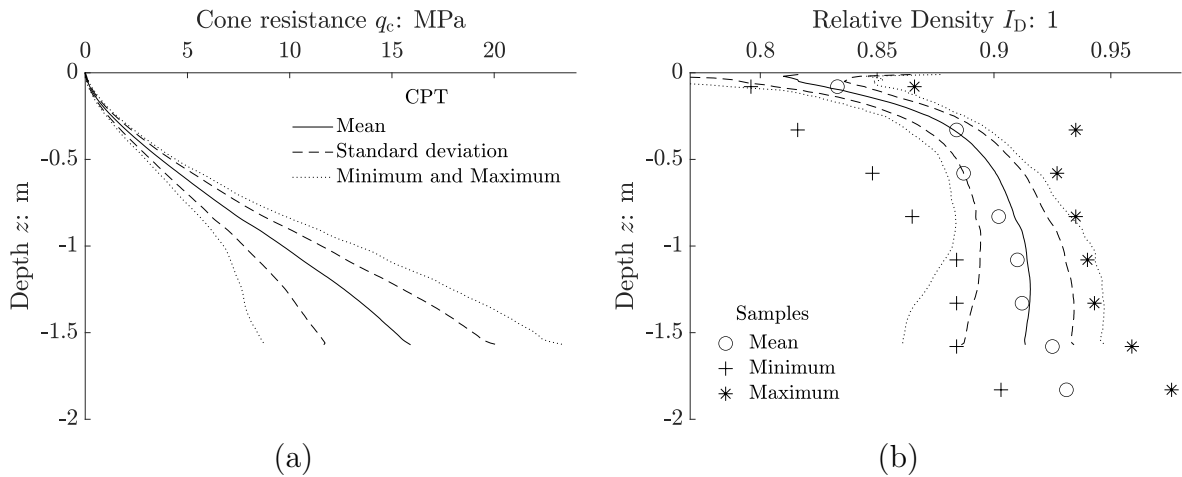
Figure 3.9: Statistical cone resistance profiles (a) and correlated relative densities along with samples (b) for 25 mm cone diameter.

of the cone resistance-profiles (see Figure 3.9). Despite variation of the measured cone resistances, the derived relative densities were only slightly affected.

3.2 Testing procedure

3.2.1 Soil preparation

The soil conditions must be repeatable and homogeneous, which was achieved by preparing the soil prior to each test. Initially, the soil was loosened by means of an upward hydraulic gradient generated by the pump (see Figure 3.1). The water pressure was increased incrementally and the soil surface commenced to elevate continuously, which indicated
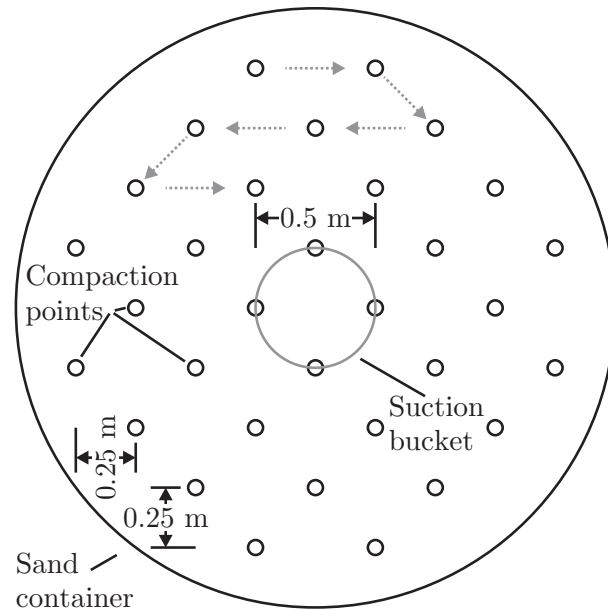
Figure 3.10: Grid for compaction of the soil.

increase of the void ratio, once a critical hydraulic gradient was exceeded (typically $i \geq 1.1$). Before local hydraulic failure took place, the pump performance was lowered so that the hydraulic gradient in the soil reduced to $i \approx 0.8$. The soil surface lowered to limited extent due to the decreased upward gradient.

While maintaining the hydraulic gradient, the soil was compacted by a horizontally oscillating vibrator that was pushed into the sand as fast as possible and pulled out slowly at constant rate. The horizontal oscillation of the vibrator provoked shear strains in the sand, which enabled the rearrangement of the grains causing densification. The compaction was successively conducted at every second point of a regular grid with a distance of 0.25 m as depicted in Figure 3.10, whereby the grey arrows indicate the order in which the points were compacted. The upward hydraulic gradient decreased the penetration resistance of the vibrator and ensured reaching the final depth (slightly above the geotextile to avoid damage). After the compaction was completed, the soil surface was levelled. For this purpose, a horizontally aligned shield (width of 1 m) was manually slid over the soil surface over the entire diameter of the sand container.

The performed sand preparation method was proven to provide homogeneous relative density of the soil in plan and depth, but provoked higher horizontal stresses as it was analysed by Massarsch et al. (2020). Furthermore, the attained relative density was high as it was intended for this study. Nonetheless, it should be noted that the high relative density affected the sand's behaviour at low stresses (see subsection 2.3.1, subsection 2.3.4 and subsection 3.1.3). Thus, the model tests have to be evaluated in the context of the soil properties as described in subsection 3.1.3, which were determined representatively for the testing facility.

3.2.2 Cone penetration testing

The relative density was controlled before each test by CPT. For the first tests, the CPTs were executed at five locations, which were equally distributed over the diameter of the sand container as shown in Figure 3.7, with a constant penetration rate of 5 mm/s. The procedure was changed at an early stage to four locations with a minimum distance of $0.5D$ from the suction bucket's skirt in order to avoid disturbance of the soil inside and in proximity to the suction bucket.

The measured cone resistance profiles were evaluated to obtain the soil's relative density as described in subsection 3.1.3 (see exemplary result in Figure 3.8 and the results for every model test in Appendix A). Further properties of the soil were deduced, namely the effective unit weight, void ratio and hydraulic conductivity. The vertical stresses were estimated and along with the previously mentioned quantities, the assumed values of the soil's stiffness and shear strength were confirmed. Finally, soil profiles consisting of up to six layers were derived (see Appendix A). Since the properties of the soil up to $|z| \approx 1.5L$ are decisive for the suction bucket's installation and bearing behaviour, the majority of soil layers were specified in the range of the suction bucket's length.

Based on the soil profile, the integral hydraulic conductivity was calculated over the embedment depth (see Equation 3.3). The chosen approach assumes that the integral hydraulic conductivity k_{int} depends on the soil layers' thicknesses and flow resistances (hydraulic conductivities) in series.

$$k_{\mathrm{int}} = \frac{z}{\sum \frac{z_{\mathrm{j}} - z_{\mathrm{j}-1}}{k_{\mathrm{f,j}}}} \tag{3.3}$$

3.2.3 Flow net calculation

To avoid hydraulic failure during the installation of the suction bucket, flow net calculations were realised by means of FE simulations. A critical exit gradient at the soil surface next to the suction bucket's skirt was adopted to evaluate the critical negative differential pressure Δu_{cr} (according to Senders and Randolph, 2009). These calculations considered the previously defined soil profiles, the geometry of the suction bucket and the boundaries of the sand container. Beside the initial state, loosening of the soil inside the suction bucket was simulated by increasing the inner permeability. The following permeability ratios were assumed: $k_{\mathrm{i}}/k_{\mathrm{o}} \in [1, 1.25, 1.5, 1.75, 2]$. Distinct embedment depths of the suction bucket were regarded to obtain profiles of the critical negative differential pressure over the entire installation process.

Beside the critical negative differential pressure, the flow net calculations provided predictions of the water volume rate q_{soil}, which was presumed to scale linearly with the applied negative differential pressure. Furthermore, the differential pressure at the locations of external DPSs as well as the DPSs at the suction bucket's skirt was evaluated to allow for

comparison with the measurements. Since the distribution of negative differential pressure in radial direction inside the suction bucket is not constant, i.e. the equipotentials are not horizontal, and depends on the actual embedment depth, the measurements of the DPS at the inner skirt required correction. Thus, a correction factor, which accounts for the location of the inner skirt's DPS, was introduced for further evaluation of the results.

3.2.4 Installation

Initially, the suction bucket was lowered until the skirt's tip came in contact with the soil surface and the load cell was zeroed so that the submerged weight of the model was excluded from the readings. Then, the first installation phase commenced. Firstly, the suction bucket was slowly jacked until $|z| = 0.2D$ having the valve on top of the lid open to avoid generation of positive differential pressure inside the suction bucket that would induce pore water seepage flow and could potentially provoke hydraulic failure outside the suction bucket. The initial jacking simulated the self-weight penetration in a controlled manner and mobilised soil resistances, which exceeded the self weight of the model.

Subsequently, the hydraulic installation was prepared by releasing the suction bucket from the actuator. Since the initial jacking force exceeded the suction bucket's self weight, no further penetration took place when the suction bucket was detached. A tube to the hydraulic system was connected with the valve on the suction bucket's lid. The hydraulic installation of the suction bucket was achieved by raising the negative differential pressure Δu as described in subsection 3.1.2 and schematically depicted in Figure 3.2. The target embedment depth was set to $|z| = 0.85L$, which was approximately achieved in every test. After reaching the final embedment depth, the negative differential pressure was removed, the penetration stagnated and certain lowering of the soil plug was observed, which was attributed to the absence of the upward hydraulic gradient.

During this installation phase, the measurements of the DT, DPSs, VS and GS were recorded. In particular, the following quantities were derived and compared with the results of the flow net calculations: differential pressure Δu, differential pressure ratios a_j as defined in Equation 3.4 (Δu_j denotes readings of an arbitrary DPS), penetration rate, plug heave, water volume rate and global hydraulic conductivity. Moreover, the additional reading of the DPS at the inside of the suction bucket's skirt enabled the determination of the soil's hydraulic conductivity inside the suction bucket as well as the permeability ratio. The evaluation of these quantities included the previously described correction factor for the inner skirt's DPS and the results are presented in Appendix A.

$$a_j = \frac{\Delta u_j}{\Delta u_{lid}} \tag{3.4}$$

Figure 3.11 summarises the plug heave during the installation of all tests with $D = 510\,\text{mm}$. In total, 29 measurements are shown, where 24 tests were installed by negative differential pressure of which the initial jacking as described above was measured in three tests. Two more tests were jacked until the final embedment depth was reached. The
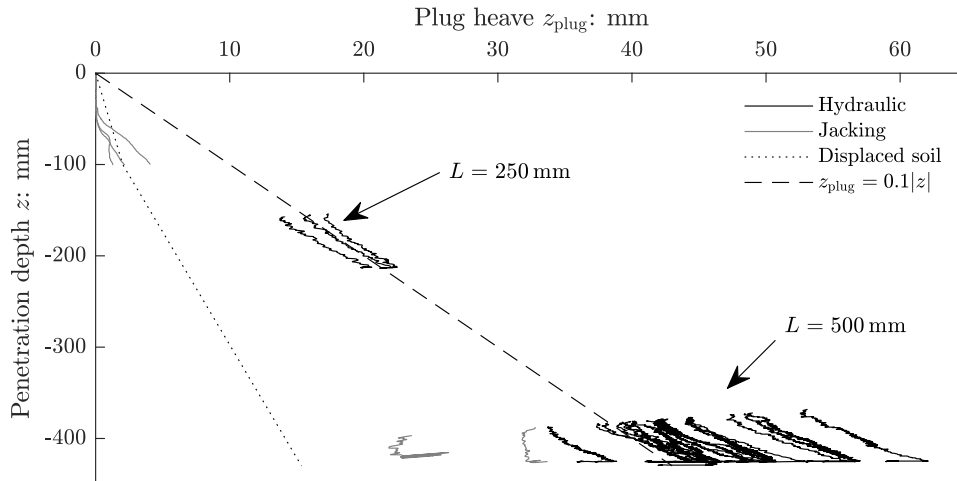
Figure 3.11: Plug heave during installation of models with $D = 510\,\text{mm}$.

measurement range of the GS was limited so that it was not possible to monitor the plug heave over the entire installation. Despite considerable scatter of the measured plug heave, the results indicate that the installation by negative differential pressure induced substantial plug heave, which tended to exceed $z_{\text{plug}} = 0.1|z|$, and was higher than in case of jacked installation. During initial jacking, plug heave commenced approximately for $|z| \geq 0.1D$.

To further facilitate the assessment of the results, the plug heave due to displacement of the soil by the suction bucket's skirt was estimated. It was assumed that during jacking, the soil displaced in equal shares to the inside and the outside of the suction bucket, but during hydraulic installation, the soil particles moved entirely inside the suction bucket. Independent of the installation method, the observed plug heave was higher than the estimation of the displaced soil, which indicates loosening of the soil inside the suction bucket (see Figure 3.11). While the jacked installation solely invoked dilation, the plug heave mechanism in hydraulic installation was an interaction of dilation and loosening due to upward hydraulic gradient. The reduction of the plug heave after complete hydraulic installation, when the negative differential pressure was removed, is noticeable as well.

3.2.5 Determination of hydraulic conductivity

The assessment of the soil's hydraulic conductivity is essential for the evaluation of the suction bucket's tensile bearing behaviour. Consequently, it was intensively investigated after every installation of the suction bucket. Similar to the procedure for hydraulic installation, distinct negative differential pressures were applied and the readings of the same sensors as during installation were recorded. Since the negative differential pressure was relatively low, neither further penetration nor plug heave were invoked. Both aspects were verified by monitoring the particular sensors. The differential pressure was incrementally increased to three arbitrary magnitudes and held constant for several minutes while the measurements were recorded. This procedure verified the linear relation

between applied negative differential pressure and the invoked pore water seepage flow. Thus, normalisation of the water volume rate according to Equation 3.5 was introduced.

$$\tilde{q}_{\text{soil}} = \frac{q_{\text{soil}}}{\Delta u} \tag{3.5}$$

The evaluation of the normalised water volume rate $\tilde{q}_{\text{soil}}$ along with results of the preceding flow net calculations facilitated the determination of the system's global hydraulic conductivity. In case of model L500D510, the additional readings of the DPS at the inside of the suction bucket's skirt enabled the direct calculation of the enclosed soil's hydraulic conductivity based on the measurements. Subsequently, the flow net calculations involving distinct permeability ratios $k_{\text{i}}/k_{\text{o}}$ were utilised to assess the actual permeability ratio. For this purpose, the normalised water volume rate was divided by the inner hydraulic conductivity. By claiming identical normalised water volume rates in model test and simulation, the permeability ratio was determined via linear interpolation (see Equation 3.6).

$$\left(\frac{\tilde{q}_{\text{soil}}(k_{\text{i}}/k_{\text{o}})}{k_{\text{i}}} \right)_{\text{FE}} \overset{!}{=} \left(\frac{\tilde{q}_{\text{soil}}}{k_{\text{i}}} \right)_{\text{model}} \tag{3.6}$$

Figure 3.12 presents exemplary results of the determination of the hydraulic conductivity and permeability ratio. In Figure 3.12 (a), the incrementally applied negative differential pressure is depicted along with the hydraulic conductivity. Since the evaluation of the hydraulic conductivity accounts for measurements of three sensors (two DPSs and VS), whose readings comprise certain sensor noise, the obtained results exhibit considerable scatter as well. The higher the applied negative differential pressure was, the lower became the spread of the calculated hydraulic conductivity, which was due to higher measured values in comparison to the sensors' noise. Two different hydraulic conductivities are presented, which either account for the soil profile derived from CPT or for homogeneous soil comprising solely a single layer. While the first mentioned represents the actual condition in the testing facility, the latter simplifies the variation of soil's relative density with depth for the implementation in FE models. Figure 3.12 (b) shows the corresponding permeability ratios and reveals that the soil inside the suction bucket had a higher permeability than outside, which underlines that soil was loosened during the installation.

The readings of the additional DPSs located in the soil and at the skirt were utilised to qualitatively verify the determined hydraulic properties. Appendix A provides comparisons of the measured quantities with the calculated ones and the permeability ratios for the tests with model L500D510. It is noted that additional hydraulic conductivities and permeability ratios, where the soil profile as defined in subsection 3.2.2 was simplified to a single layer, were derived for the retrospective FE simulations of any model test (see Figure 3.12).
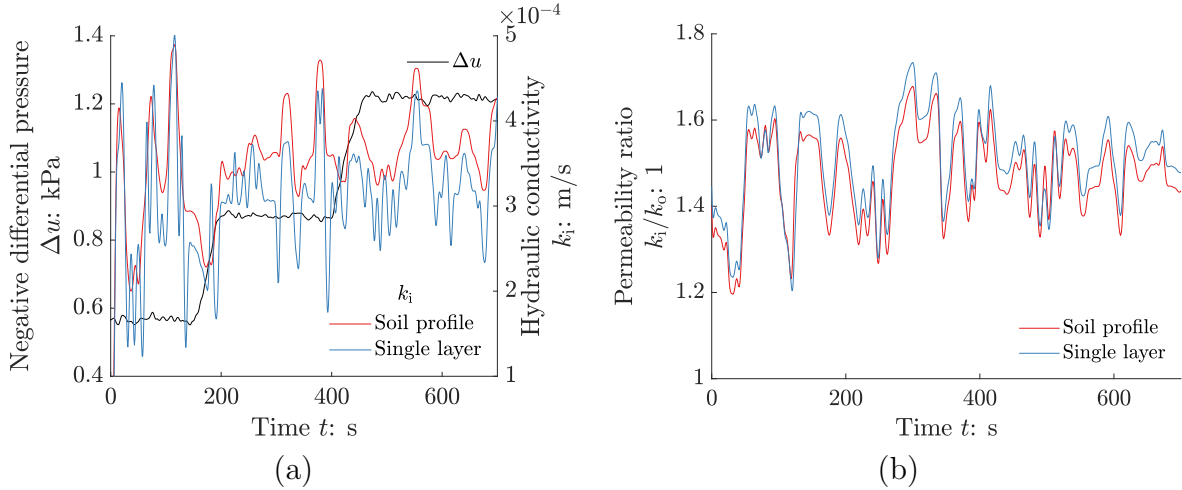
Figure 3.12: Exemplary determination of hydraulic conductivity (a) and permeability ratio (b) with model L500D510.

3.2.6 Drained resistance

Within the scope of each individual test, the drained response was analysed. In this regard, the valve on the suction bucket's lid was kept open and a very low displacement rate was applied, i.e. $v_z < 0.05\,\text{mm/s}$. Both measures prevented the generation of relevant negative differential pressure. Once a constant force was reached, the actuator was halted. To ensure an equivalent condition for the subsequent test, the tensile force was diminished by the actuator until $0\,\text{kN}$.

Figure 3.13 provides an exemplary result of a drained test with model L500D510. The negative force at the beginning of the test represents the submerged weight of the suction bucket. Initially, a very stiff response was observed, which can be essentially attributed to the weight of the model. The mobilisation of the skin friction needed higher displacement to finally evoke the drained resistance F_{dr}, which was defined as the maximum force measured during this test. Moreover, the required displacement to mobilise the drained resistance $\Delta z_{F_{\text{dr}}}$ was evaluated. These quantities are summarised in Table 3.3 supplemented with further details in Appendix A.

3.2.7 Tensile loading

Finally, the tensile bearing behaviour was investigated under various loading conditions. As defined in section 2.1, the suction bucket was subjected to either constant displacement rate, constant force or cyclic force. The following sections analyse and discuss the test results in detail. Moreover, the results of every test are given in Appendix A.
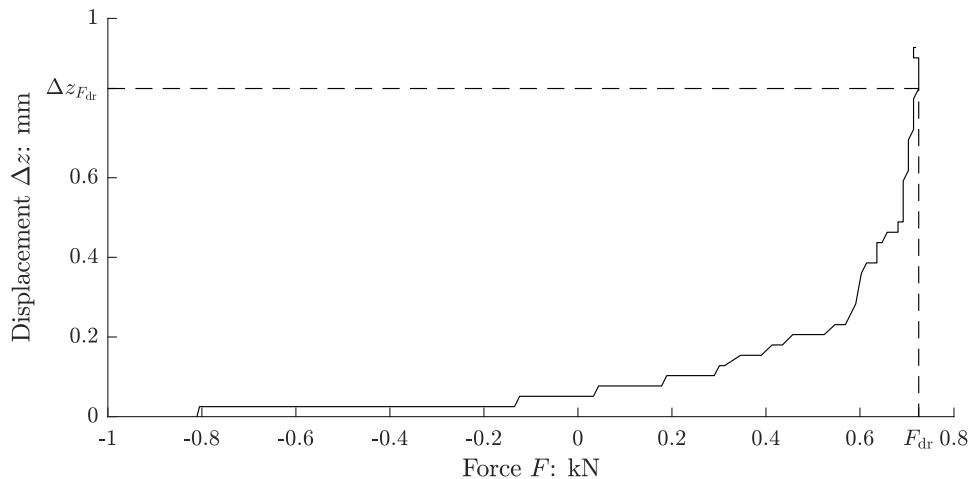
Figure 3.13: Exemplary results of drained tests with model L500D510.

3.3 General results

3.3.1 Hydraulic properties

Depending on the actual model, the determined hydraulic properties either comprise the global hydraulic conductivity k_f (L125D135, L250D260 and L250D510) or the hydraulic conductivity inside the suction bucket k_i along with the permeability ratio k_i/k_o (L500D510). The evaluation of these quantities is exemplarily shown in Figure 3.12. The hydraulic properties of all tests are summarised in Table 3.3. The provided values were derived for FE simulations, where the soil was simplified to a single layer.

The global permeability was in the range of $2.8 \times 10^{-4} \leq k_f \leq 3.4 \times 10^{-4}$, which is a rather narrow bandwidth. The inner hydraulic conductivity of the largest model L500D510 was slightly higher with $3.0 \times 10^{-4} \leq k_i \leq 4.1 \times 10^{-4}$ and had a mean value of $3.7 \times 10^{-4}\,\text{m/s}$ with a standard deviation of $0.27 \times 10^{-4}\,\text{m/s}$. The deviation from global to inner hydraulic conductivity was expected since the soil inside the suction bucket was loosened during the installation. Nevertheless, it should be noted that the difference is relatively small for this particular hydraulic property of the soil, which is usually not measured to this degree of accuracy. The permeability ratio determined with L500D510 had a mean value of 1.6 with a standard deviation of 0.1. It follows that despite deviations in individual tests, the hydraulic properties were uniform for numerous tests.

3.3.2 Drained resistance

Beside the hydraulic properties, Table 3.3 provides an overview of the measured drained resistances F_{dr} and associated displacements $\Delta z_{F_{dr}}/D$. Evidently, larger model dimensions led to higher drained resistances, which necessitated more displacement. In Table 3.3, some tests exhibit $\Delta z_{F_{dr}}/D = 0.000$ which results from rounding to three decimal digits,

Table 3.3: General results regarding the hydraulic properties and drained resistance.

Test	Hydraulic properties			Drained resistance	
	k_{f}: m/s	k_{i}: m/s	$k_{\mathrm{i}}/k_{\mathrm{o}}$: 1	F_{dr}: kN	$\Delta z_{F_{\mathrm{dr}}}/D$: 1
L500D510v0.5	*	3.7×10^{-4}	1.6	0.73	0.001
L500D510v0.8	*	3.7×10^{-4}	1.6	0.75	0.001
L500D510v1.8	*	3.0×10^{-4}	1.6	0.70	0.002
L500D510v9.6	*	3.7×10^{-4}	1.5	0.63	0.001
L250D510v0.9	2.9×10^{-4}	*	*	0.24	0.000
L250D510v1.8	2.8×10^{-4}	*	*	0.25	0.000
L250D510v9.7	2.9×10^{-4}	*	*	0.29	0.000
L250D260v1.7	3.1×10^{-4}	*	*	0.16	0.000
L250D260v9.6	3.2×10^{-4}	*	*	0.14	0.001
L250D260v19.5	3.0×10^{-4}	*	*	0.10	0.001
L250D260v48.8	3.4×10^{-4}	*	*	0.12	0.001
L125D135v9.8	3.0×10^{-4}	*	*	0.02	0.000
L125D135v19.7	3.0×10^{-4}	*	*	0.02	*
L125D135v49.1	3.0×10^{-4}	*	*	0.02	*
L500D510M1.09	*	3.0×10^{-4}	1.3	0.75	0.001
L500D510M1.58	*	3.8×10^{-4}	1.5	0.73	0.001
L500D510M2.04	*	4.1×10^{-4}	1.6	0.73	0.002
L500D510F1.02M0.86A0.18	*	4.0×10^{-4}	1.6	0.67	0.001
L500D510F1.01M0.73A0.38	*	3.7×10^{-4}	1.6	0.82	0.001
L500D510F1.01M1.06A0.25	*	3.7×10^{-4}	1.6	0.68	0.001
L500D510F1.01M0.87A0.60	*	3.8×10^{-4}	1.5	0.83	0.002
L500D510F1.01M1.24A0.38	*	3.5×10^{-4}	1.6	0.74	0.002
L500D510F1.02M1.58A0.39	*	3.7×10^{-4}	1.5	0.64	0.001
L500D510F1.01M1.29A0.89	*	3.7×10^{-4}	1.6	0.64	0.002
L500D510F1.01M2.12A0.52	*	3.6×10^{-4}	1.6	0.71	0.001
L500D510F1.01M1.90A0.99	*	3.5×10^{-4}	1.6	0.79	0.002
L500D510F0.50M0.74A0.37	*	3.6×10^{-4}	1.6	0.84	0.001
L500D510F0.51M1.04A0.45	*	3.9×10^{-4}	1.6	0.71	0.002
L500D510F0.51M1.52A0.65	*	3.7×10^{-4}	1.6	0.61	0.001
L500D510F0.51M1.90A0.81	*	3.7×10^{-4}	1.6	0.71	0.002

* No record

but Appendix A states the actual displacements with $\Delta z_{F_{\mathrm{dr}}} > 0$. For all tests, the drained resistance was mobilised within 1 mm displacement at the most, which relates to $\Delta z_{F_{\mathrm{dr}}}/D \leq 0.002$ for every model dimension and hence, the displacements were below the potential criteria of the serviceability limit state (SLS). The drained resistances for individual models were relatively uniform (e.g. L500D510 had a mean value of 0.72 kN with a standard deviation of 0.07 kN), which proves that the skin friction was akin for multiple tests. Consequently, the soil conditions were similar regarding the stress state
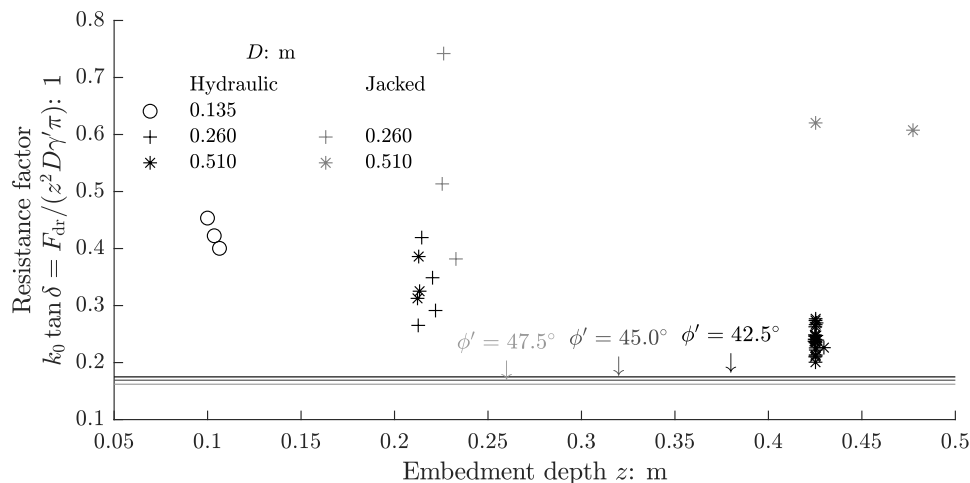
Figure 3.14: Dimensionless drained resistance factor for all model tests.

and relative density, which are the major aspects influencing the suction bucket's drained resistance.

The drained resistance depends on the size of the suction bucket due to the distinct area of the suction bucket's skirt and the soil's effective stresses at its embedment depth. In order to determine scale effects on the drained response, the drained resistances of all model tests were translated to dimensionless resistance factors (according to Hettler, 1982, see Figure 3.14). The proposed factor accounts for the model size as well as the soil's effective unit weight (with $\gamma' = 10.41\,\mathrm{kN/m^3}$) and basically represents the product of the earth pressure coefficient at rest k_0 and the friction coefficient $\tan(\delta)$. Obviously, the resistance factor decreased considerably for increasing model size. Interestingly, the tests with $D = 510\,\mathrm{mm}$ at reduced embedment depth corresponded well with those of $D = 260\,\mathrm{mm}$ at similar embedment depth. The drained resistances of the models installed by jacking were significantly higher, which was probably due to stress enhancements during installation. Therefore, the resistance factor is predominantly affected by the installation method and embedment depth, but the effect of the diameter cannot be defined reliably.

The lower effective stresses at shallower embedment depths imply higher internal friction angles and dilation angles of the sand (see Figure 3.6). Especially the enhanced dilation significantly magnifies the suction bucket's drained resistance, which is in accordance with the FE analyses of Nielsen (2019). Nielsen (2019) found that the drained resistance of a suction bucket was almost independent of the horizontal effective stresses in case of an associated flow rule, i.e. $\psi = \varphi'$. Consequently, the strong dilation dominated the soil's response and therefore dictated the suction bucket's drained resistance. Moreover, the lower embedment depth was interrelated with smaller model dimensions, where the soil inside the suction bucket tended to be more confined enhancing the drained resistance.

Additionally, Figure 3.14 includes three lines which represent theoretical resistance factors for $k_0 = 1 - sin(\varphi')$ and $\delta = 2/3\varphi'$ for internal friction angles $\varphi' \in [42.5°, 45.0°, 47.5°]$ to point out the sensitivity of the resistance factor on the internal friction angle. Evidently,

Table 3.4: Overview of model tests with constant displacement rates.

Model	Displacement rate v_z: mm/s					
L125D135				9.8	19.7	49.1
L250D260			1.7	9.6	19.5	48.8
L250D510		0.9	1.8	9.7		
L500D510	0.5	0.8	1.8	9.6		

the resistance factors of the model tests were significantly higher than the theoretical values. Nevertheless, the largest embedment depth approached the theoretical values, but it cannot be concluded that it would coincide for larger model dimensions. Assuming that there would be no scale effects on the drained response, the dimensionless resistance factor should approximately coincide for all models, which was refuted by the results depicted in Figure 3.14. However, it should be noted that the significantly higher resistance factor in comparison to the theoretical value may not be exclusively attributed to installation effects, model dimensions and enhanced dilation, but also to the sand preparation method, which probably invoked an earth pressure coefficient $k > k_0$.

3.4 Results of tests with constant displacement rate

3.4.1 Overview

Table 3.4 provides an overview of the model tests with constant displacement rates. To identify particular tests, individual names were introduced. These names comprise the names of the models, as previously defined, supplemented by the letter v and a number that represents the displacement rate v_z in mm/s. The ranges of analysed displacement rates account for the geometric dimensions of the model and the corresponding effect on the drainage, i.e. smaller models were subjected to higher displacement rates. Nevertheless, distinct displacement rates were specified to be equal for different models to directly investigate scale effects.

In subsection 3.4.2, the variation of the displacement rate is evaluated based on the results of model L500D510 so that the name of the model is not stated explicitly. Subsequently in subsection 3.4.3, the results of different models are compared and qualitative conclusions regarding the model dimensions are drawn. Additionally, the effect of the installation method on the partially drained response is analysed in subsection 3.4.4. If only selected aspects of distinct model tests are discussed, it is referred to Appendix A, where the readings of every relevant sensor are presented.
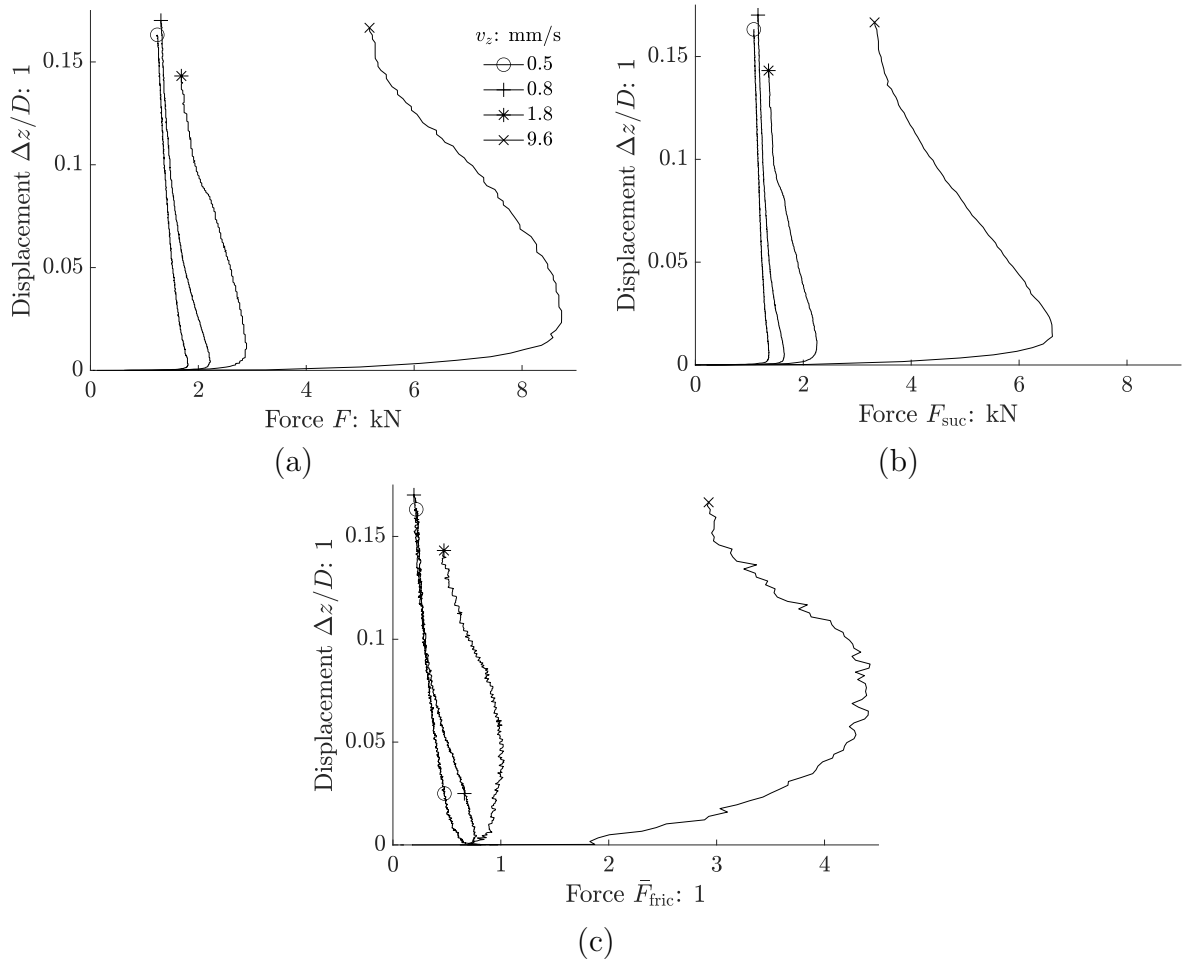
Figure 3.15: Effect of displacement rate on total force (a), suction force (b) and frictional resistance for model L500D510.

3.4.2 Displacement rate

It is evident from Figure 3.15 (a) that higher displacement rates invoked larger tensile forces. Even a slightly higher displacement rate in test v0.8 in comparison to test v0.5 led to substantial increase of the tensile resistance. In every test, distinct maximum resistances were reached within certain displacements and subsequently, the tensile forces reduced gradually. This reduction was due to continuous extraction of the suction bucket, which implied two aspects. Firstly, the frictional resistance diminished since the area of the suction bucket's skirt was reduced. Secondly, more drainage was enabled by the reduction of the embedment depth and thus, the length of the drainage path shortened.

The higher tensile resistance in case of higher displacement rate necessitated larger displacement, which resulted from the mobilisation of the suction force that required large displacement in contrast to the friction under drained condition. In particular, the displacement, where the maximum tensile resistance occurred, was in the range of $0.003 < \Delta z/D < 0.025$ for the investigated displacement rates. In section 2.1, two values of nor-

malised displacements were introduced to enable comparison with potential SLS criteria, namely $\Delta z/D = 0.009$ and $\Delta z/D = 0.013$. Thus, the model tests indicate that tensile resistances exceeding the drained resistance are attainable under partially drained to undrained conditions as long as a certain displacement would be acceptable.

The initial stiffness could not be quantified since the accuracy of the load cell and the DT were in the range of the measured values at the beginning of the tests. Nevertheless, certain tensile forces, which are less than the particular maximum tensile resistance, were achieved within less displacement in case of higher displacement rates. Therefore, the measurements suggest that the stiffness was enhanced by less drainage as qualitatively depicted in Figure 2.3. Consequently, accounting for partial drainage would decrease the required displacement to generate a particular tensile resistance.

The gain in tensile resistance was mainly due to the presence of the negative differential pressure and the invoked suction force at the suction bucket's lid (see Figure 3.15 (b)). This aspect was manifested by two aspects. Firstly, the magnitude of the suction force formed relevant share of the total force and secondly, the displacements, at which the maximum resistance and suction force appeared, coincided approximately. After the occurrence of the maximum suction force, it continuously reduced because of the previously described gain of drainage.

To assess the effect of partial drainage on the frictional resistance, the difference between total force and suction force was evaluated, i.e. $F_{\text{fric}} = F - F_{\text{suc}}$. Since the drained resistance consists solely of the frictional resistance ($F_{\text{dr}} = F_{\text{fric}}$), the frictional resistance was divided by the drained resistance to obtain $\bar{F}_{\text{fric}}$ (see Figure 3.15 (c)). A value of $\bar{F}_{\text{fric}} = 1$ states that the frictional resistance is equal to the initially measured drained resistance. The mean value of the drained resistances of the four tests was $F_{\text{dr}} = 0.72\,\text{kN}$ with a standard deviation of $0.07\,\text{kN}$ (see Table 3.3). In test v9.6, the maximum resistance was $\bar{F} > 13$ and the maximum frictional resistance was $\bar{F}_{\text{fric}} > 4$, which relates to the more undrained response due to the high displacement rate. In contrast to that, tests v0.5, v0.8 and v1.8 implied partial drainage. Consequently, the maximum resistances were only 2.5 to 4 times higher than the drained resistances, but the associated frictional resistances were even somewhat lower than under drained conditions.

Evidently, the change of drainage condition affected the frictional resistance as a result of the presence of negative differential pressure and seepage processes. Under partial drainage, the pore water seepage flow is expected to substantially diminish the inner friction. However, for increasing displacement rates, where less drainage was permitted, higher negative differential pressure was generated, which magnified the frictional resistance mainly at the outside of the suction bucket's skirt. Figure 3.15 (c) demonstrates that the generation of the maximum frictional resistance needed more displacement for higher displacement rates. This effect is probably related to the required time to develop the pore water seepage flow entirely, which affected the frictional resistance. Specifically in tests v1.8 and v9.6, the maximum suction force was reached at less displacement than the maximum frictional resistance. These findings clearly demonstrate the signifiant interaction of drainage and frictional resistance.
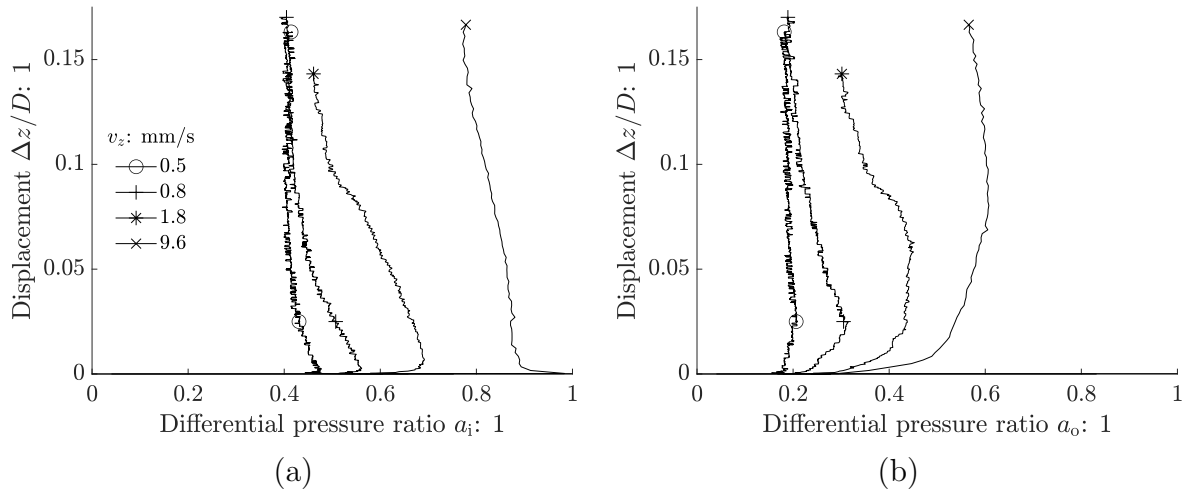
Figure 3.16: Effect of displacement rate on differential pressure ratio inside (a) and outside (b) the suction bucket's skirt for model L500D510.

The examination of the DPS readings enable the evaluation of the degree of drainage. Figure 3.16 shows the measurement of the DPS at the skirt divided by the differential pressure measured at the lid (as introduced in Equation 3.4). The higher the differential pressure ratio is, the less dissipation takes place between the two regarded locations. However, the differential pressure ratio is not exclusively driven by seepage processes, but also affected by dilation. The interaction of both effects increases the complexity of the differential pressure field and impedes the exact determination of the degree of drainage.

Theoretically, a differential pressure ratio of one states that no differential pressure would be dissipated between the two DPSs indicating undrained condition, which was immediately present inside the suction bucket's skirt at the beginning of test v9.6 (see Figure 3.16 (a)). Subsequently, the differential pressure ratio decreased rapidly until $a_i \approx 0.9$ followed by a more steady decrease during further displacement of the suction bucket. In case of tests v0.5, v0.8 and v1.8, higher amounts of differential pressure were dissipated inside the suction bucket than in test v9.6. Moreover, the three tests with the low displacement rates evinced gradual reduction rather than sudden decline (as in test v9.6) after reaching the maximum differential pressure ratio at the skirt's inside.

While the maximum differential pressure ratios on the inside were almost immediately generated, the differential pressure ratios on the outside increased steadily until larger displacements were reached and thus the flow fields were appropriately established (see Figure 3.16 (b)). As a consequence, the differential pressure ratios at the outside did not exhibit a pronounced maximum value and had minor reduction for large displacements. In general, the differential pressure ratios were lower on the outside than on the inside, which has been anticipated. Moreover, the continuous development of the differential pressures at the outside correlate with the mobilisation of the frictional resistance (see Figure 3.15 (c)).

Figure 3.17 (a) presents the development of the plug heave over the displacement of the suction bucket. Apparently, the plug heave depended on the applied displacement rate
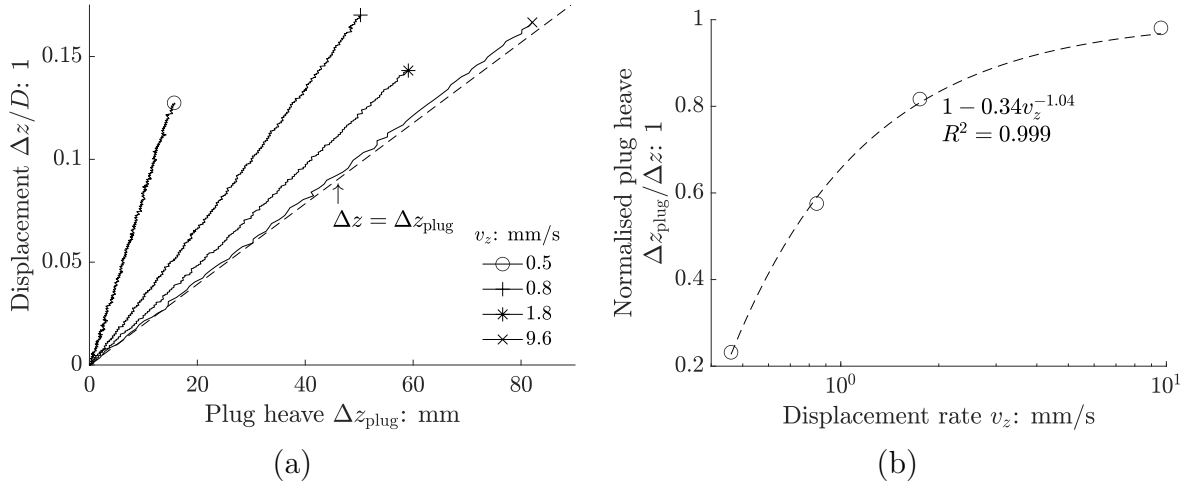
Figure 3.17: Effect of displacement rate on plug heave (a) and normalised plug heave (b) for model L500D510.

with lower displacement rates exhibiting less plug heave, since the displacement was slow enough for the water to flow inside the suction bucket and fill the gap between the suction bucket's lid and the soil surface. In contrast, partially drained to undrained conditions caused significant plug heave as evident from test v9.6. The dashed line represents equality of plug heave and displacement, which is expected to take place if drainage would be entirely prohibited.

The measured plug heave was approximately linearly related to the displacement of the suction bucket for any specific displacement rate (see Figure 3.17 (a)) so that it can be expressed as a constant normalised plug heave $\Delta z_{\mathrm{plug}}/\Delta z$ for each particular displacement rate. This quantity gives an indication for the degree of drainage and is depicted in Figure 3.17 (b). To qualitatively assess the relation between the normalised plug heave and the displacement rate, a function was regressed. For high displacement rates, where the response is almost undrained, the value approaches unity. The slower the displacement rate is, the lower is the normalised plug heave, which is expected to approach zero for drained conditions.

3.4.3 Model scale

While effects of the model scale on the drained resistance were discussed in subsection 3.3.2, Figure 3.18 depicts results of tests with partial drainage ($v_z \approx 10\,\mathrm{mm/s}$) for all model dimensions. In order to facilitate the comparison of the different geometric dimensions, the displacement was divided by the suction bucket's diameter and the generated tensile force was divided by the area of the suction bucket's lid (see Figure 3.18 (a)). The mobilisation of the tensile resistance with respect to the displacement was similar for every model, which underlines the practical relevance of the normalisation $\Delta z/D$ introduced in section 2.1. The maximum tensile resistances were attained within the range of $0.012 < \Delta z/D < 0.029$. Nevertheless, there is no explicit tendency of the displacement
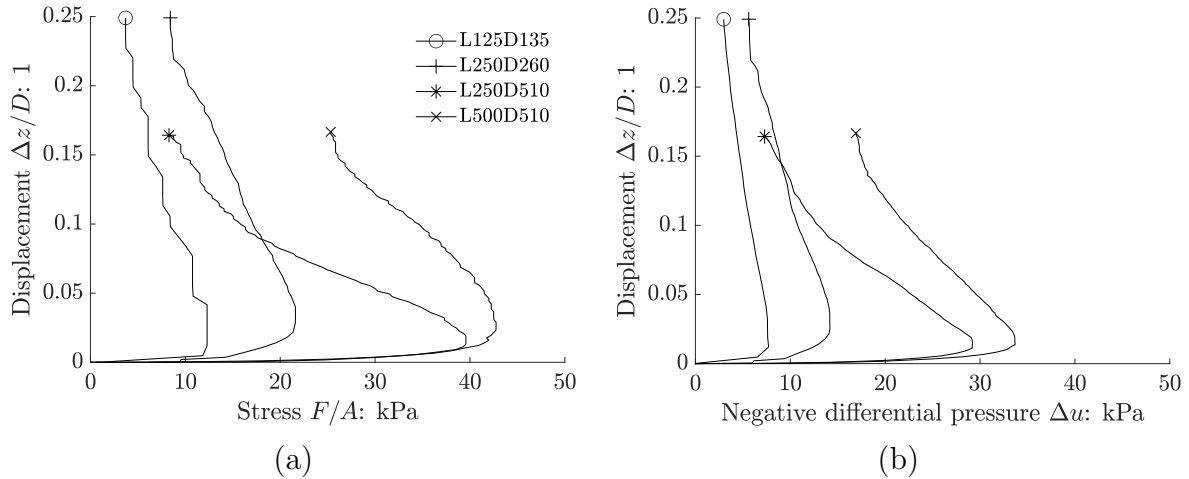
Figure 3.18: Effect of model scale on tensile resistance (a) and negative differential pressure (b) for $v_z \approx 10\,\mathrm{mm/s}$.

on the model dimension. The tensile stress increased with the scale of the model, which implies that larger diameters of suction buckets achieve higher tensile resistances not only due to their larger dimension, but also by higher tensile stresses. The comparison of the models L250D510 and L500D510 enables the evaluation of the aspect ratio. Initially, the generation of the tensile resistance was approximately identical, but the model with the larger aspect ratios finally reached higher tensile resistance at larger displacement. Firstly, the longer skirt provided larger area for the greater skin friction and secondly, the longer drainage path provoked less drainage and higher negative differential pressure (see Figure 3.18 (b)).

As presented in Figure 3.18 (b), the negative differential pressure governed the tensile resistance of every model, since it provided relevant share of the tensile stress. Moreover, the size of the model highly affected the generation of the negative differential pressure, i.e. the larger the model was, the higher negative differential pressure was measured. Comparing model L250D260 with model L250D510 highlights that doubling the diameter of the suction bucket led to an increase of the negative differential pressure by a factor of two. In terms of the generation of the negative differential pressure, it would be expected that larger model dimensions require more displacement to reach the maximum value. However, L250D510 reached the maximum negative differential pressure prior to L250D260. This might result from the normalisation of displacement $\Delta z/D$, which is demonstrated by comparing L250D510 and L500D510, where the larger model indeed required more displacement to generate the higher negative differential pressure.

Figure 3.19 evaluates the maximum tensile resistance, negative differential pressure and normalised plug heave of all model tests at constant displacement rate. The maximum tensile resistance was determined for every model test and divided by the area of the suction bucket's lid to obtain the corresponding tensile stress. Moreover, the negative differential pressure at the occurrence of the maximum tensile resistance was evaluated. These values were visualised depending on the applied displacement rate and supplemented by

regressed functions (see Figure 3.19 (a) and (b)). The constant terms in the functions presented in Figure 3.19 (a) are defined as mean values of the drained resistances of the particular models. Although the number of tests is too low to derive a specific scaling law or design recommendation, the tendency of both higher stresses and negative differential pressures for larger models is obvious and verified by larger factors in the regressed functions. To mobilise equal stresses or negative differential pressures, smaller suction bucket models required significantly higher displacement rates. Interestingly, the suction bucket's diameter for models with identical lengths had relatively small effect on the exponent (see L250D260 and L250D510), but affected the factor in the regressed function.

Following the procedure introduced in Figure 3.17, Figure 3.19 (c) summarises the normalised plug heave of all conducted tests. It would be expected that smaller dimensions of the suction bucket invoked more drainage and therefore implied less plug heave. However, the results indicate similar plug heave for all suction bucket models at distinct displacement rates. Potentially, the absolute differences in the model dimensions were too small to explicitly evoke the expected pattern so that the plug heave mechanism was overlaid by the soil being constrained inside the suction bucket. Specifically test L250D510v10 exhibited $\Delta z_{\mathrm{plug}}/\Delta z = 1.003 > 1$, which is physically questionable and might result either from soil's dilation or measurement error.

3.4.4 Installation method

Beside the analysis of the installation method regarding the drained resistance in Figure 3.14, Figure 3.20 presents results of tests under partial drainage with respect to their installation method. Two distinct displacement rates were applied on the suction bucket model L250D260, which was either installed by jacking or by applying negative differential pressure. Since the embedment depths of the test pairs differed (jacked installations reached greater embedment depths), the comparability of the results is limited. Nevertheless, relevant conclusions might be drawn.

Independent of the applied displacement rate, the maximum tensile resistance was significantly higher in case of jacked installations. At first sight, this effect cannot be definitely attributed to the installation method due to the greater embedment depth, which would qualitatively lead to higher tensile resistance, but the extent could not be quantified. Therefore, it is referred to Figure 3.18 (a), where the embedment depth of model L500D510 is twice as high as the one of model L250D510, but the increase in tensile resistance is relatively less than in Figure 3.20. This relation evinces that the difference in tensile resistance is probably mainly attributed to the installation method.

Additionally considering the suction force reveals similarity between the hydraulic and jacked installation with a tendency of slightly higher suction force for models that were installed by jacking (see Figure 3.20 (b)). It is evident that these minor differences did not essentially affect the tensile resistances. The hydraulic installation is expected to loosen the soil inside and in proximity of the suction bucket more than the jacked installation would do (see analysis of plug heave in Figure 3.11). Consequently, the generated negative
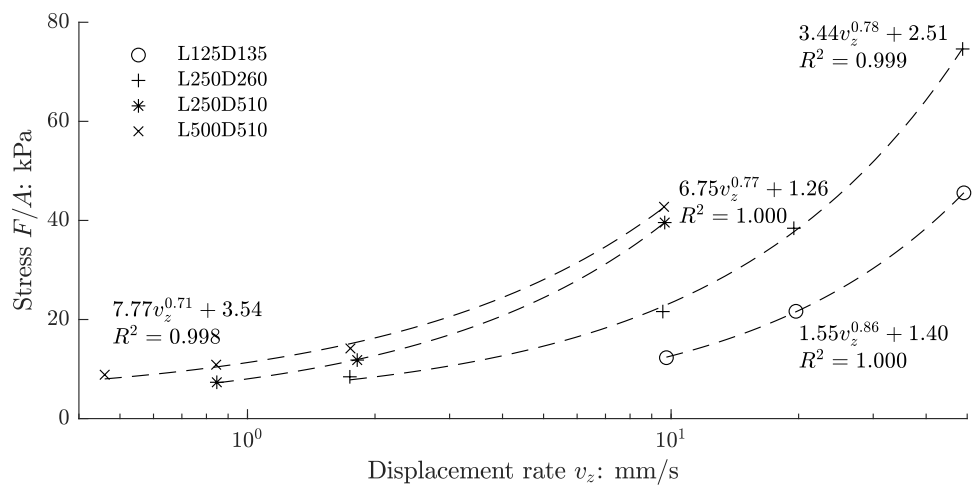
(a)
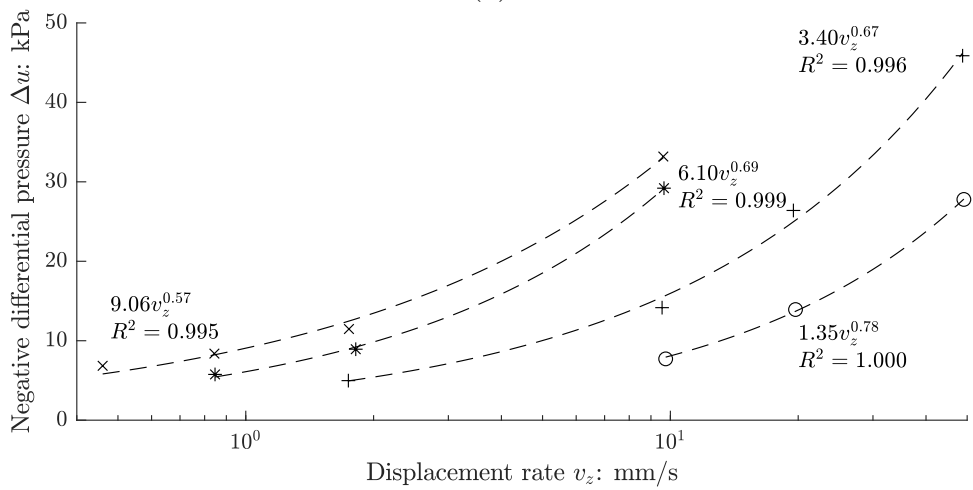
(b)
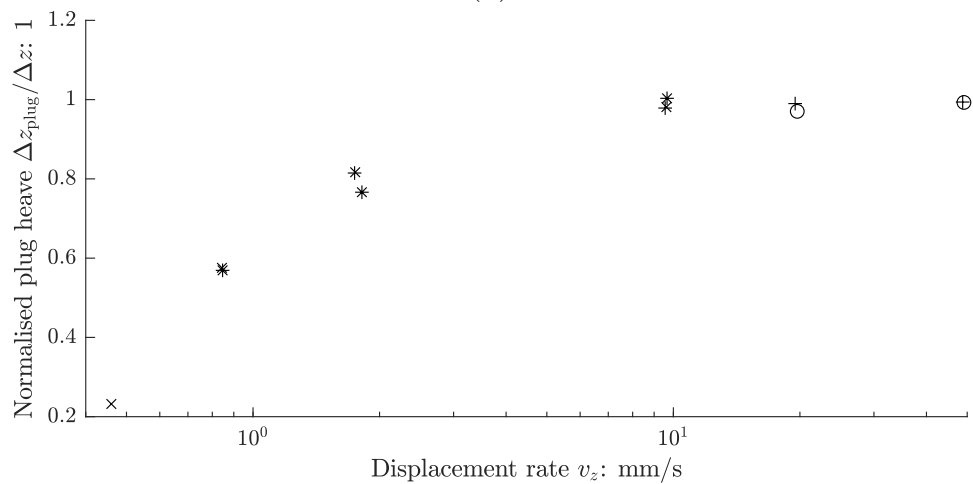
(c)

Figure 3.19: Effect of model scale on maximum stress (a), negative differential pressure (b) and normalised plug heave (c) in dependence on displacement rate.
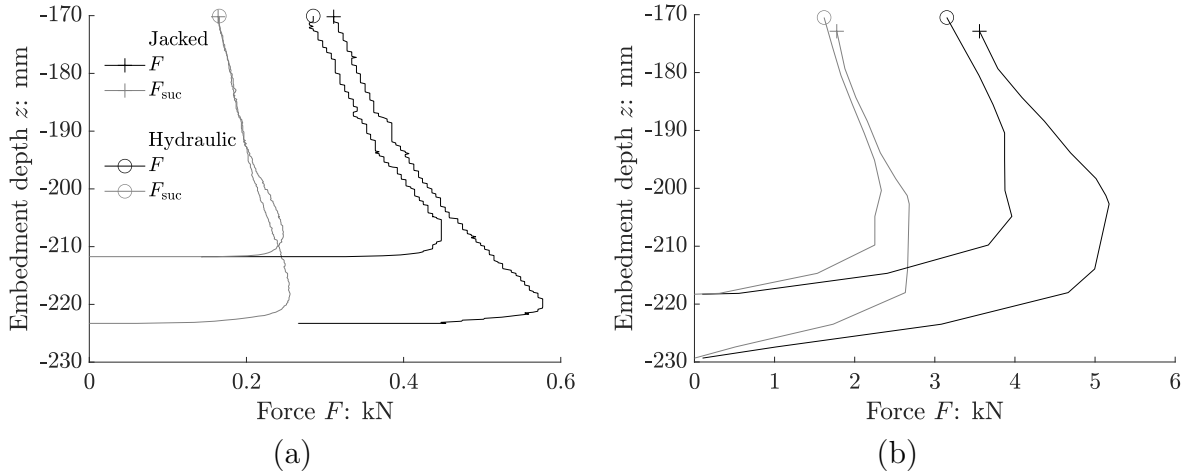
Figure 3.20: Effect of installation method on tensile resistance for $v_z \approx 2 \, \mathrm{mm/s}$ (a) and $v_z \approx 50 \, \mathrm{mm/s}$ (b) with model L250D260.

differential pressure would be less than for jacked installation as it is observed for both displacement rates in Figure 3.20. In terms of the suction force, the results indicate that the suction bucket's response was rather affected by the installation method than by the differing embedment depths.

Finally, the residual force after the occurrence of the maximum tensile resistance was higher for models installed by jacking, while the suction forces were approximately equal. These observations suggest that the frictional resistance of the suction bucket was enhanced by jacked in comparison to hydraulic installation, but the negative differential pressure was rather not affected. Apart from this, the normalised plug heave $\Delta z_{\mathrm{plug}}/\Delta z$ was found to be akin or slightly higher in case of jacked installations.

3.5 Results of tests with constant force

3.5.1 Overview

Three tests with constant forces at different load magnitudes were conducted. The applied loads were specified regarding the drained resistance, namely $\bar{F} \in [1.09, 1.58, 2.04]$. The names of the tests were specified by the letter M followed by a number that states the applied load $\bar{F}$ in 1. Since all results refer to model L500D510, the name of the model is not explicitly mentioned.

The aim of these tests was to provide a benchmark for cyclic tests. Furthermore, the load sharing and drainage were evaluated to identify potential effects of the different load magnitudes. Additionally, the tests provoked certain displacement rates that can be recursively related to the displacement-controlled tests. The presentation of the results is limited to the previously described purposes, but additional readings of particular sensors are provided in Appendix A.
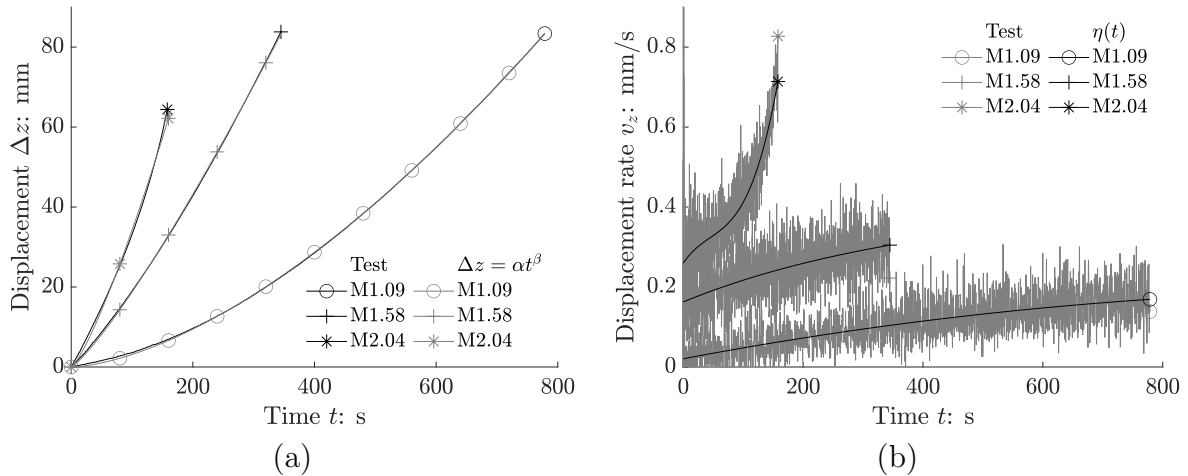
Figure 3.21: Effect of load magnitude on time-dependent displacement (a) and displacement rate (b) for model L500D510.

3.5.2 Load magnitude

Figure 3.21 (a) depicts the displacement accumulation of the aforementioned tests. Higher loads induced faster displacement of the suction bucket, which is as expected since the applied loads exceeded the drained resistances and the generation of an additional suction force required distinct displacement rates. In case of test M1.09, where the applied load was only slightly higher than the drained resistance, the displacement was relatively low at the beginning of the test. In contrast, the displacements in tests M1.58 and M2.04 were more pronounced at the beginning of the tests. Apparently, any test caused continuous acceleration.

The increase of displacement rate is underlined by Figure 3.21 (b), where the displacement rates are illustrated. The grey lines represent the numerical gradient of the measured data, which exhibits considerable scatter as it is typical for derivatives of sensor records. In order to obtain an improved estimation, the displacement versus time curves where approximated by fourth order polynomial equations, which were subsequently differentiated to attain the displacement rate (function $\eta(t)$ represented by black lines). The initial displacement rates at $t = 0\,\mathrm{s}$, where the applied load reached the target value as defined in Figure 2.2, were determined to $v_z \in [0.02, 0.16, 0.26]\,\mathrm{mm/s}$ for tests M1.09, M1.58 and M2.04 respectively. These displacement rates are lower than the ones presented in subsection 3.4.2, but the applied load magnitudes were lower than the maximum tensile resistances measured in the displacement-controlled tests as well. The lowest maximum tensile resistance was $\bar{F} = 2.5$ in test L500D510v0.5, which is at least comparable to the initial displacement rate of test L500D510M2.04, whereby the difference resulted obviously from the smaller applied load.

Figure 3.21 (b) points out that the displacement rates increased steadily during the progress of the tests M1.09 and M1.58, but the acceleration was under-linear. Opposed to that, test M2.04 initially accelerated in the same pattern, but than commenced to gain displacement rate over-linearly. The records of test M2.04 revealed that the suction bucket

Table 3.5: Regressed coefficients for constant force tests with model L500D510.

Load	Coefficients	
$\bar{F}$: 1	α: mm/s$^\beta$	β: 1
1.09	0.002	1.600
1.58	0.073	1.205
2.04	0.099	1.269

was not able to provide sufficient resistance to the applied load after $\Delta z \approx 63$ mm, which relates to the substantial acceleration during this phase of the test. As a consequence, the presented data is limited to the relevant range, where the applied load was stable.

Additionally, qualitative approximations of the displacement accumulation by regressed functions are supplemented in Figure 3.21 (a). The regressions did not aim at perfect agreement but their formulation was chosen to be rather simple comprising only two coefficients. As a result, the regressions exhibit discrepancies to the measured data especially at the beginning of each test since the chosen equation implies $v_z(t = 0\,\text{s}) = 0$ mm/s. However, the estimation is reasonable and supports the qualitative evaluation. The regressed coefficients, which indicate that a lower load implied higher non-linearity (see β), but lower initial displacement rate (see $\alpha\beta$), are summarised in Table 3.5.

The load sharing is exemplified in Figure 3.22 (a) in terms of suction force and frictional resistance (as introduced in subsection 3.4.2). Although the applied load in test M1.09 only marginally exceeded the drained resistance, the initially invoked frictional resistance was less than the drained resistance. This resulted from partial drainage caused by considerable acceleration during load application t_{acc}, which induced negative differential pressure and corresponding suction force. The continuous extraction of the suction bucket from the soil reduced the frictional resistance so that a higher suction force was required. The higher suction force related to the increasing displacement rate depicted in Figure 3.21 (b). Nevertheless, it has to be noted that in test M1.09 the frictional resistance was predominant over the suction force until $t \approx 410\,\text{s}$ and $\Delta z \approx 30$ mm.

While the shares of the resistances were approximately identical at the beginning of test M1.58, the suction force substantially exceeded the frictional resistance in test M2.04. The tendency of decreasing frictional resistance along with an increase of suction force in tests M1.58 and M2.04 was qualitatively alike to the previously discussed pattern of test M1.09. However, the reduction of the frictional resistance was much more pronounced in test M2.04. In Figure 3.15 (c), the frictional resistance was found to be reduced under partial drainage, which is confirmed by the three tests with constant force.

The records of the GS showed an initial settlement or at least no plug heave (see Figure 3.22 (b)). The settlement was probably related to densification of the soil, which was loosened during the installation, by shearing at the inside of the suction bucket's skirt. After a certain time and as the suction bucket commenced to displace more rapidly, the plug heave set on.
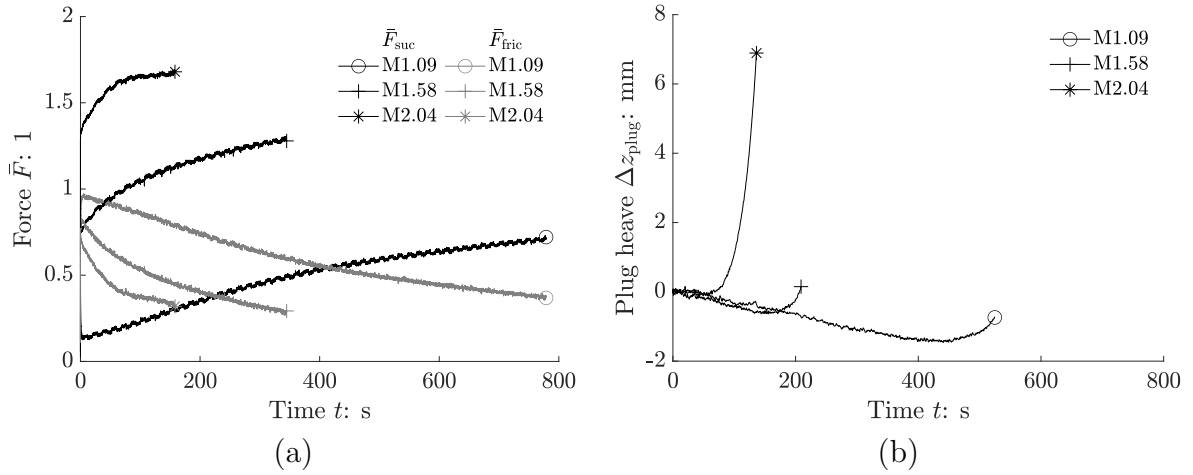
Figure 3.22: Effect of load magnitude on load sharing (a) and plug heave (b) for model L500D510.

The differential pressure ratios at the skirt's inside and outside provided indication for the drainage condition. Except for minor differences, these quantities were similar for all investigated load magnitudes (see Appendix A) so that the drainage was not essentially affected by the load magnitude. Initially, the considerable load rate within the time t_{acc} implied slightly higher differential pressure ratios in every test, but during continuous loading, their values reduced to $a_{\mathrm{i}} \approx 0.4$ and $a_{\mathrm{o}} \approx 0.15$. In tests M1.09 and M1.58, the differential pressure ratio remained almost constant over the duration of the tests. In contrast, test M2.04 exhibited an increase of both quantities by 0.05 to 0.1.

3.6 Results of tests with cyclic force

3.6.1 Overview

A total number of 13 cyclic tests was conducted with model L500D510. The load characteristics of the tests differed in terms of the load frequency (F denotes f in Hz), mean load (M denotes $\bar{F}_{\mathrm{mean}}$ in 1) and load amplitude (A denotes $\bar{F}_{\mathrm{ampl}}$ in 1). The tests are summarised in Table 3.6 in ascending order of the maximum load $\bar{F}_{\mathrm{max}}$ respecting the two distinct load frequencies. The loads were specified to be tensile swell loads and at least the maximum load exceeded the suction bucket's drained resistance, though the mean load was less than the drained resistance in some tests. Three tests exhibited load characteristics, where even the minimum load exceeded the drained resistance in every cycle, i.e. $\bar{F}_{\mathrm{min}} > \bar{F}_{\mathrm{dr}}$, which was achieved by $\bar{F}_{\mathrm{mean}} > \bar{F}_{\mathrm{ampl}} - 1 > 0$ as illustrated in Figure 3.23.

The load characteristics are graphically presented in Figure 3.23, where the grey shaded area marks the range in which the load would not have exceeded the drained resistance. Moreover, Figure 3.23 facilitates the identification of particular tests that coincide in

Table 3.6: Summary of tests with cyclic force.

Test	Maximum load	Cycles at distinct $\Delta z/D$	
	$\bar{F}_{\max}$: 1	$N_{\Delta z/D=0.009}$: 1	$N_{\Delta z/D=0.013}$: 1
F1.02M0.86A0.18	1.04	1767	1987
F1.01M0.73A0.38	1.11	411	520
F1.01M1.06A0.25	1.31	106	150
F1.01M0.87A0.60	1.47	75	106
F1.01M1.24A0.38	1.62	48	69
F1.02M1.58A0.39	1.97	28	41
F1.01M1.29A0.89	2.18	37	54
F1.01M2.12A0.52	2.64	13	20
F1.01M1.90A0.99	2.89	11	17
F0.50M0.74A0.37	1.11	203	256
F0.51M1.04A0.45	1.49	38	55
F0.51M1.52A0.65	2.17	16	24
F0.51M1.90A0.81	2.71	7	11

certain load characteristics, i.e. load frequency, mean load or load amplitude. Although the aim was to vary solely individual parameters of the load characteristics while maintaining the others, the load control of the actuator suffered from inaccuracies so that particular parameters were not perfectly equal for different tests. However, the test results were evaluated within this context and essential findings were attained.

The load frequencies were artificially chosen since there is no methodology to adequately scale the complex seepage flow due to cyclic loading (see subsection 2.3.4). Thus, the load frequencies were specified to be higher than those occurring at offshore conditions to account for the reduced scale, namely $f \in [0.5, 1.0]$ Hz. To verify suitability of the load frequencies, the results of the tests were analysed by means of retrospective FE simulations for estimating the load frequency at prototype dimension that corresponds to each particular model test. The main idea was to obtain similar normalised displacement rates $(\mathrm{d}z/D)/\mathrm{d}N$ for different scales by iteratively adjusting the load frequency at prototype scale. The results of these analyses are provided in subsection 4.2.6.

The cyclic displacement accumulation depends on the applied load and is relevant for the design of suction bucket foundations. Thus, the number of cycles that were sustained until breaching potential SLS criteria are summarised in Table 3.6. The displacement accumulation is analysed in detail in subsection 3.6.2. Beside the displacement accumulation, the evaluation of the cyclic tests focused on the accumulation of negative differential pressure and plug heave. These quantities were examined in the following regarding the variation of the load characteristics, i.e. load magnitude, mean load, load amplitude and load frequency. The differential pressure ratio a_i and a_o did not provide relevant findings with respect to the load characteristics so that the results are not explicitly discussed. However, it should be mentioned that at the beginning of the cyclic tests, the values were
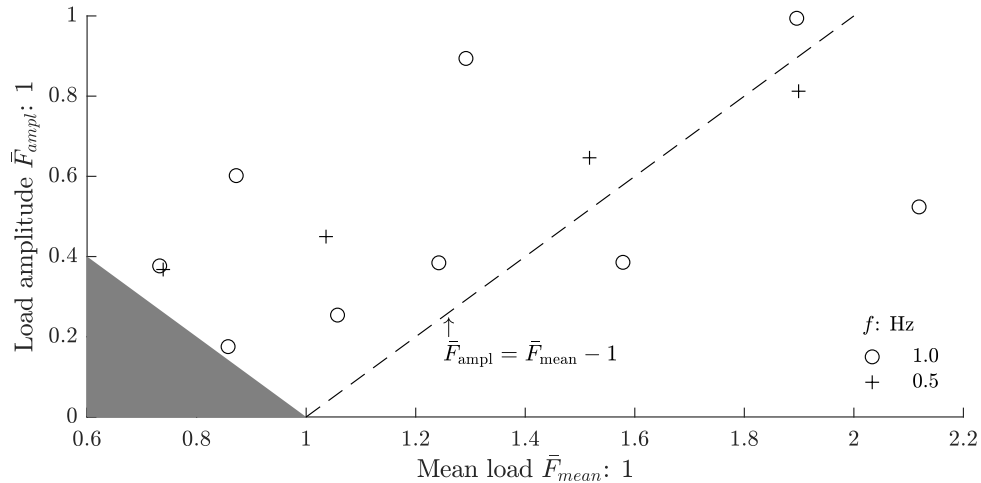
Figure 3.23: Load characteristics of cyclic tests with model L500D510.

in the range of $0.4 < a_\mathrm{i} < 0.5$ and $0.1 < a_\mathrm{o} < 0.2$. During the progress of the tests, especially the differential pressure ratio at the inside increased. Beside others, these results are provided in Appendix A.

3.6.2 Displacement accumulation

Figure 3.24 (a) presents the displacement accumulation recorded in nine tests with a load frequency of $1.0\,\mathrm{Hz}$. As it would be expected, higher loads led to faster displacement accumulation. At first sight, the maximum load $\bar{F}_\mathrm{max} = \bar{F}_\mathrm{mean} + \bar{F}_\mathrm{ampl}$ seems to be the dominating parameter, since the displacement accumulation was the greater, the higher the maximum load was. However, the comparison of the tests F1.01M1.29A0.89 and F1.02M1.58A0.39 reveals that a higher mean load evoked faster displacement accumulation, although the maximum load was lower. This effect probably resulted from more distinct unloading in every cycle of test F1.01M1.29A0.89 so that relevant duration of the loading sequence implied loads less than the drained resistance. In contrast, the tensile load in test F1.02M1.58A0.39 permanently exceeded the drained resistance. Thus, the exceptional case of tests F1.01M1.29A0.89 and F1.02M1.58A0.39 regarding the displacement accumulation might result from the fact that solely loads higher than the drained resistance induce relevant displacement. This hypothesis is further pursued in the following analyses.

The tests at lower frequency resulted in considerably higher displacement accumulation as the comparison of Figure 3.24 (a) and (b) points out. The reason for that was the longer duration of loading allowing more water to flow inside the suction bucket. This aspect is discussed extensively in subsection 3.6.6. The effect of the load magnitude is analogue to the previously described results at $f = 1.0\,\mathrm{Hz}$ with higher maximum and higher mean loads leading to more displacement accumulation (see four tests with $f = 0.5\,\mathrm{Hz}$ in Figure 3.24 (b)).
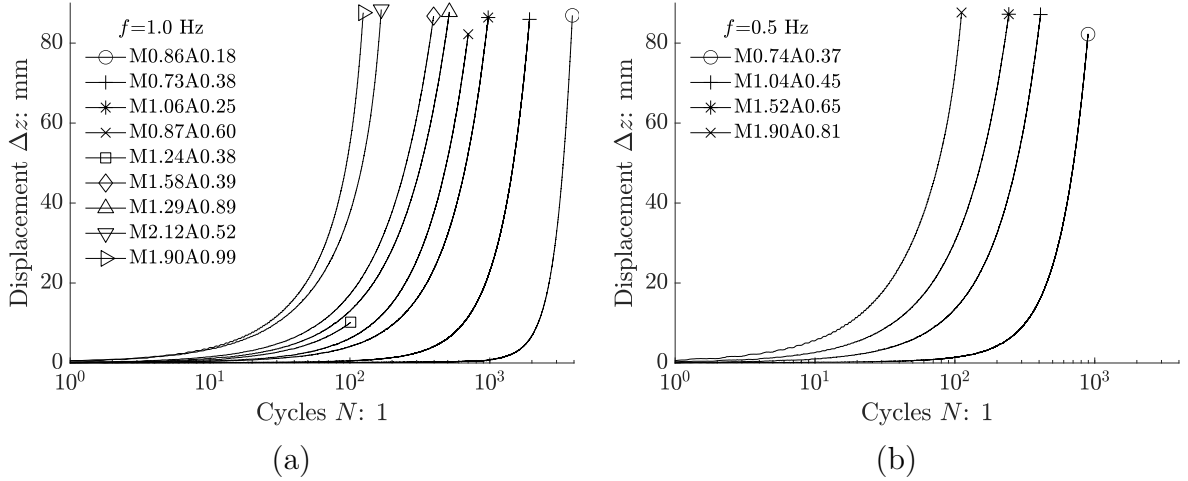
Figure 3.24: Cyclic displacement accumulation with load frequencies $f = 1.0\,\text{Hz}$ (a) and $f = 0.5\,\text{Hz}$ (b) for model L500D510.
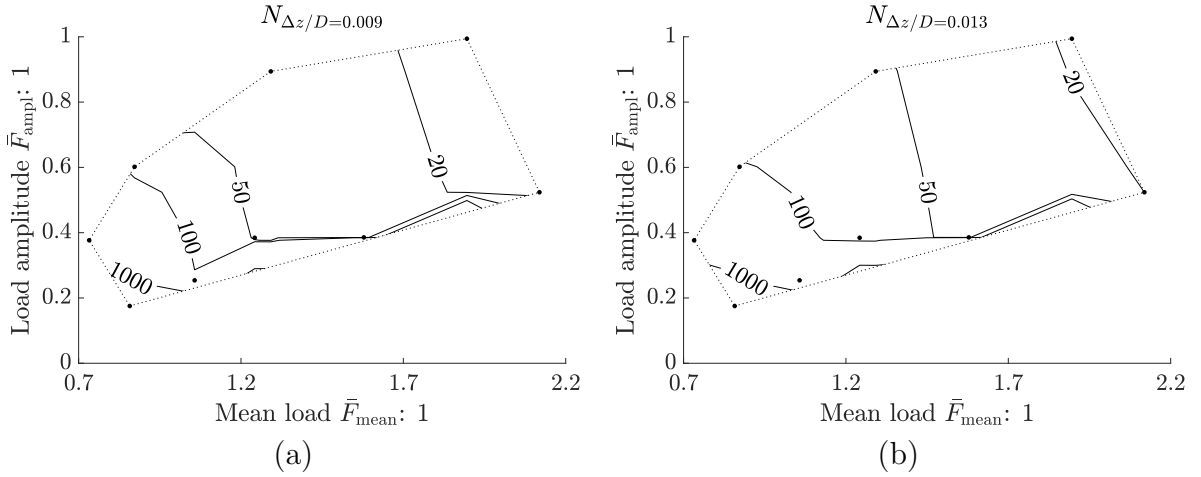
Figure 3.25: Cyclic interactions at $\Delta z/D = 0.009$ (a) and $\Delta z/D = 0.013$ (b) for $f = 1.0\,\text{Hz}$.

Figure 3.25 demonstrates the effect of the load characteristic on the displacement accumulation in terms of reaching distinct displacements for tests with $f = 1.0\,\text{Hz}$ (see Table 3.6). Although the validity of the interpolated lines representing equal number of cycles is limited by the low number of model tests, the tendency of the maximum load dominating the displacement accumulation is evident. Beside that, the mean load is predominant over the load amplitude. Evidently, a relevant number of cycles depending on the actual load characteristics was withstood until distinct displacements were breached. The comparison of Figure 3.25 (a) and (b) highlights that the qualitative effect of the cyclic load characteristics on the sustainable number of cycles did not change significantly between $\Delta z/D = 0.009$ and $\Delta z/D = 0.013$. However, the quantitative evaluation points out that if accounting for a larger displacement, substantially more cycles were borne.

The tests with constant force were considered as benchmarks for the cyclic displacement accumulation. Therefore, tests with similar monotonic and cyclic (mean) loads were com-
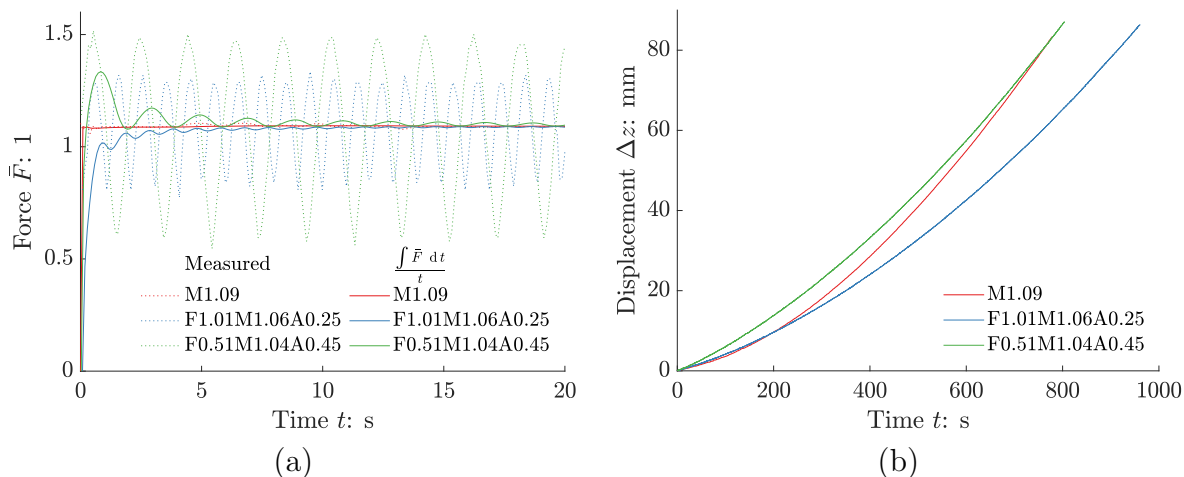
Figure 3.26: Mean load (a) and displacement accumulation (b) for tests with $\bar{F}_{\mathrm{mean}} \approx 1.0$.

pared in terms of their displacement. The evaluation of the tests in time scale enables the comparison of cyclic tests with different load frequencies and the corresponding monotonic test. Figure 3.26 presents the analysis of tests with $\bar{F}_{\mathrm{mean}} \approx 1.0$. The measured forces are depicted in Figure 3.26 (a) supplemented by the average loads (time integrated loads $\int \bar{F} \, \mathrm{d}t/t$) in order to prove comparability. Evidently, the average loads converged the longer the test continued. Thus, the considered tests applied similar average loads on the suction bucket, so that it is reasonable to examine their displacement accumulations.

The displacement accumulation is shown in Figure 3.26 (b) and reveals that the measured displacements were not equal, but qualitatively similar in the three tests. Figure 3.26 (b) points out that the displacement of the monotonic test M1.09 was initially similar to the one of cyclic test F1.01M1.06A0.26 for $t < 200\,\mathrm{s}$. Then, the displacement rate of test M.109 increased more rapidly than in test F1.01M1.06A0.26. As a consequence, the accumulated displacement of test M1.09 approached the one of test F0.51M1.04A0.45, which exhibited the most distinct displacement accumulation at the beginning of the test. After approximately $760\,\mathrm{s}$, the displacement of the monotonic test exceeded the one of test F0.51M1.04A0.45.

The cyclic loads fell below the drained resistance in every cycle as depicted in Figure 3.26 (a). It may be assumed that these loads did not substantially contribute to relevant displacements since the loads might be resisted by the frictional resistance. As a consequence, the cyclic displacement accumulation should be significantly lower than in the monotonic test. In contrast to this hypothesis, the accumulated displacements of the cyclic tests were initially similar or even higher than in the monotonic test. However, it has to be noted that the load amplitudes in the cyclic tests evoked significant maximum loads, which might have superposed the effect of the cyclic unloading below the drained resistance. Further, despite the minimum load $\bar{F}_{\mathrm{min}}$ was less than the drained resistance, the cyclic load still invoked partial drainage so that certain differential pressure arose and the suction bucket did not entirely resist the applied load by its frictional resistance. The last mentioned effects substantiate the larger displacement accumulation.
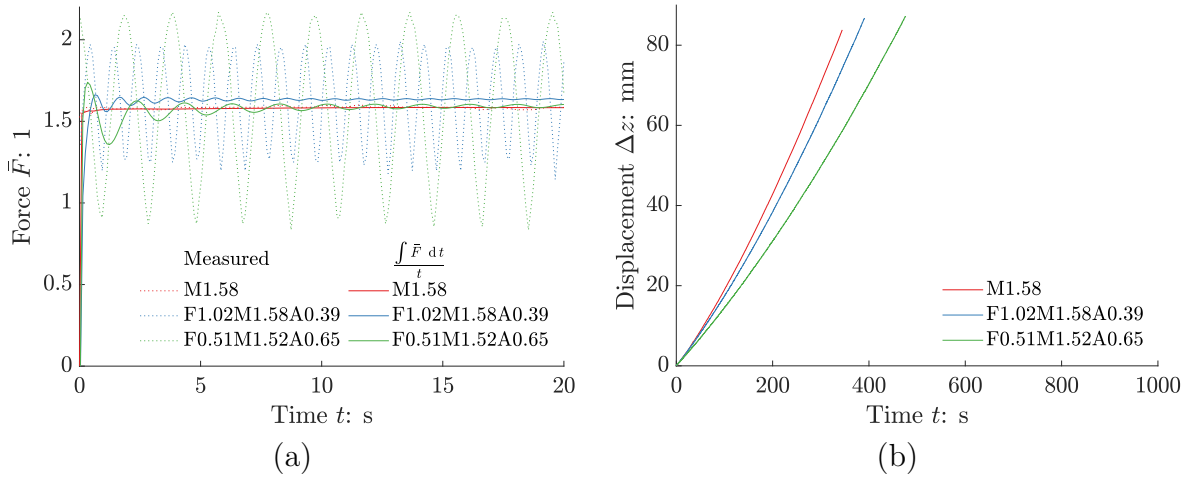
Figure 3.27: Mean load (a) and displacement accumulation (b) for tests with $\bar{F}_{\mathrm{mean}} \approx 1.5$.

In Figure 3.27, the displacement accumulation is compared for $\bar{F}_{\mathrm{mean}} \approx 1.5$. In order to facilitate the comparison with the previously presented results, the limits of the horizontal axis of Figure 3.26 (b) and Figure 3.27 (b) are identical. Apparently, the displacements accumulated faster in tests with higher mean loads. The displacements of tests M1.58 and F1.02M1.58A0.39 were akin. Potentially, the cyclic load amplitude, which did not evoke loads less than the drained resistance, caused more intense displacement of the suction bucket in each cycle. Compared to that, Figure 3.27 (a) points out that the loads in test F0.51M1.52A0.65 were slightly below the drained resistance in every cycle. As a consequence, the displacement accumulation in this test was slightly lower than in the other two tests presented in Figure 3.27 (b). Nonetheless, the displacement accumulations of the three tests were still in the same order, which essentially underlines that the load amplitude is subordinate to the maximum and mean load as derived from Figure 3.25.

It can be concluded that tests with constant forces qualitatively approximate the displacement accumulation of cyclic tests with equivalent mean load $\bar{F}_{\mathrm{mean}}$. Consequently, monotonic tests are capable to provide vague estimations of the cyclic response. However, this estimation only accounts for the displacement accumulation induced by the mean load, but does not regard for effects related to the cyclic amplitude. Especially the unloading below the suction bucket's drained resistance, which mainly depends on the load amplitude, crucially influences the displacement accumulation. The results indicate that the complex cyclic bearing behaviour might be adapted by the application of equivalent monotonic loads, but the monotonic load magnitude has to be appropriately defined and the obtained estimation must be treated as a rough approximation.

3.6.3 Load magnitude

Although the drained resistance is a reference value adopted for comparing different load magnitudes, the behaviour under cyclic loading crucially differs from drained condition. Under cyclic loading, the load rate and the closed valve on the suction bucket's lid induce

differential pressure. Exclusively for very low load frequencies, where negligible differential pressures are generated, the drained condition could be assumed. The load characteristic of tests F1.02M0.86A0.18 and F1.01M0.73A0.38 aimed at applying cyclic loads, whose maximum loads were close to the drained resistance at the most, i.e. $\bar{F}_{\max} = 1.04$ and $\bar{F}_{\max} = 1.11$ respectively. Thus, these tests are representative for the behaviour of a suction bucket under low cyclic tensile loading with partial drainage.

Figure 3.24 (a) demonstrates that in these tests, the suction bucket resisted the loading without significant displacement for numerous cycles. However, the displacement accumulation rate steadily increased with the number of cycles. Thus, after a certain number of cycles, SLS criteria were breached (see Table 3.6) and ultimately, the suction bucket was extracted from the soil. Despite the lower mean load and significant unloading due to the higher amplitude, the displacement accumulation was more pronounced in test F1.01M0.73A0.38 than in test F1.02M0.86A0.18. This finding underlines that the maximum load, which was higher in test F1.01M0.73A0.38, essentially dominated the displacement accumulation.

The development of the negative differential pressure is shown in Figure 3.28 (a). Instead of presenting the readings of the DPS in every cycle, the moving mean $\Delta \hat{u}$ over the duration of one load cycle was calculated for reasons of clarity and to clearly identify accumulation tendencies. In test F1.02M0.86A0.18, the initial negative differential pressure dissipated over about 10 cycles and subsequently, the moving mean was almost $0\,\mathrm{kPa}$ for approximately $N \leq 1000$. In this phase, the differential pressure varied in the range of $-0.18\,\mathrm{kPa} \leq \Delta u \leq 0.22\,\mathrm{kPa}$ so that positive differential pressure arose during unloading to $\bar{F}_{\min} = 0.68$ in every cycle. Then, the negative differential pressure started to accumulate rapidly with the number of cycles, which was strongly connected with the higher displacement accumulation rate (see Figure 3.24 (a)). Test F1.01M0.73A0.38 showed slightly different progress of the mean negative differential pressure. After initial dissipation, the mean negative differential pressure remained on relatively constant level of $0.1\,\mathrm{kPa}$ while varying in the bandwidth $-0.55\,\mathrm{kPa} \leq \Delta u \leq 0.75\,\mathrm{kPa}$ until it commenced to accumulate for $N > 100$. As already observed in test F1.02M0.86A0.18, the accumulation of displacement and differential pressure were related in test F1.01M0.73A0.38. The accumulation of negative differential pressure implied continuous change of the load sharing along with reduction of frictional resistance. This tendency is analogous to the tests with constant force as presented in Figure 3.22 (a) and was observed in every cyclic test.

Figure 3.28 (b) depicts the plug heave over the number of cycles. Instead of plug heave, the soil surface remained at its origin and, during the progress of the test, even settlement took place in both tests. Cyclic shearing at the interface of the suction bucket's skirt probably invoked contraction of the soil inside the suction bucket, which was loosened during the hydraulic installation. After a considerable number of cycles and along with significant increase of the displacement rate, plug heave finally set on.

Additionally, the results of tests F1.01M1.90A0.99 and F1.01M2.12A0.52, representing high cyclic load magnitudes, shall be compared. Test F1.01M1.90A0.99 had a slightly smaller mean load, but a greater load amplitude leading to a higher maximum load than
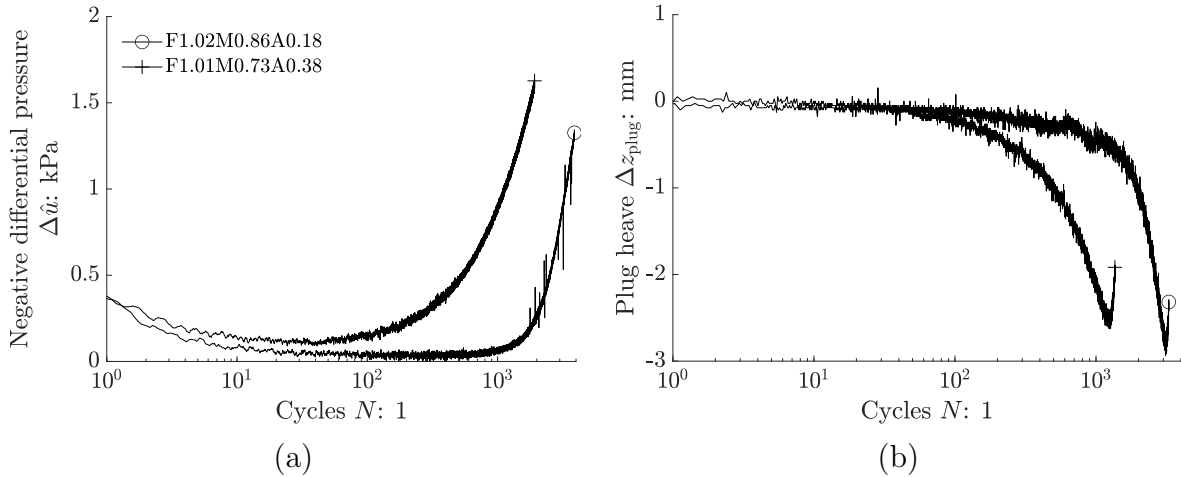
Figure 3.28: Negative differential pressure (a) and plug heave (b) for cyclic tests with low load magnitude.
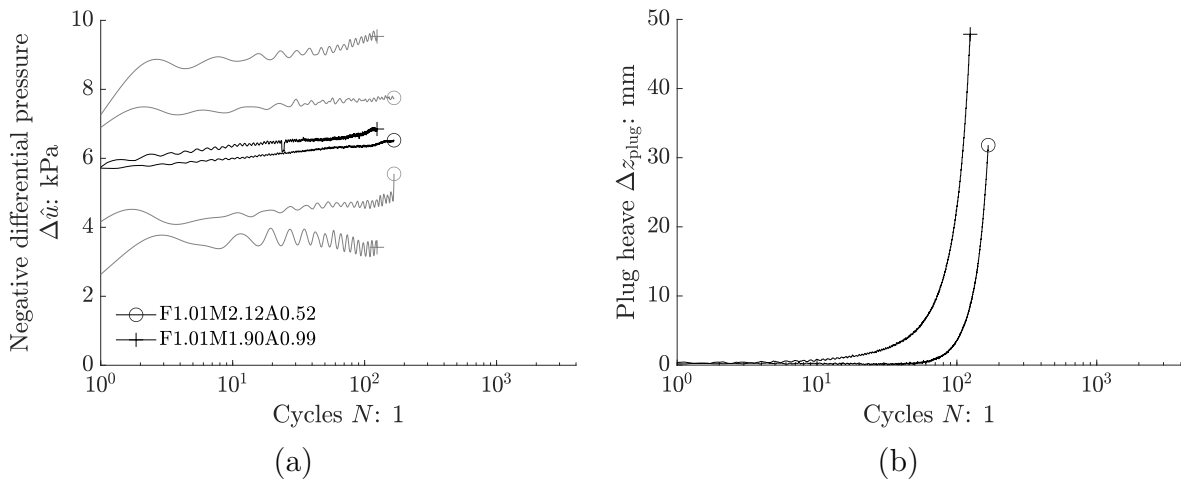
Figure 3.29: Negative differential pressure (a) and plug heave (b) for cyclic tests with high load magnitude.

test F1.01M2.12A0.52. However, both tests showed similar displacement accumulation, with test F1.01M1.90A0.99 having the larger displacement accumulation rate (see Figure 3.24 (a)). As expected, the displacement accumulation rate was much higher than in the previously discussed tests at low cyclic load level.

Figure 3.29 (a) presents the accumulation of negative differential pressure involving the moving mean (black lines) and envelopes (minima and maxima per cycle represented by grey lines). Although the mean load of test F1.01M2.12A0.52 was higher than the one of test F1.01M1.90A0.99, the mean value of the negative differential pressure was slightly lower, which probably resulted from the lower maximum load. As expected, the envelopes reveal a wider span for the higher load amplitude of test F1.01M1.90A0.99. The accumulation of differential pressure was less pronounced than in the tests with low cyclic loads (see Figure 3.28 (a)) and depended almost linearly on $\lg N$.

85
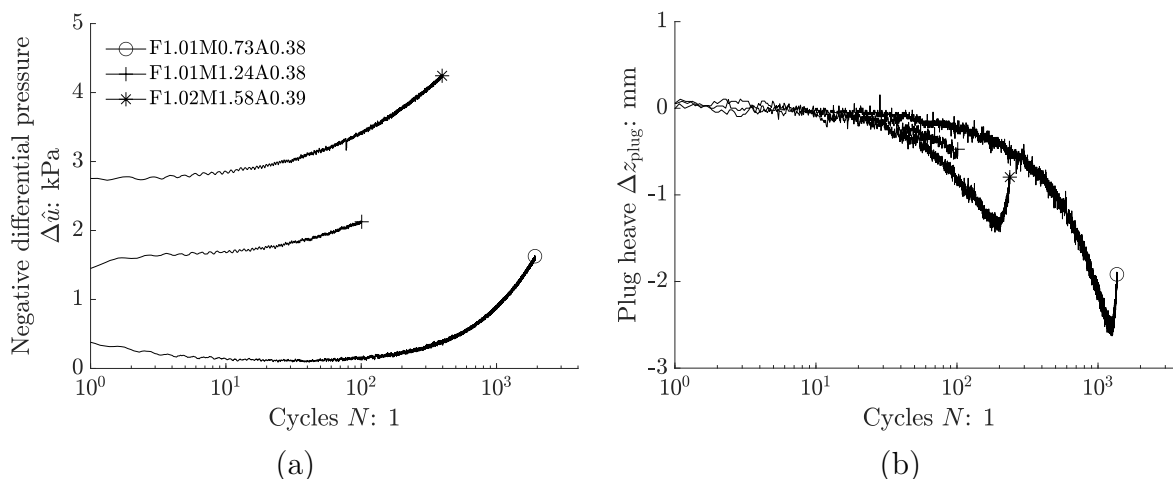
Figure 3.30: Effect of mean load in cyclic tests on negative differential pressure (a) and plug heave (b).

Furthermore, no settlement, but relatively large plug heave, occurred after few load cycles (see Figure 3.29 (b)). The plug heave observed in test F1.01M1.90A0.99 (with the higher maximum load) was considerably greater than in test F1.01M2.12A0.52, where plug heave commenced after 50 cycles, when the suction bucket was already displaced about 15 mm.

3.6.4 Mean load

The tests F1.01M0.73A0.38, F1.01M1.24A0.38 and F1.02M1.58A0.39, which had almost identical load amplitudes, were considered for evaluating the effect of different mean loads. While the load in test F1.02M1.58A0.39 permanently exceeded the drained resistance, the two other tests implied unloading below the drained resistance in every cycle. It is obvious from Figure 3.24 (a) that the higher the mean load of these tests was, the more severe displacement accumulation took place. Especially test F1.01M0.73A0.38, whose mean load was less than the drained resistance, sustained significantly more cycles until substantial displacement accumulated. In contrast, the two other tests exhibited relevant displacement from the beginning.

Figure 3.30 (a) shows the differential pressure accumulation of the three tests. In case of higher mean loads, more load had to be resisted by differential pressure, which is as expected. The development of negative differential pressure in tests F1.01M1.24A0.38 and F1.02M1.58A0.39, where the mean negative differential pressure increased almost linearly with $\lg N$ for $N \leq 100$, were quite similar. In contrast, test F1.01M0.73A0.38 exhibited no accumulation within the first 100 cycles, but showed pronounced accumulation as the test progressed further and the displacement accumulation rate increased.

The plug heave, which is depicted in Figure 3.30 (b), was similar for the three tests. The soil surface settled initially and the onset of plug heave correlated with substantial increase of the displacement accumulation rate. This behaviour is analogue to the tests at low load magnitude discussed in subsection 3.6.3.
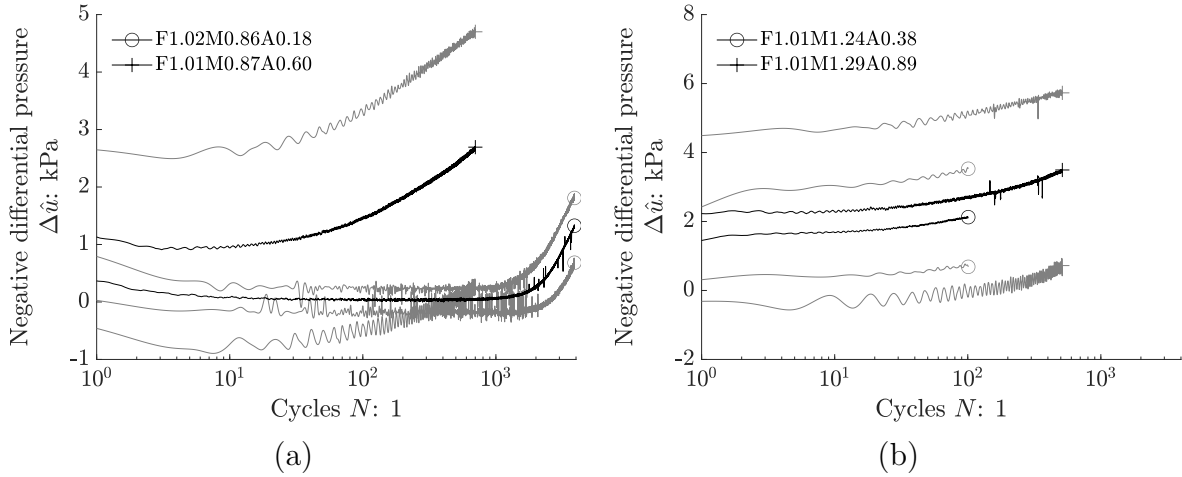
Figure 3.31: Effect of load amplitude in cyclic tests on negative differential pressure with $\bar{F}_{\mathrm{mean}} < 1$ (a) and with $\bar{F}_{\mathrm{mean}} > 1$ (b).

3.6.5 Load amplitude

The test pairs F1.02M0.86A0.18 and F1.01M0.87A0.60 as well as F1.01M1.24A0.38 and F1.01M1.29A0.89 had approximately equal mean loads, but different load amplitudes. These tests exhibited similar patterns concerning the plug heave in comparison to the previously described ones so that the measurements of the GS are not depicted and it is referred to Appendix A for detailed results.

In the tests F1.02M0.86A0.18 and F1.01M0.87A0.60, the mean load was lower than the drained resistances in both tests, but the different load amplitudes caused tensile loads either in the range of (F1.02M0.86A0.18) or higher than (F1.01M0.87A0.60) the drained resistance. This aspect highly affected the displacement accumulation, where test F1.01M0.87A0.60 experienced considerable displacement within some 100 cycles and test F1.02M0.86A0.18 revealed only slight displacement for about 1000 cycles (see Figure 3.24 (a)).

The displacement accumulation correlated with the development of the mean negative differential pressure, which is represented by the black lines in Figure 3.31 (a). Although the accumulation of negative differential pressure started much earlier in test F1.01M0.87A0.60, test F1.02M0.86A0.18 revealed a similar trend which commenced as the displacement rate increased. The larger maximum load of test F1.01M0.87A0.60 corresponded to higher mean negative differential pressure, which was already identified in Figure 3.29 (a). Moreover, the higher load amplitude evoked more pronounced variation of the differential pressure, which is demonstrated by the envelopes (see grey lines in Figure 3.31 (a)). The unloading in every cycle induced positive differential pressure in both tests, but after a distinct number of cycles and as a result of the accumulation tendency, the differential pressure became entirely negative. However, the negative differential pressure only started to accumulate more rapidly, when potential SLS criteria were already exceeded (see Table 3.6).

In contrast to tests F1.02M0.86A0.18 and F1.01M0.87A0.60, the mean loads of tests F1.01M1.24A0.38 and F1.01M1.29A0.89 were higher than their drained resistances. Despite the higher load magnitudes, a considerable number of cycles were carried until potential SLS criteria were reached (see Table 3.6). The higher load amplitude in test F1.01M1.29A0.89 invoked more rapid displacement accumulation.

The accumulation of negative differential pressure was similar for both tests, but the absolute value was higher in test F1.01M1.29A0.89 (see Figure 3.31 (b)). Consequently, the results depicted in Figure 3.29 (a) as well as Figure 3.31 (a) and (b) clearly verify that the mean negative differential pressure was higher for higher load amplitudes and maximum loads. The wider span of the envelopes of test F1.01M1.29A0.89 due to the larger amplitude in comparison to test F1.01M1.24A0.38 implied the occurrence of positive differential pressure in each cycle and for almost 300 cycles. The most significant accumulation occurred again after breaching the hypothetical SLS criteria (see Table 3.6).

3.6.6 Load frequency

The tests F1.01M0.73A0.38 and F0.50M0.74A0.37 were considered for detailed evaluation of the load frequency. Obviously, the suction bucket's displacement accumulated earlier in case of the lower frequency (see Figure 3.32 (a)). This behaviour was expected, since the load was maintained for a longer duration, which implied two aspects. Firstly considering the duration of one cycle, the suction bucket was exposed to tensile loads for a longer period provoking more displacement. Secondly, the lower load rate enabled more pore water seepage flow. Both effects are related with the need to generate certain negative differential pressure to counteract the applied load. Thus, the lower frequency facilitated more drainage and therefore required more displacement.

In terms of the negative differential pressure, the moving mean as well as the envelopes coincided as long as the displacements were almost identical (up to approximately 70 cycles, see Figure 3.32 (b)). Since these tests were force-controlled, the mobilised negative differential pressures had to be alike to resist the applied load. However, more displacement was required in case of the lower frequency, which thus caused an accumulation of negative differential pressure. This response relates to the findings of the tests at constant displacement rate presented in subsection 3.4.2. Bearing in mind the displacement accumulation of both tests, the accumulation trends of negative differential pressure were akin. The similarity of the results in terms of the displacement and differential pressure at the beginning of both tests indicates that the response of the suction bucket to the cyclic loading was initially governed by its frictional resistance.

Facilitating more water to flow inside the suction bucket should enable more gap expansion or equivalently, less plug heave. This mechanism was confirmed by the plug heave, where earlier lowering of the soil surface occurred in test F0.50M0.74A0.37 (see Figure 3.32 (c)). However, both tests exhibited similarity regarding the initial settlement and the beginning of plug heave along with the increase of the displacement accumulation rate. Although the onset of plug heave differed in terms of the number of cycles (about 600 cycles at
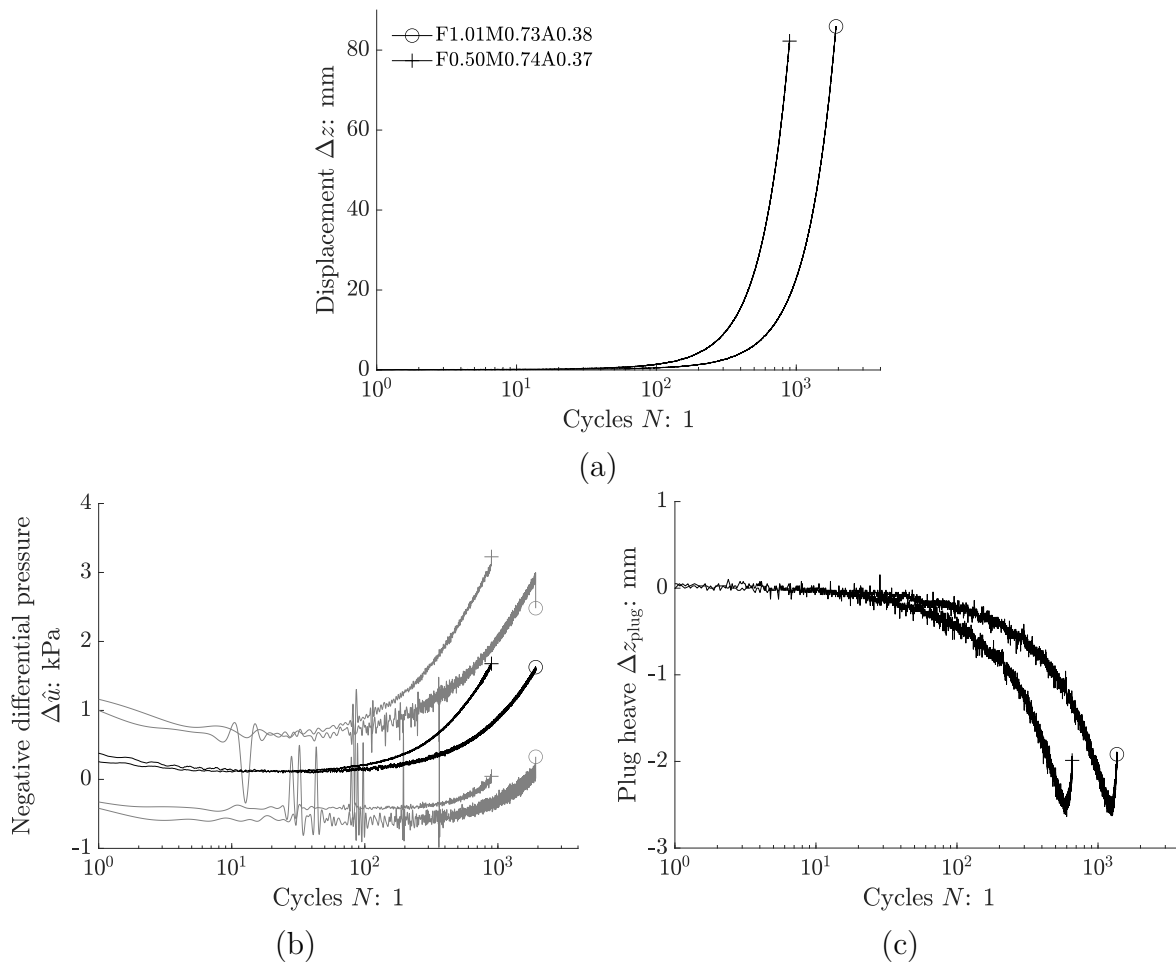
Figure 3.32: Effect of load frequency in cyclic tests on displacement (a), negative differential pressure (a) and plug heave (b).

0.5 Hz and 1300 cycles at 1.0 Hz), the corresponding displacement was related (about 35 mm at 0.5 Hz and 39 mm at 1.0 Hz). As expected, it can be concluded that the lower frequency evokes more drainage along with corresponding effects on the suction bucket's tensile bearing behaviour.

3.7 Summary

A new testing facility was erected for the purpose of investigating the suction bucket's response to different load conditions. The suction bucket model was installed by means of negative differential pressure aiming at realistic conditions. Measurements during and subsequent to the installation facilitated the determination of soil's hydraulic conductivity and permeability ratio. The soil inside the suction bucket was found to be considerably loosened due to the installation. The suction bucket's drained resistance was affected by its geometric dimension and installation method with relative enhancement for suction

buckets installed by jacking and also for lower embedment depths. Furthermore, the measured drained resistances were substantially larger than theoretical values as a result of scale effects and magnified earth pressure coefficients.

Higher displacement rates in monotonic displacement-controlled tests invoked significant increase of negative differential pressure, which provided an essential share of the partially drained tensile resistance. The analysis of the frictional resistance showed a substantial increase for a high displacement rate in comparison to the drained frictional resistance, but under partial drainage, the frictional resistance was found to be reduced. Negligible gap expansion and minor dissipation of negative differential pressure inside the suction bucket under high displacement rates were observed. Different model dimensions revealed that the maximum tensile resistance was mobilised at similar displacements $\Delta z/D$, but the tensile force divided by the area of the suction bucket's lid F/A increased significantly with absolute dimension and aspect ratio. For all models, the tensile resistance was dominated by the magnitude of the suction force. The evaluation of all model tests with respect to their displacement rates revealed that smaller geometric dimensions required much higher displacement rates in comparison to larger models to attain similar tensile resistances and suction forces. An effect of the model scale on the plug heave was not evident. The installation method with regard to the partially drained response had minor effect on the generation of negative differential pressure, but the frictional resistance was considerably higher for jacked installations.

In monotonic tests with constant forces, the loads exceeded the suction bucket's drained resistance and consequently invoked continuous displacement, which accelerated during the progress of the tests. The load magnitude was found to dictate the displacement rate, which accelerated over-linearly in case of the highest load. In respect of the load sharing, the generated suction force provided larger share for higher load magnitudes. Moreover, during the progress of the test, an increasing share of the load was resisted by the suction force and, associated therewith, the frictional resistance reduced gradually. The force-controlled tests invoked lower displacement rates than the ones investigated in displacement-controlled tests. However, this observation correlated with the lower load magnitudes applied (force-controlled) in comparison to the measured maximum tensile resistances (displacement-controlled).

The cyclic tests focussed on the investigation of the effect of the load characteristics on the displacement accumulation, where the maximum load and mean load were the most relevant parameters. If the drained tensile resistance was only marginally exceeded by $\bar{F}_{\max}$, almost no displacement accumulation occurred for numerous cycles, but finally, substantial accumulation of displacement and negative differential pressure developed. Large displacement accumulation always went along with an accumulation of negative differential pressure. As expected, the mean negative differential pressure was larger for higher maximum and mean loads. The span of the negative differential pressure was wider for higher load amplitudes. Regarding the plug heave, high cyclic load magnitudes caused the soil inside the suction bucket to be heaved within few cycles as a matter of high displacement rates. In contrast, low load magnitudes induced settlement of the soil surface. The examination of the load frequency revealed that a lower load frequency induced

earlier displacement accumulation, but comparable plug heave and negative differential pressure for distinct displacements. The comparison of displacement over time for similar mean loads in monotonic tests with constant force and cyclic tests pointed out reasonable agreement.

The boundary conditions of the model tests, such as load characteristics, soil properties and soil conditions prior to each test, were clearly defined so that sophisticated results were attained. The investigation of different load characteristics provided findings for comprehensive analyses of the tensile response of suction buckets at different scales. A major outcome of the physical model tests is a large database, which was utilised for the development, verification and validation of an FE model.

4 Finite element modelling

4.1 Model set-up

4.1.1 Requirements

The development of a sophisticated finite element (FE) model necessitates careful identification of critical aspects that dictate the system's response. A comprehensive analysis of the governing parameters leads to specific requirements for the particular model. Concerning the numerical simulation of the suction bucket's tensile bearing behaviour, the following issues were determined:

- Hydraulic-mechanical coupling with reliable and stable element formulation

- Accurate idealisation of hydraulic properties and processes

- Constitutive law, which regards for essential mechanical behaviour of the soil

- Appropriate simulation of gap expansion and transfer of the soil's pore pressure on the suction bucket's lid

- Implementation of the frictional behaviour at the skirt's soil-structure interface

- Sufficiently large calculation domain along with fine discretisation

- Exact definition of boundary conditions

- Formulation of relevant simulation steps

While some aspects in the list above require advanced modelling techniques, others are fundamental methods for establishing FE models. In the following, these issues are introduced in detail and it is described, how the particular aspects were dealt with.

The FE model was developed in the commercial Abaqus software (Dassault Systèmes, 2017) extended by user subroutines. The effective analyses of different geometric scales as well as the implementation of a large parametric study necessitated a high degree of automatisation. Therefore, additional programmes were utilised to create the models, execute numerous simulations on a high performance cluster and realise detailed post-processing.

4.1.2 Element formulation and boundary conditions

The simulation of suction buckets subjected to tensile loads requires the implementation of transient analysis procedures regarding the coupling of pore fluid flow and stresses. Since the soil is entirely submerged, complete saturation of the pores was assumed. Consequently, the soil was modelled as a continuum consisting of two phases (solid and liquid), which implied saturated flow condition. In transient coupled analyses, the effective stress approach applies, i.e. total stresses in the soil are the sum of effective stresses and pore pressure. As a result, changes in one of the fields necessarily invoke equivalent variation in the other field. Moreover, volumetric strains in the soil evoke variation of the void ratio so that under partial drainage, corresponding transition of the pore pressure field is generated. Beside this mechanism, volume continuity of the pore fluid, such as induced by the suction bucket's upward displacement, causes changes of the pore pressure. With respect to the development of pore pressure, the last mentioned effect was expected to be predominant over the soil's volumetric strains for tensile-loaded suction buckets.

Stable simulations presuppose that the shape function's order of the displacement field is higher than the one of the pore pressure field (Cuéllar et al., 2014). The utilised software provides the desired second-order element type, which is biquadratic in displacement and bilinear in pore pressure. Due to rotational symmetry of both the geometry and the loads, the system was simplified to an axisymmetric model. Thus, a continuum axisymmetric 8-node element with pore pressure degree of freedom was selected (denoted 'CAX8P' according to Dassault Systèmes, 2017). The FE model is depicted in Figure 4.1 with the symmetry axis being at $r = 0$ and the soil surface at $z = 0$ (according to Figure 2.1).

In terms of the boundary conditions, the soil surface outside the suction bucket was defined to be free to drain and displace or rotate in any direction. At the rotational axis, drainage was prohibited and an axisymmetric boundary condition was applied, i.e. displacements were fixed in radial direction and rotations about the axis vertically to the model's plane were constrained. The vertical boundary condition away from the suction bucket prevented displacements in radial direction. At the bottom of the calculation domain, the specified boundary condition inhibited vertical displacements. With respect to drainage, the two last mentioned boundaries were impermeable for the retrospective analysis of physical model tests, but permeable for the parametric study, where offshore conditions were simulated.

The tensile loads were applied on a single reference node (see Figure 4.1). The nodes on top of the suction bucket's lid were kinematically coupled to the translational and rotational degrees of freedom of this reference node. Hence, both the external load and the global response of the suction bucket were united in the reference node.

4.1.3 Discretisation and extent of simulation domain

The design of an FE model must ensure accuracy by sufficiently fine discretisation and minimise boundary effects by establishing an adequate extent of the calculation domain.
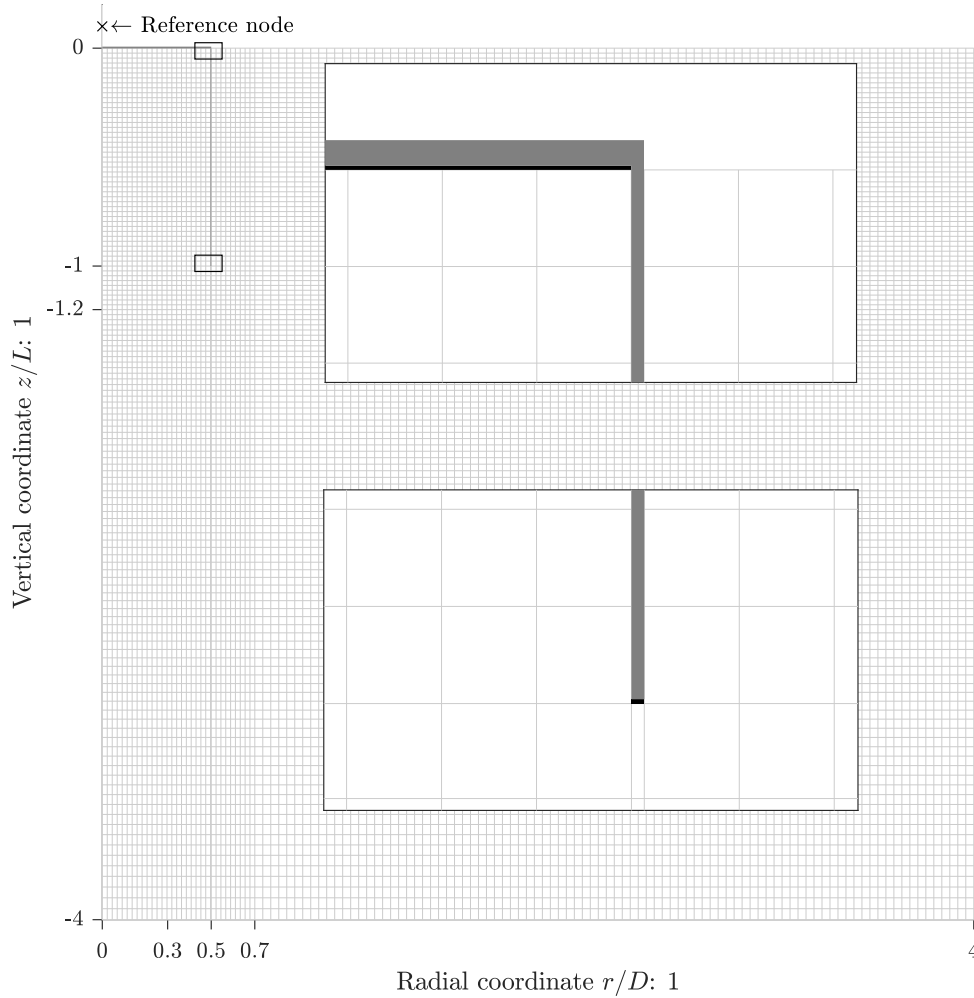
Figure 4.1: Calculation domain of the FE model and its discretisation.

Both aspects have to be defined aiming at particular optimum state in regard to the increasing computational costs for larger FE models with more elements. Most of the analyses were carried out on the cluster system at the Leibniz University Hannover, which provided immense capacities so that the computational costs were not essentially limiting the applicability of relatively fine discretisation.

The size of the calculation domain as well as its discretisation were specified in the context of a convergence study. To obtain an optimised design of the FE model, the following aspects were regarded: dimension of the calculation domain, element size, refinement in proximity to the suction bucket's skirt and increasing element sizes for elements that were further away from the suction bucket. These attributes were independently examined within a strict accuracy criterion defined as $|F_{\mathrm{j}}/F_{\mathrm{ref}} - 1| \leq 0.015$. In this formulation, F_{j} denotes the tensile force attained by an arbitrary configuration of the previously described parameters and F_{ref} represents the reference case that provided the most accurate results, i.e. largest domain or finest mesh. The convergence study accounted for prototype dimensions with $L = D = 9\,\mathrm{m}$ in very dense sand with material properties summarised

in subsection 4.1.5. Since the drainage condition potentially affected the convergence behaviour, four displacement rates ranging from drained to approximately undrained behaviour were considered, i.e. $v_z = 10^{[-12,-3,-1,0]}\,\text{m/s}$.

The size of the calculation domain was analysed by separately varying the height from $2L$ to $8L$ and width from $2D$ to $8D$. The drained response was negligibly affected by the extent of the calculation domain, but at higher displacement rates, relevant deviations were observed the closer the boundaries were to the suction bucket. This effect on the partially drained and undrained bearing behaviour was expected since the decreasing clearance between the suction bucket and the permeable boundaries changed the pattern of the pore water seepage flow. In a sufficiently large calculation domain, the majority of water infiltrated the soil surface and flew from there towards the suction bucket's inside. In contrast, the water entered the model domain from the bottom or the vertical distant boundary if these boundaries were too close to the suction bucket. Beside these hydraulic effects, the failure mechanism of the soil changed for different drainage conditions so that the undrained failure mobilised a larger soil volume, which was constrained by too small calculation domains (see Figure 2.3). It was found that these boundary effects diminished for model domains greater or equal to $4L$ in height and $4D$ in width, which were adopted hereafter (see Figure 4.1).

Because the elements were approximately square shaped inside and in proximity to the suction bucket, the element size was represented by only one length. Within the scope of the convergence study, the element size was varied from $0.007L$ to $0.050L$. Since the effect on total resistance might be less evident, the inner and outer friction as well as the suction force were examined individually. As a result, accurate and computationally efficient results were attained for element sizes, which were less or equal to $0.0225L$.

In proximity to the suction bucket's skirt and beneath the skirt's tip, the occurrence of considerable shear strains and local phenomena in terms of the pore water seepage flow were expected. In order to sophistically simulate these effects, a zone with particular mesh refinement was implemented. The extent of the mesh refinement was examined from $0.05L$ to $0.45L$ in vertical and from $0.05D$ to $0.45D$ in radial direction. Since the previously defined element size was sufficiently small, the effect of the refinement was relatively low. Consequently, the refinement zone adopted an identical element size of $0.0225L$ within a range of $0.2D$ inside and outside the suction bucket's skirt as well as $0.2L$ beneath the skirt's tip (see Figure 4.1).

Outside the refinement zone, the element size increased gradually with distance to the suction bucket. The elements adjacent to the refinement zone had approximately the same size as in the refinement zone, but each subsequent element was extended by a certain factor, which was varied from 1 to 1.1 within the context of the convergence study. As expected, the deviation from the reference case increased the larger the aforementioned factor was, while the computational effort reduced due to fewer elements. A value of 1.01 provided sufficiently accurate results considering the introduced convergence criterion, though the computational costs were not substantially reduced. The final configuration of the FE model is shown in Figure 4.1.

4.1.4 Contact definition

The soil-structure interfaces were defined as contact pairs by means of the interaction of master and slave surfaces. An augmented Lagrange procedure, which is basically the penalty method with additional iterations to improve accuracy, was adopted for the calculation of the pressure-overclosure relation of two contacting surfaces. The penalty method itself defines a hard pressure-overclosure relation that is approximated by the penalty stiffness. Thus, numerical softening occurs since little penetration of the interacting surfaces is allowed. The additional augmented Lagrange contact enforcement diminishes the penetration distance and resolves certain over-constraints, which are imposed for instance at the intersection of different surfaces. Once normal contact of two surfaces was established, these were not allowed to separate thereafter in order to avoid unrealistic void regions that were not occupied by any material.

While the pore pressure magnified the contact pressure in normal direction, the tangential interaction exclusively considered the effective stresses. At the suction bucket's skirt, the tangential contact behaviour was defined by Coulomb friction. Hence, the skin friction was limited to the effective normal contact pressure multiplied by the coefficient of friction (see Equation 4.1). The implemented model allows for little relative displacement at the interface although the contact state is sticking (denoted as elastic slip). As a consequence, the elastic slip defines certain stiffness of the friction that does not necessarily represent physical behaviour but provides numerical stabilisation. The value of the elastic slip was specified by certain slip tolerance multiplied by the characteristic element length. Since the element size was related to the length of the suction bucket (see subsection 4.1.3), the elastic slip scaled linearly likewise, which was essential for investigating different geometric dimensions ranging from laboratory to prototype scale. Moreover, the elastic slip had to be sufficiently low to prevent the contact stiffness from dominating the suction bucket's response. The default value of the slip tolerance was found to meet this requirement.

$$\tau = \sigma_r' \tan \delta \qquad (4.1)$$

The implemented plastic frictional behaviour with limited elastic slip is rather simple in comparison to more complex friction models that are capable of simulating the non-linear mobilisation of skin friction or account for degradation. Further, the adopted tangential contact stiffness was not verified by experimental results, but chosen based on FE simulations and recommendations concerning the numerical simulation of friction (Rust, 2016). To verify the applicability, subsection 4.2.2 provides evaluation of the utilised model against the measured suction bucket's drained response, which is governed by the frictional resistance.

The relatively fine discretisation of the FE model implies that large displacements exceed the length of one element at the skirt's soil-structure interface. As a result, the lowest node at the suction bucket's skirt would lose contact with the corresponding node of the soil so that the soil element would lose its bearing likewise. In order to prevent the resulting large shear strains in the soil, which would provoke numerical instabilities, the tangential

Table 4.1: Soil properties for FE analyses.

Case	e: 1	γ': kN/m^3	ν: 1	κ: 1	λ: 1	φ': °	ψ': °	$k_{\mathrm{i}}/k_{\mathrm{o}}$: 1
Model tests	0.585	10.41	0.20	350	0.4	45	20	*
Very dense	0.600	10.31	0.20	700	0.5	40	10	1.0
Medium dense	0.700	9.71	0.25	500	0.6	35	5	1.0

* Varies

contact assumed small sliding, i.e. nodes that were initially in contact remained in this state despite these nodes might displace from each other in the course of the simulation.

The effect of the differential pressure on the suction bucket must be simulated appropriately, which was addressed by adopting the methodology of 'water elements' (Cao et al., 2002; Mana et al., 2014). Beside the suction force that results from the transfer of the soil's pore pressure on the suction bucket's lid, these elements ensure continuity of the pore water volume as the gap beneath the suction bucket's lid expands. Moreover, the interaction at the skirt's tip has to be regarded. The plan area of the circular ring at the suction bucket's skirt is relatively small so that the resulting suction force could be neglected. Nevertheless, the upward displacement of the suction bucket would leave a void volume. Consequently, the 'water elements' were established beneath the suction bucket's lid and the skirt's tip. The bottom side of these elements were tied on the subjacent sand elements and their upper surface formed a contact pair with the suction bucket. The normal contact definition to the suction bucket prohibited separation and the contact pairs were tied in tangential direction.

4.1.5 Material properties

In the following, the material behaviour of the soil, suction bucket and 'water elements' are described. The adopted constitutive laws and additional definitions are provided. Certain parameters with constant values are given in the descriptions, which are supplemented by Table 4.1 summarising material properties that were specifically defined for distinct soil conditions. In particular, the soil's properties of the physical model tests were implemented as analysed in subsection 3.1.3.

The soil was modelled as elastic, perfectly plastic material. The elastic properties were defined by the Poisson's ratio ν and Young's modulus E. The Young's modulus was derived from the oedometric stiffness of the soil by Equation 4.2. As introduced in Equation 2.13, the oedometric stiffness was specified to depend non-linearly on the initial vertical effective stress. Therefore, the elastic behaviour of the soil was effectively described by the Poisson's ratio ν, the stiffness factor κ and stiffness exponent λ (see Table 4.1).

$$E = E_{\mathrm{s}} \frac{1 - \nu - 2\nu^2}{1 - \nu} \tag{4.2}$$

The soil's plasticity was modelled by the Mohr-Coulomb failure criterion without hardening (see Equation 4.3). To describe the soil's plastic response, the internal friction angle φ', dilation angle ψ and cohesion c' were required. The cohesion of saturated sands is generally negligible so that $c' = 0.1\,\text{kPa}$ was assumed. A non-associated flow rule was adopted, i.e. $\psi \neq \varphi'$. The sand's dilation angle was specified as $\psi = \varphi' - 25°$ for retrospective analyses of the physical model tests and $\psi = \varphi' - 30°$ for simulations at prototype scale. While the first case was deduced from the results of triaxial tests and consequently accounts for enhanced dilation at low stresses (see subsection 3.1.3 and Figure 3.6 (b)), the latter is in accordance with German Geotechnical Society (2014). The internal friction angle varied for distinct analyses and is summarised in Table 4.1.

$$(\sigma'_{\text{max}} - \sigma'_{\text{min}}) = (\sigma'_{\text{max}} + \sigma'_{\text{min}}) \sin\varphi' + 2c'\cos\varphi' \qquad (4.3)$$

Further material parameters of the soil are the void ratio e and the corresponding effective unit weight γ', which was determined based on sand's bulk density of $26.5\,\text{kN/m}^3$ along with the actual void ratio (see Table 4.1). The weight of the pore fluid was $\gamma_{\text{w}} = 10\,\text{kN/m}^3$. With respect to the soil's hydraulic conductivity and its dependency on the void ratio, Equation 3.1 was adopted for all simulations. Where applicable, a permeability ratio $k_{\text{i}}/k_{\text{o}}$ was incorporated (see Table 4.1). Moreover, the bulk modulus of the pore fluid K_{w} was taken into account in order to consider the compressibility of the permeating fluid in the porous soil. Since the bulk modulus of water depends on its temperature, offshore and laboratory conditions were distinguished. For in-situ conditions, $T_{\text{w}} = 10°\text{C}$ was assumed so that $K_{\text{w}} = 2.0912 \times 10^6\,\text{kPa}$, but in physical model tests, the water temperature was rather $T_{\text{w}} = 20°\text{C}$ leading to $K_{\text{w}} = 2.1786 \times 10^6\,\text{kPa}$ (Safarov et al., 2009).

Preliminary analyses were conducted with advanced constitutive laws, namely hypoplasticity (optionally with the extension for intergranular strains) and SANISAND, but both constitutive laws evinced essential deficiencies. For instance, simulations of cyclic tensile loads adopting hypoplasticity predicted downward displacement of the suction bucket, which is inconsistent with the anticipated and actual response of a suction bucket. In respect of simulations with SANISAND, questionable results were obtained for partially drained to undrained conditions, where excessive suction forces were predicted and the inner frictions approached the weight of the enclosed soil plug although certain drainage was supposed. Beside that, the calibration of SANISAND is not straightforward and it exhibited issues regarding the numerical stability.

Within this context, it is noted that the chosen soil's constitutive law is not capable of simulating the soil's mechanical response to cyclic loading. Although this detriment is an essential constraint for the simulation of many geotechnical problems involving cyclic effects, it was assumed to be less critical concerning the partially drained response of suction buckets subjected to tensile loads. It was expected that the suction bucket's bearing behaviour is dominated by hydraulic processes rather than the soil's cyclic mechanical behaviour. However, this hypothesis is crucial and required verification by means of retrospective analyses of model tests (see section 4.2). Moreover, the simplicity of the constitutive law with respect to the analyses of complex processes facilitated the clear

and precise identification of particular effects, which would be impeded if the complexity of the constitutive law complicates detailed evaluations. To underline the adequacy of the adopted constitutive law, section 4.2 comprises comparisons with studies, in which advanced constitutive laws were utilised, and discusses observed impacts of parameter variations in relation to the expected effects.

Within the scope of this study, the mechanical response of the suction bucket itself was of minor interest. Nevertheless, the axial strains in the suction bucket's skirt are potentially relevant because of their effect on the relative displacement in the soil-structure interface. In order to enable adequate simulation, linear elastic behaviour was implemented with properties for steel of $E = 210 \times 10^6$ kPa and $\nu = 0.2$. The analyses of the physical model tests accounted for the actual skirt thickness of $d = 5$ mm and for prototype conditions, a reasonable relation of $d/D = 0.003$ was assumed. The unit weight of the steel was defined to be equal to the weight of the pore fluid. As a result, the suction bucket was effectively weightless, which facilitated the evaluation of pure tensile loading and was consistent with the physical model tests, where the tensile forces accounted for the suction bucket's submerged weight.

The FE model adopted the implementation of 'water elements', which were located beneath the suction bucket's lid and the skirt's tip. The initial height of the 'water elements' was $0.001L$ and the mechanical behaviour was defined by linear elasticity with $\nu = 0$. The stiffness of the 'water elements' was initialised with $E = 1 \times 10^6$ kPa but reduced logarithmically to $E = 1 \times 10^{-9}$ kPa prior to tensile loading. To ensure that the variation of pore pressure in the 'water elements' was not constrained by their hydraulic conductivity, it was set to be 10 times higher than the initial one of the soil. The 'water elements' had the same unit weight as the pore fluid.

4.1.6 Simulation steps

The FE analyses were divided in simulation steps to adequately represent the phases to be examined. At the beginning of the simulation, the model was initialised, which comprised the definition of the elements' void ratio and saturation as well as both hydrostatic pressure and geostatic stress fields. The void ratio and saturation were constant with values as described in subsection 4.1.5. The hydrostatic pore pressure was determined via $u = \gamma'_{\mathrm{w}}(h_{\mathrm{w}} - z)$. The soil's vertical effective stresses were calculated by $\sigma_z = \gamma' z$ and the corresponding radial stresses were $\sigma_r = k_0 \gamma' z$, whereby $k_0 = 1 - \sin \varphi'$ was assumed (according to Jaky, 1948). Moreover, the soil's interaction with the pre-installed suction bucket was established and external loads were applied. These loads were the gravitational acceleration on every element as well as the hydrostatic load on the soil surface and the suction bucket's lid corresponding to the predefined water depth.

The installation of the suction bucket was not simulated. However, in terms of the retrospective analyses of the physical model test, the determined soil properties empirically implied certain installation effects. Namely, the hydraulic parameters after installation were derived from measurements and the radial stresses were estimated based on the
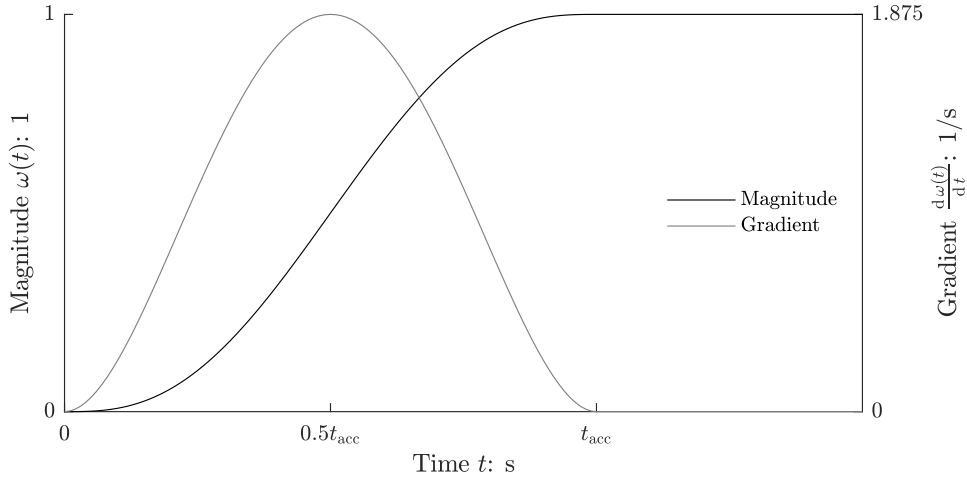
Figure 4.2: Load function for monotonic FE simulations.

drained resistance (see subsection 4.2.2). Certainly, there are several more installation effects that potentially have an influence on the tensile bearing behaviour. To mention a few, changes of the soil's void ratio, plug heave, degradation of skin friction with subsequent set-up effects and stress enhancement beneath the skirt's tip might take place during the installation but were neglected in the numerical simulation. However, at the current state, it is neither possible to accurately simulate the installation process by numerical methods, nor are there physical studies, which provide the required level of detail to implement precise effects in the FE model.

After the initialisation of the model, the dissipation of potentially arisen differential pressures was allowed for. Moreover, in this step the stiffness of the 'water elements' was diminished as described in subsection 4.1.5. The step was completed if any changes in the pore pressure field were less than 10^{-6} kPa within one time increment. Subsequently, the tensile load was applied. As introduced in section 2.1, three types of tensile loads were distinguished, namely constant displacement rate, constant force and cyclic force. Depending on the type of loading, different definitions of simulation steps were required.

The constant displacement rate was reached by a non-linear load function $\omega(t)$ to ensure numerical stability (see Equation 4.4 and Figure 4.2). This dimensionless function was multiplied with the targeted constant displacement rate to attain the variation of displacement rate with time, i.e. $v_z(t) = \omega(t)v_z$. Within the scope of the parametric study, the acceleration duration was $t_{\mathrm{acc}} = 10^{-4}$ mm/v_z. Concerning the retrospective analyses of physical model tests, the acceleration durations were specified according to the measured values. It should be noted that because of the non-linearity of $\omega(t)$, the acceleration significantly exceeded the mean value v_z/t_{acc} (see gradient in Figure 4.2). After the acceleration phase, the displacement rate was held constant until $\Delta z = 0.025L$, which was reached after $t_{\mathrm{hold}} = 0.025L/v_z$.

$$\omega(t) = \min\left[1, 10\left(\frac{t}{t_{\mathrm{acc}}}\right)^3 - 15\left(\frac{t}{t_{\mathrm{acc}}}\right)^4 + 6\left(\frac{t}{t_{\mathrm{acc}}}\right)^5\right] \tag{4.4}$$

101

The application of the constant force was alike to the constant displacement rate. The load was smoothly raised by adopting $\omega(t)$. The duration for applying the load was defined in accordance with the measurement of the model test or by $t_{\mathrm{acc}} = F/(0.5\,\mathrm{MN/s})$ in case of the parametric study. However, the non-linearity of the load function implied that the actual load rate varied over the duration of load application and was up to 1.875 times higher than the constant value of $0.5\,\mathrm{MN/s}$ for $\omega(0.5t_{\mathrm{acc}})$. The load was maintained for an arbitrarily defined time t_{hold}. Finally, unloading took place within $t_{\mathrm{unload}} = 0.1t_{\mathrm{acc}}$.

The cyclic loads considered in here were tensile swell loads so that $\bar{F}_{\mathrm{mean}} \geq \bar{F}_{\mathrm{ampl}} > 0$. Consequently, the load had to be raised up to the mean load, which was achieved by an additional preload step, prior to the cyclic load. The constant load rate within the preload step was equal to the cyclic load rate for $F = F_{\mathrm{mean}}$ (see Figure 2.2). Thus, the preload duration t_{acc} was determined by Equation 4.5. Following the preload step, the cyclic load was applied, which necessitated the specification of the number of cycles N, the load frequency f or period T, the mean load F_{mean} and load amplitude F_{ampl}. After the simulation of the last cycle, the load was reduced to $F = 0$ in an unload step, which adopted an identical, but negative load rate as for the preloading. Hence, the cyclic load ended with a half cycle and subsequent unloading.

$$t_{\mathrm{acc}} = \frac{T}{2\pi}\frac{F_{\mathrm{mean}}}{F_{\mathrm{ampl}}} \tag{4.5}$$

After force-controlled loading, a final consolidation step was conducted in which differential pressures dissipated and the suction bucket settled due to the presence of downward forces (suction force and frictional resistance). The end of the step was reached if any changes in differential pressure within a certain increment were less than $10^{-6}\,\mathrm{kPa}$, which went along with negligible incremental displacement of the suction bucket. This consolidation step enabled the determination of the residual displacement of the suction bucket after tensile loading. Although these analyses provided interesting findings, it should be noted that during upward displacement of the suction bucket, the void beneath the skirt's tip would be filled with sand, which was not accounted for in the FE simulations. Thus, the post-load consolidation facilitated more downward displacement of the suction bucket than it would take place in reality.

4.2 Verification and validation

4.2.1 Overview

The verification of the FE model was based mainly on the retrospective analyses of the physical model tests considering measured and estimated soil properties, diameter of the suction bucket and its embedment depth. The drained resistance measured in physical model tests was adopted for calibrating the initial soil's stress state (see subsection 4.2.2). The numerically simulated responses of the tensile-loaded suction bucket under partial

drainage were compared to those measured in physical model tests. Therefore, specific conditions were examined in order to assess the capability of the FE model to simulate the physical measurements with respect to different scales, drainage and load conditions (see subsection 4.2.3, subsection 4.2.4 and subsection 4.2.5).

Moreover, the results of the FE simulations were evaluated against theoretical considerations and analytical procedures in order to examine validity of the FE model as well as to highlight consistency or discrepancies of different approaches. Where appropriate, potential deviations from expected behaviour were explained and their relevance was rated.

Finally, scale effects with respect to cyclic loading were investigated. These analyses aimed at proving that the arbitrarily chosen load frequency in the model tests was reasonable. For this purpose, the load frequency at prototype scale was iteratively adjusted within the scope of FE simulations until similarity in displacement rate $(\mathrm{d}z/D)/\mathrm{d}N$ in comparison to the corresponding model test was achieved (see subsection 4.2.6).

4.2.2 Drained response

The analysis of the drained tensile response had to ensure that negligible changes in pore pressure took place. To fulfil this requirement, various displacement rates were simulated and the invoked suction forces were evaluated. For a very low displacement rate of $v_z = 10^{-12}\,\mathrm{m/s}$, almost no differential pressure developed. This displacement rate was found to guarantee the drained condition for any of the modelled scales.

Figure 4.3 depicts representative results of the measured and simulated drained response of model L500D510. Initially, the earth pressure coefficient was set to $k_0 = 1 - \sin\varphi' = 0.293$ for $\varphi' = 45°$, but the drained resistance F_{dr} was substantially underestimated. Thus, the earth pressure coefficient was iteratively increased to obtain approximately identical drained resistance in the numerical simulation compared to the physical model test, which was attained for $k_0 = 0.521$. This calibration of the radial stresses by means of adjusting the earth pressure coefficient was performed for every retrospective analysis of a model test. The distinctly calibrated earth pressure coefficients, whose values are provided in Appendix A, were further used for the subsequent analyses of the tensile response under partial drainage. The higher earth pressure coefficients resulted probably from enhanced radial stresses induced by soil preparation in the model test. Moreover, high dilation at low effective stresses, which was potentially not entirely captured by the numerical simulation, might have magnified the tensile resistance as well (see subsection 3.3.2).

The drained response simulated by the FE model was divided in three ranges. At the beginning, the skin friction increased at both sides of the suction bucket's skirt resulting in approximately linear raise of the tensile force with displacement. After a certain displacement, the outer friction reached its maximum and every node of the contact pair was slipping. Consequently, the increase of the tensile force reduced. Due to less relative displacement at the inside of the suction bucket, the inner friction increased further until its maximum was reached as well. At this particular displacement, the drained resistance was mobilised and the tensile force slightly reduced afterwards.
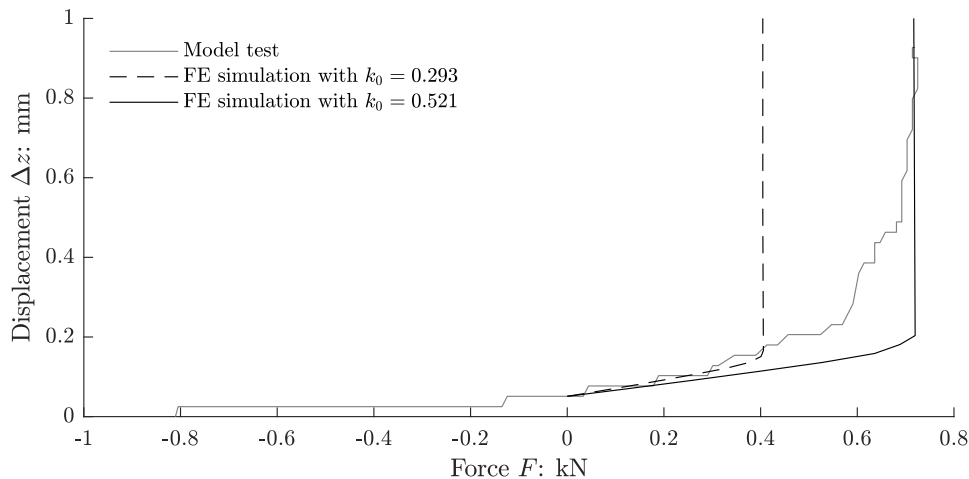
Figure 4.3: Exemplary retrospective FE analysis of drained tests with model L500D510.

The initial stiffness was accurately represented by the FE simulation (see Figure 4.3). However, the model test exhibited distinct non-linear increase of tensile force with displacement, which was not well reproduced by the numerical simulation. The FE model predicted the drained resistance to be generated within less displacement and hence overestimated the suction bucket's drained stiffness. This effect was attributed to the rather simple constitutive law that did not account for the soil's hardening. Comparative analyses with artificially changed soil's mechanical properties or advanced constitutive laws, as described in subsection 4.1.5, partly improved the accuracy of the simulation underlining the relevance of the soil's hardening with regard to the drained response. However, these approaches either failed to predict other drainage conditions or implied soil properties, which were inconsistent with those described in subsection 3.1.3. Although these modifications were not adopted, the results pointed out that beside the contact definition, the soil's constitutive law and properties had an influence on the drained response.

The suction bucket's drained resistance mainly depends on the normal stresses acting on its skirt, which are equivalent to the radial effective stresses in the soil. In particular, the variation of the soil's radial stresses as a result of the suction bucket's upward displacement is highly relevant. In order to investigate the stress relief starting from the initial geostatic state determined by $\sigma'_r = \gamma' z k_0$, Figure 4.4 examines the stress changes predicted by FE simulation and analytical calculation according to Houlsby et al. (2005b). For all presented calculations, identical input parameters were adopted. The analytical calculation required the additional parameter n, which describes the extent of stress relief outside the suction bucket and was set to $n = 1.5$ as suggested in Houlsby et al. (2005b).

The approach of Houlsby et al. (2005b) predicted similar radial stresses in comparison to the geostatic state for shallow depth. For increasing depth, the stress relief became more relevant leading to a substantial reduction of the radial stress at the depth of the skirt's tip. The stress relief was more pronounced inside the suction bucket. It must be remarked that this method effectively accounts for a reduction of vertical stresses because of the upward displacement and the provoked upward shear stresses at the skirt's
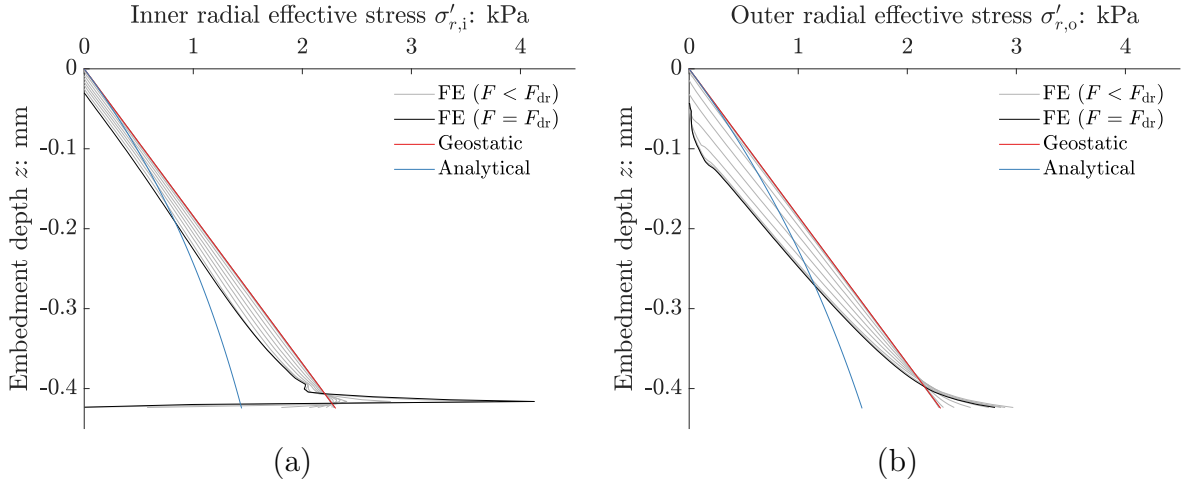
Figure 4.4: Radial effective stresses on the inside (a) and outside (b) of the suction bucket's skirt under drained condition.

interface. These vertical stresses are assumed to be proportional to the radial stresses by the constant earth pressure coefficient (Houlsby et al., 2005b).

The dependency of the stress relief on the suction bucket's displacement was illustrated by the grey lines in Figure 4.4, which represent the radial stresses on the suction bucket's skirt before reaching the drained resistance. Evidently, the stresses continuously reduced for increasing displacement starting from geostatic state. The black lines show the radial stresses at $\Delta z_{F_{dr}}$. In contrast to the analytical method, the FE model predicted major reduction of radial stresses on the outer skirt at shallow depths close to the soil surface and decreasing stress relief with depth. In comparison, the reduction of radial stresses at the inside was less distinct and rather constant over the embedment depth. On both sides of the suction bucket's skirt, an increase of radial stresses close to the skirt's tip was observed. These results pointed out that the stress relief was more pronounced where the soil's displacement was less constrained (at shallow depths), rather than close to the skirt's tip or inside the suction bucket where the soil was confined. It should be noted that the numerically simulated stress relief was qualitatively comparable to results of Shen et al. (2017), where a more sophisticated constitutive law (SANISAND) was used. Hence, the stress relief pattern did not seem to be crucially affected by the constitutive law.

The reason for the contradictory results of the analytical and numerical model can be explained by Figure 4.5, where the relative variations of distinct quantities are presented. In Figure 4.5 (a), the change of vertical effective stress was evaluated by means of its relative variation from geostatic state to the occurrence of drained resistance, i.e. $\sigma'_z(\Delta z_{F_{dr}})/\sigma'_z(\Delta z = 0) - 1$. The black lines indicate the contour where no changes of the vertical stress took place. Outside the suction bucket, the vertical stresses were reduced over a wide range of embedment depth, but close to the soil surface, the vertical stresses were slightly magnified. Assuming that the earth pressure coefficient would not change, the present stress relief would still reduce the outer friction. The stress relief was less evident inside the suction bucket and even a considerable soil volume in the lower half
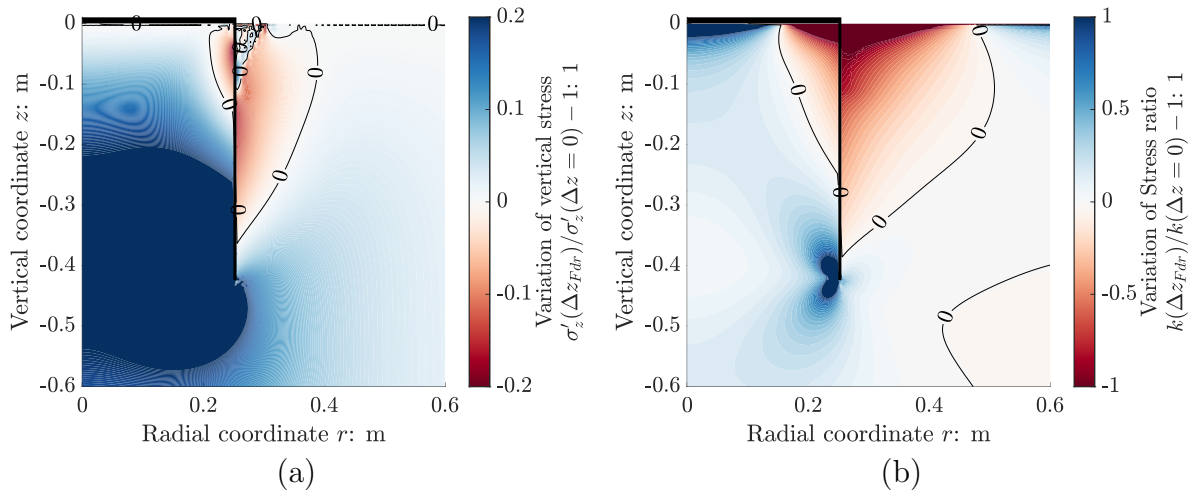
Figure 4.5: Differences in vertical effective stresses (a) and stress ratio (b) under drained condition.

of the embedment depth exhibited an increase of vertical stresses. This effect potentially resulted from the dilating soil that was confined inside the suction bucket.

The variation of stress ratio σ'_r/σ'_z, which is equivalent to the earth pressure coefficient k, was examined by $k(\Delta z_{F_{\mathrm{dr}}})/k(\Delta z = 0) - 1$ (see Figure 4.5 (b)). Considering both variations of vertical stress and stress ratio facilitated the evaluation of the stress relief and the difference between the analytical and the numerical result. The reduction of the stress ratio, which occurred at both sides of the skirt but was more distinct at the outside, diminished the radial stresses on the suction bucket's skirt and thus had a predominant effect on the drained resistance in comparison to the change in vertical stress. Close to the skirt's tip inside the suction bucket, the stress ratio increased similarly to the vertical stresses, which manifested the soil's confinement as described above. It can be concluded that the stress relief in the analytical method of Houlsby et al. (2005b) neglects the variation of the earth pressure coefficient and hence, deviations of the results from analytical calculation and FE simulation were detected. Moreover, the numerical results pointed out that the stress relief was more pronounced at shallow depths near the soil surface where the soil was less constrained.

4.2.3 Response to constant displacement rate

Figure 4.6 depicts results of physical model tests with model L500D510 along with the corresponding numerical simulations with regard to different drainage conditions, i.e. displacement rates. While subsection 3.4.2 provides detailed discussion of suction bucket's monotonic response under partial drainage, the subsequent discussion focusses on the evaluation of the numerical simulations. The retrospective FE analyses of physical model tests with constant displacement rates did not intend to represent the suction bucket's response after the occurrence of its maximum resistance so that the displacement was limited to approximately $\Delta z_{F_{\max}}$.
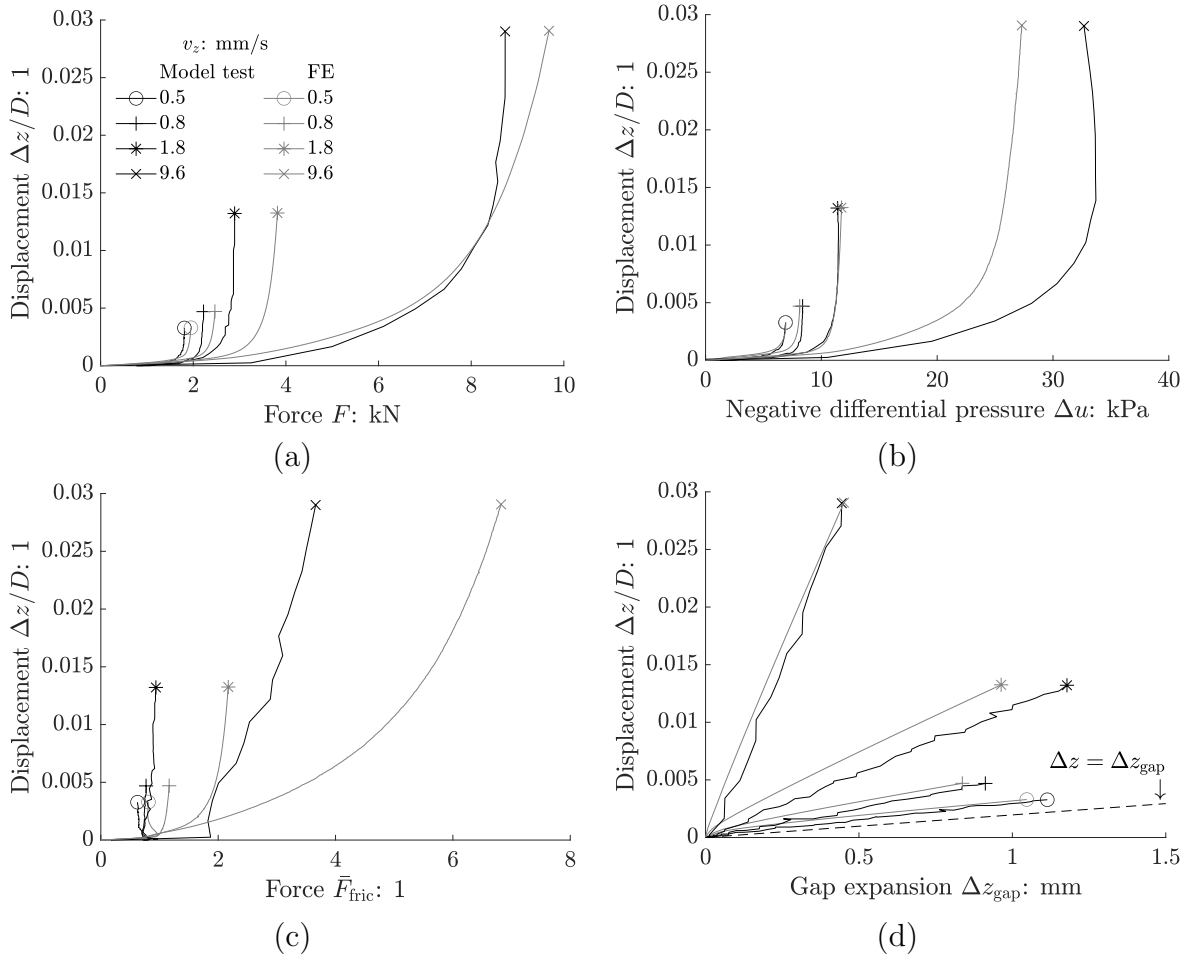
Figure 4.6: Numerical simulations of model tests with model L500D510 subjected to constant displacement rates regarding force (a), negative differential pressure (b), frictional resistance (c) and gap expansion (d).

The tensile forces of the considered tests are presented in Figure 4.6 (a). The simulations of tests v0.5, v0.8 and v9.6 exhibited minor deviations from the measured resistances with a tendency of overestimating the tensile forces. Solely the numerical simulation of test v1.8 substantially exceeded the measured tensile force. Nevertheless, the initial stiffness (increase of the resistance with displacement) of test v1.8 was still in good accordance.

Taking the development of negative differential pressure into account facilitated the estimation of the load sharing (see Figure 4.6 (b)). Apparently, the negative differential pressure of test v9.6 was significantly underestimated, but accordance was achieved for the tests v0.5 and v1.8. The negative differential pressure in test v0.8 was only slightly underestimated. It should be noted that despite detailed analysis of the measured data, the determination of the permeability and permeability ratio potentially suffered from inaccuracies due to scatter in the measurement (see exemplary measurements in Figure 3.12). Further, the utilised permeability ratio simplified the real loosening of the soil plug during the installation. The actual plug heave, which was not accounted for in the FE model, invoked a longer drainage path. This uncertainty conceivably evoked deviations as for

instance in test v9.6. However, it can be concluded that the hydraulic responses were well represented by the FE model.

The tendency of overestimating the total resistance while partly underestimating the negative differential pressure implies that the FE simulations overrated the frictional resistance of the suction bucket, which is evident from Figure 4.6 (c). Obviously, higher displacement rates led to larger deviations of the frictional resistance, which was attributed to less drainage, where the soil's effective stresses were affected by pore water seepage flow and negative differential pressure. Although it was less distinct, the measured frictional resistance was also exceeded in tests with relatively low displacement rates. Possibly, the calibration of the initial stress state based on the drained resistance was not able to accurately represent the skin friction under partial drainage, where the relative displacement at the interfaces and the soil's failure mechanism differed significantly (see Figure 2.3). While the FE model enabled the separate analysis of inner and outer friction, it was not possible to distinguish these resistances in the physical model tests, although this would have enabled further analyses of the interaction of hydraulic processes and skin friction.

Figure 4.6 (d) shows the gap expansion, which is opposed to the plug heave as discussed in subsection 3.4.2. The gap expansion correlates with the drainage condition and is therefore strongly affected by the displacement rate. The results of the numerical simulations were in good accordance with those of the model tests for the investigated range of displacement rates. Minor deviations occurred due to an underestimation of the initial gap expansion, but the continuous gap expansion rate was well predicted. With respect to the quantities analysed in Figure 4.6, the FE model successfully simulated the suction bucket's tensile response for a wide range of drainage conditions.

Figure 4.7 presents results for different model dimensions at displacement rates of $v_z \approx$ 10 mm/s. The tensile forces measured in model tests and obtained by numerical simulations were compared in Figure 4.7 (a). Except for model L250D510, the forces were in good agreement. Moreover, the simulation of the test with model L500D510 well approximated the initial response, but overrated the maximum resistance.

The negative differential pressures were underestimated by the FE simulations, whereby larger model dimensions caused greater deviations (see Figure 4.7 (b)). As a result, the frictional resistance was overestimated as already pointed out in Figure 4.6 (c). Despite certain differences, the attained results still agreed reasonably and testified the ability of the FE model to examine different geometric scales.

Although the FE model proved its capability of simulating both different drainage conditions and scales, the frictional resistance appeared to be systematically overrated. This effect was probably related to the relatively high initial radial stresses of the soil in the FE model, which resulted from the empirical calibration procedure based on the drained resistance. Two potential inaccuracies were identified. Firstly, the simulated stress relief under drained condition did not exactly represent the actual mechanism occurring in the physical model test so that the radial stresses were overestimated. Secondly, under partially drained conditions, the deformations in the soil and interface differed significantly and the stress relief might be less distinct. Hence, the calibrated drained skin friction
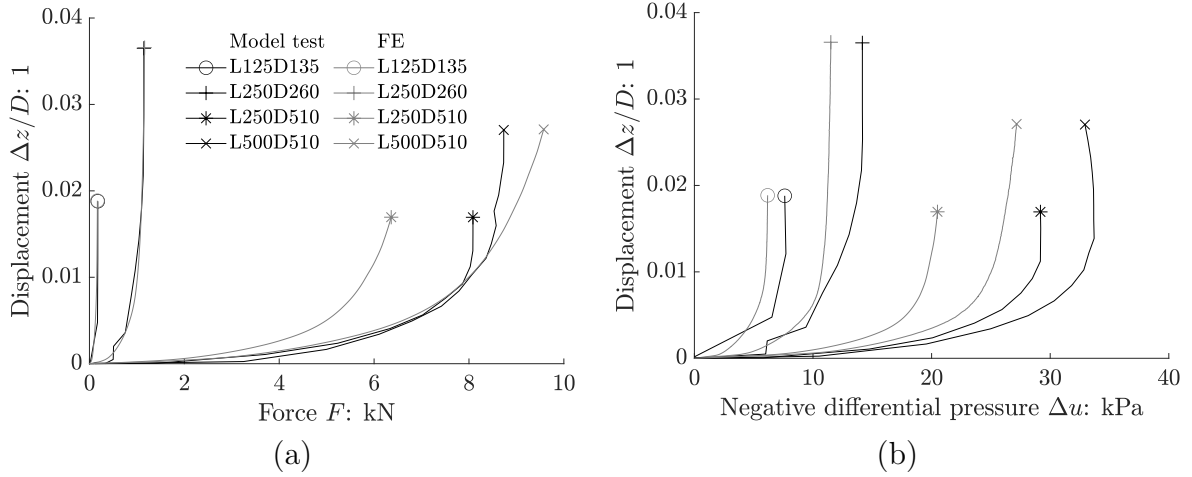
Figure 4.7: Numerical simulations of model tests with constant displacement rates $v_z \approx 10\,\mathrm{mm/s}$ concerning the model scale regarding force (a) and negative differential pressure (b).
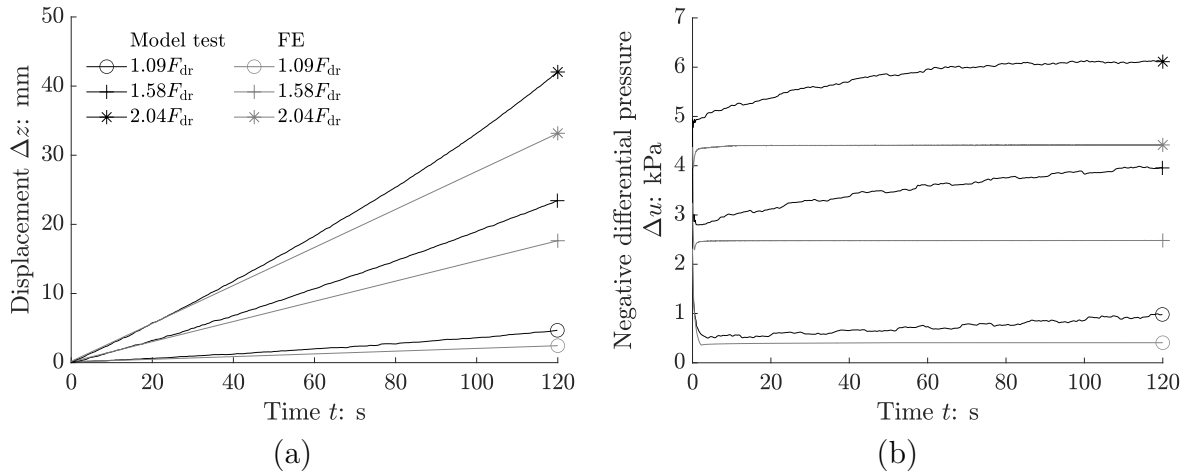
Figure 4.8: Numerical simulations of model tests with constant force regarding displacement (a) and negative differential pressure (b).

might be of restricted validity for partially drained conditions, which was manifested by larger discrepancies of the frictional resistance in case of less drainage.

4.2.4 Response to constant force

The measured and simulated results of tests with constant force are summarised in Figure 4.8, whereby only the first $120\,\mathrm{s}$ were accounted for in the FE simulations. The simulated displacement rates were higher for larger load magnitudes and particularly the initial displacement rates at the beginning of the simulations were in good agreement with those measured in the model tests (see Figure 4.8 (a)). During the progress of the physical model tests, the suction bucket accelerated continuously causing over-linear displacement with time, which was not featured by the FE simulations.

109

Figure 4.8 (b) provides the comparison of the negative differential pressures. The numerical simulations tended to underestimate the negative differential pressure, which was initially negligible for the lowest load magnitude but became more relevant for the two higher load magnitudes. Consequently, the frictional resistance was slightly overestimated. As the load was maintained, the physical model tests exhibited a variation of load sharing characterised by a reduction of frictional resistance and increase of suction force. This effect went along with an increasing displacement rate. Both aspects were not reproduced likewise by the numerical simulations. Hence, the negative differential pressure remained rather constant and the differences between the model test and FE simulation enlarged. However, the numerical results were consistent regarding the almost constant negative differential pressure along with the steady displacement rate.

Similarly to subsection 4.2.3, the tests with constant force exhibited an overestimation of the frictional resistance. Moreover, the non-linear response of the suction bucket during the progress of the test was not accounted for. In physical model tests, the length of the drainage path shortened and the skirt's area in contact with the soil diminished as the suction bucket continuously displaced upwards. Both aspects were not regarded in the FE model and were probably invoking the discussed deviations. In spite of this deficiency, the FE model well simulated the initial response of the suction bucket, but for larger displacements, differences became evident.

4.2.5 Response to cyclic force

Although every cyclic model test was numerically simulated, solely selected cyclic tests were considered for validating the FE model. The following tests were chosen to be representative: F1.02M0.86A0.18, F1.01M0.87A0.60, F1.01M1.29A0.89 and F1.01M2.12A0.52 with $f = 1.0$ Hz as well as F0.51M1.04A0.45, F0.51M1.52A0.65 and F0.51M1.90A0.81 with $f = 0.5$ Hz. The aim of the simulations was to demonstrate the capability of the FE model to qualitatively predict the cyclic bearing behaviour. Therefore, and in order to limit the computational effort, only 29.5 sinusoidal load cycles were applied in the numerical simulations. While the load in the physical model tests was raised quickly, the initial load application until reaching the mean load in the FE model was realised over a longer preload time t_{acc}, which provided stability but caused slightly higher displacement for $N \leq 0$ (see subsection 4.1.6).

Figure 4.9 (a) shows the displacement accumulation for $f = 1.0$ Hz measured in the model tests and predicted in the FE simulations. Except for test F1.02M0.86A0.18, the almost constant displacement accumulation rates were generally underestimated. However, qualitative agreement was achieved in each of the considered tests. With respect to test F1.02M0.86A0.18, the FE model predicted small displacement during the first cycles followed by stabilisation of the displacement accumulation. This was in agreement with the measurements of the model test, where relevant displacement accumulation was observed only after numerous cycles (see Figure 3.24).

Figure 4.9: Numerical simulations of model tests with cyclic force and $f = 1.0\,\text{Hz}$ regarding displacement (a) and negative differential pressure (b).

The occurrence of mean negative differential pressures $\Delta \hat{u}$ along with initial displacements was evident in tests F1.02M0.86A0.18 and F1.01M0.87A0.60 (see Figure 4.9 (b)). Subsequently, the negative differential pressure reduced within few cycles and the displacement accumulation rate diminished simultaneously. This pattern was well reproduced by the FE simulation. The higher displacement accumulation rates in tests F1.01M1.29A0.89 and F1.01M2.12A0.52 evoked larger negative differential pressures. These were generally underestimated by the FE simulations, but still in qualitative agreement.

Figure 4.10 provides results of retrospective analyses of tests with $f = 0.5\,\text{Hz}$. These results were qualitatively equivalent to those obtained for $f = 1.0\,\text{Hz}$ except for the displacement accumulation rates that slightly increased in the model tests within the depicted range of 30 cycles. Consequently, the increase in negative differential pressures was more pronounced. As already pointed out in subsection 4.2.4, this non-linear response was not accounted for in the FE model.

Although the FE model provided good qualitative estimations of the cyclic bearing behaviour and the simulation of the test F1.02M0.86A0.18 was even in quantitative agreement, the displacement accumulation rates of the FE simulations tended to be lower than the ones of the model tests (see Figure 4.9 (a) and Figure 4.10 (a)). The reason for that was probably the overestimation of the frictional resistances implying that the negative differential pressures were underestimated (see Figure 4.9 (b) and Figure 4.10 (b)). The tendency of overestimating the frictional resistance was already observed for monotonic load conditions (displacement-controlled see Figure 4.6 (c) and force-controlled see Figure 4.8). It is reminded that loads resisted by suction force necessarily require more displacement under partially drained conditions than the frictional resistance. Hence, a reduced frictional resistance would invoke both higher displacement and higher negative differential pressure.

Thus, better accordance was achieved by reducing the earth pressure coefficient at rest, which was originally calibrated by the suction bucket's drained resistance. Figure 4.11 de-
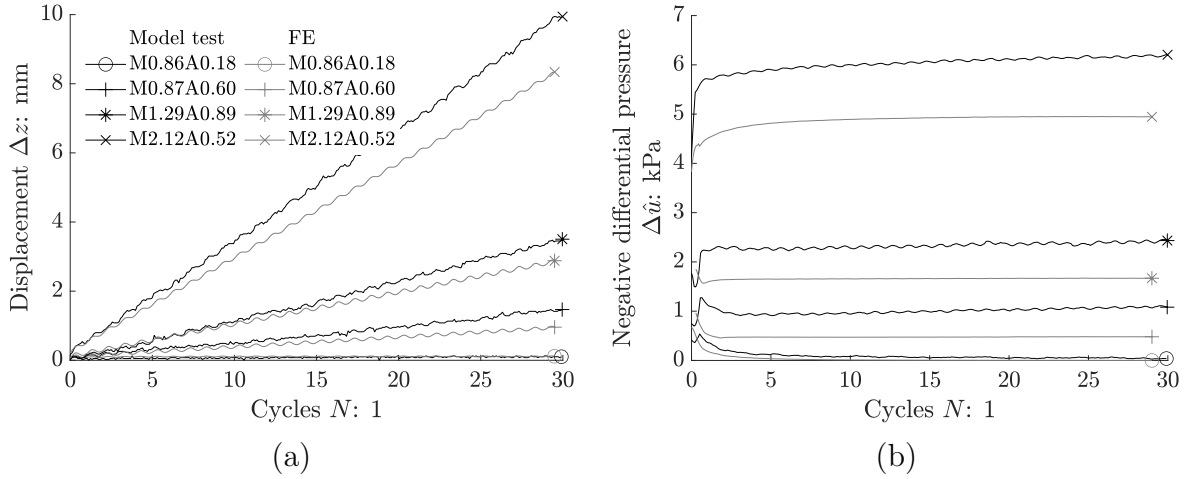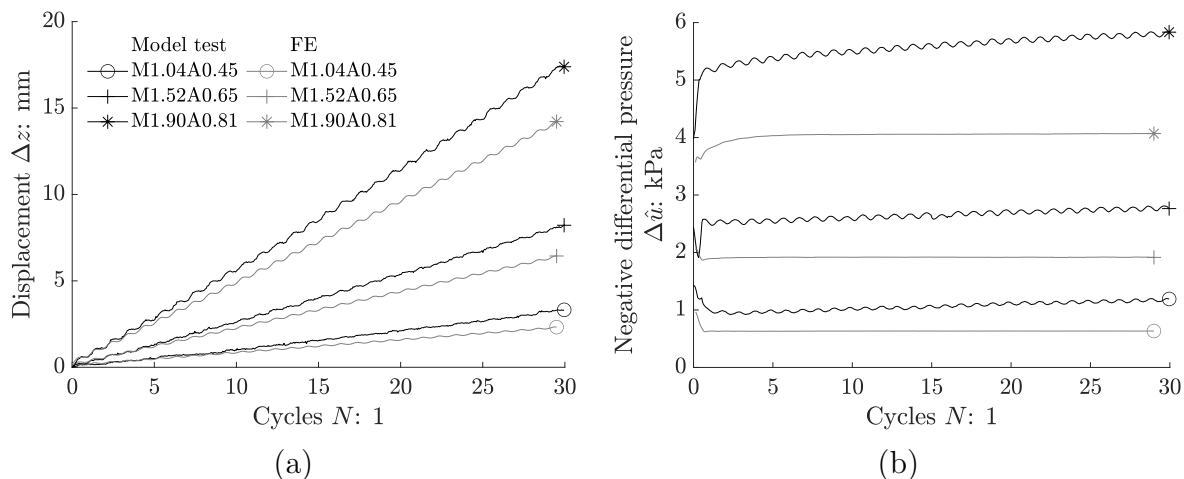
Figure 4.10: Numerical simulations of model tests with cyclic force and $f = 0.5\,\text{Hz}$ regarding displacement (a) and negative differential pressure (b).

picts exemplary results for tests F1.01M0.87A0.6, F1.01M1.29A0.8 and F1.01M2.12A0.5, where the initial stress state was empirically reduced to $0.85k_0$, $0.80k_0$ and $0.60k_0$ respectively. As expected, the frictional resistance was lowered and consequently, the displacement accumulation rate and negative differential pressure increased. Although the reason for the overestimated frictional resistance could not be determined with confidence, the presented modification provided accordance of the model tests and FE simulations.

It should be noted that perfect agreement of model test and simulation results could not be expected because of the rather simple soil's constitutive law. Highly sophisticated constitutive laws are capable of estimating volumetric strains and accounting for cyclic effects on mechanical behaviour. In contrast, the utilised constitutive law simplifies the mechanical response of the soil, but still accounts for essential aspects. Despite these limitations, plausible results were attained by the retrospective simulations of the model tests and owing to the clarity of the constitutive law, particular effects were clearly evaluable. Consequently, the hydraulic-mechanical coupling and the parameters of the FE model were generally appropriate to represent main aspects of the suction bucket's response. Moreover, the importance of the hydraulic properties and conditions along with subordinate relevance of the soil's mechanical behaviour was confirmed. Finally, it is marked that the soil's mechanical properties were adopted as originally derived in subsection 3.1.3 and the hydraulic properties were implemented as measured in the testing facility. Except for the calibration of the initial earth pressure coefficient with regard to the drained resistance (see subsection 4.2.2), no artificial modifications were applied.

4.2.6 Load frequency scaling

The approach proposed by Kelly et al. (2006a) and presented in subsection 2.3.4 shall enable the comparison of drainage conditions at different scales, but scaling of the suction bucket's cyclic response was shown to be much more complex so that it could not be
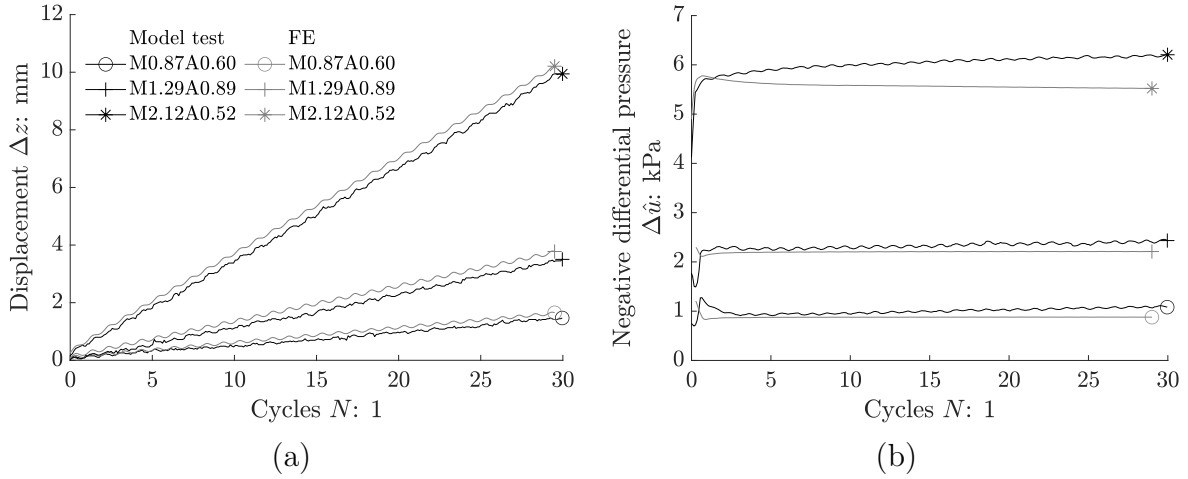
Figure 4.11: Numerical simulations of model tests with cyclic force and $f = 1.0\,\mathrm{Hz}$ considering adjusted initial stress state regarding displacement (a) and negative differential pressure (b).

simplified reliably by Equation 2.15. Hence, scale effects of the model tests were analysed with respect to the load frequency by utilising the FE model. Therefore, cyclic tests were scaled up to prototype dimension with a suction bucket diameter $D = 8\,\mathrm{m}$ while maintaining the aspect ratio z/D and skirt thickness ratio d/D. The soil properties were adopted from the individual model tests. The drained resistances of the prototype models were determined and equivalent loads $\bar{F}_{\mathrm{mean}}$ and $\bar{F}_{\mathrm{ampl}}$ were applied. Several simulations with varying load frequencies were conducted and the displacement accumulations' moving mean over one load cycle $\Delta\hat{z}$ were calculated. Subsequently, the load frequency, for which the displacement accumulation rates $(\mathrm{d}\hat{z}/D)/\,\mathrm{d}N$ coincided for both scales after a certain number of cycles, was identified. This similarity was taken as criterion to measure the scaleability and enabled the evaluation of mainly two aspects. Firstly, the determined load frequency at prototype scale was compared to typical offshore cyclic loads. Secondly, the cyclic frequency ratio $f_{\mathrm{m}}/f_{\mathrm{p}}$ pointed out the effect of the applied loads on the scaling.

Figure 4.12 (a) compares exemplarily the displacement $\Delta z/D$ of the FE simulations M0.87A0.60 at model scale and prototype scale. In contrast to the model scale, the prototype scale exhibited greater displacement due to initial load application and more pronounced displacement in each cycle (dotted lines). However, the moving means of both scales $\Delta\hat{z}/D$ (solid lines) indicated similarity and exhibited coinciding displacement accumulation rates after approximately 10 cycles. The displacement accumulation rate depicted in Figure 4.12 (b) highlights the accordance at both scales after more than 10 cycles. Thus, similarity was demonstrated for $f_{\mathrm{m}}/f_{\mathrm{p}} = 11.75$ and therefore, the load frequency of $1.01\,\mathrm{Hz}$ at model scale corresponded to $0.086\,\mathrm{Hz}$ at prototype scale, which is typical for large wave loads (see subsection 1.1.3).

Table 4.2 summarises the cyclic frequency ratios for the considered tests. For the investigated geometric scale of $D_{\mathrm{m}}/D_{\mathrm{p}} = 0.510\,\mathrm{m}/8.000\,\mathrm{m} = 1/15.69$, the cyclic frequency ratios obtained were within the range of $11.75 \leq f_{\mathrm{m}}/f_{\mathrm{p}} \leq 14.50$ and were similar for both cyclic frequencies of the model tests, but increased for higher load magnitudes. Consequently,
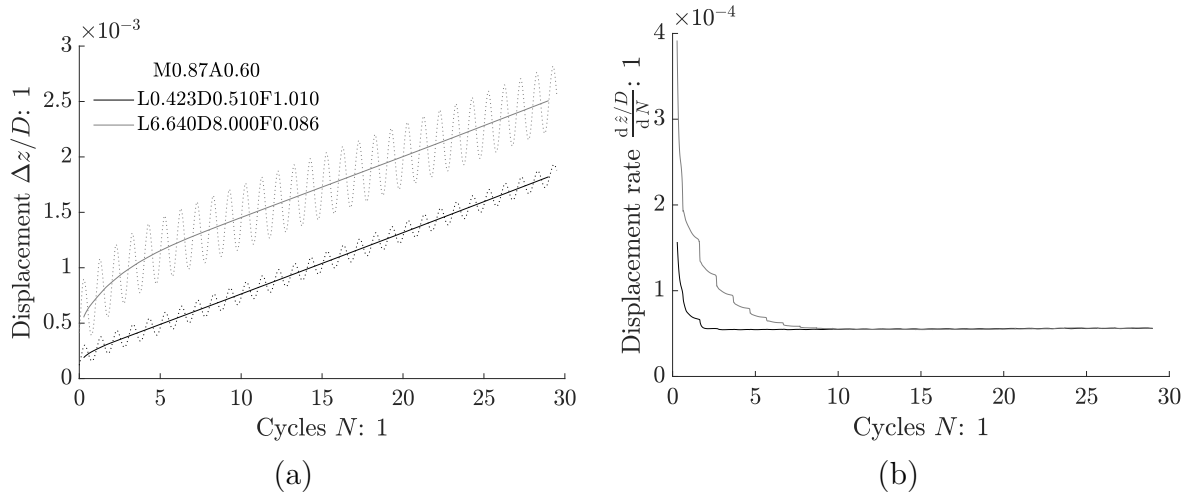
Figure 4.12: Cyclic scale analysis by means of numerical simulations regarding displacement (a) and displacement rate (b).

Table 4.2: Cyclic frequency ratios.

Cyclic load		Model scale			Prototype scale			Frequency ratio
$\bar{F}_{\mathrm{mean}}$: 1	$\bar{F}_{\mathrm{ampl}}$: 1	L: m	D: m	f: Hz	L: m	D: m	f: Hz	$f_{\mathrm{m}}/f_{\mathrm{p}}$: 1
0.86	0.18	0.4249	0.510	1.02	6.665	8.000	0.0850	≥ 12.00 *
0.87	0.60	0.4233	0.510	1.01	6.640	8.000	0.0860	11.75
1.29	0.89	0.4244	0.510	1.01	6.657	8.000	0.0856	11.80
2.12	0.52	0.4242	0.510	1.01	6.654	8.000	0.0697	14.50
1.04	0.45	0.4245	0.510	0.51	6.659	8.000	0.0418	12.20
1.52	0.65	0.4243	0.510	0.51	6.656	8.000	0.0391	13.05
1.90	0.81	0.4248	0.510	0.51	6.664	8.000	0.0352	14.50

* for $N > 120$

the scaling of tensile-loaded suction buckets did not exclusively depend on the geometric size, but also on the applied load, which was not yet accounted for in present scaling approaches (see subsection 2.3.4). In contrast to the model scale, the lowest load magnitude M0.86A0.18 at prototype scale did not lead to a negligible displacement accumulation rate within the typically simulated 29.5 cycles regardless of the load frequency. However, similarity was achieved for $N > 120$ with lower load frequencies causing higher displacements, but faster decrease of displacement accumulation rates. This pattern probably resulted from the longer drainage path at prototype scale affecting the dissipation of the negative differential pressure.

The proposed procedure is a simple approach to qualitatively assess the applicability of model tests and to estimate the effect of scaling. Moreover, the results outlined in Table 4.2 indicate that the physical model test did not require load frequencies as high as it would be estimated from Equation 2.15 to appropriately represent prototype response. In particular, it was even verified that the model tests' load frequencies represented typical

frequency ranges of environmental loads on offshore wind turbines (OWTs). However, the extent of this analysis did neither allow to entirely quantify the scaling, nor was it expected to exactly determine the prototype response. Nevertheless, the results indicated that scaling depends on an interplay of mean load $\bar{F}_{\text{mean}}$ and load amplitude $\bar{F}_{\text{ampl}}$.

4.3 Parametric study

4.3.1 Overview

Unless stated otherwise, the results of the parametric study refer to very dense sand, which was considered as reference case, with soil properties summarised in subsection 4.1.5. The suction bucket's lengths and diameters were mutually combined with $L \in [6, 9, 12]$ m and $D \in [6, 9, 12]$ m respectively, while considering the additional criterion of $L/D < 1.5$, which led to seven distinct suction bucket geometries. Each of these suction buckets was subjected to any of the loads described subsequently. Prior to the investigation of the specific loading condition, the drained resistance was determined by applying $v_z = 10^{-12}$ m/s (see subsection 4.2.2).

The load conditions comprise loading with either constant displacement rate (see subsection 4.3.3), constant force (see subsection 4.3.4) or cyclic force (see subsection 4.3.5). The considered constant displacement rates were $v_z = 10^{[-6,-5,-4,-3,-2,-1,0]}$ m/s in order to investigate a wide range of drainage conditions. Additionally, medium dense sand was accounted for in order to examine the effect of the sand's relative density on the tensile response. With respect to the constant force, four load magnitudes were applied, namely $\bar{F} = [0.5, 1, 2, 4]$, and held constant for 18 s. The loading with cyclic forces were specified to be tensile swell loads with $\bar{F}_{\text{mean}} \geq \bar{F}_{\text{ampl}}$. The mean load and load amplitude were varied independently within the range from $0.25F_{\text{dr}}$ to $2F_{\text{dr}}$. The combination of mean load and load amplitude resulted in ten different cyclic load configurations, which were further combined with two periods, namely $T \in [6, 12]$ s. These loads were applied for $N = 29.5$ cycles ending with a half cycle for subsequent unloading.

Beside the already introduced three load conditions, two more load types were considered. Firstly, the transient response of the suction bucket was examined by means of the simulation of a singular sinusoidal load with a subsequent consolidation phase (see subsection 4.3.6). This load condition accounts for the circumstance that the occurrence of a significant number of tensile cyclic loads is rather unlikely with respect to a cautious design of an OWT. Moreover, the consecutive consolidation facilitated the estimation of residual displacements. Secondly, a procedure was developed aiming at the application of an incrementally monotonic load, which induces equivalent displacement to particular cyclic load (see subsection 4.3.7). The proposed method shall enable the simplified simulation of arbitrary cyclic loads while improving the computational efficiency.
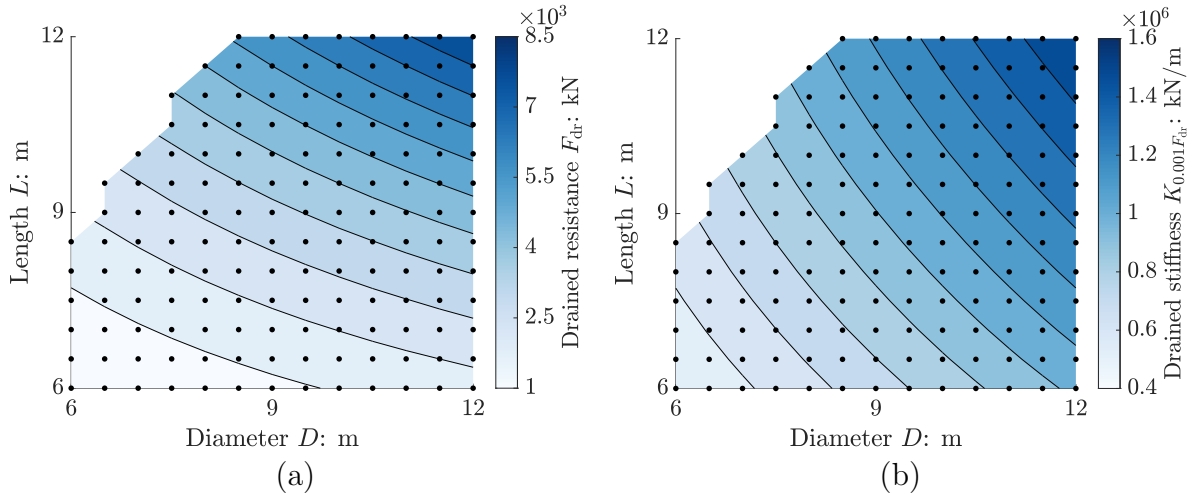
Figure 4.13: Drained resistance (a) and drained stiffness (b) in dependency of geometric dimensions.

4.3.2 Drained response

The drained resistance was determined for additional suction bucket geometries in both relative densities of the soil. Figure 4.13 (a) depicts the drained resistance in very dense sand for all geometries. As expected, larger dimensions of the suction buckets implied higher drained resistances, while the most distinct increase was observed for $L/D \approx 1$. Detailed analysis provided that the drained resistance rose over-linearly with L/D to the power of almost two. Beside that, the effect of the suction bucket's length was predominant over its diameter. Consequently, the higher skin friction in deeper embedment depth along with the linearly increasing skirt's area had a larger effect on the drained resistance than the over-linear increase of the skirt's area with the suction bucket's diameter. Based on FE simulations with an associated flow rule, Nielsen (2019) found that the drained resistance increased linearly with the suction bucket's diameter and quadratically with its length. Probably due to different assumptions of the distinct FE models, the relations of Nielsen (2019) do not coincide with Figure 4.13, but the results still confirmed the higher relevance of the suction bucket's length in comparison to its diameter.

The suction bucket's initial secant stiffness under drained condition was evaluated for the displacement at which one thousandth of the drained resistance was reached, i.e. $K_{0.001F_{dr}} = 0.001F_{dr}/\Delta z_{0.001F_{dr}}$. The results were summarised in Figure 4.13 (b) and pointed out that the initial stiffness increased almost linearly with $L/D \approx 1$. Thus, the suction bucket's length and diameter had a similar effect on the initial stiffness.

Figure 4.14 provides comparison of the drained resistances determined by FE simulation, simple soil mechanic calculation in geostatic state neglecting stress relief (see Equation 2.2 and Equation 2.3) and the analytical approach of Houlsby et al. (2005b) (see Equation 2.10). As anticipated, the calculations assuming geostatic condition provided only vague approximations of the drained resistances and generally overestimated the results of the FE simulations. In contrast, the results obtained by the method of Houlsby
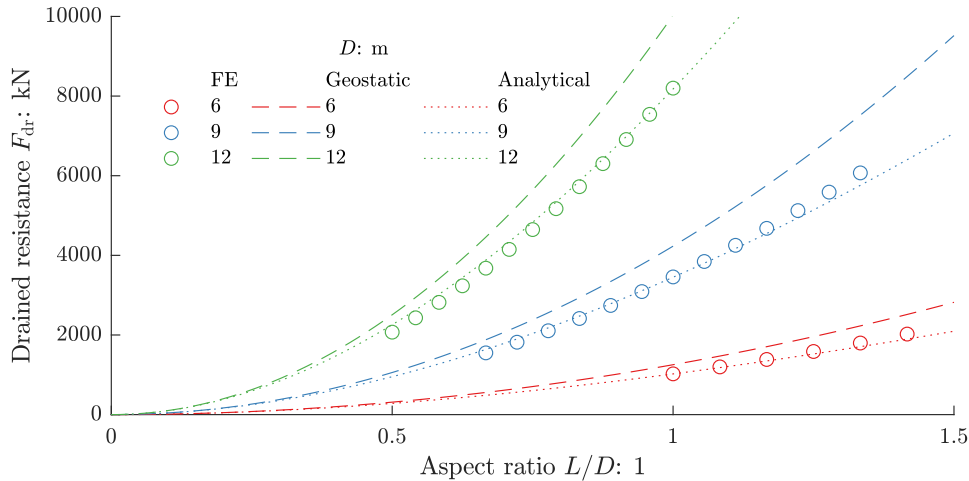
Figure 4.14: Comparison of drained resistances for different geometric dimensions.

et al. (2005b) approached those of the numerical simulation with the best approximations for $L/D = 1$. For smaller aspect ratios, the analytical method tended to overestimate the drained resistance and vice versa for $L/D > 1$. The attained accordance of the analytical method was not expected because of discrepancies in representing the stress relief (see subsection 4.2.2), but apparently, the superposition of the deviations concealed the discrepancies. Further, Figure 4.14 highlights the over-linear increase of drained resistance with increasing aspect ratio L/D as indicated in Figure 4.13 (a).

4.3.3 Constant displacement rate

The analysis of the suction bucket's response to constant displacement rates assumed the suction bucket geometry $L = D = 9\,\mathrm{m}$ in very dense sand as reference case. Starting from this configuration, a variation of the displacement rate, geometric dimension and soil's relative density was investigated. The results were presented in terms of tensile resistance, initial stiffness, gap expansion and differential pressure ratio.

Figure 4.15 depicts the tensile resistance and its individual shares, namely suction force as well as inner and outer friction, in an interaction diagram. Beside the allocation of the resistances, the influence of the displacement rate, displacement and geometric dimension of the suction bucket on the development of the tensile resistances becomes evident. To enable comparability of the two suction bucket dimensions, the resistances and displacements were divided by the suction bucket's drained resistance and diameter respectively. The drained resistances were $F_{\mathrm{dr}} = 1024\,\mathrm{kN}$ for $D = 6\,\mathrm{m}$ and $F_{\mathrm{dr}} = 3458\,\mathrm{kN}$ for $D = 9\,\mathrm{m}$. Except for minor deviations, the results presented in Figure 4.15 were qualitatively consistent with those of Thieken et al. (2014), where a more sophisticated constitutive law (hypoplasticity) was utilised.

Higher displacement rates invoked larger tensile resistances (see Figure 4.15 (a)), which mainly resulted from the increasing suction forces (see Figure 4.15 (b)). Moreover, the
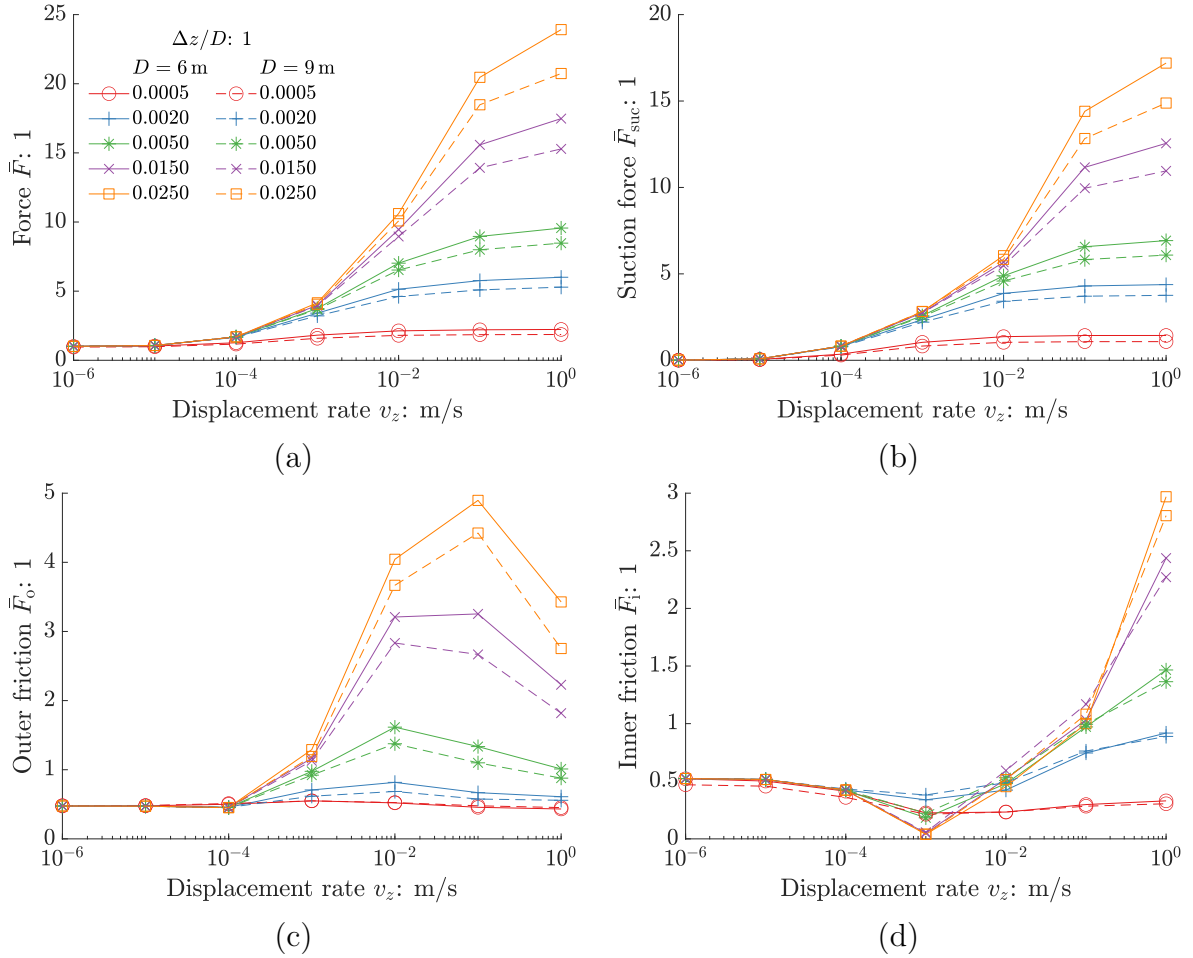
Figure 4.15: Interaction diagram for $L/D = 1$ with total resistance (a), suction force (b), outer friction (c) and inner friction (d).

outer friction increased as well with the displacement rate, but the largest magnitude was not observed for the highest displacement rate (see Figure 4.15 (c)). Consequently, the almost undrained condition caused a reduction of the outer friction in comparison to partially drained conditions. The inner friction reduced under partial drainage, i.e. $10^{-5}\,\mathrm{m/s} \le v_z \le 10^{-2}\,\mathrm{m/s}$, but increased and exceeded the drained resistance as the tensile response approached the undrained condition (see Figure 4.15 (d)). Nevertheless, the inner friction was still lower than the outer friction for the highest displacement rate.

Further, Figure 4.15 visualises the mobilisation of particular resistances in dependence of the suction bucket's displacement. Although the suction force provided major share of the tensile resistance, its generation required substantial displacements. The partially drained to undrained outer friction required significant displacement for its mobilisation as well. In contrast, the inner friction was reached within less displacement except for the almost undrained condition, where it increased crucially at large displacements.

The comparison of the two distinct sizes of the suction bucket revealed that the larger suction bucket necessitated higher displacements relative to its diameter to mobilise an
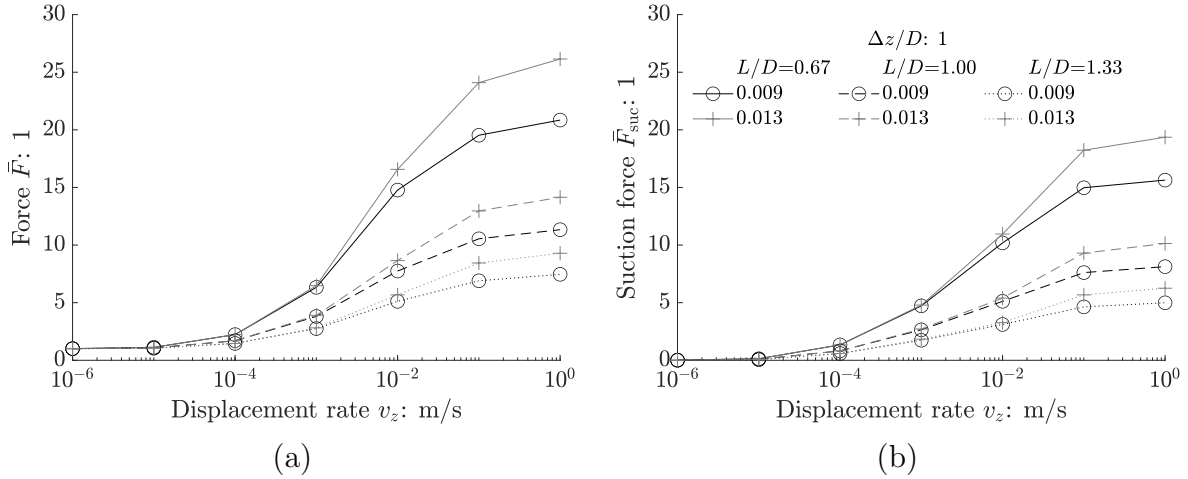
Figure 4.16: Interaction diagram for $D = 9\,\mathrm{m}$ and different aspect ratios with total resistance (a) and suction force (b).

identical resistance in relation to its drained resistance. This tendency was most obvious concerning the suction force and outer friction. Within this context, it is referred to the more than three times higher drained resistance of the larger suction bucket so that the absolute resistances were effectively higher for the larger suction bucket.

The effect of the suction bucket's aspect ratio is illustrated in Figure 4.16 for $D = 9\,\mathrm{m}$, whereby solely two displacements based on potential serviceability limit state (SLS) criteria are depicted (see section 2.1). The drained resistances were $F_{\mathrm{dr}} = 1551\,\mathrm{kN}$, $F_{\mathrm{dr}} = 3458\,\mathrm{kN}$ and $F_{\mathrm{dr}} = 6071\,\mathrm{kN}$ for $L/D = 0.67$, $L/D = 1.00$ and $L/D = 1.33$ respectively. Although the smallest aspect ratio evinced the highest rise of tensile resistance and suction force relative to its drained resistance with increasing displacement rates, the absolute resistances were still lower than the ones of the two larger aspect ratios. With respect to the load sharing, the suction force provided major resistance, which was qualitatively independent from the aspect ratio. Due to equality of the diameters, the displacements were relatively and absolutely identical. Hence, the smallest aspect ratio had the most distinct increase in tensile resistance with displacement and the two larger aspect ratios required more displacement to generate equivalent rises in tensile resistance.

Figure 4.17 compares the tensile response in dependence of the soil's relative density. The medium dense and very dense sand had different soil mechanical parameters and the permeability of the medium dense sand was almost 1.6 times higher (see subsection 4.1.5). Nevertheless, the drained resistances were similar with $F_{\mathrm{dr}} = 3458\,\mathrm{kN}$ and $F_{\mathrm{dr}} = 3363\,\mathrm{kN}$ in very dense and medium dense sand respectively. It would be expected that the drained resistance is higher in very dense sand owing the higher dilation, but it was found that the stress relief was more pronounced so that for this particular configuration of soil properties and suction bucket dimension the drained resistances were almost identical. In addition, the drained resistance is further affected by $K \tan \delta$, which was marginally higher in medium dense sand, and the soil's effective unit weight, which was slightly higher in very dense sand (see subsection 4.1.5).
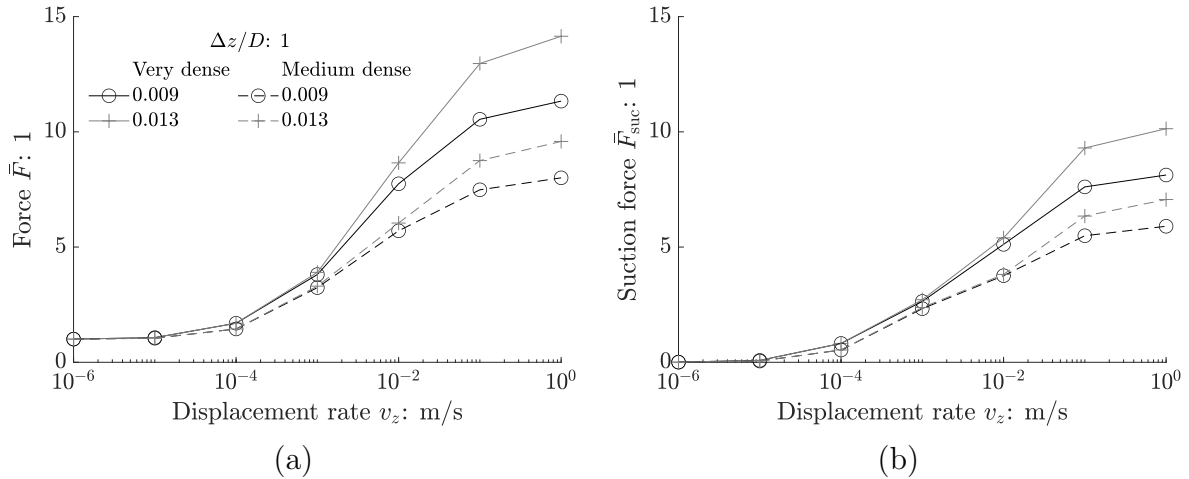
Figure 4.17: Interaction diagram for $L = D = 9\,\mathrm{m}$ in dependence of the soil's relative density with total resistance (a) and suction force (b).

Although the tensile resistance for almost drained conditions was comparable for both relative densities, the suction bucket exhibited higher tensile resistances in very dense sand under partially drained to undrained conditions (see Figure 4.17 (a)). Concerning the influence of the displacement, the increase of tensile resistance for higher displacement rates was more pronounced in very dense sand than in medium dense sand. Moreover, the lower permeability in denser soil invoked greater rise in negative differential pressure for increasing displacement rates (see Figure 4.17 (b)). Beside the larger negative differential pressure for the soil's higher relative density, the inner and outer friction were enhanced as well for partially drained to undrained conditions, which was evident from the more pronounced rise of tensile resistance for increasing displacement rates in comparison to the corresponding suction force.

While the tensile resistance of the suction bucket is of major interest regarding the ultimate limit state (ULS) of an OWT, the foundation stiffness is relevant for the design of both fatigue limit state (FLS) and SLS. The secant stiffness $K = F/\Delta z$ was evaluated for different displacement rates and loads $[0.001, 0.500]F_{\mathrm{dr}}$ with the associated displacements $\Delta z_{0.001F_{\mathrm{dr}}}$ and $\Delta z_{0.500F_{\mathrm{dr}}}$ (see markers in Figure 4.18 (a)). Additionally, Figure 4.18 (b) points out the dependency of the stiffness on the load for any $\bar{F} \leq 1$. Finally, the stiffnesses were depicted for different displacement rates and particular loads (see Figure 4.18 (c)).

The suction bucket's stiffness was higher under partially drained to undrained conditions for loads lower than the drained resistance. Even for $v_z = 10^{-6}\,\mathrm{m/s}$, where the tensile resistance was only marginally affected by minor limitation of drainage, the stiffness for $0.001F_{\mathrm{dr}}$ was enhanced in comparison to the drained condition. Moreover, the results showed a decrease of the stiffness with increasing load. This effect was more significant for drained to partially drained conditions but became less relevant for displacement rates that approach the undrained condition. For instance in case of partial drainage with $v_z = 10^{-4}\,\mathrm{m/s}$, the stiffness at $0.001F_{\mathrm{dr}}$ was almost as high as under undrained condition, but for $0.500F_{\mathrm{dr}}$, the stiffness was considerably lower.
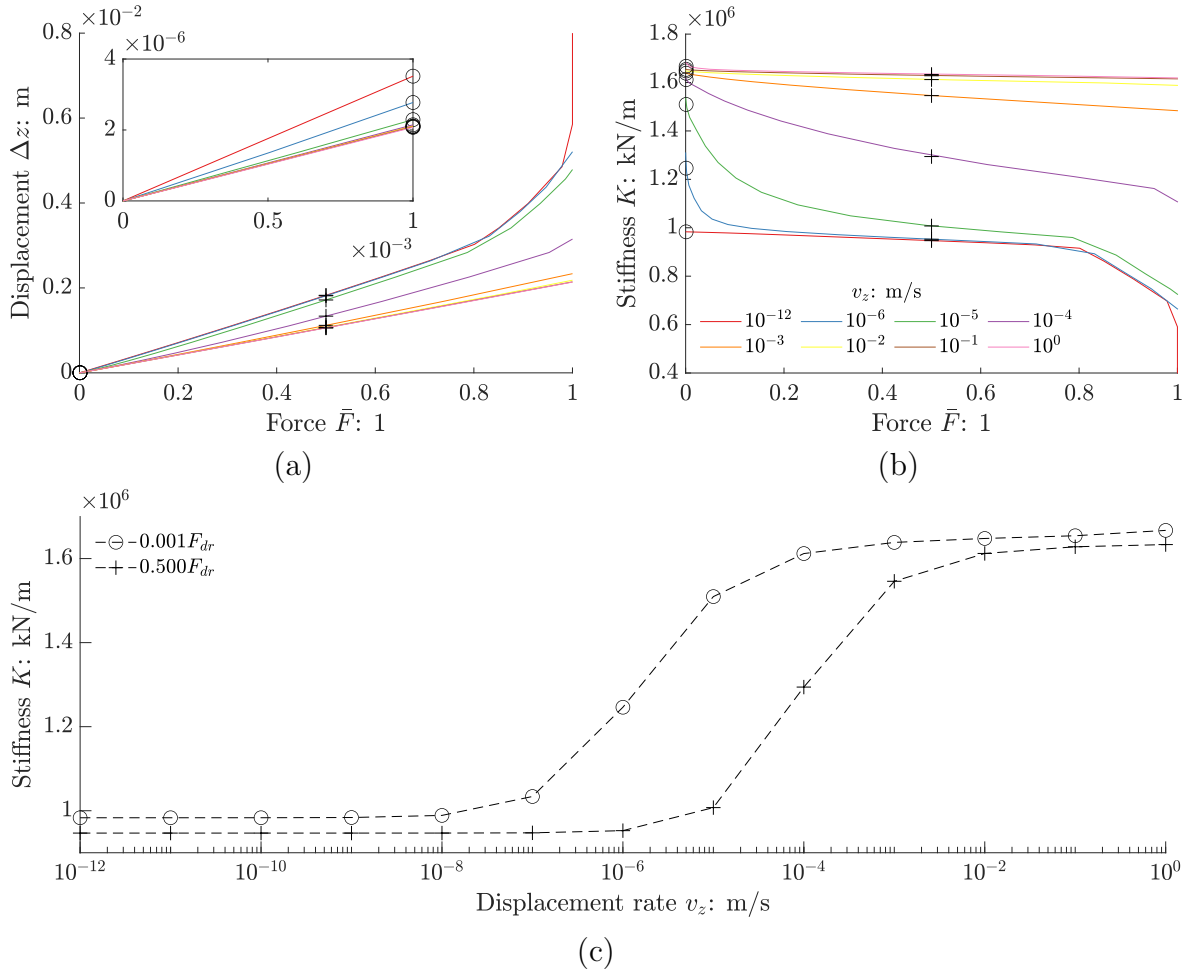
Figure 4.18: Evaluation of the initial stiffness for $L = D = 9$ m via load displacement (a), stiffness for $\bar{F} \leq 1$ (b) and stiffness in dependence of displacement rate (c).

In terms of the stiffness, Figure 4.19 generalises the results for different suction bucket dimensions. Basically, the previously described findings with respect to the displacement rates and loads applied equivalently. Figure 4.19 (a) depicts results for suction buckets with an aspect ratio of $L/D = 1$, where the stiffness increased over-linearly with increasing dimension of the suction bucket. The tendency of increasing stiffness for higher displacement rates was evident for every dimension but the largest suction bucket exhibited the most significant rise, which was because of the simultaneously decreasing drainage with increasing dimension of the suction bucket. Similarly, Figure 4.19 (b) points out that higher aspect ratios generally led to enhanced stiffness due to less drainage for high displacement rates. Furthermore, the deeper embedment depth and larger diameter correlated with higher stiffness even for low displacement rates, which is in agreement with the results for the drained condition depicted in Figure 4.13 (b).

The gap expansion beneath the suction bucket's lid is related to the actual drainage condition, whereby less drainage implies smaller gap expansion. This mechanism is visualised in Figure 4.20. Evidently, negligible gap expansion took place for $v_z \geq 10^{-2}$ m/s. Since

(a)

(b)
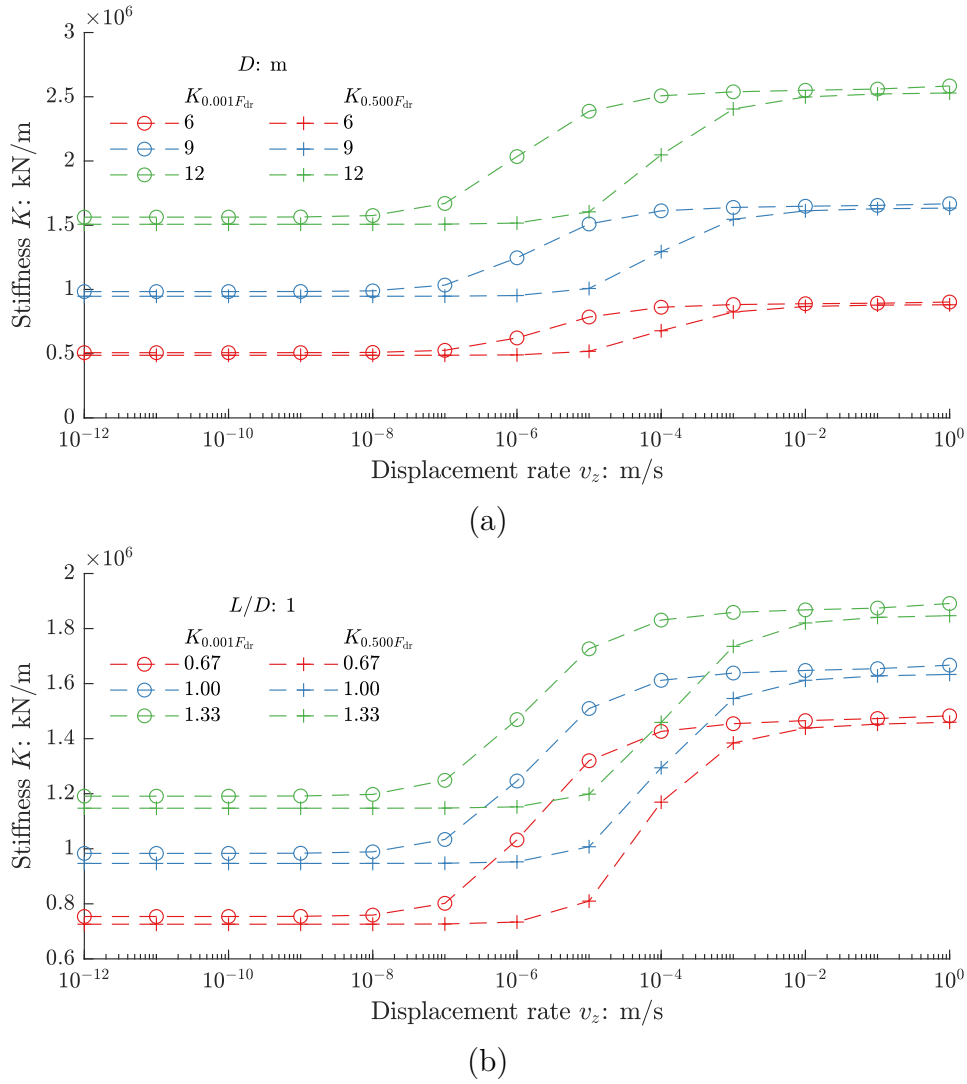
Figure 4.19: Effect of suction bucket dimensions and displacement rate on the initial stiffness for $L/D = 1$ (a) and $D = 9\,\mathrm{m}$ (b).

there was almost no gap expansion at all, the suction bucket's size and its displacement exhibited a minor effect on the gap expansion. For $v_z = 10^{-3}\,\mathrm{m/s}$, the suction bucket's response was partially drained and the gap expanded to a certain extent, which further depended on the suction bucket's displacement. This progress stagnated for $\Delta z/D = 0.025$ and led to almost constant $\Delta z_{\mathrm{gap}}/\Delta z \approx 0.22$ so that there was still continuous plug heave for advancing displacement. Moreover, it became evident that the smaller suction bucket exhibited more gap expansion due to more drainage. The influence of the displacement and dimension of the suction bucket was more pronounced for $v_z = 10^{-4}\,\mathrm{m/s}$, where significantly more drainage was enabled so that the gap expansion was almost as high as the suction bucket's displacement for $\Delta z/D = 0.025$. The two lowest displacement rates exhibited approximate equality of gap expansion and displacement proving that minor plug heave took place in case of sufficient drainage.
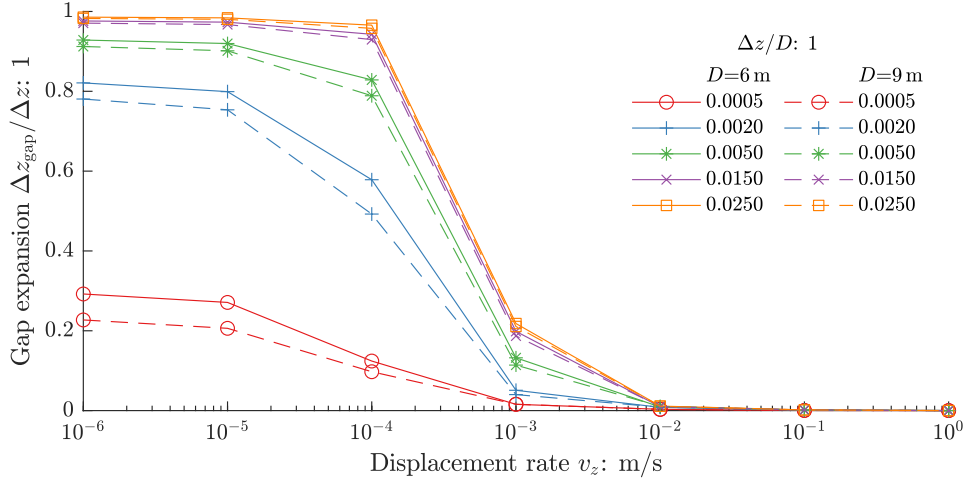
Figure 4.20: Gap expansion for $L/D = 1$ in dependence of suction bucket dimension, displacement rate and displacement.

Furthermore, the pore pressure field provided essential insights into the drainage condition. Instead of evaluating the entire field, the pore pressure close to the suction bucket's skirt in a depth of $|z/L| = 0.9$ was examined by means of the differential pressure ratio a. The less drainage takes place, the less negative differential pressure dissipates inside the suction bucket and the higher is the negative differential pressure outside the suction bucket. The occurrence of significant positive differential pressure outside the suction bucket was observed for displacement rates $v_z \geq 10^{-1}$ m/s (see Figure 4.21 (a)). This effect was related to a reduction of the soil's effective stresses because of the almost entire uplift of the soil plug inside and in proximity of the suction bucket, which was referred to nearly undrained condition. Nonetheless, the differential pressure ratio showed a gradual rise with progressing displacement of the suction bucket, which was similarly observed for $v_z = 10^{-2}$ m/s and indicated the ongoing development of the pore pressure field as a response to the constant displacement rate. As a result, negative differential pressures arose outside the suction bucket. Decreasing the displacement rate to $v_z < 10^{-2}$ m/s led to lower differential pressure ratios, which had been expected. With respect to the size of the suction bucket, the larger dimension required slightly higher displacements relative to its diameter to generate equivalent differential pressure ratios.

The differential pressure ratio at the inside was higher than the one at outside (see Figure 4.21 (b)). For $v_z \leq 10^{-1}$ m/s, the differential pressure ratios at the suction bucket's inside commenced at relatively high values and subsequently, dissipation took place with advancing displacement until the differential pressure ratios decreased to nearly constant values. This dissipation progressed faster for lower displacement rates. For $v_z \geq 10^{-1}$ m/s, the differential pressure ratio at the skirt's inside exceeded the one at the suction buckets lid, i.e. $a_i > 1$, which resulted from soil's dilation. Contrary to the dissipation observed for $v_z \leq 10^{-1}$ m/s, the highest displacement rate $v_z = 10^0$ m/s evinced an increase of the differential pressure ratio until an approximately constant level was reached. Equivalently to the outside differential pressure ratio, the larger suction bucket exhibited similar differential pressure ratios at the inside for marginally higher displacements.
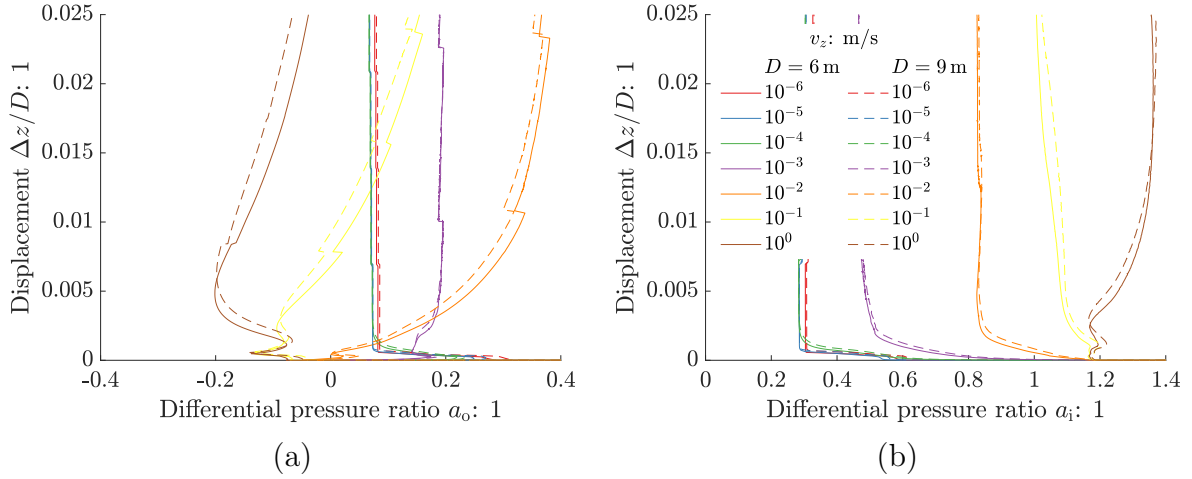
Figure 4.21: Effect of displacement rate on differential pressure ratio for $L/D = 1$ outside (a) and inside (b) the suction bucket's skirt.

4.3.4 Constant force

The suction bucket's monotonic bearing behaviour was evaluated comprehensively for constant displacement rates in subsection 4.3.3. Consequently, the discussion of the response to constant force-controlled loading focusses primarily on the most relevant aspects concerning the subsequent assessment of the cyclic bearing behaviour (see subsection 4.3.5). Thus, the displacement accumulation and load sharing are of particular interest. Further essential results of the parametric study on suction buckets subjected to constant force, such as plug heave and drainage, were summarised.

Figure 4.22 depicts exemplary results for two suction buckets with $L/D = 1$. In terms of the displacement accumulation, larger load magnitudes invoked both more displacement after load application at $t = 0\,\mathrm{s}$ and higher displacement rates during continuous loading for $t > 0\,\mathrm{s}$ (see Figure 4.22 (a)). In case of load magnitudes $\bar{F} \leq 1$, a certain initial displacement during the load application took place, but there was minor displacement accumulation for $t > 0\,\mathrm{s}$ so that the displacement remained almost constant. The displacement rates were only slightly higher for the larger suction bucket, but the absolute displacements were higher because of the initial displacements during load application. Dividing the suction buckets' displacements by their diameters led to similar initial displacements that were marginally higher for the larger suction bucket, but the displacement rates relative to the diameter v_z/D were lower.

The plug heave divided by the suction bucket's displacement $\Delta z_{\mathrm{plug}}/\Delta z$ decreased mainly during the progress of the simulation and slightly with increasing load magnitude for $\bar{F} < 4$ (see Figure 4.22 (b)). While the first aspect was related with advancing dissipation, the latter was attributed to the higher displacements for greater load magnitudes affecting the denominator of this quantity. For the highest load magnitude of $\bar{F} = 4$, substantial negative differential pressure developed invoking less drainage and considerably higher plug heave than for lower load magnitudes. Further, the dimension of the suction bucket
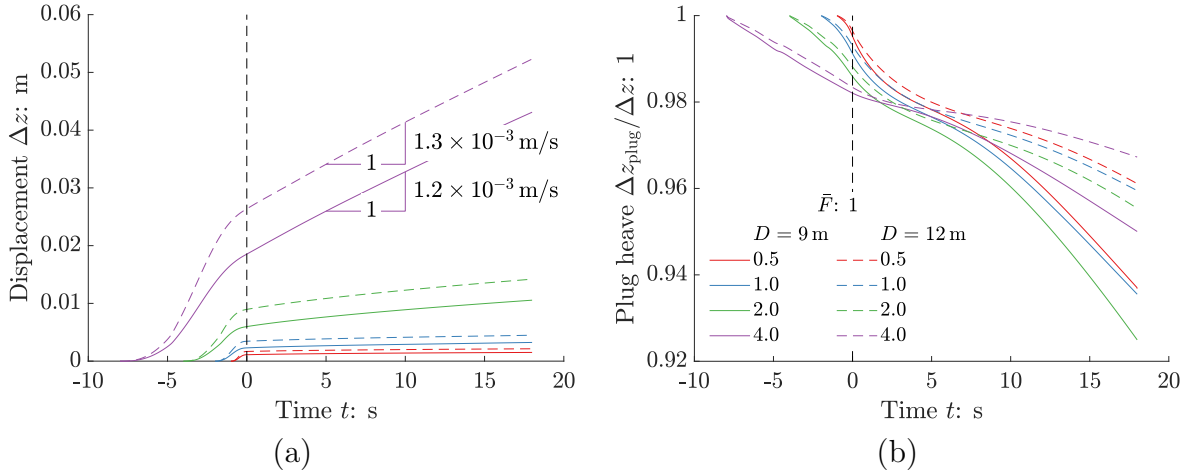
Figure 4.22: Displacement accumulation (a) and plug heave (b) in dependence of suction bucket dimension and constant load magnitude for $L/D = 1$.

affected the drainage condition and therefore influenced the plug heave. In case of the smaller suction bucket, the relative plug heave $\Delta z_{\text{plug}}/\Delta z$ was substantially lower than the one simulated with the larger suction bucket, where the displacement Δz was even higher. It is remarked additionally that the plug heave reduced until $\Delta z_{\text{plug}}/\Delta z \approx 0.8$ while maintaining the load for $t_{\text{hold}} = 18\,\text{s}$ for a suction bucket with $L = D = 6\,\text{m}$.

The corresponding suction forces are presented in Figure 4.23 (a). As a result of the load application, negative differential pressures were generated, which were higher for larger load magnitudes. For $\bar{F} \leq 1$, the suction force $\bar{F}_{\text{suc}}$ was approximately linearly related to the applied load, but for load magnitudes exceeding the drained resistance, the share of the suction force rose over-linearly. After the load was completely applied, the suction force diminished to a constant value that depended on the actual load magnitude. With respect to the suction bucket's dimension, the suction forces divided by the drained resistances were similar, but the dissipation of negative differential pressure was slower in case of the larger suction bucket, which was attributed to the longer drainage path.

During load application, the maximum outer friction was reached at $t \approx -4.6\,\text{s}$ and $t \approx -1.6\,\text{s}$ for $\bar{F} = 4$ and $\bar{F} = 2$ respectively (see Figure 4.23 (b)). Due to the further increasing load, the suction force grew at an enhanced rate afterwards. The inner friction behaved similarly at a later stage of load application (see Figure 4.23 (c)), when the load rate was much lower so that it had minor effect on the suction force. While the load was maintained and the suction force reduced, the resistances evinced redistribution with an increasing share of the inner and outer friction. This progress was related with the slight decrease of the displacement rate over the duration of the simulation. However, this deceleration was minor and therefore neglected in the evaluation. The increase of frictional resistance was most evident for the inner friction and load magnitudes $\bar{F} \leq 1$ as well as the outer friction and $\bar{F} = 4$. The latter effect indicated a crucial increase of the attainable outer friction, which was attributed to the presence of negative differential pressures at the suction bucket's skirt magnifying the effective stresses. In each of the simulations, the outer friction generally exceeded the inner friction.

125
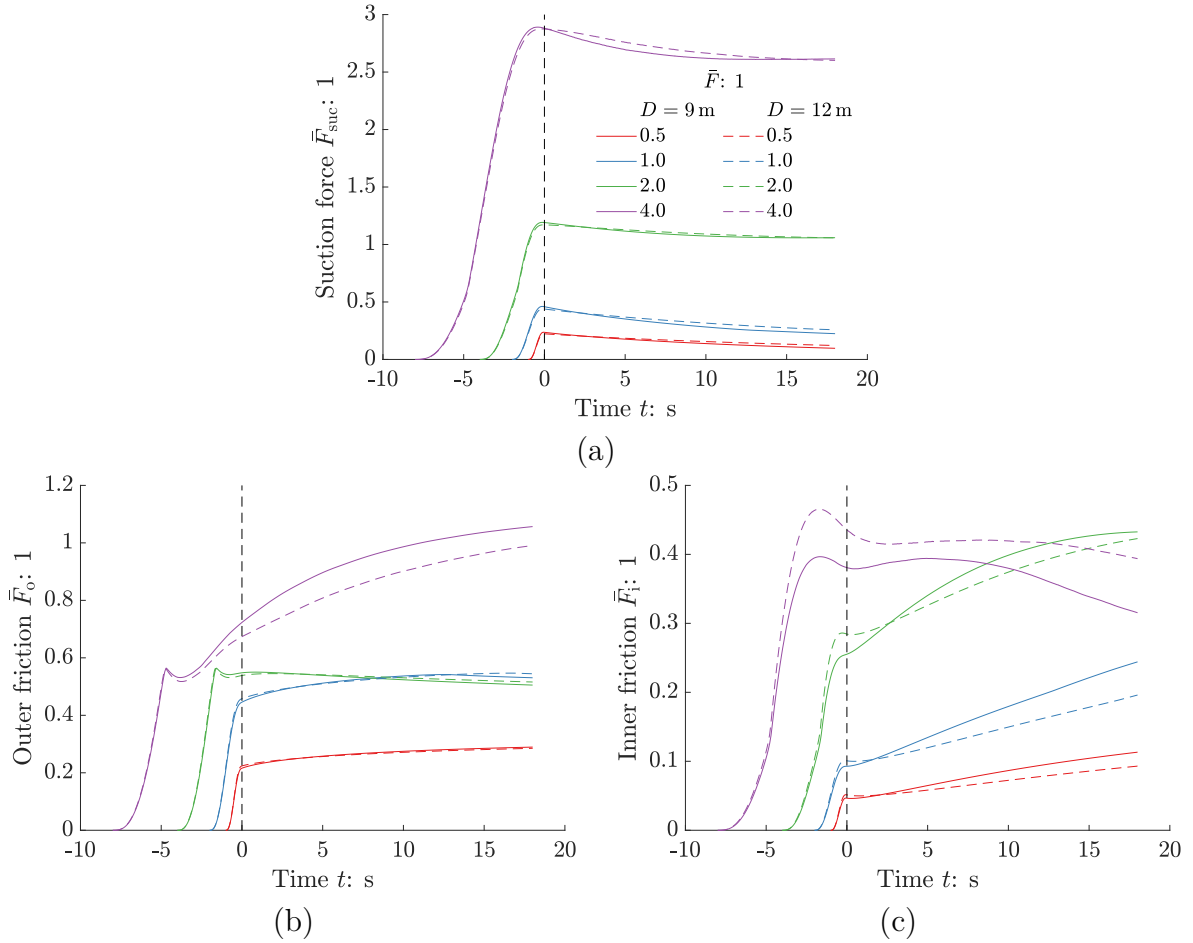
Figure 4.23: Suction force (a), outer friction (b) and inner friction (c) in dependence of suction bucket dimension and constant load magnitude for $L/D = 1$.

The displacement rates at the end of every simulation were determined in order to analyse the displacement accumulations for different suction bucket dimensions and load magnitudes. The results for $\bar{F} = 0.5$ are presented in Figure 4.24 (a) and reveal negligible displacement rates for any of the considered suction buckets. Marginally higher displacement rates occurred with increasing dimension of the suction bucket, especially for $L/D \approx 1$, which resulted from higher drained resistances implying greater absolute load magnitudes (see drained resistances in Figure 4.13 (a)). Although, the overall displacement rates for $\bar{F} = 1$ were marginal as well (see Figure 4.24 (b)), the absolute displacements resulting from the initial load application increased (see Figure 4.22 (a)). Moreover, the effect of the suction bucket's aspect ratio on the displacement ratio changed with larger aspect ratios invoking higher displacement rates.

The interrelation of load magnitude and aspect ratio became more distinct for loads above the drained resistance (see Figure 4.24 (c) and (d)). For $\bar{F} = 4$, the effect of the aspect ratio on the displacement rate was highly non-linear. Extensive analyses of the displacement accumulation with regard to the suction bucket geometry is provided in subsection 4.3.5 concerning cyclic loading.
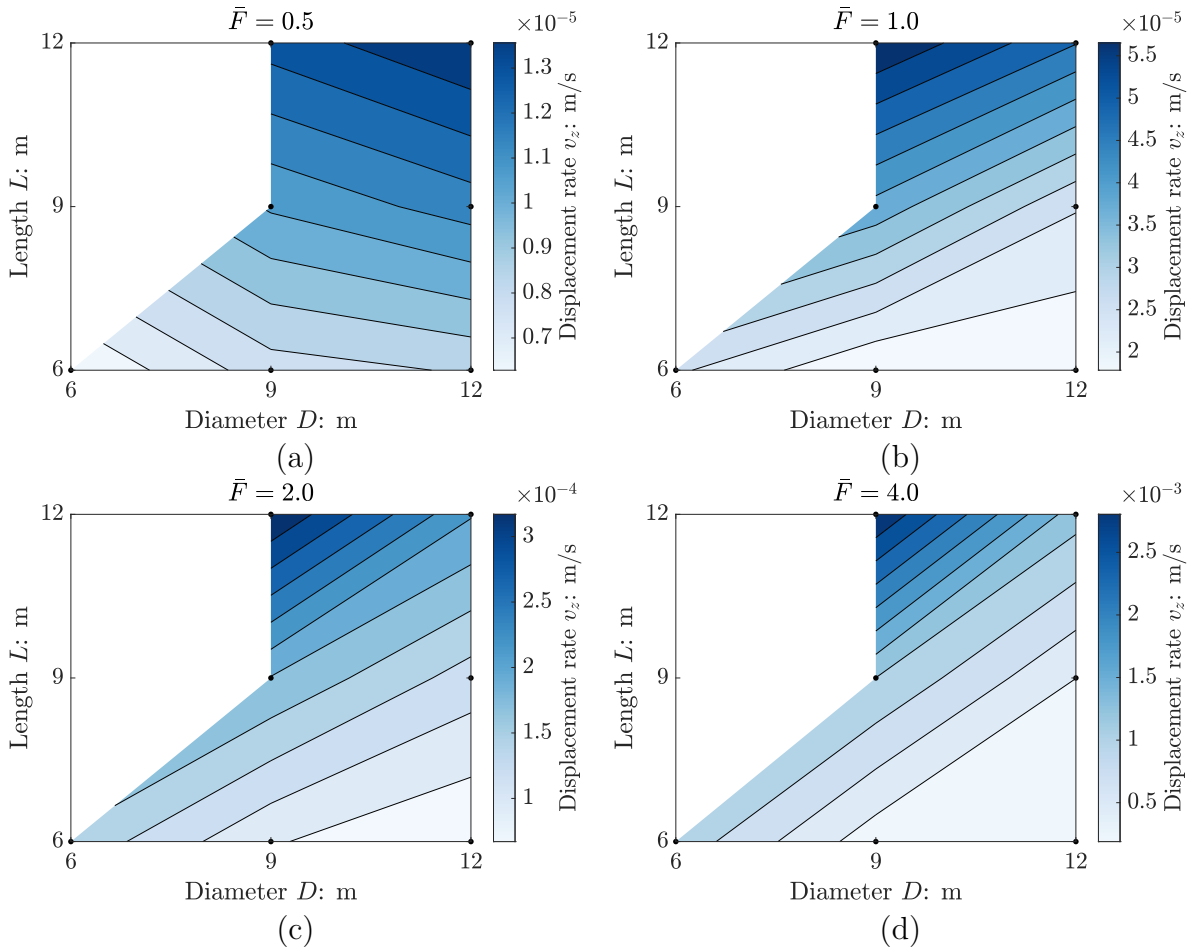
Figure 4.24: Displacement rates induced by force-controlled monotonic loading in dependence of suction bucket geometry and load magnitude with $\bar{F} = 0.5$ (a), $\bar{F} = 1.0$ (b), $\bar{F} = 2.0$ (c) and $\bar{F} = 4.0$ (d).

With respect to the evaluation of the differential pressure ratio, it is referred to simulations with constant displacement rates, were similar behaviour was observed (see Figure 4.21). For force-controlled loading, the differential pressure ratios were lower for higher load magnitudes and for $\bar{F} \leq 1$, the differential pressure ratios were almost equal and consequently negligibly affected by the load magnitude. At the beginning of the load application, the differential pressure ratio at the inside exceeded a value of one, but continuous dissipation caused steady decrease leading finally to $a_i < 1$.

The significant displacement rates due to monotonic loads above the drained resistance would have severe consequences for the entire OWT if the load would be maintained for considerable duration. This fact highlights the limited practical relevance of this loading condition so that the results were only briefly presented. However, the summarised findings regarding the monotonic displacement accumulation and load sharing were indicative and essential for the analysis of the suction bucket's cyclic bearing behaviour. Moreover, the results provided the basis for the development of an approach that simplifies the cyclic load to an equivalent load evoking similar displacement.
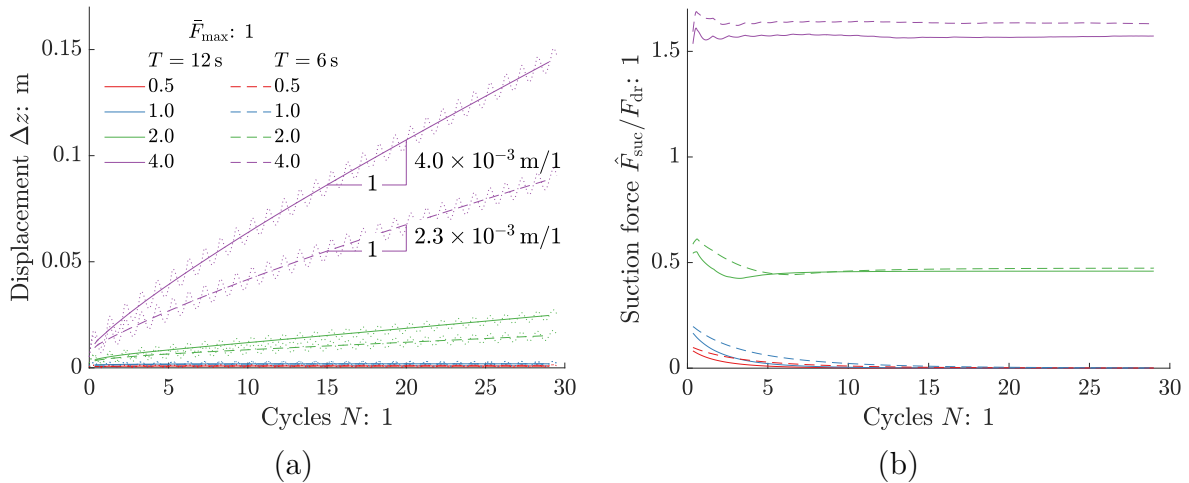
Figure 4.25: Displacement accumulation (a) and suction force (b) in dependence of load magnitude and period for $L = D = 9\,\mathrm{m}$ and cyclic loading with complete unloading in each cycle ($\bar{F}_{\mathrm{mean}} = \bar{F}_{\mathrm{ampl}}$).

4.3.5 Cyclic force

The extent of the parametric study concerning cyclic loading comprised a variation of suction buckets' geometries, mean loads, load amplitudes and periods. The combinations of these quantities led to numerous simulations exhibiting many details. However, it was beyond the scope to provide the results of every simulation in detail, especially since the cyclic bearing behaviour was described extensively with respect to the model tests in section 3.6 and their back-analysis in subsection 4.2.6. Hence, the presentation of the results concentrates on the displacement accumulation and load sharing, which are the most relevant aspects in terms of cyclic tensile loading.

Figure 4.25 depicts representative results for cyclic loading with complete unloading in each cycle, i.e. $\bar{F}_{\mathrm{mean}} = \bar{F}_{\mathrm{ampl}}$ and $\bar{F}_{\mathrm{min}} = 0$, whereby different periods and load magnitudes were accounted for. Higher displacement accumulation occurred for both higher load magnitudes $\bar{F}_{\mathrm{max}}$ and longer periods T (solid lines in Figure 4.25 (a)). Moreover, the higher the load magnitude was, the more displacement took place in each cycle, which resulted from the higher load amplitude $\bar{F}_{\mathrm{ampl}}$ (dotted lines). Maximum loads less or equal to the drained resistance did not evoke continuous displacement accumulation, but certain initial displacement during preloading and within the first cycles ($N < 10$). Nonetheless, the displacements for $\bar{F}_{\mathrm{max}} \leq 1$ were of minor relevance with respect to the range of simulated cycles. In general, the displacement accumulation rates decreased within the first cycles and approached asymptotically to distinct constant values. The constant displacement rates at the end of the simulations were used for further evaluations.

The suction force's moving mean $\hat{F}_{\mathrm{suc}}$ was determined over the duration of one load cycle and depicted in Figure 4.25 (b). The suction force was greater for higher load magnitudes in order to mobilise sufficient resistance against the tensile load. None of the simulations exhibited an accumulation of suction force, but analogously to the displacement rate, the

suction force reduced within the first cycles. This reduction was more pronounced for longer periods so that the constant suction force, which was almost not affected by the period for $\bar{F}_{\max} \leq 2$, was reached within less cycles in comparison to the shorter period. It is marked that dissipation of the pore pressure depends on the time t, in which the reduction of suction force coincided approximately for both periods, rather than the cycles N. The longer period evoked a lower suction force for $\bar{F}_{\max} = 4$. Hence, the share of the frictional resistance was greater and the suction bucket's behaviour was more drained.

The constant displacement rates at the end of the simulations were determined for every simulation of the parametric study in order to analyse the displacement accumulation. Figure 4.26 summarises the results for load configurations with complete unloading in each cycle so that the results for $T = 6\,\mathrm{s}$ depicted in Figure 4.25 (a) are directly comparable for $L = D = 9\,\mathrm{m}$ in Figure 4.26. Beside the visualisation of the global effect of the load magnitude on the displacement accumulation, the results presented in Figure 4.26 enable the examination of multiple suction buckets' geometries and their influence on the displacement accumulation. The displacement accumulation increased mainly with $L/D = 1$ for load magnitudes $\bar{F}_{\max} \leq 1$, but the actual displacement rates were negligible for any suction bucket dimension. If the maximum loads exceeded the drained resistance, the displacement rates attained considerable values and higher aspect ratios led to more significant displacement accumulation and vice versa.

The cyclic displacement accumulation depicted in Figure 4.26 was compared to the monotonic displacement accumulation shown in Figure 4.24. Because of different dimensions of the displacement rates (while cyclic accumulation referred to displacement per cycle, monotonic accumulation was defined as displacement per time), the analysis could only provide a qualitative assessment. Moreover, the monotonic forces $\bar{F}$ were persistent and the cyclic forces reached an identical magnitude only for $\bar{F}_{\max}$ and were unloaded in every cycle until $\bar{F}_{\min} = 0$.

Cyclic load magnitudes less or equal to the drained resistance did not evoke considerable displacement rates (see Figure 4.26 (a) and (b)), which was observed for monotonic load magnitudes $\bar{F} < 1$ (see Figure 4.24 (a)), but monotonic loads equal to the drained resistance caused certain, albeit minor displacement rates (see Figure 4.24 (b)). Further, significant influence of the aspect ratio became evident for a monotonic load of $\bar{F} = 1$, which was less distinct in case of cyclic loads with $\bar{F}_{\max} = 1$ (compare Figure 4.24 (b) and Figure 4.26 (b)). These findings underlined the subordinate relevance of loads below the drained resistance with regard to the displacement accumulation.

In case of loads exceeding the drained resistance, the monotonic and cyclic displacement accumulation evinced qualitative accordance in many respects. Most apparent was the agreement concerning the effect of the suction bucket geometry, which is evident from the comparison of the distribution of contour lines in Figure 4.26 (c) and (d) with the ones in Figure 4.24 (c) and (d). Furthermore, the increase of load magnitude from $2F_{\mathrm{dr}}$ to $4F_{\mathrm{dr}}$ led to approximately ten times higher displacement rates for both monotonic and cyclic loading. Consequently, these results indicated a certain similarity of the monotonic and cyclic response for distinct load magnitudes.
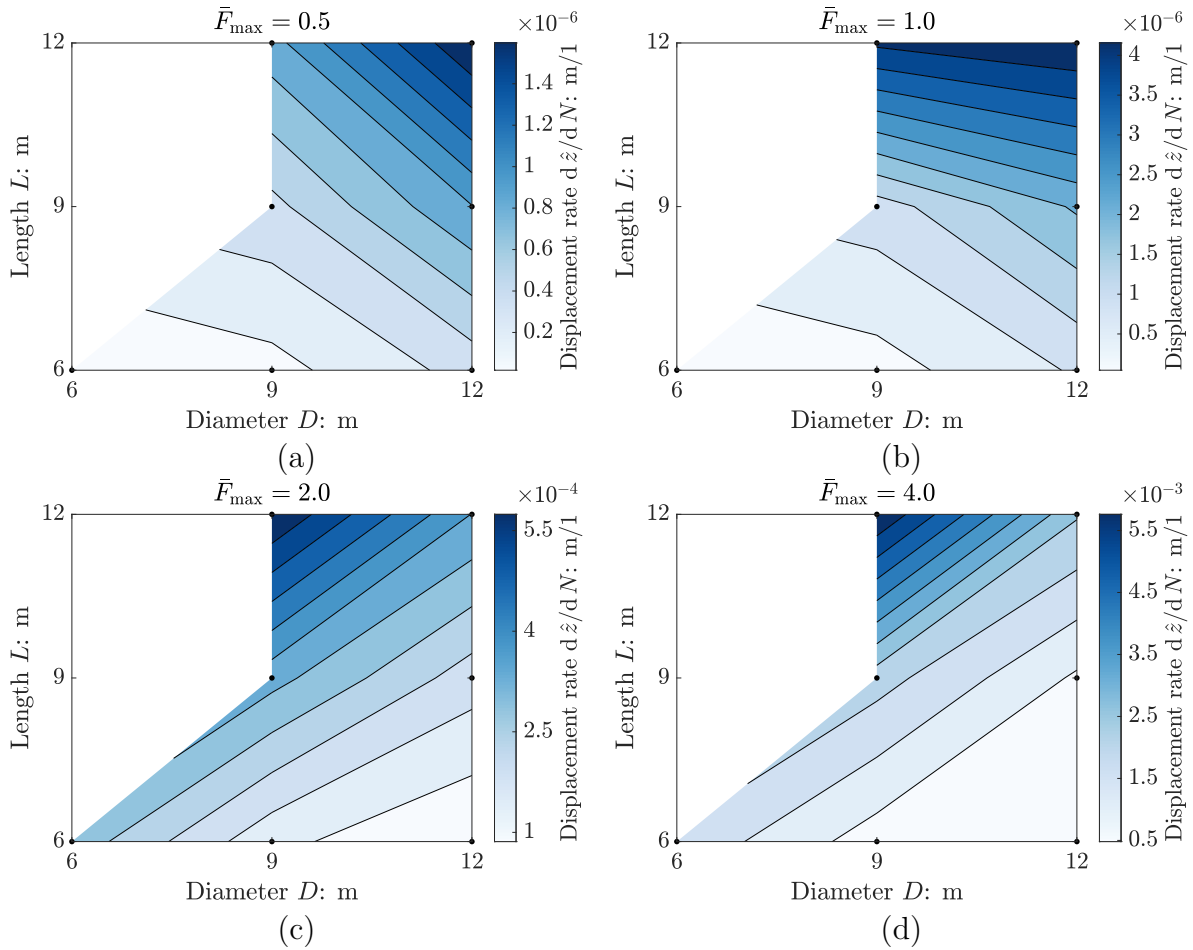
Figure 4.26: Displacement rates induced by cyclic loading with complete unloading in each cycle ($\bar{F}_\text{mean} = \bar{F}_\text{ampl}$) and period $T = 6\,\text{s}$ in dependence of suction bucket geometry and cyclic load magnitude with $\bar{F}_\text{max} = 0.5$ (a), $\bar{F}_\text{max} = 1.0$ (b), $\bar{F}_\text{max} = 2.0$ (c) and $\bar{F}_\text{max} = 4.0$ (d).

The tendency of increasing displacement accumulation for higher aspect ratios is presented in Figure 4.27 (a). Beside the larger displacement accumulation, the aspect ratio further affected the displacement amplitude in each cycle. The higher displacement accumulation rates for increasing aspect ratios stem from less dissipation of pore pressure because of longer drainage paths, which was manifested by greater suction forces (see Figure 4.27 (b)). Consequently, the share of frictional resistance was lower (see Figure 4.27 (c) and (d)). Generally, loads resisted by suction force require larger displacements in comparison to the mobilisation of frictional resistance. Hence, the different load sharing for various aspect ratios justified more displacement accumulation for higher aspect ratios. Moreover, the persisting suction force for $L/D = 1.33$ when unloading to $\bar{F}_\text{min} = 0$ led to more pronounced downward displacement in each cycle. The resulting relative displacement between the skirt's outside and the soil facilitated the generation of upward outer friction to counteract the downward displacement and provide equilibrium of the forces acting on the suction bucket (see negative sign in Figure 4.27 (c)). In contrast, the variation of frictional resistance per cycle was less pronounced and positive differential
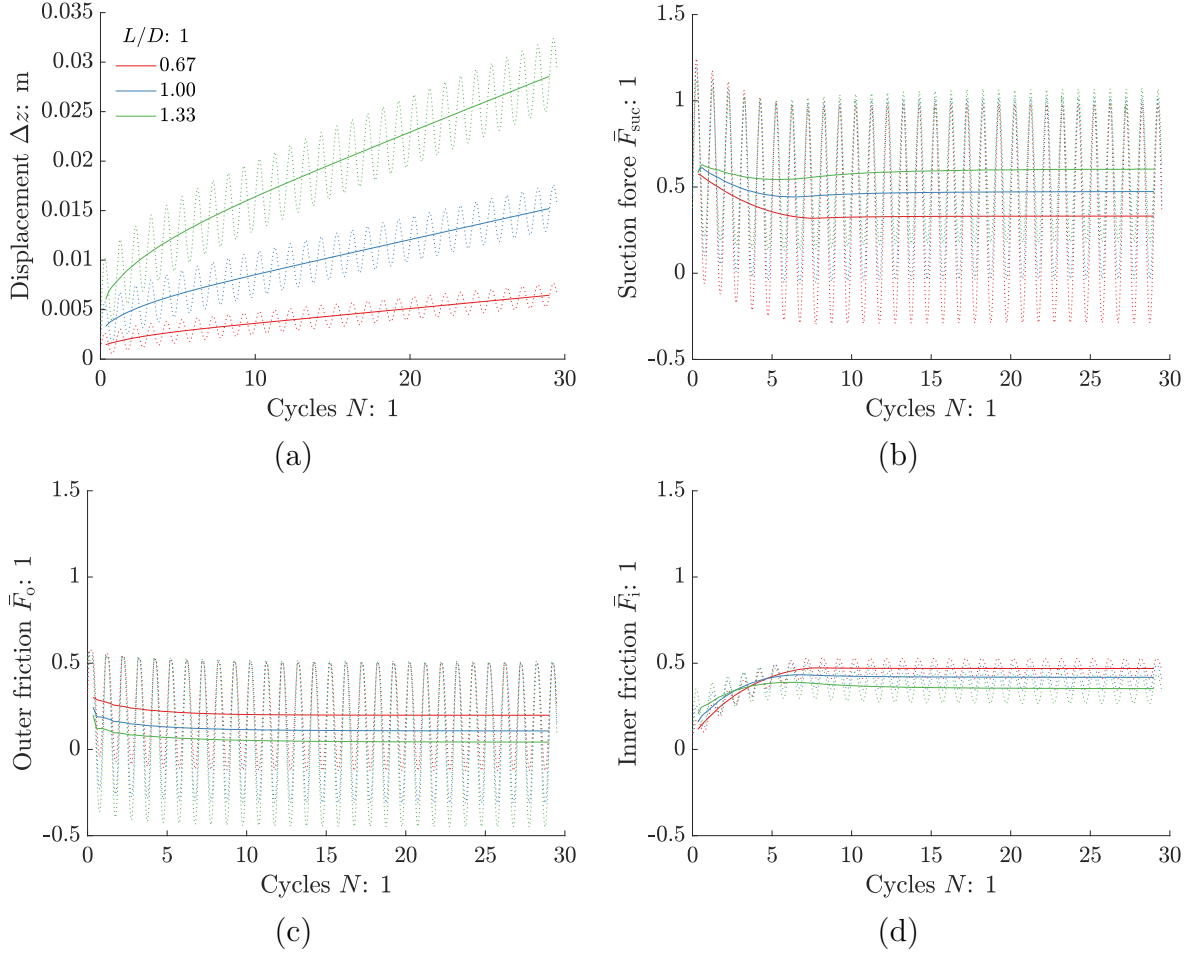
Figure 4.27: Response to cyclic loading with complete unloading in each cycle ($\bar{F}_{\mathrm{mean}} = \bar{F}_{\mathrm{ampl}} = 1$) and period $T = 6\,\mathrm{s}$ for $D = 9\,\mathrm{m}$ and different aspect ratios with displacement accumulation (a), suction force (b), outer friction (c) and inner friction (d).

pressure arose for $L/D \leq 1$, when the suction bucket was unloaded to $\bar{F}_{\mathrm{min}} = 0$, and hence proved that significantly more drainage was enabled for lower aspect ratios.

So far, the presented cyclic results of the parametric study referred to complete unloading in each cycle and were analysed concerning variations of suction bucket geometries, load magnitudes and periods. In order to provide a holistic examination, the effect of the load configuration with respect to both mean load and load amplitude shall be evaluated. Therefore, a particular reference case was introduced with $L = D = 9\,\mathrm{m}$ and $T = 6\,\mathrm{s}$ for which the displacement accumulation was depicted considering different load configurations (see Figure 4.28 (a) left with grey shaded background).

The aforementioned reference case exhibited most crucial increase of displacement rate with increasing maximum load and $\bar{F}_{\mathrm{mean}} = \bar{F}_{\mathrm{ampl}}$. Beside that, the displacement accumulation was mainly affected by the mean load for $\bar{F}_{\mathrm{ampl}} \leq 1$. In contrast, for $\bar{F}_{\mathrm{ampl}} > 1$, it appeared that the load amplitude gained prominence. However, the limited number of simulations must be noted leading to restricted validity of the contour. Nonetheless, it is
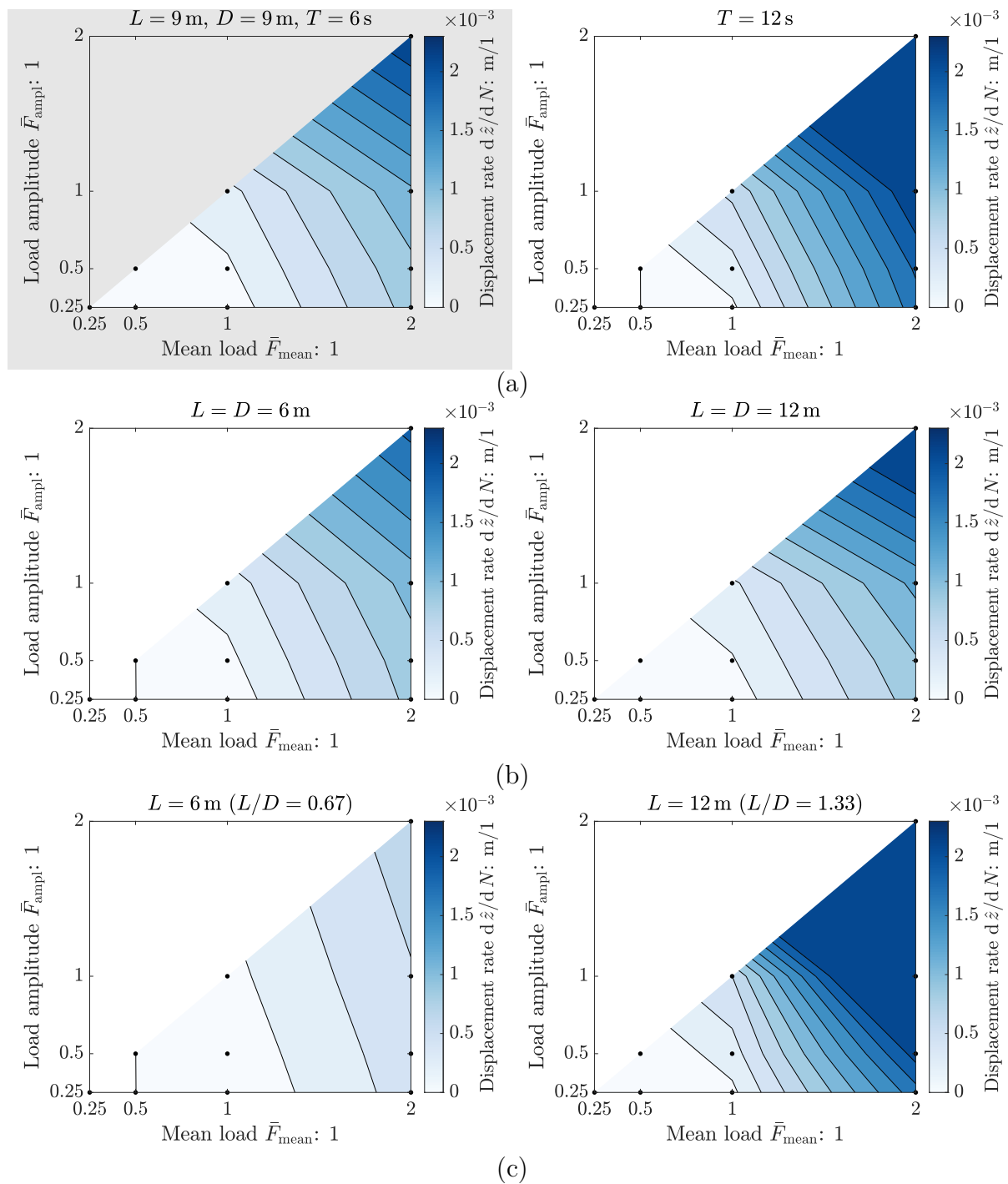
Figure 4.28: Effect of mean load and load amplitude on displacement rates with respect to period (a), suction bucket's size (b) and suction bucket's aspect ratio (c).

evident that the largest load magnitude evoked the highest displacement rate. Negligible displacement accumulation was found for $\bar{F}_{\max} \leq 1$, but even if the maximum load slightly exceeded the drained resistance for $\bar{F}_{\mathrm{mean}} = 1$ and $\bar{F}_{\mathrm{ampl}} \leq 0.5$, the induced displacement accumulations were marginal.

Certain parameters of the reference case were varied and analysed individually. The scale of the contours was set to the one of the reference case to facilitate visual comparisons. Firstly, the period was changed to $T = 12\,\mathrm{s}$ (see Figure 4.28 (a) right). As a consequence, the displacement rates increased for almost all load configurations, but the qualitative influence of both mean load and load amplitude did not change essentially. These findings were in accordance with Figure 4.25, where higher displacement accumulations were observed for longer periods. Remarkably, the displacement rates for maximum loads less or equal to the drained resistance were lower for the longer period, which resulted from more drainage enabling a higher share of the load to be resisted by the frictional resistance. Therefore, Figure 4.28 (a) generalises the previously discussed results with respect to the period for cyclic tensile swell loads exceeding the drained resistance.

The effect of the suction bucket's size was evaluated by comparing the reference case with Figure 4.28 (b), where the length and diameter were either reduced to $L = D = 6\,\mathrm{m}$ or enlarged to $L = D = 12\,\mathrm{m}$. The smaller suction bucket generally evinced lower displacement rates than the reference case, whose displacement rates were exceeded by the larger suction bucket. Similarly to the effect of the longer period, the reduced size of the suction bucket facilitated drainage so that the displacement rates for $\bar{F}_{\max} \leq 1$ were lower than those of the reference case. Beside the tendency of higher displacement rates for larger suction buckets, the influence of the mean load on the displacement accumulation was more pronounced as well.

Finally, the variation of the aspect ratio, while keeping the suction bucket's diameter to a constant value, was examined by Figure 4.28 (c). With regard to the previously discussed parameters, the variation of the aspect ratio evinced the most distinct effect on the displacement rate. A decrease of the suction bucket's length substantially enhanced drainage, which facilitated the frictional resistance, and thus led to considerably lower displacement rates. Opposed to that, the displacement rates were significantly higher for longer suction bucket's skirts, where the drainage was limited as pointed out in Figure 4.27.

4.3.6 Transient force

It was shown that persistent cyclic loading induced displacement accumulation, especially for load magnitudes exceeding the drained resistance. Since the self weight of the OWT usually invokes compressive mean loads and tensile loads might only occur as single events, the investigation of singular transient loads as schematically defined in Figure 4.29 is relevant. For this purpose, the FE model was utilised for simulating sinusoidal swell loads with different magnitudes $0.25 \leq \bar{F}_{\max} \leq 4.00$ and periods $T \in [6, 12]\,\mathrm{s}$ for a suction bucket with $L = D = 9\,\mathrm{m}$ in very dense sand. The results are depicted in terms of the displacement Δz (see Figure 4.30 (a)) and suction force divided by the load magnitude
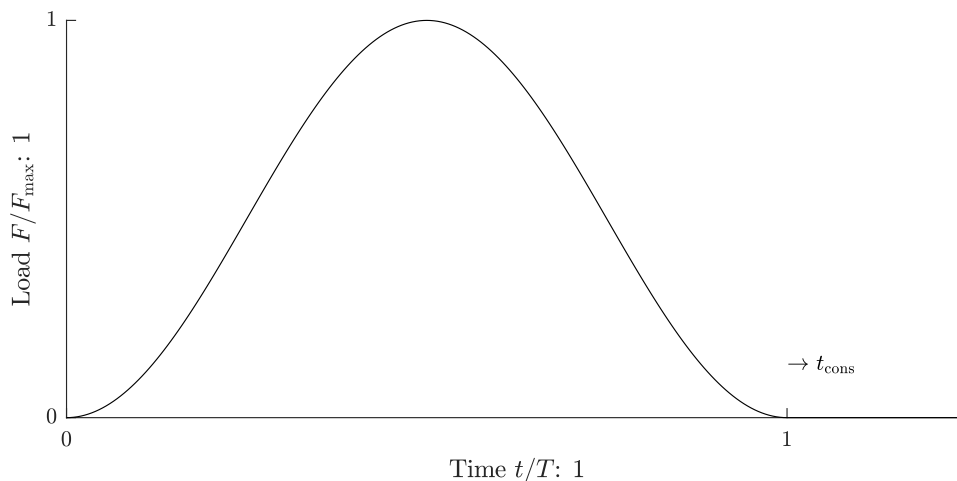
Figure 4.29: Schematic illustration of the transient load.

$\bar{F}_{\mathrm{suc}}/\bar{F}_{\mathrm{max}}$ (see Figure 4.30 (b)). Furthermore, Figure 4.30 separates the presentation of the results in two phases, namely loading on the left with time divided by period t/T and subsequent consolidation on the right with time t_{cons} in logarithmic scale.

With respect to the suction bucket's displacement, the results confirmed the previous findings in terms of the significance of the applied load magnitude (see Figure 4.30 (a)). While there was minor displacement for the lowest load magnitude during the load application ($\Delta z \approx 0.6\,\mathrm{mm}$ at the moment of the highest load $t/T = 0.5$), the displacement reached about $18\,\mathrm{mm}$ for a load magnitude $\bar{F}_{\mathrm{max}} = 4$ and $T = 12\,\mathrm{s}$. In case of $\bar{F}_{\mathrm{max}} = 4$ and $T = 6\,\mathrm{s}$, the displacement was slightly lower with $\Delta z(t/T = 0.5) \approx 15\,\mathrm{mm}$. During loading phase, the displacement was approximately proportional to the applied load magnitude for $\bar{F}_{\mathrm{max}} \leq 1$. For loads exceeding the drained resistance, the invoked displacement increased over-proportionally, which was attributed to the higher displacement that was required to mobilise sufficient suction force. Consequently, more plastic deflection took place in the soil-structure interface at the suction bucket's skirt. As the load diminished ($t/T > 0.5$), the displacement reversed in any of the simulations. During this phase, the effect of the period became distinct, as the shorter period exhibited a more pronounced displacement reduction. After completion of the singular load event, the displacements were in the range of $0.05\,\mathrm{mm}$ and $0.07\,\mathrm{mm}$ for the lowest load magnitudes, but the highest load magnitudes invoked displacements of more than $7\,\mathrm{mm}$.

The singular load was followed by consolidation, which allowed for the dissipation of negative differential pressure accompanied by displacement of the suction bucket. The consolidation was assumed to be finished when changes in pore pressure in the entire model were less than $10^{-6}\,\mathrm{kPa}$. For $\bar{F}_{\mathrm{max}} \leq 1.5$, relevant settlement occurred and the residual displacement for loads less or equal to the drained resistance could be treated as negligible with $\Delta z < 0.005\,\mathrm{mm}$. The residual displacements due to loads as high as the drained resistance were $0.03\,\mathrm{mm}$ and $0.04\,\mathrm{mm}$ for $T = 6\,\mathrm{s}$ and $T = 12\,\mathrm{s}$ respectively. The potential SLS criteria of $\Delta z/D = 0.009$ or $\Delta z/D = 0.013$ indicate the subordinate relevance of these residual displacements. Loads exceeding the drained resistance by
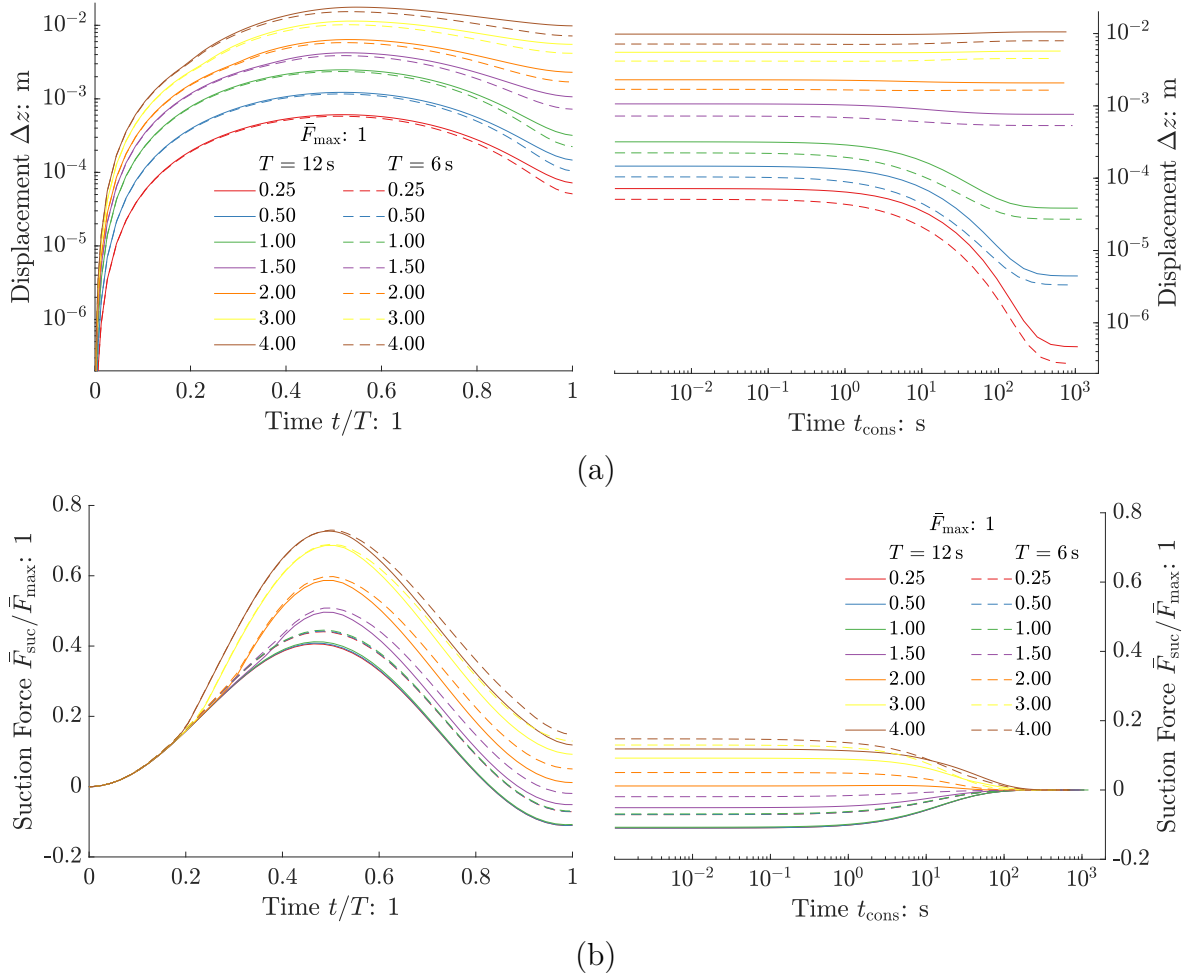
Figure 4.30: Response to transient loads for $L = D = 9\,\text{m}$ with different magnitudes and periods concerning displacement (a) and suction force (b).

the threefold or more exhibited additional upward displacements during consolidation invoking residual displacements of more than $10\,\text{mm}$. As expected, the effect of longer periods causing higher displacement did not diminish during consolidation.

The negative differential pressure was obviously higher for larger load magnitudes, since the applied load could not be resisted by the inner and outer friction (see Figure 4.30 (b)). As long as the load was lower than or equal to the drained resistance, the negative differential pressure was approximately proportional to the applied load. It has to be remarked that even the lowest load amplitude induced certain negative differential pressure (about $3\,\text{kPa}$ at the most for $t/T = 0.5$, which corresponded to $\bar{F}_\text{suc}/\bar{F}_\text{max} \approx 0.4$) so that it could not be treated as drained. This observation essentially confirmed the practical relevance of partially drained conditions. For higher load magnitudes, the frictional resistance was exceeded at an earlier state (smaller t/T) requiring higher negative differential pressure to be developed. The highest load magnitude induced a negative differential pressure of about $\Delta u \approx 165\,\text{kPa}$, which corresponded to $\bar{F}_\text{suc}/\bar{F}_\text{max} \approx 0.73$, at the most. The reduction of the load after reaching its maximum value went along with diminishing

135

negative differential pressure. Interestingly, a positive differential pressure developed for $\bar{F}_{\max} \leq 1.5$ due to the presence of downwards acting frictional resistances along the skirt, which needed a counteracting force for reaching equilibrium of the forces on the suction bucket. During consolidation, differential pressures dissipated analogously to the vertical displacement. The higher the absolute differential pressure after complete unloading was, the longer was the time required for substantial reduction of the differential pressure.

The analysis of the suction bucket's response to singular loads is essential for a cautious design of an OWT, where only particular events might evoke tensile loads on the suction bucket. Thus, it is crucial to evaluate if these individual load events might provoke substantial displacement. Moreover in order to prevent accumulation of pore pressure in the soil, the time required for a certain degree of dissipation has to be accounted for as well. The presented results indicate that singular loads up to or slightly above the drained resistance might be applicable, but their recurrence must not be in a too short period of time to provide sufficient duration for drainage. As long as SLS criteria would not be breached, the OWT could also be subjected to a much larger load, but this should only occur once in its lifetime.

4.3.7 Equivalent force

The simulation of cyclic loading is complex and in implicit formulations, each load cycle has to be divided into sufficiently small time increments to accurately represent the suction bucket's response. In order to simplify the simulation and save computational time, a methodology was sought that resulted in the same accumulated displacement as the original cyclic load had invoked. The proposed approach was based on the findings of the results of the parametric study in subsection 4.3.5 and subsection 3.6.2, where the displacement accumulations of cyclic model tests were analysed and compared with those of monotonic model tests having similar mean loads. Hence, it was assumed that exclusively loads exceeding the drained resistance contribute essentially to the displacement accumulation so that an equivalent load F_{eq} was defined as illustrated in Figure 4.31.

In particular, the cyclic load was subdivided in $\bar{F} < 1$ or $\bar{F} \geq 1$, whereby the first mentioned was discarded and the latter was regarded for determining the equivalent load ($\bar{F} \geq 1$ marked with point symbols in Figure 4.31). The loads were sorted in ascending order and the corresponding time increments for distinct load magnitudes were totalled. The initial load application was identical to the preloading of the cyclic load until the drained resistance was reached and subsequently, the equivalent load was applied. For several reasons, this methodology allowed solely for reasonable examination of the final displacement, but not for the comparison of the development of certain quantity over the load duration.

The equivalent loads were determined for every cyclic load configuration of the parametric study exceeding the drained resistance, i.e. $\bar{F}_{\max} \geq 1$. The results are summarised in Figure 4.32. The final cyclic displacement Δz_{cyc} after $N = 29.5$ was taken as reference value and compared to the displacement induced by the equivalent load Δz_{eq}. Thus, the
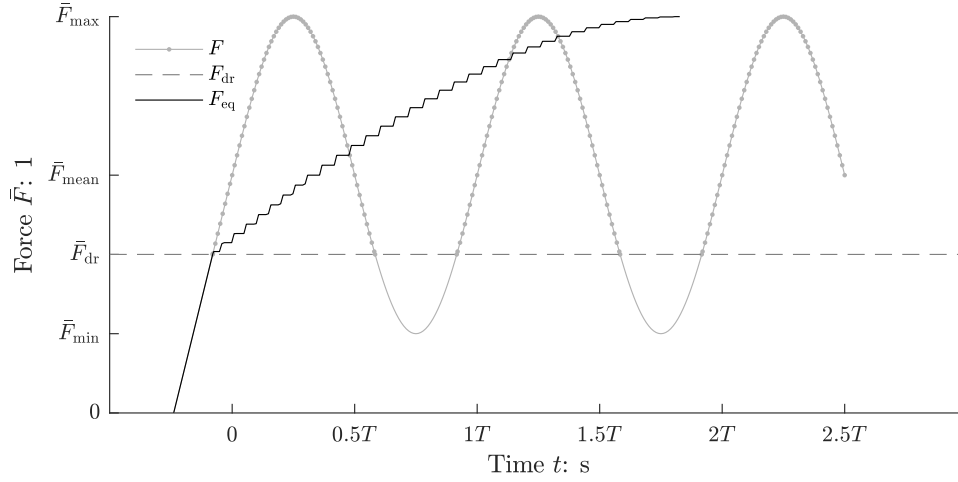
Figure 4.31: Schematic illustration of the cyclic equivalent load.
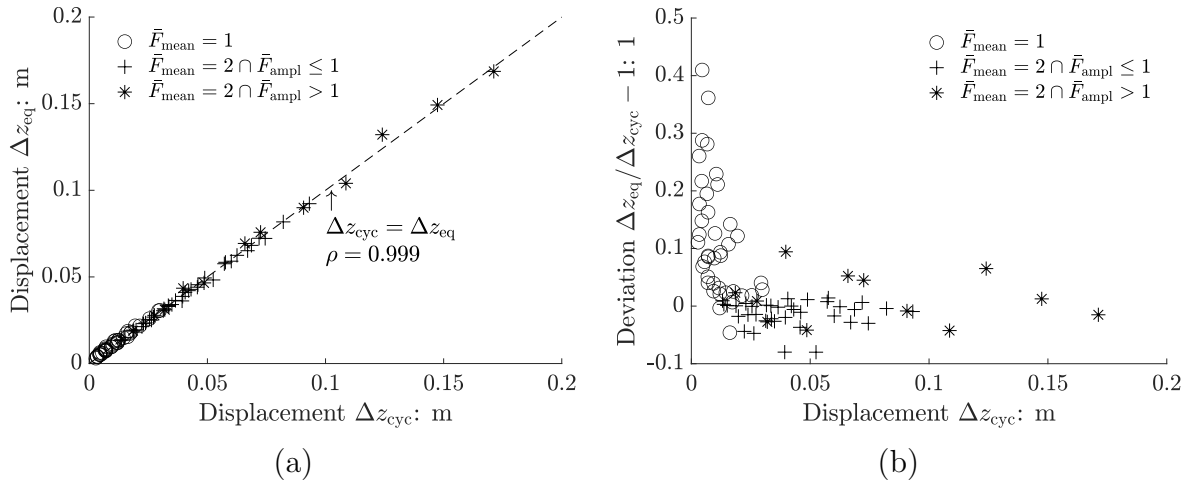
Figure 4.32: Comparison of displacement induced either by cyclic or equivalent load (a) and corresponding deviation (b).

dashed line in Figure 4.32 (a) represents the targetted cyclic displacements, which were well approximated by the equivalent loads. Different markers were adopted to highlight the effect of the load configuration on the accumulated displacement. In particular, the cyclic loads $\bar{F}_{\text{mean}} = 1$ comprised unloading below the drained resistance, i.e. $\bar{F}_{\text{min}} < 1$. The same applies for $\bar{F}_{\text{mean}} = 2 \cap \bar{F}_{\text{ampl}} > 1$, but the maximum loads were higher than for $\bar{F}_{\text{mean}} = 2 \cap \bar{F}_{\text{ampl}} \leq 1$, where the tensile loads exceeded the drained resistance during the entire load cycle, i.e. $\bar{F}_{\text{min}} \geq 1$. This classification manifests that the maximum load is the predominant parameter concerning the displacement accumulation.

While it is evident from Figure 4.32 (a) that the equivalent load attains good estimation of the absolute displacement accumulation, Figure 4.32 (b) reveals noticeable relative deviations, whereby the cyclic displacement was adopted as reference value. Therefore, the displacements of the lower load magnitudes, especially those that fell below the drained resistances, tended to be overestimated by the equivalent loads. The reason for that was

the downward movement of the suction bucket in each cycle, when the suction bucket was unloaded, which was not considered in the present approach for loads below the drained resistance. However, it is essential to remark that although the relative deviations appear to be high, the absolute deviations were rather insignificant (see Figure 4.32 (a)). Further, the relative deviations became lower for larger load magnitudes and corresponding higher displacements.

The methodology of an equivalent load facilitates the assessment of cyclic displacement accumulation and the obtained agreement demonstrated its applicability. The actual deviations were in an acceptable range for the particular degree of simplification. It should be noted that the utilised soil's mechanical constitutive law is not able to represent the drained cyclic soil mechanic response, which might have supported the attained accordance. Potentially, a further developed constitutive law would result in a slightly different cyclic displacement accumulation while the displacement predicted by the equivalent load would remain similarly resulting in larger deviations. However, reasonable accordance was achieved and the discussion on the constitutive law shall be of indicative character.

4.4 Summary

The model tests presented in chapter 3 provided essential insights into the suction bucket's complex bearing behaviour, but were not directly transferable to the response of suction buckets in-situ. Therefore, the suction bucket's response was numerically simulated at prototype scale. Hence, a sophisticated FE model was established and retrospective analyses of the physical model tests verified and validated the numerical model with respect to load conditions, drainage and geometric scale. The FE model was found to overestimate the frictional resistance by trend, which implied an underestimation of negative differential pressure or displacement accumulation in dependence of the load condition. However, potential reasons were identified and empirical calibration was provided. The validation further comprised the consideration of theoretical methods and the scaleability of the load frequency, where relevant effects of both geometric scale and load configuration were identified. As a result, approximately scaled load frequencies in model tests were successfully transferred to prototype dimensions.

The validated FE model was utilised for a comprehensive parametric study, which comprised monotonic, cyclic and transient loads. The results of the simulations with constant displacement rates enabled extensive evaluation of load sharing, drainage condition, stiffness and plug heave. The tensile resistance was substantially enhanced by increasing displacement rates, but the suction bucket necessitated larger displacements to generate the appropriate resistances of which the suction force provided the main proportion. Further, the inner and outer friction depended significantly on the drainage condition. Higher tensile resistances were reached for higher relative density of the soil, which was mainly due to larger suction forces. The secant stiffness decreased with increasing load, but was considerably greater the less drainage took place. Furthermore, higher displacement rates

138

implied larger negative differential pressures at the suction bucket's skirt and invoked more plug heave, which both depended on the suction bucket's displacement.

The force-controlled monotonic response of the suction bucket was analysed with respect to displacement accumulation in dependence of the suction bucket's geometry and load magnitude. While loads less than the drained resistance invoked negligible displacement accumulations, there were minor but still certain displacement accumulations for loads as high as the drained resistance. If the applied load exceeded the drained resistance, the crucial displacement accumulation became significantly higher for larger aspect ratios and the evoked suction force increased over-proportionally.

The investigation of the suction bucket's cyclic bearing behaviour accounted for numerous load configurations. Larger load magnitudes caused more displacement accumulation along with higher suction forces. Qualitative similarity was found between the monotonic and cyclic displacement accumulation with respect to the load magnitude and suction bucket's geometry. Cyclic loads less than the drained resistance were of subordinate relevance for the displacement accumulation. The effect of the load configuration and its interrelation to further parameters was evaluated concerning the displacement accumulation. The maximum load was most prominent, which confirmed the observations of the model tests. Moreover, an increase of the period, suction bucket dimension or aspect ratio caused higher displacement accumulation, whereby the last mentioned aspect was found to have the most distinct effect within the extent of the parametric study.

Two more load conditions were considered additionally, namely transient loading by a singular load and incrementally monotonic loading. The singular load shall represent a more realistic load event, since the occurrence of many consecutive tensile load cycles is rather unlikely. Singular loads might even exceed the drained resistance without causing significant residual displacements, but sufficient time must be provided to allow for dissipation. If the loads occur only once during the lifetime of an OWT, the loads could be even substantially larger than the drained resistance as long as certain displacement of the suction bucket is acceptable. Finally, a methodology was proposed to simplify the time series of a cyclic load to incrementally monotonic loads, which induce equivalent final displacement. The approach solely accounted for loads above the drained resistance and their corresponding duration. The comparison of the final displacements provided appropriate results.

The suction bucket's tensile bearing behaviour was evaluated holistically by means of numerical simulations with a validated FE model. Detailed insights into the interaction of monotonic tensile resistances and stiffnesses with drainage were provided. The monotonic and cyclic displacement accumulations were analysed and decisive parameters were identified. Additional load conditions, which accounted for realistic singular load events or reasonably simplified the cyclic displacement accumulation, supplemented the investigations. Particularly the equivalent load methodology is crucial for effective analyses, which could be potentially conducted by analytical approaches.

5 Analytical method

5.1 Model set-up

5.1.1 Requirements

So far, the design of suction bucket foundations is based on physical model tests and finite element (FE) simulations, whose realisations are intricate and expensive. Sophisticated analytical methods would facilitate the design process by providing an initial estimate of the suction bucket's tensile bearing behaviour. However, none of the analytical methods available is generally accepted until now and most of the methods suffer from uncertainties or inaccuracies. The methods of Deng and Carter (2002) and Iskander et al. (2002) only account for either drained or undrained condition and oversimplify the complex bearing behaviour so that the predicted tensile resistance is not precise. The method of Houlsby et al. (2005b) distinguishes four different cases of partially drained responses and provides reasonable results for the tensile resistance. Nonetheless, the design of suction bucket foundations is more likely to depend on its displacement in terms of serviceability limit state (SLS) than on the maximum tensile resistance in ultimate limit state (ULS). Senders (2009) proposed a model, which shall be able to predict the actual bearing behaviour for different drainage conditions by appropriately mobilising the particular elements. However, the model was rarely used as it is assumed to be too complex and the original definition is not straightforward. Consequently, there is a need for an adequate model, which provides reasonable predictions for distinct loads and is easy to implement.

The complexity of the suction bucket's tensile response mainly results from the interaction of hydraulic and mechanical processes. Thus, the analytical model shall be able to simulate the distinct resistances individually, i.e. suction force and frictional resistances, and regard for their interrelations. The generation of these resistances depends essentially on the suction bucket's displacement and displacement rate, so that both quantities must be considered in the analytical model. In order to account for different drainage conditions, the model shall comprise the plug heave, which further affects the relative displacement in the interface at the skirt's inside. Moreover, the effect of the differential pressure on the frictional resistance could be regarded optionally.
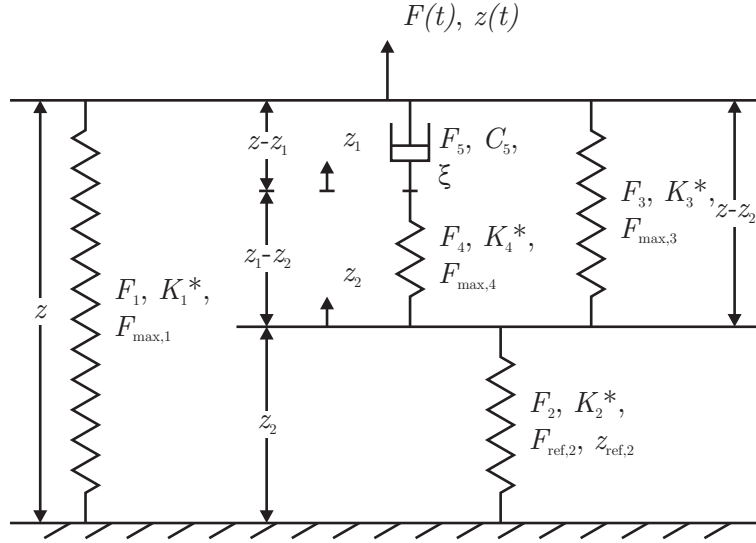
Figure 5.1: Definition of the elements and displacements of the analytical model.

Table 5.1: Denotations and dependencies of the elements of the analytical model.

Resistance	Symbol	Dependency	Symbol
Outer friction	$F_1 = F_{\mathrm{o}}$	Displacement	z
Reverse end bearing	$F_2 = F_{\mathrm{suc}} + F_{\mathrm{i}}$	Plug heave	$z_2 = z_{\mathrm{plug}}$
Inner friction	$F_3 = F_{\mathrm{i}}$	Gap height	$z - z_2 = z_{\mathrm{gap}}$
Suction force	$F_4 = F_{\mathrm{suc}}$	Water expansion	$z_1 - z_2$
Suction force	$F_5 = F_{\mathrm{suc}}$	Seepage	$z - z_1$

5.1.2 Description and formulation

The method of Senders (2009) incorporates most of the aforementioned criteria. However, it suffers from inconsistent description and formulation. In order to establish a further developed model, the layout as depicted in Figure 2.12 was adopted and a new solution scheme was proposed, which accounts for certain advancements. The analytical model distinguishes five different elements counteracting the applied load. The arrangement of these elements is presented in Figure 5.1, which utilises the numbering as proposed by Senders (2009). In particular, the elements are denoted as summarised in Table 5.1. A simple implementation of the model and a procedure for calibrating its elements were derived. In contrast to the original model of Senders (2009), no sliders were considered, but non-linear spring and damper characteristics were formulated. Figure 5.2 provides an overview on these particular functions, which are defined in detail in section 5.2.

Both frictional resistances are idealised with springs, which is appropriate for simulating the skin friction of axially loaded embedded structures. The reverse end bearing (REB) is represented by a spring, which allows for the plug heave to take place and therefore enables different relative displacements at the skirt's soil-structure interfaces outside and inside the suction bucket. Moreover, an essential feature of the REB is provided by its
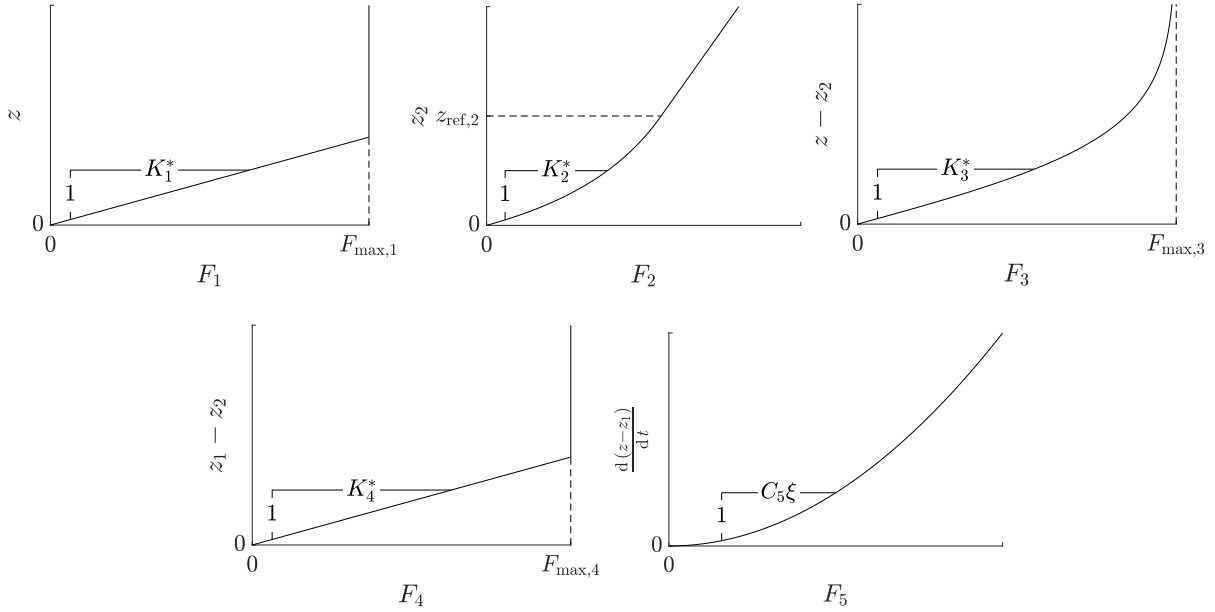
Figure 5.2: Schematic illustration of the elements' functions of the analytical model.

interrelation with the damper allowing for the simulation of different drainage conditions. Because of the arrangement in series, the force of the REB is limited by the sum of inner friction and suction force. The development of the suction force is related to the gap expansion $z_1 - z_2$ and gap expansion rate $\frac{\mathrm{d}z - z_1}{\mathrm{d}t}$, which result from the water expansion beneath the suction bucket's lid (spring) and from the pore water seepage flow (damper) respectively. The model's elements require calibration of their individual parameters, which are briefly summarised and idealised in Figure 5.2. The initial stiffnesses of the springs are defined by $K^*_{1...4}$ and the frictional resistances as well as the suction force were limited by certain maximum forces $F_{\mathrm{max},1}$, $F_{\mathrm{max},3}$ and $F_{\mathrm{max},4}$. To describe the non-linear characteristic of the spring representing the REB, additional parameters are required, namely $F_{\mathrm{ref},2}$ and $z_{\mathrm{ref},2}$. The behaviour of the damper is characterised by a coefficient C_5 and exponent ξ.

Under drained condition, minor plug heave occurs, which implies insignificant gap expansion rate along with negligible suction force. Consequently, the suction bucket's resistance is mobilised only by the outer and inner friction. Under undrained condition, the damper reacts very stiff so that almost no gap expansion takes place. As a result, substantial suction force but minor inner friction is generated. Therefore, the REB is activated, which provides the suction bucket's tensile resistance in conjunction with the outer friction. Loads invoking partially drained conditions evolve an appropriate mobilisation of distinct elements of the model depending on the degree of drainage. Hence, the arrangement of the elements intrinsically enable the simulation of different drainage conditions.

The analytical model depicted in Figure 5.1 can be solved either for arbitrary time-dependent displacement or force. Five equations were introduced to calculate the appropriate forces of each of the five elements (see section 5.2). Three additional equations account for the equilibrium between the elements as these are arranged in parallel or in

series. In total, eight equations are to be solved in order to determine the eight unknown quantities. Owing to the characteristics of the model regarding its dependency on both displacement and time, the loading $z(t)$ or $F(t)$ has to be discretised in constant time steps Δt and applied incrementally to the model. Equation 5.1 provides the equation system to be solved concerning displacement-controlled loading $z(t)$ and Equation 5.2 defines the model for force-controlled loading $F(t)$.

$$
\begin{bmatrix}
1 & & & & & & & \\
 & 1 & & & & & & -K_2 \\
 & & 1 & & & & & K_3 \\
 & & & 1 & & & -K_4 & K_4 \\
 & & & & 1 & & C_5\frac{1}{\Delta t} & \\
1 & 1 & & 1 & -1 & & & \\
 & 1 & -1 & -1 & & & & \\
 & & 1 & -1 & & & &
\end{bmatrix}
\begin{bmatrix}
\Delta F_1 \\
\Delta F_2 \\
\Delta F_3 \\
\Delta F_4 \\
\Delta F_5 \\
\Delta F \\
\Delta z_1 \\
\Delta z_2
\end{bmatrix}
=
\begin{bmatrix}
K_1\Delta z \\
0 \\
K_3\Delta z \\
0 \\
C_5\frac{\Delta z}{\Delta t} - F_{5,t-\Delta t} \\
0 \\
0 \\
0
\end{bmatrix}
\tag{5.1}
$$

$$
\begin{bmatrix}
1 & & & & & -K_1 & & \\
 & 1 & & & & & & -K_2 \\
 & & 1 & & & -K_3 & & K_3 \\
 & & & 1 & & & -K_4 & K_4 \\
 & & & & 1 & -C_5\frac{1}{\Delta t} & C_5\frac{1}{\Delta t} & \\
1 & 1 & & 1 & & & & \\
 & 1 & -1 & -1 & & & & \\
 & & 1 & -1 & & & &
\end{bmatrix}
\begin{bmatrix}
\Delta F_1 \\
\Delta F_2 \\
\Delta F_3 \\
\Delta F_4 \\
\Delta F_5 \\
\Delta z \\
\Delta z_1 \\
\Delta z_2
\end{bmatrix}
=
\begin{bmatrix}
0 \\
0 \\
0 \\
0 \\
-F_{5,t-\Delta t} \\
\Delta F \\
0 \\
0
\end{bmatrix}
\tag{5.2}
$$

The incremental solution procedure relies on the individual elements' tangent stiffnesses $K_{1...4}$. Hence, the equation system is solved for a particular time increment, but the results usually exhibit certain deviations to the exact solution within this first iteration. Based on the obtained solution, the elements' stiffnesses are changed with regard to their actual residual referring to the target value. Subsequently, the equation system is updated with the appropriate values and solved again. This convergence algorithm is iterated until a sufficiently accurate approximation of the exact solution of each element is achieved. The result for the finished load increment is stored and the system is solved for the next time increment. This procedure is repeated until the defined load is completely applied.

In order to achieve a convergent and accurate solution, the implemented procedure necessitates the definition of a certain time step, a tolerance criterion and a maximum number of iterations. The size of the time step depends on the actual load to be applied. However, the division of the load in few thousand increments is feasible without substantial computational costs. With regard to the tolerance criterion, mostly a precision of 10^{-5} is attainable but certain combinations of input parameters require the reduction to a less strict value of for instance 10^{-2}. The maximum number of iterations should be limited to a practical value to prohibit excessive computation effort but allow for convergence of the solution. Up to ten thousand iterations per increment do not crucially increase the calculation duration. It is evident that these parameters are interrelated, e.g. a shorter time step and a less strict tolerance criterion imply less iterations per increment to be

solved. The entire model was implemented and solved in commercial MATLAB software (Mathworks, 2019).

5.2 Calibration

5.2.1 Overview

In contrast to semi-empirical relations proposed by Senders (2009), the suggested calibration procedure relies on results of FE simulations and theoretical considerations. Therefore, numerous FE analyses were conducted considering appropriate conditions for the calibration of the specific elements, i.e. variation of displacement rate, bulk modulus of the pore fluid and coefficient of friction at the skirt's soil-structure interface. The calibration is described individually for every element and was conducted exemplarily for a particular reference case with $L = D = 9\,\mathrm{m}$ in very dense sand (soil properties refer to subsection 4.1.5). The elements' responses were described by simple equations, which could be easily alternated to arbitrary modified relationships.

Although the presented calibration methodology is straightforward and applicable to any desired boundary conditions, the validity of the attained parameters is limited to the particular case these were determined for. As a consequence, modifications of the suction bucket geometry or the soil properties require recalibration of the elements' parameters, which implies an essential detriment of the analytical model.

5.2.2 Outer friction

The outer friction is idealised by element 1, whose mobilisation depends on the suction bucket's displacement z. Since the outer friction is not arranged in series with any other element, there is no interaction with those. Hence, the outer friction is not affected by the actual drainage condition. Consequently, the outer friction was calibrated for the drained condition ($v_z = 10^{-12}\,\mathrm{m/s}$).

Figure 5.3 illustrates the mobilisation of the outer friction in dependence of the suction bucket's displacement. According to the results of the FE simulation, the outer friction increased approximately linearly until a maximum resistance was reached. Subsequently, the outer friction reduced because of stress relief induced by the upward displacement of the suction bucket and finally remained almost constant. The proposed calibration simplifies the response to a bi-linear characteristic (see Equation 5.3). The initial increase of outer friction versus displacement defines the element's stiffness and the maximum force is set to the residual outer friction (see Figure 5.3). Thus, the slightly higher maximum outer friction is neglected, which is a conservative assumption. Obviously, the chosen formulation well approximates the outer friction under drained condition.
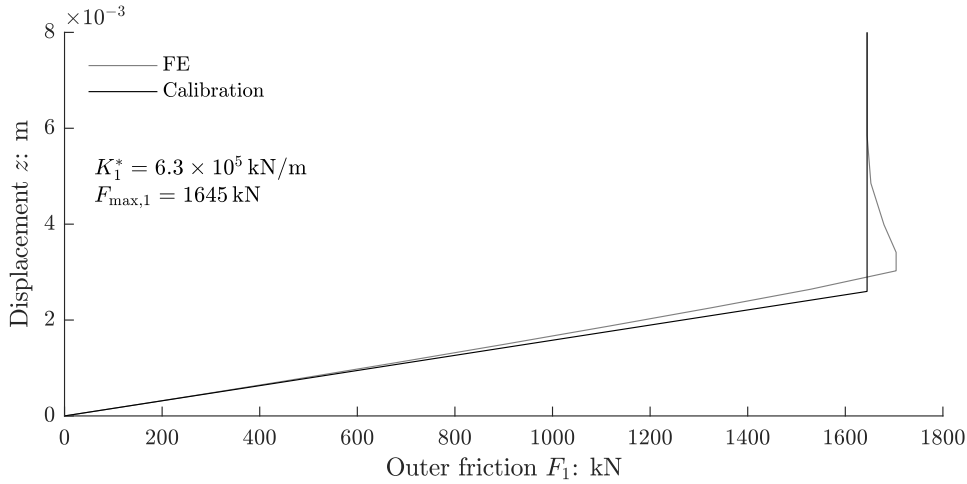
Figure 5.3: Exemplary calibration of outer friction for $L = D = 9\,\mathrm{m}$ in very dense sand.

$$F_1 = \begin{cases} K_1^* z & , \quad \text{if } z \leq F_{\mathrm{max},1}/K_1^* \\ F_{\mathrm{max},1} & , \quad \text{if } z > F_{\mathrm{max},1}/K_1^* \end{cases} \tag{5.3}$$

Under partially drained to undrained conditions, the hydraulic processes affect the soil's effective stresses, which have an influence on the outer friction. Consequently, the mathematical formulation of element 1 would have to account for hydraulic-mechanical coupling, which is not yet implemented in the model. However, the outer friction is generally enhanced due to constrained drainage so that it is more conservative to neglect this aspect.

5.2.3 Reverse end bearing

The REB describes the suction bucket's response under undrained conditions (see Figure 2.3). This mechanism is idealised by element 2 and its generation is connected to the plug heave z_2. Although the REB is partly mobilised under partially drained conditions, it becomes crucially more relevant the less drainage occurs because of magnifying suction force and plug heave, which both result from limited drainage. It follows that the REB has an insignificant effect on the drained response. In order to prohibit relevant contribution of the REB on the drained response, element 2 requires a relatively high stiffness. Consequently, the undrained condition marks the upper bound of the REB and thus was adopted for the calibration ($v_z = 10^0\,\mathrm{m/s}$).

In Figure 5.4, the REB is evaluated in dependence of the plug heave. After the significant increase of REB in the beginning, the gain in REB decreased steadily until an approximately constant rate of increase was reached. As a consequence, the calibration comprises two parts, i.e. the initial phase is approximated by a hyperbolic function followed by a linear function having the same gradient as the hyperbolic function at transition, i.e. $K_2(z_{\mathrm{ref},2})$ (see Equation 5.4). Hence, the proposed function is not limited by
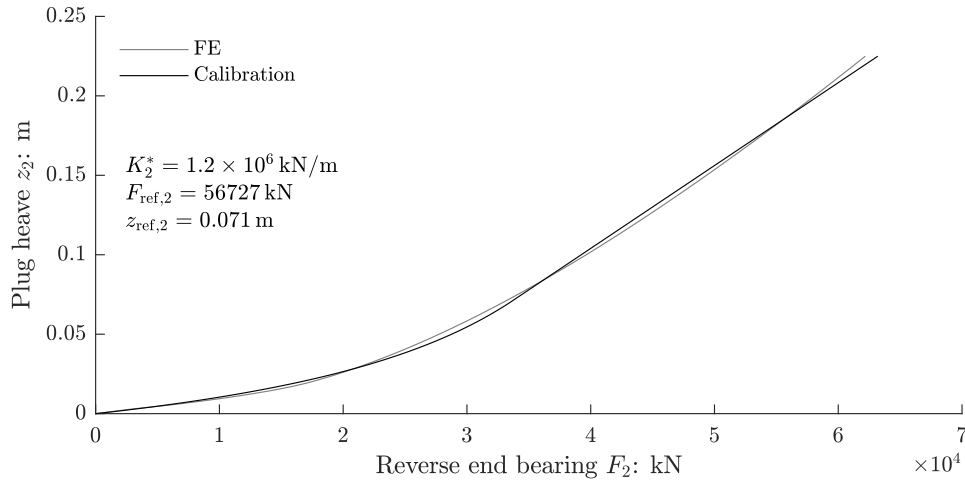
Figure 5.4: Exemplary calibration of reverse end bearing for $L = D = 9\,\mathrm{m}$ in very dense sand.

any maximum resistance, which is justified on the one hand by the results of the numerical simulations that did not indicate an upper bound. On the other hand, the REB is formed by the sum of suction force and inner friction, whose definitions regard for maximum forces (see subsection 5.2.4 and subsection 5.2.5). As pointed out in Figure 5.4, the utilised function provides a good estimation of the REB.

$$
F_2 = \begin{cases} \dfrac{z_2}{\frac{1}{K_2^*} + \frac{z_2}{F_{\mathrm{ref},2}}} & , \quad \text{if } z_2 \leq z_{\mathrm{ref},2} \\[2em] \dfrac{z_{\mathrm{ref},2}}{\frac{1}{K_2^*} + \frac{z_{\mathrm{ref},2}}{F_{\mathrm{ref},2}}} + K_2(z_{\mathrm{ref},2})(z_2 - z_{\mathrm{ref},2}) & , \quad \text{if } z_2 > z_{\mathrm{ref},2} \end{cases} \tag{5.4}
$$

It was found that even under drained to partially drained conditions, plug heave took place as a matter of the inner friction. The soil adjacent to the skirt's interface sticks initially and commences to slip along with diminishing plug heave rate after certain displacement. Since this mechanism is not related to the REB behaviour, it justifies the consideration of the undrained condition for the calibration.

5.2.4 Inner friction

Element 3 represents the inner friction, whose mobilisation is connected to the relative displacement at the soil-structure interface. Since the potentially arising plug heave reduces the relative displacement, the inner friction depends on the gap expansion $z - z_2$. In line with the calibration of the outer friction, the inner friction was calibrated under drained condition ($v_z = 10^{-12}\,\mathrm{m/s}$). Consequently, negligible plug heave occurred and the REB was practically non-existent. Nonetheless, the arrangement in series with the REB and the interaction with the suction force (arranged in parallel) allows for partial mobilisation depending on the drainage condition.

Similarly to the generation of the outer friction, the initial raise of the inner friction is almost linear and approaches certain residual force (see Figure 5.5). Before reaching the

147
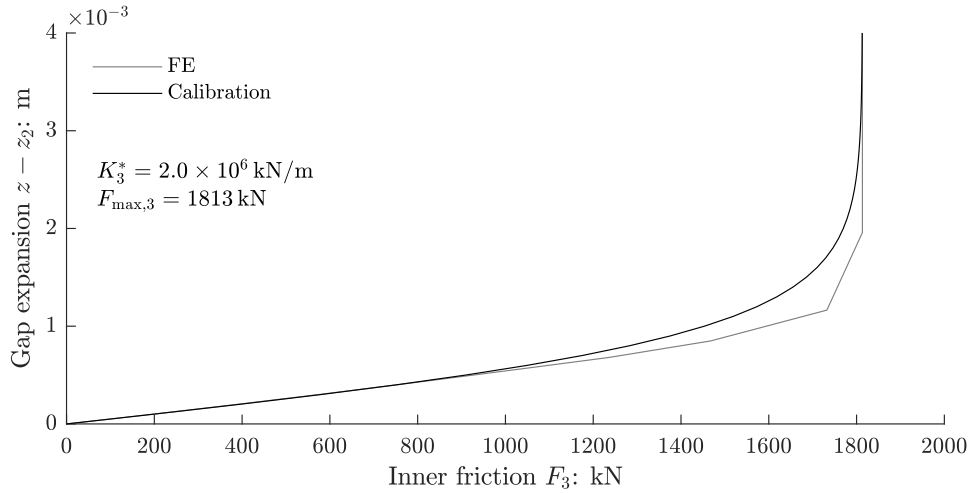
Figure 5.5: Exemplary calibration of inner friction for $L = D = 9\,\mathrm{m}$ in very dense sand.

residual inner friction, the rate of increase exhibits gradual reduction and there is neither distinct maximum resistance nor softening after reaching the maximum resistance. Hence, the hyperbolic tangent function was introduced to approximate the inner friction (see Equation 5.5). Analogous to the outer friction, two parameters describing the element's stiffness and maximum force were defined. The calibrated function attained good agreement in comparison to the results of the numerical simulation.

$$F_3 = F_{\mathrm{max},3} \tanh\left(\frac{K_3^*}{F_{\mathrm{max},3}}(z - z_2)\right) \max\left[1 - b\frac{\Delta u A}{\Delta u_{\mathrm{cr}} A}, 0\right] \tag{5.5}$$

$$\Delta u_{\mathrm{cr}} = \left[\pi - \arctan\left(5\left(\frac{L}{D}\right)^{0.85}\right)\left(2 - \frac{2}{\pi}\right)\right]\gamma' L \tag{5.6}$$

In order to consider hydraulic effects on the inner friction under partially drained to undrained conditions, Senders (2009) suggested linear reduction of the inner friction by the ratio of the suction force $F_{\mathrm{suc}} = \Delta u A$ to a critical suction force $\Delta u_{\mathrm{cr}} A$ (see Equation 5.5 and Equation 5.6 (according to Senders and Randolph, 2009)). The suction bucket's decreasing embedment depth due to its upward displacement could be implemented in Equation 5.6 by replacing L with $L - \Delta z$. However, this effect is of subordinate relevance and hence neglected. The critical negative differential pressure was originally deduced for the quasi steady-state condition during the installation of suction buckets so that its validity for transient hydraulic effects induced by tensile loading is not compulsory. Therefore, the theoretical reduction of inner friction was compared to FE simulations. In order to segregate the hydraulic effects, these FE simulations assumed frictionless interfaces at the suction bucket's skirt. Consequently, the variation of the integrated soil's radial stresses adjacent to the skirt's inside were evaluated in Figure 5.6 by means of $\int \sigma'_{r,\mathrm{i}}/\int \sigma'_{r,\mathrm{i},\Delta u=0\,\mathrm{kPa}} - 1$.
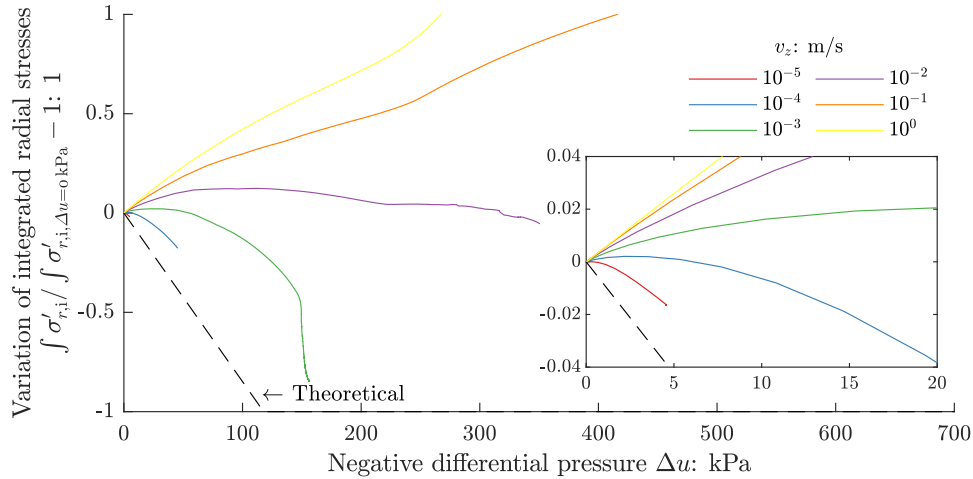
Figure 5.6: Effect of negative differential pressure on inner friction for $L = D = 9\,\text{m}$ in very dense sand.

Figure 5.6 elucidates that the interaction of drainage condition with the integrated radial stresses is much more complex than it is predicted by the theoretical approach of Senders (2009). Although the results of the FE simulations evinced that the inner friction reduced for displacement rates $v_z \leq 10^{-3}$, the reduction was less pronounced than predicted by Equation 5.5 in conjunction with Equation 5.6. Instead of reduction, the inner friction was enhanced in case of less drainage for $v_z \geq 10^{-2}$. Owing to the lack of alternative concepts, the reduction of the inner friction following Senders (2009) was implemented and augmented by an additional factor b with $0 \leq b \leq 1$, which allowed for adjustments to empirically correct Equation 5.6. As it is evident from Figure 5.6, the reduction of the inner friction by means of the critical negative differential pressure is not reasonable so that $b = 0$ was assumed for all calculations.

5.2.5 Water expansion

The enclosed water volume (and entrapped air, if present) beneath the suction bucket's lid expands due to the presence of negative differential pressure, which is limited by the cavitation of the pore fluid. In the analytical model, element 4 represents these effects. Therefore, the mobilisation of element 4 depends on the gap expansion $z_1 - z_2$.

The characteristics of the water expansion were derived from theoretical considerations. Thus, the bulk modulus of the pore fluid K_w relates to the spring's stiffness as defined by Equation 5.7. Because of the large bulk modulus of the pore fluid, the stiffness of element 4 is relatively high. Equation 5.8 introduces the maximum suction force limited by cavitation. Consequently, the suction force increases linearly with gap expansion until a maximum force corresponding to cavitation pressure is reached (see Equation 5.9). To omit infinite stiffness of the spring, the gap expansion is initially defined as $z_1 - z_2 = 0.005L$ (according to Senders, 2009). Therefore, certain initial gap expansion slightly reduces the generation of the suction force, but provides numerical stability.

$$K_4^* = K_\mathrm{w} \frac{A}{z_1 - z_2} = A \frac{\mathrm{d}u}{\mathrm{d}(z_1 - z_2)} \tag{5.7}$$

$$F_{\mathrm{max},4} = p_{\mathrm{cav}} A = (p_{\mathrm{atm}} + \gamma_\mathrm{w} h_w) A \tag{5.8}$$

$$F_4 = \begin{cases} K_4^*(z_1 - z_2) & , \quad \text{if } \Delta u \leq p_{\mathrm{cav}} \\ F_{\mathrm{max},4} & , \quad \text{if } \Delta u > p_{\mathrm{cav}} \end{cases} \tag{5.9}$$

Although water expansion is expected to be of subordinate relevance for the global response of the analytical model, it is an appropriate feature for a holistic consideration of the suction bucket's tensile bearing behaviour. Moreover, this element provides the possibility of artificial reduction of the element's stiffness to account for a certain amount of entrapped air beneath the suction bucket's lid, which would significantly affect the suction bucket's response by diminishing the generation of the suction force.

5.2.6 Seepage

The pore water seepage flow is idealised by element 5 (damper). In contrast to the previously described elements (springs), the suction force induced by seepage is mobilised by a certain displacement rate, i.e. gap expansion rate $\frac{\mathrm{d}(z-z_1)}{\mathrm{d}t}$, rather than displacement. Since the suction force further depends on the displacement rate of the suction bucket, the calibration accounts for different displacement rates. Moreover, certain boundary conditions were adopted to isolate the pore water seepage flow from further interactions. Therefore, the water was assumed to be incompressible (equivalent to infinite stiffness of element 4) and the contact at the skirt's interface was set to be frictionless (equivalent to zero stiffness of elements 1 and 3). Following these assumptions, the results of the FE simulations enabled the investigation of the interrelations of negative differential pressures and gap expansion rates as a result of the applied displacement rates.

Figure 5.7 (a) depicts exemplary results of the previously described simulations and confirms the dependency of the seepage on the applied displacement rate. The attained results were individually fitted to Equation 5.10, which accounts for the non-linear generation of the suction force. Figure 5.7 (a) points out that better approximations were achieved for simulations with lower displacement rates in which more drainage was enabled. For higher displacement rates, the estimation's quality decreased, but was still adequate. The damper's coefficient and exponent were determined for a wide range of displacement rates and illustrated in Figure 5.7 (b).

$$F_5 = C_5 \left(\frac{\mathrm{d}(z - z_1)}{\mathrm{d}t} \right)^\xi \tag{5.10}$$

The development of the suction force is highly non-linear and the fitted parameters differ significantly for the investigated displacement rates. Moreover, Equation 5.10 does not account for the suction bucket's displacement and displacement rate, which are both affecting the development of the negative differential pressure and thus possibly reduce the
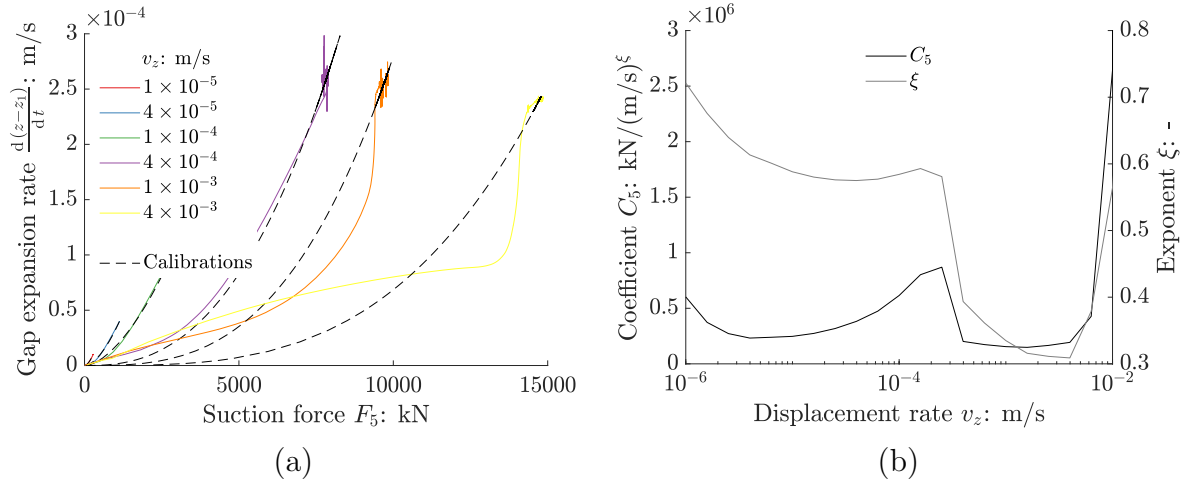
Figure 5.7: Exemplary calibration of seepage for $L = D = 9\,\text{m}$ in very dense sand (a) and its parameters.

accuracy of the approximation. Furthermore, the mobilised suction force is not unique for distinct gap expansion rates. Nevertheless, calibrating Equation 5.10 provides generally suitable approximations of the results of the FE simulations.

Figure 5.8 demonstrates that a more accurate regression of the suction force is attainable but requires substantially higher complexity of the damper's function. In this example, Equation 5.11 approximates the suction force while accounting for the gap expansion rate, suction bucket's displacement rate and displacement. The arbitrary coefficients $\eta_{1\ldots4}$, which were fitted to the results of the numerical simulations, depend on the suction bucket's displacement. Comparing Figure 5.8 (a) with Figure 5.7 (a) underlines the higher accuracy of the advanced function. The generalised results of the calibration are depicted in Figure 5.8 (b) for certain displacements, whereby the markers indicate distinct results of the FE simulations that were approximated. However, the implementation of these dependencies in the analytical model would be complex and would require additional interrelations of the individual elements and solution variables. Thus, the presentation of this alternative approach aimed at demonstrating the feasibility of more accurate prediction of the seepage rather than proposing a practical approach.

$$F_5 = \eta_1(z) + \eta_2(z) \cot\left(\eta_3(z) + \eta_4(z)\frac{\mathrm{d}(z - z_1)}{\mathrm{d}t}\frac{1}{v_z}\right) \tag{5.11}$$

5.3 Verification

5.3.1 Displacement-controlled loading

The analytical model was verified for different constant displacement rates by comparing the results with the ones of the corresponding FE simulations (see subsection 4.3.3).
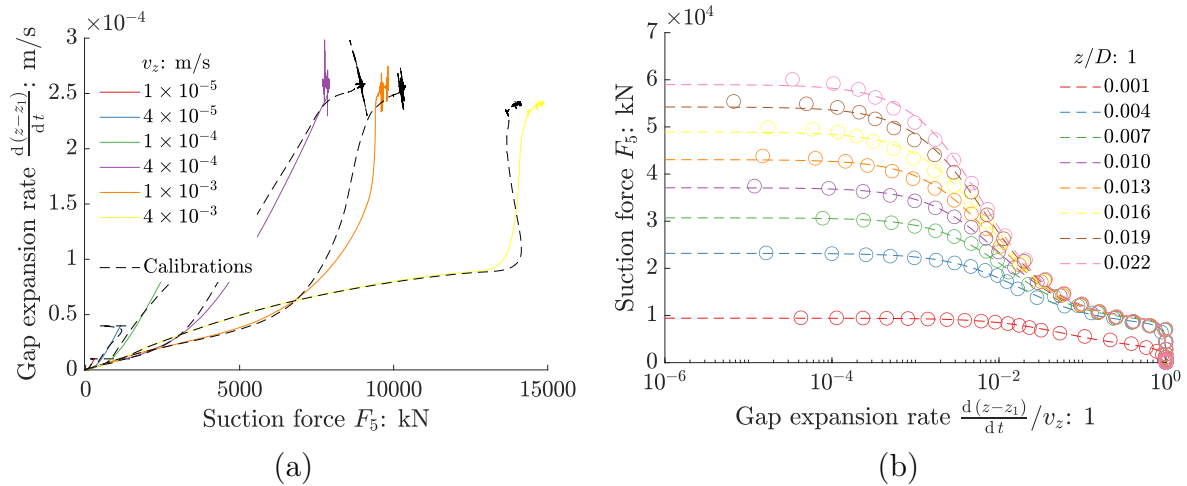
Figure 5.8: Alternative calibration of seepage for $L = D = 9\,\text{m}$ in very dense sand (a) and its generalisation (b).

Therefore, the calibrated parameters described in section 5.2 were implemented in the analytical model. The aim of this verification is to demonstrate the applicability of the model rather than presenting numerous comparisons for various boundary conditions. Nonetheless, the results presented in Figure 5.9 comprise a wide range of drainage conditions. Since the soil's mechanical properties were not varied, the drained frictional resistance remained constant. However, partial drainage implicitly involved an influence on the inner friction due to its interaction with the elements representing the suction force and the REB.

Figure 5.9 (a) illustrates results for $v_z = 10^{-6}\,\text{m/s}$, which represents the almost drained condition. Both the FE simulation and the analytical calculation predicted negligible generation of suction force. Moreover, the maximum values of the suction bucket's tensile resistance as well as the inner and outer friction agreed well. However, the suction bucket's stiffness was overestimated, which was mainly due to deviations regarding the inner friction.

The displacement rate of $v_z = 10^{-5}\,\text{m/s}$ induced certain suction force (see Figure 5.9 (b)). The non-linear generation of the suction force was well approximated qualitatively, despite less displacement was predicted in comparison to the FE simulation, which possibly relates to initial overestimation of the calibrated function of the damper (see Figure 5.7). The maximum suction force during progressing displacement was in good agreement. Similarly to Figure 5.9 (a), the stiffness was overrated mainly due to the inner friction.

Figure 5.9 (c) provides results for $v_z = 10^{-4}\,\text{m/s}$. In general, the analytical model well predicted the suction bucket's response. There were minor deviations with regard to higher suction force generated within less displacement and an overestimation of the inner friction, which slightly reduced in the FE simulations due to hydraulic effects. The overrated tensile resistance of the suction bucket was attributed to both inner and outer friction. Nevertheless, the suction bucket's stiffness was well approximated.
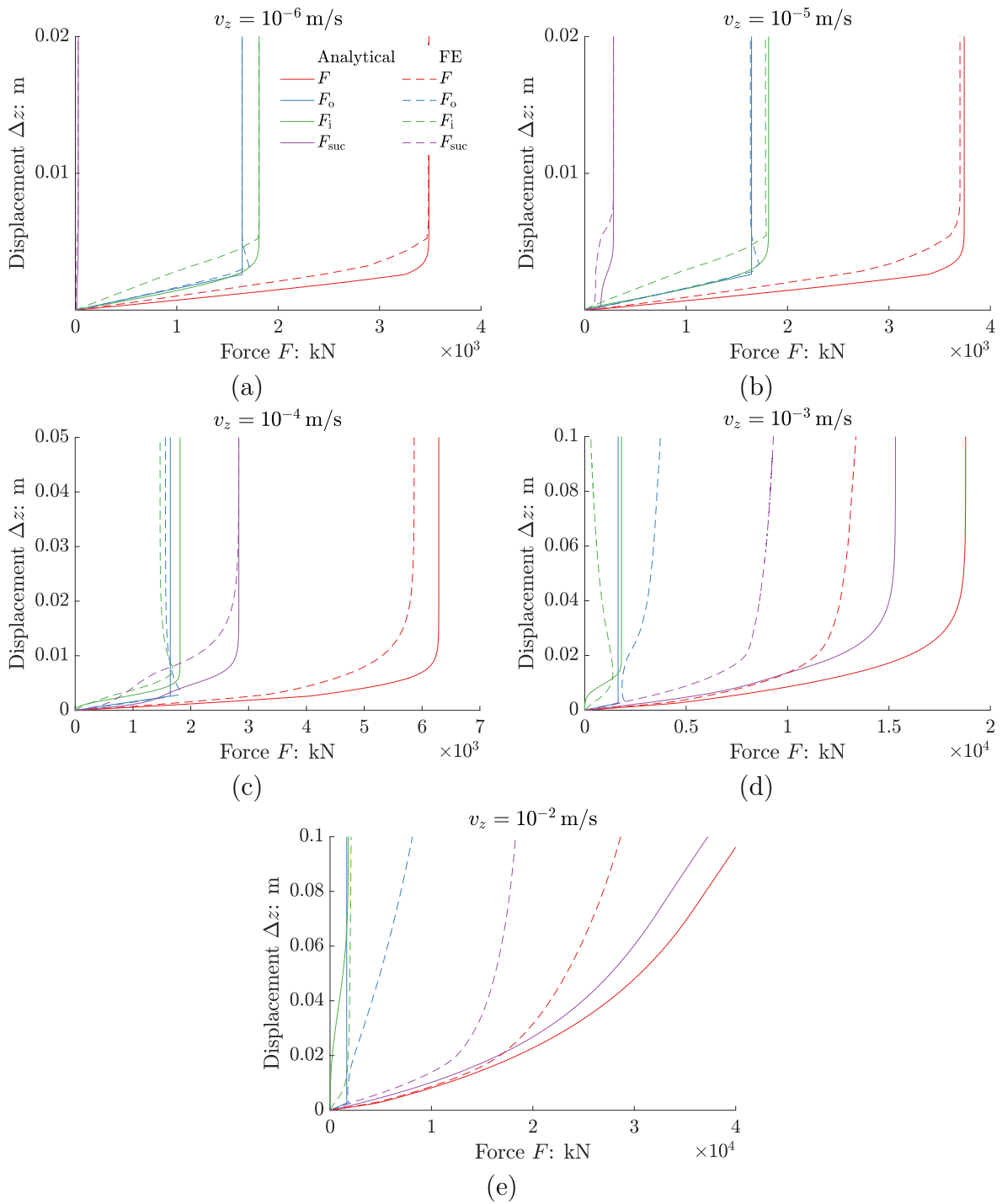
Figure 5.9: Verification of the analytical model for constant displacement rates and $L = D = 9\,\mathrm{m}$ in very dense sand with $v_z = 10^{-6}\,\mathrm{m/s}$ (a), $v_z = 10^{-5}\,\mathrm{m/s}$ (b), $v_z = 10^{-4}\,\mathrm{m/s}$ (c), $v_z = 10^{-3}\,\mathrm{m/s}$ (d) and $v_z = 10^{-2}\,\mathrm{m/s}$ (e).

153

For $v_z = 10^{-3}$ m/s the analytical model exhibited increasing deviations in comparison to the FE simulations (see Figure 5.9 (d)). These inaccuracies mainly resulted from overestimating the suction force and the inner friction. The latter evinced significant reduction in the FE simulation, which was not regarded for in the analytical calculation. Compared to this, the outer friction was enhanced by hydraulic effects, which was neglected as well. Nonetheless, the analytical model provided reasonable estimation of the numerical simulation.

Finally, Figure 5.9 (e) depicts results for $v_z = 10^{-2}$ m/s, where the drainage was constrained considerably. The approximation provided by the analytical model was rather qualitative due to crucial overestimation of the suction force. Beside this, the outer friction was significantly underestimated due to the previously described reason. It is marked that the inner friction attained by the numerical simulation exceeded the one of the analytical model, which related to an increase of the integrated radial stresses depicted in Figure 5.6.

Concerning loading with constant displacement rates, the analytical model provided at least reasonable, and partly good approximations of the results of the FE simulations. Especially the development of the inner friction and the suction force were well represented, although their courses are highly non-linear. In conclusion, the arrangement of these elements in conjunction with the REB mechanism is appropriate to simulate the suction bucket's response under partially drained conditions.

5.3.2 Force-controlled loading

The verification of the analytical model concerning force-controlled loading comprises the application of constant forces and cyclic equivalent forces. It is noted that the damper's parameters depend on the actual displacement rate, which is not constant in force-controlled loading. Since these parameters were defined initially and were not updated during the calculation process, the damper's coefficient and exponent have to be set to appropriate values. In terms of loading by constant forces, the almost constant displacement rates after sufficient holding duration were adopted. In contrast, the displacement rate varies permanently due to the incrementally increasing equivalent load, so that the mean displacement rate starting from the beginning to the final displacement was utilised.

Figure 5.10 depicts the verification for constant forces. The results of the FE model refer to subsection 4.3.4. For loads less or equal to the drained resistance, the displacements calculated by the analytical model were in good agreement with those of the FE simulations (see Figure 5.10 (a)). However, if the load magnitude exceeded the drained resistance, both displacement and displacement rate were underestimated by the analytical model with a tendency of larger deviations for higher loads. As a result of the underestimated displacement rate, the deviations of the displacements increased for longer holding durations. During the initial load application, the analytical model agreed well with the numerical simulations until a certain load magnitude was exceeded.
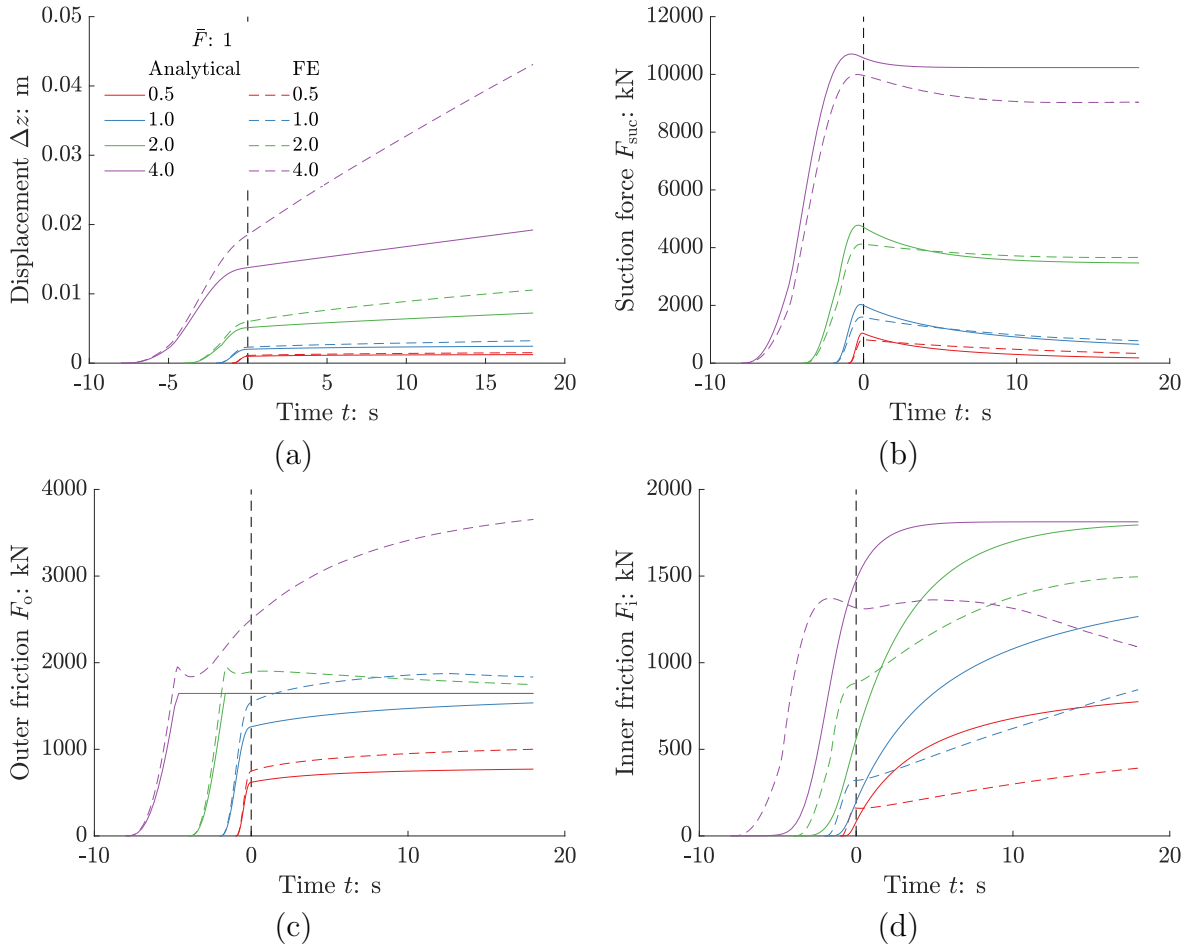
Figure 5.10: Verification of the analytical model for constant force and $L = D = 9\,\mathrm{m}$ in very dense sand with displacement (a), suction force (b), outer friction (c) and inner friction (d).

Figure 5.10 (b) elucidates that the analytical model provided good estimations of the suction force. Despite a minor overestimation in case of $\bar{F} = 4$, the results were in quantitative agreement. The analytical model predicted distinct maximum suction forces followed by subsequent reduction, which represents dissipation of the negative differential pressure underlining the model's capability of simulating transient effects. The decreasing suction force went along with slightly reducing displacement rates and a variation of load sharing. While the inner friction increased significantly, the increase of outer friction was subordinate for loads $\bar{F} \leq 1$ (see Figure 5.10 (c) and (d)). Moreover, Figure 5.10 (c) points out that the increase of outer friction resulting from higher effective stresses in the soil is neglected in the analytical model. In contrast, the inner friction would exhibit a certain reduction due to upward pore water seepage flow, which was also not accounted for in the analytical model by setting $b = 0$.

The methodology of applying incrementally constant forces to simulate the final displacement due to a particular cyclic load was employed in the analytical model. Analogue to the evaluation in subsection 4.3.7, the final displacement attained by the analytical model
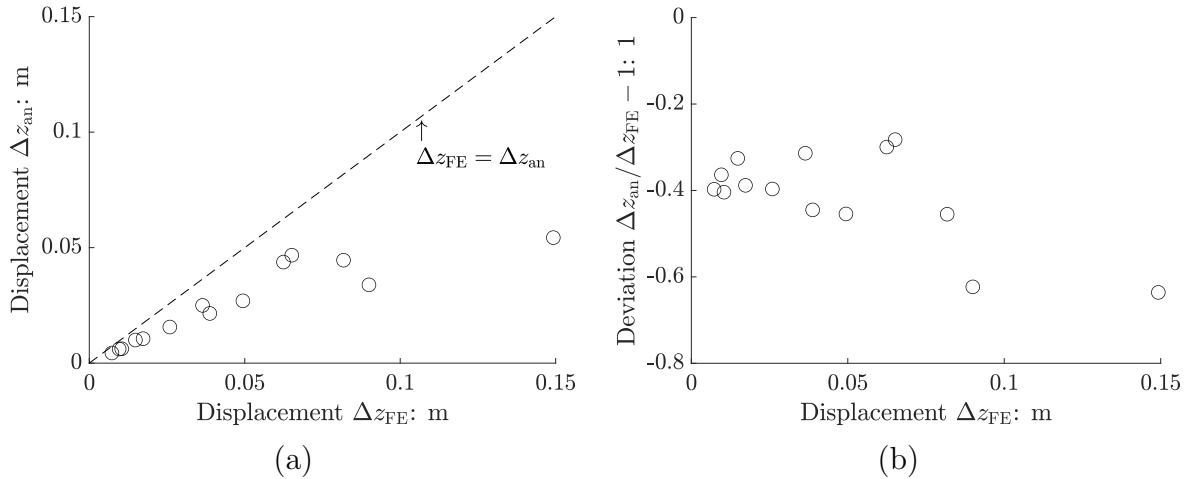
Figure 5.11: Verification of the analytical model for cyclic equivalent force and $L = D = 9\,\text{m}$ in very dense sand with displacement (a) and corresponding deviation (b).

Δz_{an} was compared to the final displacement of the cyclic equivalent load simulated by the FE model Δz_{FE} (reference case). Figure 5.11 depicts results for loads, which were equivalent to 29.5 cycles comprising different mean loads, load amplitudes and load frequencies. The analytical model underrated the final displacement by trend independently of the previously described load configurations. It appears from Figure 5.11 (a) that the underestimated displacements were related by a certain factor to the reference displacements. Figure 5.11 (b) underlines this observation by evincing approximately constant deviations for $\Delta z_{\text{FE}} < 0.085\,\text{m}$. The underestimation of the suction bucket's displacement induced by loads exceeding the drained resistance was consistent for both force-controlled load types.

Regarding the suction bucket's response to constant forces, the analytical model provided reasonable estimations of the FE simulations. The most crucial deviations were identified for the displacement rates induced by loads substantially exceeding the drained resistance. The results for the cyclic equivalent force were similar with respect to the underestimations of the final displacements. On the one hand, the long holding duration and the large number of cycles considered for the constant or equivalent force respectively magnified the deviations. Hence, the accuracy of the prediction would appear to be better for shorter holding durations or less cycles. On the other hand, the suction bucket's continuous displacement is governed by the pore water seepage flow, which was crucially simplified by the analytical model. The proposed function for describing the damper's behaviour does not account for the actual displacement of the suction bucket and further neglects the variation of the suction bucket's displacement rate during the progress of the calculation. Potentially, the agreement with the numerical simulations could be improved by continuously updating the damper's parameters or implementing a more advanced function, but these modifications would significantly affect the convergence of the model. Hence, it was chosen to demonstrate the applicability of the analytical model within the scope of the verification rather than implementing highly complex formulations for the elements.

5.4 Summary

The results of the physical model tests and numerical simulations presented in chapter 3 and chapter 4 provided essential insights in the suction bucket's tensile bearing behaviour. However, analysing the suction bucket's response by these methods involves substantial effort, which manifests the need for an effective and reliable analytical model. The model proposed by Senders (2009) was identified to be superior in comparison to the other methods and was utilised for comprehensive analyses.

The analytical model was presented in detail and modifications as well as advancements from the original version were described. The model's formulation, implementation and calibration accounted for the findings of the physical model tests and numerical simulations. In particular, incrementally linear equation systems for displacement and force-controlled loading were established, which are easy to implement in any desired computer programme. Moreover, each element of the model was discussed individually regarding its appropriate conditions, which enabled specific calibrations.

Although the FE simulations revealed that the outer friction is enhanced under partial drainage, this effect was neglected in order to establish a conservative formulation and calibration rested on the drained condition. The structure of the analytical model presupposes that the outer friction does not interact with the other elements and thus is not affected by the different drainage conditions. In contrast, the inner friction was calibrated for the drained condition, but its response is interrelated with other elements so that it implicitly accounts for different drainage conditions. It was shown that a linear reduction of the inner friction based on the critical negative differential pressure valid for installation fails to predict the actual mechanism induced by tensile loading.

The suction bucket's undrained response is dominated by the REB. However, under partially drained conditions, the REB is mobilised to a certain extent. Instead of calibrating this element for different drainage conditions, it was assumed that the undrained response is predominant. The verification for a wide range of displacement rates confirmed the applicability of the adopted condition.

The suction force is idealised by two elements requiring individual formulations. The water expansion resulting from negative differential pressure was described by the pore fluid's bulk modulus and was limited by cavitation. Moreover, the suction force induces seepage, which relates to the gap expansion rate. The calibration of the seepage implied difficulties with respect to multiple dependencies. Nonetheless, adequate results were obtained by adopting a relatively simple formulation.

The verification of the analytical model and its calibration provided reasonable results in comparison to numerical simulations for various load types. While displacement rates allowing for substantial drainage were quantitatively reproduced by the analytical model, the approximations were only qualitative in case of less drainage. With regard to force-controlled loading, the results were in good agreement for loads less or equal to the drained resistance. The application of loads exceeding the drained resistance led to an underestimation of the suction bucket's displacement and displacement rate. Detailed

analyses indicated that this inaccuracy was related to the formulation of the seepage. Nevertheless, the utilisation of the analytical model for an initial estimation was proven and it is noted that in contrast to FE simulations, the analytical model is advantageous due to its negligible computational costs. However, the model's elements require individual calibration for any particular condition, which constrains its applicability.

6 Conclusion and outlook

6.1 Discussion of the results

This thesis contributes to the current research on suction bucket foundations aiming at their economic application for offshore wind turbines (OWTs). In particular, the presented investigations dealt with the tensile bearing behaviour of suction buckets in sand under partial drainage. It is marked that the interaction of compressive and tensile loads is neglected in this thesis. The main conclusions are discussed in the following.

Installation and scale effects

During the hydraulic installation of the suction bucket, the soil's hydraulic conductivity and permeability ratio were derived from measurements. This evaluation is a novel feature in physical model testing, which confirmed the loosening of the soil during the installation by revealing an average of about 60% higher inner permeability in comparison to the outside of the suction bucket. The variation of the soil's hydraulic properties highly affected the suction bucket's tensile bearing behaviour, especially concerning the generation of the negative differential pressure. Retrospective numerical analyses verified the relevance of considering these properties accurately. Moreover, the plug heave was measured during the installation and comparisons with theoretical assumptions provided additional indication for loosening of the soil inside the suction bucket. Although these effects have already been discussed in the past, they were not measured to this extent in physical model tests so far.

The effect of the installation method and the model scale on the drained resistance was evaluated. Relatively higher drained resistances were obtained for suction buckets installed by jacking and for lower embedment depths. While the first aspect relates to the soil's confinement and stress enhancements during installation, the latter was induced by the soil's higher dilation at lower effective stresses in small-scale testing. Furthermore, the drained resistances exceeded theoretical predictions, which was attributed to the aforementioned dilation and high stress ratio in the soil because of the soil preparation method. Consequently, it is favourable to conduct model tests at maximum achievable scale, to account for the actual soil properties under appropriate conditions concerning the interpretation of the results and to hydraulically install the suction bucket rather than to jack it. Furthermore, numerical simulations of physical model tests require the implementation of the precise soil properties and the calibration of the particular stress condition. These findings emphasize the limited validity of numerous published small-scale model tests, in which the suction bucket was installed by jacking and the invoked effects were not considered in detail.

Constant displacement rate

Several studies dealt with the investigation of the suction bucket's response to constant displacement rates either in physical model tests or in numerical simulations. The results of this thesis obtained by model testing and finite element (FE) simulations essentially confirm the main findings of these studies. It was found that partial drainage led to a crucial increase of the tensile resistance in comparison to the drained resistance, but required more displacement for the generation. The enhanced tensile resistance was mainly due to the presence of the suction force. Since the mobilisation of the negative differential pressure is highly affected by the hydraulic properties, it is important to analyse those accurately as stated above. In model tests as well as numerical simulations, larger dimensions of the suction bucket and higher aspect ratios caused less drainage and therefore increased the tensile resistance. Furthermore, model tests with different model dimensions subjected to identical displacement rates reached their maximum resistances at similar displacements with respect to their diameters giving an empirical indication on scale effects, which has not been analysed in previous studies.

The variation of the pore pressure adjacent to the suction bucket's skirt affected the mobilisable skin friction. While the FE model allowed for separate analysis of the inner and outer friction, their sum was calculated from readings in the physical model tests. The measurements of the model tests revealed a decrease of the frictional resistance under partial drainage in comparison to the drained resistance, but approaching the undrained condition led to a substantial magnification. In contrast, the numerical simulations exhibited only minor decrease of the frictional resistance for displacement rates where the drainage was only marginally constrained. In case of substantially reduced drainage, the increasing outer friction overlaid the subordinate decrease of the inner friction, which increased beyond the drained resistance as the undrained condition was approached.

These findings were underlined by the evaluation of the negative differential pressure at the suction bucket's skirt. While in the model tests, these readings solely provided indication on the drainage condition, the extensive analyses of the numerical results pointed out the corresponding variation of effective stresses. The investigation of these interrelations has not been done to this extent before and it was concluded that when accounting for partial drainage, the corresponding effects on the frictional resistance shall be comprised.

In terms of the stiffness under partial drainage, it was found in FE analyses that although larger displacement was required to reach the maximum resistance, the initial stiffness was higher for lower drainage and loads lower than the drained resistance. The higher initial stiffness is beneficial for the suction bucket's bearing behaviour and essential for practical considerations. Even with regard to potential criteria for the serviceability limit state (SLS), the tensile resistance and stiffness were enhanced. Nonetheless, it is marked that the determined stiffness under tensile loading is expected to be lower than the one under compressive loading, which will be discussed below.

The measurements of the plug heave during tensile loading was innovative, gave indication on the actual drainage condition and provided an additional quantity for the validation of the FE model. In general, less drainage implied minor gap expansion, which was

observed in the physical model tests as well as numerical simulations. Furthermore, the drainage condition was also verified by measurements of the negative differential pressure at the suction bucket's skirt and in its proximity. These measurements coincided with the results of the numerical simulations by means of higher displacement rates evoking greater negative differential pressures because of less dissipation.

With respect to the installation method, the measured suction force was only marginally affected, but the frictional resistance was considerably larger for suction buckets installed by jacking. Moreover, the numerical simulations highlighted that the increase of tensile resistances was more pronounced in higher relative density, which was mainly due to higher suction forces induced by the soil's lower permeability but also because of magnified frictional resistance.

Constant force

The investigation of the suction bucket's response to constant displacement rates led to relevant insights regarding different drainage conditions. In general, the results confirmed the ones of previous studies and augmented those with innovative measurements and analyses. Subsequently, the results of force-controlled monotonic load are discussed, whereby it is noted that this load type has not been analysed in physical model tests or numerical simulations in detail so far.

While the physical model tests adopted only load magnitudes exceeding the drained resistance, the numerical model supplemented those with simulations of loads lower than the drained resistance. During load application, the relevant load rates implied partial drainage, though the actual load magnitude was below the drained resistance. Thus, negative differential pressure and corresponding suction force were generated and emphasised the importance of the suction bucket's partially drained response along with its great potential to be taken into account within the scope of design. It follows that the drained condition is rather hypothetical. As a consequence, the suction bucket's drained resistance may be adopted as a reference value, but is not transferable to the response under partially drained or undrained conditions.

Distinct continuous displacements were evoked for load magnitudes above the drained resistance. The displacement rate, which describes the tendency of displacement accumulation, was higher for larger applied loads. Loads below the drained resistance evinced slight initial displacement followed by negligible and steadily reducing displacement rates. Holding the load for substantial duration caused progressive displacement accumulation and finally led to extraction of the entire suction bucket. With respect to the load sharing, the suction force's share on the total resistance increased for higher load magnitudes. According to the results of the FE simulations, the suction force rose over-linearly for loads exceeding the drained resistance.

The FE model neglected the shortening of the drainage path and the reduction of the skirt's area in contact with the soil due to upward displacement of the suction bucket. As a result, the initial phase of the model tests were well approximated but increasing deviations evolved for longer durations. In particular, the model tests exhibited an increase of the displacement rates during the progress of the tests, which went along with

magnification of the suction forces while the frictional resistance reduced correspondingly. In contrast, the FE model predicted a dissipation of the suction force along with an increase of frictional resistance, which caused minor deceleration of the suction bucket's displacement. Although the numerical simulations failed to predict the aforementioned effects from geometric non-linearity, the simulations were in accordance with the initial response and internally consistent.

The results of the parametric study conducted with the FE model revealed larger displacement rates for higher aspect ratios and larger suction buckets due to less drainage and higher absolute loads concerning the specific drained resistance. Additionally, the force-controlled monotonic model tests were compared with appropriate displacement-controlled tests and testified validity of the results.

Cyclic force

For the first time, monotonic force-controlled loads were systematically analysed, which provided essential findings in terms of displacement accumulation and load sharing. These results are an essential benchmark for the evaluation of the cyclic bearing behaviour, but also highlight limitations of the FE model. Nevertheless, these loads are crucial idealisations of the cyclic loads acting on the foundations of OWTs. Few published physical model tests dealt with compressive mean loads, whereby cyclic excursions to tensile loads occurred, or partly accounted for tensile mean loads. Moreover, there is no numerical study, which specifically addressed the cyclic tensile bearing behaviour. Within this context, the presented results extended the available knowledge concerning cyclic tensile loads. The analyses of the physical model tests and numerical simulations were focussed on the displacement accumulation, the development of negative differential pressure, drainage condition and plug heave. The results obtained by the FE model were in good accordance with those of the model tests and widened the investigated range of parameters.

Inevitable displacement accumulation was invoked by loads exceeding the drained resistance with the maximum load being the most decisive parameter. Further effects resulting from the interaction of load parameters were observed, whereby the mean load was predominant over the load amplitude concerning the displacement accumulation. In particular, a suction bucket bore a relevant number of cycles without significant displacement, when subjected to mean loads in the range of the drained resistance and unloading in each cycle below the drained resistance. It follows that the displacement accumulation depended on both the cyclic load parameters and the expected number of cycles. Consequently, total avoidance of tensile forces acting on a suction bucket during its lifetime is not compulsory with regard to tolerable displacements defined by SLS for particular combinations of these contributing factors (even for loads exceeding the drained resistance).

However, Houlsby et al. (2005a) noted that the compressive and tensile stiffnesses differ crucially, which would severely affect the operation of OWTs. As a consequence, Houlsby et al. (2005a) recommended avoiding the occurrence of tensile loads. It is reminded that neither compressive loads nor their interaction with tensile loads was within the scope of this thesis. Therefore, the presented results only provided the indication that tensile loads below the drained resistance may be applicable with respect to the displacement

accumulation and requirements from SLS. Before these loads could be allowed for, the change in stiffness from compressive to tensile loads has to be investigated and assessed.

The measured displacement accumulations for constant and cyclic forces were compared and provided reasonable agreement for similar mean loads. This comparison was applied as well to the results of the FE simulations and qualitative accordance was confirmed concerning the load magnitude and dimension of the suction bucket. It followed that loads less than the drained resistance were of subordinate relevance and it is possible to approximate the cyclic displacement accumulation by an equivalent load (see below).

Similarly to monotonic force-controlled loads, cyclic loads intrinsically evoked partial drainage due to significant load rates. The resulting suction forces were greater for larger load magnitudes. The interrelation of displacement accumulation and increasing negative differential pressure was observed in any of the physical model tests and was consistent with the results of the monotonic force-controlled tests. Moreover, the mean value and the span of the negative differential pressure were greater for larger mean loads and load amplitudes respectively. It is concluded that an accumulation of negative differential pressure is not a critical issue provided that partial drainage is facilitated and no substantial displacement accumulation takes place.

With respect to drainage, the lower load frequency caused earlier displacement accumulation in physical model tests, but both plug heave and negative differential pressure developed similarly with respect to the suction bucket's displacement. The more pronounced displacement accumulation resulted from more drainage so that larger displacements were required to mobilise the appropriate suction force, which was confirmed by the FE simulations.

The measured initial settlement of the soil plug due to cyclic loading at low magnitudes may be critical for practical reasons as it implies wider gap expansion, which shall be avoided. However, the settlement was relatively small and took place over many cycles, which are unlikely to be allowed for in the design of an OWT. In contrast, cyclic loading at high load magnitudes induced significant plug heave within few cycles as a matter of higher displacement rates so that the gap expansion was less severe.

The comparison of the results attained by physical model tests and numerical simulations demonstrated that the relevance of the soil's cyclic mechanical behaviour is subordinate to the hydraulic properties. It remains to be clarified to what extent an advanced constitutive law affects the results of cyclic simulations.

Scaling of physical model tests is a relevant issue and the review of different scaling approaches indicated that it is questionable whether a simple scaling law, such as the one proposed by Kelly et al. (2006b), is able to accurately represent the complex cyclic tensile bearing behaviour. Thus, an alternative approach was introduced, which relies on the assumption of similarity at different scales considering the suction buckets' displacement rates divided by their diameters. Therefore, the load frequencies in numerical simulations were iteratively adjusted until accordance was achieved. This methodology is based on a fundamental hypothesis, which was derived from the results of tests with constant displacement rates at different scales (see above) and the definition of potential SLS criteria.

However, further examination and verification is needed. Nonetheless, it was shown that the frequency ratios depended on the load configuration and that the approximately scaled load frequencies at model scale were appropriate to represent the behaviour at prototype scale. While the first aspect is not considered in the approach of Kelly et al. (2006b), the latter evinces a substantial difference to the load frequency that would be required at model scale according to Kelly et al. (2006b). Although the suggested approach implies a non-verified assumption, the comparison with the rather simple scaling law clearly highlighted the need for further examinations.

Transient force

The results concerning the cyclic bearing behaviour elucidated that tensile loads may be applicable in terms of the SLS. However, at the current state, the design of suction buckets for OWT would probably not rely on a number of consecutive tensile load cycles, but potentially for singular tensile load events in consideration of the SLS and the ultimate limit state (ULS). There has been no investigations on this subject so far and hence neither the displacement nor the negative differential pressure can be predicted during loading and subsequent consolidation. This issue was investigated by means of FE simulations.

The displacement during loading and after consolidation was dictated by the load magnitude. Loads exceeding the drained resistance provoked serious displacements, but potential requirements of the SLS were still fulfilled. Hence, these loads might be acceptable in the design regarding the ULS provided that the number of occurrences is limited. In contrast to the SLS, the ULS implies that the OWT is not operating and the integrity of the OWT is the major concern. With respect to the argumentation of Houlsby et al. (2005a), the occurrence of tensile loads may be allowed for in ULS since the variation of the suction bucket's stiffness is less relevant under these conditions. It is noted that the FE model did not account for the soil's particles filling the void beneath the skirt's tip due to upward displacement, which facilitated the downward displacement. However, there were minor downward displacements during consolidation for loads substantially exceeding the drained resistance owing to the adopted weightlessness of the suction bucket along with plastic relative displacements at the skirt's interfaces and therefore this deficiency was less essential.

For transient loads less or equal to the drained resistance, negligible displacements were observed. It follows that these loads may occur a few times without breaching limitations defined by the SLS provided that sufficient time for consolidation between consecutive tensile loads is ensured. Furthermore, the induced negative differential pressure was proportional to the applied load for loads less or equal to the drained resistance since the skirt's interfaces were still in the elastic range. Over-linear rise of the negative differential pressure was found for loads higher than the drained resistance. Presupposing sufficient time for consolidation after the occurrence of a singular load prohibits the accumulation of negative differential pressure and enables downward displacement.

Equivalent force

In summary, the investigation of different load types consistently pointed out that loads higher than the drained resistance dominate the suction bucket's displacement. Based on

this conclusion, a novel approach was developed to estimate the suction bucket's displacement evoked by cyclic loads (partly) above the drained resistance. The suggested approach derives an (incrementally monotonic) equivalent load from an original cyclic load and approximates the suction bucket's final displacement. This methodology was successfully verified by comparing the final displacements of the equivalent load and cyclic load.

The most essential advantage of this approach is the reasonable simplification of the complex cyclic response (defined by the interrelation of the cyclic load parameters) by a transient load. The numerical simulation of the equivalent load causes significant reduction of the computational effort in comparison to the simulation of the original cyclic load. Moreover, the equivalent load does not necessitate an advanced constitutive law, unlike it is mostly assumed for the simulation of cyclic loads. Since the constitutive law adopted for the verification does not appropriately simulate the soil's cyclic mechanical behaviour, it might have artificially improved the achieved accordance and hence, verification with an advanced constitutive law is outstanding. Provided that the verification is successful, the equivalent load is suitable for the implementation in analytical models underlining the particular relevance of the proposed approach for practical applications.

Methods and practical applications

The discussion of the results led to distinct conclusions regarding the utilised methods and recommendations for practical applications. These aspects are briefly summarised, hereinafter.

Several published studies on numerical analyses pointed out the lack of reliable data from physical model tests or prototypes for validation purposes. This thesis provides well-documented measurements from physical model tests, which supply an essential basis for verification and validation with respect to a variety of loads and scales.

In terms of the requirements on the constitutive law in numerical models, the presented results were in reasonable agreement for any load type, although a rather simple mechanical constitutive law was implemented. This finding essentially underlined that the suction bucket's tensile response is dominated by hydraulic effects. However, this conclusion necessitates verification by further analyses with advanced constitutive laws.

The utilised analytical model was originally developed by Senders (2009), but its description was ambiguous. Thus in this thesis, it was explicitly formulated and implemented along with a proposal for calibrating the model. The verification of the analytical model confirmed its capability of predicting the suction bucket's monotonic and transient tensile response. Hence, the calibration was proven to be valid for different load conditions, although the individual elements' calibration solely assumed a specific condition. However, the model's calibration cannot be generalised for different soil types or suction bucket dimensions. In contrast to Senders (2009), where adequate results were attained only after artificial adjustments, the deviations of the presented results were discussed and suggestions for improvement were made. Moreover, solving the analytical model was proven to be highly effective, which marked a substantial advantage in comparison to physical model tests and numerical modelling, which both imply significant efforts.

165

6.2 Recommendations for further research

The results of this thesis suggested that tensile loads may be tolerated, but the current state does not allow for final recommendations. Further research shall comprise the interaction of compressive and tensile loads to be analysed in model tests and numerical studies with a developed FE model aiming at the evaluation of the suction bucket's displacement as well as compressive and tensile stiffnesses. Moreover, the augmentation of the FE model is expected to provide elaborated results by means of implementing an advanced constitutive law, considering for effects induced by hydraulic installation and accounting for reduced embedment depth of the suction bucket due to its upward displacement. These developments could enhance the certainty of the proposed procedure for evaluating scale effects with respect to the load frequency, which is also to be verified for additional model scales preferably at larger dimensions.

The approach of applying a cyclic equivalent load is promising and may assist the assessment of the suction bucket's displacement to, for instance, pseudo-random or site-specific loads. However, further verifications are required to prove adequacy and precision of this approach, whereby potential methods for verification are physical model tests and numerical simulations with sophisticated constitutive laws.

For practical applications, it is important to improve the accuracy and reliability of the analytical model. Then, a generalisation of the calibration for arbitrary conditions is necessitated to support the acceptance of the model.

Additional results attained by any method will facilitate the understanding of the complex bearing behaviour and lead to enhanced reliability as well as inclusion in current design recommendations.

7 Summary

Suction bucket foundations for offshore wind turbines (OWTs) are a promising concept, but due to incomplete understanding of their tensile bearing behaviour, especially under partial drainage and for recurring (cyclic) loads, their applicability is limited. This thesis addresses these issues for a variety of tensile conditions by means of physical model tests, numerical simulations and the advancement of an analytical model. The most essential findings are briefly summarised for the suction bucket's partially drained response in general, followed by results concerning the cyclic and transient displacement accumulation.

The effects from the suction bucket's installation affect its bearing behaviour and as a result of considerable load rates, negative differential pressure is always generated even for loads below the drained resistance. Consequently, the drained condition is a hypothetical reference rather than representing the suction bucket's actual response. Reduced drainage is further implied by larger suction bucket dimensions and higher aspect ratios implying corresponding influence on the tensile bearing behaviour. In general, larger tensile resistances are attainable under partial drainage. The maximum partially drained tensile resistance necessitates greater displacement, but the initial secant stiffness increases for decreasing drainage induced by higher load rates as well as smaller loads below the drained resistance. Moreover, reduced drainage invokes more plug heave and less dissipation in proximity to the suction bucket. While the frictional resistance potentially diminishes under partial drainage, it substantially magnifies under undrained condition.

The load magnitude acting on a suction bucket dictates its displacement accumulation. Concerning cyclic loads, the effect of the maximum load is dominant over the mean load followed by the load amplitude. The displacement induced by loads lower than the drained resistance is negligible. The comparability of monotonic and cyclic displacement accumulations along with the major relevance of forces exceeding the drained resistance on the evoked displacements allows their simplified estimation by an equivalent load.

With regard to a tolerable tilt of the OWT in serviceability limit state (SLS), the occurrence of tensile loads would be possible provided that the displacement is limited in dependence of the load characteristics and number of cycles. This includes loads above the drained resistance (presupposing that criteria from the ultimate limit state (ULS) are met) as well as those below the drained resistance, which could recur in greater numbers. However, sufficient time for subsequent consolidation must be provided enabling downward displacement of the suction bucket and dissipation of pore pressures prohibiting their accumulation.

An analytical model, constituted of several springs and a damper, is applicable to initially estimate the suction bucket's bearing behaviour and displacement accumulation. Nonetheless, the utilisation of the model should respect its limitations.

While the scope of this thesis was to analyse only suction buckets subjected to tensile loads, further research should focus on the interaction of compressive and tensile loads. The compressive loads counteract the potential upward displacement accumulation and therefore probably reduce the suction bucket's irreversible displacements. Beside that, the compressive and tensile stiffnesses differ significantly and their assessment is essential for a reliable operation of an OWT. In addition, the suggested methods for scaling physical model tests and deriving an equivalent load are to be verified for subsequent practical applications, such as in the further developed analytical model.

Bibliography

M. Achmus and C. Schröder. Installation and bearing behaviour of bucket foundations for offshore structures. *Bautechnik*, 91(9):597–608, 2014.

M. Achmus and K. Thieken. Numerical simulation of the tensile resistance of suction buckets in sand. In J. S. Chung, editor, *Proceedings of the 24th International Ocean and Polar Engineering Conference*. International Society of Offshore and Polar Engineers, 2014. ISBN 9781880653913.

O. J. Andersen and J. Løvseth. The Frøya database and maritime boundary layer wind description. *Marine Structures*, 19(2-3):173–192, 2006. URL http://www.sciencedirect.com/science/article/pii/S0951833906000542.

ANSI/API RP 2GEO. Geotechnical and foundation design considerations: ANSI/API recommended practice 2GEO; ISO 19901-4:2003 (modified), Petroleum and natural gas industries - Specific requirements for offshore structures, part 4. Recommended practice, American Petroleum Institute and American National Standards Institute, Washington, DC, 2014.

S. Bhattacharya, J. A. Cox, D. Lombardi, and D. M. Wood. Dynamics of offshore wind turbines supported on two foundations. *Proceedings of the Institution of Civil Engineers: Geotechnical Engineering*, 166(2):159–169, 2013.

B. Bienen, R. T. Klinkvort, C. D. O'Loughlin, F. Zhu, and B. W. Byrne. Suction caissons in dense sand, part II: Vertical cyclic loading into tension. *Géotechnique*, 68(11):953–967, 2018a.

B. Bienen, R. T. Klinkvort, C. D. O'Loughlin, F. Zhu, and B. W. Byrne. Suction caissons in dense sand, part I: Installation, limiting capacity and drainage. *Géotechnique*, 68(11):937–952, 2018b.

M. D. Bolton. The strength and dilatancy of sands. *Géotechnique*, 36(1):65–78, 1986.

BSH No. 7005. Minimum requirements concerning the constructive design of offshore structures within the Exclusive Economic Zone (EEZ). Standard design, Federal Maritime and Hydrographic Agency, 2015. URL https://www.bsh.de/DE/PUBLIKATIONEN/_Anlagen/Downloads/Offshore/Standards/Standard-Design_en.pdf?___blob=publicationFile&v=7.

E. Buckingham. On Physically Similar Systems; Illustrations of the Use of Dimensional Equations. *Physical Review*, 4(4):345–376, 1914.

R. Butterfield. Dimensional analysis for geotechnical engineers. *Géotechnique*, 49(3): 357–366, 1999.

BVG associates and InnoEnergy. Future renewable energy costs: Offshore wind: 57 technology innovations that will have greater impact on reducing the cost of electricity from European offshore wind farms. Technical report, 2017. URL https://bvgassociates.com/wp-content/uploads/2017/11/InnoEnergy-Offshore-Wind-anticipated-innovations-impact-2017_A4.pdf.

A. Bye, C. T. Erbrich, B. Rognlien, and T. I. Tjelta. Geotechnical Design of Bucket Foundations. In *Proceedings of the 27th Annual Offshore Technology Conference*. Offshore Technology Conference, 1995.

B. W. Byrne. *Investigations of suction caissons in dense sand*. PhD thesis, University of Oxford, 2000. URL http://ora.ox.ac.uk/objects/uuid:64c30b2e-155c-4642-9115-5e2bf5667af5/datastreams/THESIS01.

B. W. Byrne. Laboratory scale modelling for offshore geotechnical problems. In C. Gaudin and D. White, editors, *Proceedings of the 8th International Conference on Physical Modelling in Geotechnics*, volume 1. Taylor and Francis, 2014. ISBN 978-1-315-77687-3.

B. W. Byrne and G. T. Houlsby. Experimental investigations of response of suction caissons to transient vertical loading. *Journal of Geotechnical and Geoenvironmental Engineering*, 128(11):926–939, 2002.

B. W. Byrne and G. T. Houlsby. Foundations for offshore wind turbines: Philosophical Transactions of the Royal Society A: Mathematical, Physical and Engineering Sciences. *Philos. Trans. R. Soc. A Math. Phys. Eng. Sci.*, 361(1813):2909–2930, 2003.

J. Cao, R. Phillips, R. Popescu, J.M.E. Audibert, and Z. Al-Khafaji. Numerical Analysis of the Behavior of Suction Caissons in Clay. In J. S. Chung, editor, *Proceedings of the 12th International Offshore and Polar Engineering Conference*. International Society of Offshore and Polar Engineers, 2002. ISBN 9781880653586.

W. D. Carrier. Goodbye, Hazen; Hello, Kozeny-Carman. *Journal of Geotechnical and Geoenvironmental Engineering*, 129(11):1054–1056, 2003.

B. Cerfontaine, S. Levasseur, F. Collin, and R. Charlier. Axisymmetric transient modelling of a suction caisson in dense sand. In M. A. Hicks, R. B. J. Brinkgreve, and A. Rohe, editors, *Proceedings of the 8th European Conference on Numerical Methods in Geotechnical Engineering*, volume 2, pages 1243–1248. CRC Press/Balkema, 2014. ISBN 9781315751825.

B. Cerfontaine, F. Collin, and R. Charlier. Vertical transient loading of a suction caisson in dense sand. In F. Oka, A. Murakami, R. Uzuoka, and S. Kimoto, editors, *Proceedings of the 14th International Conference of International Association for Computer Methods and Recent Advances in Geomechanics*, pages 929–934. CRC Press/Balkema, 2015a. ISBN 1315733196.

B. Cerfontaine, A. C. Dieudonné, J. P. Radu, F. Collin, and R. Charlier. 3D zero-thickness coupled interface finite element: Formulation and application. *Comput. Geotech.*, 69: 124–140, 2015b.

B. Cerfontaine, A. C. Dieudonné, J. P. Radu, F. Collin, and R. Charlier. Three-node zero-thickness hydro-mechanical interface finite element for geotechnical applications. In B. A. Schrefler, E. Oñate, and M. Papadrakakis, editors, *Proceedings of the 6th International Conference on Coupled Problems in Science and Engineering*, 2015c. ISBN 978-84-943928-3-2.

B. Cerfontaine, F. Collin, and R. Charlier. Numerical modelling of transient cyclic vertical loading of suction caissons in sand. *Géotechnique*, 66(2):121–136, 2016.

P. Cuéllar, M. Baeßler, S. Georgi, and W. Rücker. Pore pressure buildup and soil stress relaxation in monopile foundations of offshore wind converters: Bautechnik. *Bautechnik*, 89(9):585–593, 2012.

P. Cuéllar, P. Mira, M. Pastor, J. A. Fernández Merodo, M. Baeßler, and W. Rücker. A numerical model for the transient analysis of offshore foundations under cyclic loading. *Comput. Geotech.*, 59:75–86, 2014.

Dassault Systèmes. Abaqus 2017, 2017.

W. Deng and J. P. Carter. A theoretical study of the vertical uplift capacity of suction caissons. *International Journal of Offshore and Polar Engineering*, 12(2):89–97, 2002.

DIN 1054:2010-12. Subsoil - Verification of the safety of earthworks and foundations - Supplementary rules to DIN EN 1997-1. German standard, Deutsches Institut für Normung e.V., Berlin, Germany, 2010.

DIN 18088-1:2019-01. Structures for wind turbines and platforms – Part 1: Basic principles and actions. German standard, Deutsches Institut für Normung e.V., Berlin, Germany, 2019.

DIN 18088-4:2019-01. Structures for wind turbines and platforms – Part 4: Soil and foundation elements. German standard, Deutsches Institut für Normung e.V., Berlin, Germany, 2019.

DIN 18125-2:2011-03. Soil investigation and testing - Determination of density of soil - Part 2: Field tests. German standard, Deutsches Institut für Normung e.V., Berlin, Germany, 2011.

DIN 18126:1996-11. Soil, investigation and testing - Determination of density of non-cohesive soils for maximum and minimum compactness. German standard, Deutsches Institut für Normung e.V., Berlin, Germany, 1996.

DIN EN 1997-1:2014-03. Eurocode 7: Geotechnical design - Part 1: General rules; German version EN 1997-1:2004 + AC:2009 + A1:2013. European standard, Deutsches Institut für Normung e.V., Berlin, Germany, 2014.

DIN EN ISO 14688-2:2018-05. Geotechnical investigation and testing - Identification and classification of soil - Part 2: Principles for a classification. International standard, International Organization for Standardization, Geneva, Switzerland, 2018.

DIN EN ISO 17892-11:2019-05. Geotechnical investigation and testing - Laboratory testing of soil - Part 11: Permeability tests. International standard, International Organization for Standardization, Geneva, Switzerland, 2019.

DIN EN ISO 17892-4:2017-04. Geotechnical investigation and testing - Laboratory testing of soil - Part 4: Determination of particle size distribution. International standard, International Organization for Standardization, Geneva, Switzerland, 2017.

DIN EN ISO 17892-5:2017-08. Geotechnical investigation and testing - Laboratory testing of soil - Part 5: Incremental loading oedometer test. International standard, International Organization for Standardization, Geneva, Switzerland, 2017.

DIN EN ISO 17892-9:2018-07. Geotechnical investigation and testing - Laboratory testing of soil - Part 9: Consolidated triaxial compression tests on water saturated soils. International standard, International Organization for Standardization, Geneva, Switzerland, 2018.

DIN EN ISO 19901-4:2017-01. Petroleum and natural gas industries - Specific requirements for offshore structures - Part 4: Geotechnical and foundation design considerations. International standard, International Organization for Standardization, Geneva, Switzerland, 2017.

DNV No. 30.4. Foundations. Classification notes, Det Norske Veritas, 1992. URL https://rules.dnvgl.com/docs/pdf/DNV/cn/1992-02/Cn30-4.pdf.

DNV-OS-J101. Design of Offshore Wind Turbine Structures. Offshore standard, Det Norske Veritas, 2014. URL https://rules.dnvgl.com/docs/pdf/DNV/codes/docs/2014-05/Os-J101.pdf.

DNVGL-ST-0126. Support structures for wind turbines. Standard, Det Norske Veritas and Germanischer Lloyd, 2018. URL https://rules.dnvgl.com/docs/pdf/DNVGL/ST/2018-07/DNVGL-ST-0126.pdf.

DNVGL-ST-0437. Loads and site conditions for wind turbines. Standard, Det Norske Veritas and Germanischer Lloyd, 2016. URL https://rules.dnvgl.com/docs/pdf/DNVGL/ST/2016-11/DNVGL-ST-0437.pdf.

J. P. Doherty and A. J. Deeks. Elastic response of circular footings embedded in a nonhomogeneous half-space. *Géotechnique*, 53(8):703–714, 2003.

J. P. Doherty, G. T. Houlsby, and A. J. Deeks. Stiffness of flexible caisson foundations embedded in nonhomogeneous elastic soil. *Journal of Geotechnical and Geoenvironmental Engineering*, 131(12):1498–1508, 2005.

A. Durakovic. Haliade-X 12 MW Nacelle Touches Down in UK, 2019a. URL https://www.offshorewind.biz/2019/11/13/haliade-x-12-mw-nacelle-touches-down-in-uk/.

A. Durakovic. Siemens Gamesa Goes to Eleven, 2019b. URL https://www.offshorewind.biz/2019/11/26/siemens-gamesa-goes-to-eleven/.

S. El-Gharbawy and R. Olson. Modeling of suction caisson foundations. In J. S. Chung, editor, *Proceedings of the 10th International Offshore and Polar Engineering Conference*, volume 2, pages 670–677. International Society of Offshore and Polar Engineers, 2000. ISBN 188065346X.

Eurostat. *Smarter, greener, more inclusive? Indicators to support the Europe 2020 strategy : 2019 edition.* Eurostat. Statistical books. Publications Office of the European Union, Luxembourg, 2019. ISBN 9276098259.

T. Feld. *Suction Buckets, a new innovation foundation concept, applied to offshore wind turbines.* PhD thesis, Aalborg University, 2001.

A. Foglia and L. B. Ibsen. Laboratory experiments of bucket foundations under cyclic loading. Technical report, Department of Civil Engineering, Aalborg University, 2014.

German Geotechnical Society. *Empfehlungen des Arbeitskreises Numerik in der Geotechnik - EANG.* Wiley, Hoboken, 2014. ISBN 9783433030806.

J. Grabe, J. Dührkop, and K. P. Mahutka. Monopile-foundations for offshore-wind power plants – generation of excess pore water pressure due to cyclic loading. *Bauingenieur*, 79(9):418–423, 2004.

K. Hasselmann, T. Barnett, E. Bouws, H. Carlson, D. Cartwright, K. Enke, J. Ewing, H. Gienapp, D. Hasselmann, P. Kruseman, A. Meerburg, P. Muller, D. Olbers, K. Richter, W. Sell, and H. Walden. Measurements of wind-wave growth and swell decay during the Joint North Sea Wave Project (JONSWAP). *Deut. Hydrogr. Z.*, 8 (12):1–95, 1973.

A. Hettler. Approximation formulae for piles under tension. In P. A. Vermeer and H. J. Luger, editors, *Deformation and failure of granular materials*, pages 603–608. Balkema, 1982. ISBN 90-6191-224-5.

A. Hettler. Possibilities and limitations of 1-g model techniques. In S. M. Springman, editor, *Proceedings of the 7th International Conference on Physical Modelling in Geotechnics*, volume 1. CRC and Taylor & Francis, 2010. ISBN 0415582202.

G. T. Houlsby. Interactions in offshore foundation design. *Géotechnique*, 66(10):791–825, 2016. URL http://dx.doi.org/10.1680/jgeot.15.RL.001.

G. T. Houlsby, L. B. Ibsen, and B. W. Byrne. Suction caissons for wind turbines. In S. Gourvenec and M. Cassidy, editors, *Proceedings of the 1st International Symposium on Frontiers in Offshore Geotechnics.* Taylor & Francis, 2005a. ISBN 9780415390637.

G. T. Houlsby, R. B. Kelly, and B. W. Byrne. The tensile capacity of suction caissons in sand under rapid loading. In S. Gourvenec and M. Cassidy, editors, *Proceedings of the 1st International Symposium on Frontiers in Offshore Geotechnics*, pages 405–410. Taylor & Francis, 2005b. ISBN 9780415390637.

G. T. Houlsby, R. B. Kelly, J. Huxtable, and B. W. Byrne. Field trials of suction caissons in sand for offshore wind turbine foundations. *Géotechnique*, 56(1):3–10, 2006.

L. C. Hung, S. Lee, N. X. Tran, and S.-R. Kim. Experimental investigation of the vertical pullout cyclic response of bucket foundations in sand. *Applied Ocean Research*, 68:325–335, 2017. URL http://www.sciencedirect.com/science/article/pii/S0141118716303819.

M. Iskander, R. Olson, and R. Pavlicek. Behavior of suction piles in sand. In P. P. Nelson, T. D. Smith, and E. C. Clukey, editors, *Design and Performance of Deep Foundations: Piles and Piers in Soil and Soft Rock*, pages 157–171. Publ by ASCE, 1993. ISBN 0872629872.

M. Iskander, S. El-Gharbawy, and R. Olson. Performance of suction caissons in sand and clay. *Canadian Geotechnical Journal*, 39(3):576–584, 2002.

J. Jaky. Pressure in silos. In *Proceedings of the second International Conference on Soil Mechanics and Foundation Engineering*, pages 103–107, 1948.

M. Jamiolkowski, D. C. F. Lo Presti, and M. Manassero. Evaluation of relative density and shear strength of sands from CPT and DMT. In J. T. Germaine, T. C. Sheahan, and R. V. Whitman, editors, *Proceedings of the symposium on soil behavior and soft ground construction*, Geotechnical special publication, pages 201–238. American Society of Civil Engineers, 2003. ISBN 978-0-7844-0659-5.

Y.-H. Jeong, J.-H. Kim, S. Manandhar, J.-G. Ha, H.-J. Park, and D.-S. Kim. Centrifuge modelling of drained pullout and compression cyclic behaviour of suction bucket. *International Journal of Physical Modelling in Geotechnics*, 20(2):59–70, 2020.

W. C. Jones, M. G. Iskander, R. E. Olson, and A. D. Goldberg. Axial capacity of suction piles in sand. In C. Chryssostomidis, M. S. Triantafyllou, A. J. Whittle, and M. S. Hoo Fatt, editors, *Proceedings of the International Conference on the Behaviour of Offshore Structures*, pages 63–75. Pergamon, 1994. ISBN 008041916X.

S. Kakasoltani, M. Zeinoddini, M. R. Abdi, and H. Arabzadeh. An Experimental Investigation Into the Pull-Out Capacity of Suction Caissons in Sand. In *Proceedings of the ASME 30th International Conference on Ocean, Offshore and Arctic Engineering - 2011*, pages 21–27. ASME, 2011. ISBN 9780791844397.

R. B. Kelly, B. W. Byrne, G. T. Houlsby, and C. M. Martin. Pressure chamber testing of model caisson foundations in sand. In T. A. Newson, editor, *Proceedings of the International Conference on Foundations: Innovations, Observations, Design and Practice*, pages 421–431, 2003. ISBN 0727732447.

R. B. Kelly, B. W. Byrne, G. T. Houlsby, and C. M. Martin. Tensile loading of model caisson foundations for structures on sand. In J. S. Chung, editor, *Proceedings of the 14th International Offshore and Polar Engineering Conference*, pages 638–641. International Society of Offshore and Polar Engineers, 2004. ISBN 9781880653623.

R. B. Kelly, G. T. Houlsby, and B. W. Byrne. A comparison of field and laboratory tests of caisson foundations in sand and clay. *Géotechnique*, 56(9):617–626, 2006a.

R. B. Kelly, G. T. Houlsby, and B. W. Byrne. Transient vertical loading of model suction caissons in a pressure chamber. *Géotechnique*, 56(10):665–675, 2006b.

K. Lesny. *Gründung von Offshore-Windenergieanlagen: Werkzeuge für Planung und Bemessung.* PhD thesis, Universität Duisburg-Essen, 2008.

D.S.K. Mana, S. Gourvenec, and M. F. Randolph. Numerical modelling of seepage beneath skirted foundations subjected to vertical uplift. *Comput. Geotech.*, 55:150–157, 2014.

K. R. Massarsch, C. Wersäll, and B. H. Fellenius. Horizontal stress increase induced by deep vibratory compaction. *Proceedings of the Institution of Civil Engineers: Geotechnical Engineering*, 173(3):228–253, 2020.

Mathworks. MATLAB 9.7 (R2019b), 2019.

K. J. McManus and R. O. Davis. Dilation-induced pore fluid cavitation in sands. *Géotechnique*, 47(1):173–177, 1997.

S. D. Nielsen. Finite element modeling of the tensile capacity of suction caissons in cohesionless soil. *Applied Ocean Research*, 90, 2019. URL http://www.sciencedirect.com/science/article/pii/S0141118719302093.

Offshore Wind Accelerator. Suction Installed Caisson Foundations for Offshore Wind: Design Guidelines. Technical report, Carbon Trust, 2019. URL https://www.carbontrust.com/resources/guides/renewable-energy-technologies/suction-installed-caisson-foundations-design-guidelines/.

J. Ohde. Zur Theorie der Druckverteilung im Baugrund. *Der Bauingenieur*, (33/34), 1939.

W. J. Pierson, Jr. and L Moskowitz. A proposed spectral form for fully developed wind seas based on the similarity theory of S. A. Kitaigorodskii. *J. Geophys. Res. (Journal of Geophysical Research)*, 69(24):5181–5190, 1964.

M. F. Randolph and S. Gourvenec. *Offshore Geotechnical Engineering.* Taylor & Francis, Hoboken, 2011. ISBN 9780415477444.

Renewables Advisory Board. Value breakdown for the offshore wind sector. Technical report, 2010. URL https://www.gov.uk/government/publications/offshore-wind-sector-value-breakdown.

Wilhelm Rust. *Nichtlineare Finite-Elemente-Berechnungen: Kontakt, Kinematik, Material.* Springer Fachmedien Wiesbaden, Wiesbaden, 3 edition, 2016. ISBN 978-3-658-13377-1.

J. Safarov, F. Millero, R. Feistel, A. Heintz, and E. Hassel. Thermodynamic properties of standard seawater: Extensions to high temperatures and pressures. *Ocean Science*, 5(3):235–246, 2009. URL https://www.ocean-sci.net/5/235/2009/os-5-235-2009.pdf.

S. Safinus, G. Sedlacek, and U. Hartwig. Cyclic response of granular subsoil under a gravity base foundation for offshore wind turbines. In *Proceedings of the ASME 30th International Conference on Ocean, Offshore and Arctic Engineering - 2011*, volume 7, pages 875–882. ASME, 2011. ISBN 9780791844397.

M. Senders. *Suction caissons in sand as tripod foundations for offshore wind turbines.* PhD thesis, The University of Western Australia, 2009.

M. Senders and M. F. Randolph. CPT-Based Method for the Installation of Suction Caissons in Sand. *Journal of Geotechnical and Geoenvironmental Engineering*, 135(1): 14–25, 2009.

K. Shen, Y. Zhang, R. T. Klinkvort, H. Sturm, H. P. Jostad, N. Sivasithemparam, and Z. Guo. Numerical simulation of suction bucket under vertical tension loading. In *Proceedings of the 8th International Offshore Site Investigation Geotechnics Conference*, pages 488–497. Society of Underwater Technology, 2017. ISBN 9780906940570.

A. Shonberg, M. Harte, A. Aghakouchak, C. S.D. Brown, M. P. Andrade, and M. A. Liingaard. Suction bucket jackets for offshore wind turbines: applications from in situ observations. In Y. Shin, editor, *Foundation Design of Offshore Wind Structures: 19th ICSMGE*, pages 65–77, 2017.

N. Skopljak. Northwester 2 Produces First Power, 2020. URL https://www.offshorewind. biz/2020/01/14/northwester-2-produces-first-power/.

E. S. Sørensen, J. Clausen, and L. Damkilde. Comparison of numerical formulations for the modeling of tensile loaded suction buckets. *Comput. Geotech.*, 83:198–208, 2017. URL http://www.sciencedirect.com/science/article/pii/S0266352X16302671.

H. E. Taşan. Numerical investigations on the behaviour of suction bucket foundations under cyclic axial compressive loads. *Bautechnik*, 92(9):595–604, 2015.

H. E. Taşan and S. A. Yilmaz. Effects of installation on the cyclic axial behaviour of suction buckets in sandy soils. *Applied Ocean Research*, 91, 2019. URL http://www. sciencedirect.com/science/article/pii/S0141118719302597.

H. E. Taşan, F. Rackwitz, and S. Savidis. Pore water pressure accumulation due to cyclic horizontally loaded monopiles with large diameters. *Bautechnik*, 87(8):449–461, 2010.

K. Terzaghi and R. Jelinek. *Theoretische Bodenmechanik.* Springer Berlin Heidelberg, Berlin, Heidelberg, 1954. ISBN 978-3-642-53245-0.

The European Parliament and the Council. Governance of the Energy Union and Climate Action, amending Regulations (EC) No 663/2009 and (EC) No 715/2009 of the European Parliament and of the Council, Directives 94/22/EC, 98/70/EC, 2009/31/EC, 2009/73/EC, 2010/31/EU, 2012/27/EU and 2013/30/EU of the European Parliament and of the Council, Council Directives 2009/119/EC and (EU) 2015/652 and repealing Regulation (EU) No 525/2013 of the European Parliament and of the Council: Regulation (EU) 2018/1999, 2018. URL https://eur-lex.europa.eu/legal-content/EN/TXT/ ?uri=OJ%3AL%3A2018%3A328%3ATOC.

K. Thieken, M. Achmus, and C. Schröder. On the behavior of suction buckets in sand under tensile loads. *Comput. Geotech.*, 60:88–100, 2014.

T. I. Tjelta. Geotechnical Aspects Of Bucket Foundations Replacing Piles For The Europipe 16/11-E Jacket. In *Proceedings of the 26th Annual Offshore Technology Conference*, pages 73–82. Offshore Technology Conference, 1994. ISBN 978-1-61399-096-4. URL https://doi.org/10.4043/7379-MS.

T. I. Tjelta. The suction foundation technology. In V. Meyer, editor, *Proceedings of the 3rd International Symposium on Frontiers in Offshore Geotechnics*, pages 85–93. CRC Press/Balkema, 2015. ISBN 9781138028487.

T. I. Tjelta and G. Haaland. Novel Foundation Concept for a Jacket Finding Its Place. In D. A. Ardus, D. Clare, A. Hill, R. Hobbs, R. J. Jardine, and J. M. Squire, editors, *Offshore Site Investigation and Foundation Behaviour*, Advances in Underwater Technology, Ocean Science and Offshore Engineering, pages 717–728. Springer Netherlands, 1993. ISBN 978-94-017-2473-9. URL https://doi.org/10.1007/978-94-017-2473-9_34.

UN Environment's Economy Division, Frankfurt School-UNEP Collaborating Centre for Climate & Sustainable Energy Finance, and Bloomberg New Energy Finance. Global Trends in Renewable Energy Investment 2018. Technical report, 2018.

Universal Foundation. Trial Installation: UK North Sea, 2014. URL https://222821-www.web.tornado-node.net/trial-installation-uk-north-sea/.

E. Vaitkunaite. *Physical Modelling of Bucket Foundations Subjected to Axial Loading*. PhD thesis, Department of Civil Engineering, Aalborg University, 2016.

E. Vaitkunaite, L. B. Ibsen, and B. N. Nielsen. New medium-scale laboratory testing of bucket foundation capacity in sand. In J. S. Chung, editor, *Proceedings of the 24th International Ocean and Polar Engineering Conference*, pages 514–519. International Society of Offshore and Polar Engineers, 2014. ISBN 9781880653913.

E. Vaitkunaite, B. N. Nielsen, and L. B. Ibsen. Comparison of design methods for axially loaded buckets in sand. In V. Meyer, editor, *Proceedings of the 3rd International Symposium on Frontiers in Offshore Geotechnics*, volume 1, pages 331–336. CRC Press/Balkema, 2015. ISBN 9781138028487.

E. Vaitkunaite, B. N. Nielsen, and L. B. Ibsen. Bucket Foundation Response Under Various Displacement Rates. *International Journal of Offshore and Polar Engineering*, 26(2):116–124, 2016.

E. Vaitkune, L. B. Ibsen, and B. N. Nielsen. Bucket foundation model testing under tensile axial loading. *Canadian Geotechnical Journal*, 54(5):720–728, 2017.

X. Wang, X. Zeng, and J. Li. Vertical performance of suction bucket foundation for offshore wind turbines in sand. *Ocean Eng.*, 180:40–48, 2019. URL http://www.sciencedirect.com/science/article/pii/S0029801818318341.

Wind Europe. Financing and investment trends: The European wind industry in 2018. Technical report, 2019a. URL https://windeurope.org/about-wind/reports/financing-and-investment-trends-2018/.

Wind Europe. Our energy, our future: How offshore wind will help Europe go carbon-neutral. Technical report, 2019b. URL https://windeurope.org/about-wind/reports/our-energy-our-future/.

Wind Europe. Wind energy in Europe in 2018: Trends and statistics. Technical report, 2019c. URL https://windeurope.org/about-wind/statistics/european/wind-energy-in-europe-in-2018/.

Wind Europe. Offshore Wind in Europe: Key trends and statistics 2019. Technical report, 2020. URL https://windeurope.org/about-wind/statistics/offshore/european-offshore-wind-industry-key-trends-statistics-2019/.

M. Zeinoddini, S. Kakasoltani, M. R. Abdi, and I. Ahmadi. Model testing of upright and tapered suction caissons in sand. *Ships and Offshore Structures*, 11(1):50–63, 2016.

Y. Zhang, D. Li, and Y. Gao. Model tests on installation and extraction of suction caissons in dense sand. *Marine Georesources and Geotechnology*, pages 1–9, 2017.

A Reports of model tests

A.1 Overview

The testing programme comprises three different test types, namely constant displacement rate (see Table A.1 and section A.2), constant force (see Table A.2 and section A.3) and cyclic force (see Table A.3 and section A.4). While the first test type implies four different model dimensions, the latter two test types were only conducted with the largest model dimension. The test name summarises the model dimension (with L and D for the length L and diameter D of the suction bucket both in mm) and the test type (with v for the constant displacement rate v_z in mm/s, M for the constant force $\bar{F}_{\mathrm{mean}}$ in 1 as well as F, M and A for the cyclic frequency f in Hz, mean load $\bar{F}_{\mathrm{mean}}$ in 1 and load amplitude $\bar{F}_{\mathrm{ampl}}$ in 1).

The results of each test are summarised in individual sections. Besides the measured data of the model test, the results of retrospective finite element (FE) simulations are included. Each section provides detailed information, such as the test summary with additional comments, the parameters of the FE model and the results presented in figures. Every model test includes preceding investigations (cone penetration testing (CPT), monitoring during installation as well as the determination of the hydraulic conductivity and the drained resistance), whose results are also provided. Although the tests proceeded until the suction bucket was entirely extracted from the soil, the post-failure response is hardly relevant (subsequent to highest force at constant displacement rate) and the permissible displacement in terms of serviceability criteria is limited (constant and cyclic force tests). Hence, the results are presented up to the occurrence of the highest force recorded for tests with constant displacement rate and up to $\Delta z \approx 90\,\mathrm{mm}$ for tests with constant or cyclic force.

It is noted that the measured hydraulic conductivity k_{f} or k_{i} in conjunction with the permeability ratio $k_{\mathrm{i}}/k_{\mathrm{o}}$ differ from the constant values, which are used for the FE simulation. This is due to the fact that the measurement considers the actual soil's relative density from CPT, but the FE simulation simplifies the soil to be homogeneous.

Table A.1: Summary of tests with constant displacement rate

Test	L in mm	D in mm	F_{dr} in kN	$\Delta z_{F_{dr}}$ in mm	v_z in mm/s	t_{acc} in s	F_{max} in kN	$\Delta z_{F_{max}}$ in mm
L500D510v0.5	500	510	0.73	0.62	0.46	1.59	1.81	1.41
L500D510v0.8	500	510	0.75	0.62	0.84	1.27	2.22	2.13
L500D510v1.8	500	510	0.70	0.87	1.75	0.71	2.89	5.51
L500D510v9.6	500	510	0.63	0.70	9.62	0.51	8.73	12.84
L250D510v0.9	250	510	0.24	0.18	0.85	0.92	1.50	2.55
L250D510v1.8	250	510	0.25	0.18	1.82	0.83	2.41	3.88
L250D510v9.7	250	510	0.29	0.12	9.66	0.40	8.08	7.66
L250D260v1.7	250	260	0.16	0.09	1.74	0.45	0.45	2.95
L250D260v9.6	250	260	0.14	0.30	9.56	0.42	1.15	8.51
L250D260v19.5	250	260	0.10	0.32	19.5	0.24	2.04	5.46
L250D260v48.8	250	260	0.12	0.24	48.8	0.25	3.96	13.44
L125D135v9.8	125	135	0.02	0.05	9.75	0.28	0.18	1.63
L125D135v19.7	125	135	0.02	*	19.7	0.40	0.31	3.99
L125D135v49.1	125	135	0.02	*	49.1	0.12	0.65	11.87

* No record

Table A.2: Summary of tests with constant force

Test	F_{dr} in kN	$\Delta z_{F_{dr}}$ in mm	$\bar{F}_{mean}$ in 1	t_{acc} in s	$t_{\Delta z=0.02D}$ in s
M1.09	0.75	0.59	1.09	0.1	207
M1.58	0.73	0.59	1.58	0.1	57
M2.04	0.73	0.80	2.04	0.2	34

Table A.3: Summary of tests with cyclic force

Test	F_{dr} in kN	$\Delta z_{F_{\mathrm{dr}}}$ in mm	f in 1/s	$\bar{F}_{\max}$ in 1	$\bar{F}_{\mathrm{mean}}$ in 1	$\bar{F}_{\mathrm{ampl}}$ in 1	$N_{\Delta z=0.02D}$ in 1
F1.02M0.86A0.18	0.67	0.59	1.02	1.04	0.86	0.18	2226
F1.01M0.73A0.38	0.82	0.72	1.01	1.11	0.73	0.38	654
F1.01M1.06A0.25	0.68	0.70	1.01	1.31	1.06	0.25	211
F1.01M0.87A0.60	0.83	0.95	1.01	1.47	0.87	0.60	149
F1.01M1.24A0.38	0.74	0.82	1.01	1.62	1.24	0.38	101
F1.02M1.58A0.39	0.64	0.72	1.02	1.97	1.58	0.39	62
F1.01M1.29A0.89	0.64	0.81	1.01	2.18	1.29	0.89	80
F1.01M2.12A0.52	0.71	0.72	1.01	2.64	2.12	0.52	30
F1.01M1.90A0.99	0.79	0.77	1.01	2.89	1.90	0.99	26
F0.50M0.74A0.37	0.84	0.74	0.50	1.11	0.74	0.37	321
F0.51M1.04A0.45	0.71	0.77	0.51	1.49	1.04	0.45	79
F0.51M1.52A0.65	0.61	0.75	0.51	2.17	1.52	0.65	36
F0.51M1.90A0.81	0.71	0.79	0.51	2.71	1.90	0.81	17

A.2 Constant displacement rate

A.2.1 L500D510v0.5

Table A.2.1.1: Test summary

L	500 mm	DPS$_{\text{ext,1}}$		DPS$_{\text{ext,2}}$	
D	510 mm	r	z	r	z
T_{w}	18.1°C	510 mm	625.0 mm	510 mm	375.5 mm

Drained resistance			Tensile test		
z	425.2	mm	z	424.4	mm
z/D	0.85		z/D	0.85	
z_{plug}	46.0	mm	z_{plug}	45.5	mm
F_{dr}	0.72	kN	F_{max}	1.81	kN
$\Delta z_{F_{\text{dr}}}$	0.64	mm	$\Delta z_{F_{\text{max}}}$	1.41	mm
			v_z	0.46	mm/s
			t_{acc}	1.59	s

Table A.2.1.2: FE model parameters

γ'	κ	λ	ν	ϕ'	ψ	k_{i}	$k_{\text{i}}/k_{\text{o}}$	k_0
10.41 kN/m^3	350	0.4	0.2	45°	20°	3.7×10^{-4} m/s	1.6	0.524

Comments:
No measurement of hydraulic conductivity due to defective sensor.

(a) (b)
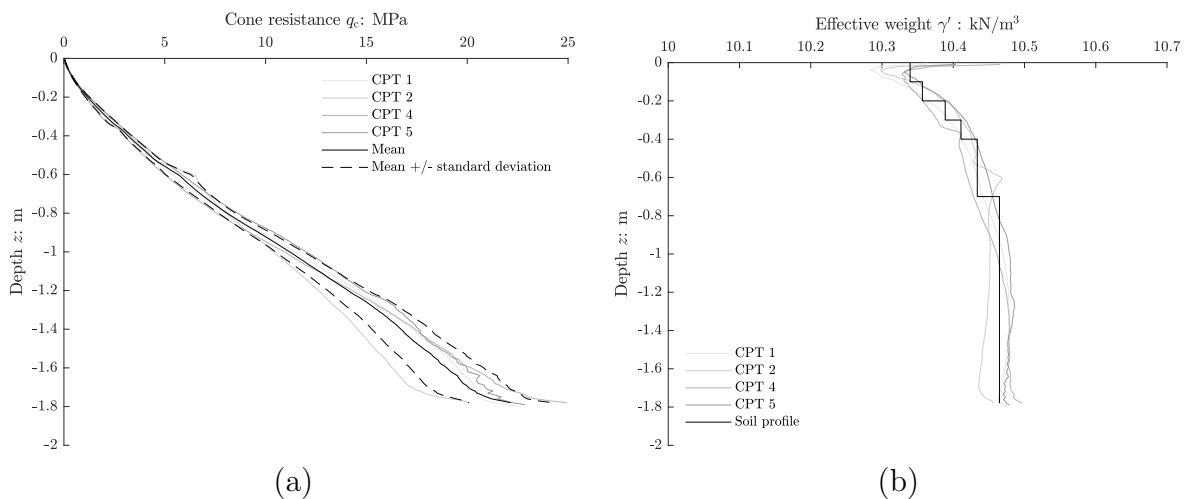
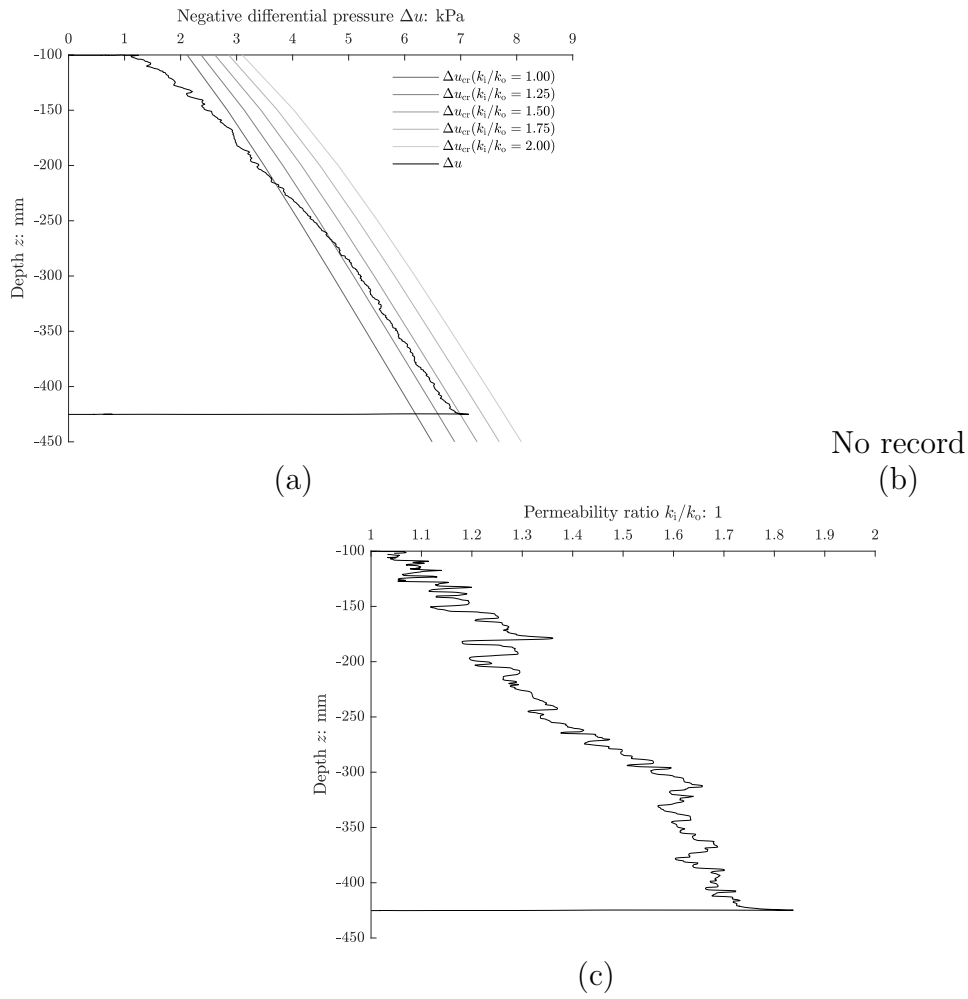*Figure A.2.1.1:* Cone penetration test: cone resistance (a) and effective weight (b).

(a)

No record

(b)

(c)

Figure A.2.1.2: Installation: negative differential pressure (a), hydraulic conductivity (b) and permeability ratio (c).
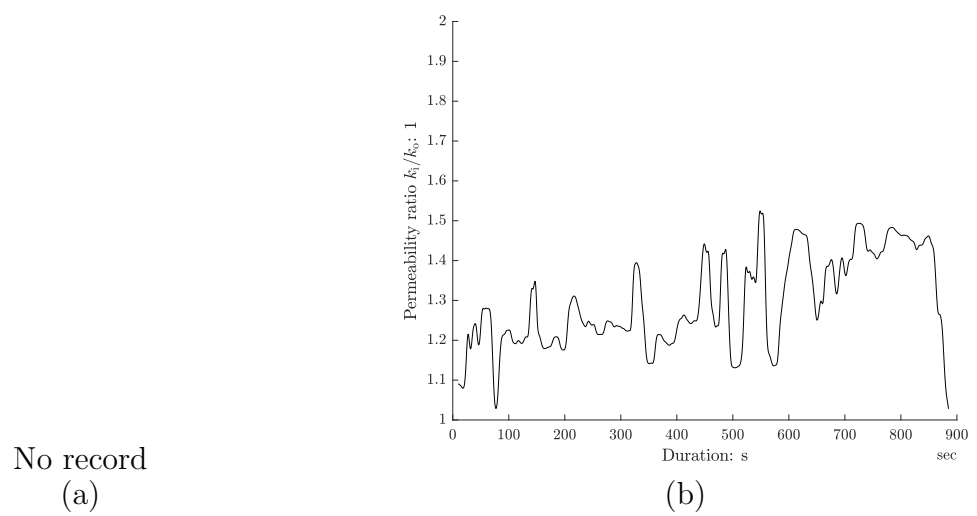
No record

(a)

(b)

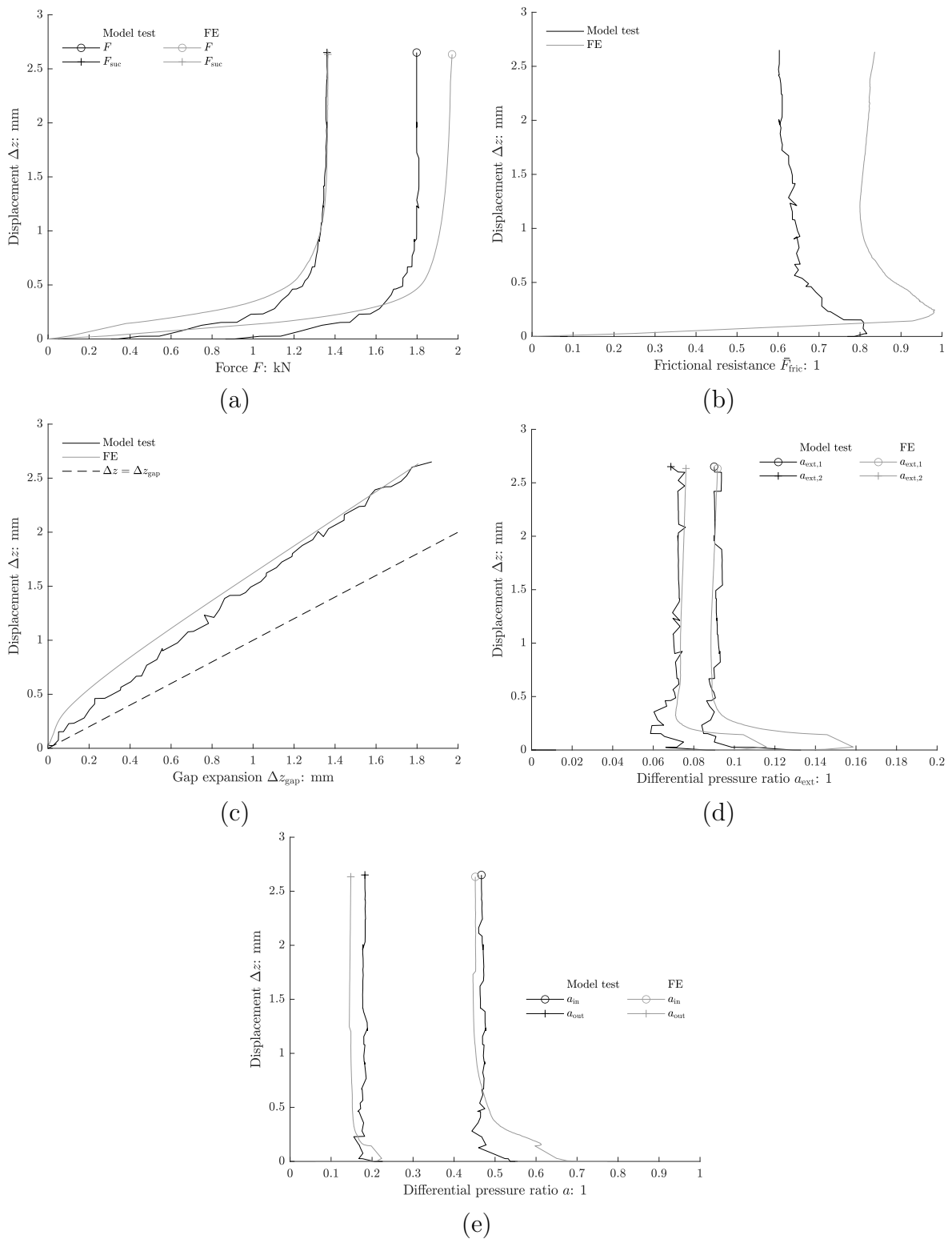*Figure A.2.1.3:* Permeability test: hydraulic conductivity (a) and permeability ratio (b).

Figure A.2.1.4: Tensile test: force and suction force (a), frictional resistance (b), gap expansion (c), differential pressure ratio (external) (d) and differential pressure ratio (skirt) (e)

A.2.2 L500D510v0.8

Table A.2.2.1: Test summary

L	$500\,\text{mm}$	$\text{DPS}_{\text{ext},1}$		$\text{DPS}_{\text{ext},2}$	
D	$510\,\text{mm}$	r	z	r	z
T_{w}	$18.6°\text{C}$	$510\,\text{mm}$	$625.0\,\text{mm}$	$510\,\text{mm}$	$378.5\,\text{mm}$

Drained resistance			Tensile test		
z	425.6	mm	z	425.2	mm
z/D	0.85		z/D	0.85	
z_{plug}	42.9	mm	z_{plug}	41.9	mm
F_{dr}	0.75	kN	F_{max}	2.22	kN
$\Delta z_{F_{\text{dr}}}$	0.62	mm	$\Delta z_{F_{\text{max}}}$	2.13	mm
			v_z	0.84	mm/s
			t_{acc}	1.27	s

Table A.2.2.2: FE model parameters

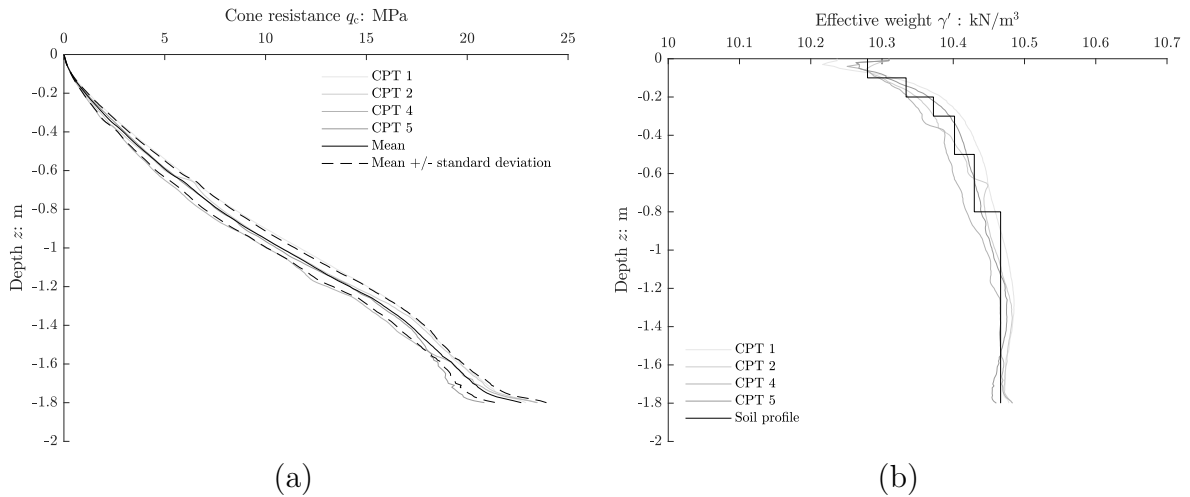| γ'	κ	λ	ν	ϕ'	ψ	k_{i}	$k_{\text{i}}/k_{\text{o}}$	k_0
$10.41\,\text{kN/m}^3$	350	0.4	0.2	$45°$	$20°$	$3.7 \times 10^{-4}\,\text{m/s}$	1.6	0.542

Comments:
-

Figure A.2.2.1: Cone penetration test: cone resistance (a) and effective weight (b).
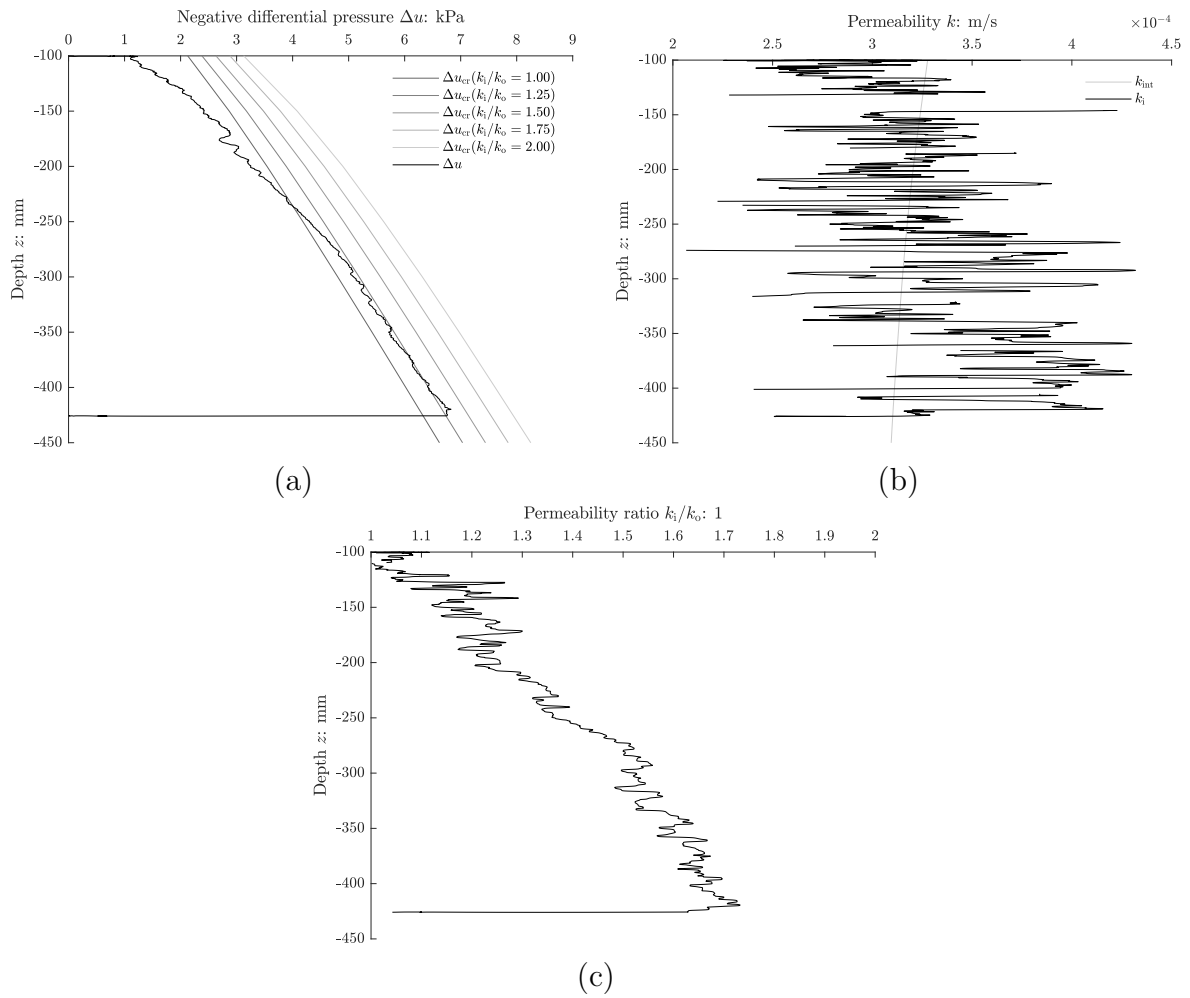
(a)

(b)

(c)

Figure A.2.2.2: Installation: negative differential pressure (a), hydraulic conductivity (b) and permeability ratio (c).
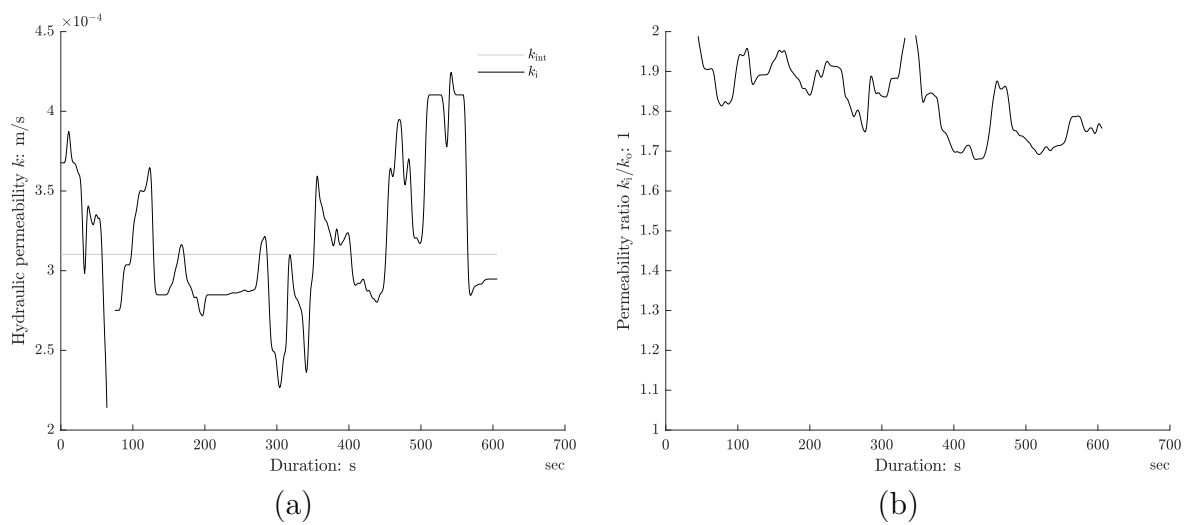

(a)

(b)

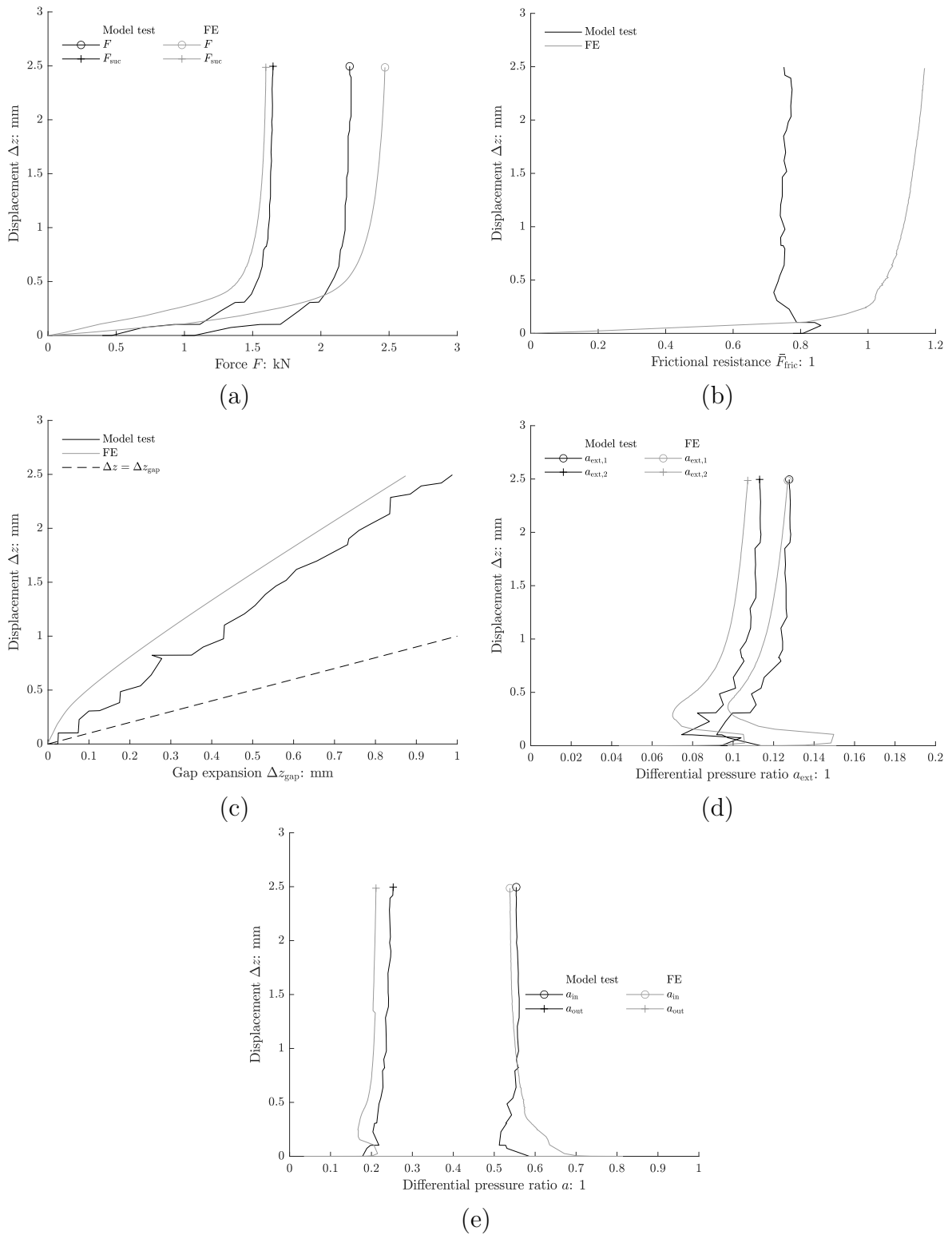*Figure A.2.2.3:* Permeability test: hydraulic conductivity (a) and permeability ratio (b).

Figure A.2.2.4: Tensile test: force and suction force (a), frictional resistance (b), gap expansion (c), differential pressure ratio (external) (d) and differential pressure ratio (skirt) (e)

A.2.3 L500D510v1.8

Table A.2.3.1: Test summary

L	500 mm	DPS$_{ext,1}$		DPS$_{ext,2}$	
D	510 mm	r	z	r	z
T_w	-	510 mm	250.0 mm	510 mm	450.0 mm

Drained resistance			Tensile test		
z	429.7	mm	z	426.9	mm
z/D	0.86		z/D	0.85	
z_{plug}	40.9	mm	z_{plug}	40.6	mm
F_{dr}	0.70	kN	F_{max}	2.89	kN
$\Delta z_{F_{dr}}$	0.87	mm	$\Delta z_{F_{max}}$	5.51	mm
			v_z	1.75	mm/s
			t_{acc}	0.71	s

Table A.2.3.2: FE model parameters

γ'	κ	λ	ν	ϕ'	ψ	k_i	k_i/k_o	k_0
10.41 kN/m^3	350	0.4	0.2	45°	20°	3.0×10^{-4} m/s	1.6	0.480

Comments:
After installation, a downward displacement of about 1 mm within more than two seconds was applied causing a compressive load and a positive differential pressure. Numerical analysis testified that the effect due to positive differential pressure can be neglected.
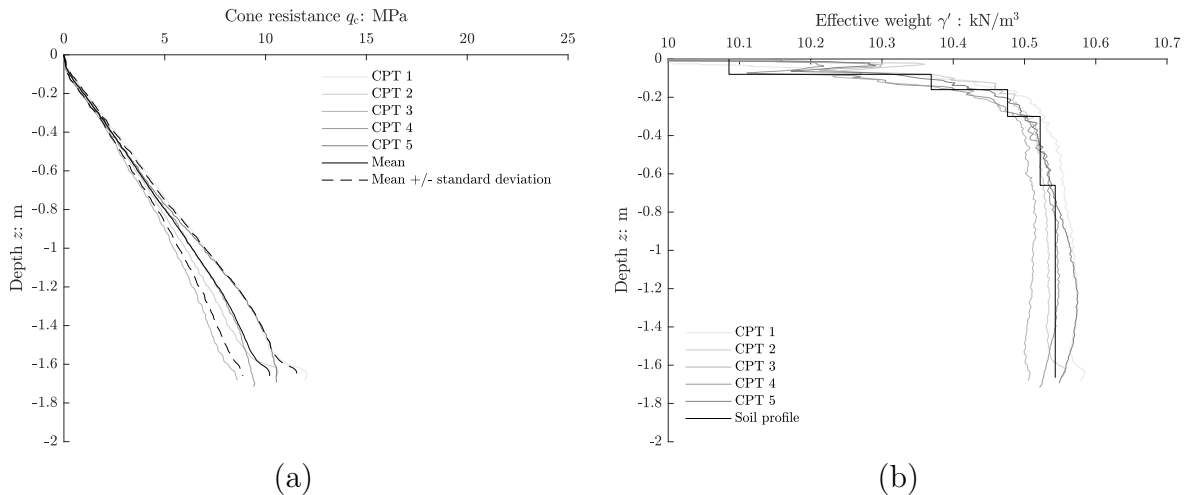

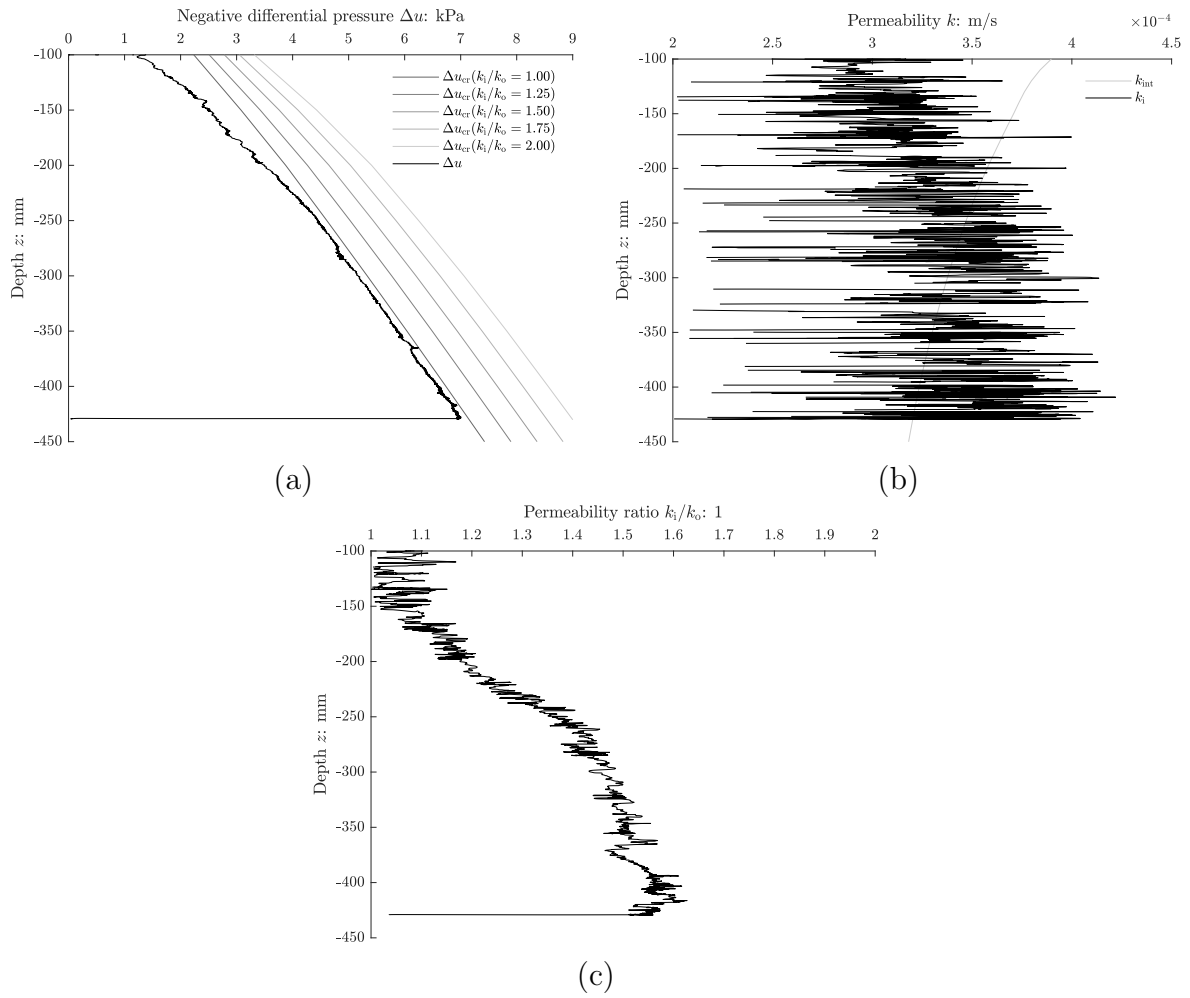*Figure A.2.3.1:* Cone penetration test: cone resistance (a) and effective weight (b).

(a)

(b)

(c)

Figure A.2.3.2: Installation: negative differential pressure (a), hydraulic conductivity (b) and permeability ratio (c).
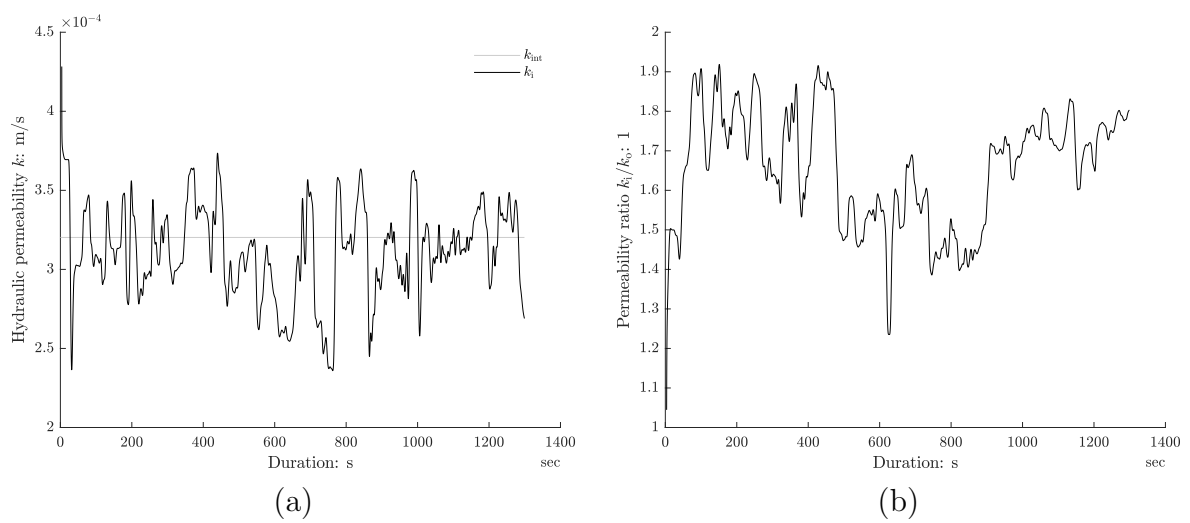

(a)

(b)

Figure A.2.3.3: Permeability test: hydraulic conductivity (a) and permeability ratio (b).
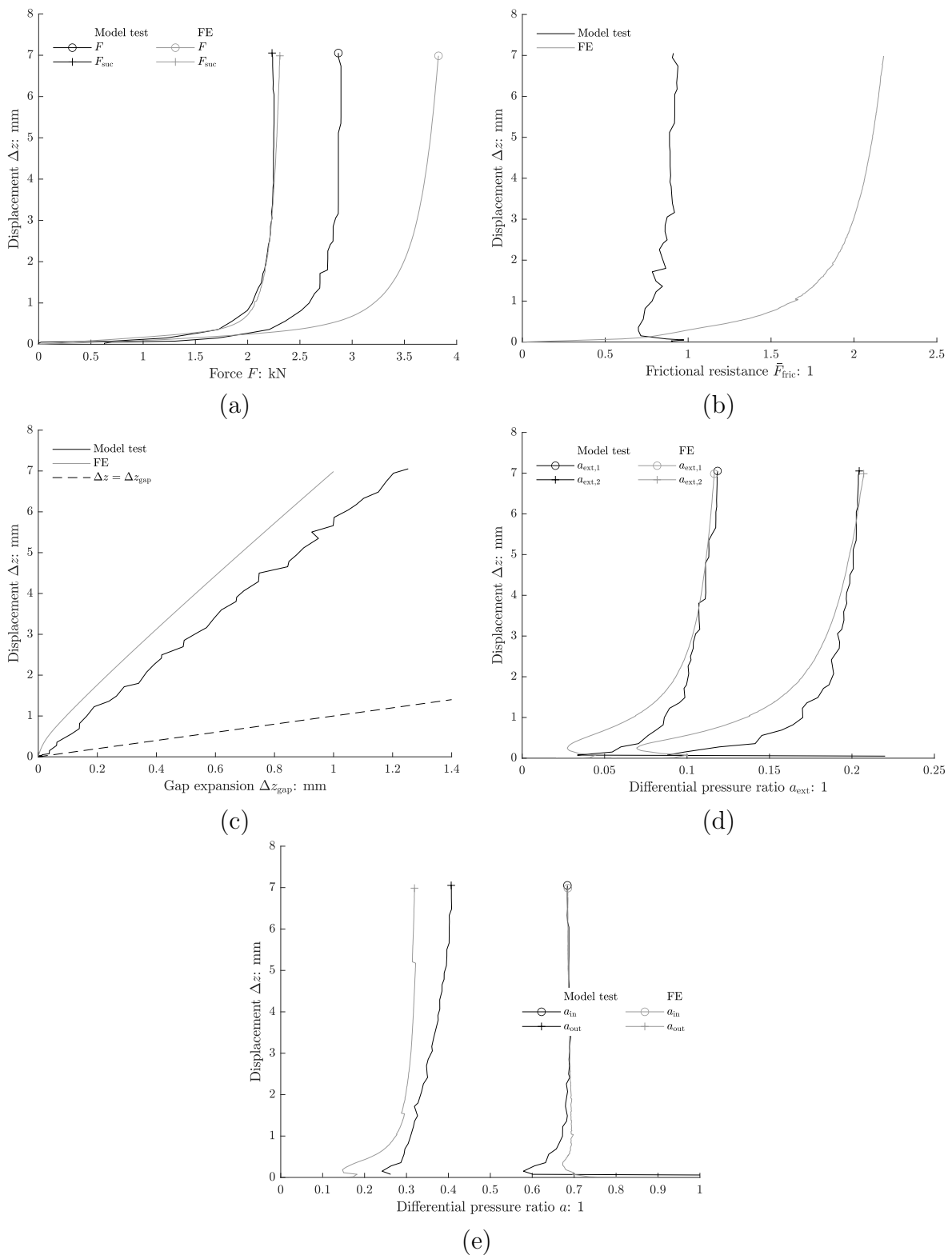
Figure A.2.3.4: Tensile test: force and suction force (a), frictional resistance (b), gap expansion (c), differential pressure ratio (external) (d) and differential pressure ratio (skirt) (e)

A.2.4 L500D510v9.6

Table A.2.4.1: Test summary

L	500 mm	DPS$_{ext,1}$		DPS$_{ext,2}$	
D	510 mm	r	z	r	z
T_w	18.3°C	510 mm	375.0 mm	510 mm	625.0 mm

Drained resistance			Tensile test		
z	425.1	mm	z	424.4	mm
z/D	0.85		z/D	0.85	
z_{plug}	52.5	mm	z_{plug}	52.0	mm
F_{dr}	0.63	kN	F_{max}	8.73	kN
$\Delta z_{F_{dr}}$	0.70	mm	$\Delta z_{F_{max}}$	12.84	mm
			v_z	9.62	mm/s
			t_{acc}	0.51	s

Table A.2.4.2: FE model parameters

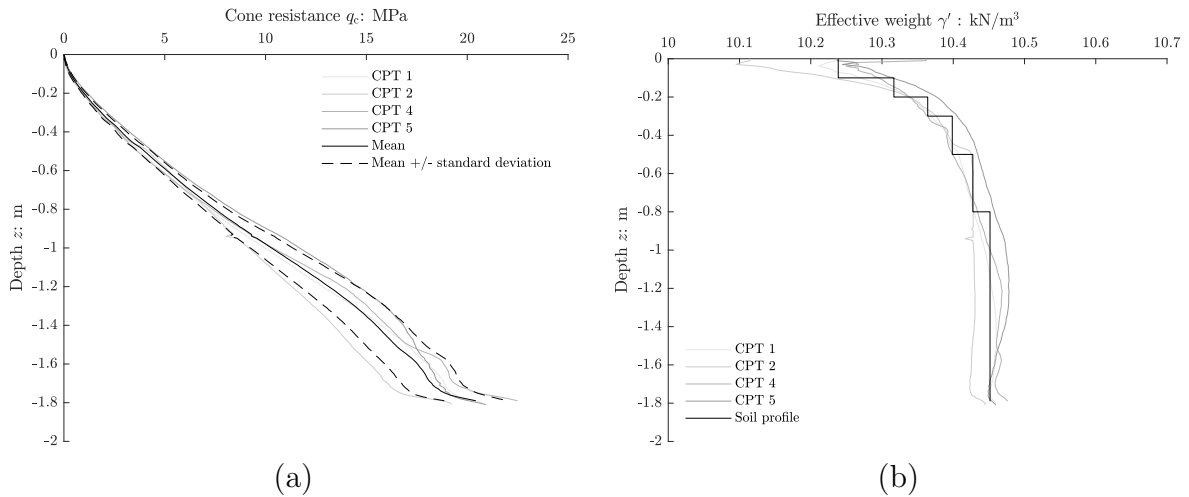| γ'	κ	λ	ν	ϕ'	ψ	k_i	k_i/k_o	k_0
10.41 kN/m³	350	0.4	0.2	45°	20°	3.7×10^{-4} m/s	1.5	0.439

Comments:

-

Figure A.2.4.1: Cone penetration test: cone resistance (a) and effective weight (b).
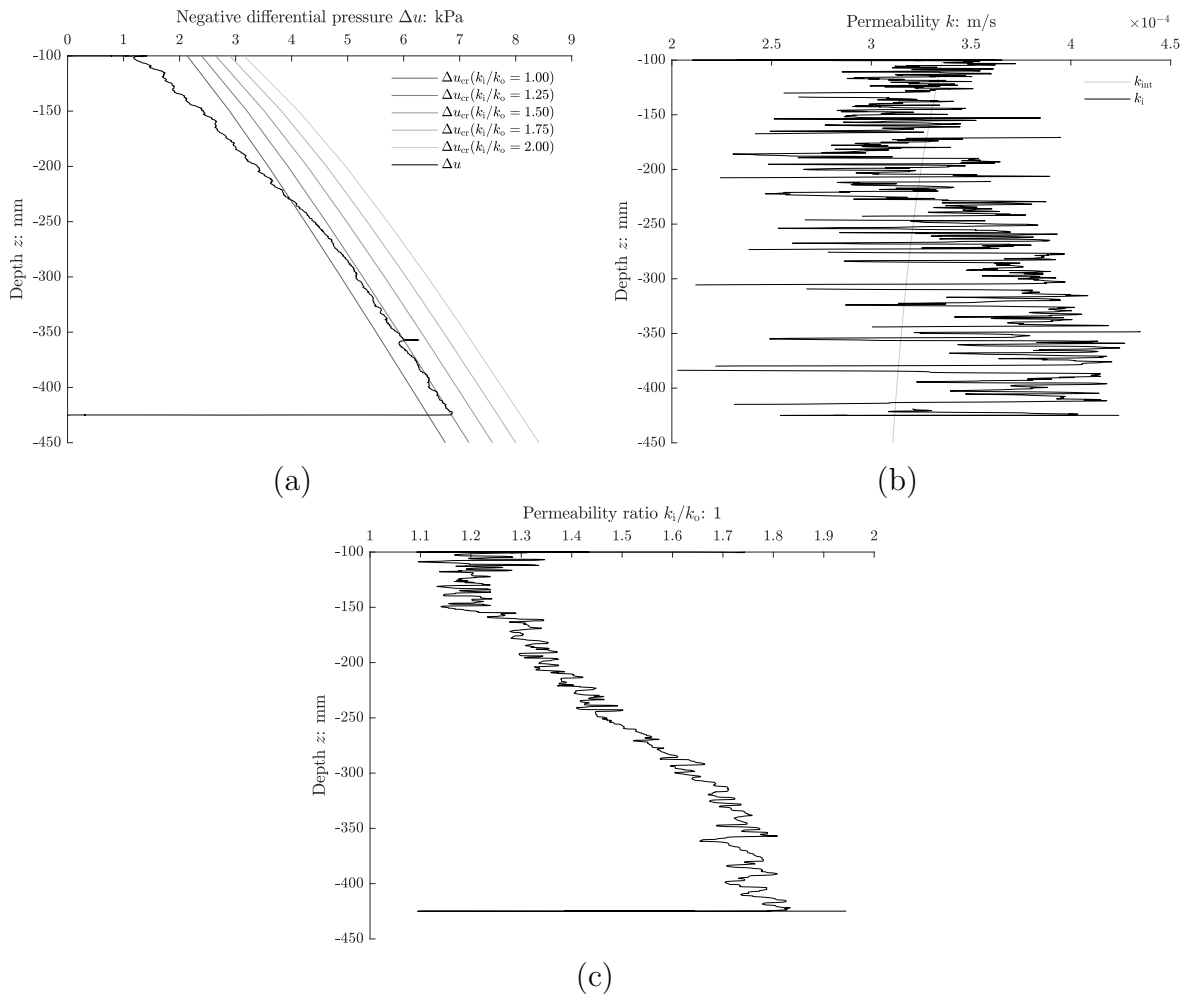
(a)

(b)

(c)

Figure A.2.4.2: Installation: negative differential pressure (a), hydraulic conductivity (b) and permeability ratio (c).
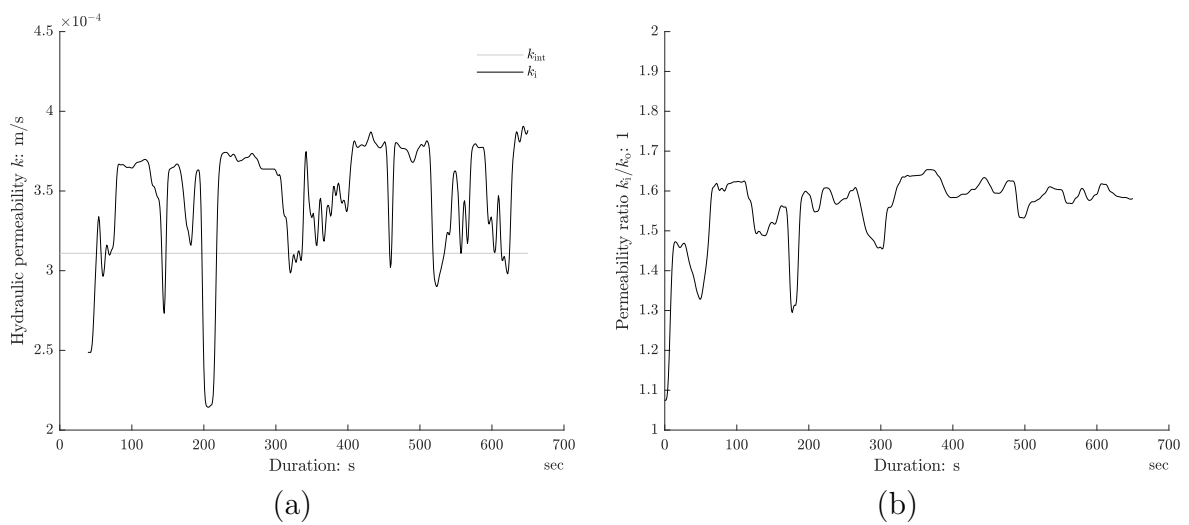

(a)

(b)

Figure A.2.4.3: Permeability test: hydraulic conductivity (a) and permeability ratio (b).
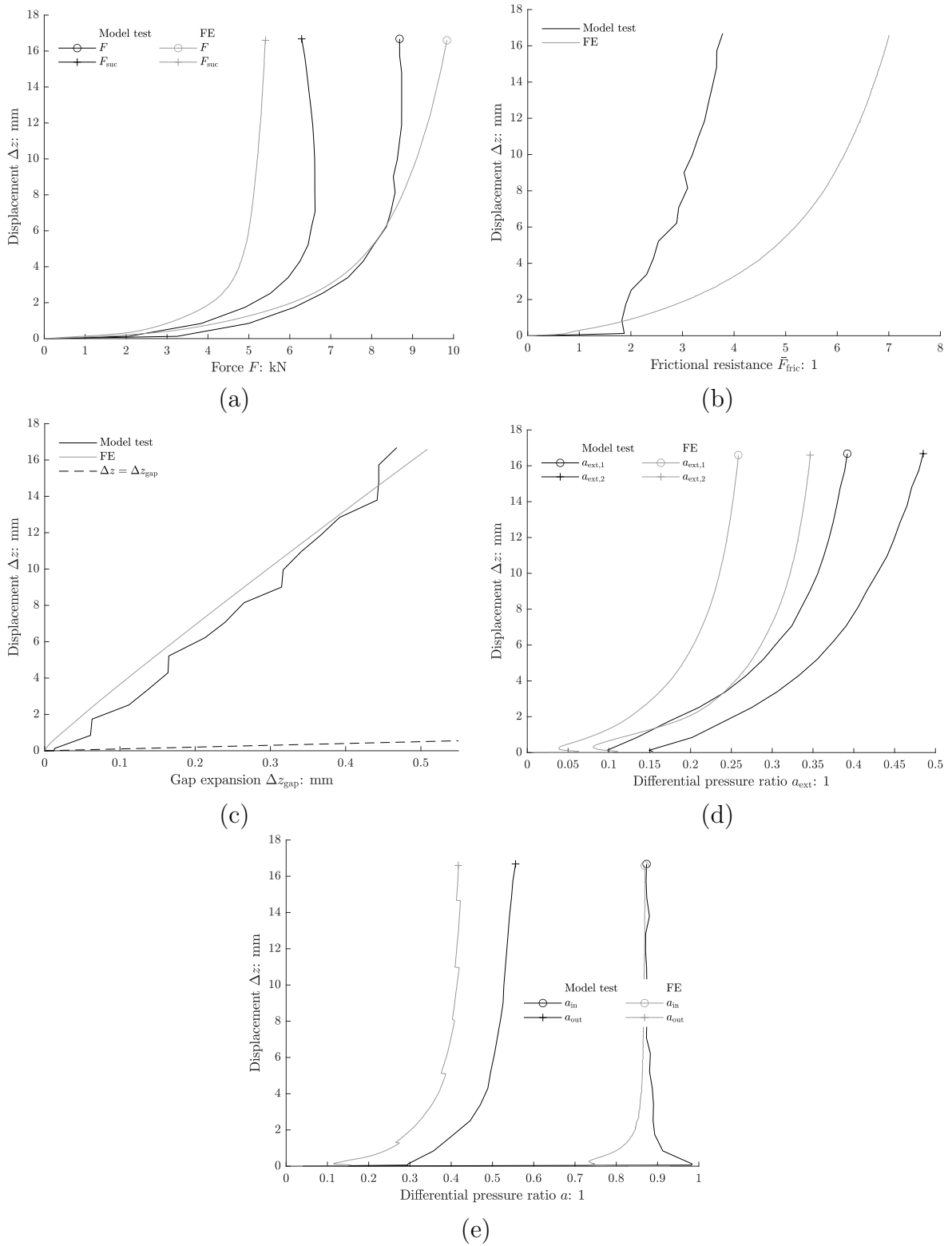
Figure A.2.4.4: Tensile test: force and suction force (a), frictional resistance (b), gap expansion (c), differential pressure ratio (external) (d) and differential pressure ratio (skirt) (e)

A.2.5 L250D510v0.9

Table A.2.5.1: Test summary

L	$250\,$mm	DPS$_{\text{ext,1}}$		DPS$_{\text{ext,2}}$	
D	$510\,$mm	r	z	r	z
T_{w}	$17.9°$C	$510\,$mm	$310.0\,$mm	$510\,$mm	$186.0\,$mm

Drained resistance			Tensile test		
z	212.3	mm	z	212.3	mm
z/D	0.85		z/D	0.85	
z_{plug}	20.2	mm	z_{plug}	19.1	mm
F_{dr}	0.24	kN	F_{max}	1.50	kN
$\Delta z_{F_{\text{dr}}}$	0.18	mm	$\Delta z_{F_{\text{max}}}$	2.55	mm
			v_z	0.85	mm/s
			t_{acc}	0.92	s

Table A.2.5.2: FE model parameters

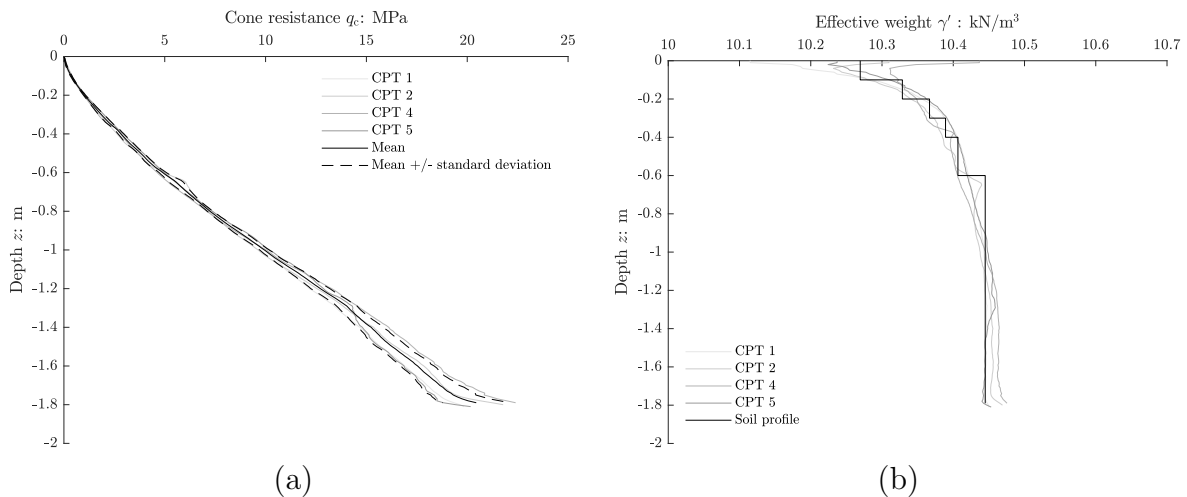| γ'	κ	λ	ν	ϕ'	ψ	k_{f}	$k_{\text{i}}/k_{\text{o}}$	k_0
$10.41\,$kN/m^3	350	0.4	0.2	$45°$	$20°$	$2.9\times10^{-4}\,$m/s	-	0.680

Comments:

-

Figure A.2.5.1: Cone penetration test: cone resistance (a) and effective weight (b).
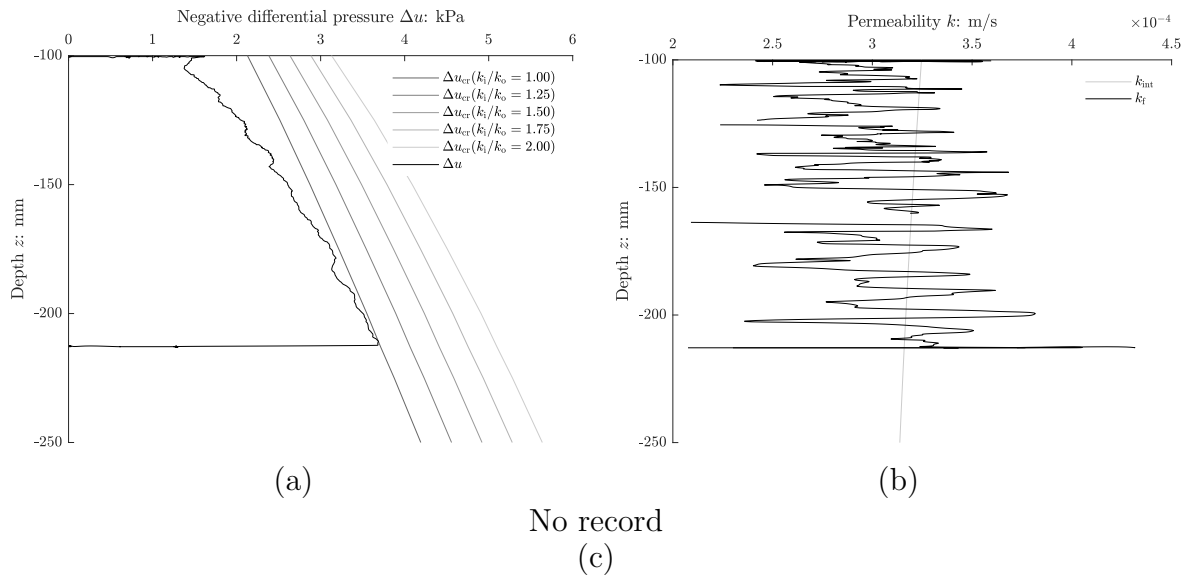
Figure A.2.5.2: Installation: negative differential pressure (a), hydraulic conductivity (b) and permeability ratio (c).
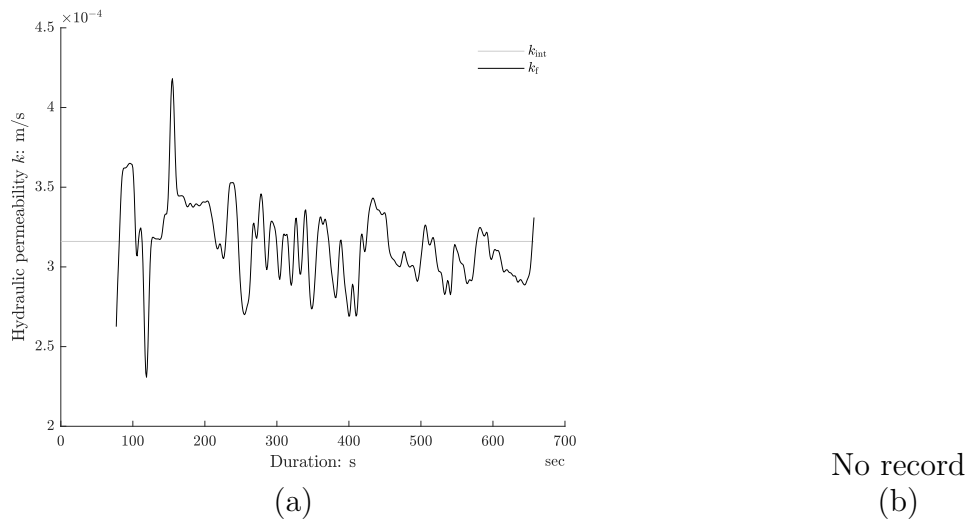

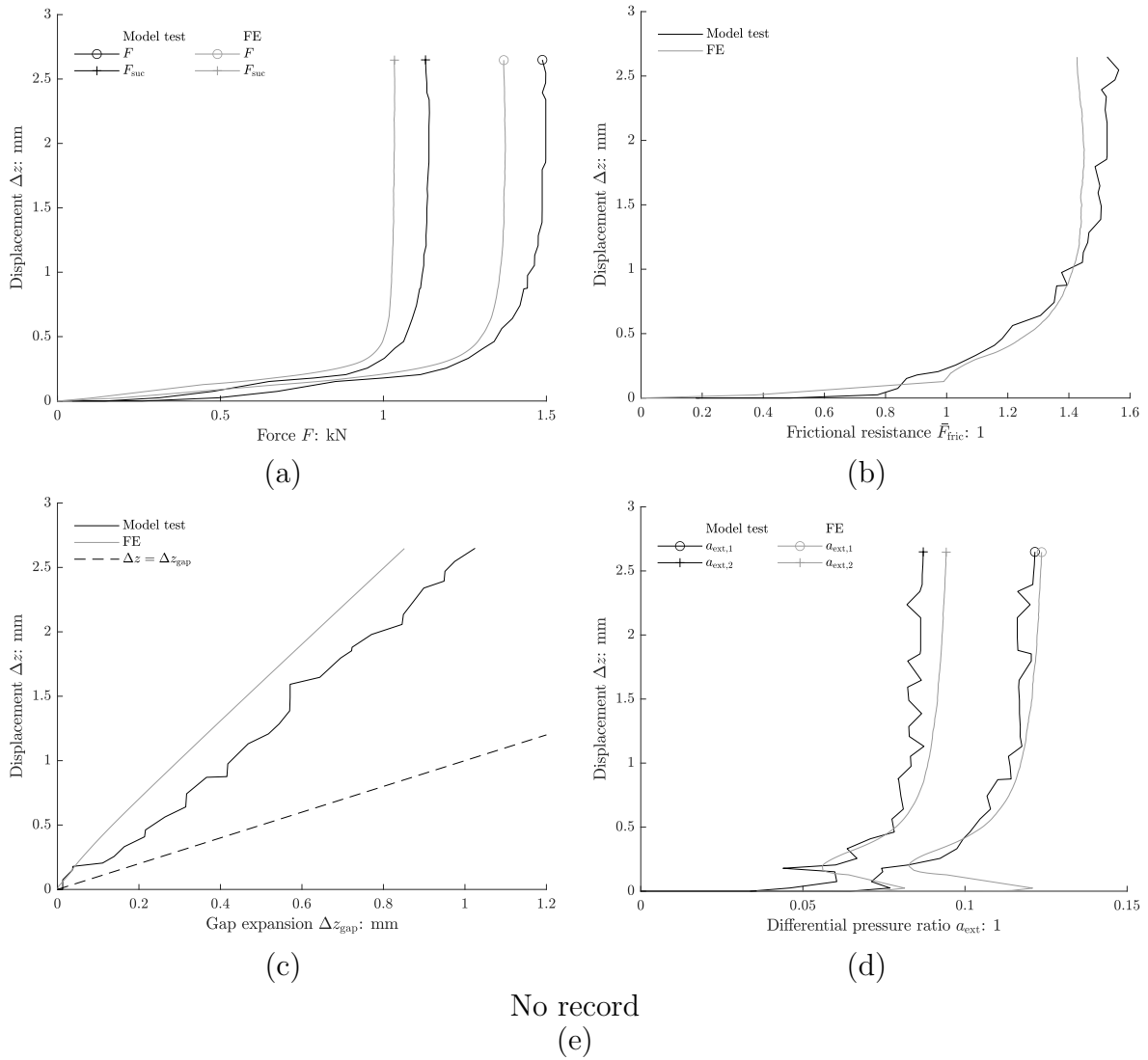*Figure A.2.5.3:* Permeability test: hydraulic conductivity (a) and permeability ratio (b).

Figure A.2.5.4: Tensile test: force and suction force (a), frictional resistance (b), gap expansion (c), differential pressure ratio (external) (d) and differential pressure ratio (skirt) (e)

A.2.6 L250D510v1.8

Table A.2.6.1: Test summary

L	250 mm	DPS$_{\text{ext},1}$		DPS$_{\text{ext},2}$	
D	510 mm	r	z	r	z
T_{w}	18.0°C	510 mm	310.5 mm	510 mm	185.5 mm

Drained resistance			Tensile test		
z	213.4	mm	z	213.0	mm
z/D	0.85		z/D	0.85	
z_{plug}	21.2	mm	z_{plug}	20.5	mm
F_{dr}	0.25	kN	F_{max}	2.41	kN
$\Delta z_{F_{\text{dr}}}$	0.18	mm	$\Delta z_{F_{\text{max}}}$	3.88	mm
			v_z	1.82	mm/s
			t_{acc}	0.83	s

Table A.2.6.2: FE model parameters

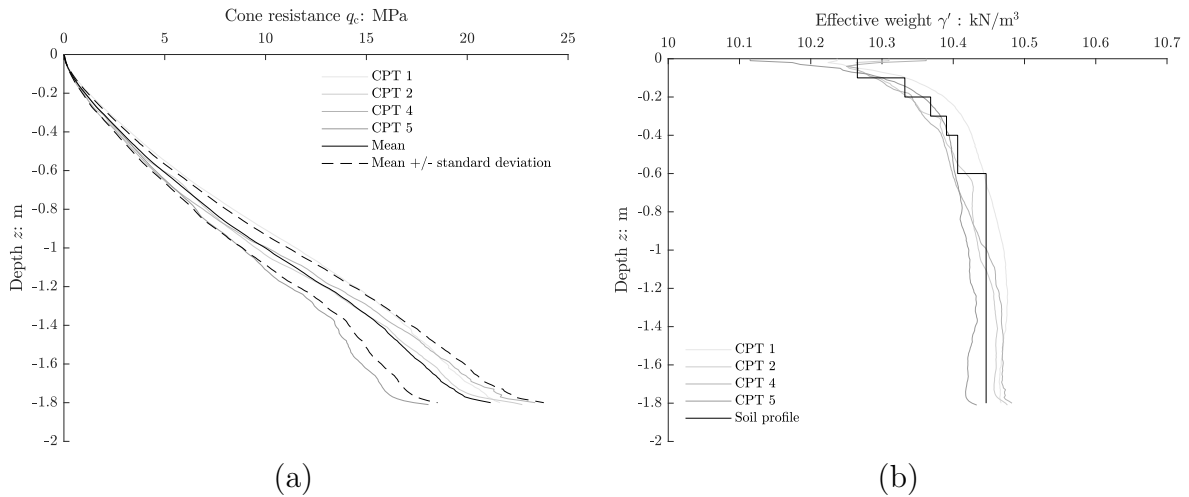| γ'	κ	λ	ν	ϕ'	ψ	k_{f}	$k_{\text{i}}/k_{\text{o}}$	k_0
10.41 kN/m³	350	0.4	0.2	45°	20°	2.8×10^{-4} m/s	-	0.688

Comments:
-

Figure A.2.6.1: Cone penetration test: cone resistance (a) and effective weight (b).
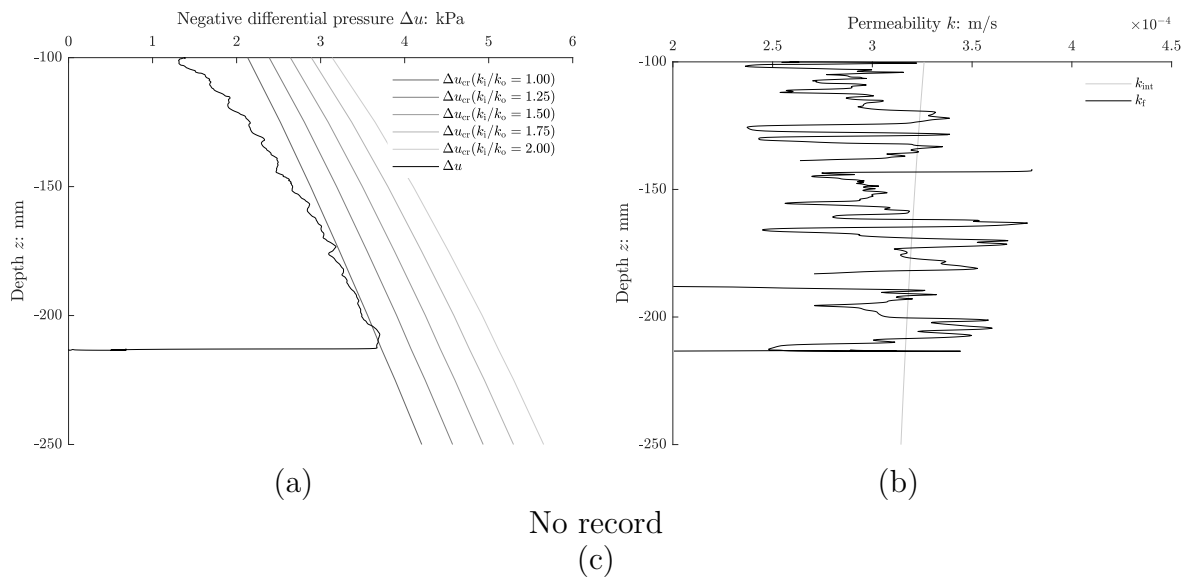
Figure A.2.6.2: Installation: negative differential pressure (a), hydraulic conductivity (b) and permeability ratio (c).
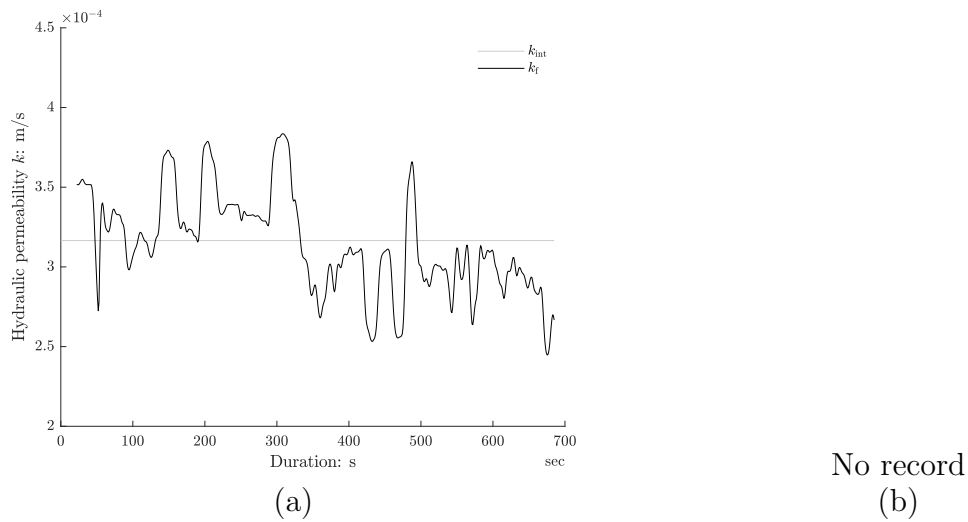

Figure A.2.6.3: Permeability test: hydraulic conductivity (a) and permeability ratio (b).
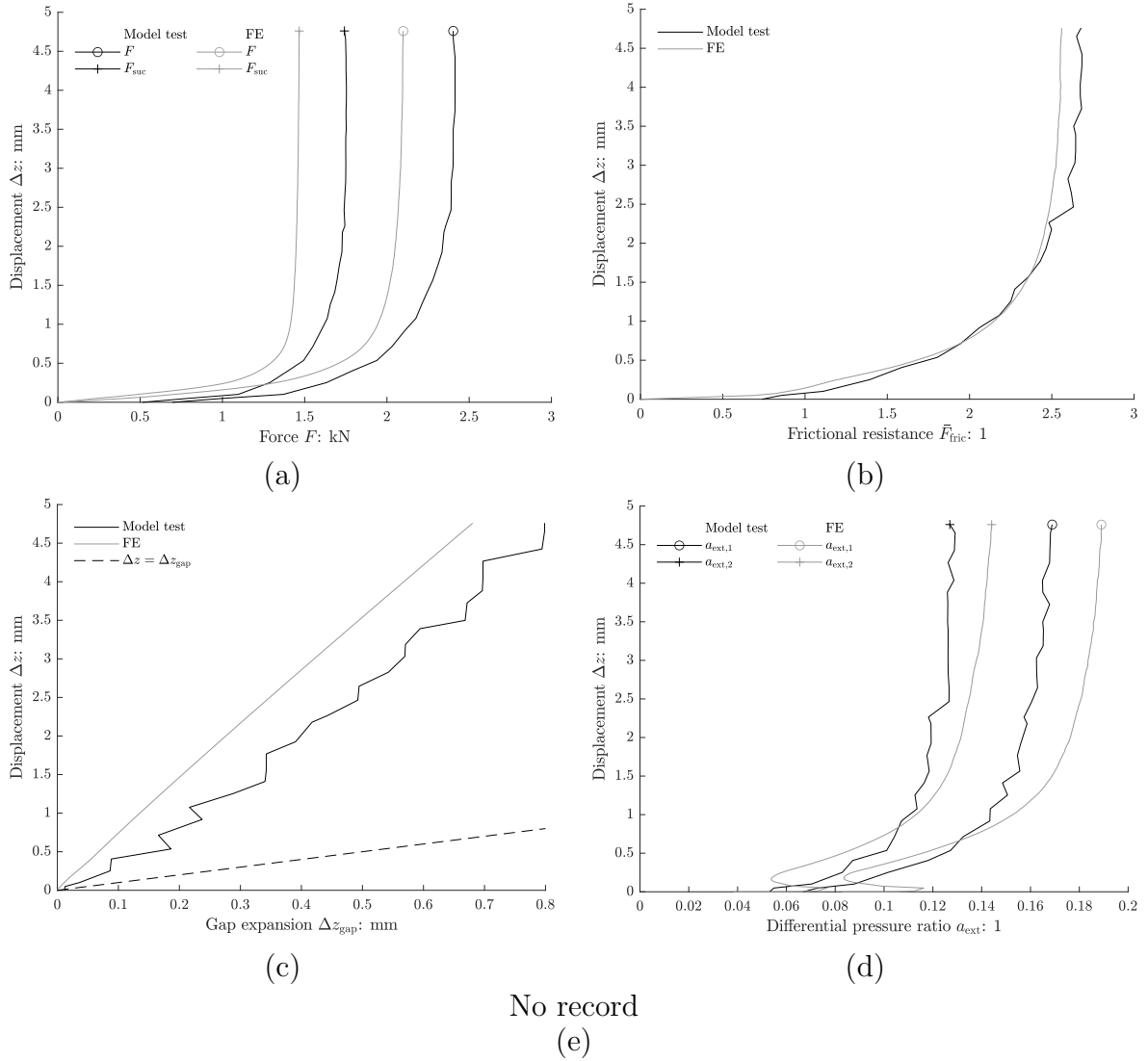
(a)

(b)

(c)

(d)

No record
(e)

Figure A.2.6.4: Tensile test: force and suction force (a), frictional resistance (b), gap expansion (c), differential pressure ratio (external) (d) and differential pressure ratio (skirt) (e)

A.2.7 L250D510v9.7

Table A.2.7.1: Test summary

L	$250\,\text{mm}$	DPS$_{\text{ext},1}$		DPS$_{\text{ext},2}$	
D	$510\,\text{mm}$	r	z	r	z
T_{w}	$18.3°\text{C}$	$510\,\text{mm}$	$310.0\,\text{mm}$	$510\,\text{mm}$	$185.0\,\text{mm}$

Drained resistance			Tensile test		
z	212.9	mm	z	212.2	mm
z/D	0.85		z/D	0.85	
z_{plug}	21.6	mm	z_{plug}	21.5	mm
F_{dr}	0.29	kN	F_{max}	8.08	kN
$\Delta z_{F_{\text{dr}}}$	0.12	mm	$\Delta z_{F_{\text{max}}}$	7.66	mm
			v_z	9.66	mm/s
			t_{acc}	0.40	s

Table A.2.7.2: FE model parameters

γ'	κ	λ	ν	ϕ'	ψ	k_{f}	$k_{\text{i}}/k_{\text{o}}$	k_0
$10.41\,\text{kN/m}^3$	350	0.4	0.2	$45°$	$20°$	$2.9\times10^{-4}\,\text{m/s}$	-	0.770

Comments:
-
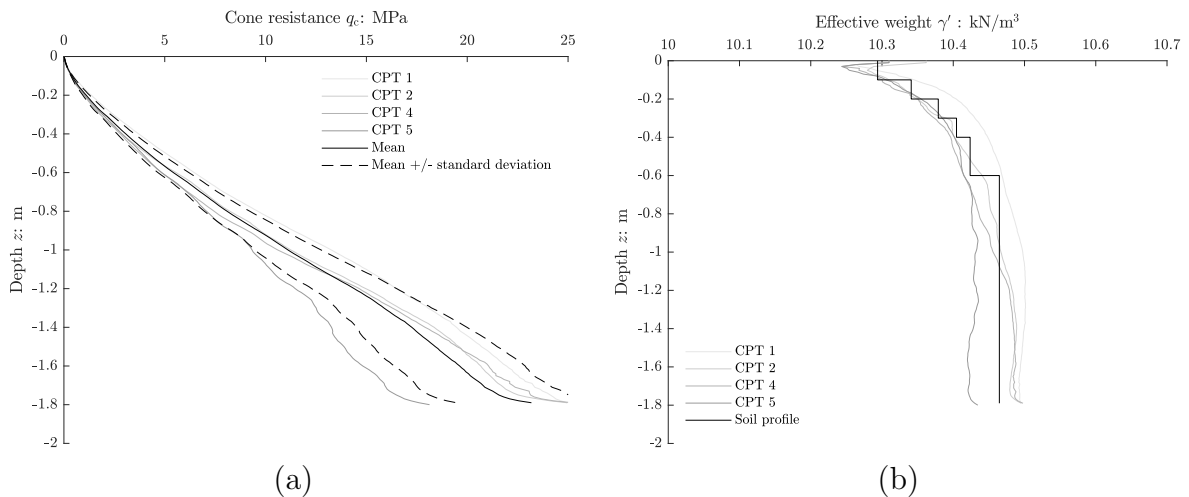
Figure A.2.7.1: Cone penetration test: cone resistance (a) and effective weight (b).

(a)

(b)

No record
(c)

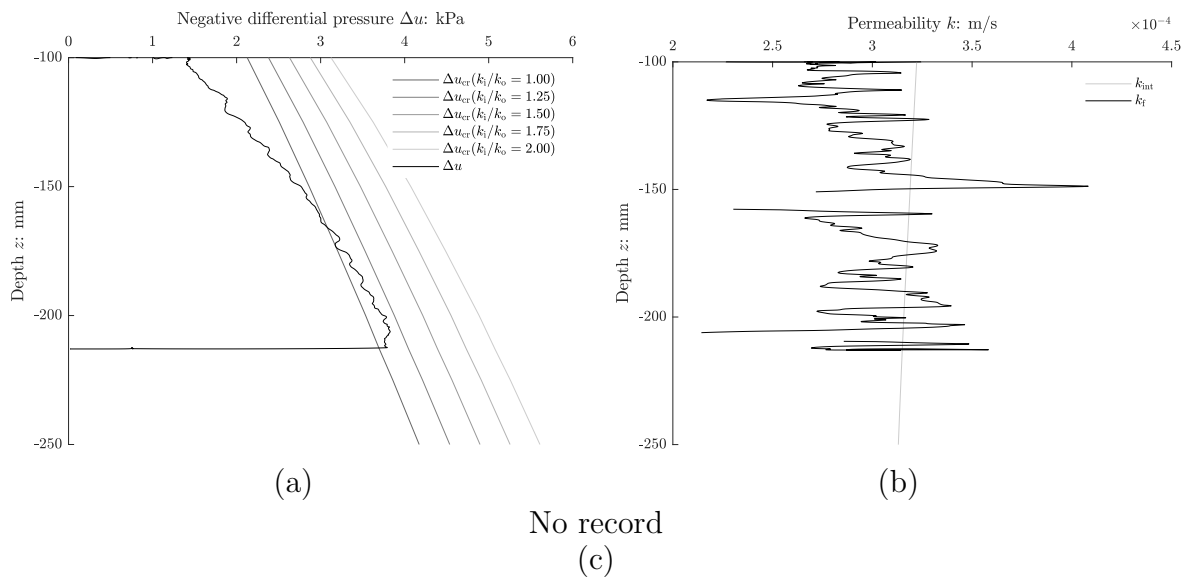*Figure A.2.7.2:* Installation: negative differential pressure (a), hydraulic conductivity (b) and permeability ratio (c).
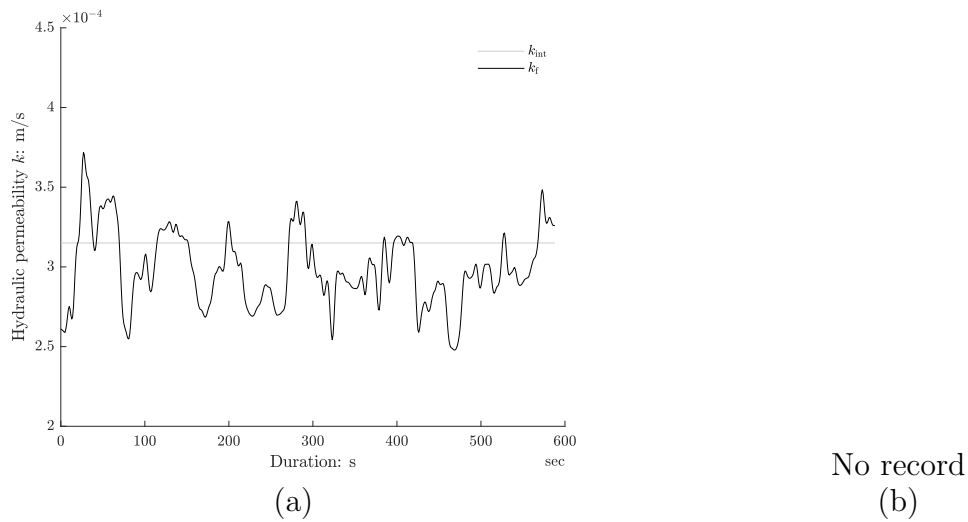

(a)

No record
(b)

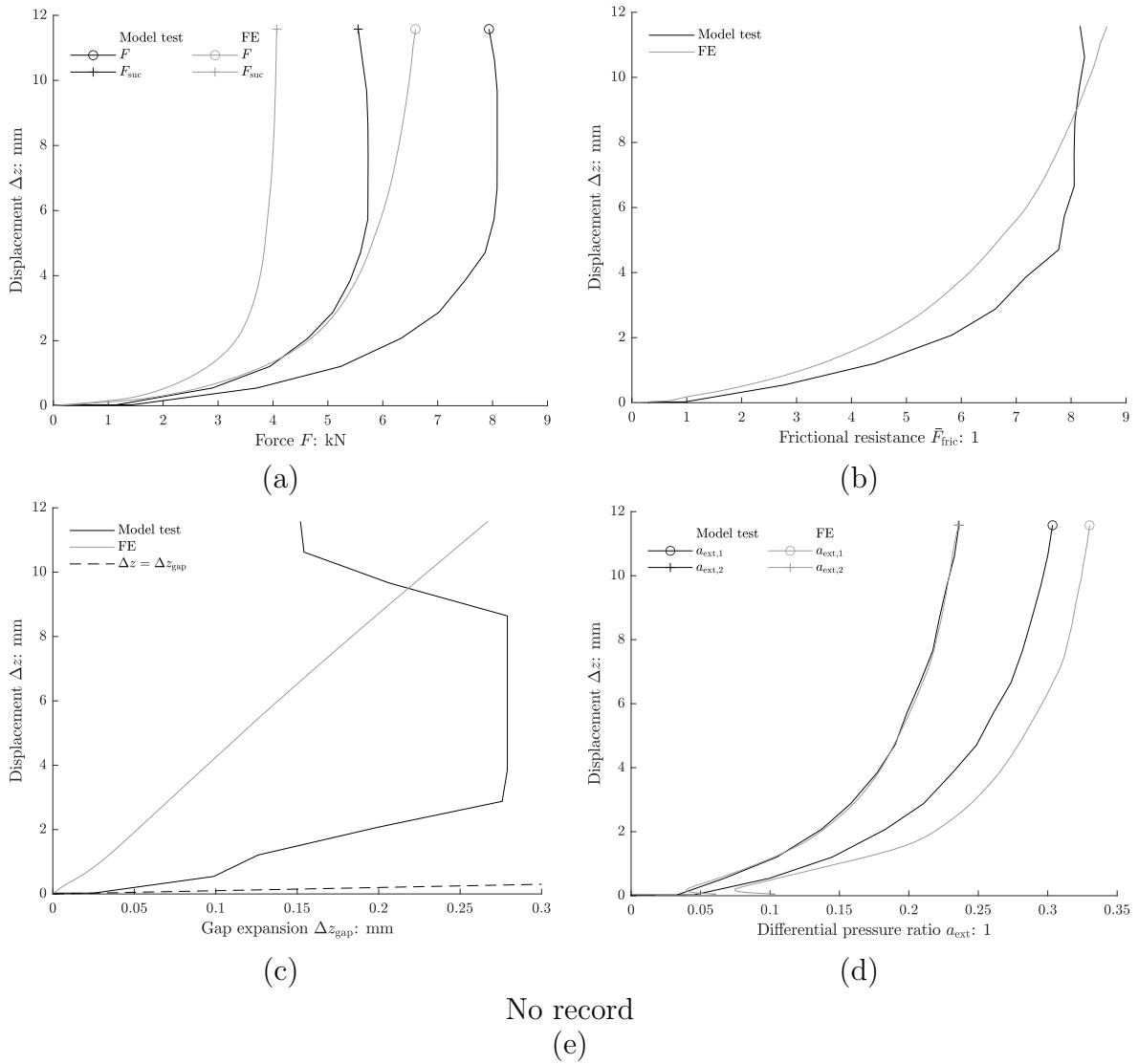*Figure A.2.7.3:* Permeability test: hydraulic conductivity (a) and permeability ratio (b).

Figure A.2.7.4: Tensile test: force and suction force (a), frictional resistance (b), gap expansion (c), differential pressure ratio (external) (d) and differential pressure ratio (skirt) (e)

A.2.8 L250D260v1.7

Table A.2.8.1: Test summary

L	250 mm	DPS$_{\text{ext},1}$		DPS$_{\text{ext},2}$	
D	260 mm	r	z	r	z
T_{w}	-	260 mm	225.0 mm	260 mm	225.0 mm

Drained resistance			Tensile test		
z	214.5	mm	z	211.8	mm
z/D	0.86		z/D	0.85	
z_{plug}	29.8	mm	z_{plug}	28.7	mm
F_{dr}	0.16	kN	F_{max}	0.45	kN
$\Delta z_{F_{\text{dr}}}$	0.09	mm	$\Delta z_{F_{\text{max}}}$	2.95	mm
			v_z	1.74	mm/s
			t_{acc}	0.45	s

Table A.2.8.2: FE model parameters

γ'	κ	λ	ν	ϕ'	ψ	k_{f}	$k_{\text{i}}/k_{\text{o}}$	k_0
10.41 kN/m^3	350	0.4	0.2	45°	20°	3.1×10^{-4} m/s	-	0.943

Comments:

-

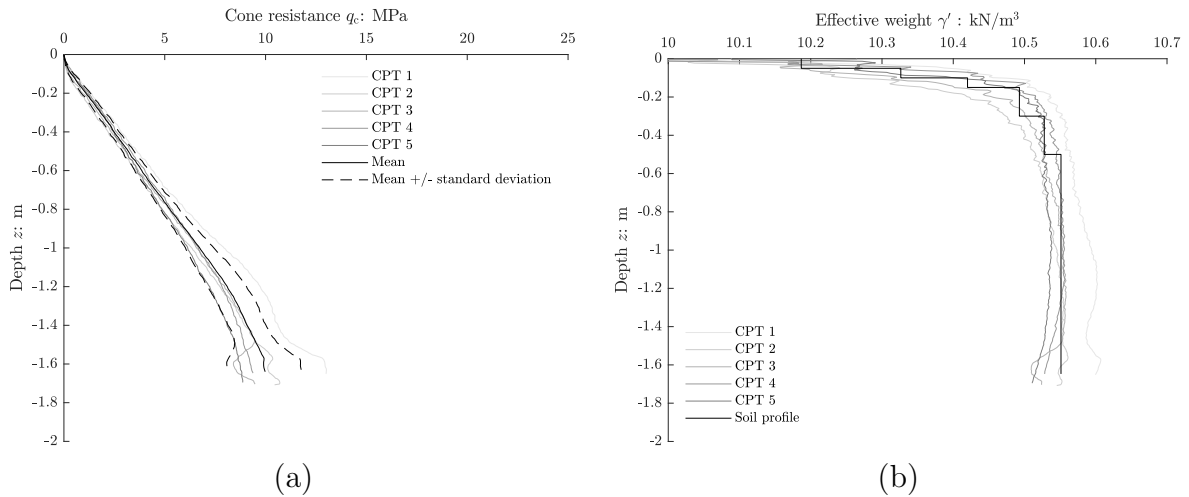*Figure A.2.8.1:* Cone penetration test: cone resistance (a) and effective weight (b).

Negative differential pressure Δu: kPa

Depth z: mm

$\Delta u_{cr}(k_i/k_o = 1.00)$
$\Delta u_{cr}(k_i/k_o = 1.25)$
$\Delta u_{cr}(k_i/k_o = 1.50)$
$\Delta u_{cr}(k_i/k_o = 1.75)$
$\Delta u_{cr}(k_i/k_o = 2.00)$
Δu

(a)

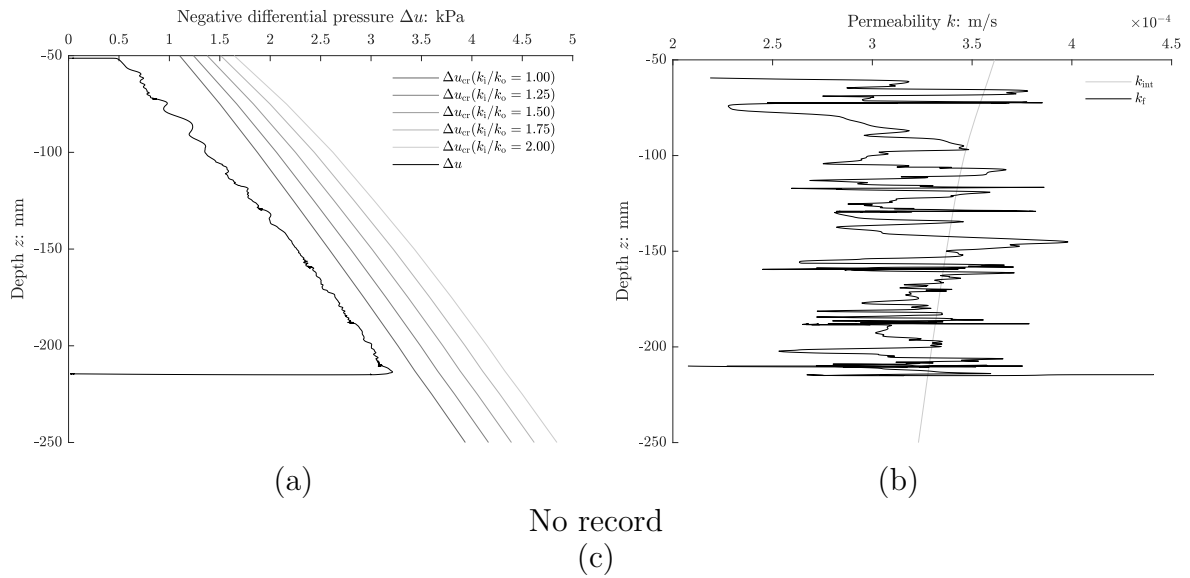Permeability k: m/s $\times 10^{-4}$

Depth z: mm

k_{int}
k_f

(b)

No record

(c)

Figure A.2.8.2: Installation: negative differential pressure (a), hydraulic conductivity (b) and permeability ratio (c).

$\times 10^{-4}$

Hydraulic permeability k: m/s

k_{int}
k_f

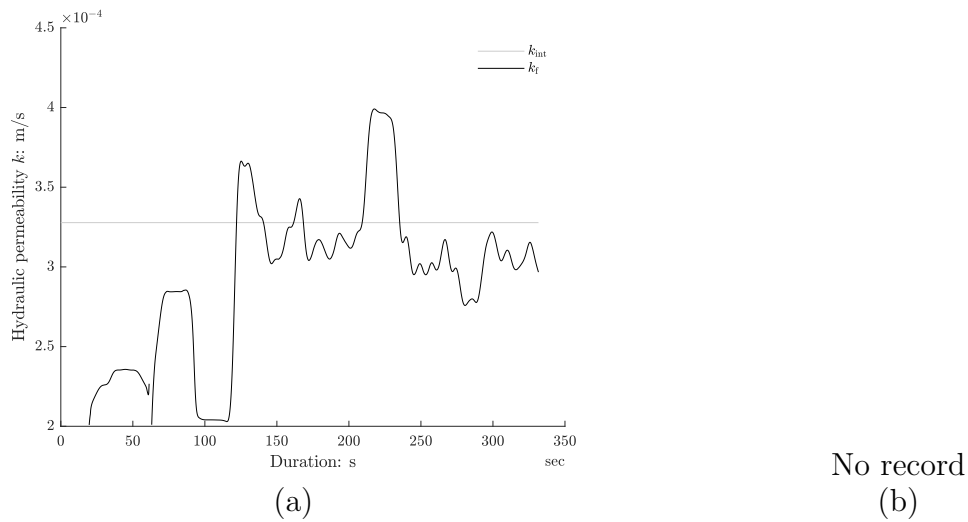Duration: s sec

(a)

No record

(b)

Figure A.2.8.3: Permeability test: hydraulic conductivity (a) and permeability ratio (b).
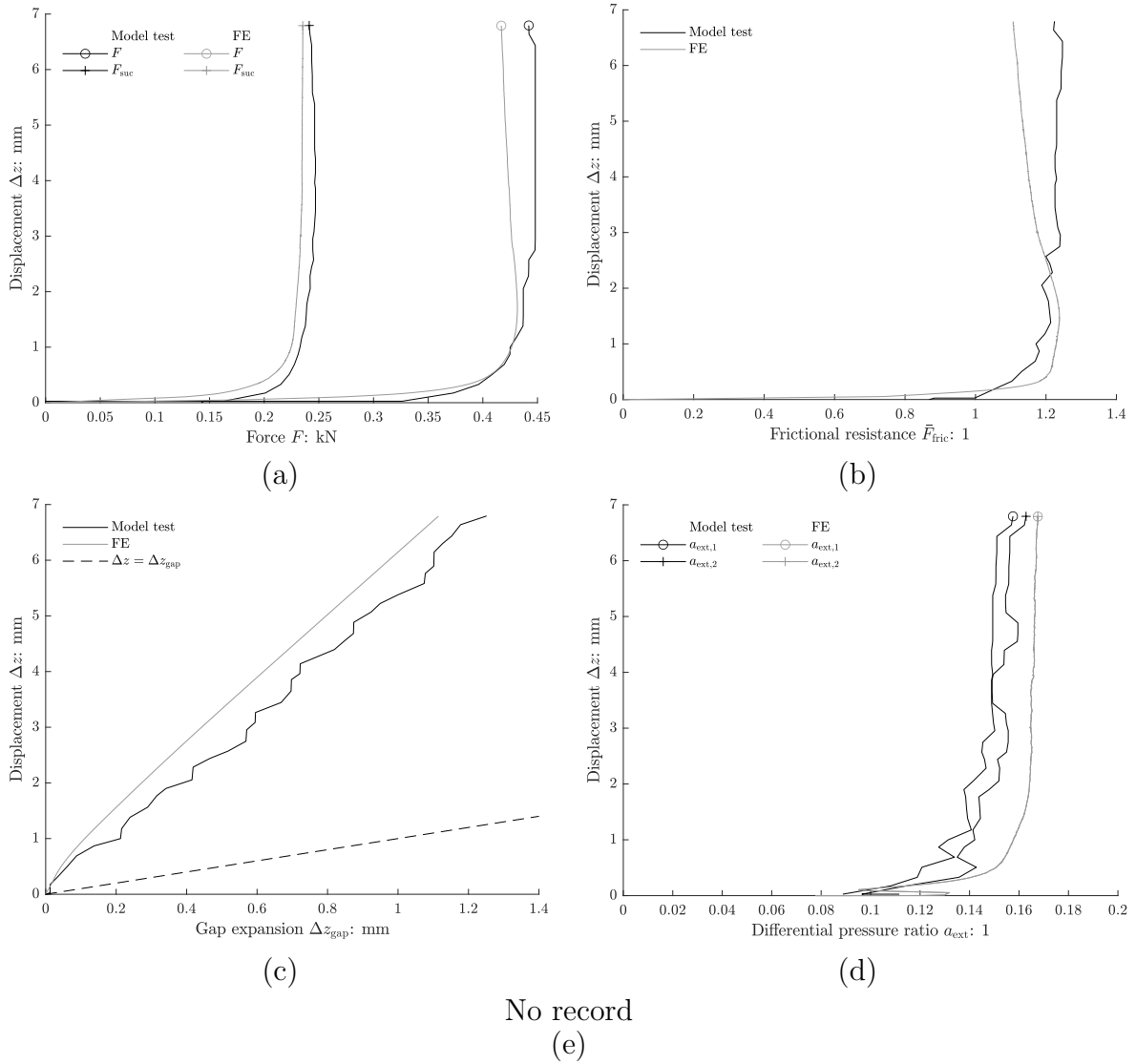
Figure A.2.8.4: Tensile test: force and suction force (a), frictional resistance (b), gap expansion (c), differential pressure ratio (external) (d) and differential pressure ratio (skirt) (e)

A.2.9 L250D260v9.6

Table A.2.9.1: Test summary

L	250 mm	DPS$_{ext,1}$		DPS$_{ext,2}$	
D	260 mm	r	z	r	z
T_w	19.2°C	260 mm	221.0 mm	260 mm	219.0 mm

Drained resistance			Tensile test		
z	220.3	mm	z	217.6	mm
z/D	0.88		z/D	0.87	
z_{plug}	21.1	mm	z_{plug}	20.6	mm
F_{dr}	0.14	kN	F_{max}	1.15	kN
$\Delta z_{F_{dr}}$	0.30	mm	$\Delta z_{F_{max}}$	8.51	mm
			v_z	9.56	mm/s
			t_{acc}	0.42	s

Table A.2.9.2: FE model parameters

γ'	κ	λ	ν	ϕ'	ψ	k_f	k_i/k_o	k_0
10.41 kN/m^3	350	0.4	0.2	45°	20°	3.2×10^{-4} m/s	-	0.776

Comments:
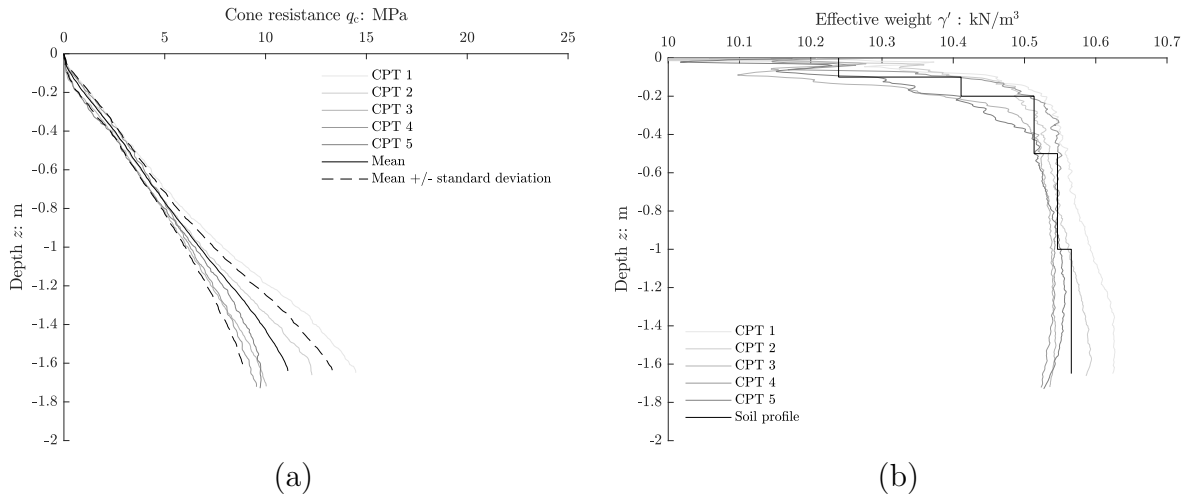No permeability test conducted.

Figure A.2.9.1: Cone penetration test: cone resistance (a) and effective weight (b).
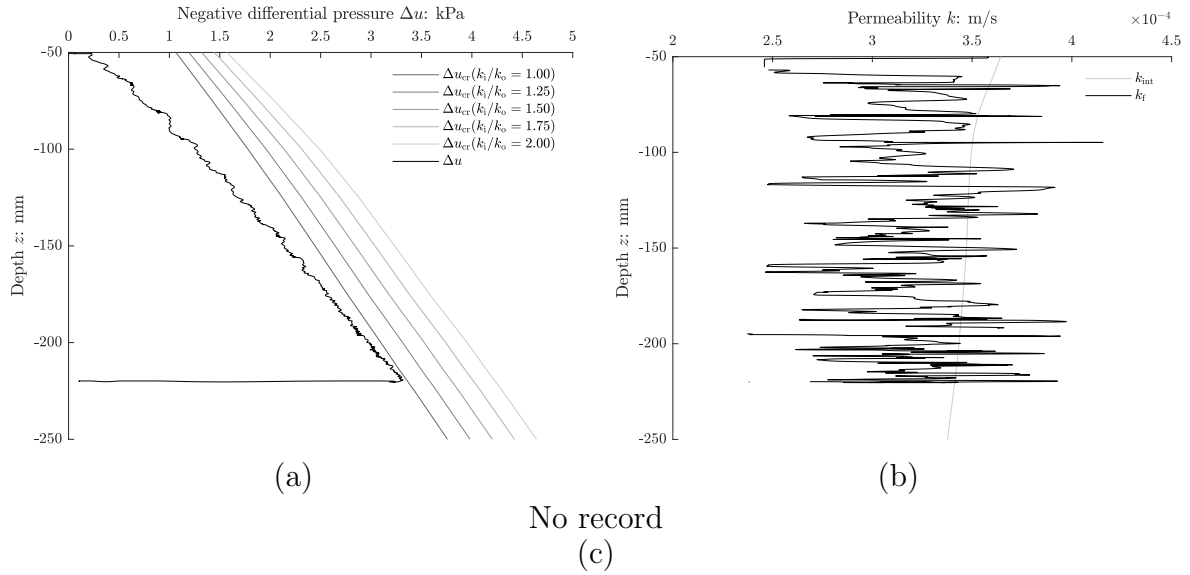
Figure A.2.9.2: Installation: negative differential pressure (a), hydraulic conductivity (b) and permeability ratio (c).

No record
(a)

No record
(b)

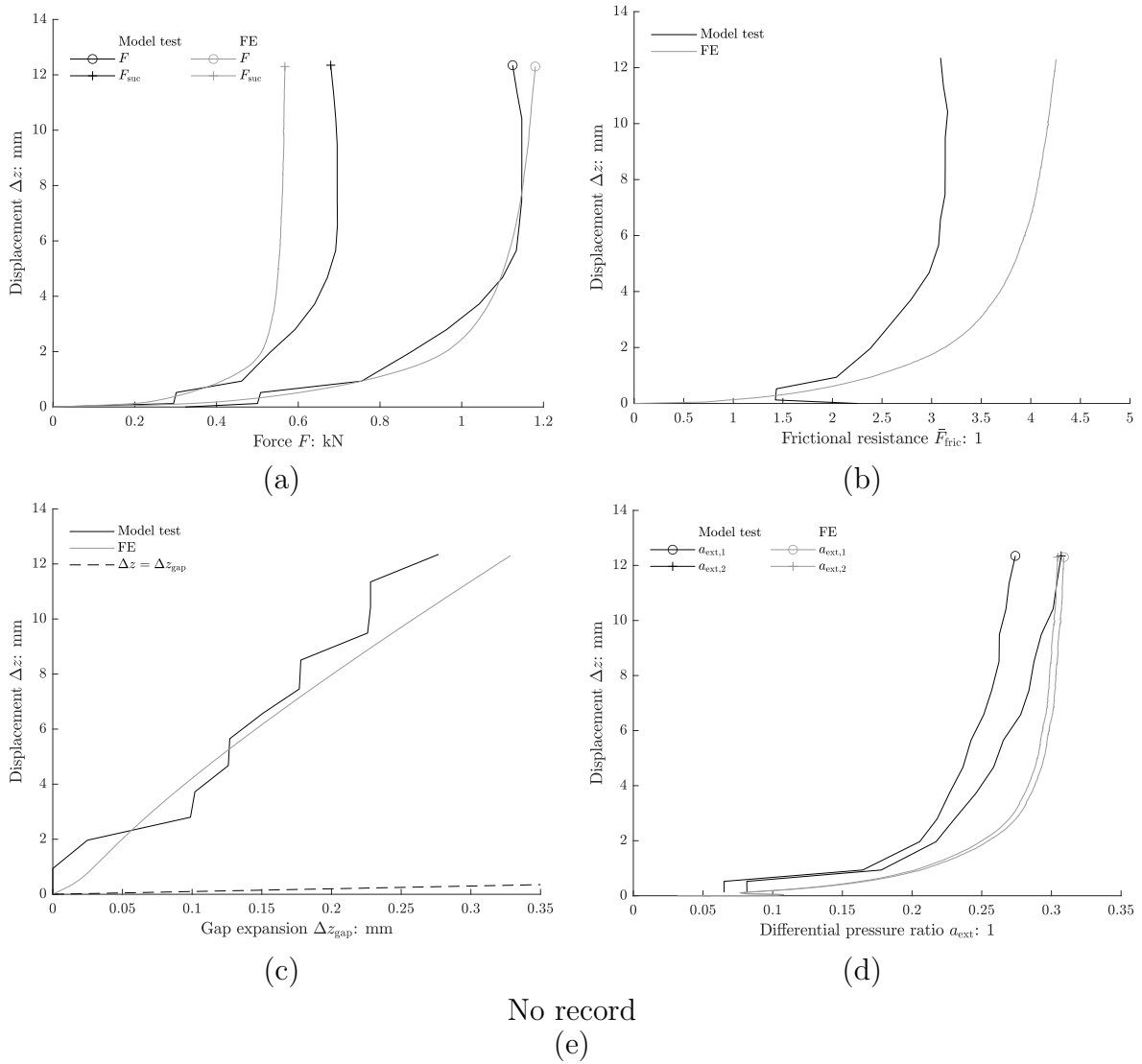*Figure A.2.9.3:* Permeability test: hydraulic conductivity (a) and permeability ratio (b).

Figure A.2.9.4: Tensile test: force and suction force (a), frictional resistance (b), gap expansion (c), differential pressure ratio (external) (d) and differential pressure ratio (skirt) (e)

A.2.10 L250D260v19.5

Table A.2.10.1: Test summary

L	250 mm	DPS$_{ext,1}$		DPS$_{ext,2}$	
D	260 mm	r	z	r	z
T_w	19.2°C	260 mm	218.0 mm	260 mm	220.0 mm

Drained resistance			Tensile test		
z	212.8	mm	z	211.5	mm
z/D	0.85		z/D	0.85	
z_{plug}	28.4	mm	z_{plug}	28.0	mm
F_{dr}	0.10	kN	F_{max}	2.04	kN
$\Delta z_{F_{dr}}$	0.32	mm	$\Delta z_{F_{max}}$	5.46	mm
			v_z	19.5	mm/s
			t_{acc}	0.24	s

Table A.2.10.2: FE model parameters

γ'	κ	λ	ν	ϕ'	ψ	k_f	k_i/k_o	k_0
10.41 kN/m³	350	0.4	0.2	45°	20°	3.0×10^{-4} m/s	-	0.589

Comments:
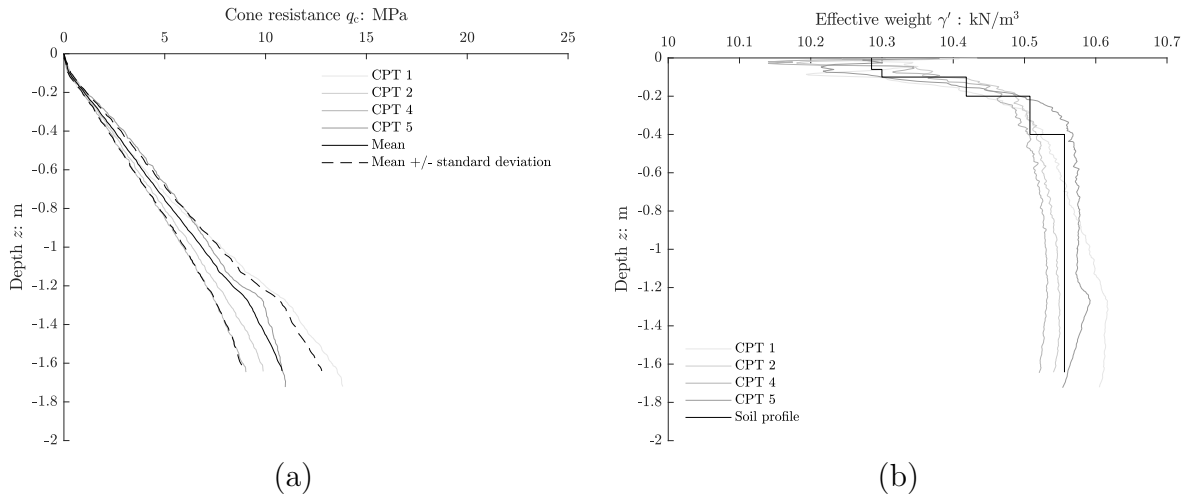No permeability test conducted.

Figure A.2.10.1: Cone penetration test: cone resistance (a) and effective weight (b).
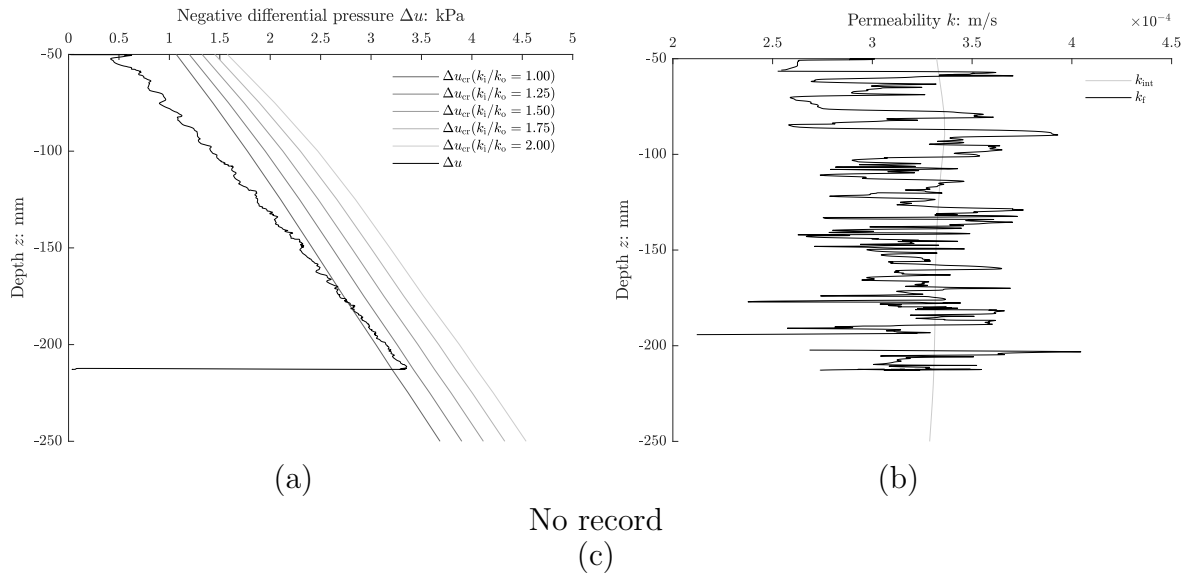
Figure A.2.10.2: Installation: negative differential pressure (a), hydraulic conductivity (b) and permeability ratio (c).

No record
(a)

No record
(b)

Figure A.2.10.3: Permeability test: hydraulic conductivity (a) and permeability ratio (b).
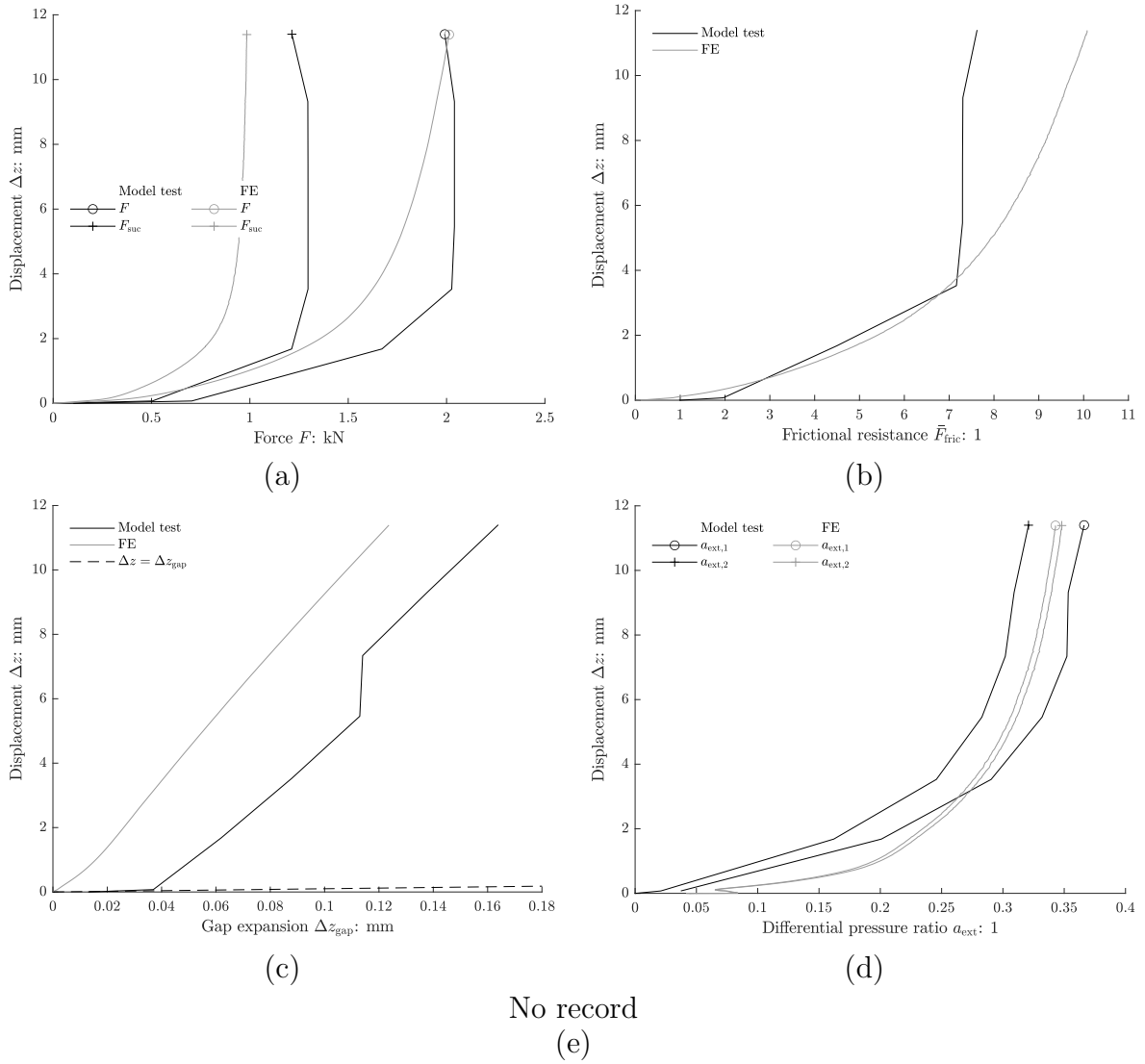
(a)

(b)

(c)

(d)

No record
(e)

Figure A.2.10.4: Tensile test: force and suction force (a), frictional resistance (b), gap expansion (c), differential pressure ratio (external) (d) and differential pressure ratio (skirt) (e)

A.2.11 L250D260v48.8

Table A.2.11.1: Test summary

L	250 mm	\multicolumn{2}{c}{DPS$_{\text{ext},1}$}	\multicolumn{2}{c}{DPS$_{\text{ext},2}$}
D	260 mm	r	z	r	z
T_{w}	-	390 mm	231.0 mm	390 mm	231.0 mm

\multicolumn{3}{c}{Drained resistance}	\multicolumn{3}{c}{Tensile test}
z	221.8	mm	z	218.3	mm
z/D	0.89		z/D	0.87	
z_{plug}	23.6	mm	z_{plug}	22.7	mm
F_{dr}	0.12	kN	F_{max}	13.44	kN
$\Delta z_{F_{\text{dr}}}$	0.24	mm	$\Delta z_{F_{\text{max}}}$	3.96	mm
			v_z	48.8	mm/s
			t_{acc}	0.25	s

Table A.2.11.2: FE model parameters

γ'	κ	λ	ν	ϕ'	ψ	k_{f}	$k_{\text{i}}/k_{\text{o}}$	k_0
10.41 kN/m^3	350	0.4	0.2	45°	20°	3.4×10^{-4} m/s	-	0.653

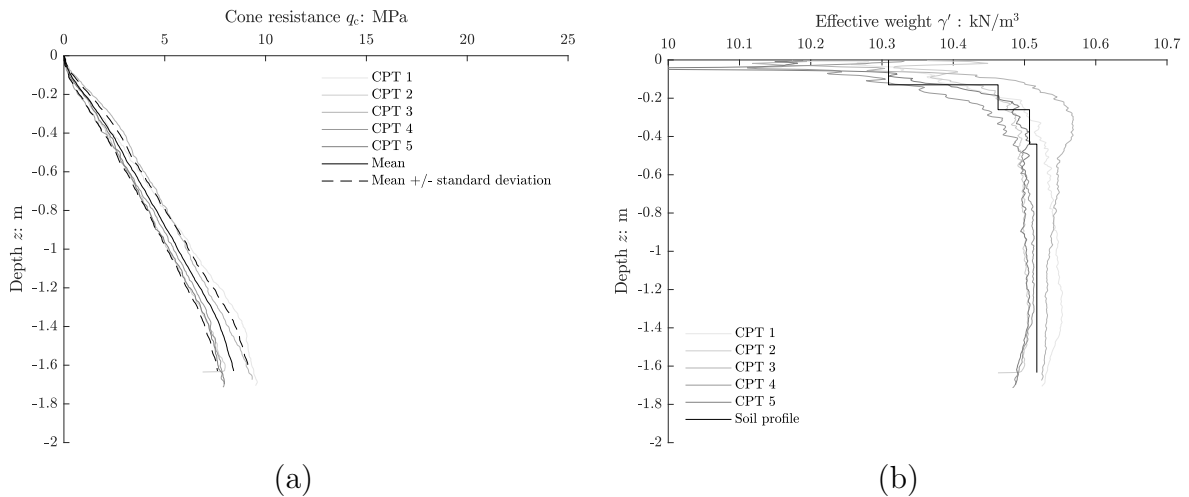Comments:
No permeability test conducted.

Figure A.2.11.1: Cone penetration test: cone resistance (a) and effective weight (b).
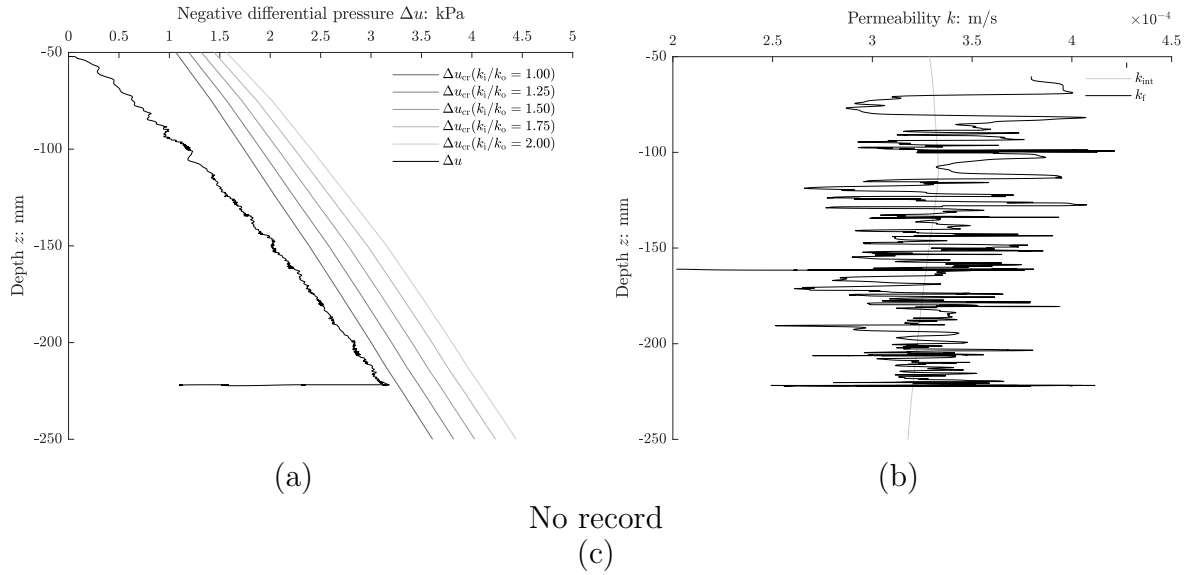
Figure A.2.11.2: Installation: negative differential pressure (a), hydraulic conductivity (b) and permeability ratio (c).

Figure A.2.11.3: Permeability test: hydraulic conductivity (a) and permeability ratio (b).
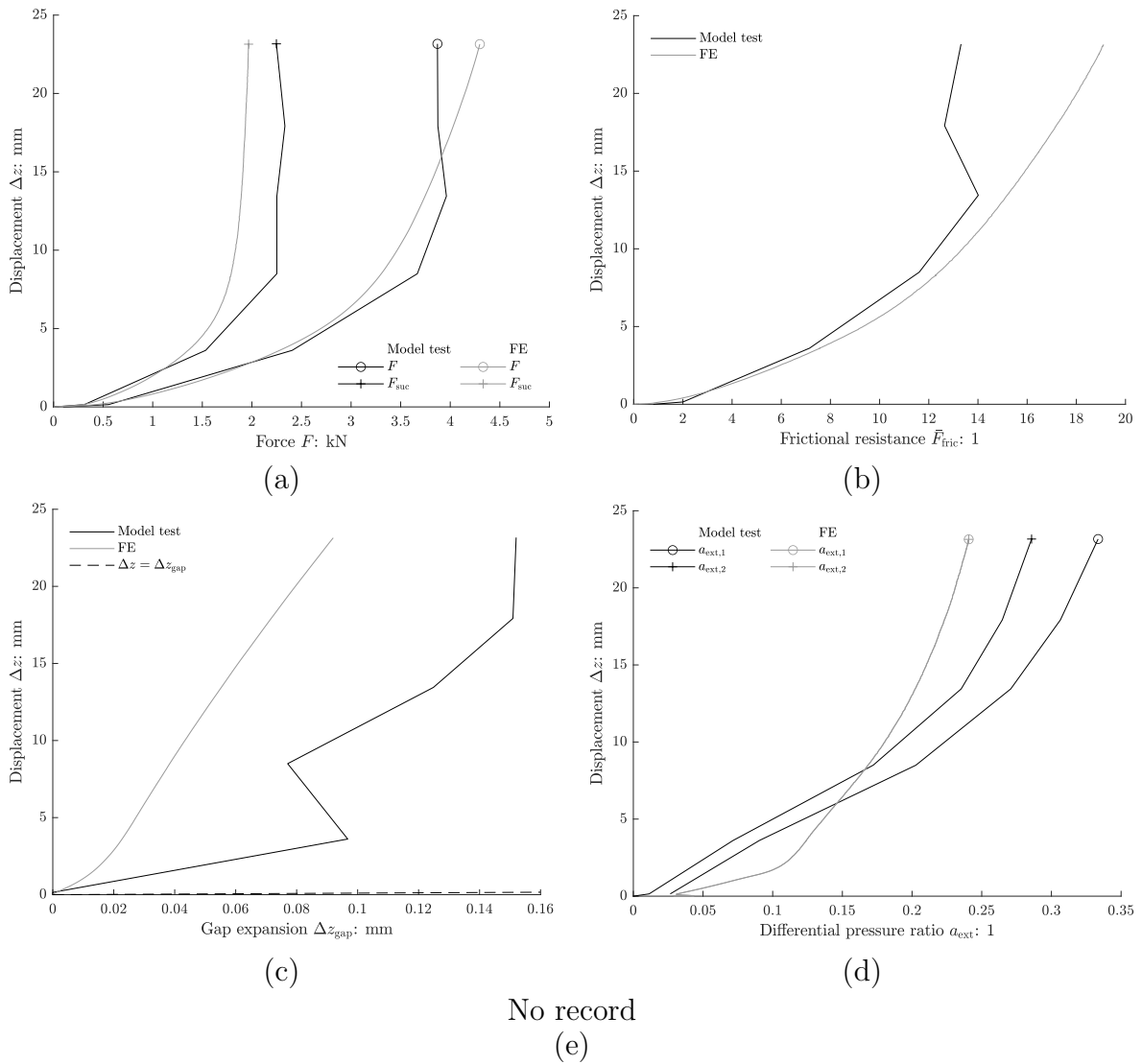
Figure A.2.11.4: Tensile test: force and suction force (a), frictional resistance (b), gap expansion (c), differential pressure ratio (external) (d) and differential pressure ratio (skirt) (e)

A.2.12 L125D135v9.8

Table A.2.12.1: Test summary

L	125 mm	DPS$_{\text{ext,1}}$		DPS$_{\text{ext,2}}$	
D	135 mm	r	z	r	z
T_{w}	19.3°C	460 mm	250.0 mm	460 mm	150.0 mm

Drained resistance			Tensile test		
z	106.4	mm	z	105.9	mm
z/D	0.85		z/D	0.85	
z_{plug}	-	mm	z_{plug}	-	mm
F_{dr}	0.02	kN	F_{max}	0.18	kN
$\Delta z_{F_{\text{dr}}}$	0.05	mm	$\Delta z_{F_{\text{max}}}$	1.63	mm
			v_z	9.75	mm/s
			t_{acc}	0.28	s

Table A.2.12.2: FE model parameters

γ'	κ	λ	ν	ϕ'	ψ	k_{f}	$k_{\text{i}}/k_{\text{o}}$	k_0
10.41 kN/m^3	350	0.4	0.2	45°	20°	3.0×10^{-4} m/s	-	0.905

Comments:
No measurement of gap expansion due to defective sensor.
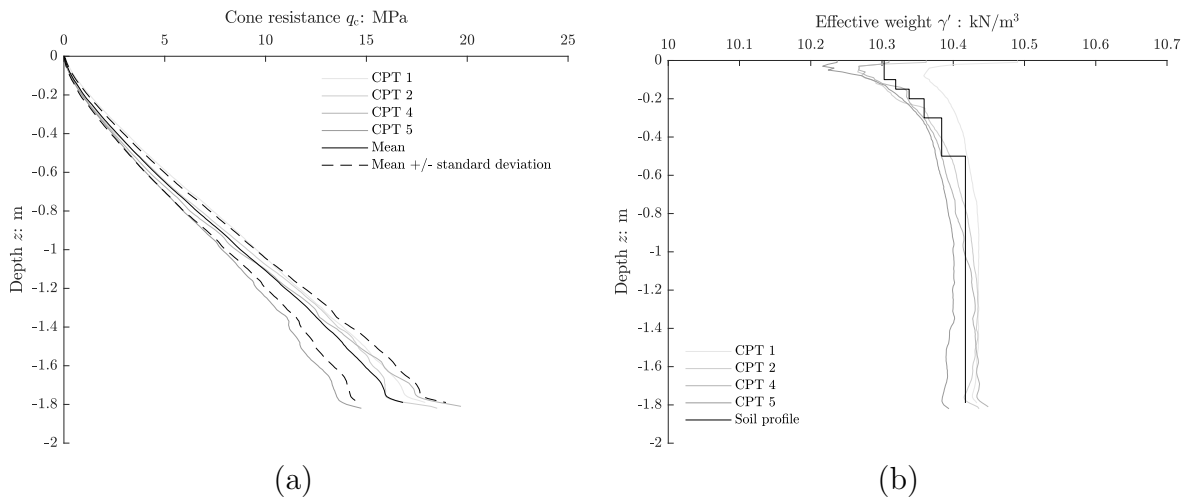The hydraulic conductivity cannot be determined from measured data; k_{f} is assumed.

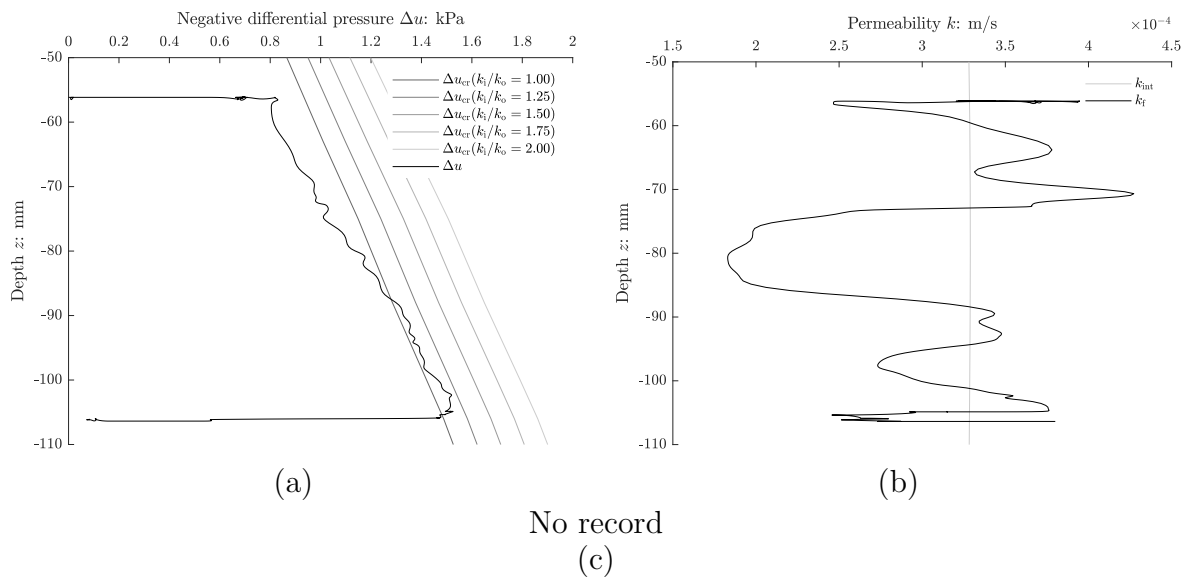*Figure A.2.12.1:* Cone penetration test: cone resistance (a) and effective weight (b).

Negative differential pressure Δu: kPa

Permeability k: m/s

(a)

(b)

No record

(c)

Figure A.2.12.2: Installation: negative differential pressure (a), hydraulic conductivity (b) and permeability ratio (c).

(a)

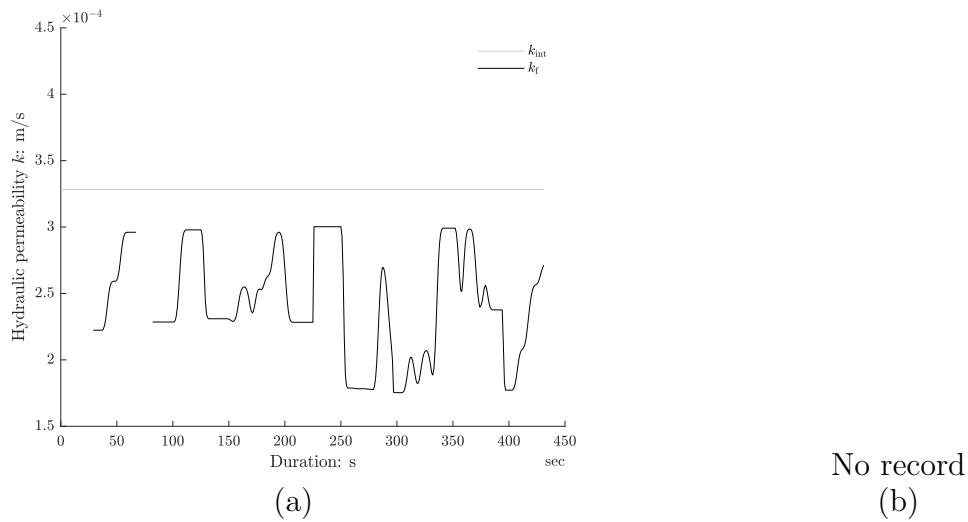No record

(b)

Figure A.2.12.3: Permeability test: hydraulic conductivity (a) and permeability ratio (b).
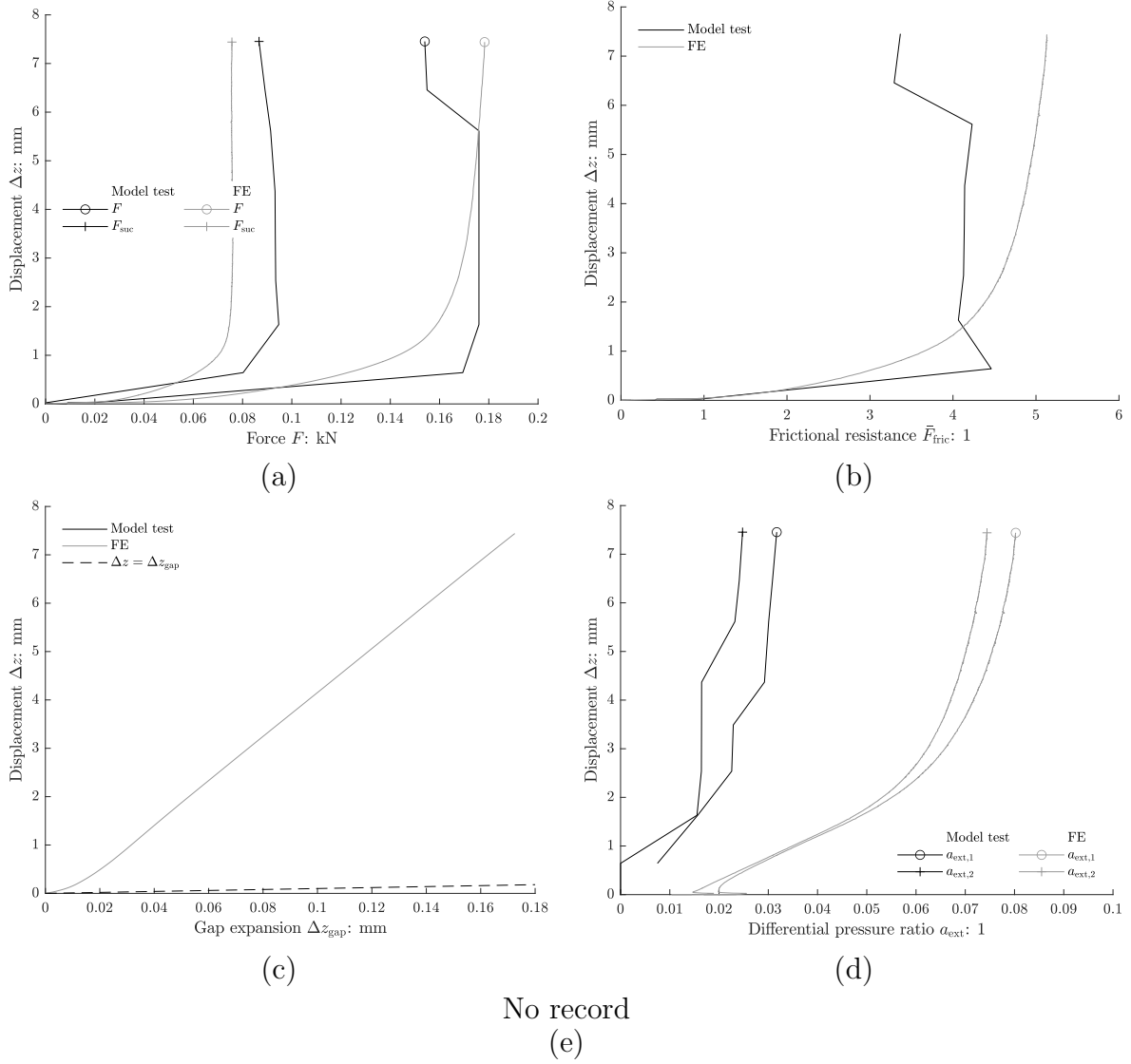
(a)

(b)

(c)

(d)

No record
(e)

Figure A.2.12.4: Tensile test: force and suction force (a), frictional resistance (b), gap expansion (c), differential pressure ratio (external) (d) and differential pressure ratio (skirt) (e)

A.2.13 L125D135v19.7

Table A.2.13.1: Test summary

			DPS$_{ext,1}$		DPS$_{ext,2}$	
L	125 mm		r	z	r	z
D	135 mm		-	-	-	-
T_w	19.1°C					

Drained resistance			Tensile test		
z	103.6	mm	z	102.6	mm
z/D	0.83		z/D	0.82	
z_{plug}	15.9	mm	z_{plug}	16.1	mm
F_{dr}	0.02	kN	F_{max}	0.31	kN
$\Delta z_{F_{dr}}$	-	mm	$\Delta z_{F_{max}}$	3.99	mm
			v_z	19.7	mm/s
			t_{acc}	0.40	s

Table A.2.13.2: FE model parameters

γ'	κ	λ	ν	ϕ'	ψ	k_f	k_i/k_o	k_0
10.41 kN/m^3	350	0.4	0.2	45°	20°	3.0×10^{-4} m/s	-	0.961

Comments:
No external differential pressure sensors used.
The hydraulic conductivity cannot be determined from measured data; k_f is assumed.
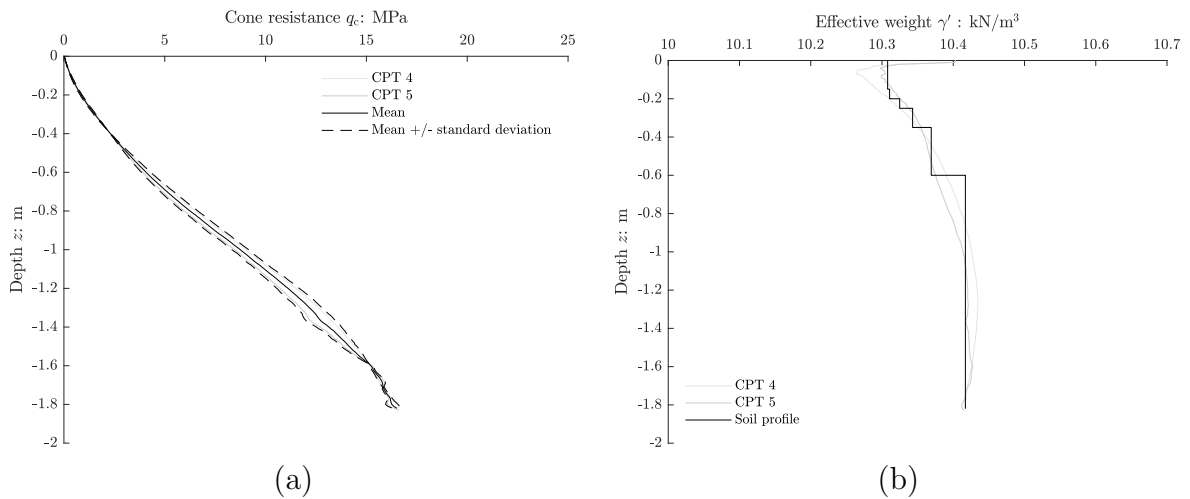

Figure A.2.13.1: Cone penetration test: cone resistance (a) and effective weight (b).
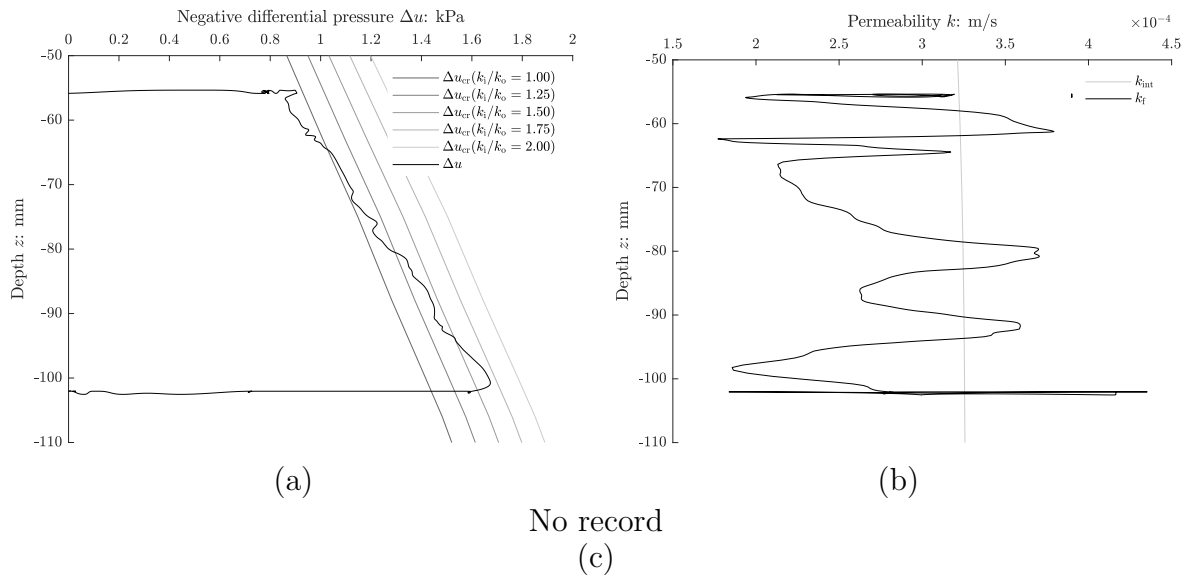
Figure A.2.13.2: Installation: negative differential pressure (a), hydraulic conductivity (b) and permeability ratio (c).
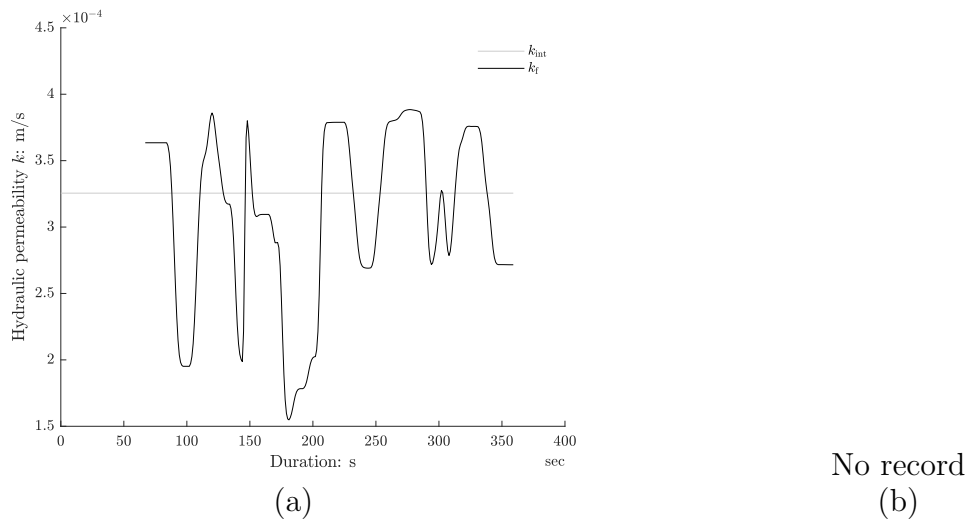

Figure A.2.13.3: Permeability test: hydraulic conductivity (a) and permeability ratio (b).
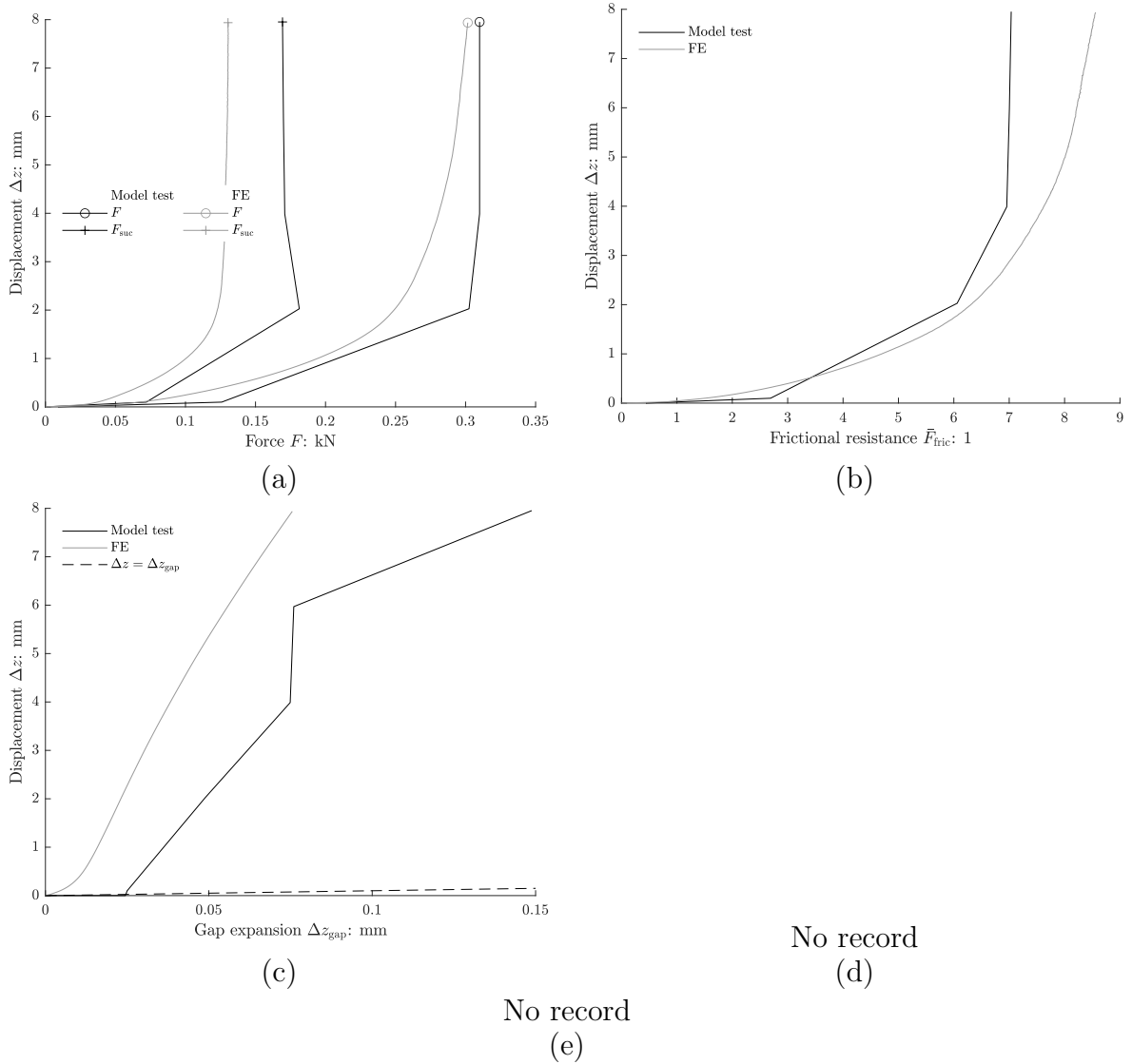
(a)

(b)

(c)

No record

(d)

No record

(e)

Figure A.2.13.4: Tensile test: force and suction force (a), frictional resistance (b), gap expansion (c), differential pressure ratio (external) (d) and differential pressure ratio (skirt) (e)

A.2.14 L125D135v49.1

Table A.2.14.1: Test summary

L	125 mm	DPS$_{\text{ext,1}}$		DPS$_{\text{ext,2}}$	
D	135 mm	r	z	r	z
T_{w}	19.1°C	-	-	-	-

Drained resistance			Tensile test		
z	100.0	mm	z	99.4	mm
z/D	0.80		z/D	0.80	
z_{plug}	18.8	mm	z_{plug}	18.5	mm
F_{dr}	0.02	kN	F_{max}	0.65	kN
$\Delta z_{F_{\text{dr}}}$	-	mm	$\Delta z_{F_{\text{max}}}$	11.87	mm
			v_z	49.1	mm/s
			t_{acc}	0.12	s

Table A.2.14.2: FE model parameters

γ'	κ	λ	ν	ϕ'	ψ	k_{f}	$k_{\text{i}}/k_{\text{o}}$	k_0
10.41 kN/m^3	350	0.4	0.2	45°	20°	3.0×10^{-4} m/s	-	1.031

Comments:
No external differential pressure sensors used.
The hydraulic conductivity cannot be determined from measured data; k_{f} is assumed.
Test was conducted after test L125D135v19.7 without new sand preparation. Centre distance between both tests was 1.1 m.

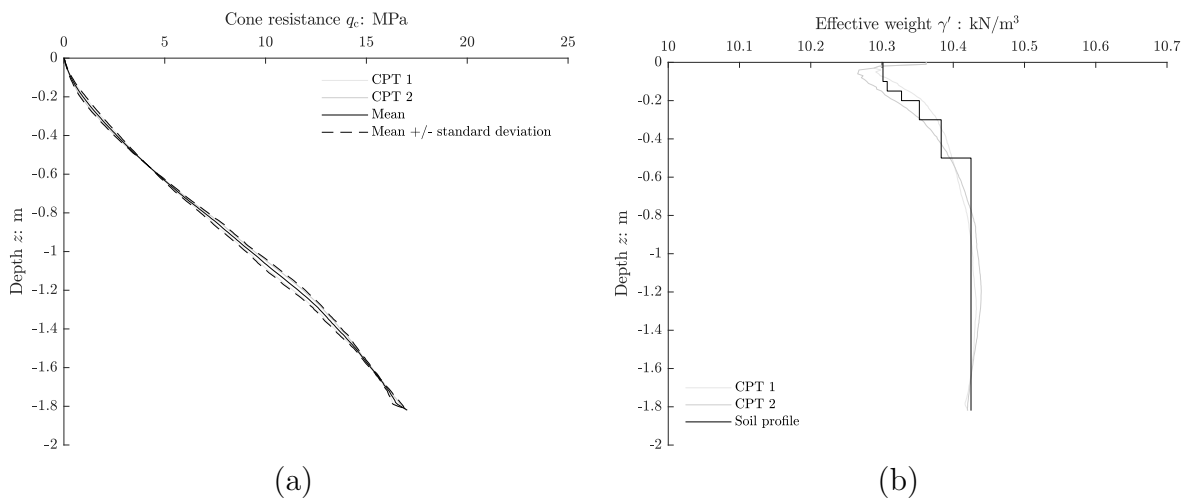(a)   (b)

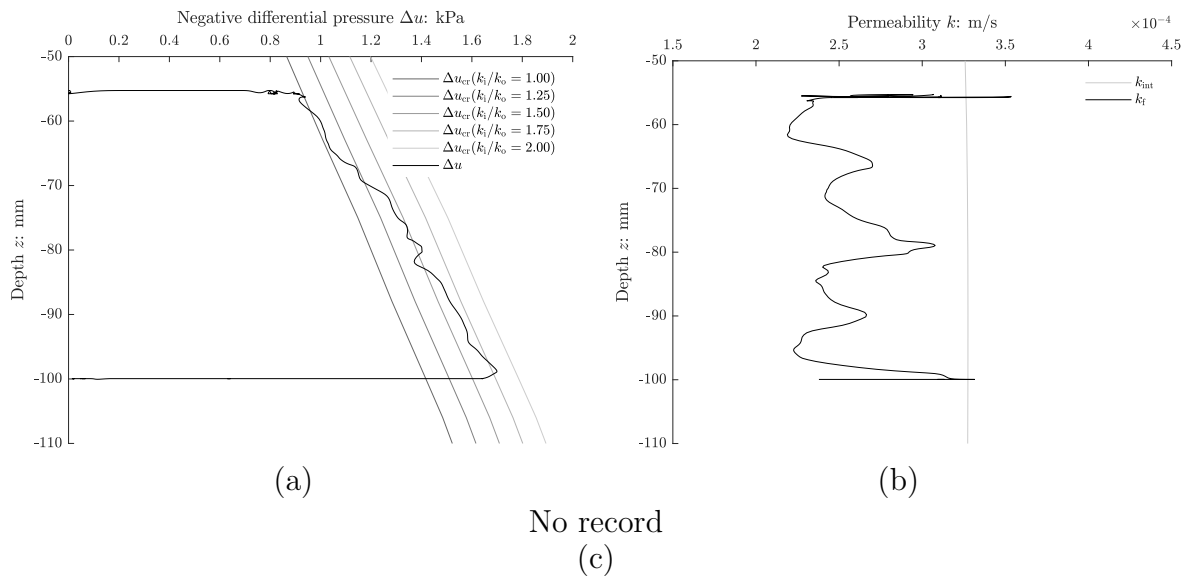*Figure A.2.14.1:* Cone penetration test: cone resistance (a) and effective weight (b).

(a)

(b)

No record

(c)

Figure A.2.14.2: Installation: negative differential pressure (a), hydraulic conductivity (b) and permeability ratio (c).
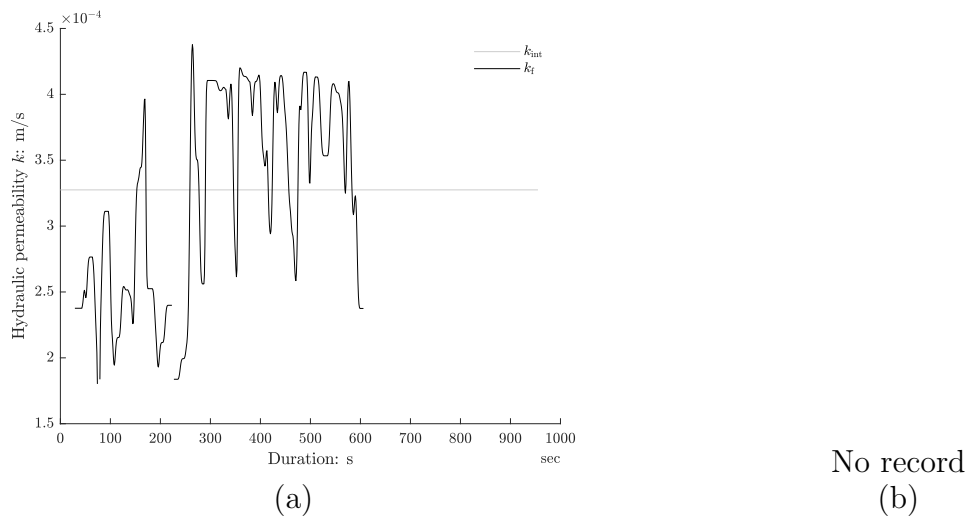

(a)

No record

(b)

Figure A.2.14.3: Permeability test: hydraulic conductivity (a) and permeability ratio (b).
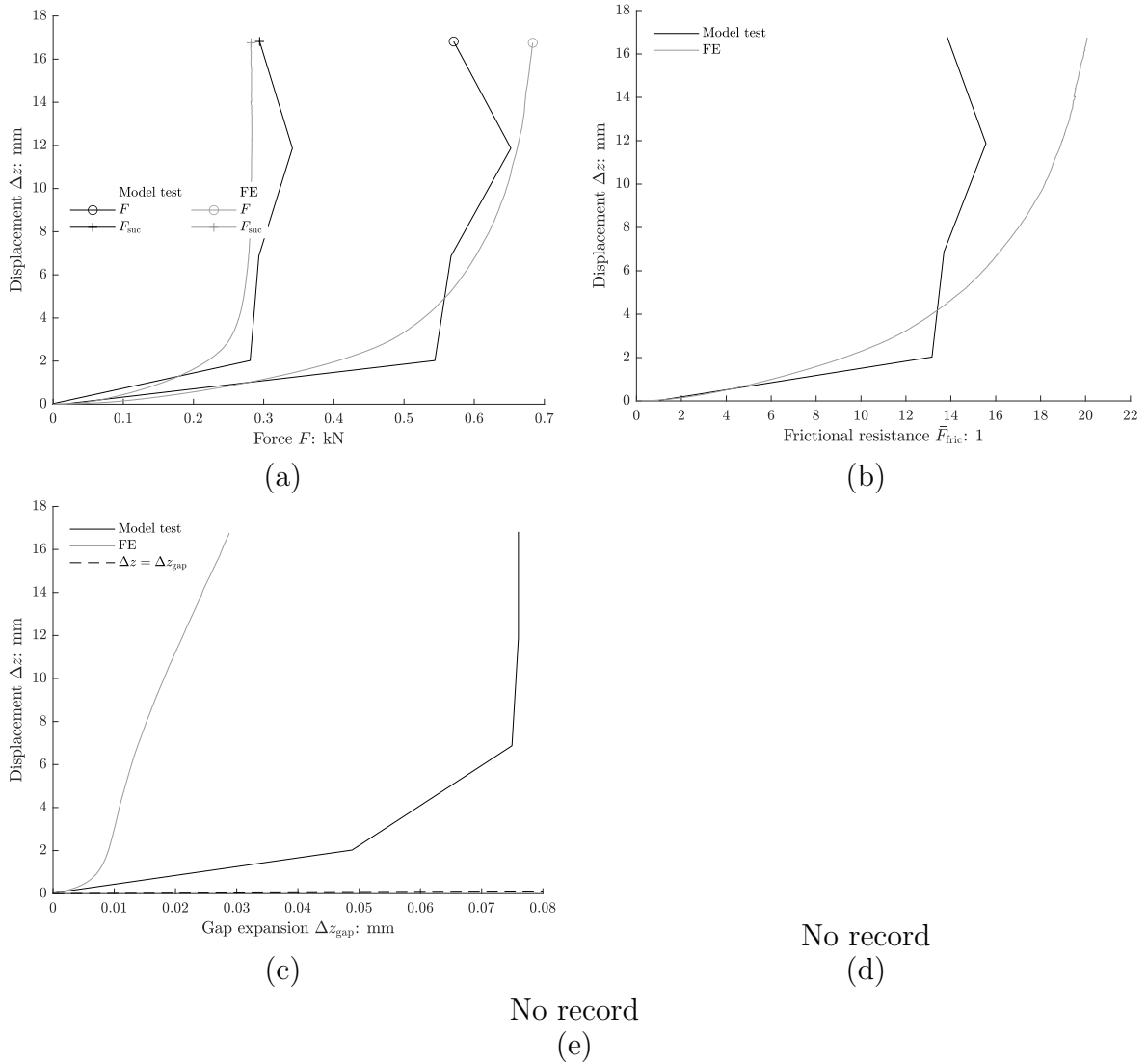
Figure A.2.14.4: Tensile test: force and suction force (a), frictional resistance (b), gap expansion (c), differential pressure ratio (external) (d) and differential pressure ratio (skirt) (e)

A.3 Constant force

A.3.1 M1.09

Table A.3.1.1: Test summary

L	500 mm	DPS$_{\text{ext,1}}$		DPS$_{\text{ext,2}}$	
D	510 mm	r	z	r	z
T_{w}	18.6°C	460 mm	250.0 mm	460 mm	150.0 mm

Drained resistance			Tensile test		
z	425.2	mm	z	424.4	mm
z/D	0.85		z/D	0.85	
z_{plug}	42.8	mm	z_{plug}	41.8	mm
F_{dr}	0.75	kN	$\bar{F}_{\text{mean}}$	1.09	1
$\Delta z_{F_{\text{dr}}}$	0.59	mm	t_{acc}	0.1	s
			Regression ($\Delta z = \alpha t^{\beta}$)		
			α	0.0020	mm/s$^{\beta}$
			β	1.5997	1

Table A.3.1.2: FE model parameters

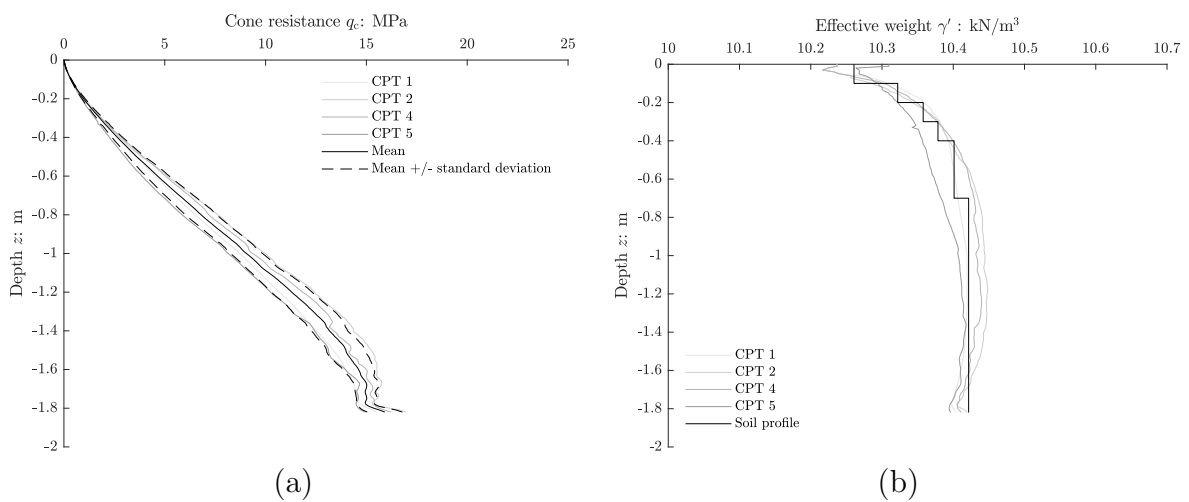| γ'	κ	λ	ν	ϕ'	ψ	k_{i}	$k_{\text{i}}/k_{\text{o}}$	k_0
10.41 kN/m^3	350	0.4	0.2	45°	20°	3.0×10^{-4} m/s	1.3	0.545

Comments:
-

Figure A.3.1.1: Cone penetration test: cone resistance (a) and effective weight (b).
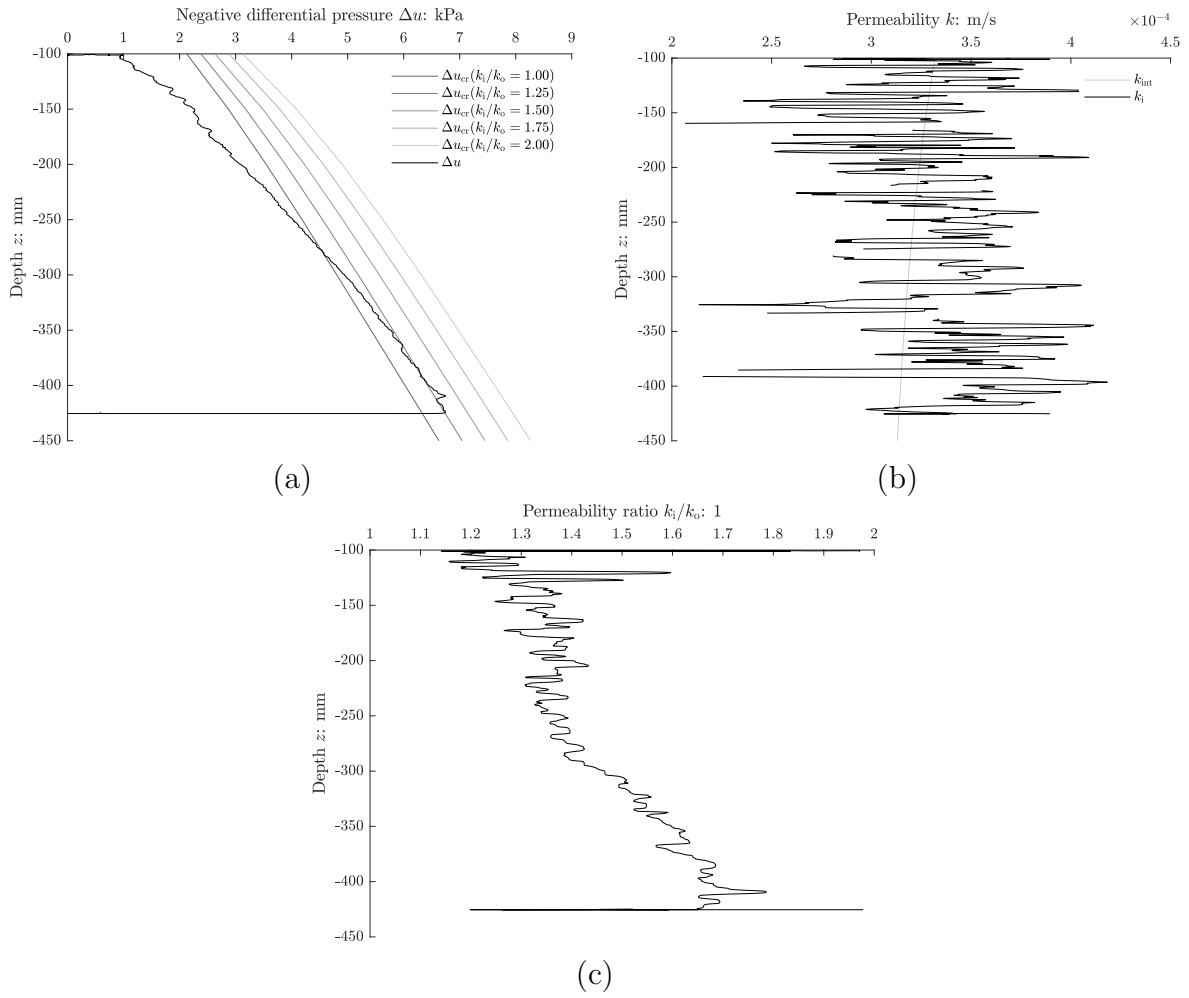
(a)

(b)

(c)

Figure A.3.1.2: Installation: negative differential pressure (a), hydraulic conductivity (b) and permeability ratio (c).
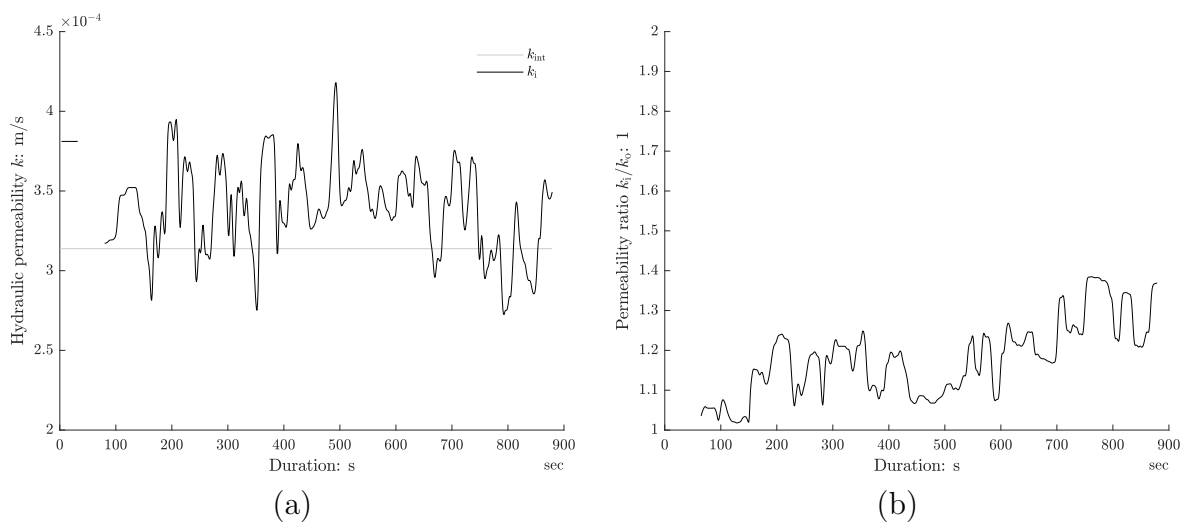

(a)

(b)

Figure A.3.1.3: Permeability test: hydraulic conductivity (a) and permeability ratio (b).
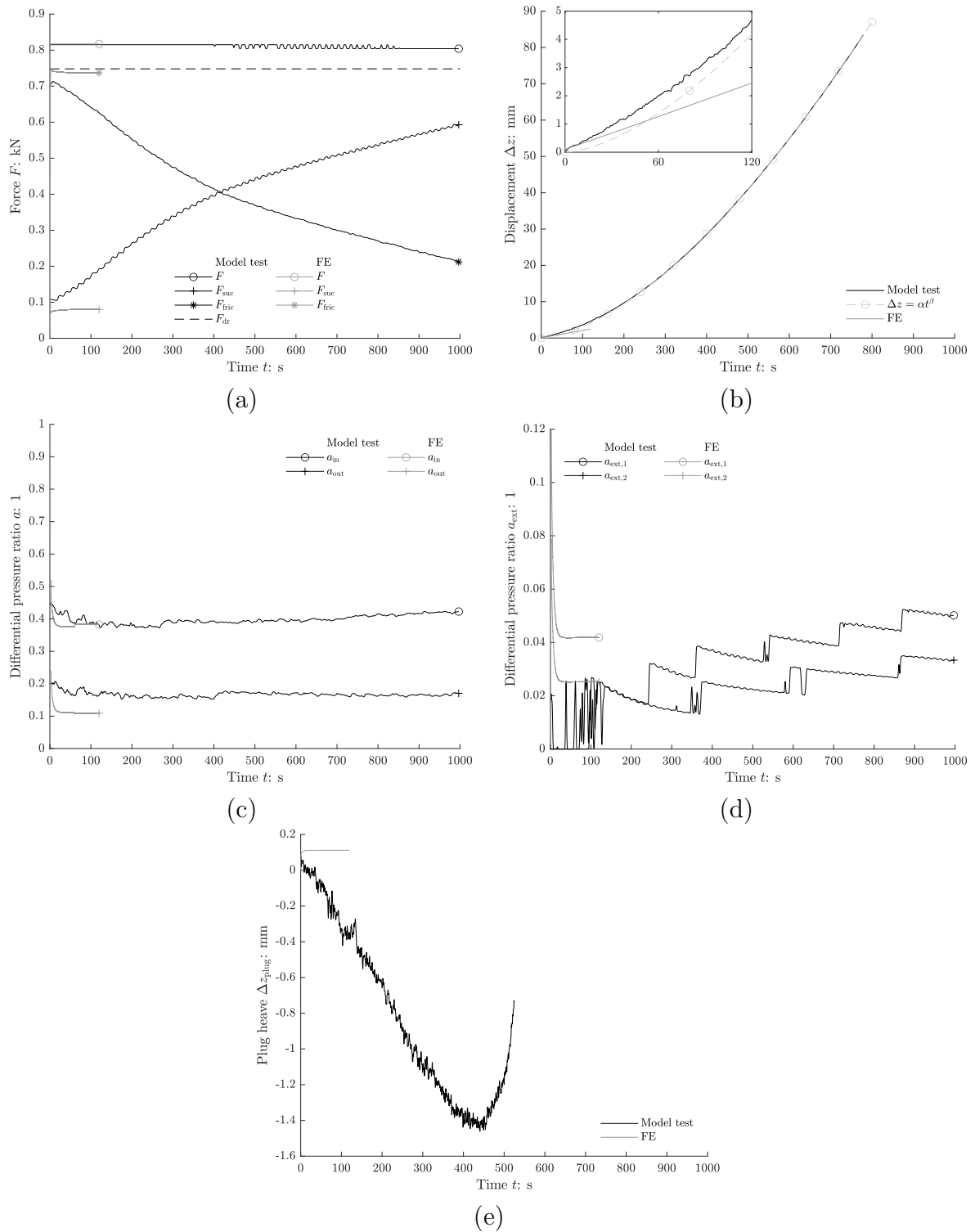
Figure A.3.1.4: Tensile test: load sharing (a), displacement (b), differential pressure ratio (skirt) (c), differential pressure ratio (external) (d) and plug heave (e).

A.3.2 M1.58

Table A.3.2.1: Test summary

L	500 mm	DPS$_{\text{ext},1}$		DPS$_{\text{ext},2}$	
D	510 mm	r	z	r	z
T_{w}	18.3°C	510 mm	625.0 mm	510 mm	375.0 mm

Drained resistance			Tensile test		
z	425.9	mm	z	424.9	mm
z/D	0.85		z/D	0.85	
z_{plug}	41.5	mm	z_{plug}	41.3	mm
F_{dr}	0.73	kN	$\bar{F}_{\text{mean}}$	1.58	1
$\Delta z_{F_{\text{dr}}}$	0.59	mm	t_{acc}	0.1	s
			Regression ($\Delta z = \alpha t^{\beta}$)		
			α	0.0730	mm/s$^{\beta}$
			β	1.2047	1

Table A.3.2.2: FE model parameters

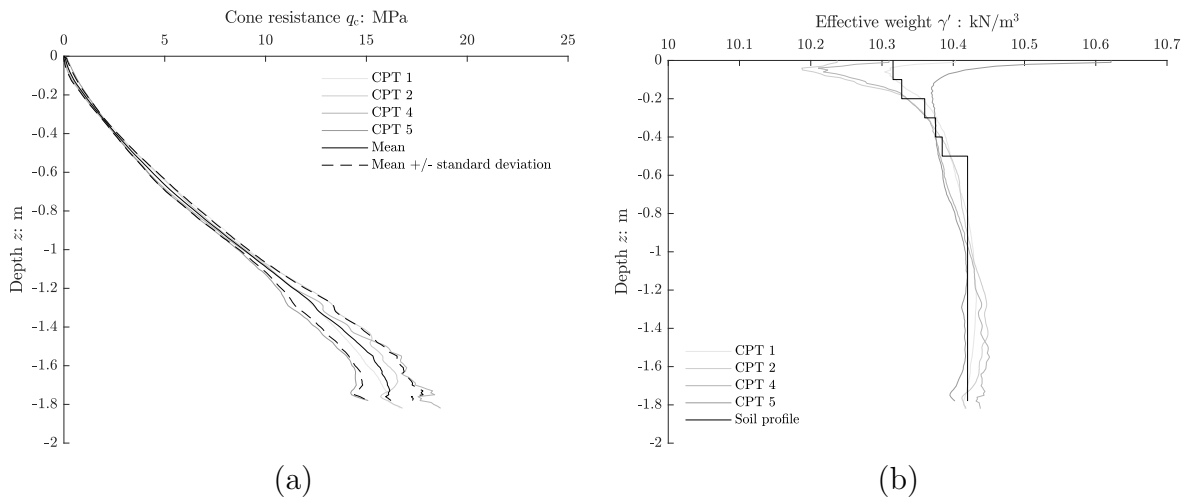| γ'	κ	λ	ν	ϕ'	ψ	k_{i}	$k_{\text{i}}/k_{\text{o}}$	k_0
10.41 kN/m³	350	0.4	0.2	45°	20°	3.8×10^{-4} m/s	1.5	0.521

Comments:
-

Figure A.3.2.1: Cone penetration test: cone resistance (a) and effective weight (b).
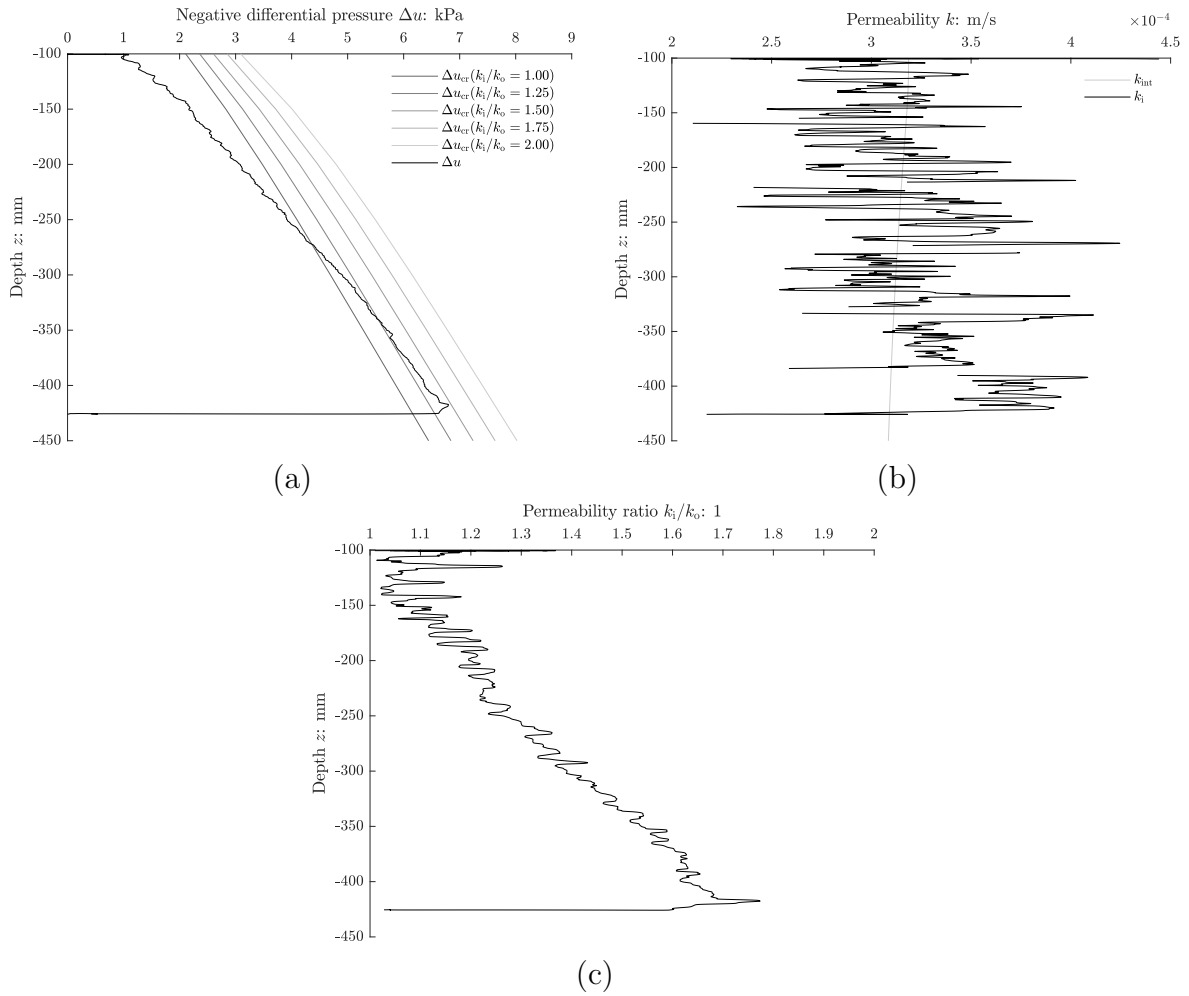
(a)

(b)

(c)

Figure A.3.2.2: Installation: negative differential pressure (a), hydraulic conductivity (b) and permeability ratio (c).
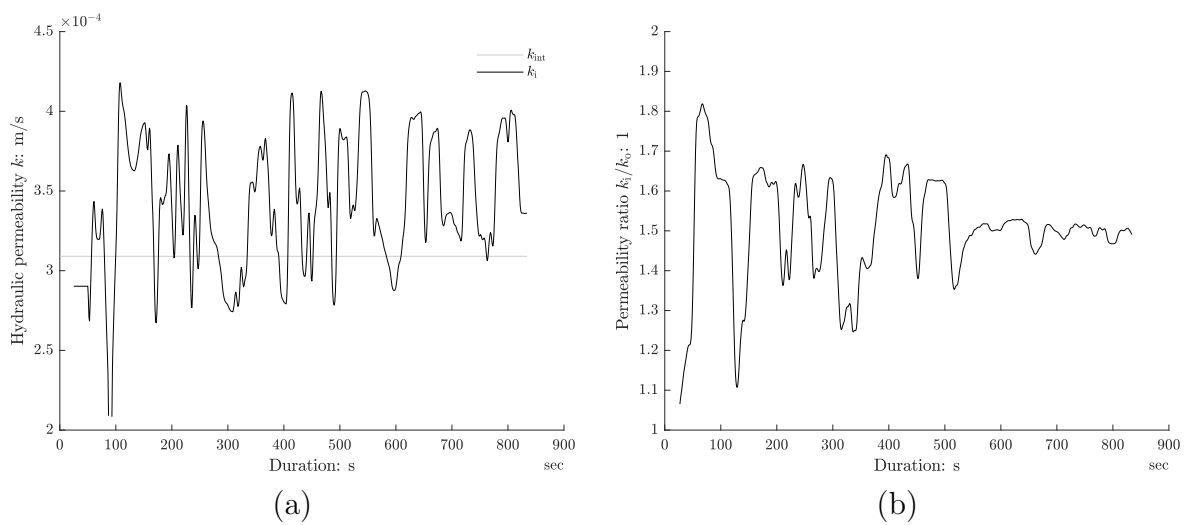

(a)

(b)

Figure A.3.2.3: Permeability test: hydraulic conductivity (a) and permeability ratio (b).
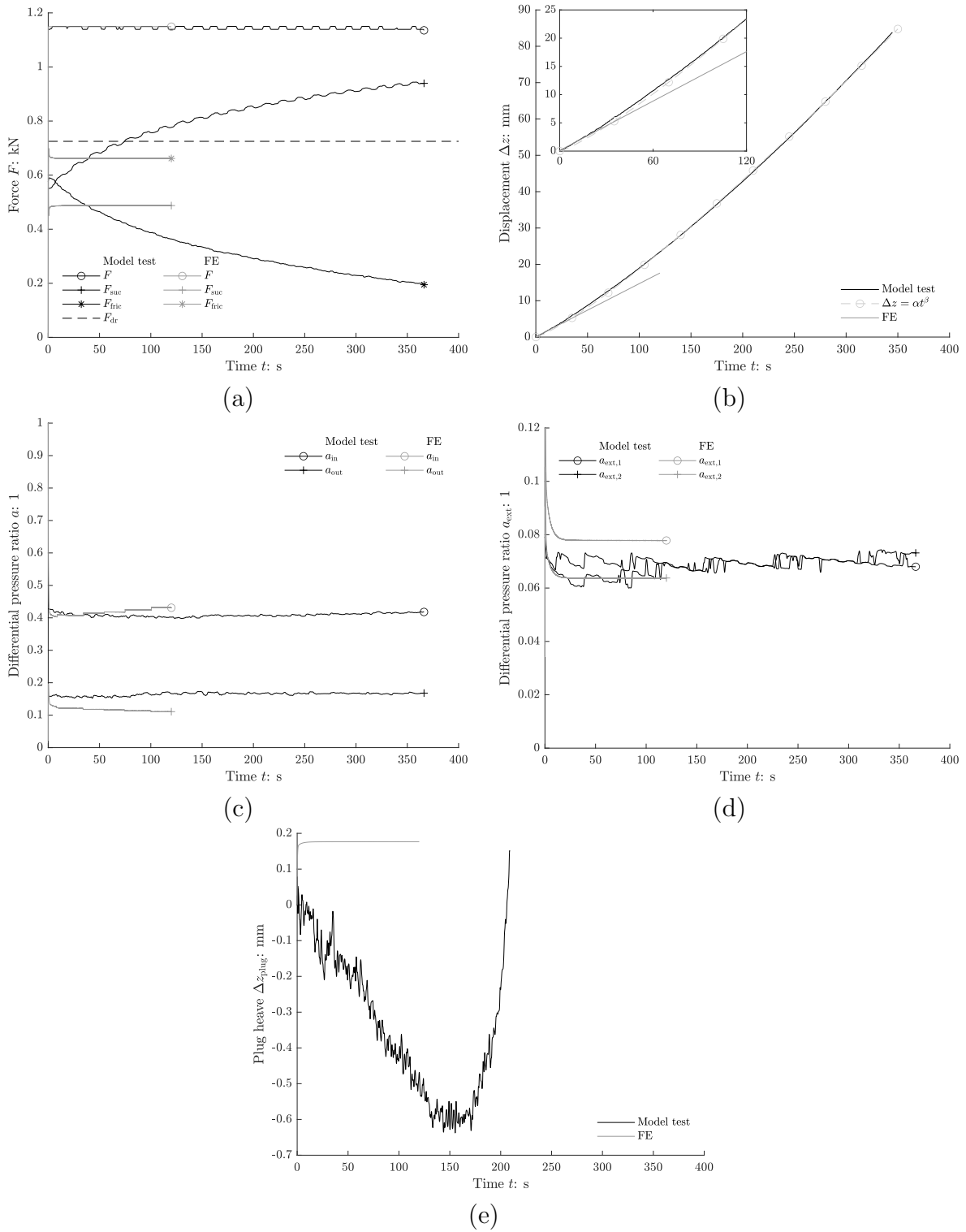
Figure A.3.2.4: Tensile test: load sharing (a), displacement (b), differential pressure ratio (skirt) (c), differential pressure ratio (external) (d) and plug heave (e).

A.3.3 M2.04

Table A.3.3.1: Test summary

L	500 mm	DPS$_{\text{ext},1}$		DPS$_{\text{ext},2}$	
D	510 mm	r	z	r	z
T_{w}	18.2°C	510 mm	625.0 mm	510 mm	376.0 mm

Drained resistance			Tensile test		
z	424.8	mm	z	424.0	mm
z/D	0.85		z/D	0.85	
z_{plug}	41.4	mm	z_{plug}	40.9	mm
F_{dr}	0.73	kN	$\bar{F}_{\text{mean}}$	2.04	1
$\Delta z_{F_{\text{dr}}}$	0.80	mm	t_{acc}	0.2	s
			Regression ($\Delta z = \alpha t^{\beta}$)		
			α	0.0991	mm/s$^{\beta}$
			β	1.2693	1

Table A.3.3.2: FE model parameters

γ'	κ	λ	ν	ϕ'	ψ	k_{i}	$k_{\text{i}}/k_{\text{o}}$	k_0
10.41 kN/m^3	350	0.4	0.2	45°	20°	4.1×10^{-4} m/s	1.6	0.521

Comments:
Permeability test did not provide reasonable data; k_{i} and $k_{\text{i}}/k_{\text{o}}$ are derived from installation.
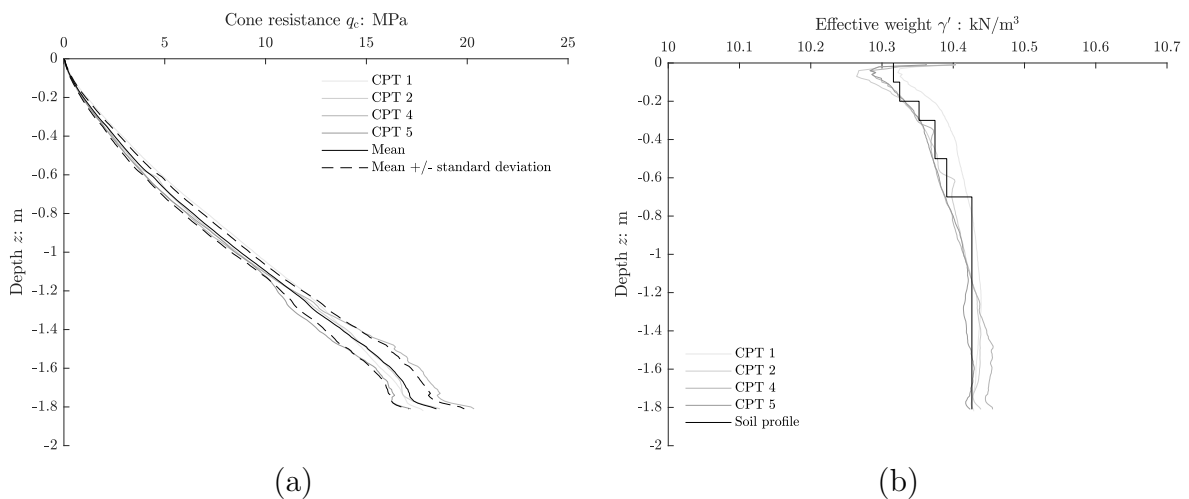

Figure A.3.3.1: Cone penetration test: cone resistance (a) and effective weight (b).
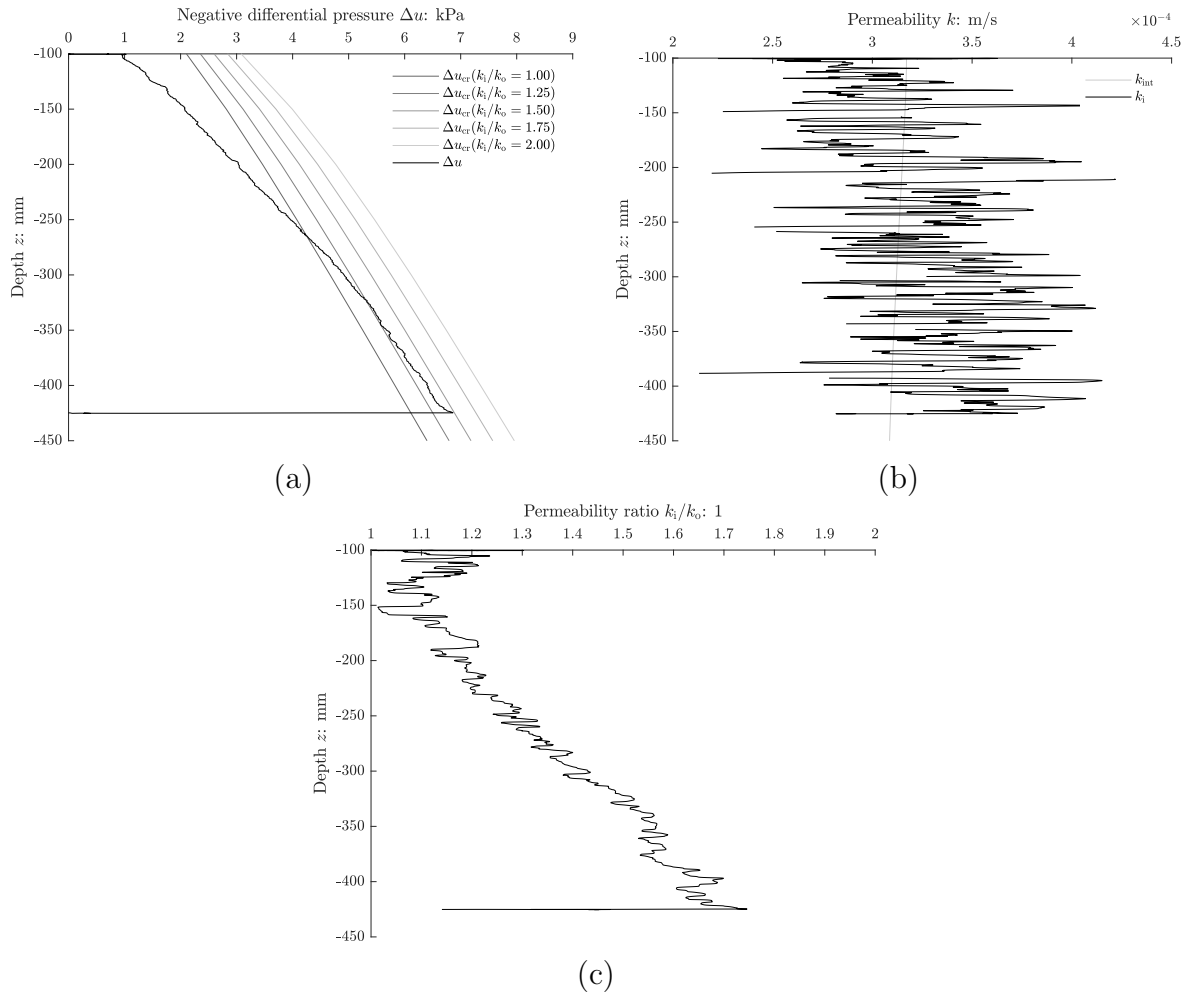
(a)

(b)

(c)

Figure A.3.3.2: Installation: negative differential pressure (a), hydraulic conductivity (b) and permeability ratio (c).
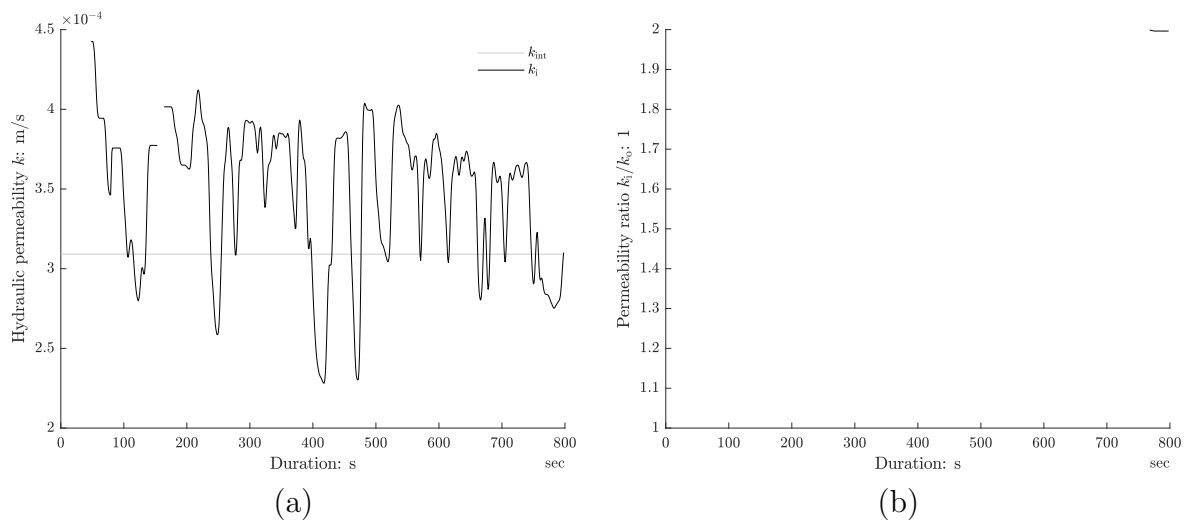

(a)

(b)

Figure A.3.3.3: Permeability test: hydraulic conductivity (a) and permeability ratio (b).
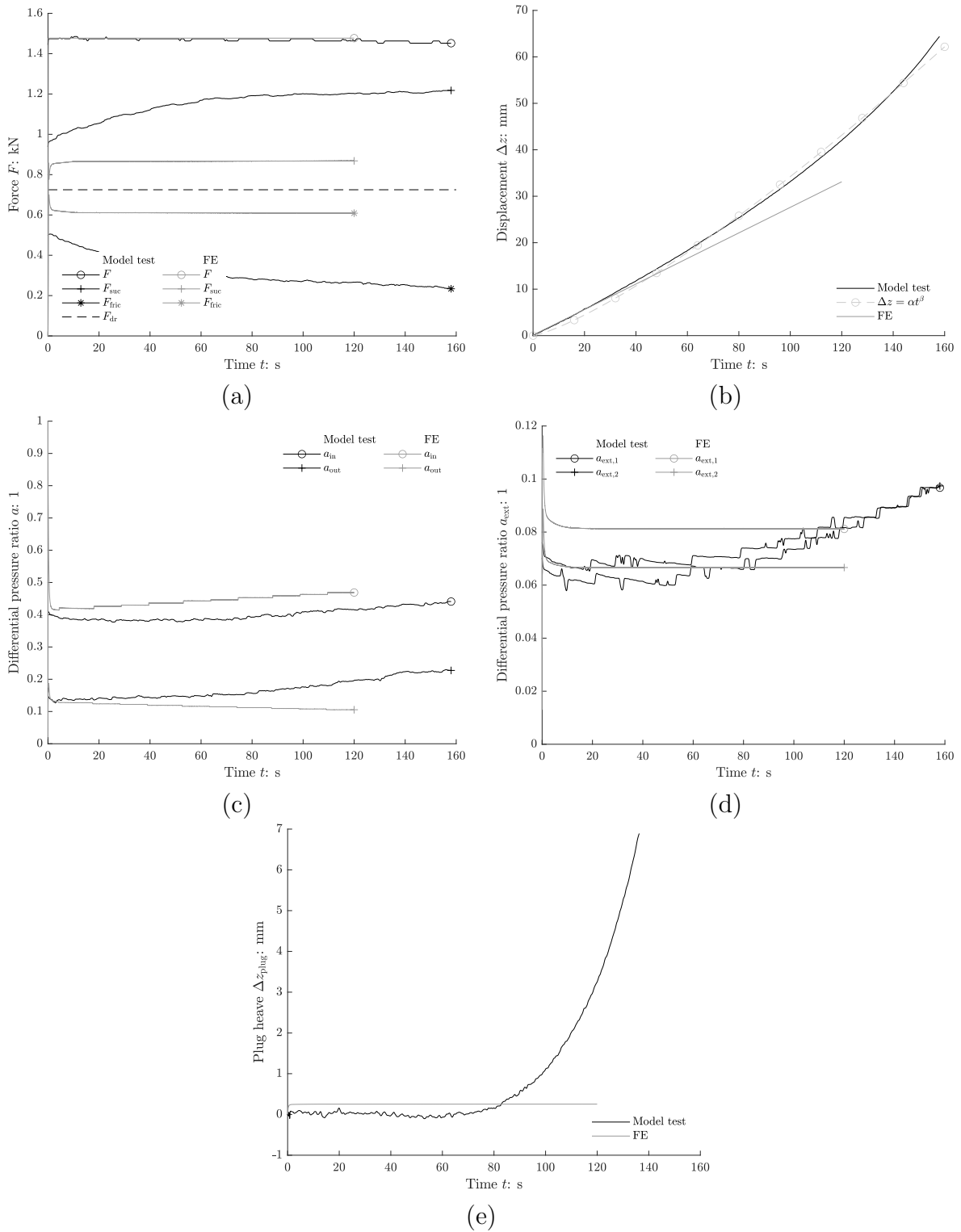
(a)

(b)

(c)

(d)

(e)

Figure A.3.3.4: Tensile test: load sharing (a), displacement (b), differential pressure ratio (skirt) (c), differential pressure ratio (external) (d) and plug heave (e).

A.4 Cyclic force

A.4.1 F1.02M0.86A0.18

Table A.4.1.1: Test summary

L	500 mm	DPS$_{ext,1}$		DPS$_{ext,2}$	
D	510 mm	r	z	r	z
T_w	18.0°C	510 mm	375.5 mm	510 mm	474.5 mm

Drained resistance			Tensile test		
z	425.3	mm	z	424.9	mm
z/D	0.85		z/D	0.85	
z_{plug}	45.4	mm	z_{plug}	44.7	mm
F_{dr}	0.67	kN	f	1.02	1/s
$\Delta z_{F_{dr}}$	0.59	mm	$\bar{F}_{mean}$	0.86	
			$\bar{F}_{ampl}$	0.18	
			Regression ($\Delta z = \alpha N^\beta$)		
			α	1.7523e-12	mm/1$^\beta$
			β	3.8159	1

Table A.4.1.2: FE model parameters

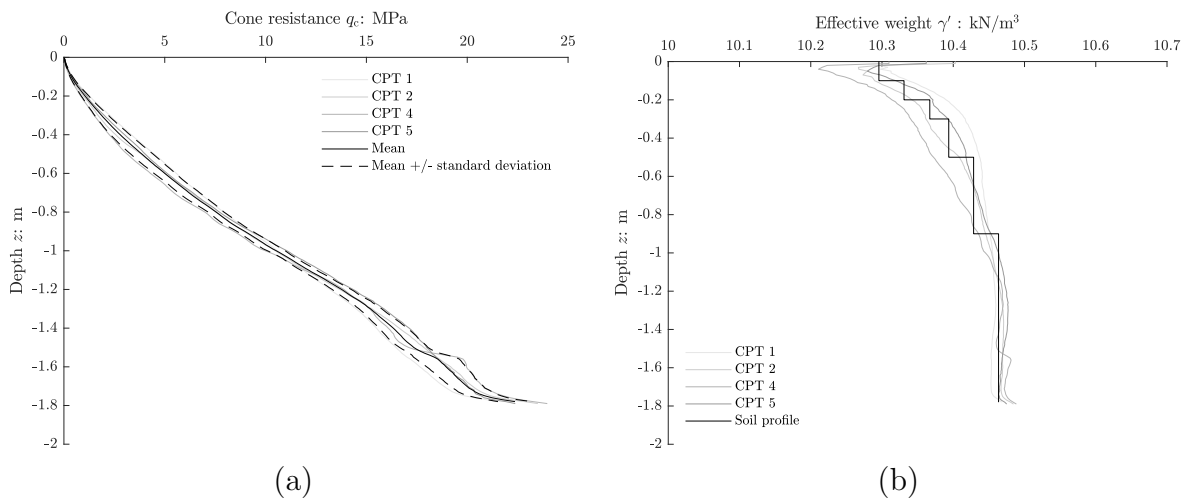| γ'	κ	λ	ν	ϕ'	ψ	k_i	k_i/k_o	k_0
10.41 kN/m^3	350	0.4	0.2	45°	20°	4.0×10^{-4} m/s	1.6	0.483

Comments:
-

Figure A.4.1.1: Cone penetration test: cone resistance (a) and effective weight (b).
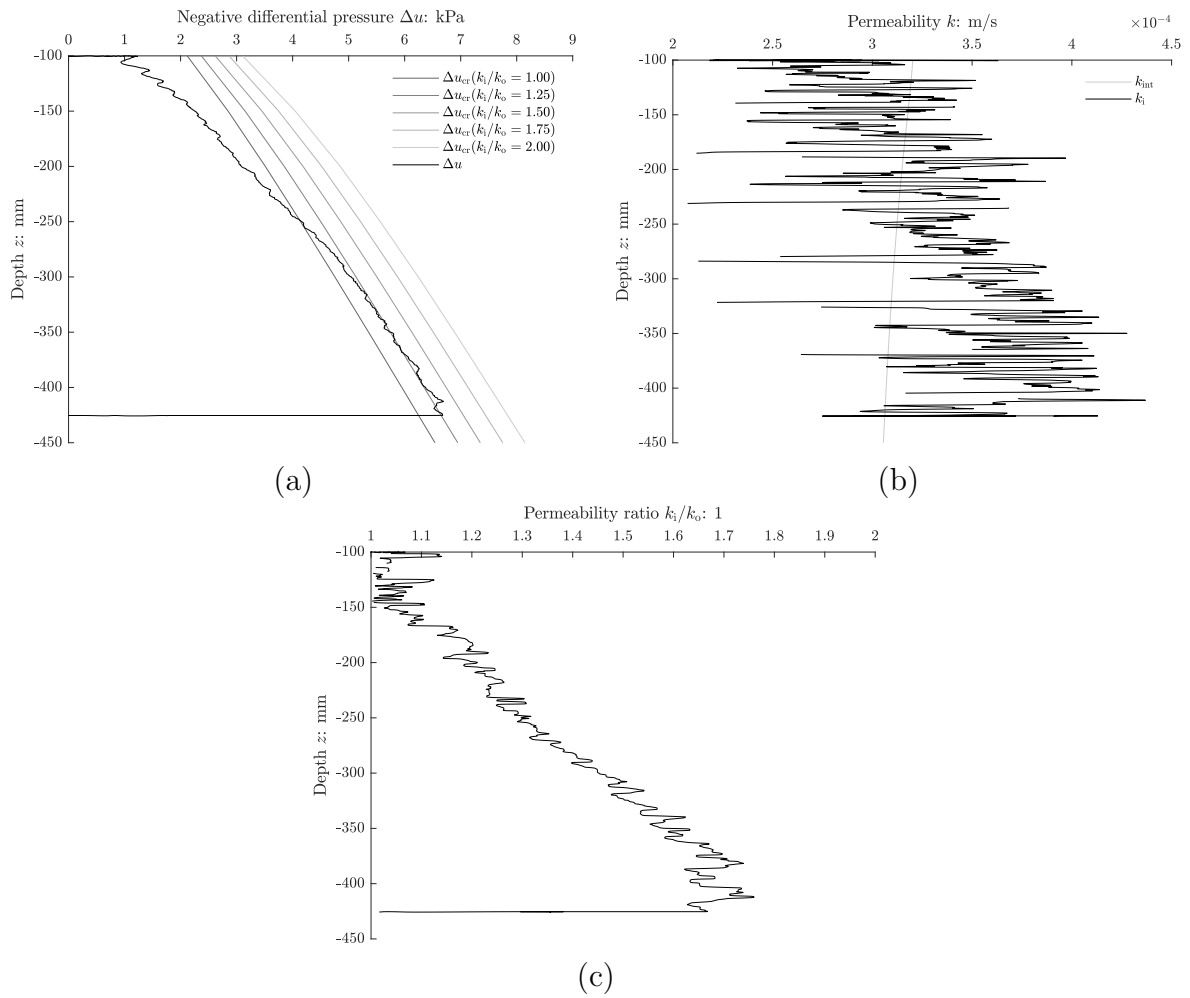
(a)

(b)

(c)

Figure A.4.1.2: Installation: negative differential pressure (a), hydraulic conductivity (b) and permeability ratio (c).
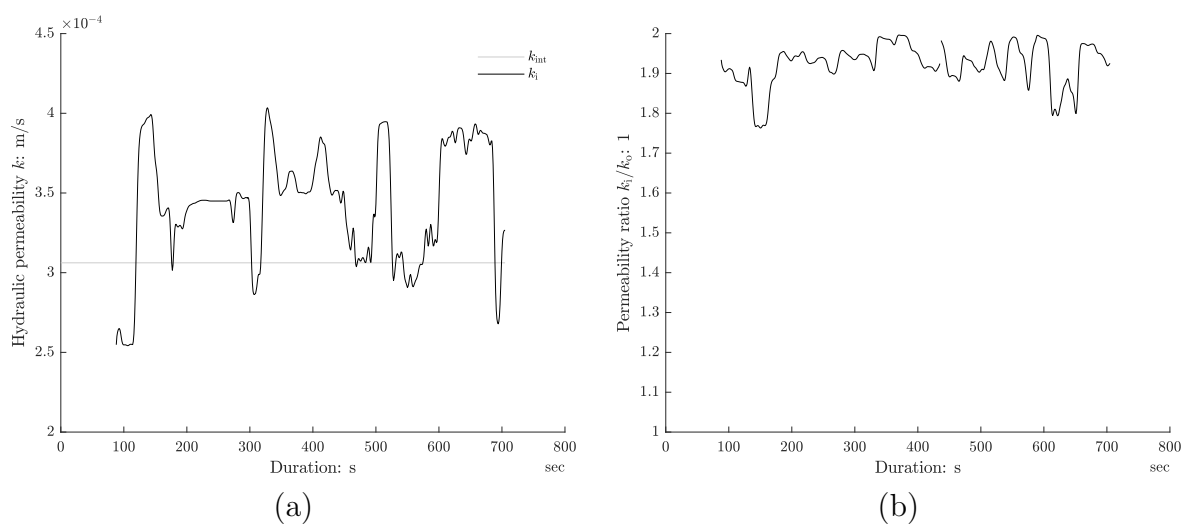

(a)

(b)

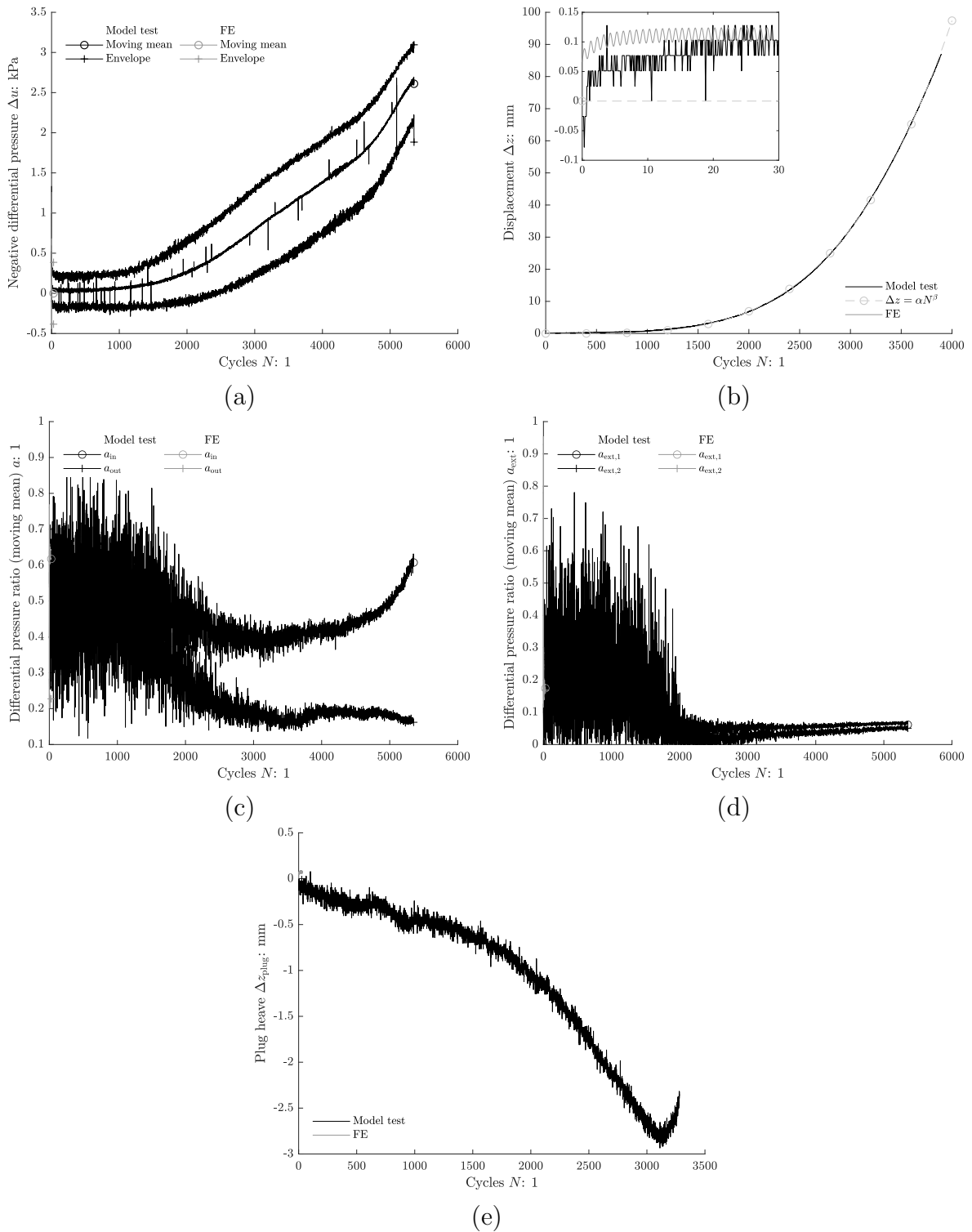*Figure A.4.1.3:* Permeability test: hydraulic conductivity (a) and permeability ratio (b).

Figure A.4.1.4: Tensile test: negative differential pressure (a), displacement (b), differential pressure ratio (skirt) (c), differential pressure ratio (external) (d) and plug heave (e).

A.4.2 F1.01M0.73A0.38

Table A.4.2.1: Test summary

L	500 mm	DPS$_{\text{ext},1}$		DPS$_{\text{ext},2}$	
D	510 mm	r	z	r	z
T_{w}	17.5°C	510 mm	625.0 mm	510 mm	375.0 mm

Drained resistance			Tensile test		
z	425.8	mm	z	425.0	mm
z/D	0.85		z/D	0.85	
z_{plug}	41.3	mm	z_{plug}	40.3	mm
F_{dr}	0.82	kN	f	1.01	1/s
$\Delta z_{F_{\text{dr}}}$	0.72	mm	$\bar{F}_{\text{mean}}$	0.73	
			$\bar{F}_{\text{ampl}}$	0.38	
			Regression ($\Delta z = \alpha N^{\beta}$)		
			α	2.2063e-5	mm/1$^{\beta}$
			β	2.0061	1

Table A.4.2.2: FE model parameters

γ'	κ	λ	ν	ϕ'	ψ	k_{i}	$k_{\text{i}}/k_{\text{o}}$	k_0
10.41 kN/m³	350	0.4	0.2	45°	20°	3.7×10^{-4} m/s	1.6	0.592

Comments:
No measurement of hydraulic conductivity due to defective sensor.
Extra weight in the amount of the suction bucket's self weight added during installation.
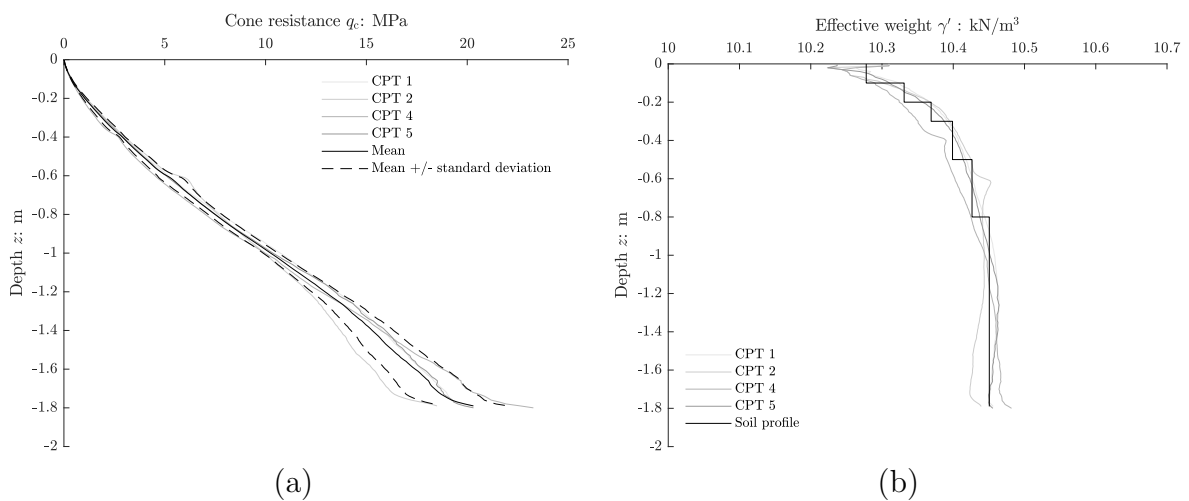

Figure A.4.2.1: Cone penetration test: cone resistance (a) and effective weight (b).

(a)

No record

(b)

(c)

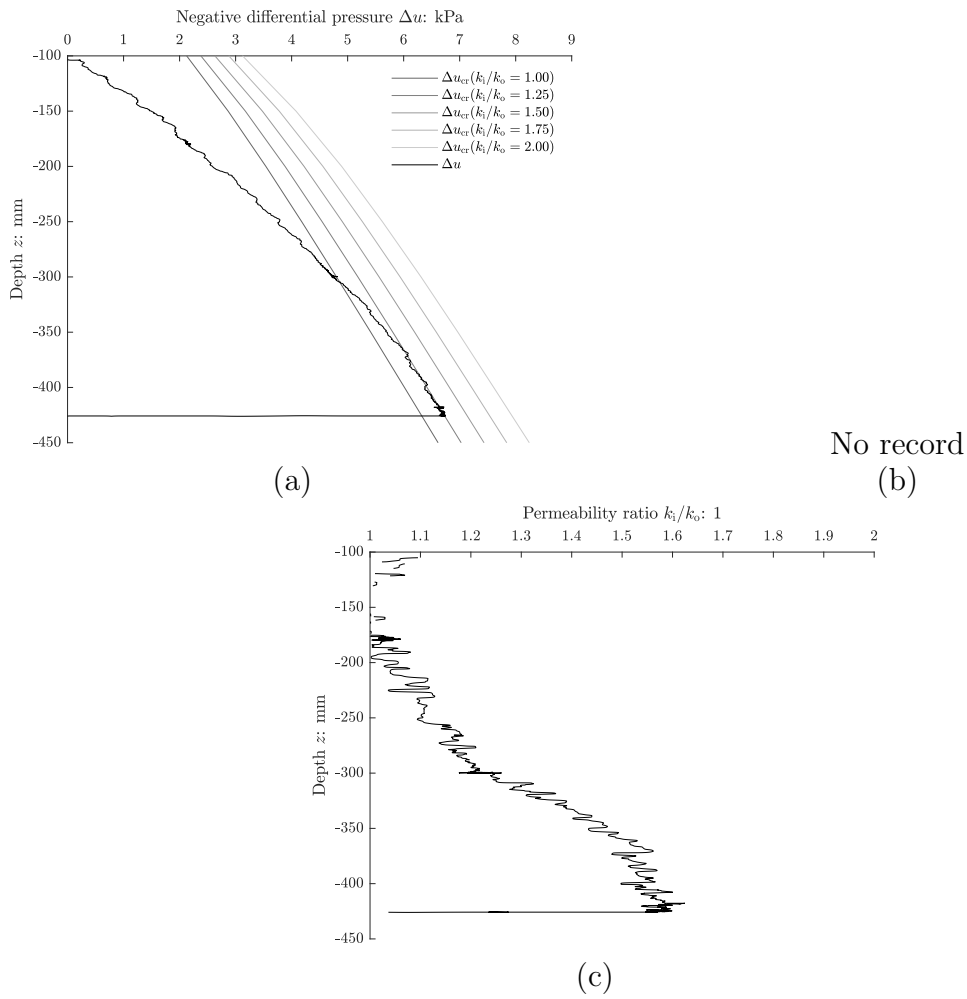*Figure A.4.2.2:* Installation: negative differential pressure (a), hydraulic conductivity (b) and permeability ratio (c).

No record

(a)

(b)

Figure A.4.2.3: Permeability test: hydraulic conductivity (a) and permeability ratio (b).

237

(a)

(b)

(c)

(d)

(e)
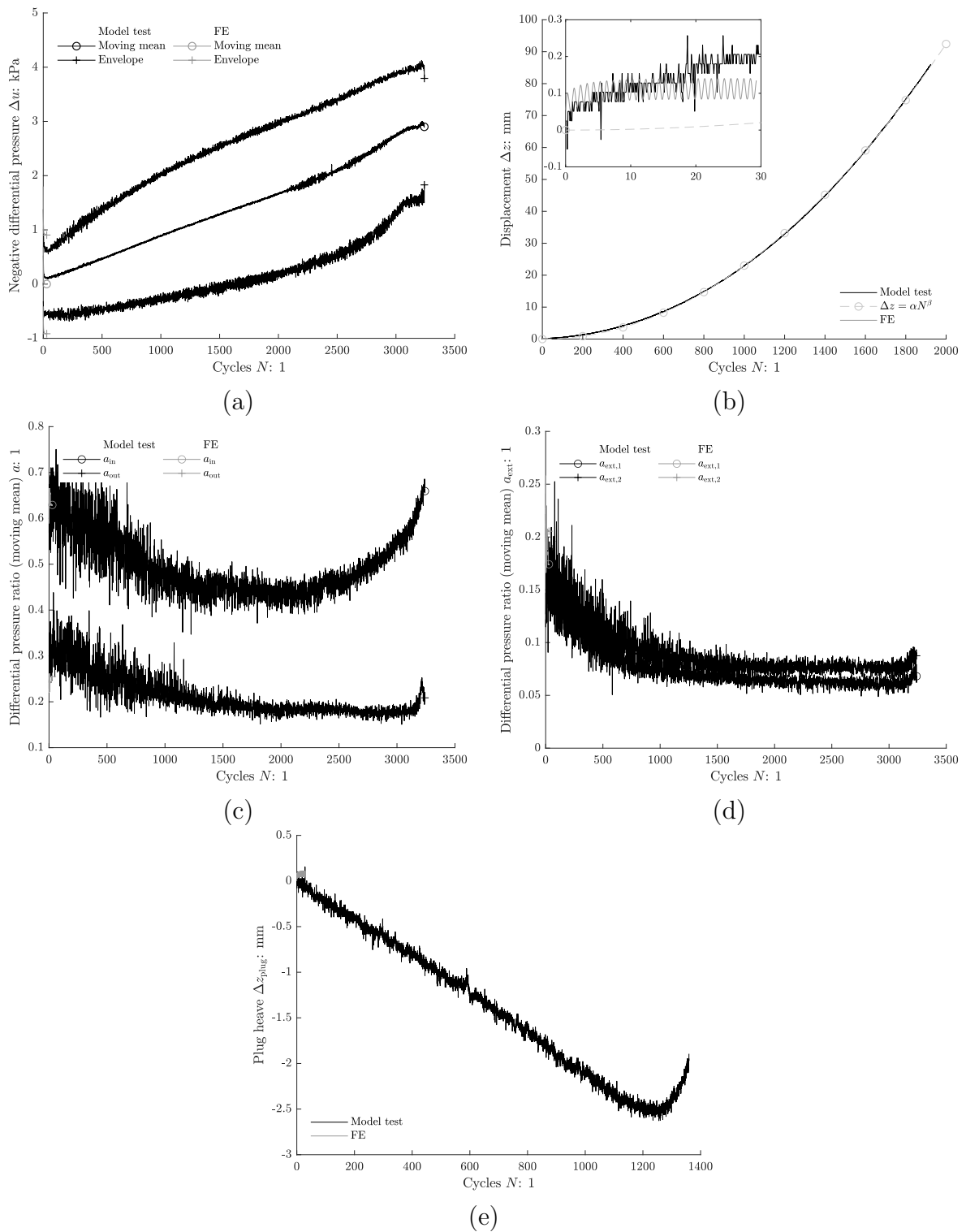
Figure A.4.2.4: Tensile test: negative differential pressure (a), displacement (b), differential pressure ratio (skirt) (c), differential pressure ratio (external) (d) and plug heave (e).

A.4.3 F1.01M1.06A0.25

Table A.4.3.1: Test summary

L	$500\,\mathrm{mm}$	DPS$_{\mathrm{ext,1}}$		DPS$_{\mathrm{ext,2}}$	
D	$510\,\mathrm{mm}$	r	z	r	z
T_{w}	$18.7°\mathrm{C}$	$510\,\mathrm{mm}$	$376.0\,\mathrm{mm}$	$510\,\mathrm{mm}$	$475.0\,\mathrm{mm}$

Drained resistance			Tensile test		
z	425.3	mm	z	424.9	mm
z/D	0.85		z/D	0.85	
z_{plug}	54.1	mm	z_{plug}	53.1	mm
F_{dr}	0.68	kN	f	1.01	1/s
$\Delta z_{F_{\mathrm{dr}}}$	0.70	mm	$\bar{F}_{\mathrm{mean}}$	1.06	
			$\bar{F}_{\mathrm{ampl}}$	0.25	
			Regression $(\Delta z = \alpha N^{\beta})$		
			α	0.0041	mm/1^{β}
			β	1.4457	1

Table A.4.3.2: FE model parameters

γ'	κ	λ	ν	ϕ'	ψ	k_{i}	$k_{\mathrm{i}}/k_{\mathrm{o}}$	k_0
$10.41\,\mathrm{kN/m^3}$	350	0.4	0.2	45°	20°	$3.7 \times 10^{-4}\,\mathrm{m/s}$	1.6	0.483

Comments:
No permeability test conducted.

Figure A.4.3.1: Cone penetration test: cone resistance (a) and effective weight (b).

(a)

(b)

(c)

Figure A.4.3.2: Installation: negative differential pressure (a), hydraulic conductivity (b) and permeability ratio (c).
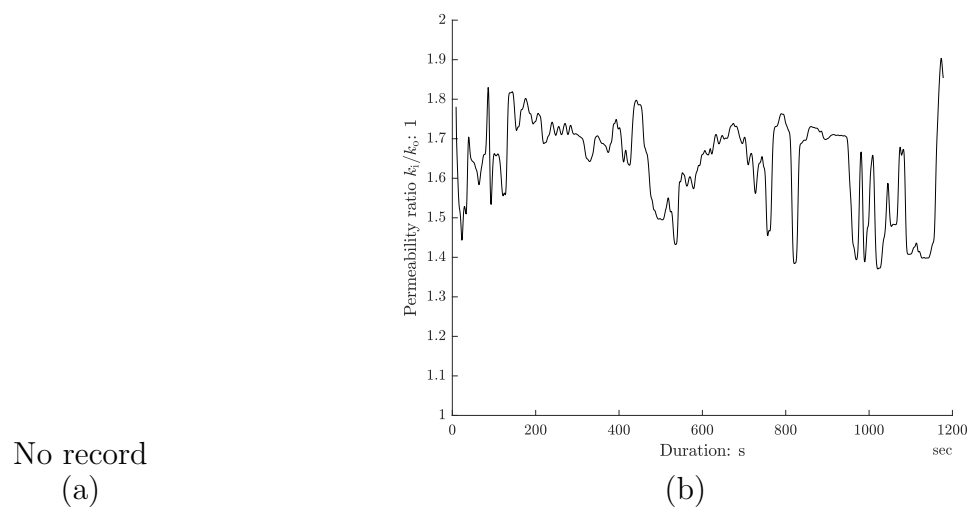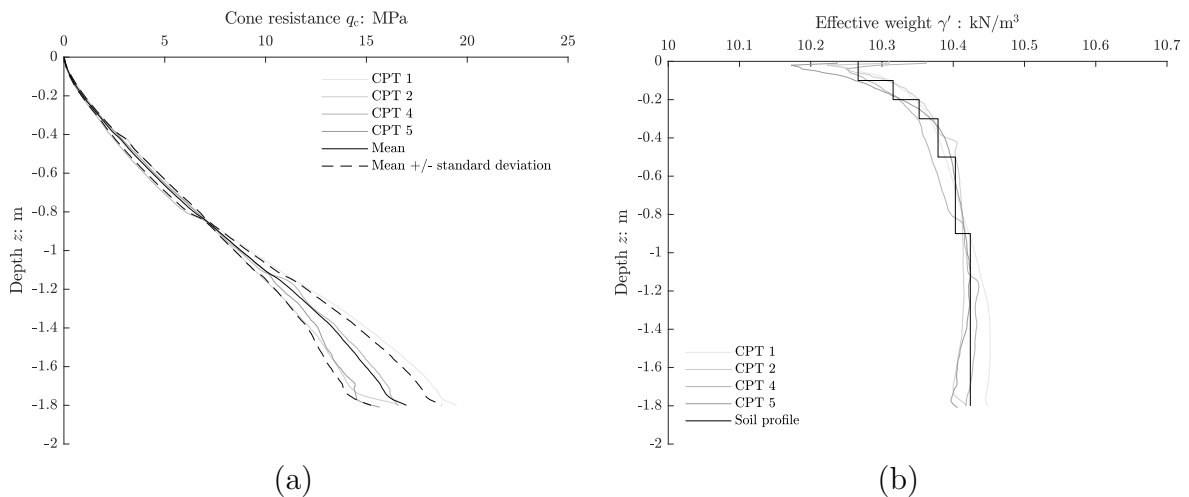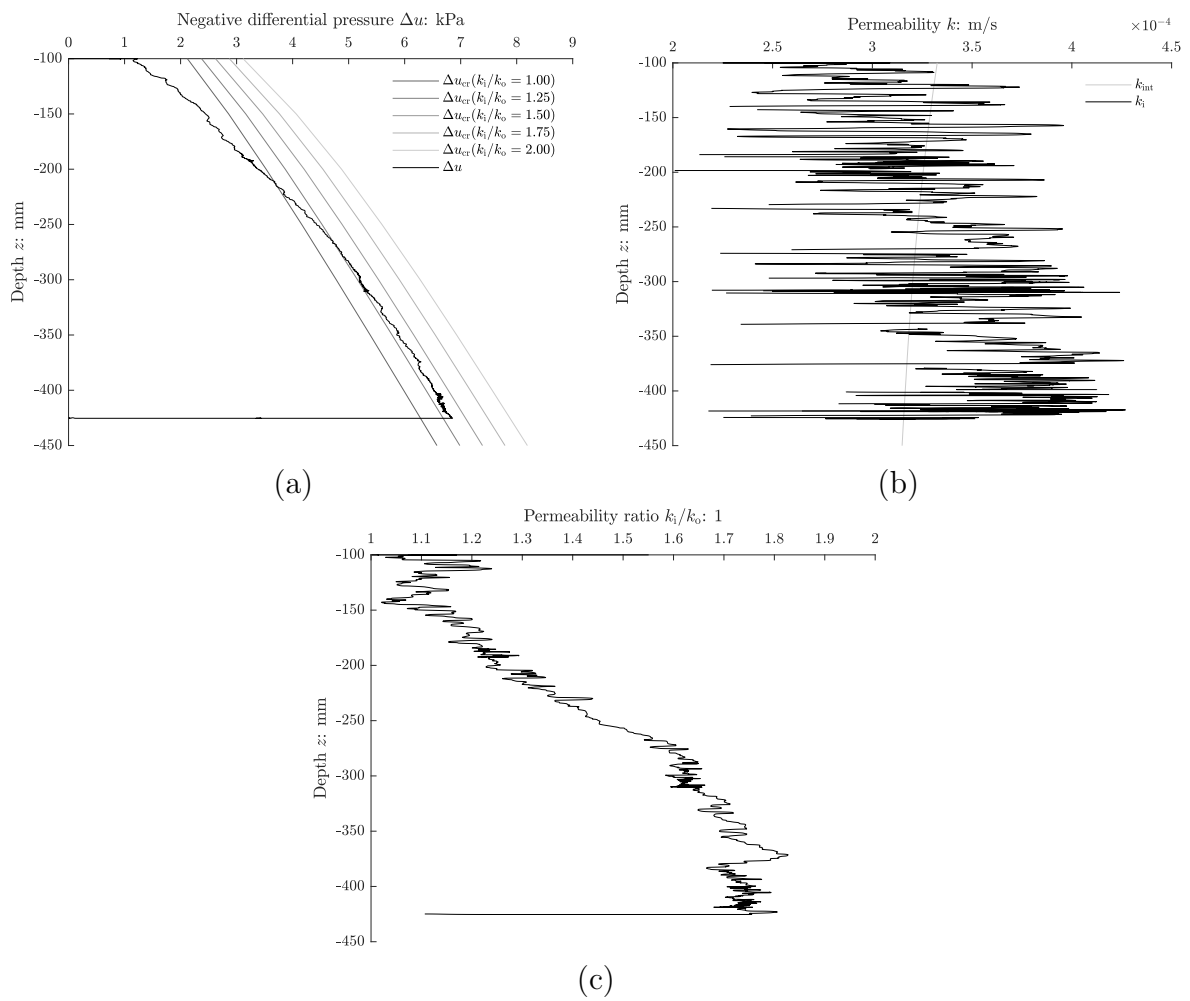
No record
(a)

No record
(b)

Figure A.4.3.3: Permeability test: hydraulic conductivity (a) and permeability ratio (b).
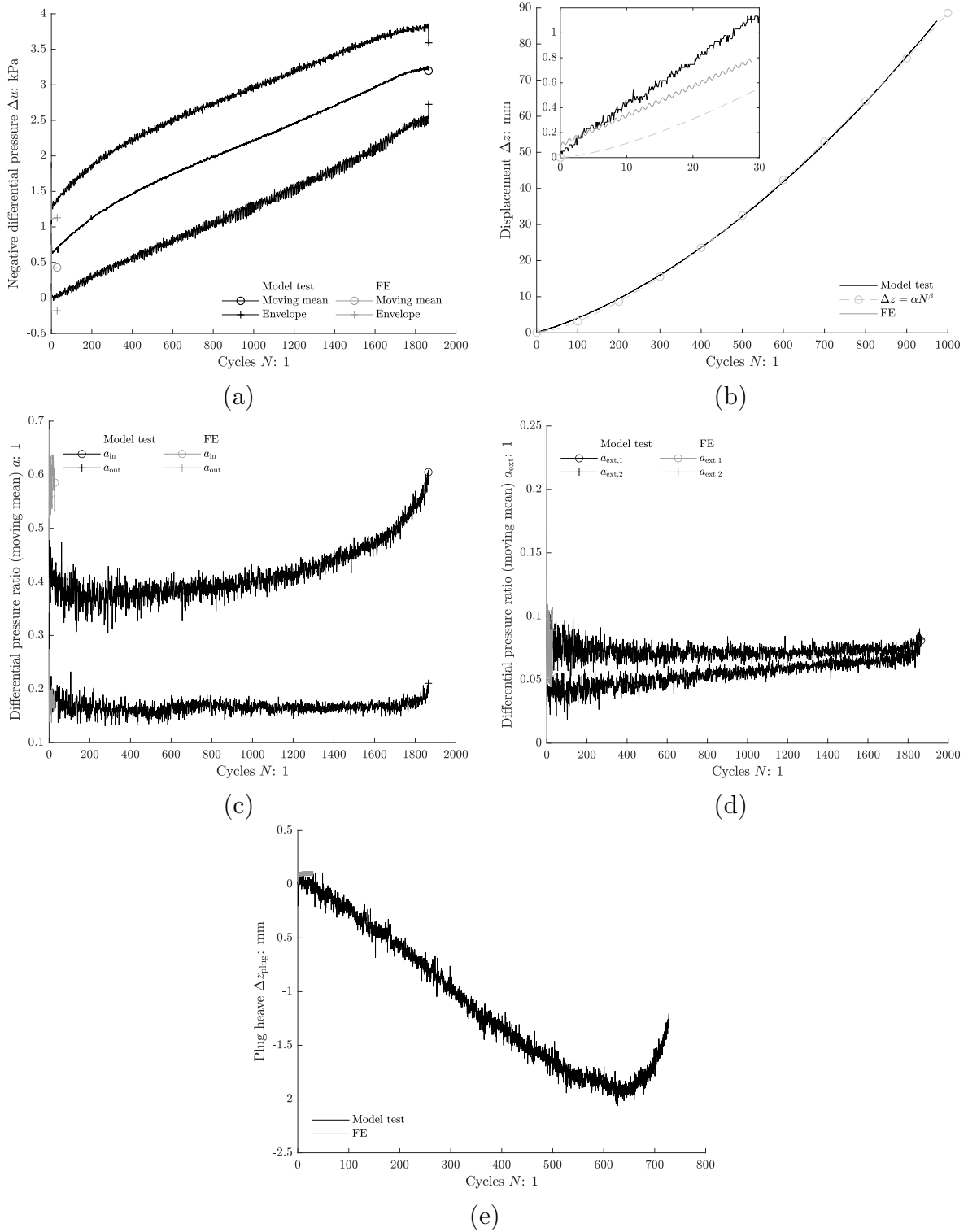
(a)

(b)

(c)

(d)

(e)

Figure A.4.3.4: Tensile test: negative differential pressure (a), displacement (b), differential pressure ratio (skirt) (c), differential pressure ratio (external) (d) and plug heave (e).

A.4.4 F1.01M0.87A0.60

Table A.4.4.1: Test summary

L	$500\,\mathrm{mm}$	$\mathrm{DPS_{ext,1}}$		$\mathrm{DPS_{ext,2}}$	
D	$510\,\mathrm{mm}$	r	z	r	z
T_w	$17.9°\mathrm{C}$	$510\,\mathrm{mm}$	$380.0\,\mathrm{mm}$	$510\,\mathrm{mm}$	$475.0\,\mathrm{mm}$

Drained resistance			Tensile test		
z	425.2	mm	z	423.3	mm
z/D	0.85		z/D	0.85	
z_plug	35.6	mm	z_plug	35.3	mm
F_dr	0.83	kN	f	1.01	1/s
Δz_{F_dr}	0.95	mm	$\bar{F}_\mathrm{mean}$	0.87	
			$\bar{F}_\mathrm{ampl}$	0.60	
			Regression ($\Delta z = \alpha N^\beta$)		
			α	0.0107	$\mathrm{mm}/1^\beta$
			β	1.3647	1

Table A.4.4.2: FE model parameters

γ'	κ	λ	ν	ϕ'	ψ	k_i	$k_\mathrm{i}/k_\mathrm{o}$	k_0
$10.41\,\mathrm{kN/m^3}$	350	0.4	0.2	45°	20°	$3.8 \times 10^{-4}\,\mathrm{m/s}$	1.5	0.592

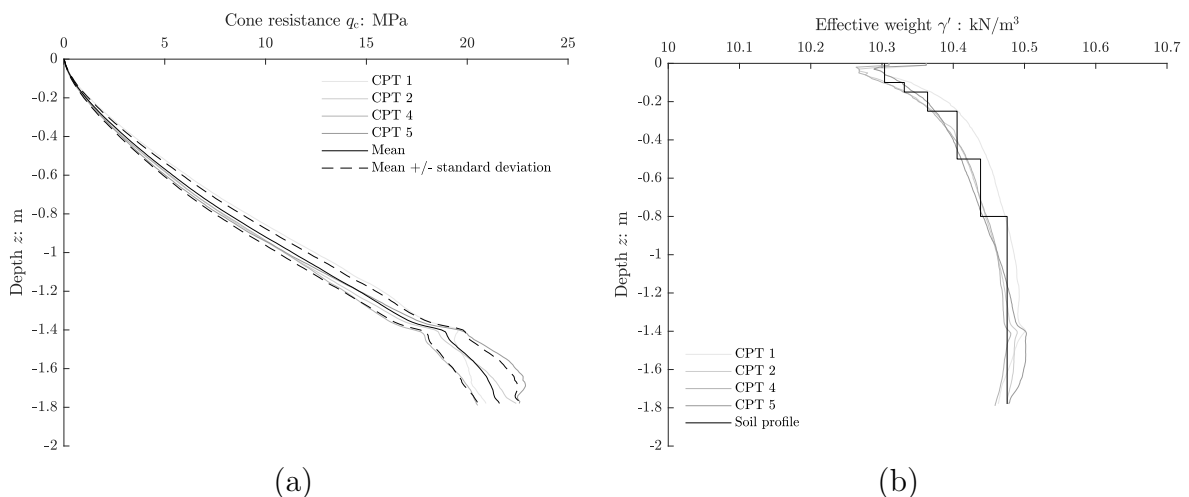| Comments: |
|---|
| No permeability test conducted. |

Figure A.4.4.1: Cone penetration test: cone resistance (a) and effective weight (b).
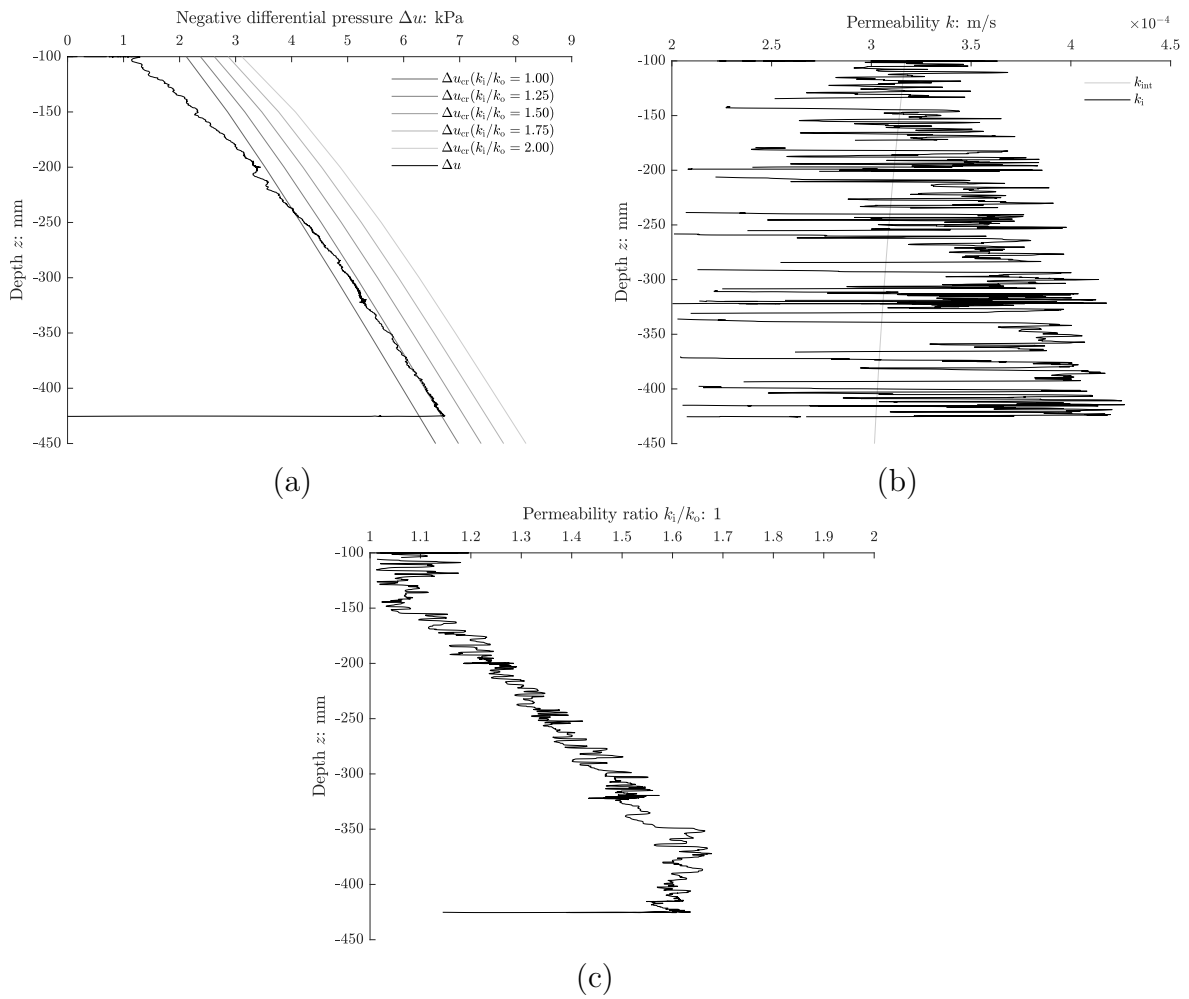
Figure A.4.4.2: Installation: negative differential pressure (a), hydraulic conductivity (b) and permeability ratio (c).

No record
(a)

No record
(b)

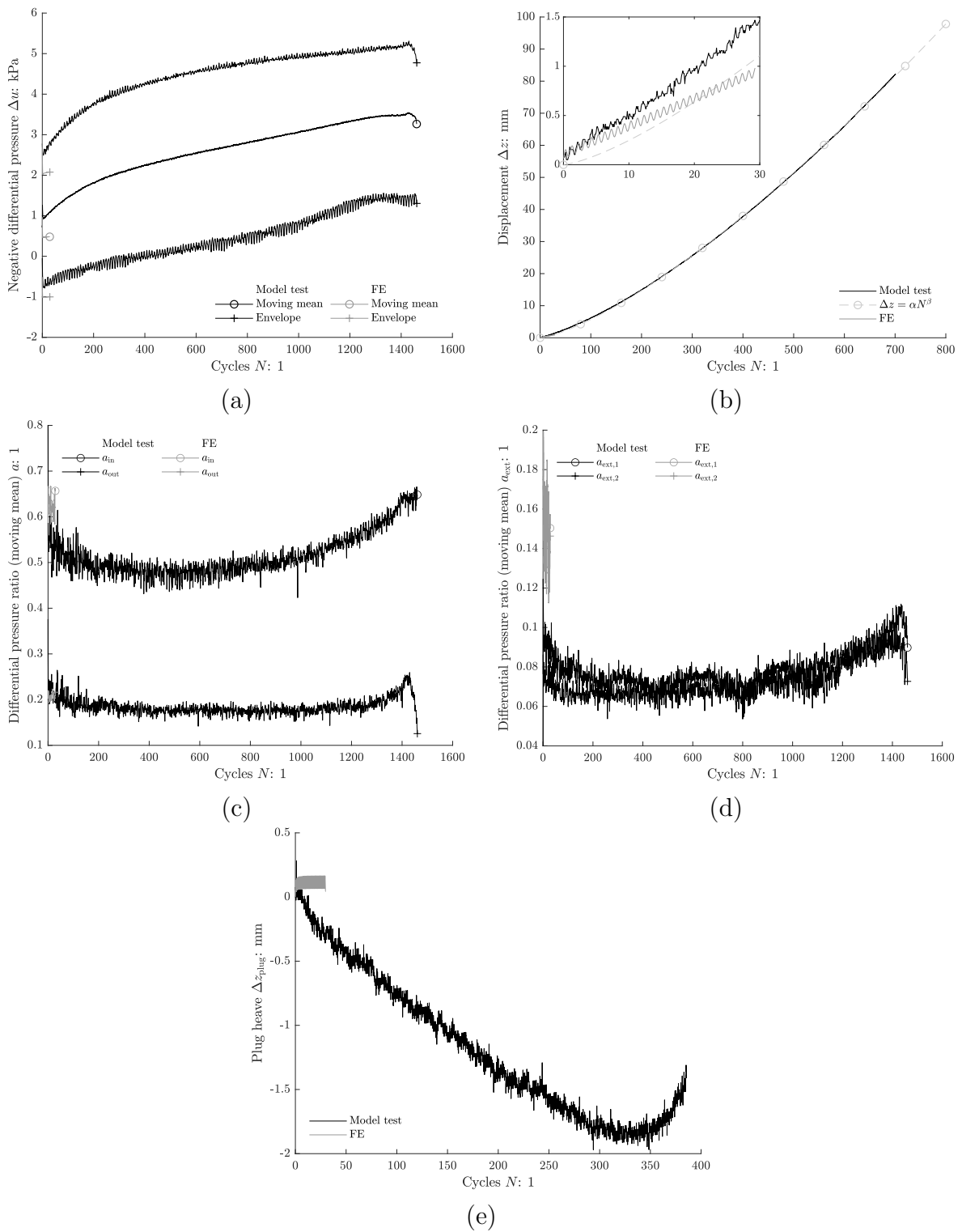*Figure A.4.4.3:* Permeability test: hydraulic conductivity (a) and permeability ratio (b).

Figure A.4.4.4: Tensile test: negative differential pressure (a), displacement (b), differential pressure ratio (skirt) (c), differential pressure ratio (external) (d) and plug heave (e).

A.4.5 F1.01M1.24A0.38

Table A.4.5.1: Test summary

L	500 mm	DPS$_{\text{ext,1}}$		DPS$_{\text{ext,2}}$	
D	510 mm	r	z	r	z
T_{w}	18.4°C	510 mm	376.5 mm	510 mm	425.0 mm

Drained resistance			Tensile test		
z	425.0	mm	z	424.3	mm
z/D	0.85		z/D	0.85	
z_{plug}	44.5	mm	z_{plug}	43.8	mm
F_{dr}	0.74	kN	f	1.01	1/s
$\Delta z_{F_{\text{dr}}}$	0.82	mm	$\bar{F}_{\text{mean}}$	1.24	
			$\bar{F}_{\text{ampl}}$	0.38	
			Regression ($\Delta z = \alpha N^{\beta}$)		
			α	0.0633	mm/1$^{\beta}$
			β	1.0991	1

Table A.4.5.2: FE model parameters

γ'	κ	λ	ν	ϕ'	ψ	k_{i}	$k_{\text{i}}/k_{\text{o}}$	k_0
10.41 kN/m³	350	0.4	0.2	45°	20°	3.5×10^{-4} m/s	1.6	0.542

Comments:
Test was prematurely terminated when reaching $\Delta z = 0.02D$ due to inaccurate load application.

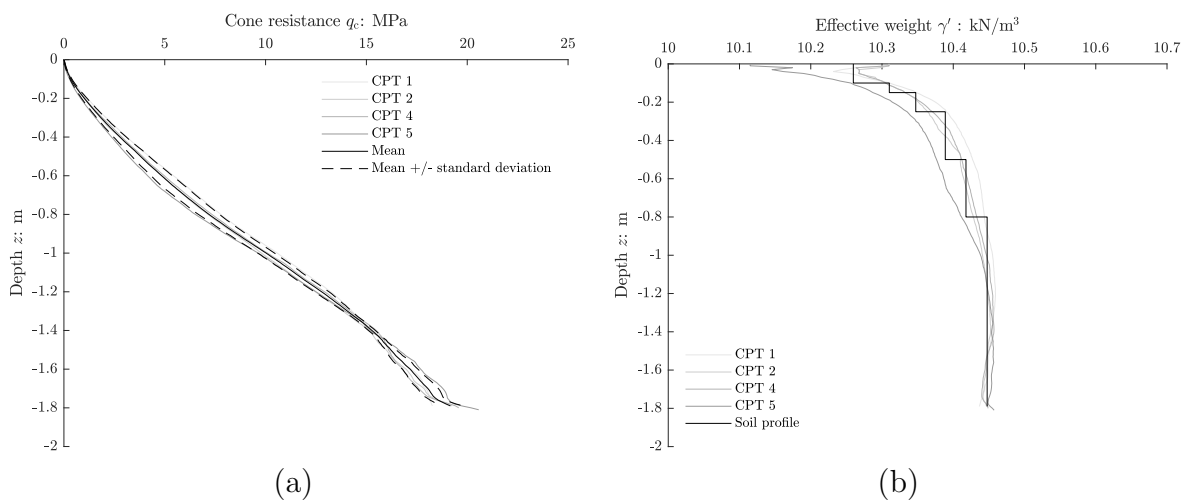*Figure A.4.5.1:* Cone penetration test: cone resistance (a) and effective weight (b).
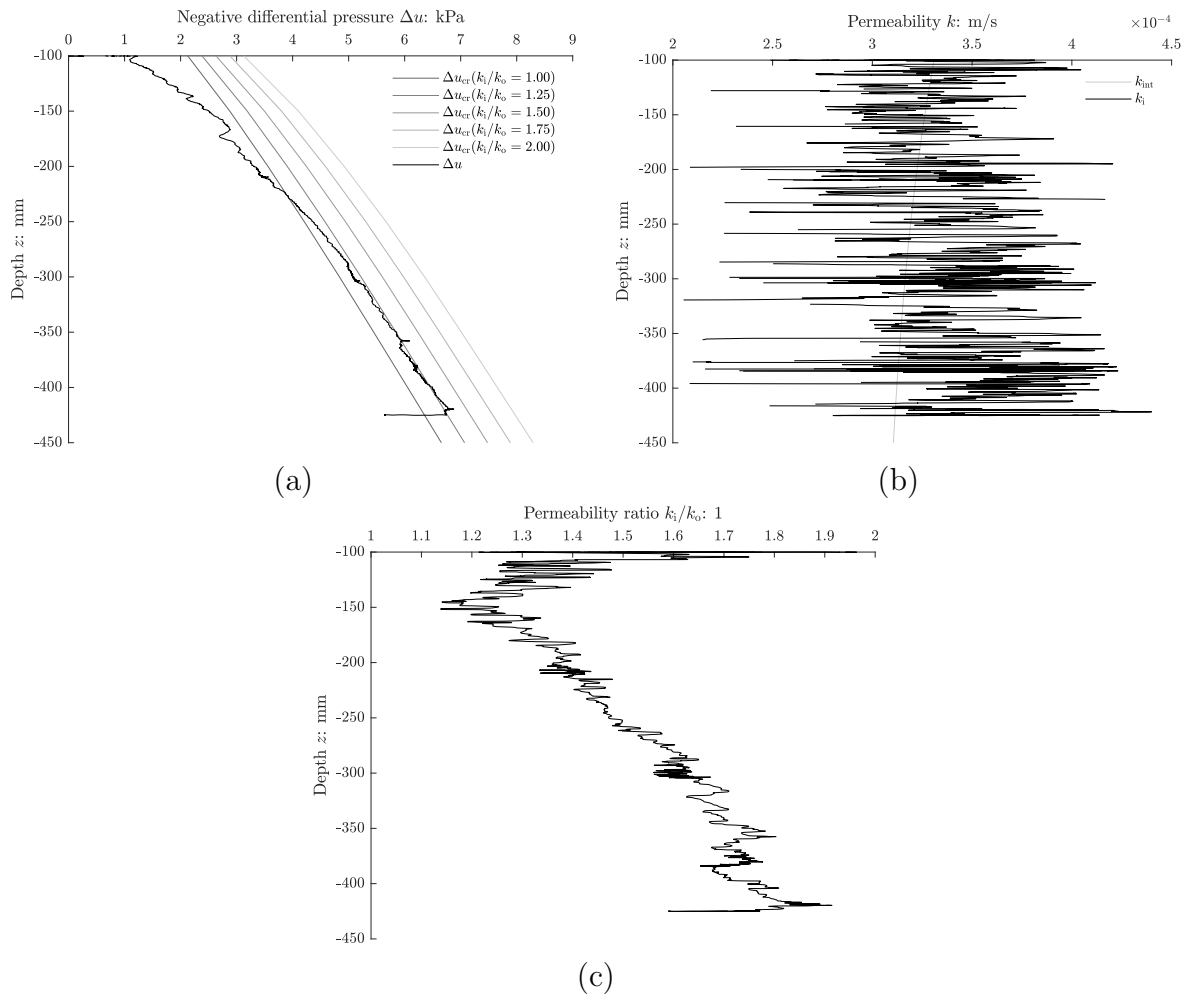
(a)

(b)

(c)

Figure A.4.5.2: Installation: negative differential pressure (a), hydraulic conductivity (b) and permeability ratio (c).
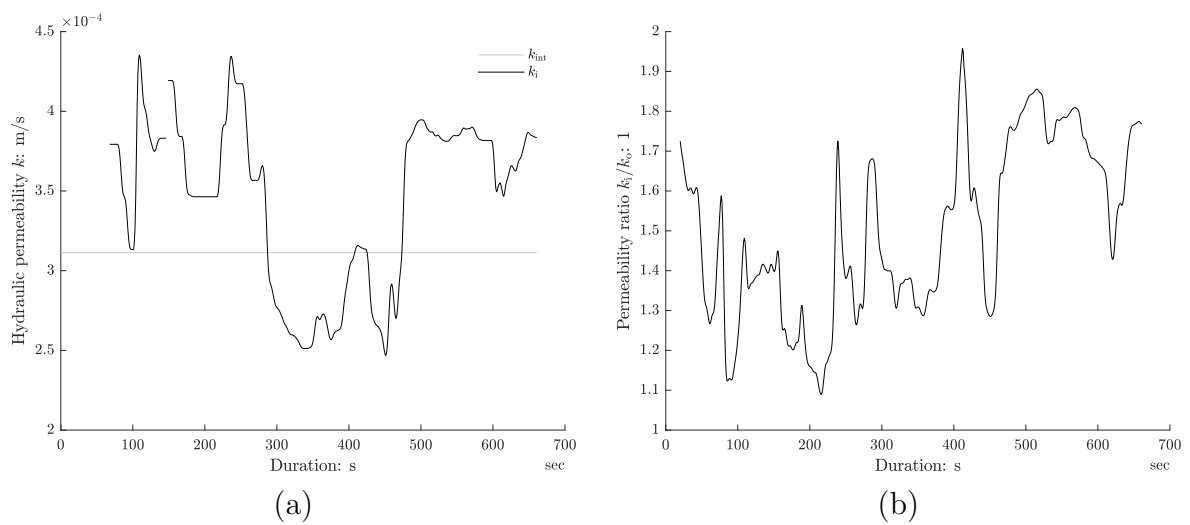

(a)

(b)

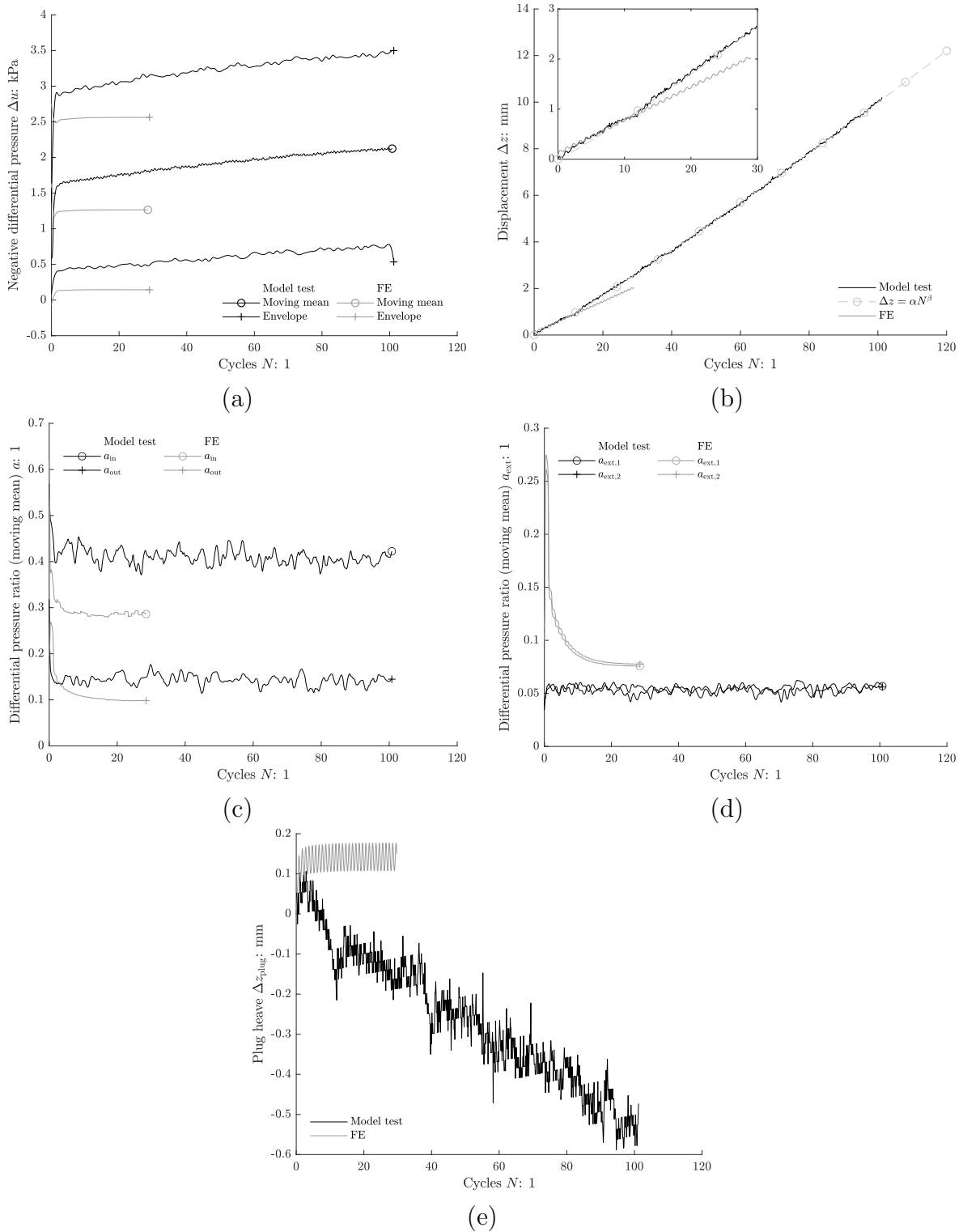*Figure A.4.5.3:* Permeability test: hydraulic conductivity (a) and permeability ratio (b).

Figure A.4.5.4: Tensile test: negative differential pressure (a), displacement (b), differential pressure ratio (skirt) (c), differential pressure ratio (external) (d) and plug heave (e).

A.4.6 F1.02M1.58A0.39

Table A.4.6.1: Test summary

L	$500\,\mathrm{mm}$	$\mathrm{DPS_{ext,1}}$		$\mathrm{DPS_{ext,2}}$	
D	$510\,\mathrm{mm}$	r	z	r	z
T_w	$18.7^\circ\mathrm{C}$	$510\,\mathrm{mm}$	$1150.0\,\mathrm{mm}$	$510\,\mathrm{mm}$	$426.0\,\mathrm{mm}$

Drained resistance			Tensile test		
z	425.3	mm	z	424.4	mm
z/D	0.85		z/D	0.85	
z_plug	43.8	mm	z_plug	43.7	mm
F_dr	0.64	kN	f	1.02	1/s
Δz_{F_dr}	0.72	mm	$\bar{F}_\mathrm{mean}$	1.58	
			$\bar{F}_\mathrm{ampl}$	0.39	
			Regression $(\Delta z = \alpha N^\beta)$		
			α	0.0706	$\mathrm{mm}/1^\beta$
			β	1.1874	1

Table A.4.6.2: FE model parameters

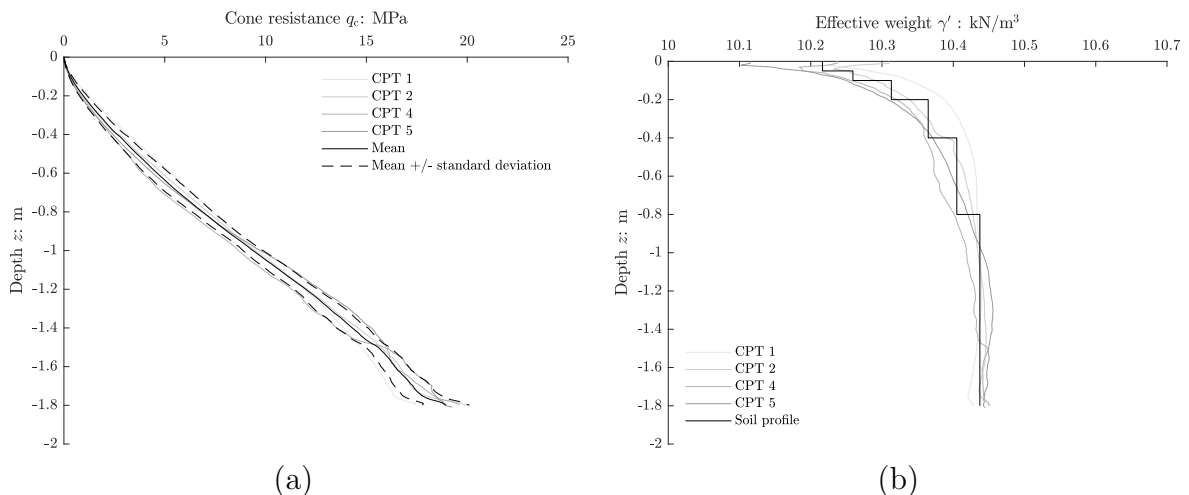| γ'	κ	λ	ν	ϕ'	ψ	k_i	$k_\mathrm{i}/k_\mathrm{o}$	k_0
$10.41\,\mathrm{kN/m^3}$	350	0.4	0.2	45°	20°	$3.7\times10^{-4}\,\mathrm{m/s}$	1.5	0.454

Comments:
No permeability test conducted.

Figure A.4.6.1: Cone penetration test: cone resistance (a) and effective weight (b).
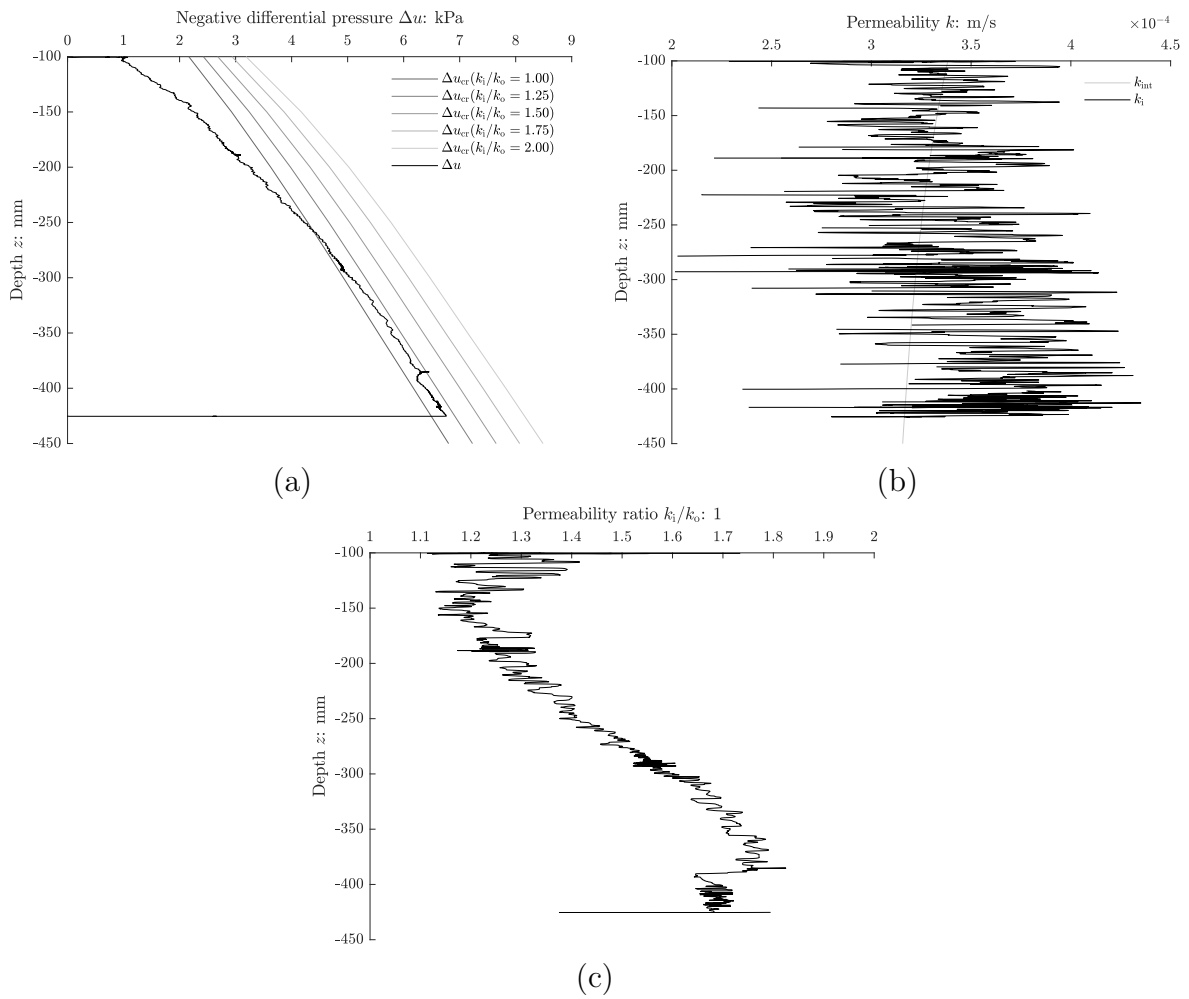
Figure A.4.6.2: Installation: negative differential pressure (a), hydraulic conductivity (b) and permeability ratio (c).

No record
(a)

No record
(b)

Figure A.4.6.3: Permeability test: hydraulic conductivity (a) and permeability ratio (b).
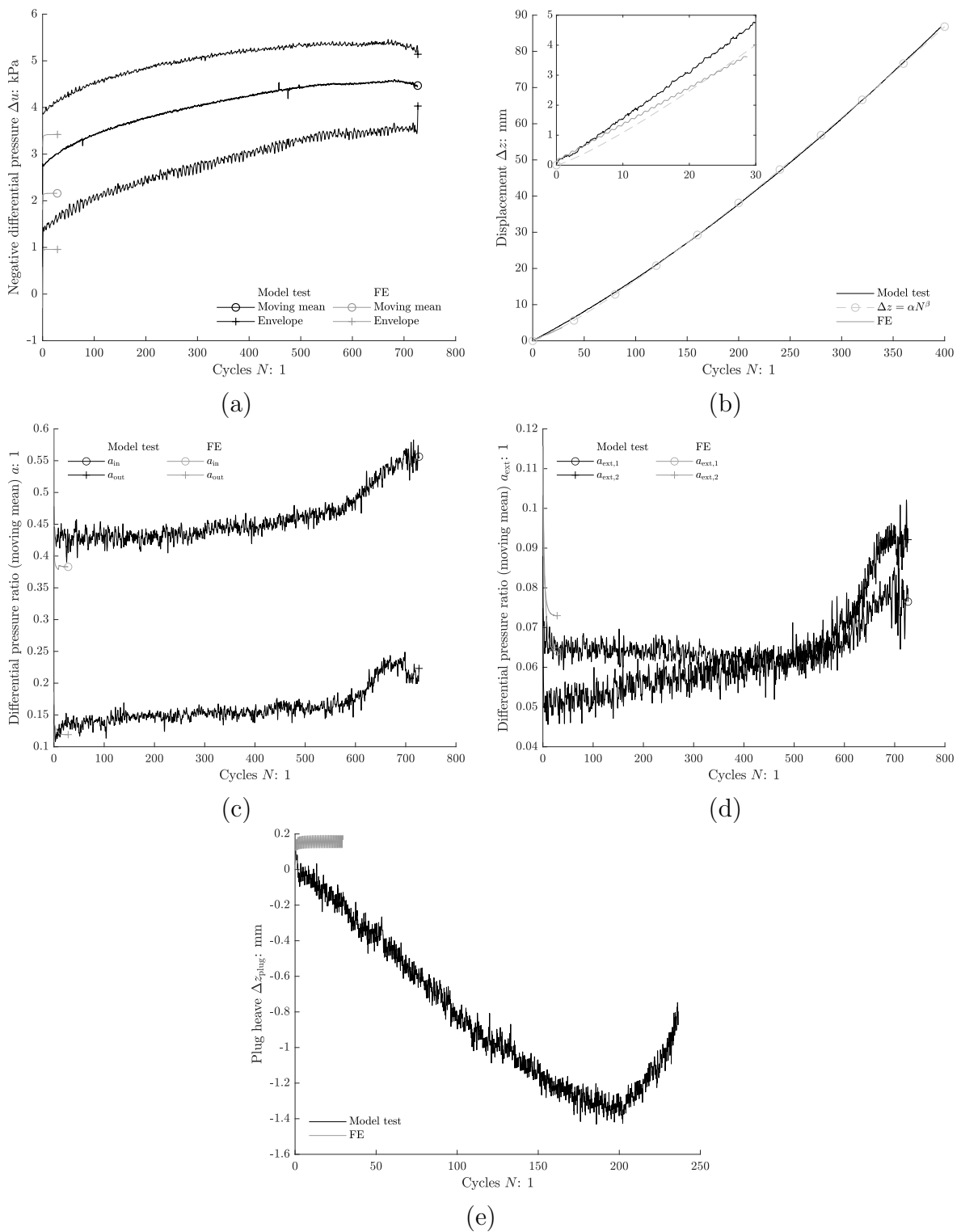
(a)

(b)

(c)

(d)

(e)

Figure A.4.6.4: Tensile test: negative differential pressure (a), displacement (b), differential pressure ratio (skirt) (c), differential pressure ratio (external) (d) and plug heave (e).

A.4.7 F1.01M1.29A0.89

Table A.4.7.1: Test summary

L	500 mm	DPS$_{\text{ext,1}}$		DPS$_{\text{ext,2}}$	
D	510 mm	r	z	r	z
T_{w}	18.1°C	510 mm	550.0 mm	510 mm	375.0 mm

Drained resistance			Tensile test		
z	425.3	mm	z	424.4	mm
z/D	0.85		z/D	0.85	
z_{plug}	47.0	mm	z_{plug}	46.5	mm
F_{dr}	0.64	kN	f	1.01	1/s
$\Delta z_{F_{\text{dr}}}$	0.81	mm	$\bar{F}_{\text{mean}}$	1.29	
			$\bar{F}_{\text{ampl}}$	0.89	
			Regression ($\Delta z = \alpha N^\beta$)		
			α	0.0528	mm/1$^\beta$
			β	1.1867	1

Table A.4.7.2: FE model parameters

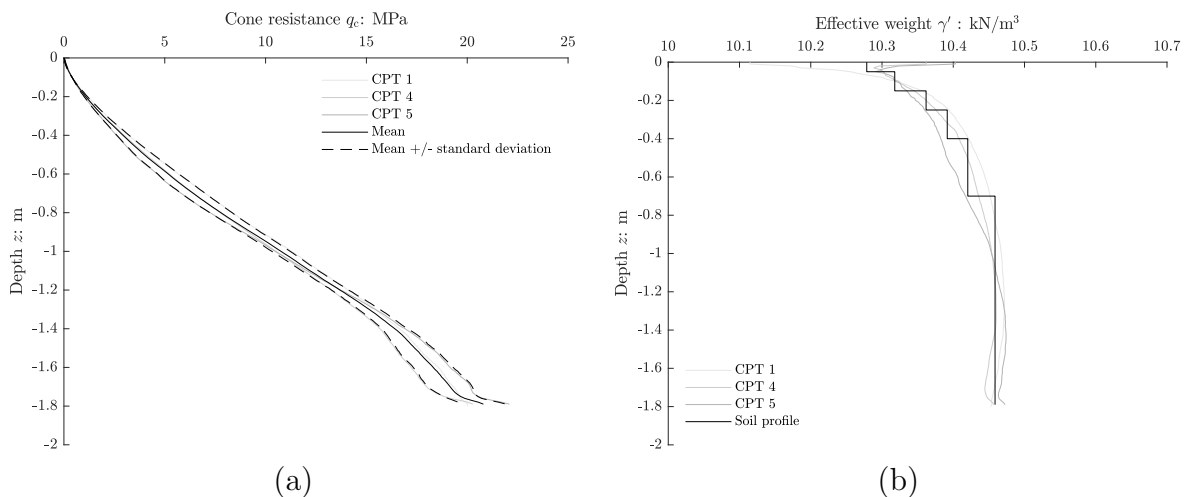| γ'	κ	λ	ν	ϕ'	ψ	k_{i}	$k_{\text{i}}/k_{\text{o}}$	k_0
10.41 kN/m^3	350	0.4	0.2	45°	20°	3.7×10^{-4} m/s	1.6	0.463

Comments:

-

Figure A.4.7.1: Cone penetration test: cone resistance (a) and effective weight (b).
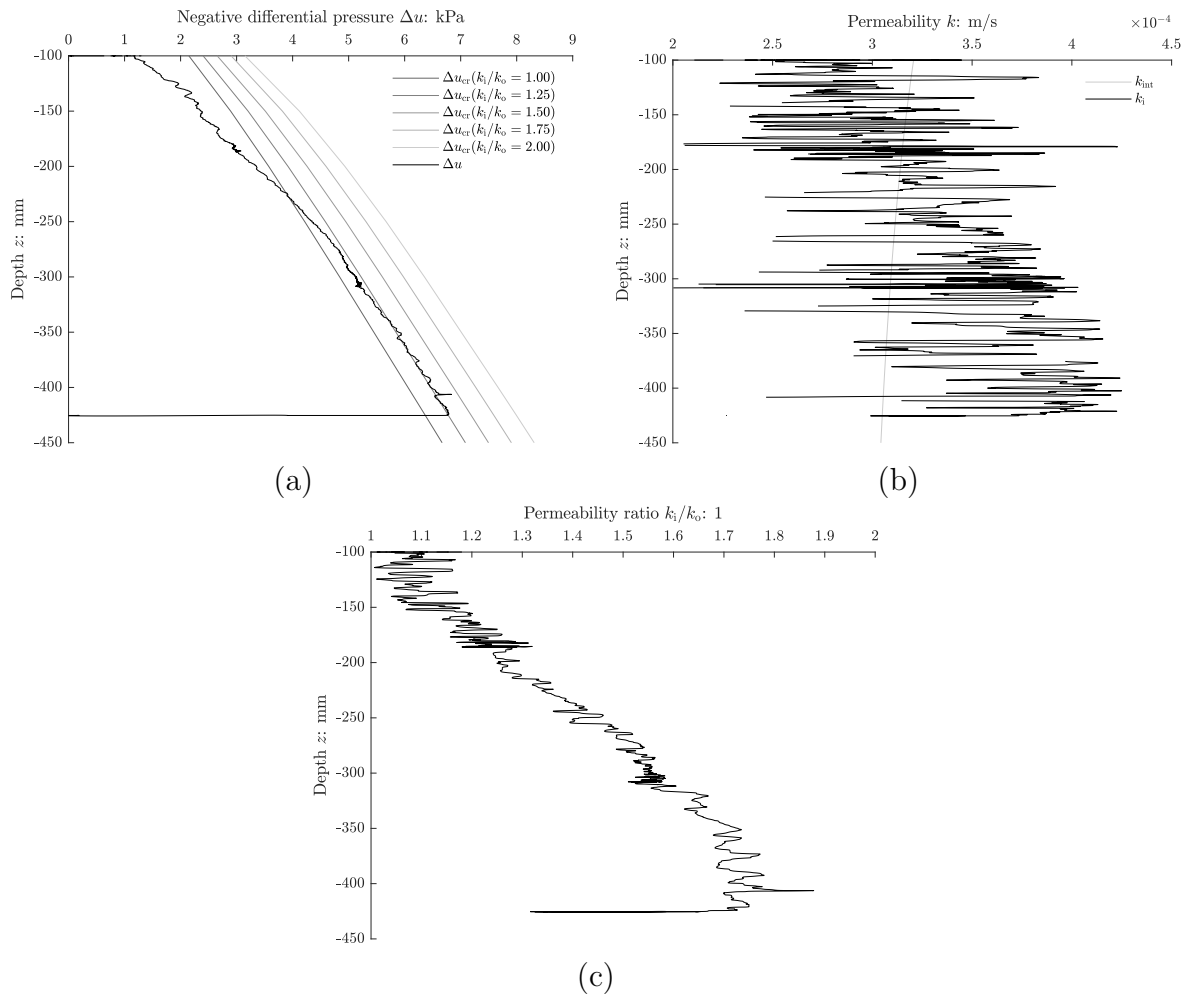
(a)

(b)

(c)

Figure A.4.7.2: Installation: negative differential pressure (a), hydraulic conductivity (b) and permeability ratio (c).
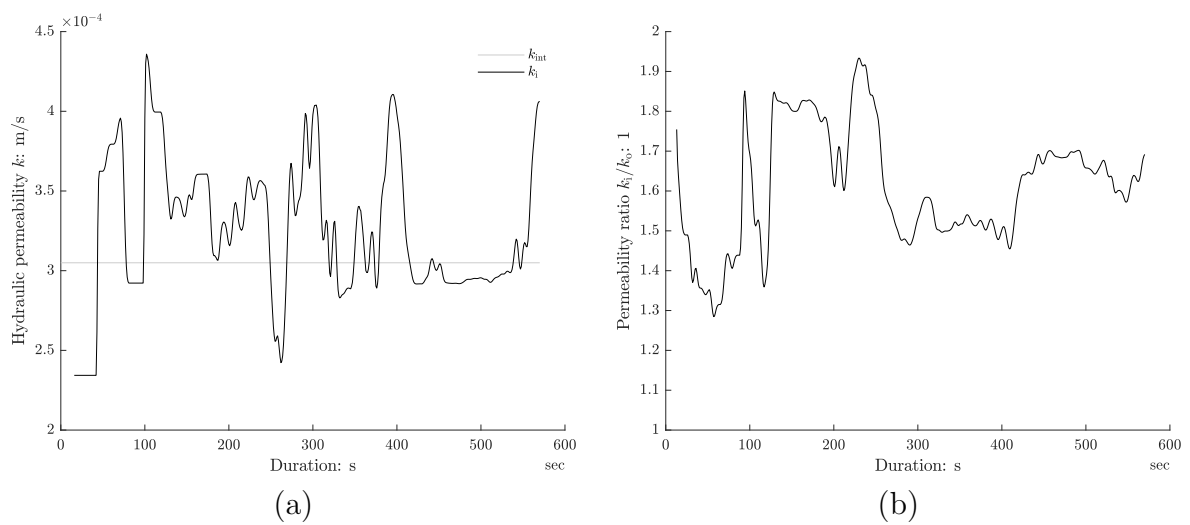

(a)

(b)

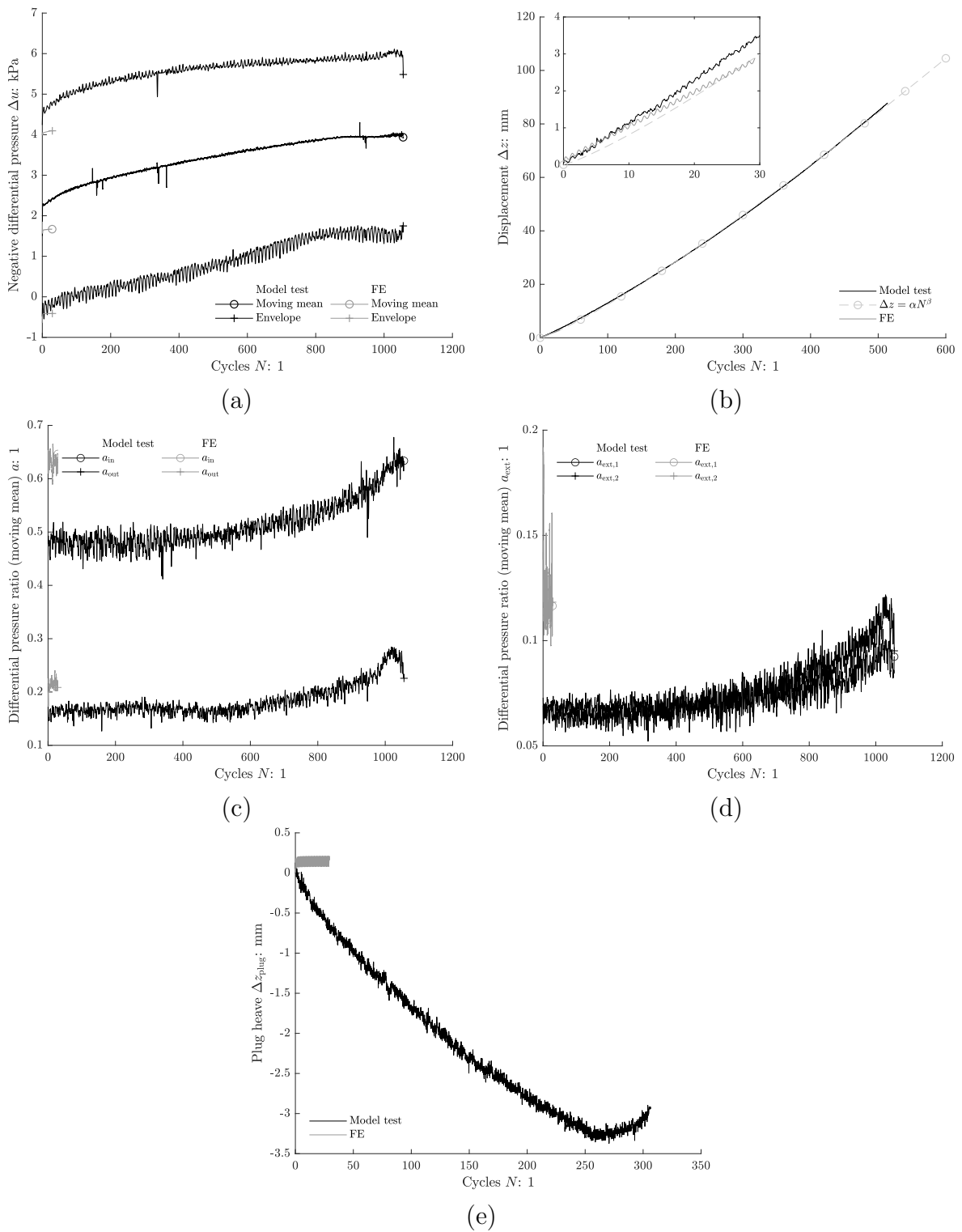*Figure A.4.7.3:* Permeability test: hydraulic conductivity (a) and permeability ratio (b).

Figure A.4.7.4: Tensile test: negative differential pressure (a), displacement (b), differential pressure ratio (skirt) (c), differential pressure ratio (external) (d) and plug heave (e).

A.4.8 F1.01M2.12A0.52

Table A.4.8.1: Test summary

L	500 mm	DPS$_{\text{ext},1}$		DPS$_{\text{ext},2}$	
D	510 mm	r	z	r	z
T_{w}	18.4°C	510 mm	1500.0 mm	510 mm	425.0 mm

Drained resistance			Tensile test		
z	424.8	mm	z	424.2	mm
z/D	0.85		z/D	0.85	
z_{plug}	59.2	mm	z_{plug}	58.6	mm
F_{dr}	0.71	kN	f	1.01	1/s
$\Delta z_{F_{\text{dr}}}$	0.72	mm	$\bar{F}_{\text{mean}}$	2.12	
			$\bar{F}_{\text{ampl}}$	0.52	
			Regression ($\Delta z = \alpha N^{\beta}$)		
			α	0.0630	mm/1$^{\beta}$
			β	1.3976	1

Table A.4.8.2: FE model parameters

γ'	κ	λ	ν	ϕ'	ψ	k_{i}	$k_{\text{i}}/k_{\text{o}}$	k_0
10.41 kN/m^3	350	0.4	0.2	45°	20°	3.6×10^{-4} m/s	1.6	0.515

Comments:
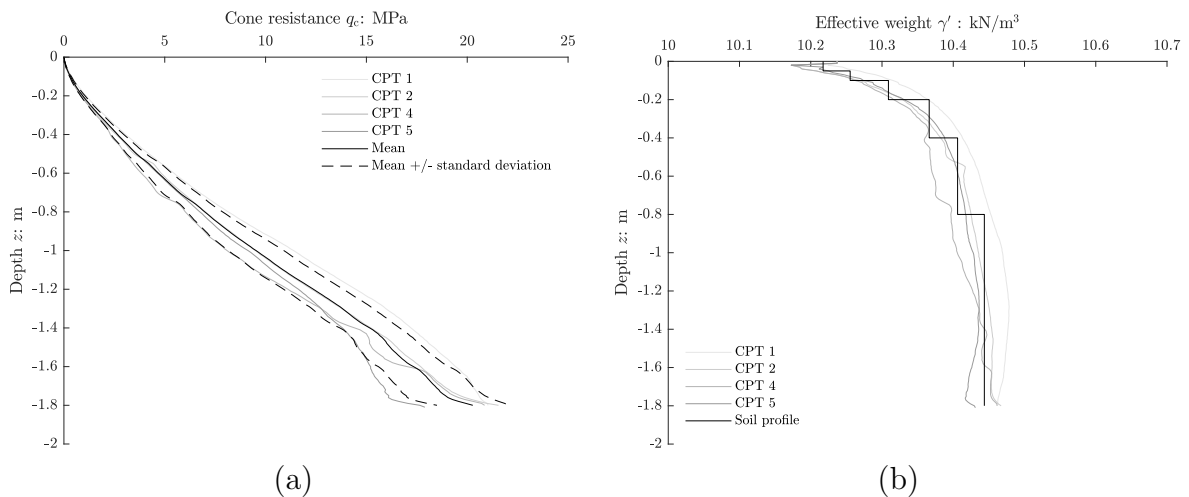No permeability test conducted.

Figure A.4.8.1: Cone penetration test: cone resistance (a) and effective weight (b).
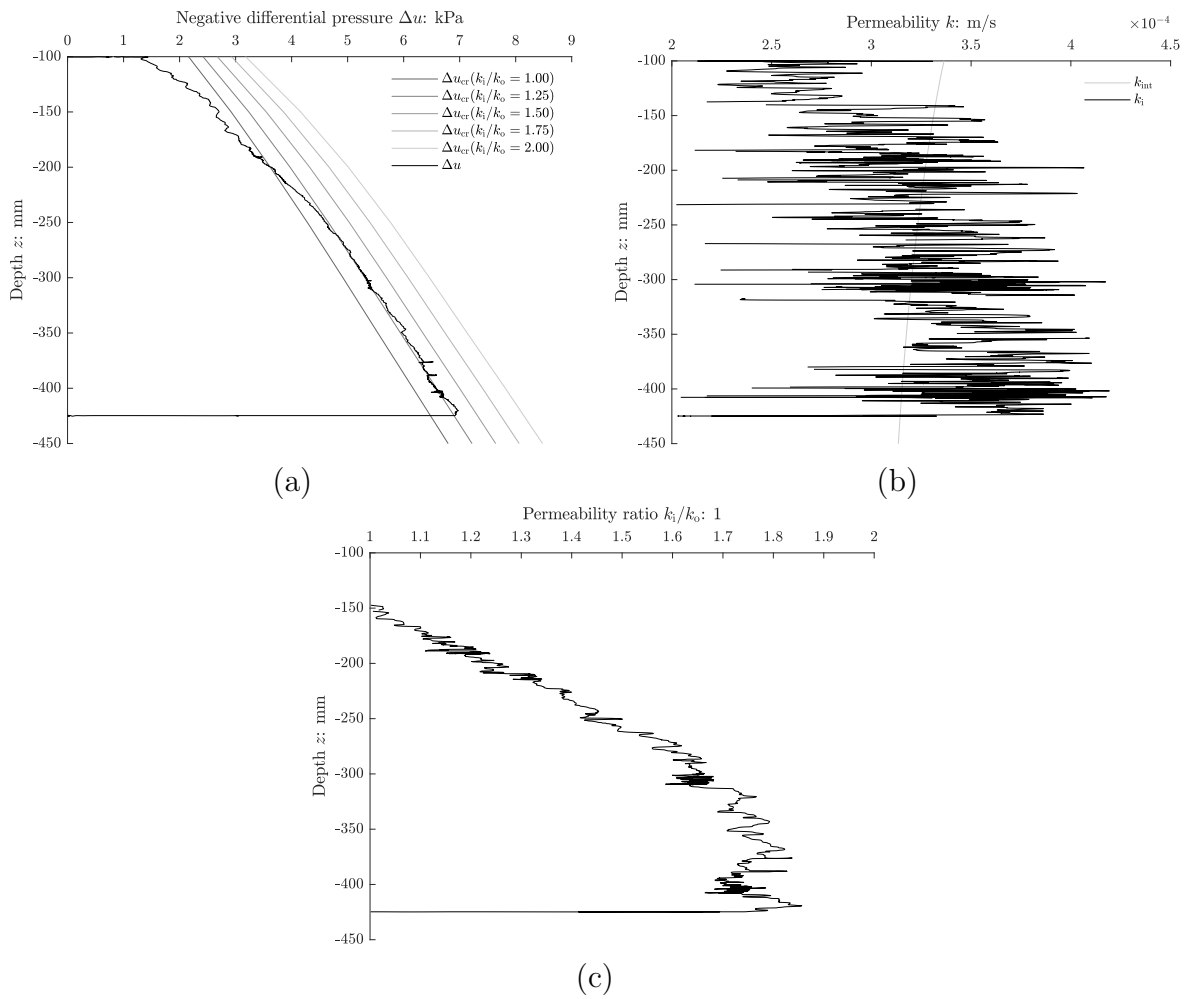
Figure A.4.8.2: Installation: negative differential pressure (a), hydraulic conductivity (b) and permeability ratio (c).

No record
(a)

No record
(b)

Figure A.4.8.3: Permeability test: hydraulic conductivity (a) and permeability ratio (b).
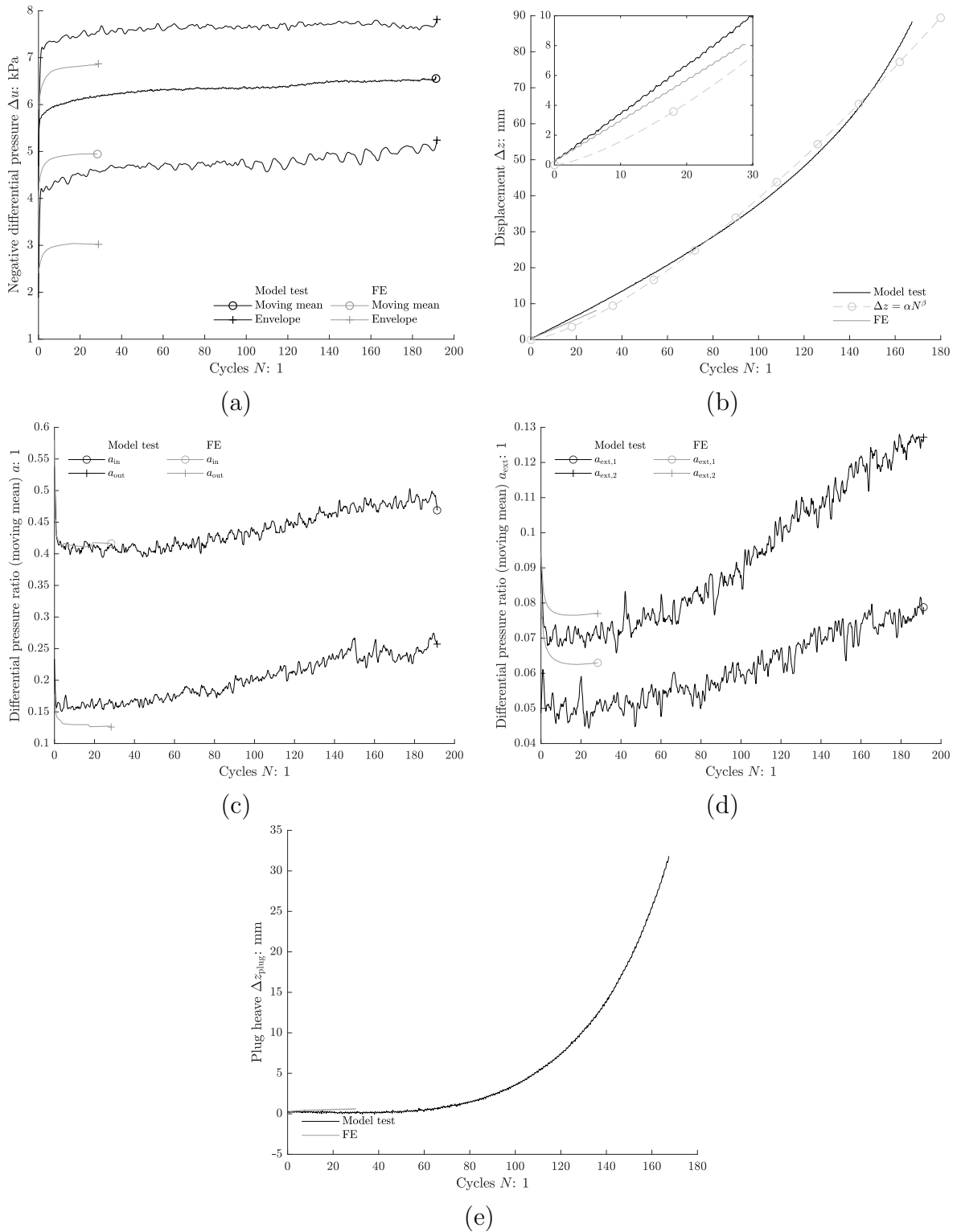
(a)

(b)

(c)

(d)

(e)

Figure A.4.8.4: Tensile test: negative differential pressure (a), displacement (b), differential pressure ratio (skirt) (c), differential pressure ratio (external) (d) and plug heave (e).

A.4.9 F1.01M1.90A0.99

Table A.4.9.1: Test summary

L	500 mm	$DPS_{ext,1}$		$DPS_{ext,2}$	
D	510 mm	r	z	r	z
T_w	18.3°C	510 mm	1600.0 mm	510 mm	554.0 mm

Drained resistance			Tensile test		
z	425.1	mm	z	424.1	mm
z/D	0.85		z/D	0.85	
z_{plug}	46.1	mm	z_{plug}	45.7	mm
F_{dr}	0.79	kN	f	1.01	1/s
$\Delta z_{F_{dr}}$	0.77	mm	$\bar{F}_{mean}$	1.90	
			$\bar{F}_{ampl}$	0.99	
			Regression ($\Delta z = \alpha N^\beta$)		
			α	0.0464	mm/1^β
			β	1.5454	1

Table A.4.9.2: FE model parameters

γ'	κ	λ	ν	ϕ'	ψ	k_i	k_i/k_o	k_0
10.41 kN/m³	350	0.4	0.2	45°	20°	3.5×10^{-4} m/s	1.6	0.574

Comments:
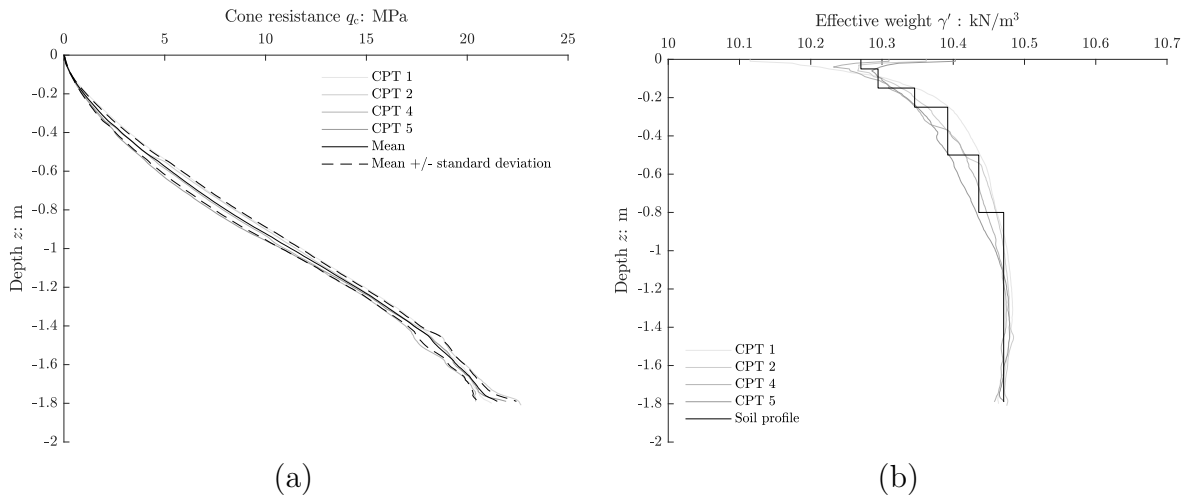No permeability test conducted.

Figure A.4.9.1: Cone penetration test: cone resistance (a) and effective weight (b).
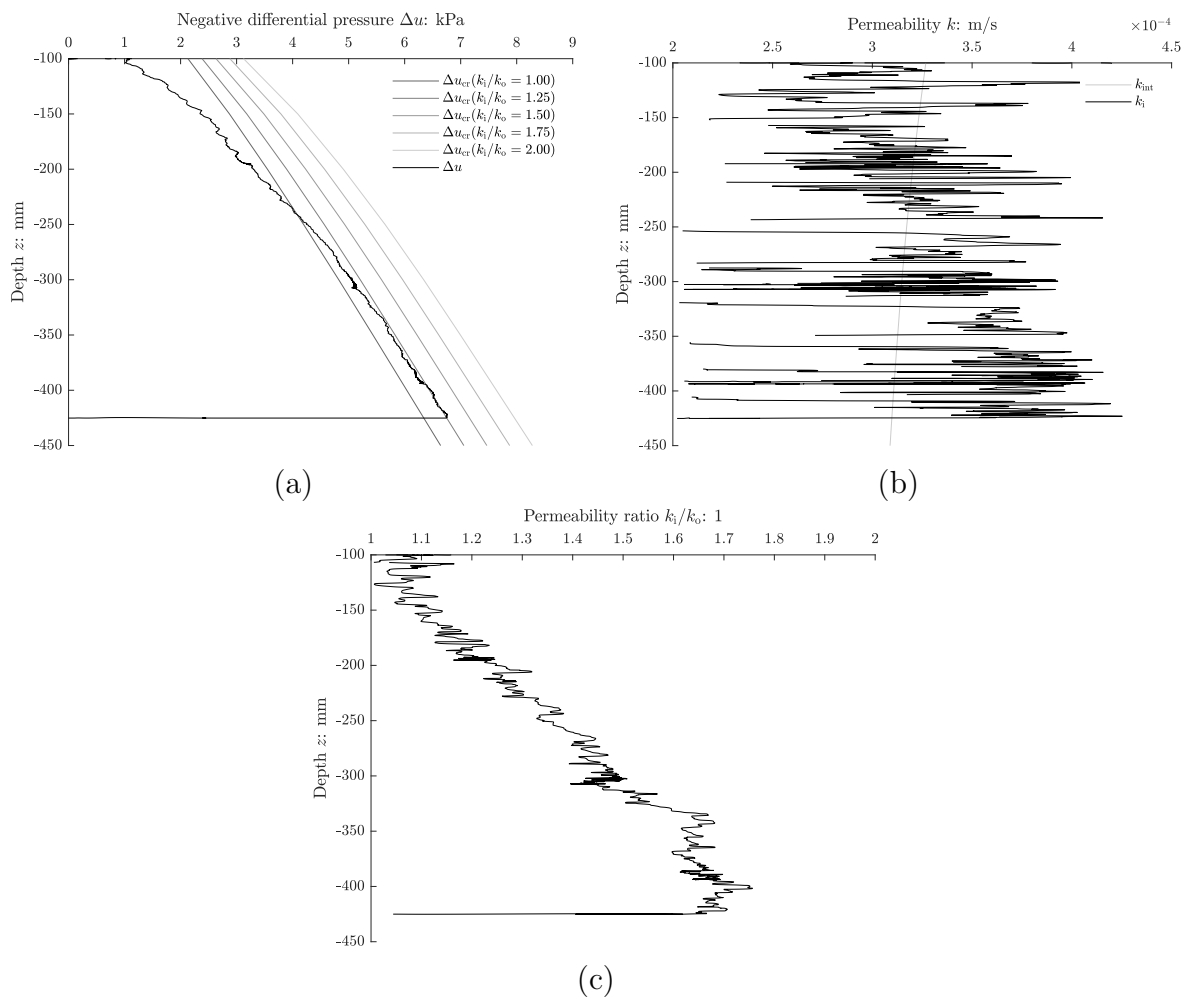
(a)

(b)

(c)

Figure A.4.9.2: Installation: negative differential pressure (a), hydraulic conductivity (b) and permeability ratio (c).

No record
(a)

No record
(b)

Figure A.4.9.3: Permeability test: hydraulic conductivity (a) and permeability ratio (b).
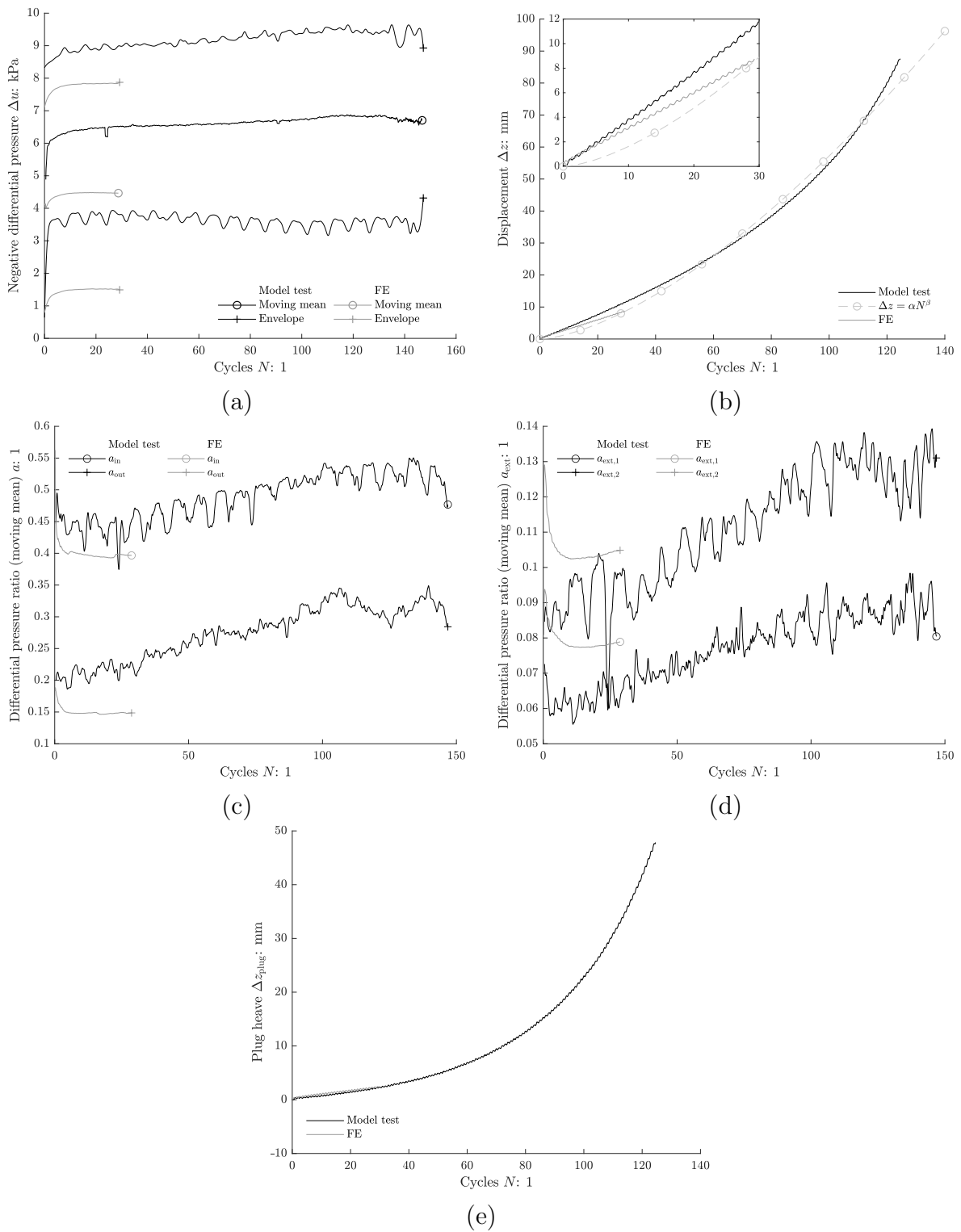
(a)

(b)

(c)

(d)

(e)

Figure A.4.9.4: Tensile test: negative differential pressure (a), displacement (b), differential pressure ratio (skirt) (c), differential pressure ratio (external) (d) and plug heave (e).

A.4.10 F0.50M0.74A0.37

Table A.4.10.1: Test summary

L	500 mm	DPS$_{\text{ext},1}$		DPS$_{\text{ext},2}$	
D	510 mm	r	z	r	z
T_{w}	17.8°C	510 mm	625.0 mm	510 mm	375.0 mm

Drained resistance			Tensile test		
z	425.3	mm	z	424.3	mm
z/D	0.85		z/D	0.85	
z_{plug}	42.3	mm	z_{plug}	41.1	mm
F_{dr}	0.84	kN	f	0.50	1/s
$\Delta z_{F_{\text{dr}}}$	0.74	mm	$\bar{F}_{\text{mean}}$	0.74	
			$\bar{F}_{\text{ampl}}$	0.37	
			Regression ($\Delta z = \alpha N^{\beta}$)		
			α	6.5587e-5	mm/1$^{\beta}$
			β	2.0653	1

Table A.4.10.2: FE model parameters

γ'	κ	λ	ν	ϕ'	ψ	k_{i}	$k_{\text{i}}/k_{\text{o}}$	k_0
10.41 kN/m^3	350	0.4	0.2	45°	20°	3.6×10^{-4} m/s	1.6	0.606

Comments:
Extra weight in the amount of the suction bucket's self weight added during installation.
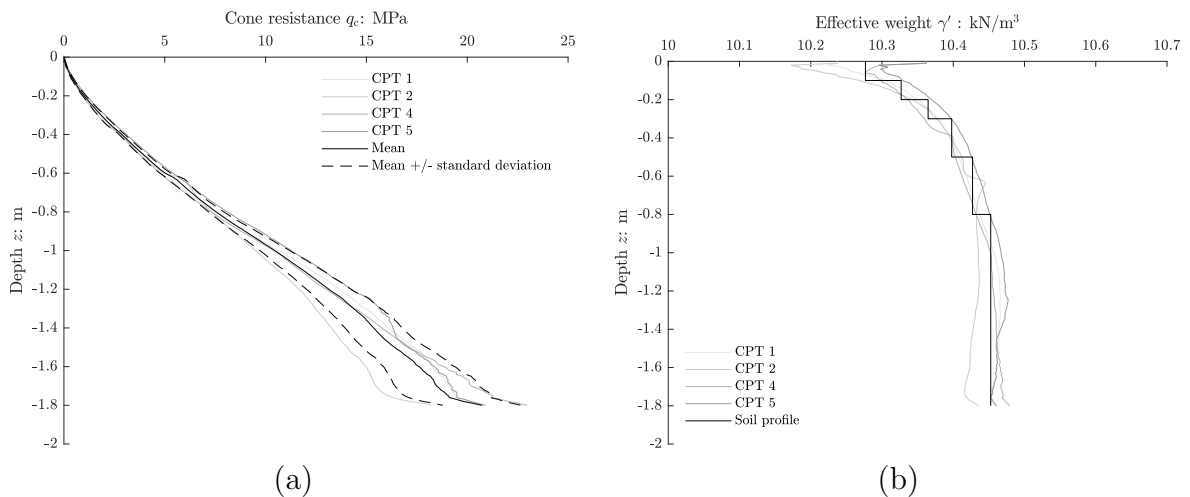

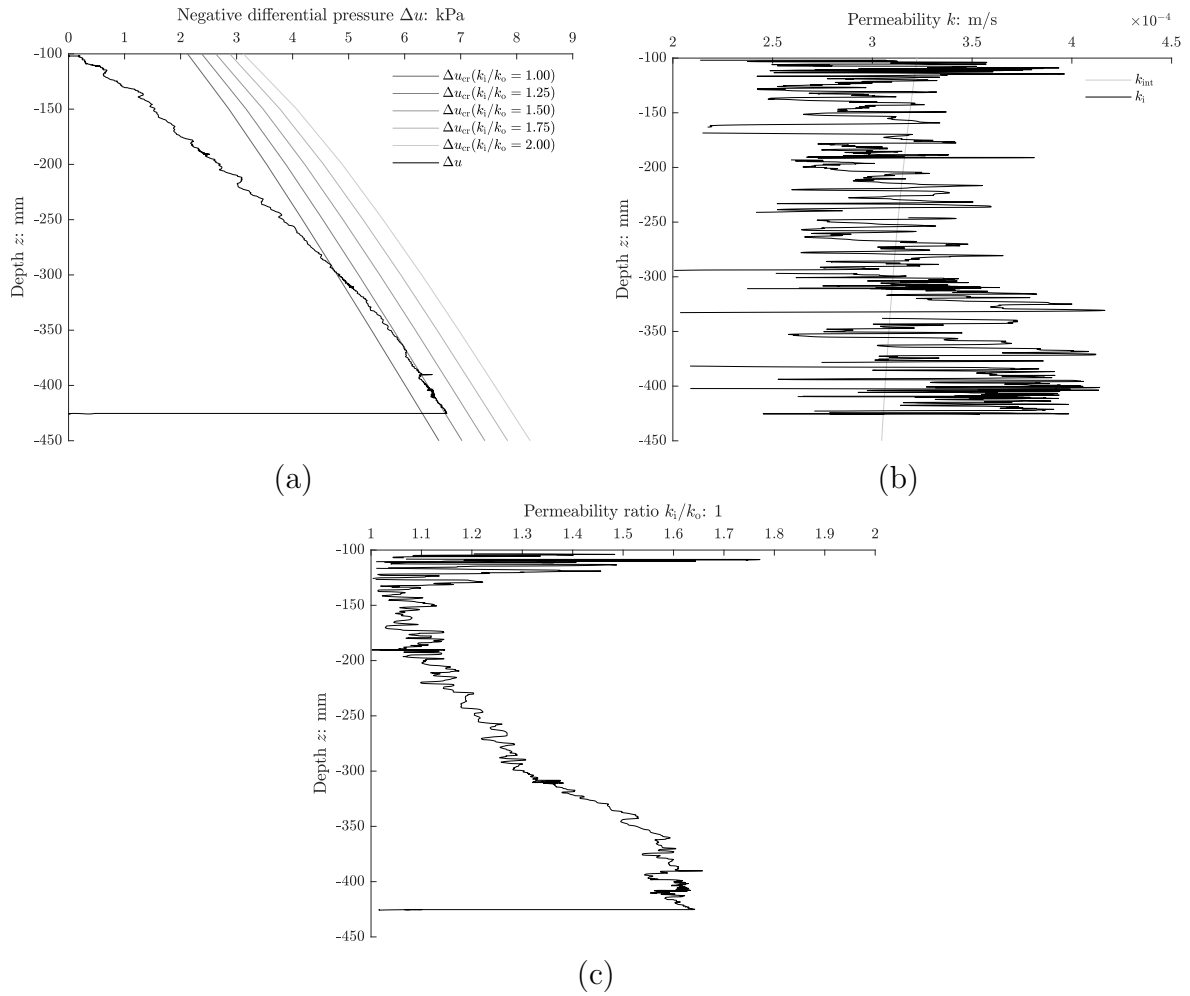*Figure A.4.10.1:* Cone penetration test: cone resistance (a) and effective weight (b).

(a)

(b)

(c)

Figure A.4.10.2: Installation: negative differential pressure (a), hydraulic conductivity (b) and permeability ratio (c).
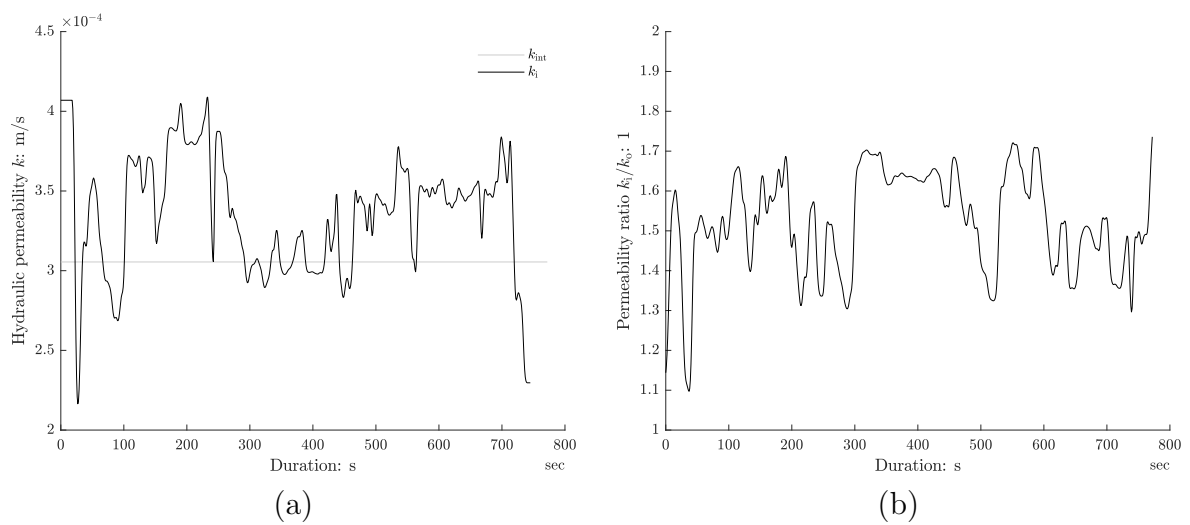

(a)

(b)

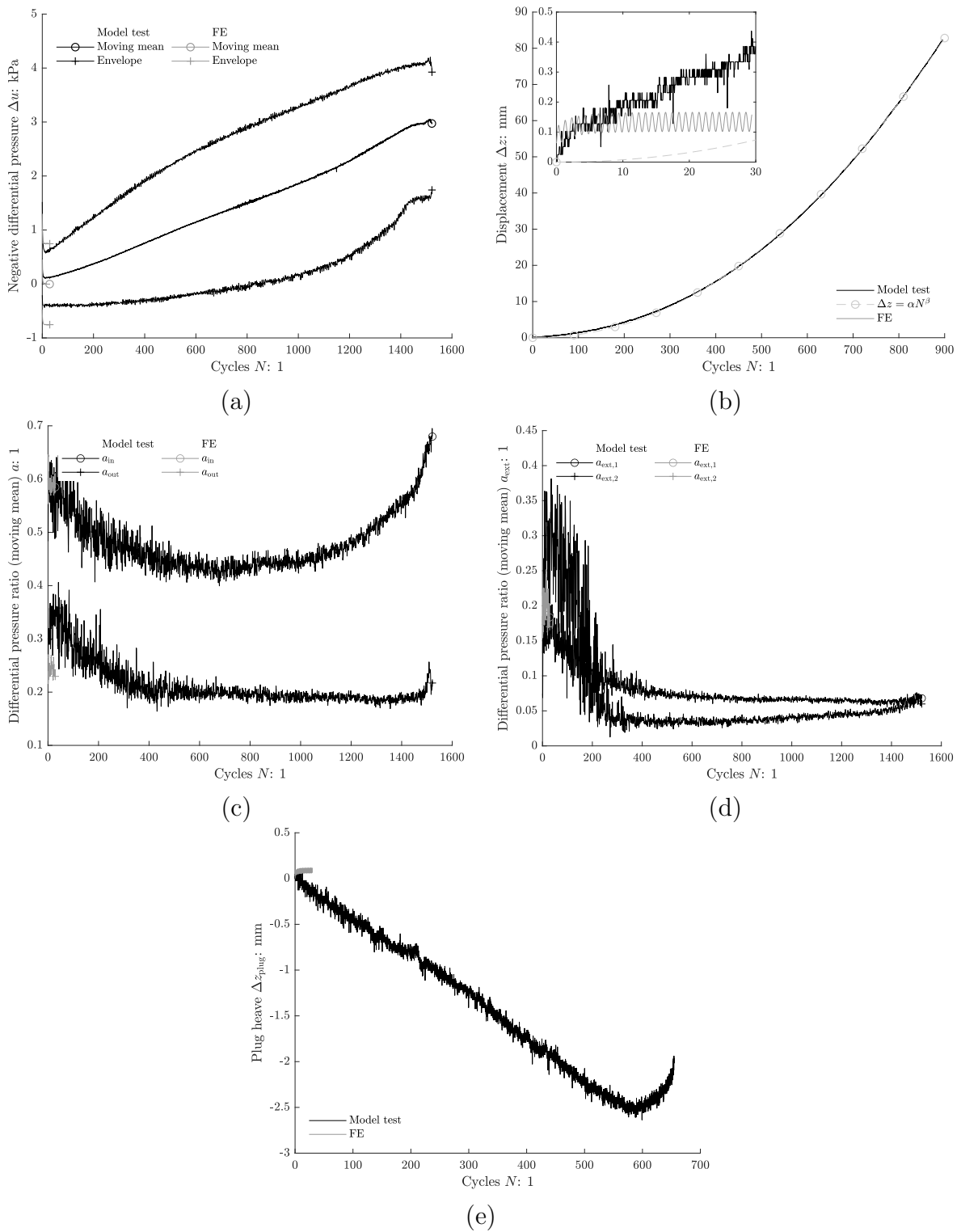*Figure A.4.10.3:* Permeability test: hydraulic conductivity (a) and permeability ratio (b).

Figure A.4.10.4: Tensile test: negative differential pressure (a), displacement (b), differential pressure ratio (skirt) (c), differential pressure ratio (external) (d) and plug heave (e).

A.4.11 F0.51M1.04A0.45

Table A.4.11.1: Test summary

L	500 mm	DPS$_{ext,1}$		DPS$_{ext,2}$	
D	510 mm	r	z	r	z
T_w	18.0°C	510 mm	376.5 mm	462 mm	376.5 mm

Drained resistance			Tensile test		
z	425.1	mm	z	424.8	mm
z/D	0.85		z/D	0.85	
z_{plug}	49.8	mm	z_{plug}	48.8	mm
F_{dr}	0.71	kN	f	0.51	1/s
$\Delta z_{F_{dr}}$	0.77	mm	$\bar{F}_{mean}$	1.04	
			$\bar{F}_{ampl}$	0.45	
			Regression ($\Delta z = \alpha N^\beta$)		
			α	0.0255	mm/1$^\beta$
			β	1.3506	1

Table A.4.11.2: FE model parameters

γ'	κ	λ	ν	ϕ'	ψ	k_i	k_i/k_o	k_0
10.41 kN/m^3	350	0.4	0.2	45°	20°	3.9×10^{-4} m/s	1.6	0.513

Comments:
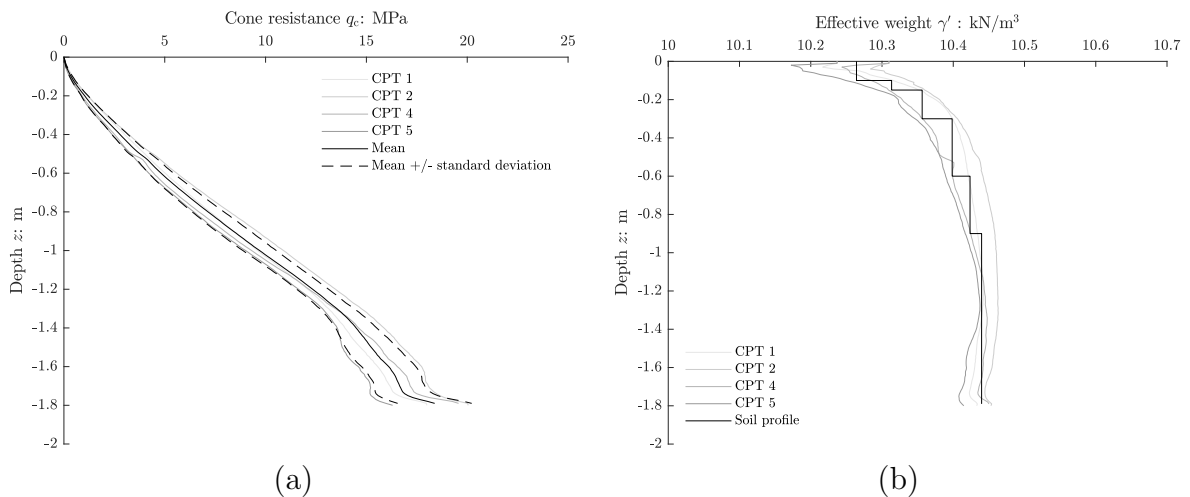No permeability test conducted.

Figure A.4.11.1: Cone penetration test: cone resistance (a) and effective weight (b).
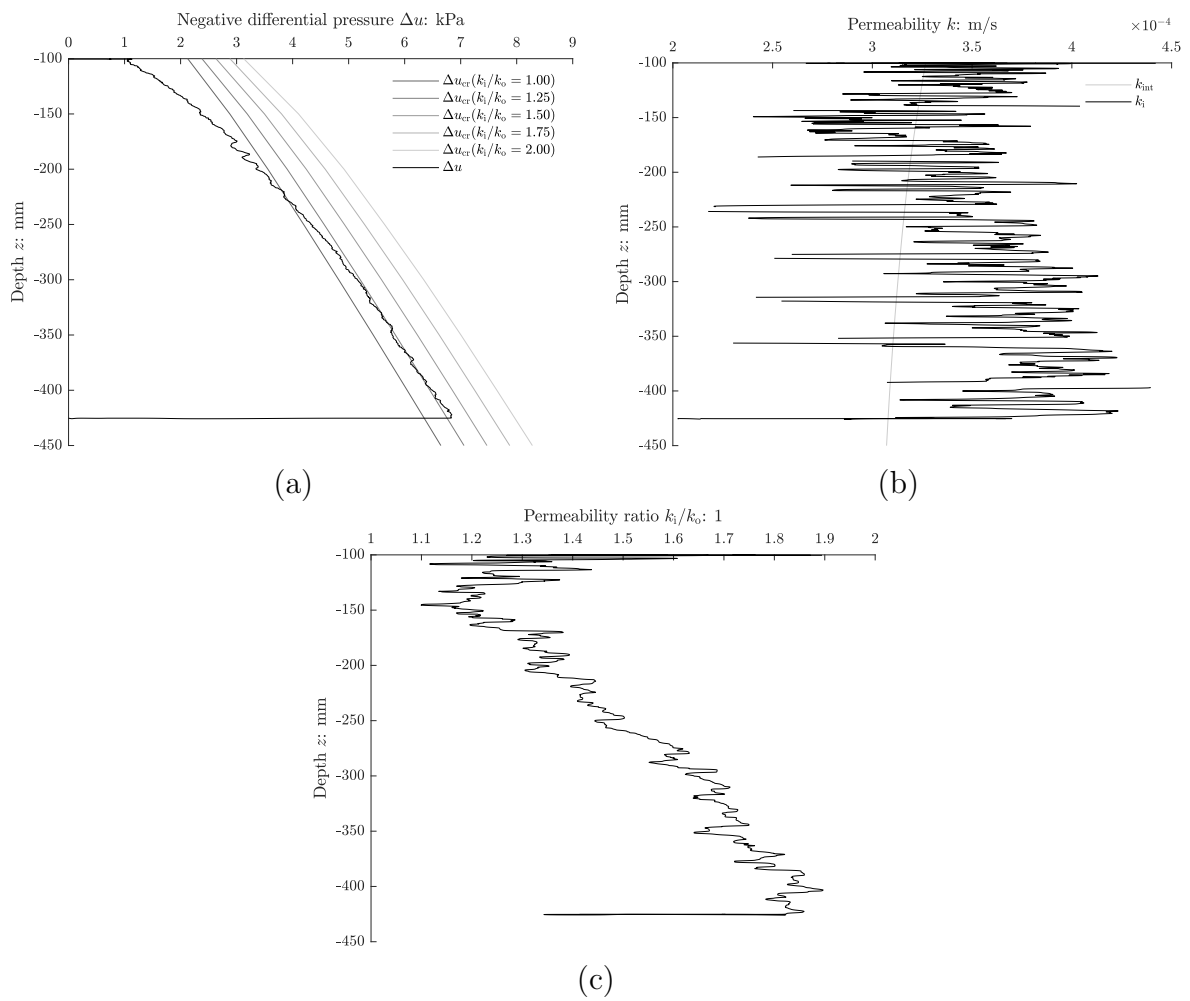
(a)

(b)

(c)

Figure A.4.11.2: Installation: negative differential pressure (a), hydraulic conductivity (b) and permeability ratio (c).

No record
(a)

No record
(b)

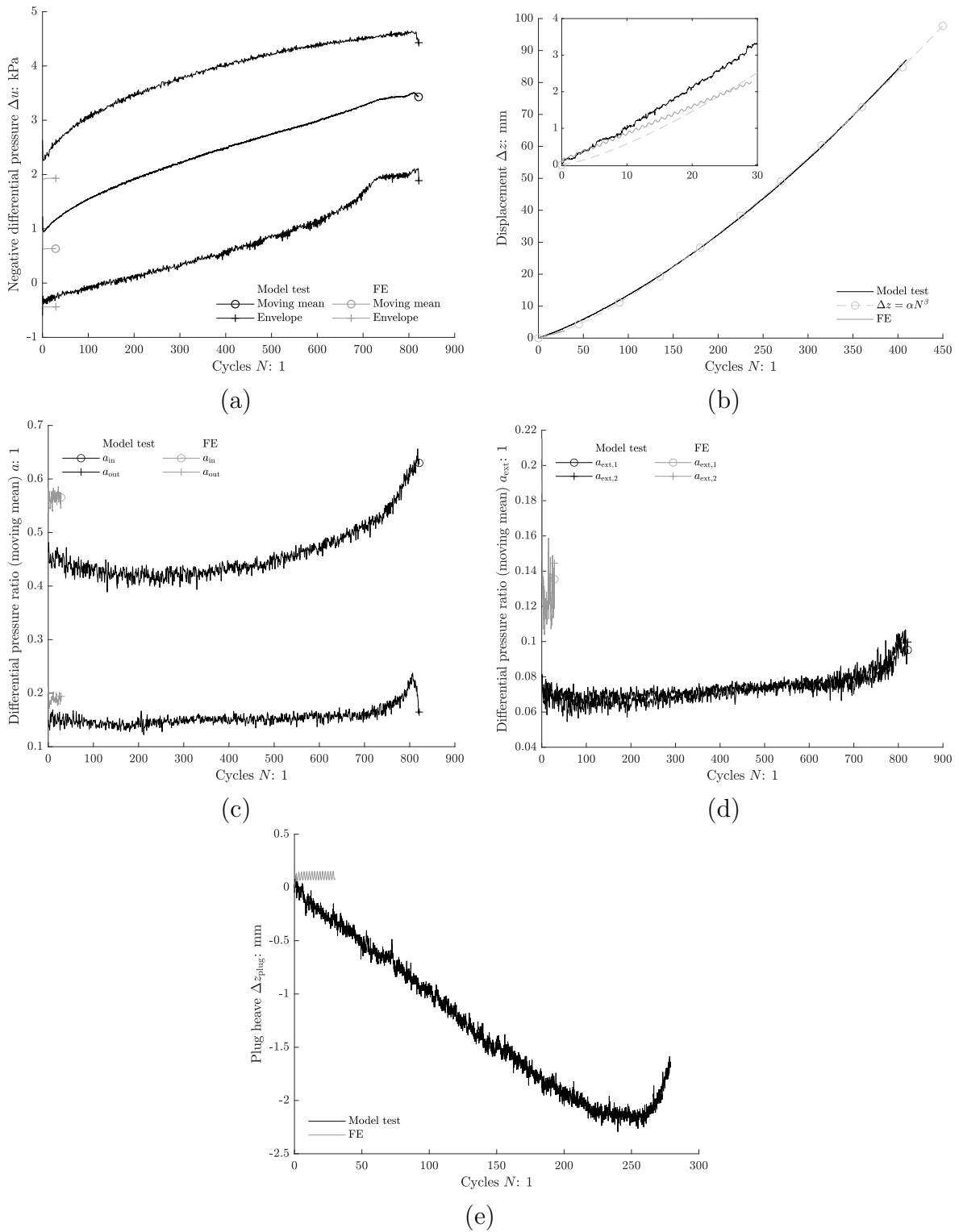*Figure A.4.11.3:* Permeability test: hydraulic conductivity (a) and permeability ratio (b).

Figure A.4.11.4: Tensile test: negative differential pressure (a), displacement (b), differential pressure ratio (skirt) (c), differential pressure ratio (external) (d) and plug heave (e).

A.4.12 F0.51M1.52A0.65

Table A.4.12.1: Test summary

L	500 mm	DPS$_{\text{ext,1}}$		DPS$_{\text{ext,2}}$	
D	510 mm	r	z	r	z
T_{w}	17.9°C	510 mm	526.0 mm	510 mm	526.0 mm

Drained resistance			Tensile test		
z	425.2	mm	z	424.3	mm
z/D	0.85		z/D	0.85	
z_{plug}	48.7	mm	z_{plug}	48.4	mm
F_{dr}	0.61	kN	f	0.51	1/s
$\Delta z_{F_{\text{dr}}}$	0.75	mm	$\bar{F}_{\text{mean}}$	1.52	
			$\bar{F}_{\text{ampl}}$	0.65	
			Regression ($\Delta z = \alpha N^\beta$)		
			α	0.1379	mm/1$^\beta$
			β	1.1722	1

Table A.4.12.2: FE model parameters

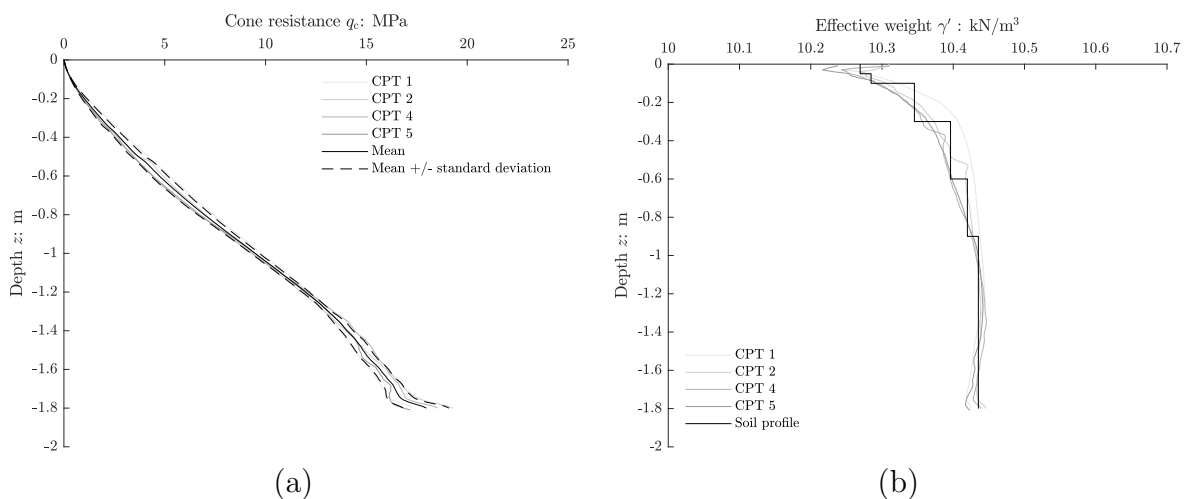| γ'	κ	λ	ν	ϕ'	ψ	k_{i}	$k_{\text{i}}/k_{\text{o}}$	k_0
10.41 kN/m^3	350	0.4	0.2	45°	20°	3.7×10^{-4} m/s	1.6	0.431

Comments:

-

Figure A.4.12.1: Cone penetration test: cone resistance (a) and effective weight (b).
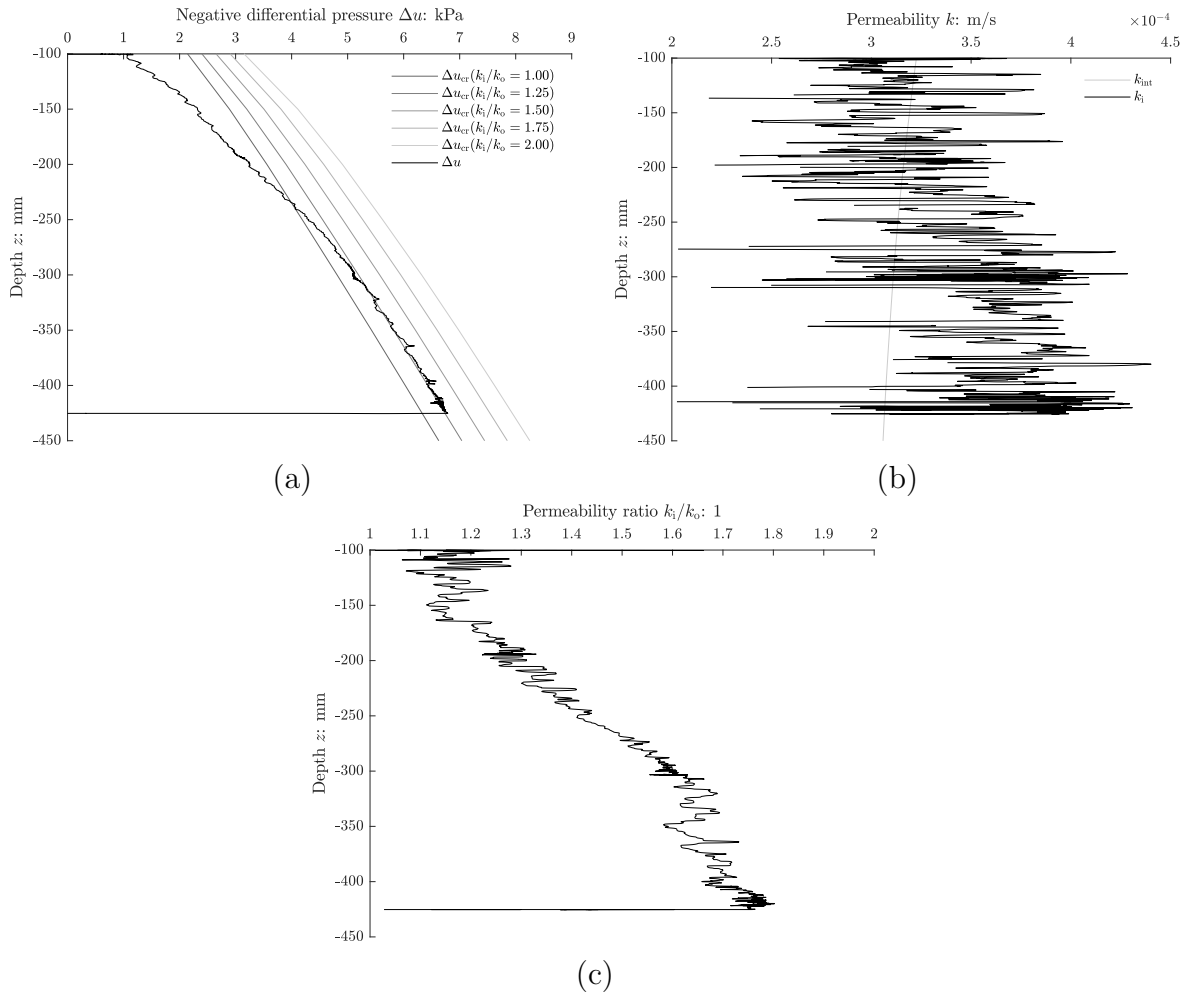
(a)

(b)

(c)

Figure A.4.12.2: Installation: negative differential pressure (a), hydraulic conductivity (b) and permeability ratio (c).
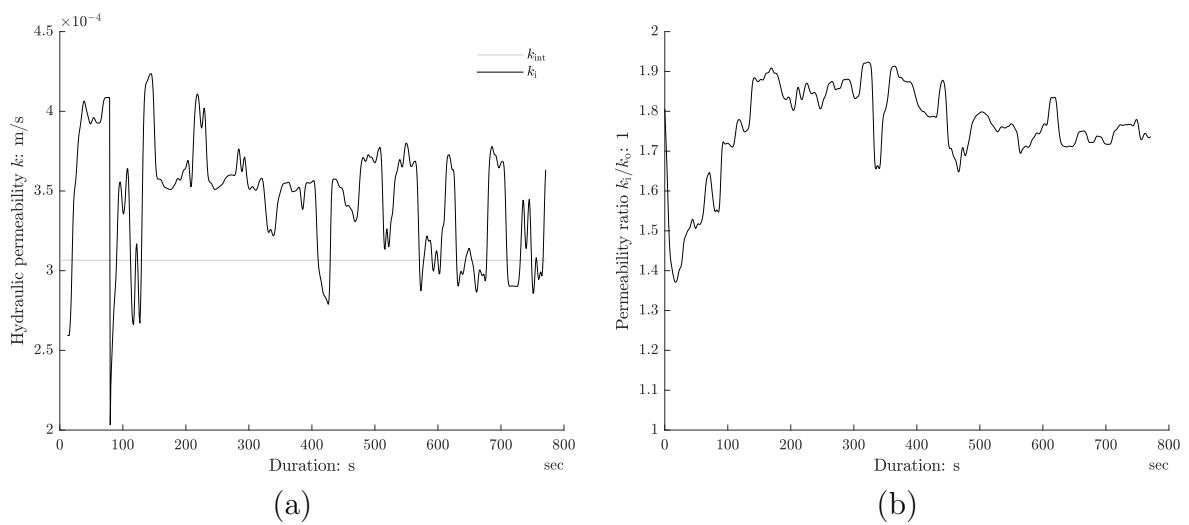

(a)

(b)

Figure A.4.12.3: Permeability test: hydraulic conductivity (a) and permeability ratio (b).
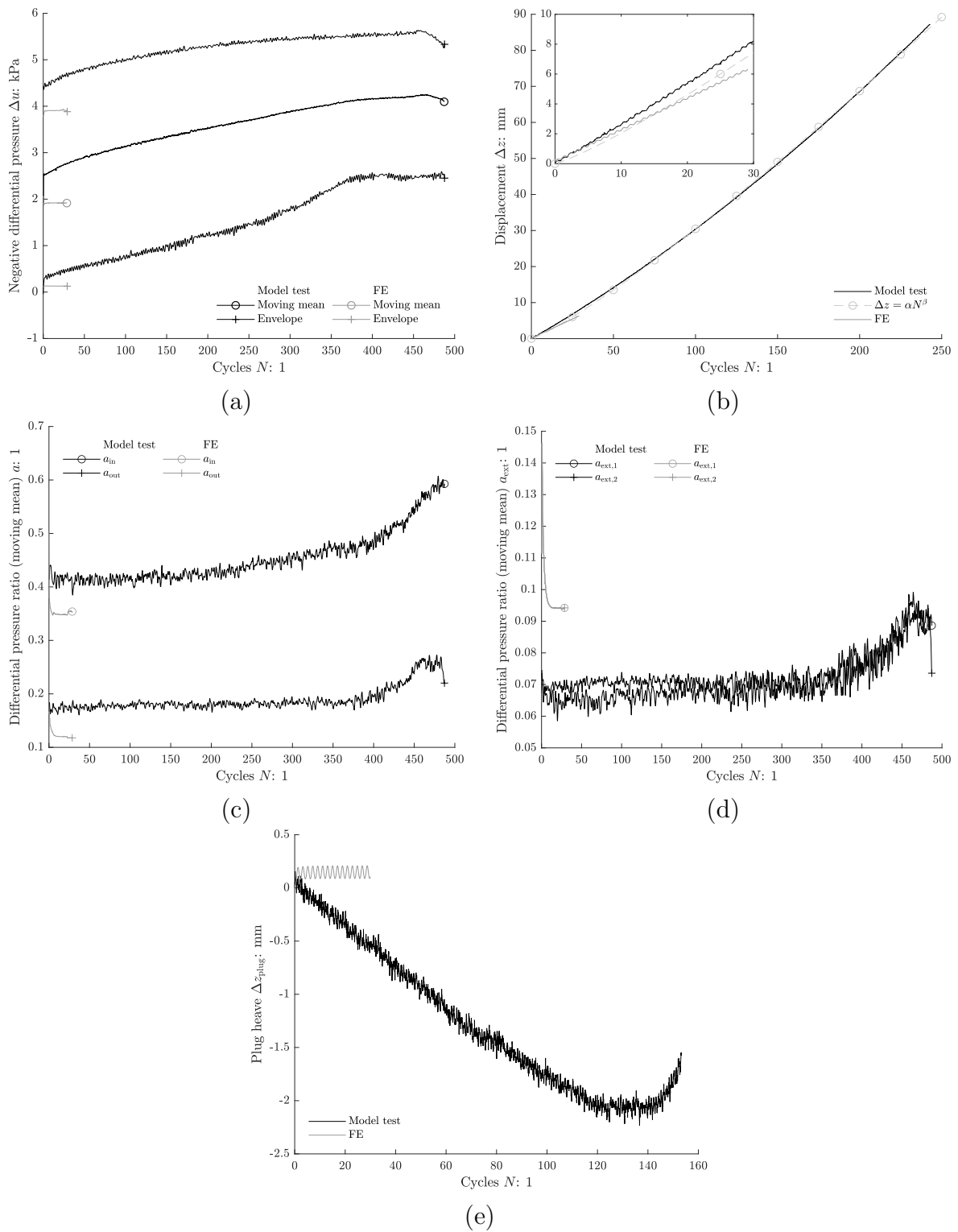
(a)

(b)

(c)

(d)

(e)

Figure A.4.12.4: Tensile test: negative differential pressure (a), displacement (b), differential pressure ratio (skirt) (c), differential pressure ratio (external) (d) and plug heave (e).

A.4.13 F0.51M1.90A0.81

Table A.4.13.1: Test summary

L	$500\,\text{mm}$	DPS$_{\text{ext,1}}$		DPS$_{\text{ext,2}}$	
D	$510\,\text{mm}$	r	z	r	z
T_{w}	$18.0°\text{C}$	$510\,\text{mm}$	$375.0\,\text{mm}$	$510\,\text{mm}$	$526.0\,\text{mm}$

Drained resistance			Tensile test		
z	425.2	mm	z	424.5	mm
z/D	0.85		z/D	0.85	
z_{plug}	47.8	mm	z_{plug}	45.0	mm
F_{dr}	0.71	kN	f	0.51	1/s
$\Delta z_{F_{\text{dr}}}$	0.79	mm	$\bar{F}_{\text{mean}}$	1.90	
			$\bar{F}_{\text{ampl}}$	0.81	
			Regression ($\Delta z = \alpha N^{\beta}$)		
			α	0.2438	mm/1$^{\beta}$
			β	1.2352	1

Table A.4.13.2: FE model parameters

γ'	κ	λ	ν	ϕ'	ψ	k_{i}	$k_{\text{i}}/k_{\text{o}}$	k_0
$10.41\,\text{kN/m}^3$	350	0.4	0.2	45°	20°	$3.7 \times 10^{-4}\,\text{m/s}$	1.6	0.510

Comments:
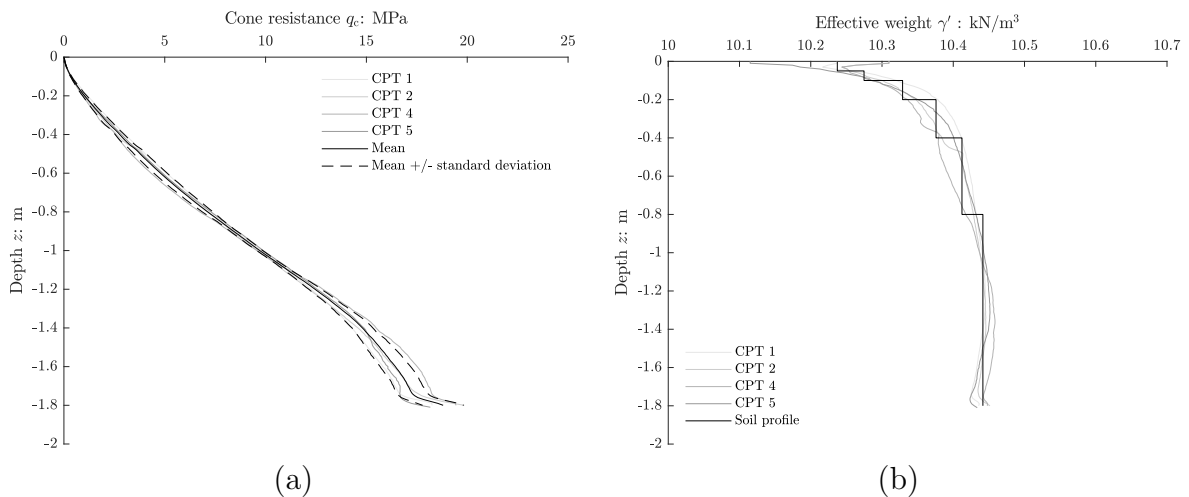No permeability test conducted.

Figure A.4.13.1: Cone penetration test: cone resistance (a) and effective weight (b).
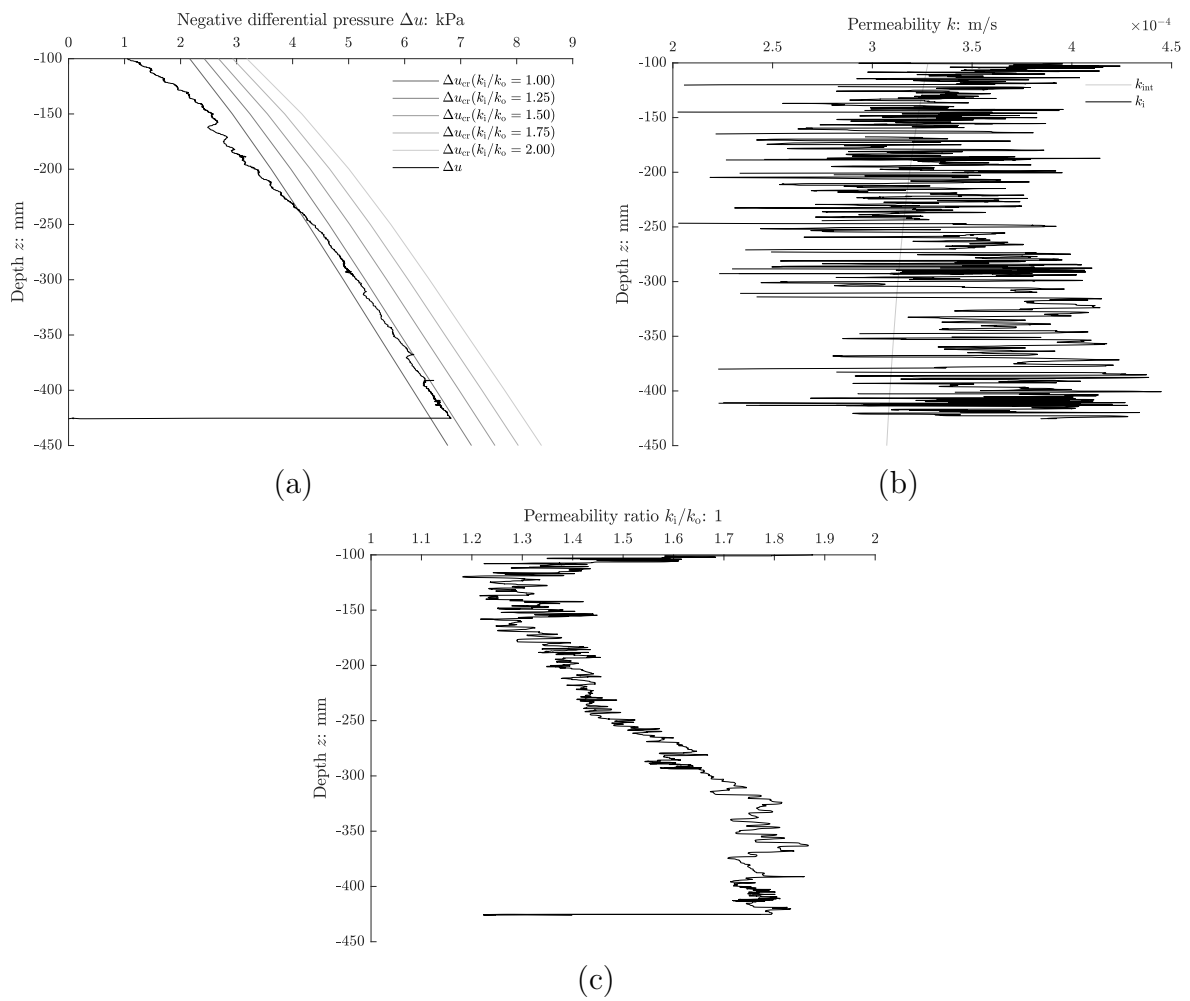
Figure A.4.13.2: Installation: negative differential pressure (a), hydraulic conductivity (b) and permeability ratio (c).

No record
(a)

No record
(b)

Figure A.4.13.3: Permeability test: hydraulic conductivity (a) and permeability ratio (b).
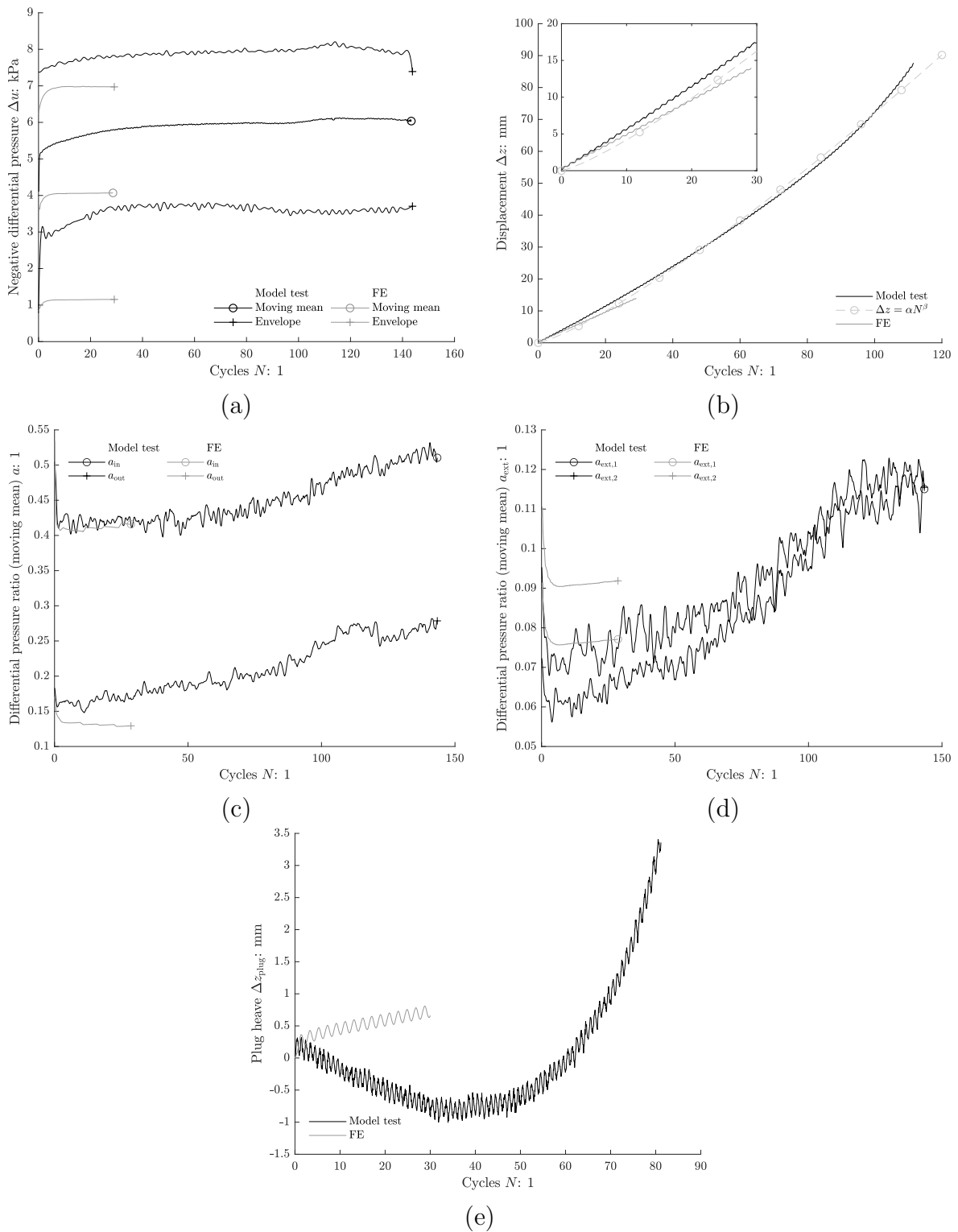
Figure A.4.13.4: Tensile test: negative differential pressure (a), displacement (b), differential pressure ratio (skirt) (c), differential pressure ratio (external) (d) and plug heave (e).

Curriculum vitae

Personal details ————————————————————————————

Patrick Sven Gütz

Born on 29th March 1988 in Berlin, Germany

married, one child

Work experience ————————————————————————————

03/2015 – present **Research Assistant**
Institute for Geotechnical Engineering, Leibniz University Hannover, Hannover

2016 – 2020 **Occasional Freelancer**
ACP Prof. Achmus + CRP Ingenieurgesellschaft für Grundbau mbH

10/2012 – 02/2015 **Construction Manager**
Gottlieb Tesch Kanal- und Rohrleitungsbau GmbH (formerly Trapp Rohrbau GmbH), Stahnsdorf near Berlin

Education ————————————————————————————

10/2008 – 09/2012 **Leibniz University Hannover, Hannover**
Diploma in civil engineering

10/2007 – 09/2008 **Technische Fachhochschule Berlin, Berlin**
(now Beuth University of Applied Sciences Berlin)
Aspired degree: Bachelor of Engineering in Civil Engineering

06/2007 **Romain-Rolland-Gymnasium, Berlin**
General higher education entrance qualification (Abitur)